

UC Berkeley

UC Berkeley Electronic Theses and Dissertations

Title

Cooperative Adsorbents for Carbon Dioxide Separations

Permalink

<https://escholarship.org/uc/item/9zj6h5wv>

Author

Siegelman, Rebecca Leigh

Publication Date

2019

Peer reviewed|Thesis/dissertation

Cooperative Adsorbents for Carbon Dioxide Separations

By

Rebecca L. Siegelman

A dissertation submitted in partial satisfaction of the

requirements for the degree of

Doctor of Philosophy

in

Chemistry

in the

Graduate Division

of the

University of California, Berkeley

Committee in charge:

Professor Jeffrey R. Long, Chair

Professor Omar M. Yaghi

Professor Alexander Katz

Summer 2019

Abstract

Cooperative Adsorbents for Carbon Dioxide Separations

By

Rebecca L. Siegelman

Doctor of Philosophy in Chemistry

University of California, Berkeley

Professor Jeffrey R. Long, Chair

Carbon dioxide separations are likely to play an important role in mitigating greenhouse gas emissions and preventing further increases in global temperature. To perform these separations efficiently at scale, new materials are needed with greater efficiencies in the capture and release of CO₂ from the emissions of fossil fuel-fired power plants and industrial process streams. In recent years, metal–organic frameworks, constructed from inorganic ions or clusters connected by organic bridging units, have shown particular promise in improving the efficiency of CO₂ separations. Specifically, a new class of metal–organic frameworks of the form M₂(dobpdc)(diamine)₂ (M = Mg, Mn, Fe, Co, Zn; dobpdc⁴⁻ = 4,4'-dioxidobiphenyl-3,3'-dicarboxylate) have been found to capture CO₂ through a cooperative mechanism involving the switch-like, reversible polymerization of CO₂ in ammonium carbamate chains along the pore axis.

Chapter 1 introduces the concept of carbon capture and sequestration, beginning with an overview of common adsorbent classes employed for CO₂ capture applications. Opportunities and challenges are subsequently discussed for CO₂ removal from individual potential target streams, including the flue emissions of power plants, industrial process streams, and air. Specific reports are selected to highlight recent advances in overcoming stream-specific challenges, such as stability to common adsorbent poisons. The chapter concludes with a discussion of key needs from the materials research community to accelerate greater adoption of carbon capture technologies.

Chapter 2 describes the development of alkylethylenediamine-appended variants of Mg₂(dobpdc) for carbon capture applications. Small modifications to the diamine structure are shown to shift the threshold pressure for cooperative CO₂ adsorption by over 4 orders of magnitude at a given temperature. The observed trends are rationalized on the basis of crystal structures of the isostructural zinc frameworks obtained by *in situ* single-crystal X-ray diffraction experiments. The structure–activity relationships derived from these results are subsequently shown to enable the optimization of adsorbent design to match the conditions of a given CO₂ separation process, thereby minimizing the energetic cost of CO₂ capture.

Chapter 3 leverages the results of *Chapter 2* in the design of a diamine-appended framework for cooperative CO₂ capture from the flue emissions of natural gas combined cycle power plants. Due to growing adoption of natural gas as a fuel source, the emissions of gas-fired plants are contributing a growing portion of global CO₂ emissions, but CO₂ capture from these power plants is hindered by the low CO₂ concentration and high oxygen and water content of the flue

stream. In this chapter, functionalization of $\text{Mg}_2(\text{dobpdc})$ with the cyclic diamine 2-(aminomethyl)piperidine (2-ampd) is shown to produce an adsorbent that is capable of >90% CO_2 capture from a humid natural gas flue emission stream, as confirmed by breakthrough measurements. Multicomponent adsorption experiments, infrared spectroscopy, magic angle spinning solid-state NMR spectroscopy, and van der Waals-corrected density functional theory studies suggest that water enhances CO_2 capture in 2-ampd- $\text{Mg}_2(\text{dobpdc})$ through hydrogen-bonding interactions with the carbamate groups of the ammonium carbamate chains formed upon CO_2 adsorption, thereby increasing the thermodynamic driving force for CO_2 binding. The exceptional thermal, oxidative, and cycling stability of this material are subsequently demonstrated, indicating that 2-ampd- $\text{Mg}_2(\text{dobpdc})$ is a promising adsorbent for this important separation.

Chapter 4 describes the development of a diamine-appended framework for CO_2 removal from crude natural gas. Due to its low CO_2 emission intensity compared to coal, natural gas is favored as a cleaner-burning fuel. However, for many natural gas reserves, CO_2 contamination must be removed at the wellhead to meet pipeline specifications. In this chapter, the framework ee-2- $\text{Mg}_2(\text{dobpdc})$ (ee-2 = *N,N*-diethylethylenediamine) is demonstrated as a next-generation CO_2 capture material for high-pressure natural gas purification. This material can be readily regenerated with a minimal change in temperature or pressure and maintains its CO_2 capacity in the presence of water. Moreover, consistent with the results in *Chapter 3*, breakthrough experiments reveal that water enhances the CO_2 capture performance of ee-2- $\text{Mg}_2(\text{dobpdc})$ by reducing or eliminating “slip” of CO_2 prior to full breakthrough. As in *Chapter 3*, spectroscopic characterization and multicomponent isobars suggest that the enhanced performance under humid conditions arises from preferential stabilization of the CO_2 -inserted phase in the presence of water. The favorable performance of ee-2- $\text{Mg}_2(\text{dobpdc})$ is further demonstrated through comparison with a benchmark material for this separation, zeolite 13X, as well as through extended pressure cycling experiments.

Finally, *Chapter 5* builds upon the previous chapters in this work to advance a diamine-appended framework toward commercialization in upgrading crude biogas to biomethane, a renewable natural gas equivalent. Using the principles outlined in previous chapters, the material dmpn- $\text{Mg}_2(\text{dobpdc})$ (dmpn = 2,2-dimethyl-1,3-diaminopropane) is identified as a promising candidate for this separation, and its performance in capturing CO_2 from CO_2/CH_4 mixtures is first demonstrated at the laboratory scale. Through a collaboration with Mosaic Materials, a start-up company working to commercialize cooperative adsorbents for CO_2 separations, the performance of dmpn- $\text{Mg}_2(\text{dobpdc})$ is then demonstrated in breakthrough experiments with composite pellets at the 30–50 g scale. Importantly, these experiments enable simultaneous monitoring of heat and mass transfer in the adsorbent bed, resulting in data suitable to inform the development of a process model. Finally, in partnership with the Davis Wastewater Treatment Plant, slipstream tests are conducted with a crude biogas stream containing water, oxygen, H_2S , and siloxanes. These early results suggest that dmpn- $\text{Mg}_2(\text{dobpdc})$ is relatively robust to H_2S and can withstand short-term exposure to crude biogas feeds, representative of a process failure in upstream pretreatment units. These results represent a promising step toward the commercialization of cooperative adsorbents for CO_2 separations.

Table of Contents

List of Figures	v
List of Tables	vii
Acknowledgements	viii
Chapter 1. Porous Materials for Carbon Dioxide Separations to Mitigate Greenhouse Gas Emissions	1
1.1. Introduction	1
1.2. Overview of Adsorbent Classes	3
1.2.1. Activated Carbons	3
1.2.2. Zeolites	4
1.2.3. Amine-Functionalized Silicas	4
1.2.4. Porous Organic Networks	5
1.2.5. Metal–Organic Frameworks	5
1.3. Target Separations and Case Studies	6
1.3.1 The Power Sector	7
1.3.2 Biogas and Crude Natural Gas	9
1.3.3 Other Industrial CO ₂ Streams	10
1.3.4 Direct CO ₂ Capture from Air	11
1.4. Outlook and Key Needs from the Materials Community	12
1.5. Acknowledgements	13
1.6. References	13
Chapter 2. Controlling Cooperative CO₂ Adsorption in Diamine-Appended Mg₂(dobpdc) Metal–Organic Frameworks	23
2.1. Introduction	23
2.2. Experimental Procedures	25
2.2.1. General Synthesis and Characterization Methods	25
2.2.2. Synthesis of Mg ₂ (dobpdc)	25
2.2.3. Synthesis of Diamine-Appended Mg ₂ (dobpdc) Frameworks	25
2.2.4. Synthesis of Zn ₂ (dobpdc) Single Crystals	26
2.2.5. Synthesis of Diamine-Appended Zn ₂ (dobpdc) Single Crystals	26
2.2.6. Gas Dosing of Diamine-Appended Zn ₂ (dobpdc) Single Crystals	26
2.2.7. Single-Crystal X-ray Diffraction	27
2.2.8. Thermogravimetric Analysis	27
2.2.9. High-Throughput Gas Adsorption Isotherm Measurements	28
2.2.10. Calculation of Differential Enthalpies and Entropies of Adsorption	28
2.3. Results and Discussion	28
2.3.1. Selection of Diamines and Synthesis of Adsorbents	28
2.3.2. Structural Characterization of Diamine Binding in M ₂ (dobpdc)(diamine) ₂	30
2.3.3. Isobaric Characterization of CO ₂ Adsorption	31
2.3.4. X-ray Single-Crystal Structures of CO ₂ -Inserted Diamine-Appended Frameworks	33
2.3.5. Process Considerations Derived from High-Throughput CO ₂ Adsorption Isotherms	36
2.3.6. Thermodynamics of CO ₂ Adsorption	39

2.4.	Conclusions	41
2.5.	Acknowledgements	42
2.6.	Supporting Information	43
2.6.1	Additional Experimental Details	43
2.6.2	Equivalent Energy Calculation Details	45
2.6.3	Langmuir Surface Areas	47
2.6.4	Powder X-ray Diffraction	47
2.6.5	Infrared Spectra	49
2.6.6	<i>In Situ</i> Infrared Spectra	50
2.6.7	NMR Digestion	51
2.6.8	Thermogravimetric Decomposition	52
2.6.9	CO ₂ Adsorption and Desorption Isobars	54
2.6.10	High-Throughput N ₂ Isotherms	57
2.6.11	High-Throughput H ₂ O Isotherms	58
2.6.12	Equivalent Energy Results	59
2.6.13	Supplementary Structure Figures and Crystallographic Data	61
2.7	References	68
Chapter 3. Water Enables Efficient CO₂ Capture from Natural Gas Flue Emissions in an Oxidation-Resistant Diamine-Appended Metal–Organic Framework		73
3.1.	Introduction	73
3.2.	Experimental Procedures	74
3.2.1.	General Synthesis and Characterization Methods	74
3.2.2.	Infrared Spectra	75
3.2.3.	Diamine Grafting Procedure	76
3.2.4.	Thermogravimetric Analysis and Cycling Measurements	76
3.2.5.	Gas Adsorption Measurements	76
3.2.6.	Calculation of Differential Enthalpies and Entropies of Adsorption	77
3.2.7.	Breakthrough Measurements	77
3.2.8.	Solid-State Magic Angle Spinning (MAS) NMR Experiments	77
3.2.9.	Single-Crystal X-ray Diffraction	78
3.2.10.	Density Functional Theory Calculations	78
3.3.	Results and Discussion	78
3.3.1	Adsorbent Design for NGCC Post-Combustion Capture	78
3.3.2	Single-Component Adsorption Experiments	80
3.3.3	Mixed-Gas Adsorption Experiments	81
3.3.4	Fixed-Bed Adsorption Experiments	84
3.3.5	Influence of Water on CO ₂ Adsorption	86
3.3.6	Thermal, Oxidative, and Cycling Stability	91
3.4.	Conclusions	93
3.5.	Acknowledgements	93
3.6.	Supporting Information	94
3.6.1	Preparation of M ₂ (dobpdc) (M = Mg, Mn, Co, Ni, Zn) and Mg ₂ (dotpdc)	94
3.6.2	Characterization of 2-ampd–Mg ₂ (dobpdc)	98
3.6.3	Calculation of the Approximate Regeneration Energy of 2-ampd–Mg ₂ (dobpdc)	107
3.6.4	Synthesis and Characterization of 2-ampd–Mg ₂ (dotpdc)	110

3.6.5	Variants of Mg ₂ (dobpdc) Appended with Acyclic <i>Primary,Secondary</i> 1,3-Diaminopropanes	112
3.6.6	Variants of Mg ₂ (dobpdc) Appended with Additional Cyclic <i>Primary,Secondary</i> Diamines	114
3.6.7	Relationship Between Isobaric and Isothermal Measurements	121
3.6.8	Effect of Humidity on CO ₂ Adsorption in 2-ampd–Mg ₂ (dobpdc) in Isobaric Measurements	123
3.6.9	Ramp Rate Effects on Adsorption Isobars	135
3.6.10	Predicting Breakthrough Curves from Step-Shaped Adsorption Isotherms	138
3.6.11	Breakthrough Experiments with 2-ampd–Mg ₂ (dobpdc)	142
3.6.12	Synthesis of 2-ampd–Zn ₂ (dobpdc) Single Crystals	148
3.6.13	Synthesis and Characterization of Molecular 2-ampd–CO ₂ Single Crystals	149
3.6.14	Single-Crystal X-ray Diffraction	150
3.6.15	Synchrotron Powder X-ray Diffraction	153
3.6.16	Accelerated Decomposition of Diamine-Appended Variants of Mg ₂ (dobpdc)	155
3.6.17	Comparison of 2-ampd–Mg ₂ (dobpdc) and MCM-41-PEI-50	162
3.6.18	Adsorption/Desorption Cycling of 2-ampd–Mg ₂ (dobpdc)	167
3.6.19	Synthesis and Characterization of 2-ampd–M ₂ (dobpdc) (M = Mn, Co, Ni, Zn)	169
3.6.20	Additional Solid-State Magic Angle Spinning (MAS) NMR Spectra and Details	173
3.6.21	Additional DFT Figures and Details	176
3.7.	References	181
Chapter 4. A Cooperative Adsorbent for Switch-Like CO₂ Capture from Crude Natural Gas		191
4.1.	Introduction	191
4.2.	Experimental Procedures	193
4.2.1.	General Materials and Methods	193
4.2.2.	Gram-Scale Synthesis of Diamine-Appended M ₂ (dobpdc)	193
4.2.3.	Volumetric Gas Adsorption Experiments	194
4.2.4.	Thermogravimetric Analysis	195
4.2.5.	Breakthrough Experiments and Pressure Cycling	196
4.2.6.	Infrared Spectra	196
4.3.	Results and Discussion	197
4.3.1.	Material Design Considerations	197
4.3.2.	Pressure-Swing Adsorption with a Cooperative Adsorption Threshold at Atmospheric Pressure	198
4.3.3.	Evaluation of ee-2–Mg ₂ (dobpdc) for Natural Gas Purification	200
4.3.4.	Performance Under Humid Conditions	203
4.3.5.	Mechanism of CO ₂ Adsorption and Proposed Role of Water	204
4.3.6.	Mechanical Pressure Cycling	207
4.4.	Conclusions	207
4.5.	Acknowledgements	208
4.6.	Supporting Information	210
4.6.1.	Characterization of Mg ₂ (dobpdc)	210

4.6.2.	Additional Characterization of ii-2-Mg ₂ (dobpdc)	211
4.6.3.	Additional Characterization of ee-2-Mg ₂ (dobpdc)	214
4.6.4.	Isotherm Backgrounds and Fits	217
4.6.5.	Additional Isotherms, Fits, and Thermodynamic Data for ii-2-Mg ₂ (dobpdc)	218
4.6.6.	Additional Isotherms, Fits, and Thermodynamic Data for ee-2-Mg ₂ (dobpdc)	223
4.6.7.	Adsorption Isotherms, Fits, and Thermodynamic Data for Zeolite 13X	231
4.6.8.	Heat Capacity Measurements with Dynamic Scanning Calorimetry	235
4.6.9.	Kinetics Experiments with Dynamic Scanning Calorimetry	236
4.6.10.	<i>In Situ</i> Infrared Spectra for ee-2-Mg ₂ (dobpdc)	238
4.6.11.	Effect of Humidity on CO ₂ Adsorption in ee-2-Mg ₂ (dobpdc)	238
4.6.12.	Predicting Breakthrough Curves from Step-Shaped Adsorption Isotherms	244
4.6.13.	Additional Experimental Details for Breakthrough Measurements	246
4.6.14.	Additional Breakthrough Experiments with ii-2-Mg ₂ (dobpdc)	249
4.6.15.	Additional Breakthrough Experiments with ee-2-Mg ₂ (dobpdc)	252
4.6.16.	Characterization of ee-2-Mg ₂ (dobpdc) Following Extended Pressure Cycling	255
4.6.17.	Synchrotron Powder X-ray Diffraction	258
4.6.18.	Single-Crystal X-ray Diffraction	260
4.7.	Notes and References	263
Chapter 5. A Cooperative Adsorbent for Biogas Upgrading		269
5.1.	Introduction	269
5.2.	Experimental Procedures	270
5.3.	Results and Discussion	270
5.4.	Conclusions	277
5.5.	Acknowledgements	277
5.6.	Supporting Information	278
5.6.1.	Additional Adsorption Data, Fits, and Thermodynamic Calculations	278
5.6.2.	Additional Breakthrough Details and Results	281
5.6.3.	Additional Characterization Following Exposure Tests	284
5.7.	References	286

List of Figures

Figure 1.1.	Global energy consumption by fuel, and CO ₂ emissions by sector and fuel	2
Figure 1.2.	Illustrative examples of the structures of CO ₂ capture adsorbents	6
Figure 1.3.	Minimum work for CO ₂ capture as a function of CO ₂ concentration	11
Figure 2.1.	Structure of Mg ₂ (dobpdc), and depiction of diamine functionalization and cooperative CO ₂ insertion	24
Figure 2.2.	Structures of Zn ₂ (dobpdc) and alkylethylenediamine-appended variants	30
Figure 2.3.	Adsorption isobars under pure CO ₂ for alkylethylenediamine-appended Mg ₂ (dobpdc)	32
Figure 2.4.	Structures of Zn ₂ (dobpdc)(m-2-m-CO ₂) _{1.5} , Zn ₂ (dobpdc)(e-2-e)(e-2-e-CO ₂), Zn ₂ (dobpdc)(i-2)(i-2-CO ₂), and Zn ₂ (dobpdc)(e-2-CO ₂) _{1.5}	33
Figure 2.5.	Structures of two conformations of Zn ₂ (dobpdc)(m-2-CO ₂) _{1.62}	36
Figure 2.6.	High-throughput CO ₂ adsorption isotherms for m-2-, e-2-, i-2-, mm-2-, ee-2-, and ii-2-Mg ₂ (dobpdc)	37
Figure 2.7.	High-throughput CO ₂ adsorption isotherms for m-2-m- and e-2-e-Mg ₂ (dobpdc)	38
Figure 2.8.	Differential enthalpy vs. differential entropy of CO ₂ adsorption for alkylethylenediamine-appended Mg ₂ (dobpdc)	41
Figure 3.1.	Structure of 2-ampd-Zn ₂ (dobpdc)	75
Figure 3.2.	Pure CO ₂ adsorption isotherms for 2-ampd-Mg ₂ (dobpdc)	79
Figure 3.3.	Dry and humid isobars at atmospheric pressure for 2-ampd-Mg ₂ (dobpdc) under pure CO ₂ , 4% CO ₂ in N ₂ , 0.4% CO ₂ in N ₂ , and pure N ₂	82
Figure 3.4.	Breakthrough experiments with 2-ampd-Mg ₂ (dobpdc) under dry and humid simulated NGCC flue emission streams	85
Figure 3.5.	Infrared spectra of 2-ampd-Mg ₂ (dobpdc) under dry N ₂ and dry and humid CO ₂	87
Figure 3.6.	Solid-state NMR spectra of 2-ampd-Mg ₂ (dobpdc) dosed with dry and humid CO ₂	88
Figure 3.7.	DFT-calculated structures and binding energies for CO ₂ insertion, H ₂ O adsorption, and co-adsorption of CO ₂ and H ₂ O in <i>L</i> -2-ampd- <i>R</i> -Mg ₂ (dobpdc)	89
Figure 3.8.	Dry CO ₂ isobars of 2-ampd-Mg ₂ (dobpdc) following exposure to air and humid CO ₂ at elevated temperatures	91

Figure 3.9.	Extended simulated temperature-swing cycling data for 2-ampd-Mg ₂ (dobpdc) with simulated NGCC flue gas	92
Figure 4.1.	Structure of diamine-functionalized Mg ₂ (dobpdc), schematic of cooperative CO ₂ insertion, and idealized isotherm illustrating pressure-swing adsorption	192
Figure 4.2.	Schematic of a “shock–wave–shock” breakthrough profile anticipated for an adsorbent with a step-shaped isotherm	197
Figure 4.3.	High-pressure CO ₂ and CH ₄ adsorption isotherms for ii-2-Mg ₂ (dobpdc)	199
Figure 4.4.	Breakthrough profile for ii-2-Mg ₂ (dobpdc) under 300 sccm of dry 10% CO ₂ in CH ₄ at 70 bar and 30 °C	200
Figure 4.5.	Low- and high-pressure CO ₂ and high-pressure CH ₄ adsorption isotherms for ee-2-Mg ₂ (dobpdc)	201
Figure 4.6.	Breakthrough and corresponding temperature profile for ee-2-Mg ₂ (dobpdc) under 300 sccm of dry 10% CO ₂ in CH ₄ at 70 bar and 30 °C	202
Figure 4.7.	Dry and humid qualitative breakthrough curves for ee-2-Mg ₂ (dobpdc) and zeolite 13X	204
Figure 4.8.	Structure of ee-2-Zn ₂ (dobpdc) before and after CO ₂ insertion to form ammonium carbamate chains	205
Figure 4.9.	Dry and humid CO ₂ adsorption and desorption isobars for ee-2-Mg ₂ (dobpdc)	206
Figure 4.10.	Schematic showing generation of a single-shock breakthrough profile for an adsorbent with a step-shaped isotherm	207
Figure 5.1.	Schematic showing a PSA process for hypothetical adsorbents with Langmuir vs. step-shaped isotherms, and the structure of dmpn-Zn ₂ (dobpdc) and proposed CO ₂ adsorption mechanism for dmpn-Mg ₂ (dobpdc)	271
Figure 5.2.	High-pressure CO ₂ and CH ₄ adsorption isotherms for dmpn-Mg ₂ (dobpdc)	272
Figure 5.3.	Temperature-swing cycling of dmpn-Mg ₂ (dobpdc) at atmospheric pressure with adsorption under 10% CO ₂ in N ₂ at 40 °C and desorption under pure CO ₂ at 100 °C	273
Figure 5.4.	Small-scale breakthrough experiment with binderless pellets of dmpn-Mg ₂ (dobpdc) under 3 sccm of dry 50% CO ₂ in CH ₄ at ~1 bar and 40 °C	274
Figure 5.5.	Large-scale breakthrough experiment and corresponding temperature profile with composite pellets of dmpn-Mg ₂ (dobpdc) under 75 sccm of dry 36.5% CO ₂ in CH ₄ at ~1 bar and 22 °C	275
Figure 5.6.	Pure CO ₂ adsorption isobars for composite pellets of dmpn-Mg ₂ (dobpdc) after varying exposure times to a crude biogas stream	276

List of Tables

Table 1.1.	Representative CO ₂ concentrations in process streams	7
Table 2.1.	Alkylethylenediamine structures and nomenclature system	29
Table 4.1.	Target total stream pressure, CO ₂ partial pressure, and CO ₂ adsorption step pressure for natural gas purification	198

Acknowledgements

I am incredibly grateful for the support of my research group, collaborators, friends, and family in the creation of this work. I would first like to acknowledge my advisor, Jeff Long, whose patience, trust, high standards, and attention to detail have guided my development as a researcher, writer, and presenter. I'm thankful for the many opportunities he has given me and for the incredible group of people he has gathered in his laboratory. Jeff's leadership has created an exceptionally collaborative and supportive group atmosphere, and I am lucky to work with so many scientists and engineers who have invested so deeply in both their research and each other. I would also like to thank Jen for her enthusiasm and encouraging words during many group holiday parties and barbecues.

I am grateful to the many other mentors and teachers I have had at Berkeley, Columbia, Dow, and Walton. In particular, I would like to thank Professor Jonathan Owen, who welcomed me into his research laboratory at Columbia early in my undergraduate career. Despite his many obligations as an early career professor, Jon always made time to discuss research, and his passion for chemistry and careful approach have always inspired me. The members of the Owen group were equally dedicated and supportive, and I learned a great deal from each of them. I would also like to thank Professor Ken Raymond, who shared his knowledge of crystallography with me during my two semesters as his Graduate Student Instructor. Additionally, I would like to thank my dissertation and qualifying exam committee members. Professor Omar Yaghi helped to inspire my appreciation for the structures of framework materials, and Professors Alex Katz and Angy Stacy raised many thoughtful discussion points about my research.

I would like to thank my family for their constant love and encouragement. My parents, Barbara and David, have been incredibly supportive in all of my endeavors. I'm grateful for the example they have always set and for their dedication to picking up MOF-related jargon. My brother Philip, grandparents, aunts, and uncles have also been a source of comfort throughout, and I am grateful for every phone call, email, and text. You are all so important to me.

I would like to offer my thanks to many others below who have supported this work. Although the sentiments here are brief, my gratitude is immense:

To Miguel Gonzalez, a mentor, inspiration, and lifelong friend deserving of a thesis-sized acknowledgement section of his own. Thank you, Miguel!

To Phill Milner and Jeff Martell, co-captains of our CO₂ crew, who have shaped the way I view science and made the lab a fantastically collaborative place. And to the rest of team CO₂—Alex Forse, Jung-Hoon Lee, Eugene Kim, Surya Parker, Ziting Zhu, Bhavish Dinakar, Victor Mao, and Steph Didas—for countless invigorating discussions and the kind of “cowboy style” experiments that involve occasional use of duct tape. Alex Forse and Professor Jeff Reimer performed the solid-state NMR spectroscopy in this work, while Jung-Hoon Lee and Professor Jeff Neaton completed the DFT studies.

To Tom McDonald, who discovered and introduced me to the class of materials discussed in this work, and who has remained an excellent advisor and friend throughout. To Jarad Mason, a role model who selflessly gave his time to train me and whose legacy reminds me to dig deeper.

To our crystallography “beam team” of Miguel Gonzalez, Naomi Biggins, Ari Turkiewicz, Job Chakarawet, Alex Vincent, and Eugene Kim for all of the overnight X-ray adventures.

To Kristen Colwell, my year-mate and fast friend; Mercedes Taylor, my fellow literati; Lucy Darago, my voice of reason; and Julia Oktawiec, my Columbia compatriot, for so much joy. To Mike Ziebel, who has shared late-night laughs while shouldering so many safety and group organizational responsibilities. To David Jaramillo, for many energy-related discussions; Henry

Jiang, co-proprietor of Tiny Tools; Colin Gould, a chemistry sandwich artist; Ryan Murphy, a wellspring of ideas and physics knowledge; Rodi Torres-Gavosto, another companion for late-night laughs; and Ever Velasquez, co-member of the Wildcat rescue squad. To my other fellow graduate students, who deserve more thanks than I can fit here: Katie Engler, Kaipeng Hou, Daniel Lussier, Maria Paley, Jesse Park, and Adam Uliana.

To many other senior graduate students who led the way when I joined the group: Mike Aubrey, Jordan Axelson, Jon Bachman, Phil Bunting, Xiaowen Feng, Matt Kapelewski, Dana Levine, Katie Meihaus (now also our group editor), Doug Reed, Brian Wiers, Dianne Xiao, and David Zee; as well as several skilled undergraduates: David Gygi, Jo Melville, and Raymond Yu. Each of you shared many lessons and laughs, and I hope I have thanked you properly in person.

To the other postdoctoral scientists and visiting scholars, professors, and students from across the globe who have shared Lewis and Hildebrand Halls with me: Brandon Barnett, Dominik Halter, Megan Jackson, Adam Jaffe, Jovan Kamcev, Mike McGuirk, Dong-Myeong Shin, Ben Snyder, Yusuke Mukae, Yuto Yabuuchi, Gokan Barin, Aravind Chandiran, Selly Demir, Keith Keitz, Jiwoong Lee, Hye Jeong Park, Tomce Runcevski, Farshid Ramezanipour, Zach Smith, Günther Thiele, Yang Yang, Guillem Aromi, Leoni Barrios, Jason Chen, Sid Das, Lucie Norel, Durga Parajuli, Manabu Tanaka, Jenny Vitillo, Christina Legendre, and Lingchang Jiang. I hope our paths cross again and look forward to following your research for many years to come.

To Kenna Eames, Kristin Stangl, and Shela Deguzman, who have helped keep the laboratory running smoothly, and to Hiro Furukawa, who has been a valuable resource in proper gas adsorption measurement techniques, Industrial Alliances, and instrument repairs.

To the excellent members of the wood, glass, electrical, and machine shops who have saved me from countless jams and who always stop to offer a friendly word. To our industrial collaborators at Chevron, Exxon, and Mosaic Materials, for the opportunity to learn from you and for the inspiration to think bigger. To Simon Teat and Laura McCormick, who made the small-molecule crystallography beamline at the Advanced Light Source feel like a home away from home.

To Emily, Michelle, Nate, and Chelsea, who feel like family. To Erica, for the welcome distraction of your fiction and warm reality of your friendship. And to many other friends—Eric, Tyler, Shawn, Chris, Sydney, James, Evelyn, Alina, Kevin, Nicole, Andreana, Maddie, JP, Anicia, and Stephen—for laughter and perspective. To Mimmi.

To the teachers, classmates, colleagues, collaborators, staff, friends, and family beyond the above who have been there in ways big and small: I am thankful for you.

Let's capture some CO₂.

Chapter 1. Porous Materials for Carbon Dioxide Separations to Mitigate Greenhouse Gas Emissions

1.1. Introduction

Driven by economic and population growth, global CO₂ emissions from fossil fuel combustion have more than doubled since the 1970s, reaching over 32 Gt CO₂ per year in 2016.¹⁻³ As a result, human activities have generated an estimated increase of 0.8–1.2 °C in global temperature since pre-industrial levels, and as of 2018, the Intergovernmental Panel on Climate Change (IPCC) anticipates that current trends will lead to 1.5 °C of warming by 2030 to 2052.⁴ Warming at these levels has been correlated with a number of increased risks for people, economies, and ecosystems, including sea level rise, extreme weather events, species extinction, and threats to human health, security, food, and water.⁴ Combatting these changes will require political, economic, and technological investment at a global scale toward the rapid deployment of decarbonization strategies. The materials community can play a key role in these efforts through the development of technologies to manage carbon emissions.

In particular, carbon capture and sequestration (CCS), in which CO₂ is selectively captured and permanently stored underground, has been recognized as a vital component of pathways to limit warming below 2 °C.^{1,5,6} Industrial development of carbon capture technology dates to the 1930s, when aqueous amine scrubbing was first patented for the selective removal of CO₂ from crude natural gas.⁷ Supported largely by economic incentives related to enhanced oil recovery, CO₂ transport and storage have also already achieved commercialization.⁵ However, deployment of commercial-scale CCS projects specifically for the purposes of emissions mitigation has been slow. At the time of writing, the Global CCS Institute lists a total of 44 large-scale CCS facilities, of which 18 are currently operational.⁸ While these facilities capture approximately 40 million tons per annum (Mtpa) of CO₂, and while over 230 Mt of CO₂ has been sequestered underground to date, an estimated 2500 CCS facilities with a capture capacity of 1.5 Mtpa each may be needed by 2040 to limit warming to the 2 °C target set in the 2016 Paris Agreement (Global CCS Institute, on the basis of the Sustainable Development Scenario of the International Energy Agency).⁹ A recent review by Bui and coworkers⁵ provides an excellent broader discussion of the current status of CCS, including remaining commercial and political barriers to large-scale deployment.

Research efforts toward CCS have focused in large part on post-combustion capture from fossil fuel-fired power plants, which are attractive targets due to their emission of large quantities CO₂ at relatively high concentrations (~4–15%).¹⁰ Indeed, in 2016, the production of electricity and heat generated 42% of global CO₂ emissions (Figure 1.1a), and thus decarbonization of the power sector will be a critical component of emissions mitigation efforts during the transition to renewable or other low-carbon energy sources.² Beyond fossil fuel sources, bioenergy production may also be coupled with CCS, enabling the potential for net CO₂ removal from the atmosphere (“negative emissions”) in a process termed BECCS (bioenergy with carbon capture and sequestration). Furthermore, CCS technology can be deployed to capture carbon from a number of other CO₂-containing streams beyond the power sector. For example, carbon capture technology can assist in the production of cleaner-burning natural gas or renewable biomethane to reduce global reliance on coal, which emits approximately twice as much CO₂ per unit electricity produced. The industrial sector, which contributes 19% of global CO₂ emissions, also offers a number of opportunities for decarbonization in cement production, oil refineries, iron and steel mills, and the pulp and paper industry.² Finally, CO₂ can be captured directly from air

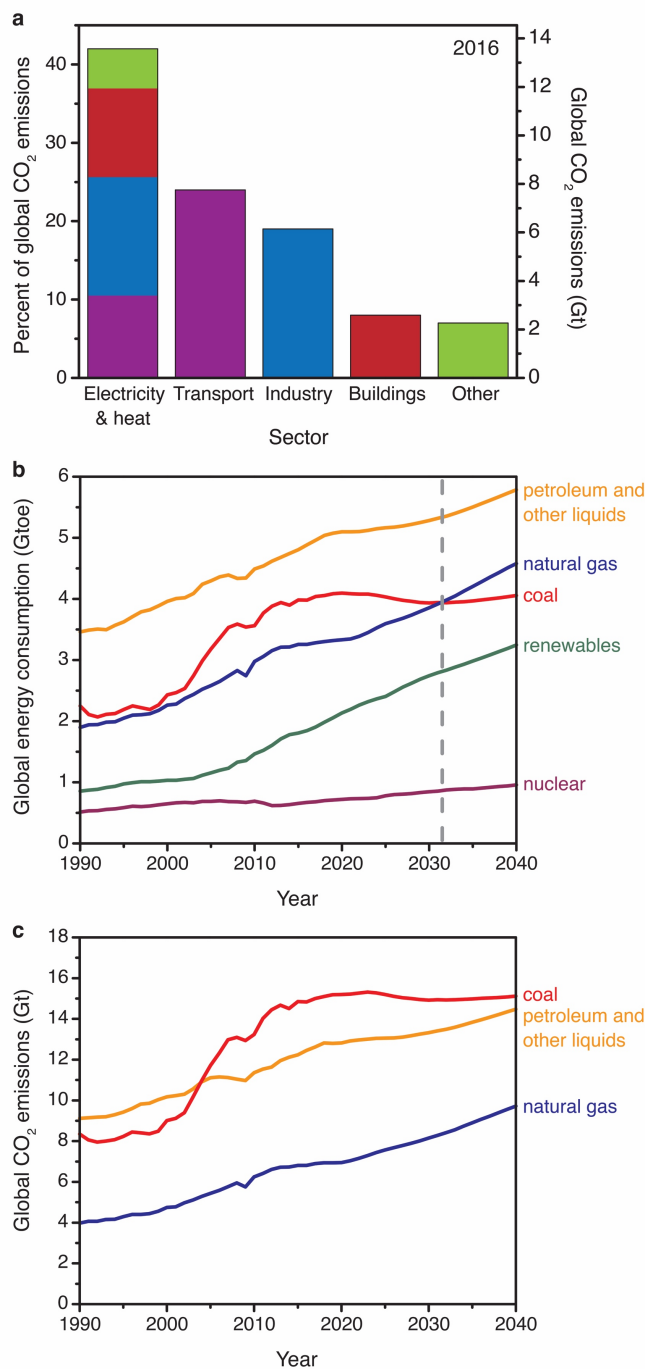


Figure 1.1. (a) Global CO₂ emissions by sector in 2016 (most recent year available), with emissions from electricity and heat further subdivided by end-use sector; based on data from the International Energy Agency (IEA, 2018), all rights reserved, as modified by the authors.² (b) Historical and projected global energy consumption by fuel from 1990–2040, suggesting that consumption of natural gas will match that of coal by ~2032 (dashed grey line). (c) Historical and projected global CO₂ emissions by source from 1990–2040. Data in (b) and (c) from the U.S. Energy Information Administration (EIA, 2017).³ Gt = gigatonnes, Gtoe = gigatonnes oil equivalent. Data in (b) were obtained in units of quadrillion Btu and were converted to units of Gtoe using a factor of 39.68 quad/Gtoe.

(DAC, direct air capture), a complementary strategy to BECCS with the potential for negative

emissions.¹¹

With traditional aqueous amine-based capture systems, the capture step currently comprises 60–80% of total cost of CCS (capture, compression, transport, and storage),¹² but learning curves from the commercialization of comparable processes suggest that significant improvements may be possible.¹³ Accordingly, a vast array of new capture technologies have been reported for CCS in recent years. Amine solutions, which capture CO₂ through the reversible formation of carbamate or bicarbonate species, remain the most technologically advanced systems, and ongoing research has led to proprietary blends with enhanced performance over the historical benchmark, monoethanolamine (MEA).¹⁴ Despite their significant advantage of proven performance at commercial scale, amine solutions suffer from issues with volatilization, oxidation, corrosivity, and high energy requirements to desorb bound CO₂.¹⁵ Although at an earlier stage of development, water-lean solvents offer the potential for improved efficiency by reducing the specific heat compared to aqueous systems while maintaining chemically specific capture.¹⁶ In addition, membranes,¹⁷ metal oxides,¹⁸ and encapsulated liquid sorbents¹⁹ may offer advantages in increasing the efficiency of CCS.

As another alternative, porous materials have received growing attention in recent years due to their potential to achieve intrinsically lower energy consumption in CO₂ capture processes.²⁰ Here, we discuss the state of the art in low-temperature CO₂ capture with porous materials, beginning with an overview of the primary adsorbent classes. We then examine individual target separations, with a focus on remaining barriers to deployment, such as stream-specific contaminants that can act as adsorbent poisons. Throughout this section, we highlight recent developments in materials design toward overcoming stream-specific CCS challenges. We then conclude with a discussion of key needs from the materials community.

1.2. Overview of Adsorbent Classes

A wide array of porous inorganic, organic, and organic–inorganic hybrid structures have been proposed for adsorptive CO₂ capture. Key metrics for evaluating the utility of an adsorbent for CCS include (1) the CO₂ swing capacity of the adsorbent in adsorption–desorption cycling, (2) the CO₂ selectivity of the adsorbent in the presence of all mixture components, (3) the stability of the adsorbent to chemical and mechanical stresses during extended cycling, (4) the energy required to cycle or regenerate the adsorbent, (5) the kinetics of adsorption and desorption, and (6) the viability of the adsorbent in a cradle-to-grave lifecycle assessment. Ultimate evaluation of an adsorbent requires analysis of a structured material (*e.g.* pellets, fibers, monoliths) within a full-scale process, with a number of possible cycling configurations (*e.g.* temperature swing, pressure or vacuum swing, concentration swing) and adsorption unit configurations (*e.g.* fixed bed, fluidized bed, rotating bed). Although these engineering considerations are critical to the overall process efficiency, we focus here on recent developments in the optimization of the fundamental adsorbent design for CCS. The primary adsorbent classes evaluated for CCS to date are introduced below.

1.2.1. Activated Carbons

Activated carbons are among the most industrial mature adsorbents, with applications in air and water purification, solvent recovery systems, and decolorization of sugar and other products through the removal of trace organic species.²¹ Preparation of activated carbon involves pyrolysis of biomass followed by high-temperature activation (typically at 700–1100 °C) using

physical agents including steam, CO₂, O₂, or other gases.²¹ Alternatively, chemical activation agents can be used to access higher surface areas or incorporate specific surface functionalities, such as nitrogenous groups to increase basicity.^{21,22} Porosity in activated carbons is generated through random stacking of microcrystalline graphite domains and can be controlled through modulation of the pyrolysis and activation conditions.²¹ For CCS, activated carbons offer the desirable features of potential low-cost feedstocks, such as waste biomass,²² as well as generally nonpolar, hydrophobic surfaces, which can enable CO₂ capture in the presence of moisture.²³ However, nonpolar surfaces also limit the equilibrium CO₂/N₂ selectivity and CO₂ capacity of typical carbons at conditions relevant to CO₂ capture from flue gases ($\leq 15\%$ CO₂), and these limitations must be addressed if carbons are to be deployed for CCS.²³

1.2.2. Zeolites

Zeolites are crystalline, microporous aluminosilicates that can be extracted as minerals or produced synthetically. These materials have already achieved commercialization in industrial gas separations, and a wealth of knowledge is available regarding their incorporation into engineered forms within full-scale processes.²⁴ For carbon capture applications, the mechanism of separation typically relies upon preferential interaction of the quadrupole moment of CO₂ with the electric field of cations within the zeolite pores, enabling strong CO₂ binding at low partial pressures.^{25,26} The crystalline nature of these materials and the comprehensive library of known and predicted structures make zeolites particularly well-suited for computational evaluation; indeed, previous studies have leveraged these properties to predict the optimal zeolites for CO₂ capture from both coal²⁷ and natural gas²⁸ flue emissions. However, zeolites such as 13X that operate via equilibrium adsorption mechanisms suffer from a critical limitation: water typically outcompetes CO₂ at cationic binding sites, leading to loss of selectivity for CO₂ in humid gas streams.^{23,29,30} Future research in zeolite-based processes for CO₂ capture must take this limitation into account by designing innovative process configurations or materials (Figure 1.2a, discussed in greater detail below) or by incorporating increased capital and operating costs to pre-dry the flue gas stream.³¹ Despite this challenge, zeolites remain attractive candidates for separations due to their advanced state of development and high thermal, oxidative, and hydrolytic stability, a product of the strong tetrahedral Al–O and Si–O bonds and the relatively small increase in energy for permanently porous phases compared to analogous condensed structures.³²

1.2.3. Amine-Functionalized Silicas

The impregnation (class 1) or covalent grafting (class 2) of (poly)amines within porous silicas has been demonstrated as a strategy to generate highly selective CO₂ capture adsorbents (Figure 1.2b).^{15,33–35} These materials typically bind CO₂ by chemisorption to form ammonium carbamate and/or carbamic acid species, depending on the identity and proximity of amine functionalities.³⁶ Importantly, chemisorption of CO₂ enables many amine-functionalized silicas to preserve selectivity for CO₂ in the presence of water, typically with improved capacities, due to the formation of bicarbonate species.^{33,37} Key remaining challenges for this class of materials include amine oxidation, urea formation, leaching of amines from class 1 materials, and slow adsorption/desorption kinetics in certain diffusion-limited variants.^{20,33} Recent work has demonstrated that the incorporation of longer alkyl spacers between amines,³⁸ integration of hydrogen bonding groups,³⁹ and addition of small amounts of chelators to remove oxidation-

catalyzing trace metal impurities⁴⁰ can dramatically improve the oxidative stability of these materials. These recent findings support continued study toward the application of amine-functionalized silicas for CO₂ capture.

1.2.4. Porous Organic Networks

Permanently porous organic materials can be prepared via crosslinking of multitopic organic monomers to achieve amorphous porous organic polymers or crystalline covalent–organic frameworks. These materials offer a number of advantages in carbon capture processes, including modular pore size and surface functionality, high stability, and the potential for high gravimetric capacities through the use of light elements in the polymer backbone.^{41–44} Porous polymers bearing amine functionalities or other CO₂ chemisorption sites (Figure 1.2c) are likely to be most promising for CCS, particularly for CO₂ capture from low partial pressure streams.⁴³ Due to the constituent covalent bonds, many porous organic networks possess significant hydrothermal stability.⁴⁵ While the oxidative stability of polymers has been studied more broadly over the past several decades,⁴⁶ further work is needed to probe the oxidative stability of porous polymer networks under the gas compositions and higher temperatures relevant to flue gases and other industrial streams. Kinetics data, cycling tests, and multicomponent experiments incorporating H₂O and other contaminants are also needed to support further evaluation of porous polymers for CCS applications. In addition, the ability of these materials to be synthesized at scale and formulated into industrially relevant structured forms remains to be demonstrated.

1.2.5. Metal–Organic Frameworks

Metal–organic frameworks consist of inorganic ions or clusters connected by bridging organic ligands, enabling control of pore size, shape, and surface chemistry to target strong and selective binding of specific adsorbates.^{47,48} As with zeolites, metal–organic frameworks possess crystalline structures that facilitate precise characterization of framework–guest interactions. The multitude of possible structures accessible with metal–organic frameworks has led to a proliferation of synthetic and computational reports on these materials for carbon capture, with a particular emphasis on post-combustion capture from coal-fired power plants.^{49–54} Many studies have focused on the use of metal–organic frameworks bearing metals with open coordination sites to bind CO₂ selectively over N₂. However, these binding sites can suffer from the same water passivation issues encountered with cationic binding sites in zeolites.^{23,55–57} As one possible solution, amine-functionalized metal–organic frameworks can combine the advantages of crystalline materials with the selective reactivity toward CO₂ demonstrated by amine-grafted silicas, amine-functionalized porous organic polymers, and amine solutions (Figure 1.2d).^{58,59} Despite promising advances in fundamental materials design, several challenges remain in advancing metal–organic frameworks toward industrial application. As discussed for porous polymers, further work is needed to develop metal–organic frameworks in industrially-viable structured forms. Additionally, limited hydrothermal stability remains a barrier for many frameworks due to the lability of metal–ligand coordination bonds.⁶⁰ Oxidative stability is likewise a challenge for many metal–organic frameworks, with oxidation possible at the metal node⁶¹ and/or the organic linker,⁶² particularly in the presence of both O₂ and H₂O.^{63–65} Furthermore, development of metal–organic frameworks at scales relevant to CCS will require thoughtful selection of earth-abundant metals, inexpensive organic bridging units, and

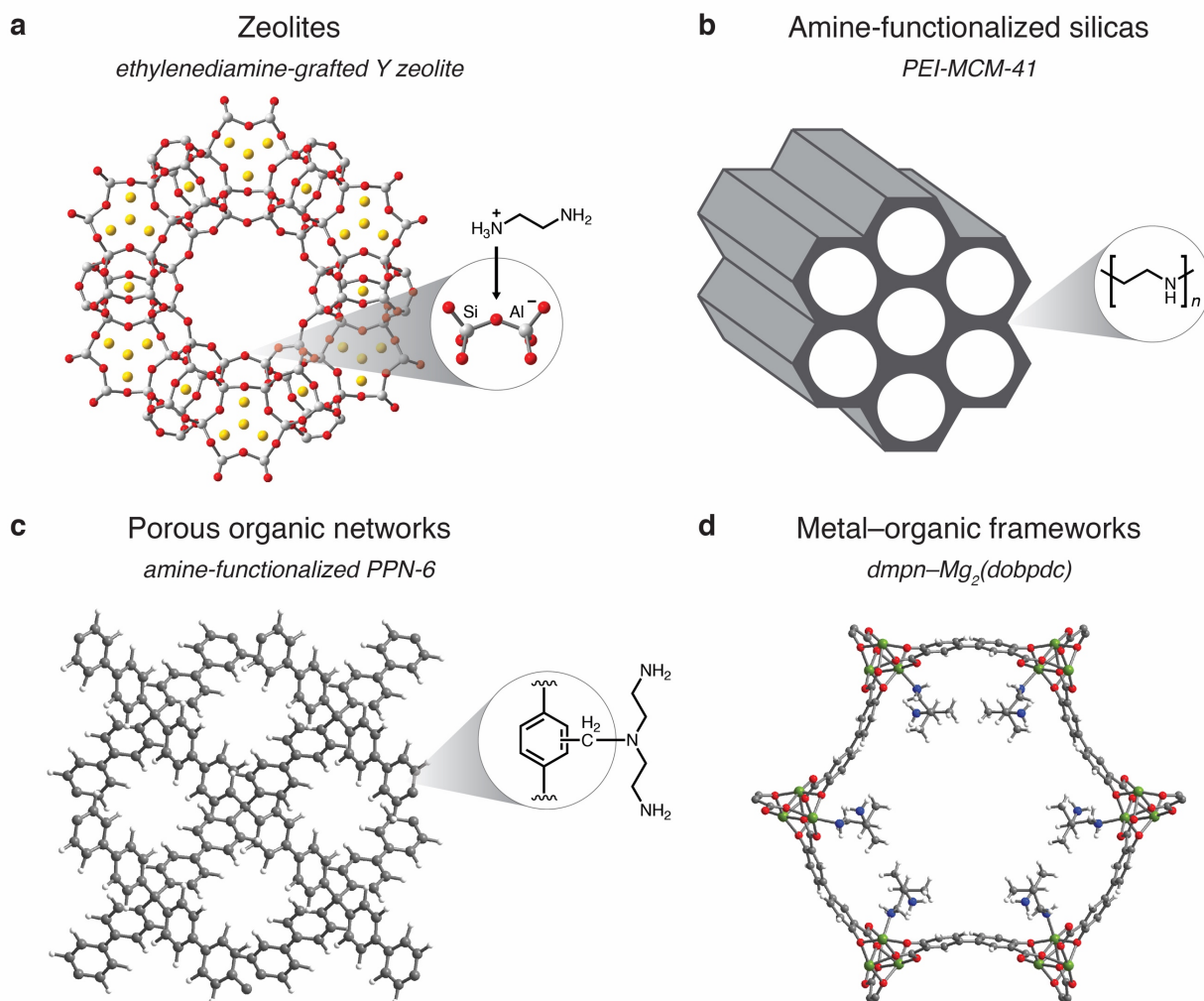


Figure 1.2. Illustrative examples discussed in this work for structures of various adsorbent classes. Silver, red, yellow, gray, green, blue, and white spheres represent Al/Si, O, Na, C, Mg, N, and H atoms, respectively. The structure in (c) shows one proposed local environment within the amorphous material PPN-6 (PAF-1) and is adapted from reference 44; structures in (a) and (d) are adapted from refs. 78 and 75, respectively.

environmentally friendly synthetic routes.

1.3. Target Separations and Case Studies

As shown in Table 1.1, potential target streams for CCS contain CO₂ concentrations spanning several orders of magnitude. Opportunities for adsorptive CCS from individual streams are discussed in greater detail below, along with recent advances in materials design toward overcoming stream-specific challenges.

Table 1.1. Representative CO₂ concentrations in process streams.^{10,12,66–69}

Process	CO ₂ concentration (vol %)
<i>Power plant flue gas</i>	
Coal-fired boiler	10–15
Natural gas-fired boiler	8
Natural gas combined cycle	4
Coal-oxygen combustion	>80%
Natural gas partial oxidation	40
<i>Crude CH₄ streams</i>	
Anaerobic digester biogas	30–50
Landfill biogas	25–47
Crude natural gas	up to 80%
<i>Blast furnace gas</i>	
Before combustion	20
After combustion	27
<i>Cement kiln off-gas</i>	14–33
<i>Oil refineries and petrochemical plant fired boiler</i>	8
<i>Air</i>	0.041

1.3.1 The Power Sector

Responsible for 42% of global annual CO₂ emissions, the production of electricity and heat is a natural target for CO₂ emission mitigation efforts.² A number of potential separation strategies may be used to reduce or eliminate CO₂ emissions from thermal power plants.²⁰ In pre-combustion capture, synthesis gas (syngas, H₂ and CO) is produced from gasified fuel and sent to a shift reactor, which oxidizes CO to CO₂ and reduces H₂O to produce additional H₂. The resulting CO₂/H₂ mixture is then separated into H₂ for fuel and CO₂ for subsequent compression and storage. In oxy-fuel combustion, pure oxygen is used in place of air during the combustion of a hydrocarbon fuel, resulting in a flue gas containing only CO₂ and easily-condensable H₂O. In this case, the primary energy of separation is consumed in the separation of O₂ from N₂ in air at the beginning of the process. In this review, we focus on post-combustion CO₂ capture, in which CO₂ is removed from a flue gas containing primarily CO₂, N₂, O₂, and H₂O.

In 2016, coal supplied 27% of global primary energy and generated 44% of global CO₂ emissions (Figure 1.1b–c),^{2,3} due to its heavy carbon intensity (26–29 tons of carbon per TJ, vs 15 tC/TJ for natural gas).² A typical coal-fired power plant emits a flue gas stream at ambient pressure that can be cooled to a minimum of 40–60 °C and that contains 70–75% N₂, 10–15% CO₂, 8–10% H₂O, 3–4% O₂, and trace SO_x, NO_x, and other impurities.¹² As the largest point-source emitters of CO₂, coal-fired power plants have garnered significant attention in the CCS community, and the relatively high concentration of CO₂ in the flue gas stream is favorable for adsorptive CO₂ capture. Thus, the primary challenge for adsorptive post-combustion CCS from coal-fired plants is not typically separation of CO₂ from N₂, but instead the selective capture of CO₂ in the presence of H₂O and other contaminants. Water has long been known to outcompete CO₂ at sites such as exposed metal cations, which are often the primary binding sites in zeolites or metal–organic frameworks with equilibrium selectivity for CO₂.^{23,30,70–72,56} Indeed, a recent evaluation of 15 activated carbons, zeolites, mesoporous silicas, and metal–organic frameworks found that only adsorbents functionalized with alkylamines maintained appreciable CO₂ capacity in ternary (CO₂/N₂/H₂O) equilibrium experiments simulating coal flue gas.²³ Of these, the

material $\text{mmen-Mg}_2(\text{dobpdc})$ ($\text{mmen} = N,N'$ -dimethylethylenediamine, $\text{dobpdc}^{4-} = 4,4'$ -dioxidobiphenyl-3,3'-dicarboxylate) was identified as particularly promising.⁷³ This material features step-shaped CO_2 adsorption isotherms resulting from cooperative, reversible insertion of CO_2 into the metal-amine bonds to form chains of ammonium carbamate along the pore axis.⁷⁴ Subsequently, incorporation of the diamine dmpn (2,2-dimethyl-1,3-diaminopropane) in place of mmen was found to shift the cooperative adsorption pressure to an optimal range for coal flue gas capture and to improve the stability of the material (Figure 1.2d).⁷⁵ In a related approach, the metal-organic frameworks $\text{M}^{\text{II}}\text{M}^{\text{III}}(\text{OH})\text{Cl}_2(\text{bbta})$ ($\text{M} = \text{Mn}, \text{Co}$; $\text{H}_2\text{bbta} = 1H,5H$ -benzo(1,2-*d*:4,5-*d'*)bistriazole) were found to capture large quantities of CO_2 under simulated coal flue gas conditions through the reversible formation of metal-bound bicarbonate at surface sites bearing monodentate hydroxide ligands.⁷⁶ Likewise, incorporation of amines within the organic linkers of metal-organic frameworks has been demonstrated as an effective strategy to achieve CO_2 capture under humid conditions.⁷⁷ Furthermore, amine-functionalized silicas have long been valued for their ability to bind CO_2 selectively in the presence of water, and these materials often show improved CO_2 capture performance under humid conditions due to bicarbonate formation.^{33,37} Amine-functionalized zeolites have also been demonstrated to enable CO_2 capture from humid streams.^{78–82} As a notable recent example, a chemically grafted ethylenediamine-Y zeolite (Figure 1.2a) was shown to possess high thermal stability to 180 °C, resistance to urea formation, and CO_2 selectivity in the presence of water.⁷⁸

Another key challenge for post-combustion capture from coal-fired power plants is the presence of SO_x , NO_x , Hg, and particulate matter in the flue gas stream. In a comprehensive two-part study of class 1 and class 2 aminosilica materials, Rezaei and Jones found that these adsorbents were typically unaffected by NO but irreversibly bound NO_2 at high concentrations (200 ppm, 35 °C) to form nitrates, resulting in a dramatic loss of CO_2 capacity.^{83,84} The authors also found that exposure to 20 ppm SO_2 at 35 °C reduced the CO_2 capacity of aminosilicate materials from dry 10% CO_2 streams, due to proposed formation of sulfates and/or sulfites on the surface.⁸³ Further research is needed to determine the influence of H_2O on the competitive adsorption of CO_2 , SO_x , and NO_x on these materials. Critically, deactivation of amine-based binding sites by SO_x and NO_x has also been observed for other amine-based capture materials,^{85,86} including aqueous amine solutions, which form heat-stable salts.⁸⁷ Early evaluation of the stability of metal-organic frameworks to acid gases also suggests that humid SO_2 will compromise the stability and/or CO_2 capacity of many of these adsorbents,^{88,89} although the zeolitic imidazolate framework ZIF-71 ($\text{Zn}(\text{dcim})_2$, $\text{dcim} = 4,5$ -dichloroimidazolate, RHO topology) was found to withstand humid SO_2 exposure.⁸⁹ As a result, CCS processes may require additional pre-treatment, such as a sacrificial adsorbent layer or NaOH-based polishing scrubber, to reduce the SO_2 concentration beyond typical flue gas desulfurization levels (~37 ppmv for wet limestone forced oxidation).¹⁰ Alternatively, new CO_2 capture materials with high CO_2 swing capacities in the presence of H_2O , SO_x , and NO_x would be highly desirable. Although carbon-based materials have shown strong stability to cycling under real flue gas, their CO_2 working capacities may not be sufficient to allow them to be cost-competitive with aqueous amines.⁸⁶ Similarly, zeolites may offer attractive stability, but SO_2 , along with H_2O , will likely outcompete CO_2 at exposed metal cation sites.⁹⁰ Considering other flue gas contaminants, limited experimental data have been reported regarding the effect of particulate matter and Hg on the performance of CO_2 capture materials. However, the degradative nature of these contaminants on the adsorbent structure is likely to be minimal compared to the degradation risks associated with oxygen and acid gases.³³ Notably, adsorbents may support Hg emission control efforts in

separate pretreatment steps such as activated carbon injection, in which vapor-phase Hg is captured by activated carbon dispersed in the flue gas ductwork.⁹¹

Beyond CCS at coal-fired power plants, adsorptive CO₂ capture will also be valuable in post-combustion capture from natural gas-fired power plants.⁹² Due to increasingly available reserves and its low greenhouse gas footprint among fossil fuels, natural gas is anticipated to surpass coal in its contribution to primary energy by 2030 (New Policies Scenario, IEA)^{2,93} or 2032 (EIA, Figure 1.1b).³ The flue gas of natural gas combined cycle (NGCC) power plants may be more favorable for adsorptive CCS due to its lower levels of SO_x, particulate matter, and Hg compared to coal flue gas. However, NGCC flue gas contains lower CO₂ concentrations (~4%) and higher O₂ concentrations (~12%) compared to coal flue gas (~10–15% CO₂, 3–4% O₂), as well as similar H₂O concentrations (~8% H₂O). Therefore, adsorbents for CCS from NGCC power stations must possess strong oxidative stability as well as binding sites capable of selective CO₂ capture from more dilute, humid streams. While amine-based capture materials possess the chemical selectivity to achieve this separation, the high oxygen content of NGCC flue gas is likely to lead to deleterious reaction pathways. For example, solution-phase amines tend to generate soluble iron and copper species through equipment corrosion, and these trace metals act to catalyze oxidation reactions of the mobile amine species.^{33,94} Tethering amines to an adsorbent surface has therefore been proposed to offer generally improved oxidation resistance over solution-phase amines by reducing the likelihood of equipment corrosion.^{33,94} Nonetheless, reactions of amine-functionalized materials with oxygen to form imines, amides, and other carbonyl-containing species remain a challenge for these adsorbents in CCS from oxygen-rich streams.⁹⁴ Notably, the use of poly(propylenimine) (PPI) in place of polyethylenimine (PEI) in aminopolymer structures was recently found to afford enhanced oxidative stability at elevated temperatures.³⁸ Additionally, the incorporation of hydrogen bonding groups and phosphate or phosphonate sodium salt chelators to capture trace-metal oxidation catalysts have been found to enhance the oxidative stability of aminosilica materials.⁴⁰ Other amine-functionalized materials, such as derivatives of the biphenyl-based, diamond-like porous polymer network PPN-6 (Figure 1.2c), have been computationally predicted as efficient adsorbents for CCS from dry NGCC flue streams,²⁸ but further experimental evaluation of their oxidative stability is needed. Likewise, further work is needed to engineer new metal–organic frameworks with both CO₂ selectivity from low partial pressure streams and oxidative and hydrolytic stability.

As a third option in the power sector, BECCS has been included in several of the IPCC Integrated Assessment Models (IAMs) as a necessary technology to meet climate targets.^{1,5,95,96} In BECCS, biomass is cultivated both to sequester CO₂ and generate energy. If the CO₂ generated during energy production from biomass is then captured and sequestered, net removal of CO₂ from the atmosphere can be achieved. The composition of the target CCS stream in a BECCS process can vary significantly based on the fuel composition, but post-combustion streams will likely contain SO_x, NO_x, particulate matter, and trace alkali and transition metals.⁹⁵ BECCS remains an underexplored area for adsorbents, and additional research is needed to accelerate the deployment of this important technology.

1.3.2 Biogas and Crude Natural Gas

In addition to reducing the emissions of thermal power plants, adsorptive CO₂ capture is also valuable in the production of renewable or low-carbon fuels. Specifically, biomethane, a renewable natural gas equivalent, can be produced by removing CO₂ contamination from crude biogas (~25–50% CO₂ in CH₄) generated through the anaerobic digestion of plant or animal

waste. Biomethane production offers the dual environmental benefit of harnessing otherwise harmful methane emissions from organic waste for energy production while also supporting intermittencies of other renewable sources, such as wind and solar power. Further emissions reductions can be achieved if biomethane consumption is coupled with CCS, an example of BECCS, as discussed above. Adsorptive CO₂ capture can also be used to purify crude natural gas to meet pipeline specifications, although the carbon balance for natural gas, a CO₂-emitting fossil fuel, is less favorable than for biomethane. Nonetheless, highly efficient NGCC power plants are considered a bridge technology in place of coal-fired plants to reduce the carbon footprint of the power sector in the near-term, provided that fugitive CH₄ emissions are minimized.¹ Furthermore, gas processing facilities have provided much of the early support for commercial CCS demonstrations and will likely remain major contributors to long-term CCS efforts.⁵

Desirable adsorbents for renewable and non-renewable gas processing will reduce CO₂ concentrations to pipeline-acceptable levels (typically $\leq 2\%$), achieve high CH₄ recovery, and tolerate—and ideally remove—H₂S present in the stream.⁹⁷ In the case of biogas, adsorbents may also need to tolerate siloxanes present as a waste product from consumer goods, although these species may be removed in pretreatment beds containing activated carbon, molecular sieves, or polymer beads.⁹⁸ As one notable approach, “trapdoor” zeolites have been developed with high selectivity for CO₂ over CH₄ arising from temporary and reversible displacement of pore-blocking cations to admit CO₂.⁹⁹ Computational approaches have also proven valuable in identifying zeolites with optimal properties for gas processing.^{100,101} In addition, metal–organic frameworks have received increasing attention for CO₂/CH₄ separations.¹⁰² A recently reported fluorinated framework, NiAlF₅(H₂O)(pyr)₂ (KAUST-8, AlFFIVE-1-Ni; pyr = pyrazine), was found to enable simultaneous removal of CO₂ and H₂S from CH₄, a result that the authors attribute to a favorable pore volume and segregated binding sites for CO₂ and H₂S.¹⁰³ For selective H₂S removal, metal–organic frameworks with amine-functionalized linkers¹⁰⁴ and “molecular basket” aminosilica adsorbents such as TMHDA/SBA-15 (TMHDA = tetramethyl hexanediamine)¹⁰⁵ have recently been demonstrated as effective materials. To meet pipeline specifications, natural gas must typically contain <4% total inerts, which may further necessitate nitrogen removal.⁹⁷ In this case, titanosilicate materials with adjustable pore apertures, such as ETS-4, remain particularly interesting technologies that operate by a commercialized “molecular gate” process of size-selective gas sieving.¹⁰⁶

1.3.3 Other Industrial CO₂ Streams

In addition to natural gas processing, a number of other industrial CO₂-containing streams provide ample opportunities for decarbonization.^{5,107,108} The iron and steel industry generates the largest fraction of industrial emissions (31%), but deployment of CCS in this sector is complicated by the large number of CO₂-emitting processes within each mill.¹⁰⁸ Post-combustion capture from the blast furnace, the largest point source in an integrated steel mill, is under active investigation,¹⁰⁸ and adsorbents may play a role in reducing the costs of capture compared to traditional liquid amine scrubbers. The cement industry, another attractive target, generates approximately 5% of global CO₂ emissions, a result of both fuel consumption to power the kiln (40% of cement industry emissions) and unavoidable emissions associated with production of the cement precursor CaO from limestone (CaCO₃).⁵ Many process configurations have been proposed for CCS from cement plants, including post-combustion capture, which has largely focused on aqueous amine technology to date.¹⁰⁹ However, a pilot-scale demonstration incorporating PEI-functionalized silica was undertaken in a collaboration between RTI and

Norcem at the first cement plant CCS test center in Brevik, Norway.¹¹⁰ In the refining industry, CCS deployment may be favored by the significant relevant expertise in this sector, as well as the relatively small cost of CCS compared to typical price differentials routinely managed by the industry in the cost of crude oil.⁵ The compositions, volumes, and physical properties of CO₂-containing industrial streams vary widely, and increased investigation of adsorbents for industrial CCS will help identify suitable avenues for entry while accelerating decarbonization across this sector.

1.3.4 Direct CO₂ Capture from Air

Along with BECCS, DAC has received growing attention in recent years as a potential negative emissions technology (NET).¹¹ Proponents highlight the necessity of DAC for carbon dioxide removal (CDR) if warming overshoots target limits.⁵ In the near term, DAC may accelerate the development of capture technologies by circumventing technical challenges associated with integration with power plants or other industrial facilities. However, to achieve net negative emissions, DAC facilities must be coupled with transport and storage infrastructure, and the energy consumed to power DAC systems must emit less CO₂ than is sequestered. In terms of capture, the primary technical challenge in DAC arises from the low concentration of CO₂ in air (410 ppm at the time of writing),⁶⁹ which is over 100 times more dilute than the exhausts of fossil fuel-fired power plants (4–15%).¹⁰ As a result, the theoretical minimum work to separate CO₂ from air (19–21 kJ/mol CO₂) is 2–4 times greater than that required for CCS from the emissions of power plants fired by gas (6–9 kJ/mol) or coal (5–7 kJ/mol, Figure 1.3).¹¹¹ As discussed above, amine-functionalized materials, including porous polymers,¹¹² metal–organic frameworks,¹¹³ and silicas,¹¹⁴ often possess the requisite CO₂ selectivity at low partial pressures. To increase the efficiency of DAC processes, alternative mechanisms for adsorptive

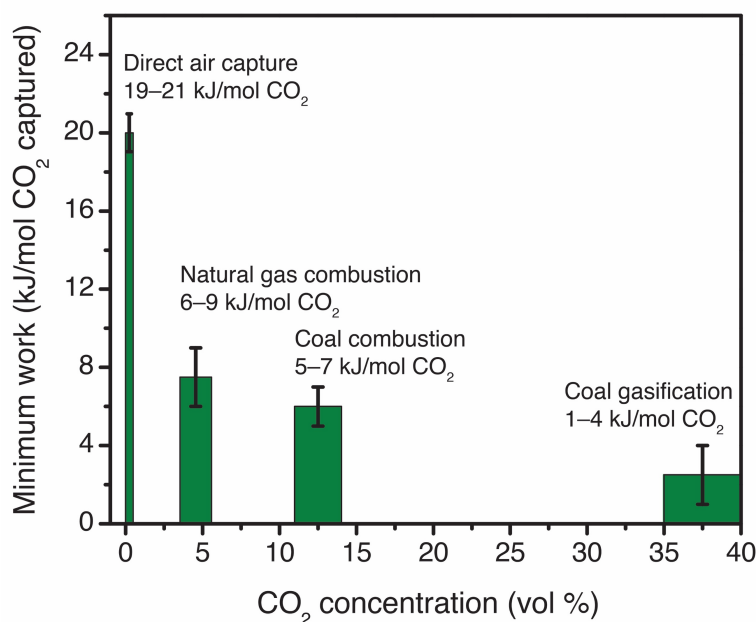


Figure 1.3. Theoretical minimum work required for CO₂ capture as a function of CO₂ concentration, adapted from ref. 111. Black bars and ranges indicate the variation in minimum work anticipated for 50% CO₂ capture at 80% purity (lower bound) to 90% CO₂ capture at 99% purity (upper bound).

capture and release of CO₂ have also been proposed. Notably, an amine-functionalized anion-exchange resin has been shown to bind CO₂ when dry and release it when wet, a cycling configuration termed “moisture swing” that may offer advantages over traditional pressure- or temperature-swing cycling processes.¹¹⁵ Steam has also been proposed as a desorption medium, and promising early results have been demonstrated with amine-functionalized silica and γ -alumina adsorbents.^{116–119} The low concentration of CO₂ in air further requires the processing of large quantities of air with a low pressure drop, which has prompted the development of fiber-based adsorbents, such as a recently reported PEI-functionalized cellulose acetate/SiO₂ composite.¹²⁰ Finally, the oxidative stability¹¹⁴ and kinetics¹²¹ of CO₂ capture are critical to consider for dilute streams.

1.4. Outlook and Key Needs from the Materials Community

The materials community has made significant strides toward overcoming barriers to the deployment of adsorbents for CCS. Nonetheless, continued investment is needed to identify the most promising materials for a given separation and to accelerate the development of these materials beyond the laboratory to the pilot, demonstration, and ultimately commercial scale. Throughout this process, computational efforts will be essential in the prediction or down-selection of top candidate adsorbents.²⁷ For experimentalists, continued iteration of adsorbent design is needed to achieve impurity tolerance and overcome other source-specific challenges. Additionally, close collaboration among materials scientists, process engineers, and power plant personnel is needed from the earliest stages of development in order to accelerate large-scale deployment.^{12,122} Increased utilization of test centers, such as the Technology Centre Mongstad (Norway), the National Carbon Capture Center (NCCC, USA) or the Pilot-Scale Advanced Capture Technology facility (PACT, UK), will likewise be crucial to accelerated deployment of CCS technologies.⁸ While these centers are largely focused on scale-up and de-risking of technologies beyond the laboratory scale, we propose that test centers could also play a key role in evaluating technologies at an earlier stage of development. For example, a slipstream testing unit capable of exposing a bank of early-stage (milligram- to gram-scale) samples to crude process streams would enable experimentalists to probe adsorbent stability to realistic process conditions that may be difficult to simulate in the laboratory. In this manner, iteration of the material structure to achieve suitable stability could be prioritized from the initial stages of adsorbent design.

Beyond fundamental adsorbent development, the expertise of the materials community is also needed in the development of adsorbents at large scale and in structured forms. Critically, while adsorbents are typically synthesized as powders, commercial deployment will likely require the use of shaped particles, such as pellets, or other structured contactors, such as monoliths or fibers.¹²³ Industrial-scale formulation is well understood for traditional adsorbents such as zeolites, but continued development is still needed for newer materials, such as metal–organic frameworks. The ultimate structure of the commercial material will strongly influence the pressure and thermal gradients across the adsorption unit, which in turn will dictate factors such as the bed size, cycle times, and overall energy demand.¹²³ For temperature-swing processes, innovative contactor configurations may further enable heat integration to make use of the sorption enthalpy at other stages of the separation process.¹²³

Finally, as new materials are accelerated toward commercial deployment for CCS, developing technologies must be evaluated within full lifecycle assessments.^{124,125} Proposed synthetic routes must be safe and atom-efficient at scales relevant to CCS, with minimal synthetic steps and high

space-time yields. In the case of metal–organic frameworks for CCS from coal-fired power plants, these requirements will likely restrict the base metals that could be used, with frameworks incorporating vanadium or cobalt—and likely also chromium, zirconium, or nickel—likely to place untenable strain on the global reserves of these metals.¹²⁶ Recyclability and ultimate management of waste streams must also be considered.¹²⁴ Furthermore, continued expansion of commercial-scale CCS operations will raise new questions about allocation of water and land resources. In 2011, 39% of freshwater withdraws in the US were associated with thermal power plants, and liquid amine-based CCS systems are projected to approximately double the water consumption of coal-fired power plants.¹²⁷ For BECCS, land availability remains a highly debated issue, because land for the cultivation of biomass fuel may compete with land for the production of food.^{5,95}

While many of these challenges remain far beyond the scope of early-stage materials research, framing this work within the broader context of global food, energy, and water resources can help guide materials discovery toward sustainable solutions. Meeting ambitious decarbonization targets will require political, economic, and technological alignment at a global scale to manage these resources while deploying a suite of mitigation solutions. Carbon capture and sequestration is widely recognized as a vital component of least-cost pathways to limit warming below 2 °C, and porous materials are likely to form the basis of next-generation capture technologies. Continued research by the materials community will accelerate the deployment of CCS within the power and industrial sectors and for negative emissions technologies. Together with continued growth of renewable energy, as well as solutions such as improved vehicle and building efficiency, CCS can help secure a cleaner future for generations to come.

1.5. Acknowledgements

Sections 1.2.2 to 1.2.5 were partially reproduced from reference 92, with permission from the Royal Society of Chemistry.

1.6. References

- (1) Pachauri, R. K.; Allen, M. R.; Barros, V. R.; Broome, J.; Cramer, W.; Christ, R.; Church, J. A.; Clarke, L.; Dahe, Q.; Dasgupta, P. *Climate Change 2014: Synthesis Report. Contribution of Working Groups I, II and III to the Fifth Assessment Report of the Intergovernmental Panel on Climate Change*; IPCC, 2014.
- (2) *CO₂ Emissions from Fuel Combustion 2018*; International Energy Agency: Paris, France, 2018.
- (3) *International Energy Outlook 2017*; DOE/EIA-0484(2017); Energy Information Administration, U.S. Department of Energy, 2017.
- (4) Intergovernmental Panel on Climate Change. *Global Warming of 1.5°C*; SR15; Intergovernmental Panel on Climate Change, 2018.
- (5) Bui, M.; Adjiman, C. S.; Bardow, A.; Anthony, E. J.; Boston, A.; Brown, S.; Fennell, P. S.; Fuss, S.; Galindo, A.; Hackett, L. A.; Hallett, J. P.; Herzog, H. J.; Jackson, G.; Kemper, J.; Krevor, S.; Maitland, G. C.; Matuszewski, M.; Metcalfe, I. S.; Petit, C.; Puxty, G.; Reimer, J.; Reiner, D. M.; Rubin, E. S.; Scott, S. A.; Shah, N.; Smit, B.; Trusler, J. P. M.; Webley, P.; Wilcox, J.; Mac Dowell, N. Carbon Capture and Storage (CCS): The Way Forward. *Energy Environ. Sci.* **2018**, *11*, 1062–1076. <https://doi.org/10.1039/C7EE02342A>.

- (6) Boot-Handford, M. E.; Abanades, J. C.; Anthony, E. J.; Blunt, M. J.; Brandani, S.; Mac Dowell, N.; Fernández, J. R.; Ferrari, M.-C.; Gross, R.; Hallett, J. P.; Haszeldine, R. S.; Heptonstall, P.; Lyngfelt, A.; Makuch, Z.; Mangano, E.; Porter, R. T. J.; Pourkashanian, M.; Rochelle, G. T.; Shah, N.; Yao, J. G.; Fennell, P. S. Carbon Capture and Storage Update. *Energy Environ. Sci.* **2014**, *7* (1), 130–189. <https://doi.org/10.1039/C3EE42350F>.
- (7) Rochelle, G. T. Amine Scrubbing for CO₂ Capture. *Science* **2009**, *325* (5948), 1652–1654. <https://doi.org/10.1126/science.1176731>.
- (8) Facilities - Global CCS Institute <https://co2re.co/FacilityData> (accessed Apr 20, 2019).
- (9) *The Global Status of CCS: 2018*; Global CCS Institute: Australia, 2018.
- (10) *Cost and Performance Baseline for Fossil Energy Plants. Volume 1a: Bituminous Coal (PC) and Natural Gas to Electricity. Revision 3*; DOE/NETL-2015/1723; U.S. Department of Energy, National Energy Technology Laboratory, 2015.
- (11) Sanz-Pérez, E. S.; Murdock, C. R.; Didas, S. A.; Jones, C. W. Direct Capture of CO₂ from Ambient Air. *Chem. Rev.* **2016**, *116* (19), 11840–11876. <https://doi.org/10.1021/acs.chemrev.6b00173>.
- (12) Bhowan, A. S.; Freeman, B. C. Analysis and Status of Post-Combustion Carbon Dioxide Capture Technologies. *Environ. Sci. Technol.* **2011**, *45* (20), 8624–8632. <https://doi.org/10.1021/es104291d>.
- (13) *The Costs of CO₂ Capture, Transport and Storage*; European Technology Platform for Zero Emission Fossil Fuel Power Plants (ZEP), 2011.
- (14) Rochelle, G. T. 3 - Conventional Amine Scrubbing for CO₂ Capture. In *Absorption-Based Post-combustion Capture of Carbon Dioxide*; Feron, P. H. M., Ed.; Woodhead Publishing, 2016; pp 35–67. <https://doi.org/10.1016/B978-0-08-100514-9.00003-2>.
- (15) Dutcher, B.; Fan, M.; Russell, A. G. Amine-Based CO₂ Capture Technology Development from the Beginning of 2013—A Review. *ACS Appl. Mater. Interfaces* **2015**, *7* (4), 2137–2148. <https://doi.org/10.1021/am507465f>.
- (16) Heldebrant, D. J.; Koech, P. K.; Glezakou, V.-A.; Rousseau, R.; Malhotra, D.; Cantu, D. C. Water-Lean Solvents for Post-Combustion CO₂ Capture: Fundamentals, Uncertainties, Opportunities, and Outlook. *Chem. Rev.* **2017**, *117* (14), 9594–9624. <https://doi.org/10.1021/acs.chemrev.6b00768>.
- (17) Du, N.; Park, H. B.; Dal-Cin, M. M.; Guiver, M. D. Advances in High Permeability Polymeric Membrane Materials for CO₂ Separations. *Energy Environ. Sci.* **2012**, *5* (6), 7306–7322. <https://doi.org/10.1039/C1EE02668B>.
- (18) Wang, S.; Yan, S.; Ma, X.; Gong, J. Recent Advances in Capture of Carbon Dioxide Using Alkali-Metal-Based Oxides. *Energy Environ. Sci.* **2011**, *4* (10), 3805–3819. <https://doi.org/10.1039/C1EE01116B>.
- (19) Vericella, J. J.; Baker, S. E.; Stolaroff, J. K.; Duoss, E. B.; Hardin Iv, J. O.; Lewicki, J.; Glogowski, E.; Floyd, W. C.; Valdez, C. A.; Smith, W. L.; Satcher, J. H.; Bourcier, W. L.; Spadaccini, C. M.; Lewis, J. A.; Aines, R. D. Encapsulated Liquid Sorbents for Carbon Dioxide Capture. *Nat. Commun.* **2015**, *6*, 6124. <https://doi.org/10.1038/ncomms7124>.
- (20) Choi, S.; Drese, J. H.; Jones, C. W. Adsorbent Materials for Carbon Dioxide Capture from Large Anthropogenic Point Sources. *ChemSusChem* **2009**, *2* (9), 796–854. <https://doi.org/10.1002/cssc.200900036>.
- (21) Ruthven, D. M. *Principles of Adsorption and Adsorption Processes*; John Wiley & Sons: New York, 1984.

- (22) Creamer, A. E.; Gao, B. Carbon-Based Adsorbents for Postcombustion CO₂ Capture: A Critical Review. *Environ. Sci. Technol.* **2016**, *50* (14), 7276–7289. <https://doi.org/10.1021/acs.est.6b00627>.
- (23) Mason, J. A.; McDonald, T. M.; Bae, T.-H.; Bachman, J. E.; Sumida, K.; Dutton, J. J.; Kaye, S. S.; Long, J. R. Application of a High-Throughput Analyzer in Evaluating Solid Adsorbents for Post-Combustion Carbon Capture via Multicomponent Adsorption of CO₂, N₂, and H₂O. *J. Am. Chem. Soc.* **2015**, *137* (14), 4787–4803. <https://doi.org/10.1021/jacs.5b00838>.
- (24) Kulprathipanja, S. *Zeolites in Industrial Separation and Catalysis*; John Wiley & Sons, 2010.
- (25) Bae, T.-H.; Hudson, M. R.; Mason, J. A.; Queen, W. L.; Dutton, J. J.; Sumida, K.; Micklash, K. J.; Kaye, S. S.; Brown, C. M.; Long, J. R. Evaluation of Cation-Exchanged Zeolite Adsorbents for Post-Combustion Carbon Dioxide Capture. *Energy Env. Sci* **2013**, *6* (1), 128–138. <https://doi.org/10.1039/C2EE23337A>.
- (26) Cheung, O.; Hedin, N. Zeolites and Related Sorbents with Narrow Pores for CO₂ Separation from Flue Gas. *RSC Adv* **2014**, *4* (28), 14480–14494. <https://doi.org/10.1039/C3RA48052F>.
- (27) Lin, L.-C.; Berger, A. H.; Martin, R. L.; Kim, J.; Swisher, J. A.; Jariwala, K.; Rycroft, C. H.; Bhowan, A. S.; Deem, M. W.; Haranczyk, M.; Smit, B. In Silico Screening of Carbon-Capture Materials. *Nat. Mater.* **2012**, *11* (7), 633–641. <https://doi.org/10.1038/nmat3336>.
- (28) Huck, J. M.; Lin, L.-C.; Berger, A. H.; Shahrak, M. N.; Martin, R. L.; Bhowan, A. S.; Haranczyk, M.; Reuter, K.; Smit, B. Evaluating Different Classes of Porous Materials for Carbon Capture. *Energy Environ. Sci.* **2014**, *7* (12), 4132–4146. <https://doi.org/10.1039/C4EE02636E>.
- (29) Brandani, F.; Ruthven, D. M. The Effect of Water on the Adsorption of CO₂ and C₃H₈ on Type X Zeolites. *Ind. Eng. Chem. Res.* **2004**, *43* (26), 8339–8344. <https://doi.org/10.1021/ie040183o>.
- (30) Li, G.; Xiao, P.; Webley, P.; Zhang, J.; Singh, R.; Marshall, M. Capture of CO₂ from High Humidity Flue Gas by Vacuum Swing Adsorption with Zeolite 13X. *Adsorption* **2008**, *14* (2–3), 415–422. <https://doi.org/10.1007/s10450-007-9100-y>.
- (31) Lee, K. B.; Sircar, S. Removal and Recovery of Compressed CO₂ from Flue Gas by a Novel Thermal Swing Chemisorption Process. *AIChE J.* **2008**, *54* (9), 2293–2302. <https://doi.org/10.1002/aic.11531>.
- (32) Cheetham, A. K.; Férey, G.; Loiseau, T. Open-Framework Inorganic Materials. *Angew. Chem. Int. Ed.* **1999**, *38* (22), 3268–3292. [https://doi.org/10.1002/\(SICI\)1521-3773\(19991115\)38:22<3268::AID-ANIE3268>3.0.CO;2-U](https://doi.org/10.1002/(SICI)1521-3773(19991115)38:22<3268::AID-ANIE3268>3.0.CO;2-U).
- (33) Bollini, P.; Didas, S. A.; Jones, C. W. Amine-Oxide Hybrid Materials for Acid Gas Separations. *J. Mater. Chem.* **2011**, *21* (39), 15100–15120. <https://doi.org/10.1039/C1JM12522B>.
- (34) Ünveren, E. E.; Monkul, B. Ö.; Sariođlan, Ş.; Karademir, N.; Alper, E. Solid Amine Sorbents for CO₂ Capture by Chemical Adsorption: A Review. *Petroleum* **2017**, *3* (1), 37–50. <https://doi.org/10.1016/j.petlm.2016.11.001>.
- (35) Chen, C.; Kim, J.; Ahn, W.-S. CO₂ Capture by Amine-Functionalized Nanoporous Materials: A Review. *Korean J. Chem. Eng.* **2014**, *31* (11), 1919–1934. <https://doi.org/10.1007/s11814-014-0257-2>.

- (36) Foo, G. S.; Lee, J. J.; Chen, C.-H.; Hayes, S. E.; Sievers, C.; Jones, C. W. Elucidation of Surface Species through in Situ FTIR Spectroscopy of Carbon Dioxide Adsorption on Amine-Grafted SBA-15. *ChemSusChem* **2017**, *10* (1), 266–276. <https://doi.org/10.1002/cssc.201600809>.
- (37) Xu, X.; Song, C.; Miller, B. G.; Scaroni, A. W. Influence of Moisture on CO₂ Separation from Gas Mixture by a Nanoporous Adsorbent Based on Polyethylenimine-Modified Molecular Sieve MCM-41. *Ind. Eng. Chem. Res.* **2005**, *44* (21), 8113–8119. <https://doi.org/10.1021/ie050382n>.
- (38) Pang, S. H.; Lee, L.-C.; Sakwa-Novak, M. A.; Lively, R. P.; Jones, C. W. Design of Aminopolymer Structure to Enhance Performance and Stability of CO₂ Sorbents: Poly(propylenimine) vs Poly(ethylenimine). *J. Am. Chem. Soc.* **2017**, *139* (10), 3627–3630. <https://doi.org/10.1021/jacs.7b00235>.
- (39) Srikanth, C. S.; Chuang, S. S. C. Spectroscopic Investigation into Oxidative Degradation of Silica-Supported Amine Sorbents for CO₂ Capture. *ChemSusChem* **2012**, *5* (8), 1435–1442. <https://doi.org/10.1002/cssc.201100662>.
- (40) Min, K.; Choi, W.; Kim, C.; Choi, M. Oxidation-Stable Amine-Containing Adsorbents for Carbon Dioxide Capture. *Nat. Commun.* **2018**, *9* (1), 726. <https://doi.org/10.1038/s41467-018-03123-0>.
- (41) Dawson, R.; Cooper, A. I.; Adams, D. J. Chemical Functionalization Strategies for Carbon Dioxide Capture in Microporous Organic Polymers. *Polym. Int.* **2013**, *62* (3), 345–352. <https://doi.org/10.1002/pi.4407>.
- (42) Zeng, Y.; Zou, R.; Zhao, Y. Covalent Organic Frameworks for CO₂ Capture. *Adv. Mater.* **2016**, *28* (15), 2855–2873. <https://doi.org/10.1002/adma.201505004>.
- (43) Zou, L.; Sun, Y.; Che, S.; Yang, X.; Wang, X.; Bosch, M.; Wang, Q.; Li, H.; Smith, M.; Yuan, S.; Perry, Z.; Zhou, H.-C. Porous Organic Polymers for Post-Combustion Carbon Capture. *Adv. Mater.* **2017**, *29* (37), 1700229. <https://doi.org/10.1002/adma.201700229>.
- (44) Thomas, J. M. H.; Trewin, A. Amorphous PAF-1: Guiding the Rational Design of Ultraporous Materials. *J. Phys. Chem. C* **2014**, *118* (34), 19712–19722. <https://doi.org/10.1021/jp502336a>.
- (45) Slater, A. G.; Cooper, A. I. Function-Led Design of New Porous Materials. *Science* **2015**, *348* (6238), aaa8075. <https://doi.org/10.1126/science.aaa8075>.
- (46) Celina, M. C. Review of Polymer Oxidation and Its Relationship with Materials Performance and Lifetime Prediction. *Polym. Degrad. Stab.* **2013**, *98* (12), 2419–2429. <https://doi.org/10.1016/j.polymdegradstab.2013.06.024>.
- (47) Li, J.-R.; Kuppler, R. J.; Zhou, H.-C. Selective Gas Adsorption and Separation in Metal–Organic Frameworks. *Chem. Soc. Rev.* **2009**, *38* (5), 1477–1504. <https://doi.org/10.1039/B802426J>.
- (48) Furukawa, H.; Cordova, K. E.; O’Keeffe, M.; Yaghi, O. M. The Chemistry and Applications of Metal–Organic Frameworks. *Science* **2013**, *341* (6149), 1230444. <https://doi.org/10.1126/science.1230444>.
- (49) Li, J.-R.; Ma, Y.; McCarthy, M. C.; Sculley, J.; Yu, J.; Jeong, H.-K.; Balbuena, P. B.; Zhou, H.-C. Carbon Dioxide Capture-Related Gas Adsorption and Separation in Metal–Organic Frameworks. *Coord. Chem. Rev.* **2011**, *255* (15–16), 1791–1823. <https://doi.org/10.1016/j.ccr.2011.02.012>.

- (50) González-Zamora, E.; Ibarra, I. A. CO₂ Capture under Humid Conditions in Metal–Organic Frameworks. *Mater. Chem. Front.* **2017**, *1* (8), 1471–1484. <https://doi.org/10.1039/C6QM00301J>.
- (51) Lin, Y.; Kong, C.; Zhang, Q.; Chen, L. Metal-Organic Frameworks for Carbon Dioxide Capture and Methane Storage. *Adv. Energy Mater.* **2017**, *7* (4), 1601296. <https://doi.org/10.1002/aenm.201601296>.
- (52) Yu, J.; Xie, L.-H.; Li, J.-R.; Ma, Y.; Seminario, J. M.; Balbuena, P. B. CO₂ Capture and Separations Using MOFs: Computational and Experimental Studies. *Chem. Rev.* **2017**, *117* (14), 9674–9754. <https://doi.org/10.1021/acs.chemrev.6b00626>.
- (53) Madden, D. G.; Scott, H. S.; Kumar, A.; Chen, K.-J.; Sanii, R.; Bajpai, A.; Lusi, M.; Curtin, T.; Perry, J. J.; Zaworotko, M. J. Flue-Gas and Direct-Air Capture of CO₂ by Porous Metal–Organic Materials. *Phil Trans R Soc A* **2017**, *375* (2084), 20160025. <https://doi.org/10.1098/rsta.2016.0025>.
- (54) Ding, M.; Flaig, R. W.; Jiang, H.-L.; Yaghi, O. M. Carbon Capture and Conversion Using Metal–Organic Frameworks and MOF-Based Materials. *Chem. Soc. Rev.* **2019**. <https://doi.org/10.1039/C8CS00829A>.
- (55) Liu, J.; Wang, Y.; Benin, A. I.; Jakubczak, P.; Willis, R. R.; LeVan, M. D. CO₂/H₂O Adsorption Equilibrium and Rates on Metal–Organic Frameworks: HKUST-1 and Ni/DOBDC. *Langmuir* **2010**, *26* (17), 14301–14307. <https://doi.org/10.1021/la102359q>.
- (56) Kizzie, A. C.; Wong-Foy, A. G.; Matzger, A. J. Effect of Humidity on the Performance of Microporous Coordination Polymers as Adsorbents for CO₂ Capture. *Langmuir* **2011**, *27* (10), 6368–6373. <https://doi.org/10.1021/la200547k>.
- (57) Yu, J.; Balbuena, P. B. Water Effects on Postcombustion CO₂ Capture in Mg-MOF-74. *J. Phys. Chem. C* **2013**, *117* (7), 3383–3388. <https://doi.org/10.1021/jp311118x>.
- (58) Lin, Y.; Kong, C.; Chen, L. Amine-Functionalized Metal–Organic Frameworks: Structure, Synthesis and Applications. *RSC Adv.* **2016**, *6* (39), 32598–32614. <https://doi.org/10.1039/C6RA01536K>.
- (59) Emerson, A. J.; Chahine, A.; Batten, S. R.; Turner, D. R. Synthetic Approaches for the Incorporation of Free Amine Functionalities in Porous Coordination Polymers for Enhanced CO₂ Sorption. *Coord. Chem. Rev.* **2018**, *365*, 1–22. <https://doi.org/10.1016/j.ccr.2018.02.012>.
- (60) Burtch, N. C.; Jasuja, H.; Walton, K. S. Water Stability and Adsorption in Metal–Organic Frameworks. *Chem. Rev.* **2014**, *114* (20), 10575–10612. <https://doi.org/10.1021/cr5002589>.
- (61) Bloch, E. D.; Murray, L. J.; Queen, W. L.; Chavan, S.; Maximoff, S. N.; Bigi, J. P.; Krishna, R.; Peterson, V. K.; Grandjean, F.; Long, G. J.; Smit, B.; Bordiga, S.; Brown, C. M.; Long, J. R. Selective Binding of O₂ over N₂ in a Redox–Active Metal–Organic Framework with Open Iron(II) Coordination Sites. *J. Am. Chem. Soc.* **2011**, *133* (37), 14814–14822. <https://doi.org/10.1021/ja205976v>.
- (62) Cozzolino, A. F.; Brozek, C. K.; Palmer, R. D.; Yano, J.; Li, M.; Dincă, M. Ligand Redox Non-Innocence in the Stoichiometric Oxidation of Mn₂(2,5-dioxidoterephthalate) (Mn-MOF-74). *J. Am. Chem. Soc.* **2014**, *136* (9), 3334–3337. <https://doi.org/10.1021/ja411808r>.
- (63) Zhang, Z.; Wang, Y.; Jia, X.; Yang, J.; Li, J. The Synergistic Effect of Oxygen and Water on the Stability of the Isostructural Family of Metal–Organic Frameworks [Cr₃(BTC)₂]

- and $[\text{Cu}_3(\text{BTC})_2]$. *Dalton Trans.* **2017**, 46 (44), 15573–15581. <https://doi.org/10.1039/C7DT02957H>.
- (64) Tu, B.; Pang, Q.; Xu, H.; Li, X.; Wang, Y.; Ma, Z.; Weng, L.; Li, Q. Reversible Redox Activity in Multicomponent Metal–Organic Frameworks Constructed from Trinuclear Copper Pyrazolate Building Blocks. *J. Am. Chem. Soc.* **2017**, 139 (23), 7998–8007. <https://doi.org/10.1021/jacs.7b03578>.
- (65) Vitillo, J. G.; Bordiga, S. Increasing the Stability of $\text{Mg}_2(\text{dobpdc})$ Metal–Organic Framework in Air through Solvent Removal. *Mater Chem Front* **2017**, 1 (3), 444–448. <https://doi.org/10.1039/C6QM00220J>.
- (66) Mondal, M. K.; Balsora, H. K.; Varshney, P. Progress and Trends in CO_2 Capture/Separation Technologies: A Review. *Energy* **2012**, 46 (1), 431–441. <https://doi.org/10.1016/j.energy.2012.08.006>.
- (67) Yang, L.; Ge, X.; Wan, C.; Yu, F.; Li, Y. Progress and Perspectives in Converting Biogas to Transportation Fuels. *Renew. Sustain. Energy Rev.* **2014**, 40, 1133–1152. <https://doi.org/10.1016/j.rser.2014.08.008>.
- (68) Burgers, W. F. J.; Northrop, P. S.; Kheshgi, H. S.; Valencia, J. A. Worldwide Development Potential for Sour Gas. *Energy Procedia* **2011**, 4 (Supplement C), 2178–2184. <https://doi.org/10.1016/j.egypro.2011.02.104>.
- (69) Dlugokencky, E.; Tans, P. ESRL Global Monitoring Division - Global Greenhouse Gas Reference Network www.esrl.noaa.gov/gmd/ccgg/trends/ (accessed Jan 25, 2017).
- (70) Wang, Y.; LeVan, M. D. Adsorption Equilibrium of Binary Mixtures of Carbon Dioxide and Water Vapor on Zeolites 5A and 13X. *J. Chem. Eng. Data* **2010**, 55 (9), 3189–3195. <https://doi.org/10.1021/je100053g>.
- (71) Liu, J.; Wang, Y.; Benin, A. I.; Jakubczak, P.; Willis, R. R.; LeVan, M. D. $\text{CO}_2/\text{H}_2\text{O}$ Adsorption Equilibrium and Rates on Metal–Organic Frameworks: HKUST-1 and Ni/DOBDC. *Langmuir* **2010**, 26 (17), 14301–14307. <https://doi.org/10.1021/la102359q>.
- (72) Liu, J.; Benin, A. I.; Furtado, A. M. B.; Jakubczak, P.; Willis, R. R.; LeVan, M. D. Stability Effects on CO_2 Adsorption for the DOBDC Series of Metal–Organic Frameworks. *Langmuir* **2011**, 27 (18), 11451–11456. <https://doi.org/10.1021/la201774x>.
- (73) McDonald, T. M.; Lee, W. R.; Mason, J. A.; Wiers, B. M.; Hong, C. S.; Long, J. R. Capture of Carbon Dioxide from Air and Flue Gas in the Alkylamine-Appended Metal–Organic Framework $\text{mmen-Mg}_2(\text{dobpdc})$. *J. Am. Chem. Soc.* **2012**, 134 (16), 7056–7065. <https://doi.org/10.1021/ja300034j>.
- (74) McDonald, T. M.; Mason, J. A.; Kong, X.; Bloch, E. D.; Gygi, D.; Dani, A.; Crocellà, V.; Giordanino, F.; Odoh, S. O.; Drisdell, W. S.; Vlasisavljevich, B.; Dzubak, A. L.; Poloni, R.; Schnell, S. K.; Planas, N.; Lee, K.; Pascal, T.; Wan, L. F.; Prendergast, D.; Neaton, J. B.; Smit, B.; Kortright, J. B.; Gagliardi, L.; Bordiga, S.; Reimer, J. A.; Long, J. R. Cooperative Insertion of CO_2 in Diamine-Appended Metal–Organic Frameworks. *Nature* **2015**, 519 (7543), 303–308. <https://doi.org/10.1038/nature14327>.
- (75) Milner, P. J.; Siegelman, R. L.; Forse, A. C.; Gonzalez, M. I.; Runčevski, T.; Martell, J. D.; Reimer, J. A.; Long, J. R. A Diaminopropane-Appended Metal–Organic Framework Enabling Efficient CO_2 Capture from Coal Flue Gas via a Mixed Adsorption Mechanism. *J. Am. Chem. Soc.* **2017**, 139 (38), 13541–13553. <https://doi.org/10.1021/jacs.7b07612>.
- (76) Liao, P.-Q.; Chen, H.; Zhou, D.-D.; Liu, S.-Y.; He, C.-T.; Rui, Z.; Ji, H.; Zhang, J.-P.; Chen, X.-M. Monodentate Hydroxide as a Super Strong yet Reversible Active Site for

- CO₂ Capture from High-Humidity Flue Gas. *Energy Environ. Sci.* **2015**, *8* (3), 1011–1016. <https://doi.org/10.1039/C4EE02717E>.
- (77) Flaig, R. W.; Osborn Popp, T. M.; Fracaroli, A. M.; Kapustin, E. A.; Kalmutzki, M. J.; Altamimi, R. M.; Fathieh, F.; Reimer, J. A.; Yaghi, O. M. The Chemistry of CO₂ Capture in an Amine-Functionalized Metal–Organic Framework under Dry and Humid Conditions. *J. Am. Chem. Soc.* **2017**, *139* (35), 12125–12128. <https://doi.org/10.1021/jacs.7b06382>.
- (78) Kim, C.; Cho, H. S.; Chang, S.; Cho, S. J.; Choi, M. An Ethylenediamine-Grafted Y Zeolite: A Highly Regenerable Carbon Dioxide Adsorbent via Temperature Swing Adsorption without Urea Formation. *Energy Environ. Sci.* **2016**, *9* (5), 1803–1811. <https://doi.org/10.1039/C6EE00601A>.
- (79) Jadhav, P. D.; Chatti, R. V.; Biniwale, R. B.; Labhsetwar, N. K.; Devotta, S.; Rayalu, S. S. Monoethanol Amine Modified Zeolite 13X for CO₂ Adsorption at Different Temperatures. *Energy Fuels* **2007**, *21* (6), 3555–3559. <https://doi.org/10.1021/ef070038y>.
- (80) Fisher, J. C.; Tanthana, J.; Chuang, S. S. C. Oxide-supported Tetraethylenepentamine for CO₂ Capture. *Environ. Prog. Sustain. Energy* **2009**, *28* (4), 589–598. <https://doi.org/10.1002/ep.10363>.
- (81) Su, F.; Lu, C.; Kuo, S.-C.; Zeng, W. Adsorption of CO₂ on Amine-Functionalized Y-Type Zeolites. *Energy Fuels* **2010**, *24* (2), 1441–1448. <https://doi.org/10.1021/ef901077k>.
- (82) Nguyen, T. H.; Kim, S.; Yoon, M.; Bae, T.-H. Hierarchical Zeolites with Amine-Functionalized Mesoporous Domains for Carbon Dioxide Capture. *ChemSusChem* **2016**, *9* (5), 455–461. <https://doi.org/10.1002/cssc.201600004>.
- (83) Rezaei, F.; Jones, C. W. Stability of Supported Amine Adsorbents to SO₂ and NO_x in Postcombustion CO₂ Capture. 1. Single-Component Adsorption. *Ind. Eng. Chem. Res.* **2013**, *52* (34), 12192–12201. <https://doi.org/10.1021/ie4019116>.
- (84) Rezaei, F.; Jones, C. W. Stability of Supported Amine Adsorbents to SO₂ and NO_x in Postcombustion CO₂ Capture. 2. Multicomponent Adsorption. *Ind. Eng. Chem. Res.* **2014**, *53* (30), 12103–12110. <https://doi.org/10.1021/ie502024z>.
- (85) Khatri, R. A.; Chuang, S. S. C.; Soong, Y.; Gray, M. Thermal and Chemical Stability of Regenerable Solid Amine Sorbent for CO₂ Capture. *Energy Fuels* **2006**, *20* (4), 1514–1520. <https://doi.org/10.1021/ef050402y>.
- (86) Sjostrom, S.; Krutka, H. Evaluation of Solid Sorbents as a Retrofit Technology for CO₂ Capture. *Fuel* **2010**, *89* (6), 1298–1306. <https://doi.org/10.1016/j.fuel.2009.11.019>.
- (87) Uyanga, I. J.; Idem, R. O. Studies of SO₂- and O₂-Induced Degradation of Aqueous MEA during CO₂ Capture from Power Plant Flue Gas Streams. *Ind. Eng. Chem. Res.* **2007**, *46* (8), 2558–2566. <https://doi.org/10.1021/ie0614024>.
- (88) Mangano, E.; Kahr, J.; Wright, P. A.; Brandani, S. Accelerated Degradation of MOFs under Flue Gas Conditions. *Faraday Discuss.* **2016**, *192* (0), 181–195. <https://doi.org/10.1039/C6FD00045B>.
- (89) Bhattacharyya, S.; Han, R.; Kim, W.-G.; Chiang, Y.; Jayachandrababu, K. C.; Hungerford, J. T.; Dutzer, M. R.; Ma, C.; Walton, K. S.; Sholl, D. S.; Nair, S. Acid Gas Stability of Zeolitic Imidazolate Frameworks: Generalized Kinetic and Thermodynamic Characteristics. *Chem. Mater.* **2018**, *30* (12), 4089–4101. <https://doi.org/10.1021/acs.chemmater.8b01394>.
- (90) Rouf, S. A.; Eić, M. Adsorption of SO₂ from Wet Mixtures on Hydrophobic Zeolites. *Adsorption* **1998**, *4* (1), 25–33. <https://doi.org/10.1023/A:1008883219403>.

- (91) Sjoström, S.; Durham, M.; Bustard, C. J.; Martin, C. Activated Carbon Injection for Mercury Control: Overview. *Fuel* **2010**, *89* (6), 1320–1322. <https://doi.org/10.1016/j.fuel.2009.11.016>.
- (92) Siegelman, R. L.; Milner, P. J.; Kim, E. J.; Weston, S. C.; Long, J. R. Challenges and Opportunities for Adsorption-Based CO₂ Capture from Natural Gas Combined Cycle Emissions. *Energy Environ. Sci.* **2019**, *Advance Article*. <https://doi.org/10.1039/C9EE00505F>.
- (93) *World Energy Outlook 2018*; International Energy Agency, 2018. <https://doi.org/10.1787/weo-2018-en>.
- (94) Bollini, P.; Choi, S.; Drese, J. H.; Jones, C. W. Oxidative Degradation of Aminosilica Adsorbents Relevant to Postcombustion CO₂ Capture. *Energy Fuels* **2011**, *25* (5), 2416–2425. <https://doi.org/10.1021/ef200140z>.
- (95) *Biomass Energy and Carbon Capture and Storage (BECCS): Unlocking Negative Emissions*, First edition.; Gough, C., Thornley, P., Mander, S., Vaughan, N., Falano, T., Eds.; John Wiley & Sons: Hoboken, NJ, 2018.
- (96) Kemper, J. Biomass and Carbon Dioxide Capture and Storage: A Review. *Int. J. Greenh. Gas Control* **2015**, *40*, 401–430. <https://doi.org/10.1016/j.ijggc.2015.06.012>.
- (97) Rufford, T. E.; Smart, S.; Watson, G. C. Y.; Graham, B. F.; Boxall, J.; Diniz da Costa, J. C.; May, E. F. The Removal of CO₂ and N₂ from Natural Gas: A Review of Conventional and Emerging Process Technologies. *J. Pet. Sci. Eng.* **2012**, *94* (Supplement C), 123–154. <https://doi.org/10.1016/j.petrol.2012.06.016>.
- (98) Schweigkofler, M.; Niessner, R. Removal of Siloxanes in Biogases. *J. Hazard. Mater.* **2001**, *83* (3), 183–196. [https://doi.org/10.1016/S0304-3894\(00\)00318-6](https://doi.org/10.1016/S0304-3894(00)00318-6).
- (99) Shang, J.; Li, G.; Singh, R.; Gu, Q.; Nairn, K. M.; Bastow, T. J.; Medhekar, N.; Doherty, C. M.; Hill, A. J.; Liu, J. Z.; Webley, P. A. Discriminative Separation of Gases by a “Molecular Trapdoor” Mechanism in Chabazite Zeolites. *J. Am. Chem. Soc.* **2012**, *134* (46), 19246–19253. <https://doi.org/10.1021/ja309274y>.
- (100) First, E. L.; Hasan, M. M. F.; Floudas, C. A. Discovery of Novel Zeolites for Natural Gas Purification through Combined Material Screening and Process Optimization. *AIChE J.* **2014**, *60* (5), 1767–1785. <https://doi.org/10.1002/aic.14441>.
- (101) Braun, E.; Zurhelle, A. F.; Thijssen, W.; Schnell, S. K.; Lin, L.-C.; Kim, J.; Thompson, J. A.; Smit, B. High-Throughput Computational Screening of Nanoporous Adsorbents for CO₂ Capture from Natural Gas. *Mol. Syst. Des. Eng.* **2016**, *1* (2), 175–188. <https://doi.org/10.1039/C6ME00043F>.
- (102) Chaemchuen, S.; Kabir, N. A.; Zhou, K.; Verpoort, F. Metal–Organic Frameworks for Upgrading Biogas via CO₂ Adsorption to Biogas Green Energy. *Chem. Soc. Rev.* **2013**, *42* (24), 9304–9332. <https://doi.org/10.1039/C3CS60244C>.
- (103) Belmabkhout, Y.; Bhatt, P. M.; Adil, K.; Pillai, R. S.; Cadiau, A.; Shkurenko, A.; Maurin, G.; Gongping, L.; Koros, W. J.; Eddaoudi, M. Natural Gas Upgrading Using a Fluorinated MOF with Tuned H₂S and CO₂ Adsorption Selectivity. *Nat. Energy* **2018**, *1*. <https://doi.org/10.1038/s41560-018-0267-0>.
- (104) Joshi, J. N.; Zhu, G.; Lee, J. J.; Carter, E. A.; Jones, C. W.; Lively, R. P.; Walton, K. S. Probing Metal–Organic Framework Design for Adsorptive Natural Gas Purification. *Langmuir* **2018**, *34* (29), 8443–8450. <https://doi.org/10.1021/acs.langmuir.8b00889>.

- (105) Quan, W.; Wang, X.; Song, C. Selective Removal of H₂S from Biogas Using Solid Amine-Based “Molecular Basket” Sorbent. *Energy Fuels* **2017**, *31* (9), 9517–9528. <https://doi.org/10.1021/acs.energyfuels.7b01473>.
- (106) Kuznicki, S. M.; Bell, V. A.; Nair, S.; Hillhouse, H. W.; Jacubinas, R. M.; Braunbarth, C. M.; Toby, B. H.; Tsapatsis, M. A Titanosilicate Molecular Sieve with Adjustable Pores for Size-Selective Adsorption of Molecules. *Nature* **2001**, *412* (6848), 720–724. <https://doi.org/10.1038/35089052>.
- (107) *Technology Roadmap - Carbon Capture and Storage in Industrial Applications*; International Energy Agency and United Nations Industrial Development Organization, 2011.
- (108) Leeson, D.; Mac Dowell, N.; Shah, N.; Petit, C.; Fennell, P. S. A Techno-Economic Analysis and Systematic Review of Carbon Capture and Storage (CCS) Applied to the Iron and Steel, Cement, Oil Refining and Pulp and Paper Industries, as Well as Other High Purity Sources. *Int. J. Greenh. Gas Control* **2017**, *61*, 71–84. <https://doi.org/10.1016/j.ijggc.2017.03.020>.
- (109) Hills, T.; Leeson, D.; Florin, N.; Fennell, P. Carbon Capture in the Cement Industry: Technologies, Progress, and Retrofitting. *Environ. Sci. Technol.* **2016**, *50* (1), 368–377. <https://doi.org/10.1021/acs.est.5b03508>.
- (110) Nelson, T. O.; Coleman, L. J. I.; Mobley, P.; Kataria, A.; Tanthana, J.; Lesemann, M.; Bjerge, L.-M. Solid Sorbent CO₂ Capture Technology Evaluation and Demonstration at Norcem’s Cement Plant in Brevik, Norway. *Energy Procedia* **2014**, *63*, 6504–6516. <https://doi.org/10.1016/j.egypro.2014.11.686>.
- (111) Wilcox, J.; Haghpanah, R.; Rupp, E. C.; He, J.; Lee, K. Advancing Adsorption and Membrane Separation Processes for the Gigaton Carbon Capture Challenge. *Annu. Rev. Chem. Biomol. Eng.* **2014**, *5* (1), 479–505. <https://doi.org/10.1146/annurev-chembioeng-060713-040100>.
- (112) Lu, W.; Sculley, J. P.; Yuan, D.; Krishna, R.; Zhou, H.-C. Carbon Dioxide Capture from Air Using Amine-Grafted Porous Polymer Networks. *J. Phys. Chem. C* **2013**, *117* (8), 4057–4061. <https://doi.org/10.1021/jp311512q>.
- (113) Liu, J.; Wei, Y.; Zhao, Y. Trace Carbon Dioxide Capture by Metal–Organic Frameworks. *ACS Sustain. Chem. Eng.* **2019**, *7* (1), 82–93. <https://doi.org/10.1021/acssuschemeng.8b05590>.
- (114) Pang, S. H.; Lively, R. P.; Jones, C. W. Oxidatively-Stable Linear Poly(propylenimine)-Containing Adsorbents for CO₂ Capture from Ultradilute Streams. *ChemSusChem* **2018**, *11* (15), 2628–2637. <https://doi.org/10.1002/cssc.201800438>.
- (115) Wang, T.; Lackner, K. S.; Wright, A. Moisture Swing Sorbent for Carbon Dioxide Capture from Ambient Air. *Environ. Sci. Technol.* **2011**, *45* (15), 6670–6675. <https://doi.org/10.1021/es201180v>.
- (116) Li, W.; Choi, S.; Drese, J. H.; Hornbostel, M.; Krishnan, G.; Eisenberger, P. M.; Jones, C. W. Steam-Stripping for Regeneration of Supported Amine-Based CO₂ Adsorbents. *ChemSusChem* **2010**, *3* (8), 899–903. <https://doi.org/10.1002/cssc.201000131>.
- (117) Sakwa-Novak, M. A.; Jones, C. W. Steam Induced Structural Changes of a Poly(ethylenimine) Impregnated γ -Alumina Sorbent for CO₂ Extraction from Ambient Air. *ACS Appl. Mater. Interfaces* **2014**, *6* (12), 9245–9255. <https://doi.org/10.1021/am501500q>.

- (118) Min, K.; Choi, W.; Choi, M. Macroporous Silica with Thick Framework for Steam-Stable and High-Performance Poly(ethyleneimine)/Silica CO₂ Adsorbent. *ChemSusChem* **2017**, *10* (11), 2518–2526. <https://doi.org/10.1002/cssc.201700398>.
- (119) Potter, M. E.; Lee, J. J.; Darunte, L. A.; Jones, C. W. Exploring Steam Stability of Mesoporous Alumina Species for Improved Carbon Dioxide Sorbent Design. *J. Mater. Sci.* **2019**, *54* (10), 7563–7575. <https://doi.org/10.1007/s10853-019-03418-7>.
- (120) Sujan, A. R.; Pang, S. H.; Zhu, G.; Jones, C. W.; Lively, R. P. Direct CO₂ Capture from Air Using Poly(ethylenimine)-Loaded Polymer/Silica Fiber Sorbents. *ACS Sustain. Chem. Eng.* **2019**, *7* (5), 5264–5273. <https://doi.org/10.1021/acssuschemeng.8b06203>.
- (121) Darunte, L.; Sen, T.; Bhawanani, C.; Walton, K. S.; Sholl, D. S.; Realff, M. J.; Jones, C. W. Moving Beyond Adsorption Capacity in Design of Adsorbents for CO₂ Capture from Ultra-Dilute Feeds: Kinetics of CO₂ Adsorption in Materials with Stepped Isotherms. *Ind. Eng. Chem. Res.* **2019**, *58* (1), 366–377. <https://doi.org/10.1021/acs.iecr.8b05042>.
- (122) Miller, D. C.; Syamlal, M.; Mebane, D. S.; Storlie, C.; Bhattacharyya, D.; Sahinidis, N. V.; Agarwal, D.; Tong, C.; Zitney, S. E.; Sarkar, A.; Sun, X.; Sundaresan, S.; Ryan, E.; Engel, D.; Dale, C. Carbon Capture Simulation Initiative: A Case Study in Multiscale Modeling and New Challenges. *Annu. Rev. Chem. Biomol. Eng.* **2014**, *5* (1), 301–323. <https://doi.org/10.1146/annurev-chembioeng-060713-040321>.
- (123) DeWitt, S. J. A.; Sinha, A.; Kalyanaraman, J.; Zhang, F.; Realff, M. J.; Lively, R. P. Critical Comparison of Structured Contactors for Adsorption-Based Gas Separations. *Annu. Rev. Chem. Biomol. Eng.* **2018**, *9* (1), 129–152. <https://doi.org/10.1146/annurev-chembioeng-060817-084120>.
- (124) Assen, N. von der; Voll, P.; Peters, M.; Bardow, A. Life Cycle Assessment of CO₂ Capture and Utilization: A Tutorial Review. *Chem. Soc. Rev.* **2014**, *43* (23), 7982–7994. <https://doi.org/10.1039/C3CS60373C>.
- (125) Cuéllar-Franca, R. M.; Azapagic, A. Carbon Capture, Storage and Utilisation Technologies: A Critical Analysis and Comparison of Their Life Cycle Environmental Impacts. *J. CO₂ Util.* **2015**, *9*, 82–102. <https://doi.org/10.1016/j.jcou.2014.12.001>.
- (126) Sathre, R.; Masanet, E. Prospective Life-Cycle Modeling of a Carbon Capture and Storage System Using Metal–Organic Frameworks for CO₂ Capture. *RSC Adv.* **2013**, *3* (15), 4964–4975. <https://doi.org/10.1039/C3RA40265G>.
- (127) Zhai, H.; Rubin, E. S.; Versteeg, P. L. Water Use at Pulverized Coal Power Plants with Postcombustion Carbon Capture and Storage. *Environ. Sci. Technol.* **2011**, *45* (6), 2479–2485. <https://doi.org/10.1021/es1034443>.

Chapter 2. Controlling Cooperative CO₂ Adsorption in Diamine-Appended Mg₂(dobpdc) Metal–Organic Frameworks

2.1. Introduction

With the atmospheric CO₂ concentration now exceeding 400 ppm,¹ rapid implementation of carbon management strategies will be essential to limit further rise in the average global temperature. The energy sector alone accounts for 68% of global anthropogenic greenhouse gas emissions, including more than 32 Gt of CO₂ per year.² While decarbonization of the energy sector will ultimately require long-term restructuring of current energy systems, emission mitigation strategies are needed in the near term to minimize the environmental impact of the existing energy infrastructure.³ Carbon capture and sequestration, in which CO₂ is selectively removed from point sources such as the flue gas of power plants, has been proposed as a particularly promising emission mitigation strategy.⁴ As a complementary approach, separating CO₂ from crude gas reserves can favor greater production and use of natural gas, which is nearly half as emission intensive as coal on a tons of carbon per terajoule basis.⁵ In a third strategy, removal of CO₂ from crude biogas could enable greater adoption of biomethane as a renewable fuel.⁶ Each of these strategies requires materials capable of efficiently capturing CO₂ from a variety of gas mixtures over a wide range of temperatures and pressures. As a result, a tunable CO₂ capture material would be highly desirable to maximize the energy efficiency of each individual process through a coupled optimization of adsorbent design and process engineering.

Aqueous amine absorbers, dating to the 1930s, remain the most mature technology available for large-scale CO₂ separations.⁷ Despite their advanced state of development, these solutions suffer from inherent limitations arising from thermal and oxidative amine degradation as well as corrosion issues, which necessitate the use of dilute amine solutions that possess low working capacities for CO₂.⁸ Furthermore, while thermal integration and the development of new amines enable a moderate degree of flexibility in targeting specific CO₂ separations, future advances are anticipated to afford only incremental savings in the regeneration energy of absorption-based processes.⁹

Recently, solid adsorbents with large working capacities and inherently lower regeneration energy requirements have shown promise in significantly reducing the energetic and economic costs of CO₂ separations.^{10,11} In particular, amine-functionalized adsorbents, as with aqueous amine solutions, leverage Lewis acid–base chemistry between CO₂ and amines to form ammonium carbamate or bicarbonate species. These reactions enable highly selective binding of CO₂ from gas mixtures even in the presence of water, which typically passivates adsorbents relying on exposed metal ions as binding sites.¹²

Metal–organic frameworks, a class of crystalline, porous materials consisting of metal ions or clusters bridged by organic ligands, offer the potential to incorporate the desirable properties of amine-based CO₂ capture in highly modular systems with well-defined binding sites.^{13–17} Specifically, the grafting of alkyldiamines onto frameworks bearing coordinatively unsaturated metal centers has been demonstrated as an effective approach to realize strong and selective binding of CO₂.^{18–29} This strategy led to the recent discovery of an exceptional set of diamine-appended adsorbents, mmen–M₂(dobpdc) (mmen = *N,N'*-dimethylethylenediamine; M = Mg, Mn, Fe, Co, Zn; dobpdc⁴⁻ = 4,4'-dioxidobiphenyl-3,3'-dicarboxylate) (Figure 2.1a), that exhibit step-shaped CO₂ adsorption isotherms.^{21,23} Unlike conventional Langmuir-type adsorption, significant CO₂ adsorption in mmen–M₂(dobpdc) occurs only above a critical partial pressure that dramatically increases with temperature. This switch-like adsorption behavior enables

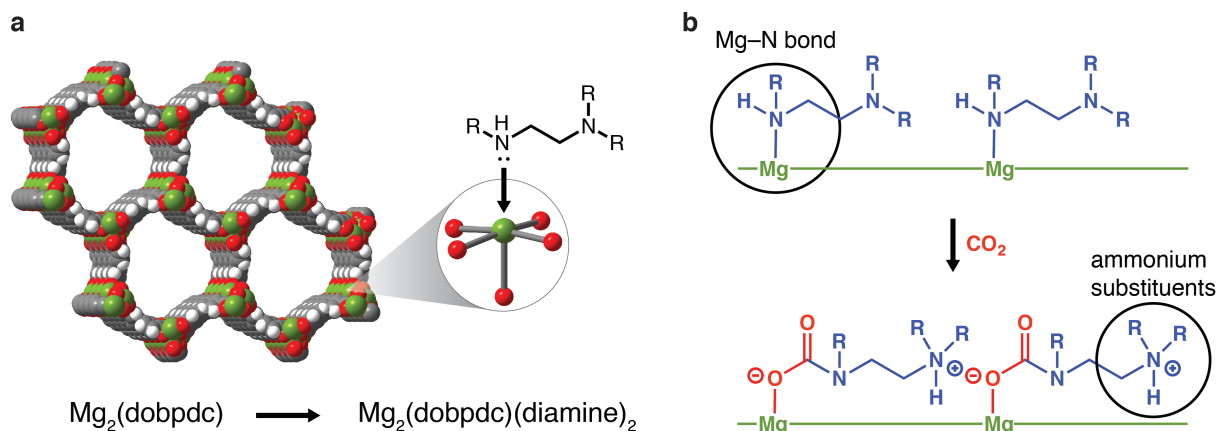


Figure 2.1. (a) Representative structure of the metal–organic framework $Mg_2(dobpdc)$. Green, red, gray, and white spheres represent Mg, O, C, and H atoms, respectively. The inset shows a single open Mg^{II} site appended with a diamine molecule. (b) Depiction of cooperative CO_2 insertion into a row of Mg^{II} –diamine sites to form ammonium carbamate chains along the pore axis. The threshold conditions for cooperative adsorption can be tuned by modifying the diamine structure to adjust the strength of the metal–amine bond and the ammonium carbamate ion-pairing interaction.

separations in which the full CO_2 capacity of the material can be accessed using a minimal temperature swing for each adsorption/desorption cycle.

Remarkably, CO_2 binds in these materials through cooperative insertion into the metal–amine bonds to form ammonium carbamate chains.^{23,30} As a result, the adsorption step pressure can be tuned by altering the metal–amine bond strength. Specifically, varying the framework metal(II) cations led to a shift in step pressure following the order $Mg < Mn < Fe < Zn < Co$,²³ consistent with the anticipated metal–ligand bond strengths for divalent, octahedral metal complexes.³¹ However, this approach to developing tunable CO_2 adsorbents is limited by the range of metals with which the framework can be synthesized. In addition, at industrial scale, the flexibility of this strategy is further restricted to metals for which precursor salts can be sourced economically.

As an alternative strategy, the appended diamine can be varied to change the position of the CO_2 adsorption step.^{22,24,28,29} We envisioned that this approach would provide a straightforward and versatile route to a broader library of adsorbents tailored to specific CO_2 capture applications. This method further enables the adsorption step pressure to be tuned for a specific metal variant of $M_2(dobpdc)$. To maximize the ultimate industrial viability of the adsorbents, we focused our efforts on the base framework $Mg_2(dobpdc)$ due to the low cost of Mg^{II} precursor salts, the stability and scalability of the material, and the high gravimetric capacities achievable with the resulting diamine-appended adsorbents.

Recognizing that the cooperative adsorption threshold is dictated by the relative stability of the amine-bound and CO_2 -inserted phases, we sought to probe the influence of the diamine structure on the strength of both the metal–amine bond and the ammonium carbamate ion-pairing interaction (Figure 2.1b). Here, we present the evaluation of nine diamine-appended $Mg_2(dobpdc)$ frameworks using thermogravimetric analysis and a custom-made, high-throughput, volumetric gas adsorption instrument.¹² Structural insight from *in situ* single-crystal X-ray diffraction experiments with the isostructural zinc frameworks further revealed precise correlations between diamine structure and the cooperative CO_2 adsorption properties of these materials. Altogether, these studies outline the critical principles for the design of diamine-

appended metal–organic frameworks with adsorption properties optimized for specific CO₂ separations.

2.2. Experimental Procedures

2.2.1. General Synthesis and Characterization Methods

The compound 4,4'-dihydroxy-(1,1'-biphenyl)-3,3'-dicarboxylic acid (H₄dobpdc) was either obtained from Combi-Blocks and purified by recrystallization from a 3:1 (v:v) acetone:water mixture or synthesized as previously reported.³² All other reagents and solvents were obtained from commercial suppliers at reagent grade purity or higher and were used without further purification. Ultrahigh purity (99.999%) He and N₂ and research grade (99.998%) CO₂ were used for all adsorption experiments. Elemental analyses were conducted at the Microanalytical Laboratory of the University of California, Berkeley, using a PerkinElmer 2400 Series II combustion analyzer.

2.2.2. Synthesis of Mg₂(dobpdc)

The framework Mg₂(dobpdc) was synthesized by a solvothermal method scaled from a previous report.²³ The ligand H₄dobpdc (9.89 g, 36.1 mmol) and Mg(NO₃)₂·6H₂O (11.5 g, 44.9 mmol) were dissolved in 200 mL of a 55:45 (v:v) methanol:*N,N*-dimethylformamide (DMF) mixture using sonication. The solution was filtered to remove any undissolved particulates and added to a 350 mL glass pressure vessel with a glass stirbar. The reactor was sealed with a Teflon cap and heated in a silicone oil bath at 120 °C for 20 h. The crude white powder was isolated by filtration and soaked three times in 200 mL of DMF for a minimum of 3 h at 60 °C, followed by solvent exchange by soaking three times in 200 mL of methanol for a minimum of 3 h at 60 °C. The methanol-solvated framework was collected by filtration and heated *in vacuo* or under flowing N₂ for 12 h at 250 °C to yield fully desolvated Mg₂(dobpdc) as a white powder. Combustion elemental analysis calculated for C₁₄H₆O₆Mg₂: C, 52.74; H, 1.90. Found: C, 53.00; H, 1.56. Representative Langmuir surface areas, powder X-ray diffraction patterns, and infrared spectra are presented in Figures 2.S1, 2.S2 and 2.S5.

2.2.3. Synthesis of Diamine-Appended Mg₂(dobpdc) Frameworks

Samples of diamine-appended Mg₂(dobpdc) frameworks used for collection of high-throughput isotherm data were prepared following conditions reported previously.²³ For each analogue, a solution of 20% (v/v) diamine in toluene was stirred over freshly ground CaH₂, and a quantity corresponding to a 10-fold molar excess of diamine per metal site was added to approximately 100 mg of desolvated Mg₂(dobpdc) under N₂ by syringe or cannula transfer. The slurry was sonicated for 15 min under N₂ and left undisturbed under N₂ for a minimum of 12 h. The solid was then isolated by filtration in air and washed with 30 mL of dry toluene followed by 30 mL of dry hexanes at room temperature. Prior to adsorption measurements, the samples were desolvated by heating *in vacuo* at 120 °C for 12 h.

For all subsequent experiments, it was found that identical CO₂ adsorption performance could be achieved through direct diamine-grafting of methanol-solvated Mg₂(dobpdc), enabling rapid sample preparation by eliminating time-consuming activation of the parent framework. In this rapid procedure, approximately 30 mg of methanol-solvated Mg₂(dobpdc) was isolated by

filtration, washed with 30 mL of toluene, and submerged in 5 mL of a 20% (v/v) solution of diamine in toluene. After 12 h, the solid was isolated by filtration and washed with 30 mL of fresh toluene to remove excess diamine.

Powder X-ray diffraction patterns, infrared spectra, and representative diamine loadings obtained from NMR spectra upon digestion of the material are presented in Figures 2.S3 and 2.S4 and Table 2.S2.

2.2.4. Synthesis of Zn₂(dobpdc) Single Crystals

In a 20 mL vial, H₄dobpdc (23 mg, 0.084 mmol) was dissolved in 2.8 mL of dimethylacetamide (DMA). In a second 20 mL vial, Zn(NO₃)₂·6H₂O (62 mg, 0.21 mmol) was dissolved in a mixture of 2.8 mL of ethanol and 2.8 mL of water. Several thick-walled borosilicate tubes were each charged with 0.2 mL of ligand stock solution and 0.4 mL of Zn stock solution. The resulting reaction solutions (10 mM H₄dobpdc, 2.5 equiv Zn(NO₃)₂·6H₂O, 0.6 mL of 1:1:1 (v:v:v) DMA:ethanol:water) were degassed by four freeze–pump–thaw cycles, after which the tubes were flame-sealed and placed in an oven preheated to 100 °C. After 48 h, pale yellow, needle-shaped crystals suitable for single-crystal X-ray diffraction had formed. The crystals were transferred from the reaction solution to a 10 mL Schlenk flask, sealed under N₂, and soaked three times in 10 mL of dry DMA for a minimum of 3 h, followed by three times in 10 mL of dry methanol for a minimum of 3 h at room temperature. The solution was replaced three times with 10 mL of dry toluene, and the toluene-suspended crystals were degassed by four freeze–pump–thaw cycles. The crystals were then transferred to a N₂-filled glovebox and stored under dry toluene until use.

2.2.5. Synthesis of Diamine-Appended Zn₂(dobpdc) Single Crystals

Samples of Zn₂(dobpdc) crystals were removed from the glovebox under 2 mL of toluene in individual 4 mL vials. For each analogue, 12 µL of the desired diamine was added to the vial, which was then left undisturbed for 4 h. Excess diamine was removed by decanting and washing three times with fresh toluene. For crystals appended with 1°/2° diamines, the crystals were transferred to plastic centrifuge tubes prior to addition of diamine to avoid adhesion of the crystals to the borosilicate glass. The toluene-solvated crystals were analyzed by single-crystal X-ray diffraction within 24 h of preparation.

2.2.6. Gas Dosing of Diamine-Appended Zn₂(dobpdc) Single Crystals

For CO₂-inserted structures of Zn₂(dobpdc) appended with *N,N'*-dimethylethylenediamine (m-2-m), *N,N'*-diethylethylenediamine (e-2-e), and *N*-isopropylethylenediamine (i-2), diamine-appended crystals were first soaked in hexanes or diethyl ether to facilitate removal of residual toluene from the pores. A single crystal was then mounted on a MiTeGen loop using a minimal amount of epoxy, taking care to avoid the ends of the rod-shaped crystals to preserve access to the hexagonal pores for gas diffusion. The sample was then transferred to a custom-made gas cell consisting of a quartz capillary with a vacuum-tight O-ring seal and Beswick ball valves for gas dosing.³³ Within the cell, the crystal was desolvated under reduced pressure for 45 min at an external temperature of 50 °C using an Oxford Cryosystems cryostream and a turbomolecular pump. After solving the structure to confirm removal of residual solvent from the pores, the

crystal was cooled to 25 °C, dosed with 1 bar of CO₂, and rapidly cooled to 195 K for the final data collection.

To obtain CO₂-inserted X-ray single-crystal structures of Zn₂(dobpdc) appended with *N*-methylethylenediamine (m-2) and *N*-ethylethylenediamine (e-2), single crystals were first washed with dry hexanes, transferred to a glass measurement tube sealed with a Micromeritics *TranSeal*, and heated *in vacuo* at 100 °C (m-2) or 50 °C (e-2) for 1 h on an ASAP 2420 gas adsorption instrument. The sample was then transferred air-free to the analysis port of the instrument and dosed with 1.1 bar of CO₂. The tube was sealed under CO₂, removed from the manifold, and stored over dry ice for 3 h. The crystals were coated with Paratone oil immediately after the tube was opened, and a single crystal was rapidly mounted and flash-cooled to 100 K using an Oxford Cryosystems cryostream prior to data collection.

2.2.7. Single-Crystal X-ray Diffraction

All single-crystal X-ray diffraction data were collected at Beamline 11.3.1 at the Advanced Light Source, Lawrence Berkeley National Laboratory using synchrotron radiation ($\lambda = 0.7749$, 0.7293, or 0.8856 Å; see Table 2.S4) and a Bruker AXS D8 diffractometer equipped with a Bruker PHOTON 100 CMOS detector. Single-crystal structures of diamine-appended Zn₂(dobpdc) frameworks without CO₂ were collected at 100 K using an Oxford Cryosystems Cryostream 700 Plus. Structures with CO₂ were collected at either 195 K (Zn₂(dobpdc)(m-2-m-CO₂)_{1.5}, Zn₂(dobpdc)(e-2-e)(e-2-e-CO₂), and Zn₂(dobpdc)(i-2)(i-2-CO₂)) or 100 K (Zn₂(dobpdc)(m-2-CO₂)_{1.62} and Zn₂(dobpdc)(e-2-CO₂)_{1.5}). All crystals were refined in space group *P*3₂21 or *P*3₁21 as inversion twins based on Flack parameter values near 0.5. Raw data were corrected for Lorentz and polarization effects using Bruker AXS SAINT software³⁴ and were corrected for absorption using SADABS.³⁵ The structures were solved using SHELXT³⁶ and refined using SHELXL³⁷ operated in the OLEX2³⁸ interface. Thermal parameters were refined anisotropically for all non-hydrogen atoms. All hydrogen atoms were placed geometrically and refined using a riding model.

For structures without CO₂, the appended diamines were found to be disordered over a minimum of two positions. The reported formula and final refinement were fixed to reflect the freely refined occupancy of each diamine. However, the occupancy of the bound nitrogen was fixed at 1 to account for solvent or water bound on sites where the diamine was absent. Similarly, for CO₂-inserted structures, the occupancy of the bound oxygen of the carbamate was fixed at 1 to account for CO₂, solvent, or water where the ammonium carbamate chains were absent, but the reported formula reflects the oxygen content for the freely refined ammonium carbamate chains alone. Displacement parameter restraints (RIGU and SIMU) and distance restraints (SADI, and in select cases DFIX) were necessary to model disorder of the free diamines and the ammonium carbamate chains.

2.2.8. Thermogravimetric Analysis

Thermogravimetric analyses (TGA) were conducted using a TA Instruments TGA Q5000 with a flow rate of 25 mL/min for all gases. Masses were uncorrected for buoyancy effects. For isobars under 100% CO₂, samples were first activated under flowing N₂ at 120–150 °C for 30 min, after which the temperature was rapidly increased to the highest plotted temperature for each adsorption (cooling) isobar. The gas was then switched to 100% CO₂ and the mass normalized to 0. Cooling and heating rates of 1 °C/min were used for isobars unless otherwise

specified. For *N,N*-diisopropylethylenediamine (ii-2)-appended Mg₂(dobpdc), the sample was held isothermally for 45 min at 30 °C prior to switching from adsorption to desorption. Adsorption isobar step temperatures were determined as the inflection points of the isobars based on the peak of the temperature derivative. Desorption isobar step temperatures were determined as the point of closure of the hysteresis loop (Table 2.S3).

Thermogravimetric decomposition traces were collected under 100% N₂ with a temperature ramp rate of 1.5 °C/min (Figures 2.S7 and 2.S9). Comparison of derivative plots (dT_G, mg/min vs temperature) was performed using data collected from diamine-appended samples prepared from the same batch of Mg₂(dobpdc) (Figure 2.S8).

2.2.9. High-Throughput Gas Adsorption Isotherm Measurements

Adsorption isotherms for CO₂, N₂, and H₂O were collected in parallel for all diamine-appended Mg₂(dobpdc) analogues at 25, 40, 50, 75, 100, and 120 °C using a custom-built, 28-channel volumetric gas adsorption instrument designed by Wildcat Discovery Technologies. Calibration and verification of this instrument have been described in detail in a previous report.¹² Samples were heated *in vacuo* for 12 h at 120 °C prior to collection of each isotherm. Additional experimental details, as well as N₂ and H₂O isotherms, can be found in the Supporting Information (Figures 2.S13 and 2.S14).

2.2.10. Calculation of Differential Enthalpies and Entropies of Adsorption

The differential enthalpy (Δh_{ads}) of cooperative CO₂ adsorption for each diamine-appended Mg₂(dobpdc) framework was calculated from the high-throughput adsorption isotherms using the Clausius–Clapeyron relationship (eq 2.1).³⁹

$$(\ln P)_n = \frac{\Delta h_{\text{ads}}}{RT} + C \quad (2.1)$$

Here, P is the pressure, T is the temperature, R is the universal gas constant, and C is a constant equal to $-\Delta s_{\text{ads}}/R$, where Δs_{ads} is the differential entropy of adsorption.³⁹ Lines of constant loading at $n = 1$ mmol/g (within the cooperative adsorption region) were obtained using linear interpolation for a minimum of three adsorption isotherms over a range of 25–120 °C. (Note that previous studies^{21,23} have shown Δh_{ads} to be relatively constant throughout the cooperative adsorption region.) From the plots of $\ln P$ vs $1/T$, Δh_{ads} and Δs_{ads} were obtained from the slope and y -intercept, respectively. Standard errors were calculated from the deviations of the best-fit lines of constant loading. For ii-2–Mg₂(dobpdc), only two isotherms could be used due to the step pressure exceeding the accessible pressure range at higher temperatures, and thus a comparable standard error could not be obtained in this case. Further details are provided in Table 2.S3.

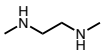
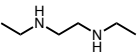
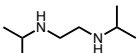
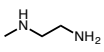
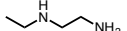
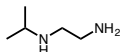
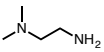
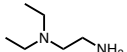
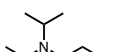
2.3. Results and Discussion

2.3.1. Selection of Diamines and Synthesis of Adsorbents

In this study, nine carefully chosen diamine-appended Mg₂(dobpdc) frameworks were synthesized and analyzed to determine the correlation between the diamine structure and the thermodynamic threshold for cooperative CO₂ adsorption. On the basis of the metal dependence of the adsorption properties in the mmen–M₂(dobpdc) series, we hypothesized that for a given

metal, increasing the metal–amine bond strength would increase the isothermal step pressure for cooperative CO₂ adsorption (or, equivalently, decrease the isobaric step temperature) by stabilizing the amine-bound phase relative to the CO₂-inserted phase. We further postulated that the same effect could be achieved by increasing the steric profile of the unbound amine to decrease the stability of the ammonium carbamate chains. Both of these effects were probed by preparing adsorbents bearing 2°/2°, 1°/2°, and 1°/3° diamines with substituents of varying size. To simplify the nomenclature of this class of adsorbents, a diamine naming scheme was devised following the pattern RR-*n*-R, where each R signifies methyl (m), ethyl (e), or isopropyl (i) substituents on each amine, and *n* indicates the number of carbons on the alkyl bridge connecting the amines (Table 2.1). Note that in order to adsorb CO₂ by cooperative insertion, the diamine must possess at least one proton to form a charge-balancing ammonium cation.

Table 2.1. Diamine structures and nomenclature system.

Diamine name	Structure	Abbreviation
<i>N,N'</i> -dimethylethylenediamine		m-2-m (mmen)
<i>N,N'</i> -diethylethylenediamine		e-2-e
<i>N,N'</i> -diisopropylethylenediamine		i-2-i
<i>N</i> -methylethylenediamine		m-2
<i>N</i> -ethylethylenediamine		e-2
<i>N</i> -isopropylethylenediamine		i-2
<i>N,N</i> -dimethylethylenediamine		mm-2
<i>N,N</i> -diethylethylenediamine		ee-2
<i>N,N</i> -diisopropylethylenediamine		ii-2

The framework Mg₂(dobpdc), an expanded variant of the well-studied framework Mg₂(dobdc)⁴⁰ and an isomer of the isorecticular framework IRMOF-74-II,⁴¹ was readily synthesized on a multigram scale by modification of the previously reported²³ solvothermal reaction of H₄dobpdc with Mg(NO₃)₂·6H₂O in 55:45 MeOH:DMF at 120 °C. After washing the as-synthesized framework with DMF and exchanging the bound solvent with methanol, diamine-appended Mg₂(dobpdc) analogues were rapidly prepared by submerging aliquots of the framework in 20% (v/v) solutions of diamine in toluene. While previous reports of diamine-appended M₂(dobpdc) frameworks stipulated removal of bound solvent molecules by heating *in vacuo* at 250 °C prior to diamine grafting,^{21–24,28} we determined that functionalization with diamines could be achieved directly with methanol-solvated Mg₂(dobpdc). In this activation-free procedure, a greater excess of diamine (~50 equiv per Mg^{II} site) is typically required, as compared to ~10 equiv in the procedure involving activation. However, the synthetic ease of the activation-free procedure enables analysis of a wide array of diamine-appended analogues within a short time period. Furthermore, for large-scale preparations, the excess diamine solution can

easily be recycled, and the activation-free procedure eliminates the need for hazardous diamine drying agents, such as CaH_2 , employed in previous reports.

For all diamine-appended frameworks, completeness of diamine grafting was confirmed by examining the CO_2 saturation loading (discussed below), the ^1H NMR spectra of samples digested in $\text{DCI/DMSO-}d_6$ (Table 2.S2), and the thermogravimetric decomposition curves (Figure 2.S7). Attempts to synthesize the tetramethylethylenediamine-appended framework $\text{mm-2-mm-Mg}_2(\text{dobpdc})$ revealed that diamine loadings higher than 15% could not be achieved, even with addition of a large excess of diamine to the activated framework.

2.3.2. Structural Characterization of Diamine Binding in $\text{M}_2(\text{dobpdc})(\text{diamine})_2$

To understand the influence of the diamine on the stability of the amine-bound phase, we sought to characterize the structure of the diamine-appended frameworks prior to CO_2 adsorption by single-crystal X-ray diffraction. While we were unable to prepare suitable single crystals of the $\text{Mg}_2(\text{dobpdc})$ analogues, we developed a new synthetic route to grow millimeter-sized single crystals of the isostructural Zn framework. These crystals were washed and grafted with diamines following a procedure similar to that implemented for $\text{Mg}_2(\text{dobpdc})$, enabling the characterization of the resulting diamine-appended crystals by single-crystal X-ray diffraction (Figure 2.2).

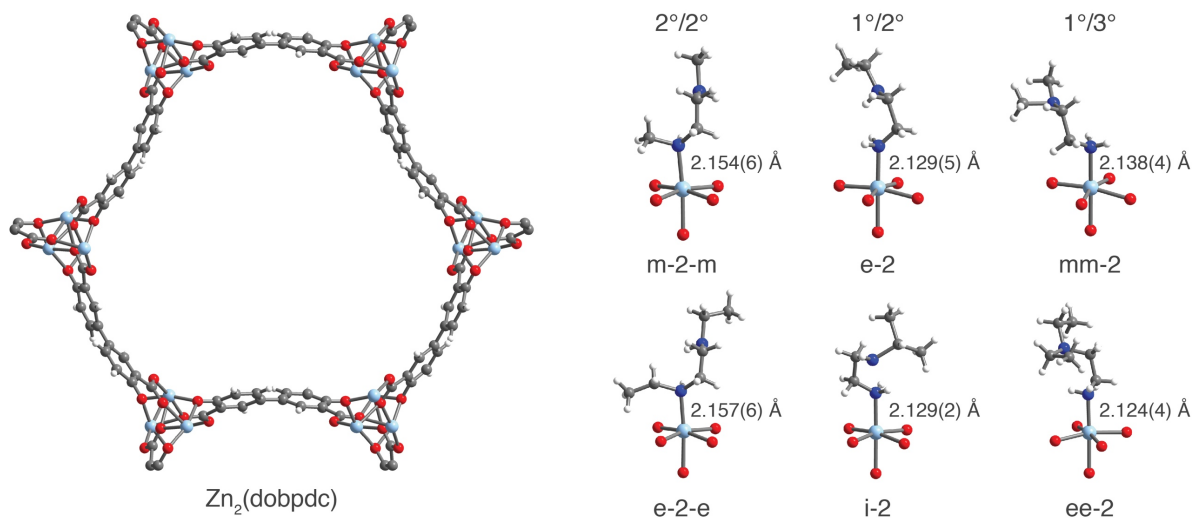


Figure 2.2. Structures of $\text{Zn}_2(\text{dobpdc})$ and toluene-solvated, diamine-appended variants, as determined by single-crystal X-ray diffraction at 100 K. Left: A portion of the crystal structure of $\text{Zn}_2(\text{dobpdc})(\text{DMA})_2$ as viewed along the c axis (N,N -dimethylacetamide molecules have been excluded for clarity). Right: First coordination spheres for the Zn^{II} centers in a series of diamine-appended frameworks examined in this work. Structures were refined as inversion twins in either space group $P3_121$ or $P3_221$, and the diamines were found to be disordered over a minimum of two positions. For clarity, only the dominant conformation is depicted in space group $P3_221$. Light blue, blue, red, gray, and white spheres represent Zn, N, O, C, and H atoms, respectively.

In all cases, disorder of the appended diamine over a minimum of two positions was observed, indicating that the diamines have conformational degrees of freedom within the pores prior to CO_2 insertion. With the exception of m-2, all $1^\circ/2^\circ$ and $1^\circ/3^\circ$ diamines were found to bind exclusively through the primary amine in the 100 K structures. Although the disorder in m-2–

Zn₂(dobpdc) could not be modeled satisfactorily, preliminary refinements suggested the presence of a mixture of primary amine-bound and secondary amine-bound structures.

Diamines bound through a primary amine were found to exhibit Zn–N bond lengths 0.03(1) Å shorter on average than those of diamines bound through a secondary amine, consistent with primary amine-bound diamines possessing greater metal–amine bond strengths. This trend likely results from the decrease in steric repulsion between the framework and coordinated primary amines compared to secondary amines. Within a class of diamines (2°/2°, 1°/2°, or 1°/3°), small differences in Zn–N bond lengths were within the estimated standard deviations.

The influence of M–N bond strength was further investigated through analysis of the thermogravimetric decomposition traces of Mg₂(dobpdc)(diamine)₂ frameworks (Figure 2.S8). For each analogue, the temperature of the maximum rate of diamine volatilization was identified by plotting the derivative of mass loss (dTG, mg/min) with respect to temperature. This T_{\max} was then plotted as a function of diamine boiling point for all alkylethylenediamine–Mg₂(dobpdc) analogues. For 1°/2° and 1°/3° analogues, T_{\max} of diamine volatilization increases linearly from the methyl to ethyl to isopropyl variants. This increased T_{\max} for larger substituents likely arises from the increasing diamine molecular weight and greater van der Waals contacts with the framework. In contrast, for the 2°/2° analogues, T_{\max} of diamine volatilization decreases with increasing diamine boiling point, moving from m-2-m to e-2-e to i-2-i. This finding is consistent with a reduction in metal–amine bond strength upon increasing the substituent size on the metal-bound amine.

2.3.3. Isobaric Characterization of CO₂ Adsorption

Thermogravimetric adsorption isobars enable rapid comparison of cooperative adsorption step temperatures for a variety of diamine structures. The adsorption isobars of the Mg₂(dobpdc)(diamine)₂ series under pure CO₂ at ambient pressure reveal that altering the steric profile of each amine causes dramatic changes in the isobaric threshold temperature for cooperative adsorption (Figure 2.3). In all cases, the frameworks were found to possess sharp, step-shaped adsorption isobars with saturation values consistent with a loading of 1 CO₂ per diamine–Mg^{II} site. For 2°/2° diamines (Figure 2.3a), moving from m-2-m to e-2-e increases the step temperature from 125 °C to 151 °C. The higher cooperative adsorption temperature for the diethyl variant is consistent with a reduced metal–amine bond strength upon functionalization of the bound amine with larger alkyl substituents. By destabilizing the amine-bound phase, the transition to CO₂-inserted, O-bound carbamates becomes favorable at a higher temperature with e-2-e compared to m-2-m. Notably, a second step in the e-2-e–Mg₂(dobpdc) isobar was observed at approximately half occupancy. This second step is the subject of ongoing investigation in our laboratory and can likely be attributed to the formation of a secondary conformation or rearrangement of the ammonium carbamate chains at half occupancy.

Attempts to collect CO₂ adsorption isobars or isotherms for the 2°/2° diisopropylethylenediamine-appended framework i-2-i–Mg₂(dobpdc) were ultimately unsuccessful (Figure 2.S10). While the ¹H NMR spectrum of material digested with DCl in DMSO-*d*₆ indicated up to 70% diamine loading with respect to the quantity of Mg^{II} sites in the framework (Table 2.S2), the diamine was rapidly liberated from the framework upon activation under flowing N₂ or vacuum (Figure 2.S7). This result further supports the conclusion that increasing the substituent size on the metal-bound amine decreases the metal–amine bond strength.

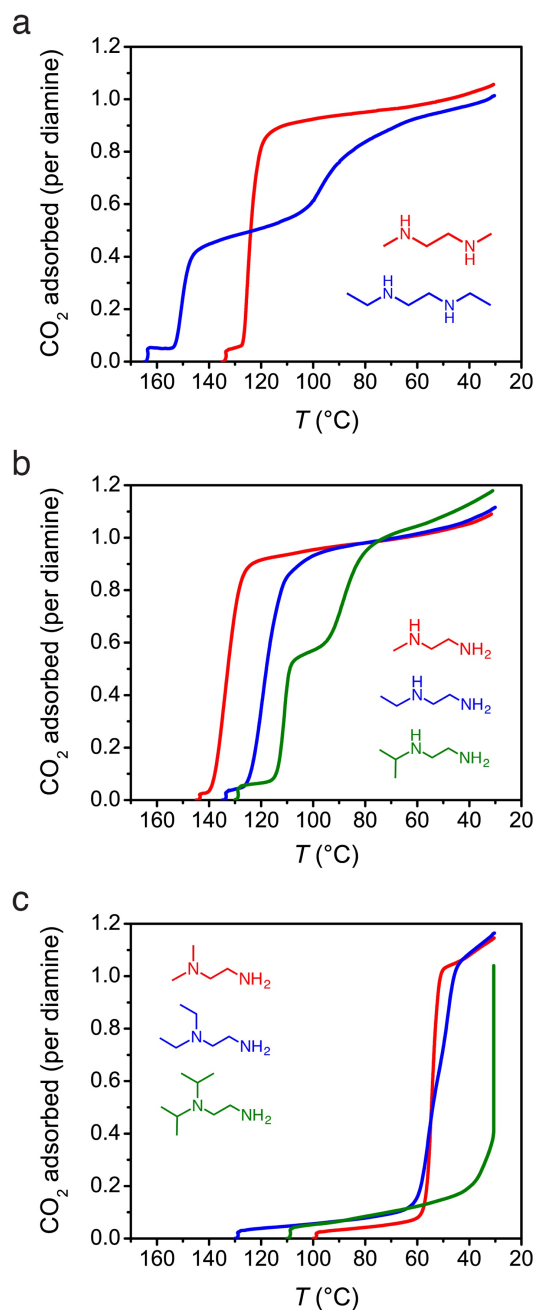


Figure 2.3. Adsorption isobars under pure CO₂ for (a) 2°/2°, (b) 1°/2°, and (c) 1°/3° diamine-appended Mg₂(dobpdc) frameworks, demonstrating the effect of diamine structure on the cooperative adsorption step temperature.

For 1°/2° diamine-appended Mg₂(dobpdc) frameworks (Figure 2.3b), increasing the steric profile of the unbound amine decreases the threshold temperature for cooperative adsorption from 134 °C for m-2 to 120 °C for e-2 and 111 °C for i-2. As with the e-2-e-appended framework, a second adsorption step is apparent for i-2-Mg₂(dobpdc). The steric trend is maintained with 1°/3° diamine-appended Mg₂(dobpdc) frameworks (Figure 2.3c), for which the step temperature decreases to approximately 55 °C for mm-2 and ee-2 and 30 °C for ii-2. The

reduction in step temperature with increasing substituent size is consistent with weaker ammonium carbamate ion pairing upon CO₂ insertion with more sterically encumbered secondary and tertiary amines.

The steric influence of the diamine also accounts for differences in the CO₂ adsorption isobars among 2°/2°, 1°/2°, and 1°/3° diamines bearing substituents of the same size. For example, in the series of ethyl-substituted diamines, the primary amine-bound e-2-Mg₂(dobpdc) decreases the CO₂ step temperature to 120 °C as compared to e-2-e-Mg₂(dobpdc), where the adsorption step occurs at 151 °C. This is likely due to the stronger interaction of the metal with e-2 as compared to e-2-e, which causes CO₂ insertion to become thermodynamically less favorable. For ee-2-Mg₂(dobpdc), the adsorption step temperature is further reduced to approximately 56 °C, consistent with the above observation of lower step temperatures for diamines with larger substituents on the ammonium-forming amine. In general, isobaric step temperatures follow the order 2°/2° > 1°/2° > 1°/3° for a given substituent class (methyl, ethyl, or isopropyl). The adsorbent m-2-Mg₂(dobpdc), which shows a higher threshold temperature than m-2-m-Mg₂(dobpdc), is an exception to this trend and will be discussed in subsequent sections.

2.3.4. X-ray Single-Crystal Structures of CO₂-Inserted Diamine-Appended Frameworks

To better understand the influence of diamine structure on the stability of the ammonium carbamate chains, *in situ* single-crystal X-ray diffraction experiments were conducted using an environmental gas cell³³ designed at Beamline 11.3.1 of the Advanced Light Source (Figure 2.4). While a number of single-crystal structures have been reported characterizing CO₂ binding sites for adsorbents demonstrating Langmuir-type physisorption of CO₂,^{33,42–45} analogous experiments are exceedingly rare for phase-change adsorbents, such as flexible metal–organic frameworks.^{46,47} The dramatic change in unit cell volume that accompanies adsorption-induced phase changes in these materials typically leads to difficulty in maintaining single crystallinity

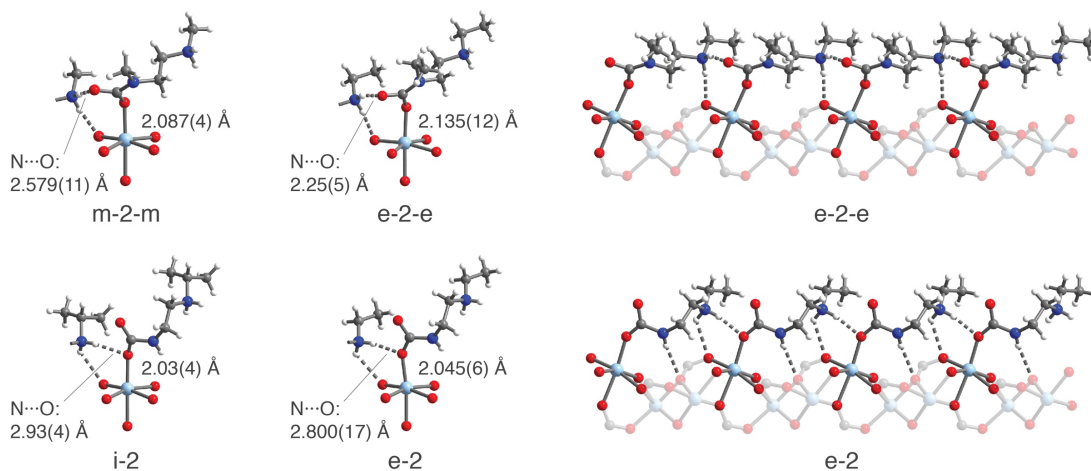


Figure 2.4. Representative structures of CO₂-inserted diamine-appended Zn₂(dobpdc) frameworks as determined by single-crystal X-ray diffraction. Left: First coordination spheres for the Zn^{II} centers in Zn₂(dobpdc)(m-2-m-CO₂)_{1.5}, Zn₂(dobpdc)(e-2-e)(e-2-e-CO₂), and Zn₂(dobpdc)(i-2)(i-2-CO₂) at 195 K and the dominant conformation of Zn₂(dobpdc)(e-2-CO₂)_{1.5} at 100 K. Right: A portion of the ammonium carbamate chains along the pore axis of the material for Zn₂(dobpdc)(e-2-e-CO₂) and Zn₂(dobpdc)(e-2-CO₂)_{1.5}. For clarity, all structures are depicted in space group *P*3₂21. Light blue, blue, red, gray, and white spheres represent Zn, N, O, C, and H atoms, respectively.

throughout the transition. In contrast, diamine-appended analogues of $M_2(\text{dobpdc})$ benefit from the framework acting as a relatively rigid, crystalline scaffold during formation of ammonium carbamate chains, as well as the high degree of order induced by the CO_2 insertion mechanism. These experiments afford unprecedented precision in determining the structural nuances governing the cooperative adsorption process. To the best of our knowledge, these structures, together with the previously reported structure of $\text{Mn}_2(\text{dobpdc})(\text{m-2-m-CO}_2)_2$ obtained by powder X-ray diffraction,²³ represent the only crystallographically characterized examples of chemisorption of CO_2 to form ammonium carbamate species in a porous material.

Single crystals of diamine-appended $\text{Zn}_2(\text{dobpdc})$ frameworks were again used for these experiments, owing to their greater crystallinity compared to the isostructural magnesium frameworks. Importantly, isobaric adsorption measurements with diamine-appended $\text{Zn}_2(\text{dobpdc})$ powders under pure CO_2 confirm that the zinc and magnesium analogues follow the same trends in CO_2 adsorption step temperature (Figure 2.S12). Larger alkyl substituents increase the threshold temperature for $\text{Zn}_2(\text{dobpdc})$ frameworks appended with 2°/2° diamines (55 °C for m-2-m versus >75°C for e-2-e) but decrease the threshold temperature for frameworks with 1°/2° diamines (52 °C for e-2 versus 47 °C for i-2).

The single-crystal structure of CO_2 -dosed m-2-m- $\text{Zn}_2(\text{dobpdc})$ at 195 K shows full insertion of CO_2 into the Zn–N bonds to produce O-bound carbamate species with Zn–O distances of 2.087(4) Å. The unbound carbamate oxygen atom interacts with an ammonium cation from a neighboring diamine, forming an ion pair with an N···O distance of 2.579(11) Å. The structure is in very good agreement with the previously published powder X-ray diffraction structure of m-2-m- $\text{Mn}_2(\text{dobpdc})$, for which Mn–O distances of 2.10(2) Å and N···O distances of 2.61(10) Å were observed.²³ Similar Zn–O distances of 1.919(3)–1.995(4) Å have also been reported for molecular zinc(II) carbamate complexes,^{48–51} and the N···O distances observed here are consistent with those of purely organic ammonium carbamate networks formed from reaction of CO_2 with alkylethylenediamines (N···O distances of 2.664(5)–2.810(2) Å).⁵²

In addition, hydrogen bonding between an ammonium proton and the nonbridging carboxylate oxygen atom of the dobpdc^{4-} ligand was observed with an N···O distance of 2.806(9) Å. The sum of these interactions stabilizes a single, highly-ordered ammonium carbamate chain conformation, in contrast to the significant disorder of the diamine observed in the structure prior to CO_2 insertion. Importantly, space-filling models (Figures 2.S16–2.S19) reveal that m-2-m- $\text{Zn}_2(\text{dobpdc})$ and other diamine-appended analogues maintain significant porosity even following CO_2 insertion, a feature that should facilitate rapid gas diffusion through the pores.

The structure of CO_2 -dosed e-2-e- $\text{Zn}_2(\text{dobpdc})$ at 195 K shows a similar network of electrostatic interactions. In this case, a Zn–O(carbamate) bond length of 2.135(12) Å was observed, which is 0.048(16) Å longer than that of the Zn–O(carbamate) bond with m-2-m. The ammonium carbamate chains refined to an occupancy of 0.501(15), yielding a formula of $\text{Zn}_2(\text{dobpdc})(\text{e-2-e})(\text{e-2-e-CO}_2)$. The ethyl substituents of the ammonium nitrogen atoms appear to overlap in the *ab* plane, which, in conjunction with the apparent second adsorption step in the CO_2 adsorption isobar of e-2-e- $\text{Mg}_2(\text{dobpdc})$ (Figure 2.3a), suggests that a structural rearrangement must occur at half loading to accommodate complete filling (1 CO_2 per diamine) of the CO_2 inserted phase.

We were further able to obtain the first structures showing CO_2 insertion into 1°/2° diamine-appended $\text{Zn}_2(\text{dobpdc})$ frameworks. For e-2- and i-2- $\text{Zn}_2(\text{dobpdc})$, CO_2 inserts into the bond between the metal and the 1° amine, while the secondary amine forms the corresponding

ammonium cation. In both structures, a dominant conformation could be identified and refined to approximately 50% occupancy. The ammonium carbamate chains in these structures exhibit different hydrogen-bonding and ion-pairing networks upon CO₂ insertion compared to those found in the 2°/2° diamine structures. Specifically, the 1°/2° CO₂-inserted structures show ion pairing of the ammonium with the bound oxygen atom of the carbamate instead of the unbound oxygen. The preference for ion-pairing with the bound oxygen may be explained by the ability of these ammonium carbamate chains to approach the framework more closely, due to the absence of substituents on the carbamate-forming amine. As with the ammonium carbamate chains formed by 2°/2° diamines, the chains formed by 1°/2° diamines also interact with the framework through hydrogen bonding of the ammonium with the ligand. An additional hydrogen bonding interaction was identified between the proton on the carbamate nitrogen and the bridging carboxylate oxygen atom of the ligand. These structures suggest that the ammonium carbamate phases of the 1°/2° diamines are more stable than their 2°/2° analogues. However, this is offset by the stronger M–N bond, ultimately resulting in slightly less favorable CO₂ adsorption in these materials.

A second chain conformation with an occupancy of 26.4(1.3)% was found in the CO₂-inserted structure of e-2–Zn₂(dobpdc) (Figure 2.S18). In contrast to the dominant conformation, this chain structure shows an ion-pairing interaction between the ammonium and the unbound carbamate oxygen atom. As a result, the ethyl groups on the ammonium are shifted toward the pore interior, alleviating steric crowding in the *a/b* plane. However, the resulting loss of the hydrogen bonding interaction between the ammonium and the framework ligand likely makes this conformation less energetically favorable. While a second chain conformation could not be identified in the CO₂-inserted structure of i-2–Zn₂(dobpdc), a similar conformational change must occur to accommodate CO₂ loadings of greater than 50% due to the apparent overlap of the isopropyl groups in the *a/b* plane. Furthermore, a secondary conformational shift would explain the second step in the adsorption isobars and isotherms for i-2–Mg₂(dobpdc).

In the structure of CO₂-inserted m-2–Zn₂(dobpdc) at 100 K, two conformations were identified (Figure 2.5). The dominant conformation (51.7(9)% occupancy relative to Zn) is similar to that of e-2 and i-2 but features ion-pairing interactions between the ammonium and both carbamate oxygen atoms (Figure 2.5, bottom). Additionally, a second ammonium carbamate chain conformation was resolved in which the primary amine forms the ammonium and the secondary amine forms the carbamate. In this conformation, refined at 29.2(9)% occupancy, one of the ammonium protons interacts with both the bound oxygen atom of the carbamate of the same site, as well as with the unbound oxygen atom of the neighboring carbamate along the *c* axis (Figure 2.5, top). This conformation is unique among the diamine-appended frameworks investigated in this study and likely forms due to the comparatively small size of m-2. The stabilization of the CO₂-inserted phase resulting from these additional ion-pairing and hydrogen-bonding interactions may explain the increase in adsorption step temperature for m-2–Mg₂(dobpdc) relative to m-2–Mg₂(dobpdc), a deviation from the trend of decreasing step temperature observed for other 1°/2° diamines relative to their 2°/2° counterparts.

Efforts to observe CO₂ insertion crystallographically with 1°/3° diamine-appended frameworks are ongoing. Nonetheless, the step-like CO₂ adsorption behavior of the 1°/3° diamine-appended Mg₂(dobpdc) analogues suggests that they also form ammonium carbamate chains. Further support for CO₂ insertion with 1°/3° analogues is provided by the similar C–O (~1650 cm⁻¹) and C–N (~1330 cm⁻¹) carbamate vibrations in the infrared spectra of CO₂-dosed 1°/3° diamine-appended Mg₂(dobpdc) frameworks compared to the 1°/2° and 2°/2° diamine-

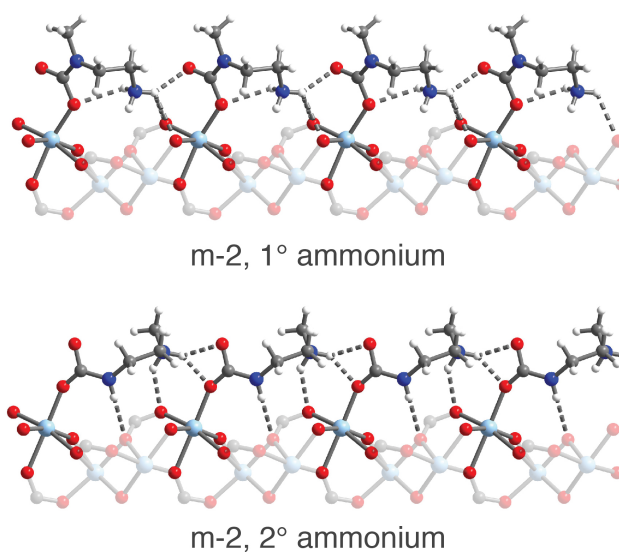


Figure 2.5. Structures of two conformations of the ammonium carbamate chains in $\text{Zn}_2(\text{dobpdc})(\text{m-2-CO}_2)_{1.62}$ at 100 K as determined by single-crystal X-ray diffraction. A primary ammonium forms in the first conformation (top, 29.2(9)% occupancy relative to Zn^{II}), while a secondary ammonium forms in the second conformation (bottom, 51.7(9)% occupancy). Light blue, blue, red, gray, and white spheres represent Zn, N, O, C, and H atoms, respectively.

appended analogues (Figure 2.S6 and Table 2.S1). The envisioned ammonium carbamate chains for $1^\circ/3^\circ$ diamines cannot achieve the hydrogen-bonding interactions observed for the $1^\circ/2^\circ$ and $2^\circ/2^\circ$ diamines between the ammonium or carbamate protons and the oxygen atoms of the ligand. The loss of these interactions is consistent with reduced stability of the ammonium carbamate phase and the resulting lower adsorption step temperatures observed by thermogravimetric analysis (Figure 2.3).

2.3.5. Process Considerations Derived from High-Throughput CO_2 Adsorption Isotherms

Using a custom-built, high-throughput, volumetric adsorption instrument,¹² CO_2 adsorption isotherms were collected at six temperatures for each diamine-appended $\text{Mg}_2(\text{dobpdc})$ analogue. These measurements establish the characteristic range and temperature dependence of the adsorption step pressures for each material at temperatures relevant to typical CO_2 separations, thereby guiding the development and selection of diamine-appended adsorbents for specific capture applications. In addition, N_2 isotherms were collected and confirm the high CO_2/N_2 selectivity of these adsorbents (Figure 2.S13).

The CO_2 adsorption isotherms of the diamine-appended $\text{Mg}_2(\text{dobpdc})$ series (Figures 2.6 and 2.7) demonstrate the wide range of step pressures accessible through systematic modification of the diamine structure. Sharp CO_2 adsorption steps were observed for each analogue, following trends consistent with the isobaric adsorption data. The isotherms highlight the minimal uptake of CO_2 prior to the adsorption step, the defining feature of these materials that gives rise to their high CO_2 adsorption capacities. Desorption isobars under pure CO_2 (Figure 2.S10) confirm that the full capacity of the ammonium carbamate chains can be accessed to yield high gravimetric capacities on the order of 3.5–4.0 mmol/g for the adsorbents in this work. These gravimetric

capacities correspond to volumetric capacities of 79–84 v/v, as calculated using the crystallographic densities.⁵³

To design a promising cooperative adsorbent for a target application, the partial pressure of CO₂ in the target gas stream must first be considered, as this will dictate the upper bound for the CO₂ adsorption step pressure at the temperature of interest. However, the cooperative adsorption step must be positioned at a sufficiently low pressure for capture to occur at the lowest concentration needed to achieve the desired capture rate or product gas purity. Importantly, this concern is intrinsic to all materials possessing step-shaped isotherms, as these materials will cease adsorption as soon as the adsorbate partial pressure in the bed drops below the threshold pressure for adsorption.

As an example, any material that saturates with CO₂ at a pressure below 150 mbar will be able to bind CO₂ from a stream of coal flue gas containing 150 mbar of CO₂. However, in order to capture 90% of the CO₂ from this stream, the adsorbent must possess a step that enables CO₂ insertion at a partial pressure as low as 10% of 150 mbar, or 15 mbar, at the target adsorption temperature. Likewise, achieving 90% CO₂ capture from a natural gas flue gas stream containing 40 mbar of CO₂ requires adsorption at a CO₂ partial pressure of 4 mbar. At the standard adsorption temperature of 40 °C, the coal and natural gas 90% capture conditions are satisfied by each of the 1°/2° diamines, which possess 40 °C step pressures of <0.2, <0.7, and <1 mbar for m-2-, e-2-, and i-2-Mg₂(dobpdc), respectively, as determined from the inflection points within the adsorption step. In addition, desorption isobars of CO₂-saturated 1°/2° diamine-appended frameworks indicate that these materials can be fully regenerated under a flow of pure CO₂ at

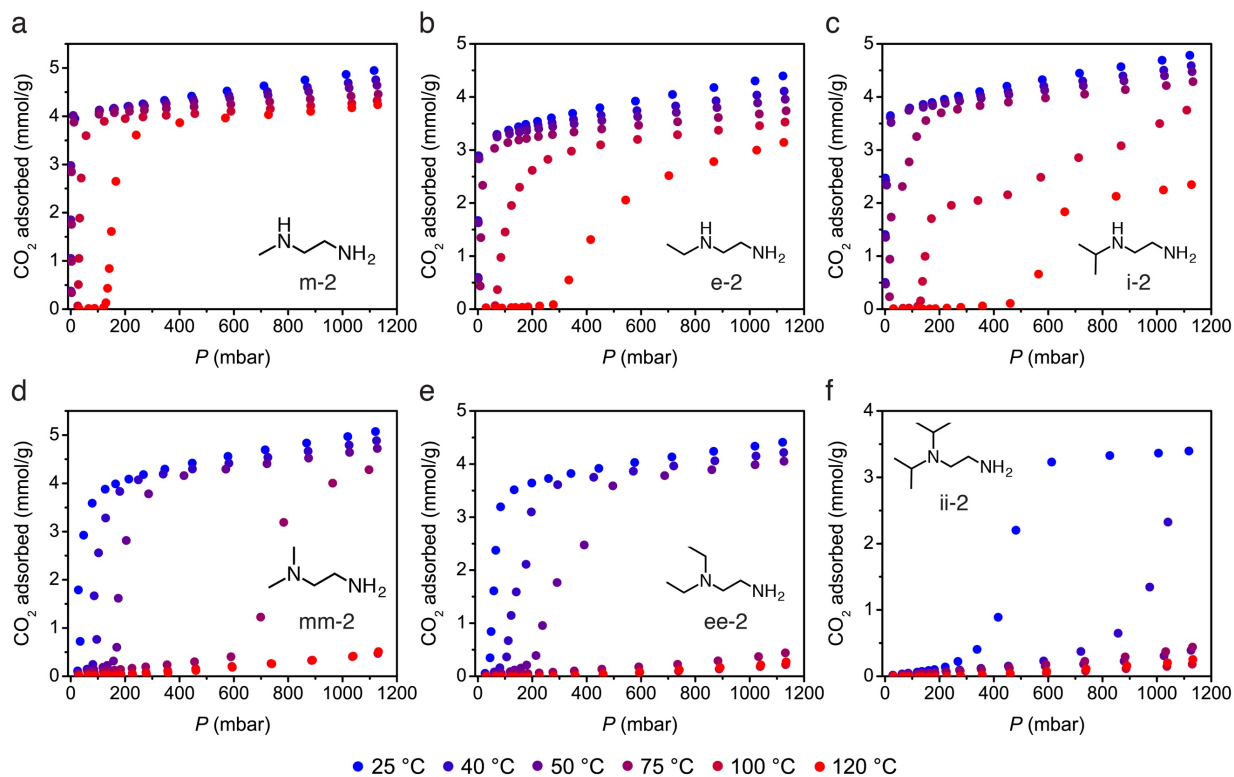


Figure 2.6. High-throughput CO₂ adsorption isotherms over a range of 25–120 °C for the 1°/2° and 1°/3° diamine-appended Mg₂(dobpdc) frameworks examined in this work.

temperatures of 148, 134, and 123 °C for m-2-, e-2-, and i-2-Mg₂(dobpdc), respectively (Figure 2.S10, Table 2.S3). These moderate regeneration temperatures underscore the potential utility of these materials in temperature swing adsorption processes.

For the 1°/3° diamines, the isothermal cooperative threshold pressures are greatly increased compared to 2°/2° and 1°/2° diamines, owing to the combined stabilization of the amine-bound phase (stronger metal-amine bond) and destabilization of the product phase (weaker ion pairing). At 40 °C, the frameworks mm-2- and ee-2-Mg₂(dobpdc) display step pressures of approximately 100 mbar, while that of ii-2-Mg₂(dobpdc) is close to 1 bar. Desorption isobars indicate that mm-2-, ee-2-, and ii-2-Mg₂(dobpdc) can be regenerated at 88, 73, and 68 °C, respectively under pure CO₂ (Figure 2.S10, Table 2.S3). Desorption at temperatures below 100 °C allows the use of much lower quality steam for thermal regeneration of these materials, enabling significant energy savings. The low desorption temperature of mm-2-Mg₂(dobpdc) led to its prior evaluation for separation of CO₂ from coal flue gas.²⁴ However, these 1°/3° diamine-appended frameworks can only achieve a maximum of 33% capture from a coal flue gas stream at 40 °C. As a result, practical use of these adsorbents is limited to cases where a lower capture rate is acceptable or where an inlet stream at lower temperature or higher CO₂ partial pressure

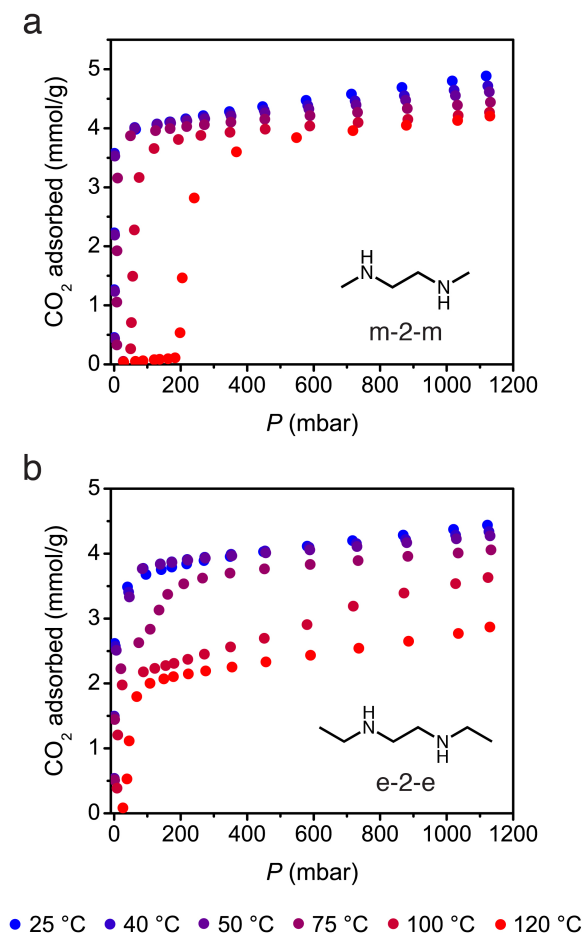


Figure 2.7. High-throughput CO₂ adsorption isotherms over a range of 25 to 120 °C for m-2-m- and e-2-e-Mg₂(dobpdc).

can be obtained.

As an additional advantage, frameworks appended with 1°/3° diamines exhibit reduced water uptake in the absence of CO₂ compared to frameworks appended with 2°/2° and 1°/2° diamines (Figure 2.S14). Therefore, modification of the diamine structure allows control not only over the threshold for CO₂ adsorption but also over the hydrophobicity of the framework pores. Importantly, previous multicomponent equilibrium experiments under simulated coal flue gas confirmed that cooperative CO₂ adsorption is preserved in these materials in the presence of water.¹² By segregating the CO₂ and H₂O binding sites and minimizing water coadsorption, significant savings in regeneration energy can thus be achieved with diamine-appended frameworks by diminishing the energetic costs associated with desorption of large quantities of water between cycles. Moving forward, additional multicomponent experiments under realistic mixed-gas conditions will be a central focus in advancing these materials toward specific applications, as single-component isotherms on the diamine-bound phase may not adequately reflect the affinity of other species in a mixture for the CO₂-inserted phase.

The CO₂ adsorption isotherms for m-2-m-Mg₂(dobpdc) reported here display step positions in good agreement with those observed previously (Figure 2.7a).^{21,23} For e-2-e-Mg₂(dobpdc), destabilization of the amine-bound phase reduces the CO₂ insertion step pressure for the first step by an order of magnitude at each temperature, with step pressures of approximately 1, 10, and 50 mbar occurring at 75, 100, and 120 °C, respectively (Figure 2.7b). Thus, adsorbents capable of scrubbing CO₂ at ultradilute concentrations can be designed through the use of sterically encumbered amines that facilitate weak dative metal–amine interactions. Indeed, the ability of m-2-m-Mg₂(dobpdc) to capture CO₂ from air (400 ppm) has been demonstrated previously,²¹ and the lower step pressures of e-2-e-Mg₂(dobpdc) would enable an increased capture rate from air or capture from streams containing even lower partial pressures of CO₂.

Calculation of equivalent energy (MJ/kg of CO₂ captured and compressed to 150 bar) as a function of the adsorption partial pressure of CO₂ indicates that energies on the order of 1.1 MJ/kg CO₂ can be achieved with 2°/2° and 1°/2° diamine-appended frameworks for dilute CO₂ streams (Figure 2.S15a,b, Table 2.S3). For more concentrated CO₂ streams (> 120 mbar CO₂), equivalent energies approaching 0.5 MJ/kg CO₂ captured may be possible with 1°/3° diamine-appended Mg₂(dobpdc) frameworks (Figure 2.S15c, Table 2.S3). Considering CO₂ capture from a supercritical coal-fired power plant as an example, these numbers compare favorably with the Department of Energy baseline for absorption-based capture with the amine solution Cansolv,⁵⁴ for which an analogous calculation yields an equivalent energy of 0.935 MJ/kg CO₂ for capture over the range from 128.8 to 16.3 mbar of CO₂ (Figure 2.S15).

Novel process configurations that leverage the step-shaped adsorption within these materials may afford further savings in regeneration energy. For example, while Langmuir-type adsorbents require adsorption at the lowest possible temperature to maximize the working capacity, cooperative adsorbents can operate at higher adsorption temperatures, with the maximum adsorption temperature dictated by the desired CO₂ capture rate and purity. Pressure and vacuum swing adsorption processes may likewise afford savings in regeneration energy as well as decreased cycle times. The potential engineering advantages of these materials have already received attention,²⁷ and we and others are exploring additional process configurations to achieve further reductions in the capital and operating costs of CO₂ capture.

2.3.6. Thermodynamics of CO₂ Adsorption

Characterization of the thermodynamics of CO₂ adsorption in these materials imparts further insight on the influence of diamine structure on cooperative adsorption and provides key parameters necessary for industrial applications. The differential enthalpies and entropies of cooperative CO₂ adsorption (Δh_{ads} and Δs_{ads}) for the diamine-appended Mg₂(dobpdc) series were obtained using the Clausius–Clapeyron relationship. For each framework, lines at a constant loading of 1 mmol/g (0.2–0.3 mmol of CO₂/mmol of Mg) were calculated across all temperatures by linear interpolation within the CO₂ isotherm step. Plotting the corresponding pressures and temperatures as $\ln P$ vs $1/T$ afforded the differential enthalpy and entropy of adsorption from the slope and y-intercept, respectively, of the resulting lines.

As shown in Figure 2.8 and Table 2.S3, more exothermic CO₂ adsorption correlates with more negative adsorption entropies. As $|\Delta h_{\text{ads}}|$ increases, the ammonium carbamate units in the CO₂-inserted phase interact more strongly with one another and with the framework walls, leading to a greater loss of entropy upon CO₂ adsorption. Similar compensating effects have been observed previously for both gas adsorption^{55,56} and a number of other chemical processes.⁵⁷ Furthermore, large $|\Delta h_{\text{ads}}|$ values were found to correlate with lower step pressures, a result consistent with the need to offset the larger gas-phase entropy of CO₂ at low pressures.

Relative to the 2°/2° diamines, the 1°/2° diamines show an increase in the stability of the CO₂-inserted phase due to the additional hydrogen-bonding interactions, as observed crystallographically. However, the 1°/2° diamines also show increased Mg–N bond strengths relative to the 2°/2° frameworks. The combined stabilization of the amine-bound and CO₂-bound phases leads to similar $-\Delta h_{\text{ads}}$ and $-\Delta s_{\text{ads}}$ values for 1°/2° and 2°/2° analogues. For the 1°/3° frameworks, stabilization of the amine-bound phase and destabilization of the ammonium carbamate ion pairing results in the lowest $|\Delta h_{\text{ads}}|$ and $|\Delta s_{\text{ads}}|$ values (and thus the highest CO₂ adsorption step pressures) of the series.

Beyond demonstrating the enthalpy–entropy tradeoff for CO₂ adsorption in diamine-appended frameworks, these plots can be used to illustrate thermodynamic cutoffs for specific separation and capture targets. At equilibrium,

$$\Delta g_{\text{ads}} = RT \ln \left(\frac{p}{p_0} \right) \quad (2.2)$$

Here, Δg_{ads} is the free energy of adsorption, R is the universal gas constant, p is the partial pressure of CO₂, and $p_0 = 1$ bar is the reference pressure. Using this relationship, the Δg_{ads} required to achieve a target separation can be determined from the adsorption temperature T and minimum adsorption partial pressure p , which in turn is determined from the inlet CO₂ concentration and desired capture rate. Using the relation

$$\Delta g_{\text{ads}} = \Delta h_{\text{ads}} - T \Delta s_{\text{ads}} \quad (2.3),$$

lines of constant Δg_{ads} and T can be drawn on the enthalpy–entropy correlation plot as a visual guide for predicting the viability of an adsorbent for a given process. An example is shown in Figure 2.8, where a line of $\Delta g_{\text{ads}} = -10.9$ kJ/mol has been drawn to represent the target differential enthalpy and entropy needed to achieve 90% CO₂ capture from coal flue gas (step pressure of 15 mbar at 40 °C). Adsorbents above this line, including all 2°/2° and 1°/2° diamine-appended frameworks explored in this work, are predicted to meet the separation target, while those below the line will fall short of the 90% CO₂ capture rate. Similar analyses can be performed for other mixtures of interest, such as natural gas flue gas (see Table 2.S3). Materials that fall on the line will operate with the highest thermodynamic efficiency in a given process by

minimizing the regeneration energy. Importantly, for diamine-appended frameworks, energetic savings can be achieved not only by modifying the adsorbent structure to match the target Δg_{ads} but also by modifying the process configuration (for example, increasing the adsorption temperature) to shift the Δg_{ads} line toward the known adsorbent points.

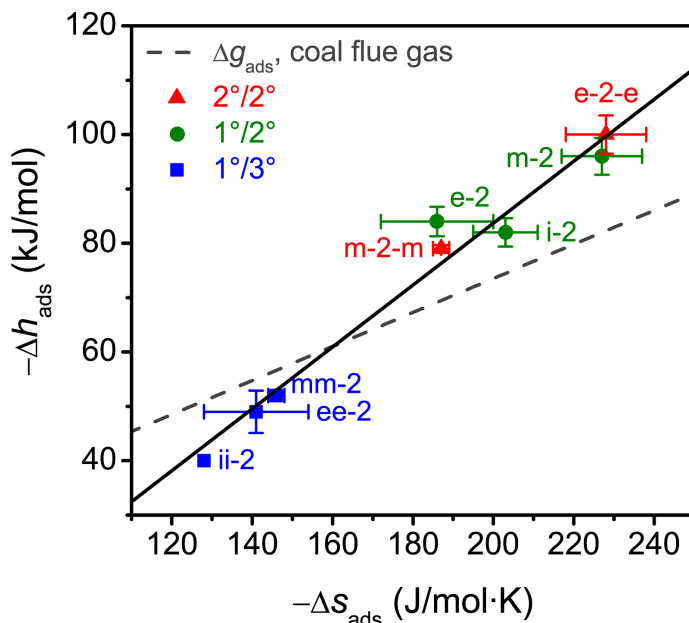


Figure 2.8. Plot of the differential enthalpy (Δh_{ads}) vs. differential entropy (Δs_{ads}) of CO_2 adsorption for alkylethylenediamine-appended $\text{Mg}_2(\text{dobpdc})$ frameworks, as calculated using a Clausius–Clapeyron relationship at a loading of 1 mmol/g (within the first step of the cooperative adsorption region) for isotherms over a range of 25–120 °C. A black line is provided to guide the eye, suggesting enthalpy–entropy compensation for cooperative CO_2 adsorption in this class of materials. (We note that statistical significance of the apparent linear correlation has not been definitively proven in this case.) Materials above the dashed gray line are predicted to be capable of capturing >90% of the CO_2 from a coal flue gas stream (15% CO_2 in N_2 at 40 °C and a total pressure of 1 bar).

2.4. Conclusions

The foregoing results demonstrate that variation of the diamine structure can be used to control cooperative CO_2 adsorption in diamine-appended $\text{M}_2(\text{dobpdc})$ frameworks. Gas adsorption measurements coupled with *in situ* single-crystal X-ray diffraction experiments enabled identification of the principal structural features that influence CO_2 adsorption. First, steric bulk on the metal-bound amine leads to lower step pressures by destabilizing the diamine-bound phase. Second, adding substituents on the terminal amine increases the step pressure due to weaker ion-pairing interactions within ammonium carbamate chains formed upon CO_2 insertion. Third, specific ion-pairing and hydrogen-bonding interactions stabilize the CO_2 -inserted phase and consequently decrease the threshold pressure for cooperative CO_2 adsorption. These structural considerations result in a compensating effect between the differential enthalpy and entropy of adsorption, as revealed by thermodynamic analysis of the gas adsorption isotherms of these materials.

The structural and thermodynamic relationships identified here allow the selection or design of diamine-appended frameworks with CO_2 step positions ideally suited to minimize the energy

consumed in a temperature or pressure swing process. In ongoing work, we are studying the application of these materials to specific CO₂ separations, including CO₂ capture from flue gases, biogas, and crude methane streams. Critically, we are working to characterize all parameters necessary for complete process modeling, with particular attention to the kinetics of adsorption and the stability of these materials to cycling in the presence of water and other impurities. We further anticipate that these materials will afford engineering opportunities to design new process configurations, such as high-temperature operation, to maximize the utility of the cooperative adsorption mechanism.

2.5. Acknowledgements

This chapter is a permitted reproduction of the following article: Siegelman, R. L.; McDonald, T. M.; Gonzalez, M. I.; Martell, J. D.; Milner, P. J.; Mason, J. A.; Berger, A. H.; Bhowm, A. S.; Long, J. R. Controlling Cooperative CO₂ Adsorption in Diamine-Appended Mg₂(dobpdc) Metal–Organic Frameworks. *J. Am. Chem. Soc.* **2017**, *139* (30), 10526–10538. <https://doi.org/10.1021/jacs.7b05858>. Copyright 2017, American Chemical Society.

Materials synthesis and collection of adsorption data were funded by the Advanced Research Projects Agency – Energy (ARPA-E), U.S. Department of Energy, under award number DE-AR0000402. Structural studies were supported by the Center for Gas Separations Relevant to Clean Energy Technologies, an Energy Frontier Research Center supported by the U.S. Department of Energy, Office of Science, Office of Basic Energy Sciences, under Award DE-SC0001015. Single-crystal X-ray diffraction data were collected on Beamline 11.3.1 at the Advanced Light Source at Lawrence Berkeley National Laboratory, which is supported by the Director, Office of Science, Office of Basic Energy Sciences, of the U.S. Department of Energy under Contract No. DE-AC02-05CH11231. We gratefully acknowledge Dr. Hye Jeong Park for the development of a gram-scale synthesis of Zn₂(dobpdc) powder and Dr. Simon Weston for helpful discussions.

2.6. Supporting Information

2.6.1 Additional Experimental Details

Gram-Scale Synthesis of $\text{Zn}_2(\text{dobpdc})$ Powder. The previously published synthetic route for $\text{Zn}_2(\text{dobpdc})$ powder²³ was found to be readily scalable at increased concentration. In a roundbottom flask, 2.74 g (10.0 mmol) $\text{H}_4(\text{dobpdc})$ and 8.35 g (32.0 mmol) $\text{ZnBr}_2 \cdot 2\text{H}_2\text{O}$ were dissolved in a mixture of 250 mL of ethanol and 250 mL of *N,N*-dimethylformamide (DMF). The solution was stirred for 12 h at 120 °C, producing an off-white powder. The reaction solution was decanted, and the powder was soaked three times in 200 mL of DMF for 6 h at 60 °C and three times in 200 mL of methanol for 6 h at 60 °C. The material was then filtered and fully desolvated by heating at 250 °C under dynamic vacuum for 12 h. Following desolvation, the activated material was stored in a N_2 -filled glovebox.

Synthesis of Diamine-Appended $\text{Zn}_2(\text{dobpdc})$ Powders. The frameworks m-2-m- $\text{Zn}_2(\text{dobpdc})$ (m-2-m = “mmen” = *N,N'*-dimethylethylenediamine), e-2-e- $\text{Zn}_2(\text{dobpdc})$ (e-2-e = *N,N'*-diethylethylenediamine), e-2- $\text{Zn}_2(\text{dobpdc})$ (e-2 = *N*-ethylethylenediamine), and i-2- $\text{Zn}_2(\text{dobpdc})$ (i-2 = *N*-isopropylethylenediamine) were prepared through modification of the previously reported procedure for the mmen- $\text{M}_2(\text{dobpdc})$ series of frameworks. For m-2-m- $\text{Zn}_2(\text{dobpdc})$, 15 mg of fully desolvated $\text{Zn}_2(\text{dobpdc})$ was submerged in 0.8 mL of 20% (v/v) dry m-2-m in hexanes (20 equiv diamine per Zn^{2+}) in a 4 mL vial in a N_2 -filled glovebox. For e-2-e-, e-2-, and i-2- $\text{Zn}_2(\text{dobpdc})$, solutions of 20% (v/v) diamine in hexanes (e-2-e) or toluene (e-2, i-2) were dried by stirring over CaH_2 for 3 h at 60 °C. In a N_2 -filled glovebag, a quantity of diamine solution corresponding to 10 (e-2), 30 (e-2-e), or 50 (i-2) equiv diamine per Zn^{2+} was transferred by syringe to a 4 mL scintillation vial containing 20 mg of fully-desolvated $\text{Zn}_2(\text{dobpdc})$. In all cases, the suspension was left undisturbed for a minimum of 4 h. For m-2-m and e-2-e, the resulting diamine-appended powder was soaked three times in 4 mL-portions of dry hexanes and was stored under dry hexanes. For e-2 and i-2, the diamine-appended powder was filtered and washed with three 10 mL portions of toluene followed by three 10 mL portions of hexanes. All diamine-appended $\text{Zn}_2(\text{dobpdc})$ frameworks were stored under nitrogen and characterized by thermogravimetric analysis within 24 h of preparation. Note that attempts to prepare m-2- $\text{Zn}_2(\text{dobpdc})$ (m-2 = *N*-methylethylenediamine) following this procedure resulted in loss of crystallinity of the powder.

CO_2 Isobars of Diamine-Appended $\text{Zn}_2(\text{dobpdc})$ Powders. Isobars of diamine-appended $\text{Zn}_2(\text{dobpdc})$ powders under 100% CO_2 were collected using a TA Instruments Q5000 TGA with a flow rate of 25 mL/min for all gases. Masses were uncorrected for buoyancy effects. The frameworks m-2-m- and e-2-e- $\text{Zn}_2(\text{dobpdc})$ were transferred as slurries in hexanes to the tared aluminum analysis pans, while the frameworks e-2- and i-2- $\text{Zn}_2(\text{dobpdc})$ were transferred rapidly in air as dry powders. The frameworks were first activated under flowing N_2 using the following conditions: 1 h at 50 °C for m-2-m- and e-2-e- $\text{Zn}_2(\text{dobpdc})$; 45 min at 50 °C for i-2- $\text{Zn}_2(\text{dobpdc})$; and 25 min at 100 °C for e-2- $\text{Zn}_2(\text{dobpdc})$. To observe the cooperative adsorption step temperature, the cooling branch of the isobar must start at a temperature above the step temperature. Therefore, prior to cooling, the temperature was rapidly increased to 80 °C for m-2-m, e-2-e, and e-2, or to 120 °C for i-2. Upon reaching the set temperature, the gas was switched to 100% CO_2 , the mass was normalized to 0, and the cooling branch of the isobar was initiated. For e-2-e- $\text{Zn}_2(\text{dobpdc})$, the maximum temperature of initial CO_2 exposure was restricted to 80 °C to minimize diamine volatilization; however, the rapid rise in CO_2 adsorption upon exposure to CO_2 at 80 °C is consistent with a CO_2 insertion threshold at or above this

temperature. Note that this additional heating step between activation and CO₂ was not required for the single-crystal experiments, in which CO₂ was dosed at 25 °C following activation.

Powder X-Ray Diffraction. Laboratory powder X-ray diffraction patterns were collected using a Bruker AXS D8 Advance diffractometer with Cu K α radiation ($\lambda = 1.5418 \text{ \AA}$), a Göbel mirror, and a Lynxeye linear position-sensitive detector, and the following optics: fixed divergence slit (0.6 mm), receiving slit (3 mm), and secondary-beam Soller slits (2.5°). Generator settings were 40 kV and 40 mA. All powder X-ray diffraction patterns were collected at room temperature in air on as-synthesized samples immediately following filtration.

Surface Area Measurements. Langmuir surface area measurements were performing using a Micromeritics ASAP 2420 instrument. In a typical measurement, 50–200 mg of powder was transferred to a pre-weighed glass measurement tube under a N₂ atmosphere and capped with a Micromeritics *Transeal*. The sample was then degassed on the adsorption instrument at the specified activation temperature until the outgas rate was less than 3 $\mu\text{bar}/\text{min}$. The evacuated tube was then weighed to determine the mass of the degassed sample. The sample was then fitted with an isothermal jacket and transferred to the analysis port of the adsorption instrument, where the outgas rate was again confirmed to fall below 3 $\mu\text{bar}/\text{min}$. The Langmuir surface areas were measured in a 77 K liquid N₂ bath and calculated using the Micromeritics software with a cross-sectional area of 16.2 \AA for N₂.

High-Throughput CO₂, N₂, and H₂O Adsorption Isotherm Measurements. Equilibrium adsorption isotherms for CO₂, N₂, and H₂O were collected for all diamine-appended Mg₂(dobpdc) samples in parallel using an instrument custom-built by Wildcat Discovery Technologies.¹² For each analogue, 50–100 mg of activated adsorbent was loaded into a tared 4 mL vial in a N₂-filled glovebox. The 4 mL vials were then sealed in aluminum sample assemblies that can hold up to 7 vials each, where the seal above each vial is equipped with a Schrader valve that can be actuated by the instrument. The sample assemblies were loaded into the high-throughput adsorption instrument, and the headspace above each sample was evacuated prior to actuation of the Schrader valve. Prior to collection of each adsorption isotherm, the samples were activated under vacuum for 12 h at 120 °C using heating elements under the sample holders. The instrument temperature was monitored and recorded continuously by eight thermocouples throughout activation and data collection.

¹H NMR Analysis of Digested Metal–Organic Frameworks. To analyze diamine loading, ~5 mg of each diamine-appended Mg₂(dobpdc) powder was digested in a solution of 20 μL of 35 wt. % DCl in D₂O and 1 mL of DMSO-*d*₆. The solution was sonicated and/or heated at 60 °C until the solid fully dissolved. ¹H NMR spectra were acquired on Bruker AV-300, ABV-400, or AVQ-400 instruments at the University of California, Berkeley NMR facility. Diamine loadings were determined from the ratios of the integrated diamine resonances to those of the ligand.

Infrared Spectroscopy. Infrared spectra were collected using a PerkinElmer Avatar Spectrum 400 FTIR spectrophotometer equipped with a Pike attenuated total reflectance (ATR) accessory. Spectra for all diamine-appended Mg₂(dobpdc) analogues were collected for as-synthesized samples. For m-2-m-, e-2-e-, m-2-, e-2-, mm-2-, and ee-2-Mg₂(dobpdc), *in situ* FTIR spectra were collected on activated and CO₂-dosed samples at room temperature by enclosing the ATR accessory within a plastic glovebag with positive gas pressure. Prior to collecting spectra, the glovebag was evacuated and exchanged with the desired gas three times and then purged for 1 h. Spectra of activated samples were collected within the glovebag under positive N₂ pressure at room temperature following activation of the samples in 20 mL

scintillation vials under flowing N₂ for 2 h at 120 °C. Spectra of CO₂-dosed samples were collected following collection of spectra under N₂ using the same sample aliquots.

2.6.2 Equivalent Energy Calculation Details

Energy Consumption of CCS Process. The equivalent energy of a CO₂ capture process is a metric that describes the total loss in electrical production of a power plant due to CO₂ capture and compression. CO₂ capture requires thermal energy to heat the sorbent and desorb CO₂ as the final product. This thermal energy is supplied by diverting steam to the adsorbent beds, instead of sending it to turbines to make electricity, effectively reducing the net power output from the plant. Once relatively pure CO₂ is removed from the adsorbent beds, it is mechanically compressed to supercritical conditions, which requires electrical energy from the power plant. In our model, the compression of the product CO₂ is modeled as a series of intercooled compressors with maximum pressure ratio of 2.5, an isentropic efficiency of 85% for each stage of compression, and intercooling between each compressor to 313 K. The fluid properties were determined using real gas data from the REFPROP⁵⁸ software package developed by NIST.

The thermal energy needed to heat and regenerate the adsorbent includes heating the adsorbent, adsorbed components, and interstitial gases as well as providing the heat of desorption for CO₂ and any N₂. Moisture was not included in this analysis. The thermal energy is supplied by steam extraction from the steam cycle of the power plant and can be calculated using power plant models. The steam extraction occurs at the saturation pressure that corresponds to a saturation temperature that is 10 °C warmer than the warmest temperature in the regeneration step. The properties of the extracted steam were then calculated from the steam condition in the low-pressure (LP) turbine at the extraction pressure. The loss in electrical generation from this steam extraction was determined from GateCycle⁵⁹ simulations of steam extraction at varying extraction pressures in regenerative reheat steam cycles. Results from these simulations show a linear correlation for the lost electrical work E_{lost} as a function of the heating requirement $Q_{heating}$ throughout all possible LP turbine extractions and follows the equation:⁶⁰

$$E_{lost} = (-0.08037 + 0.002326 * T) * Q_{heating} \quad (2.S1)$$

where T is the saturation temperature in Celsius of the extracted steam.

The capture process was modeled as a single-bed equilibrium adsorption model with fixed adsorption and regeneration temperatures. The difference in total CO₂ and N₂ uptake in the bed between the final adsorption and final desorption conditions was taken to be the produced gas and determined the product purity.

CO₂ adsorption was assumed to take place at 1 bar in a dry stream of CO₂ and balance N₂. The concentration of CO₂ was varied from 0 to 99% and optimal process conditions and performance was calculated for each concentration. The lowest temperature of adsorption allowed was 313 K. The regeneration was also modeled at 1 bar, 99% CO₂ with the balance N₂. The temperature of regeneration was allowed to take any value to minimize the equivalent energy of the full capture process.

The model for CO₂ adsorption was developed from a 1-D lattice gas adsorption model with interaction between adjacent sites.⁶¹ When the interaction parameter ω is sufficiently large with respect to ΔH , a clear step change emerges.

$$P_{CO_2} e^{-\Delta H/RT} = \frac{1}{q} \left(\frac{\beta - 1 + 2\theta}{\beta + 1 - 2\theta} \right) \quad (2.S2),$$

with

$$\beta = \left[\left(1 - 4 \left(1 - e^{-\frac{\omega}{RT_0}} \right) \right) \theta (1 - \theta) \right]^{-\frac{1}{2}} \quad (2.S3),$$

where P_{CO_2} is the partial pressure of CO₂, ΔH is the heat of adsorption for CO₂ at a site with one neighboring site adsorbed with CO₂, q is the Henry's constant at a reference temperature T_0 times $e^{\Delta H/RT_0}$, R is the universal gas constant, T is the temperature at which we are calculating the CO₂ uptake, θ is the fraction of sites on the adsorbent that are loaded with CO₂, and ω is the additional heat of adsorption experienced by CO₂ binding at a site with one adjacent site occupied compared to no adjacent sites occupied.

For each adsorbent, the values of ΔH , q , ω as well as a maximum loading parameter were fit to the experimental isotherm data. For the dual step materials, the second step-change isotherm was modeled as having the same maximum loading, but the ΔH , q , and ω terms were fit independently. An additional Langmuir isotherm term was added to generate a complete fit of the data to account for the non-cooperative adsorption properties of the adsorbent. The complete isotherm was created by adding the different adsorption terms together. The total heat of adsorption for the CO₂ adsorbed on the system was calculated independently for each type of site assuming constant values for ΔH and ω and summed to create a total value. The N₂ isotherm was modeled as a linear isotherm as described for mmen-Mg₂(dobpdc)²¹ with CO₂ uptake of 0.079 mol/kg adsorbent at 0.75 bar N₂, at 25°C, $\Delta H = -14000$ J/mol N₂.

Calculation of Baseline Amine Energy Consumption. The equivalent energy for a baseline was calculated by summing the electrical impact of the steam extraction and the electrical energy required for CO₂ compression. Other auxiliary loads such as pumping, pressure loss, and reclaimer heating were not included. The U.S. Department of Energy has established baseline performance data for amine solvents deployed on power plants.⁵⁴ For the DOE baseline case 12B, CO₂ capture and compression on a supercritical power plant, the approach outlined above resulted in an equivalent energy of 934.7 kJ/kg CO₂, of which 71.4% is from the steam extraction for solvent regeneration in the reboiler and 28.6% is from CO₂ compression.

2.6.3 Langmuir Surface Areas

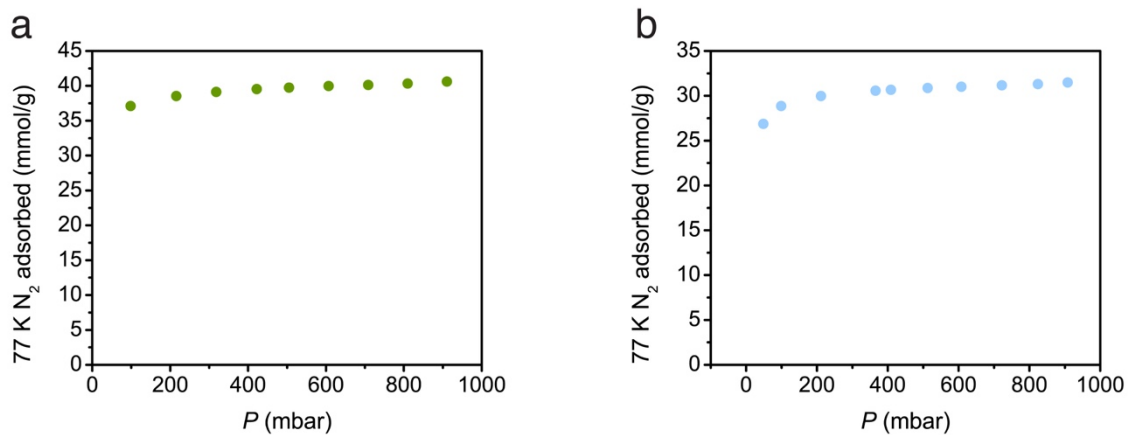


Figure 2.S1. 77 K N_2 adsorption isotherms for gram-scale syntheses of (a) $Mg_2(dobpdc)$ and (b) $Zn_2(dobpdc)$ following activation at 250 °C. The calculated Langmuir surface areas are 4001(5) m^2/g for $Mg_2(dobpdc)$ and 3104(4) m^2/g for $Zn_2(dobpdc)$.

2.6.4 Powder X-ray Diffraction

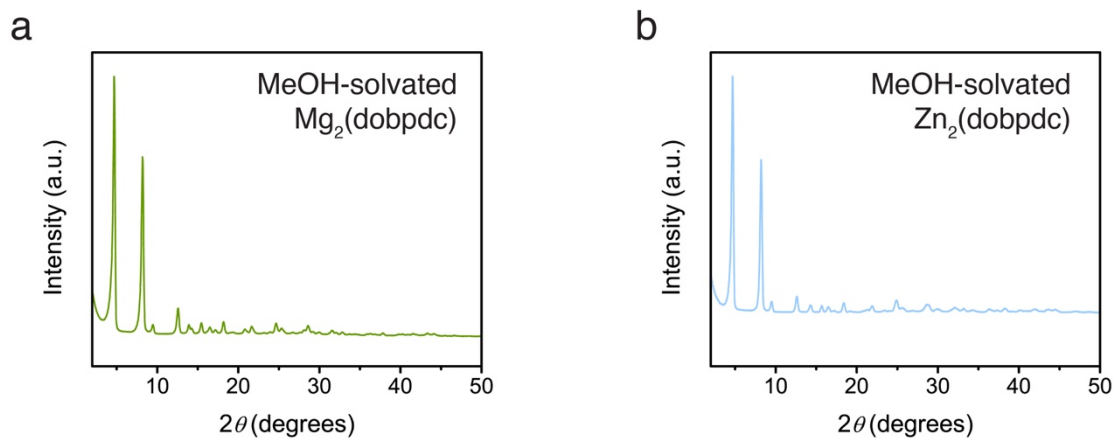


Figure 2.S2. Powder X-ray diffraction patterns ($\lambda = 1.5418 \text{ \AA}$) for gram-scale syntheses of methanol-solvated (a) $Mg_2(dobpdc)$ and (b) $Zn_2(dobpdc)$.

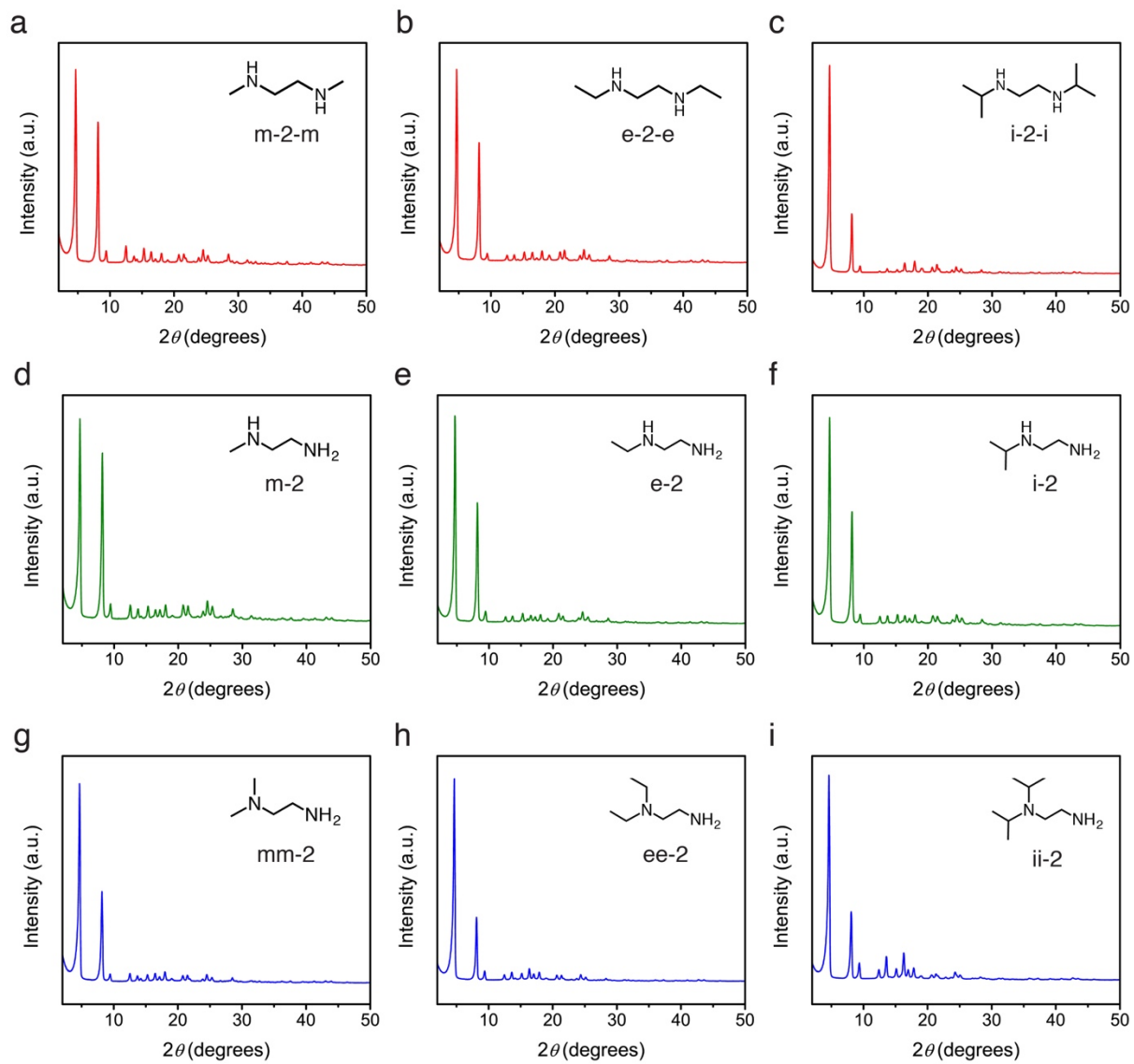


Figure 2.S3. Powder X-ray diffraction patterns ($\lambda = 1.5418 \text{ \AA}$) for the as-synthesized diamine-terminated $\text{Mg}_2(\text{dobpdc})$ analogues discussed in this work.

2.6.5 Infrared Spectra

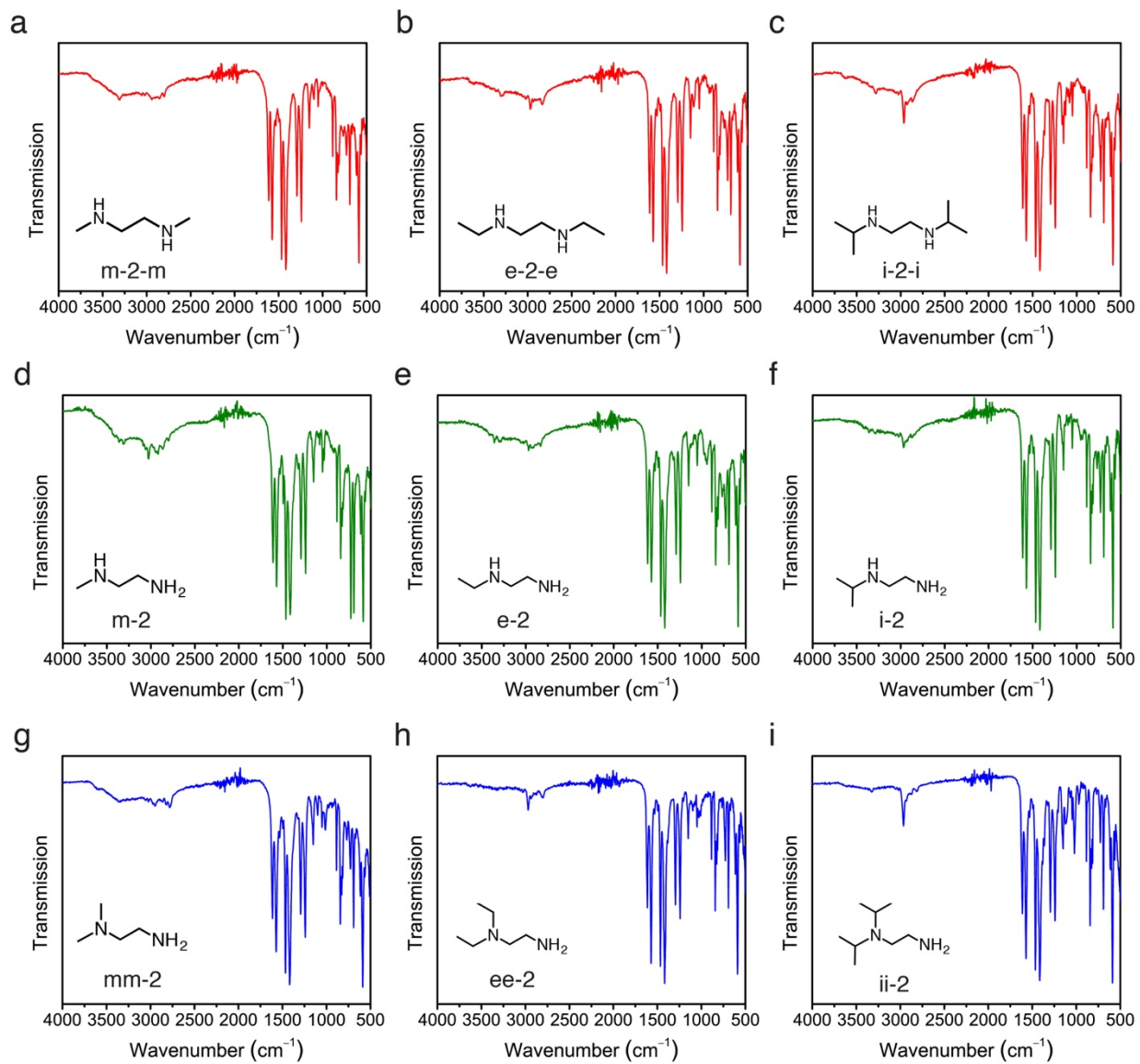


Figure 2.S4. Infrared spectra for the as-synthesized diamine-appended Mg₂(dobpdc) analogues discussed in this work.

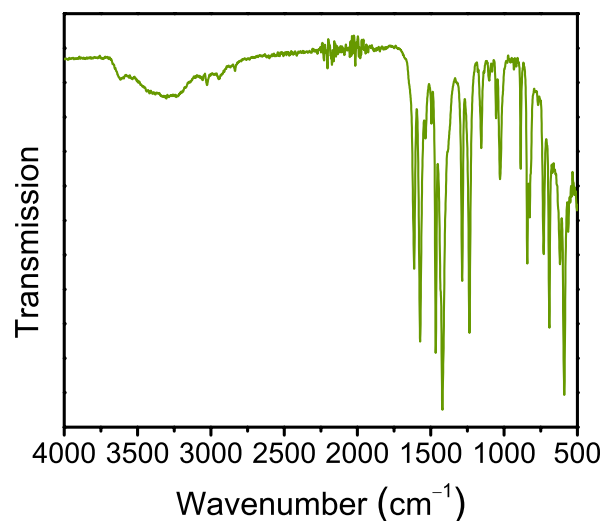


Figure 2.S5. Infrared spectra for methanol-solvated $\text{Mg}_2(\text{dobpdc})$ washed with toluene.

2.6.6 *In Situ* Infrared Spectra

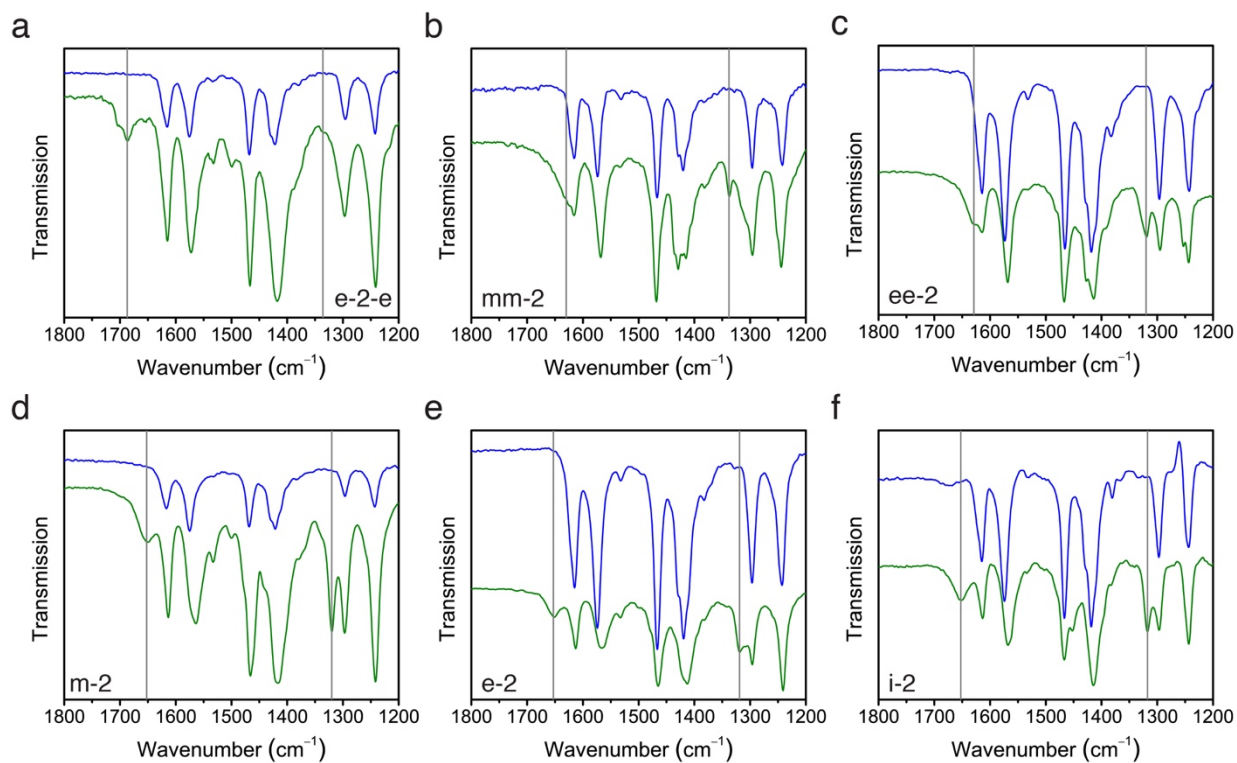


Figure 2.S6. *In situ* infrared spectra at room temperature under N_2 (blue) and CO_2 (green) for activated samples of the diamine- appended $\text{Mg}_2(\text{dobpdc})$ analogues discussed in this work. Gray lines mark the diagnostic carbamate $\nu(\text{C}-\text{O})$ ($1630\text{--}1690\text{ cm}^{-1}$) and $\nu(\text{C}-\text{N})$ ($\sim 1320\text{ cm}^{-1}$) bands.

Table 2.S1. Carbamate stretching frequencies for CO₂-dosed diamine-appended Mg₂(dobpdc) analogues.

	$\nu(\text{C-N})$ (cm ⁻¹)	$\nu(\text{C-O})$ (cm ⁻¹)
m-2-m	1334	1690
e-2-e	1336	1687
m-2	1320	1652
e-2	1319	1653
i-2	1318	1653
mm-2	1338	~1630
ee-2	1320	1629

2.6.7 NMR Digestion

Table 2.S2. Representative diamine loadings for diamine-appended Mg₂(dobpdc) analogues calculated from the ratio of diamine peak integral(s) to ligand peak integrals by ¹H NMR following sample digestion with DCl in DMSO-*d*₆. For samples in which more than one diamine peak could be integrated cleanly, the reported diamine loading is an average of the ratios calculated using each diamine peak. Error is estimated as ± 5%. All samples were prepared through the newly developed rapid synthetic method of submerging methanol-solvated Mg₂(dobpdc) in a 20 v/v% solution of diamine in toluene.

	Diamine loading (% per Mg ²⁺)
m-2-m*	93%
e-2-e*	93%
i-2-i*	70%
m-2	118%
e-2	103%
i-2	102%
mm-2	104%
ee-2	102%
ii-2	103%

* Dry toluene and dry diamine were required to achieve high diamine loadings for 2°/2° diamines.

2.6.8 Thermogravimetric Decomposition

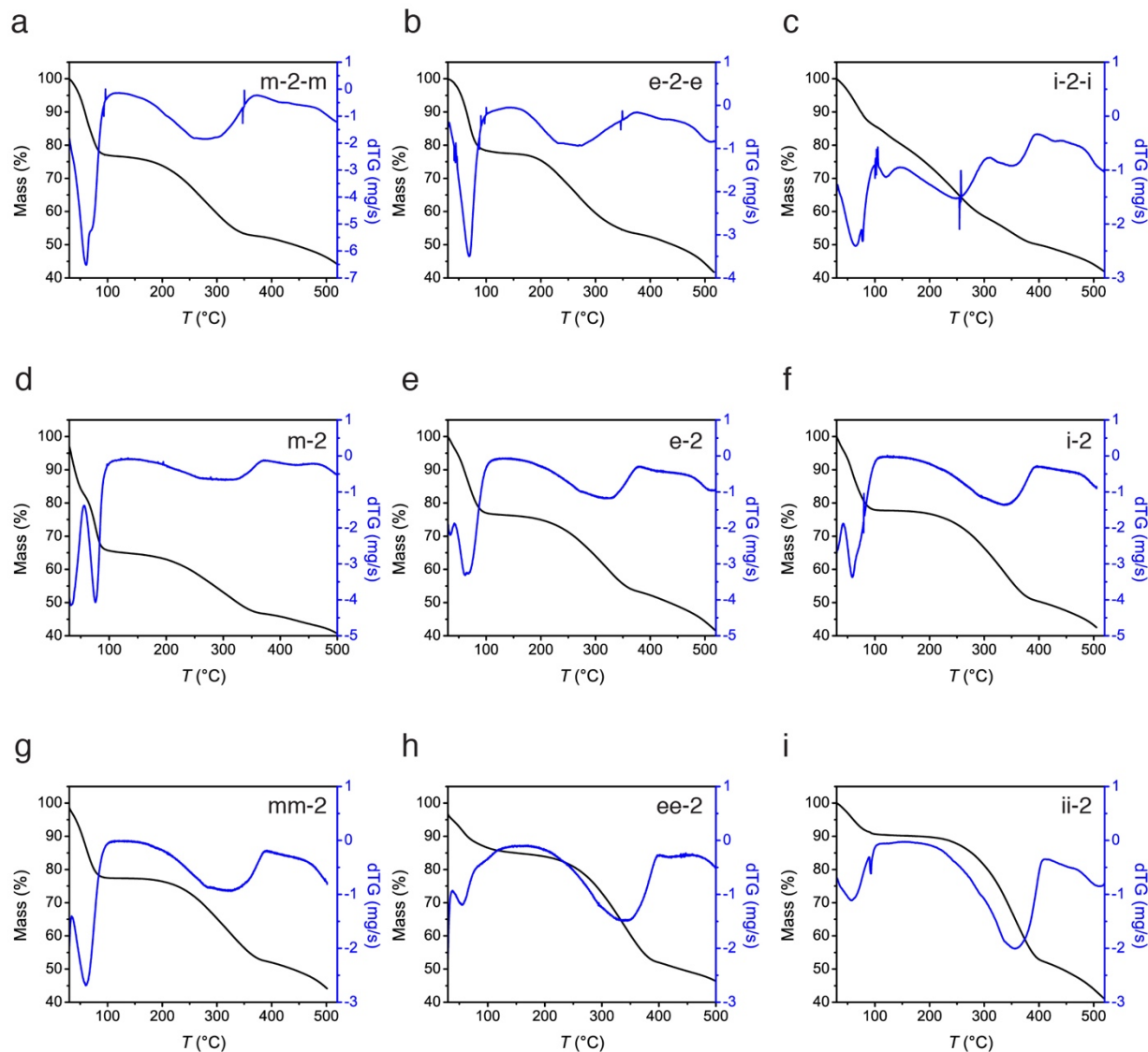


Figure 2.S7. Thermogravimetric decomposition traces (black) and derivative decomposition traces (dTG, blue) for diamine-appended $\text{Mg}_2(\text{dobpdc})$ analogues discussed in this work. Temperature ramp rates of $1.5\text{ }^\circ\text{C}/\text{min}$ were used. The dTG peak at lowest temperature is due to excess solvent (toluene or hexanes) in the framework pores, while the higher temperature peak is due to volatilization of the diamine. For $\text{m-2-Mg}_2(\text{dobpdc})$, the additional low-temperature mass loss is consistent with partial solvation by diamine observed in NMR digestion experiments. Derivative plots were smoothed through a 20-point adjacent averaging technique.

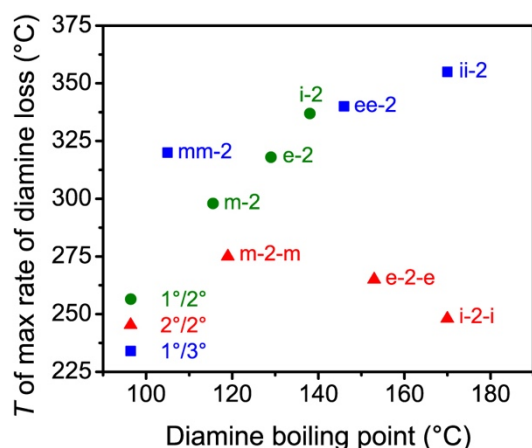


Figure 2.S8. Plot of the temperature of maximum rate of diamine volatilization (as determined from the peak of the dTG decomposition plots for each diamine) as a function of diamine boiling point. A linear relationship can be seen for each class of diamines ($1^\circ/2^\circ$, $2^\circ/2^\circ$, $1^\circ/3^\circ$). For diamines predominately bound through primary amines ($1^\circ/2^\circ$ and $1^\circ/3^\circ$ diamines), the temperature at which the diamine is volatilized from the framework increases linearly with diamine boiling point as the substituent size is increased. For $2^\circ/2^\circ$ diamines, the trend is reversed, and diamines with larger substituents are more easily volatilized despite the increase in diamine boiling point. All diamine-appended analogues in this plot were prepared from the same batch of $Mg_2(dobpdc)$. Note that the temperature of the max rate of diamine loss is plotted here due to ease of identification and comparison; however, the temperature of the *onset* of volatilization is of greater relevance for minimizing diamine loss in an adsorption process.

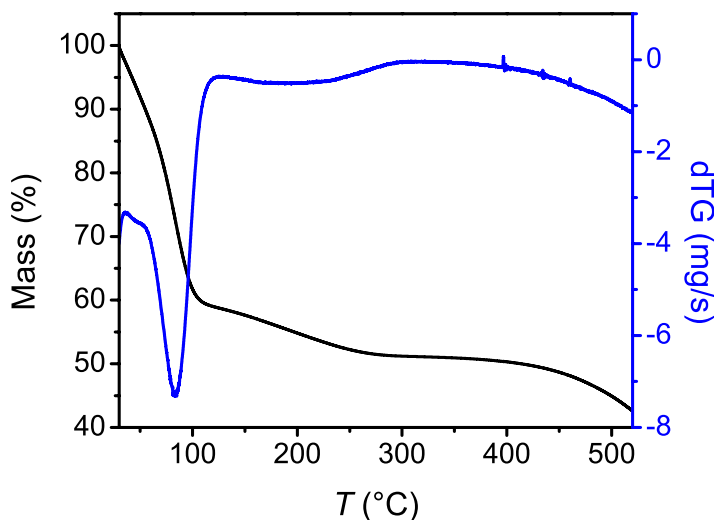


Figure 2.S9. Thermogravimetric decomposition trace (black) and derivative decomposition trace (dTG, blue) for methanol-solvated $Mg_2(dobpdc)$.

2.6.9 CO₂ Adsorption and Desorption Isobars

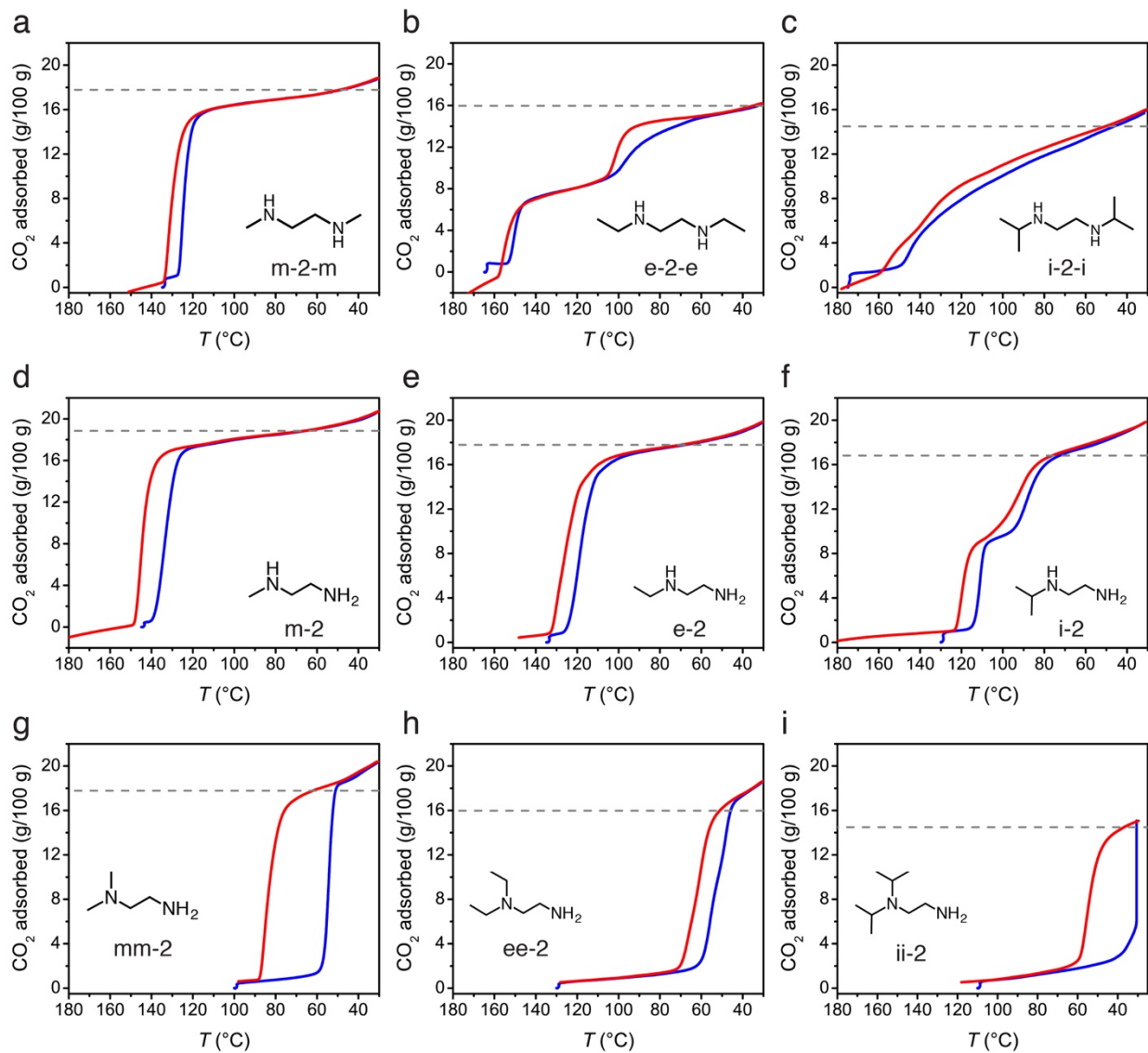


Figure 2.S10. Thermogravimetric adsorption (cooling, blue) and desorption (heating, red) isobars at atmospheric pressure under pure CO_2 for the diamine-apped $\text{Mg}_2(\text{dobpdc})$ analogues discussed in this work. The dashed grey lines mark the theoretical CO_2 capacity of 1 CO_2 per diamine- Mg^{2+} site. Temperature ramp rates of $1^\circ\text{C}/\text{min}$ were used. For ii-2- $\text{Mg}_2(\text{dobpdc})$, the temperature was held isothermally at 30°C for 45 min prior to beginning the desorption branch of the isobar.

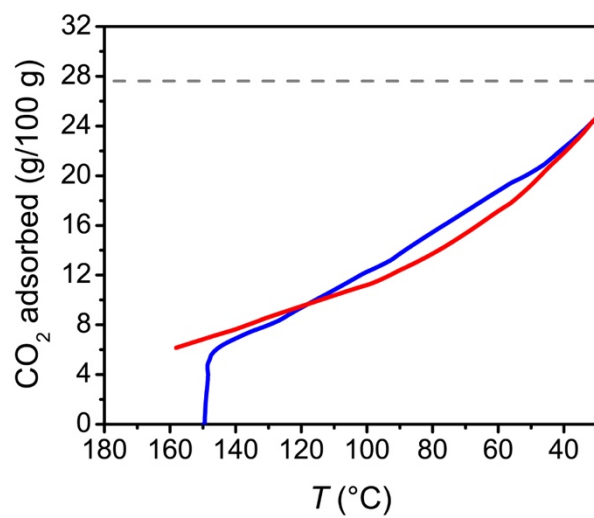


Figure 2.S11. Thermogravimetric adsorption (cooling, blue) and desorption (heating, red) isobars at atmospheric pressure under pure CO₂ for activated Mg₂(dobpdc), which displays Langmuir adsorption. A temperature ramp rate of 1 °C/min was used.

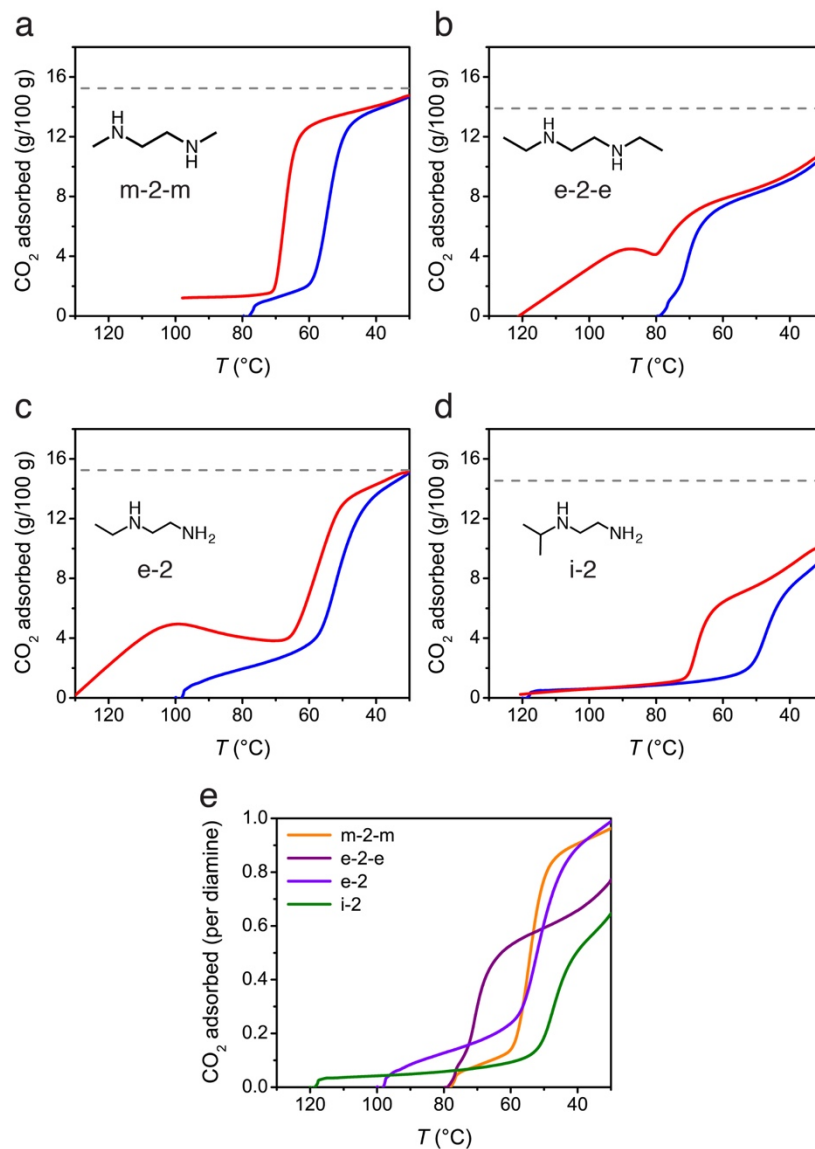


Figure 2.S12. (a–d) Thermogravimetric adsorption (cooling, blue) and desorption (heating, red) isobars at atmospheric pressure under pure CO₂ for diamine-appended Zn₂(dobpdc) powders. (e) Overlay of pure CO₂ adsorption isobars on a per-diamine basis for diamine-appended Zn₂(dobpdc) powders. Temperature ramp rates of 2 °C/min were used.

2.6.10 High-Throughput N₂ Isotherms

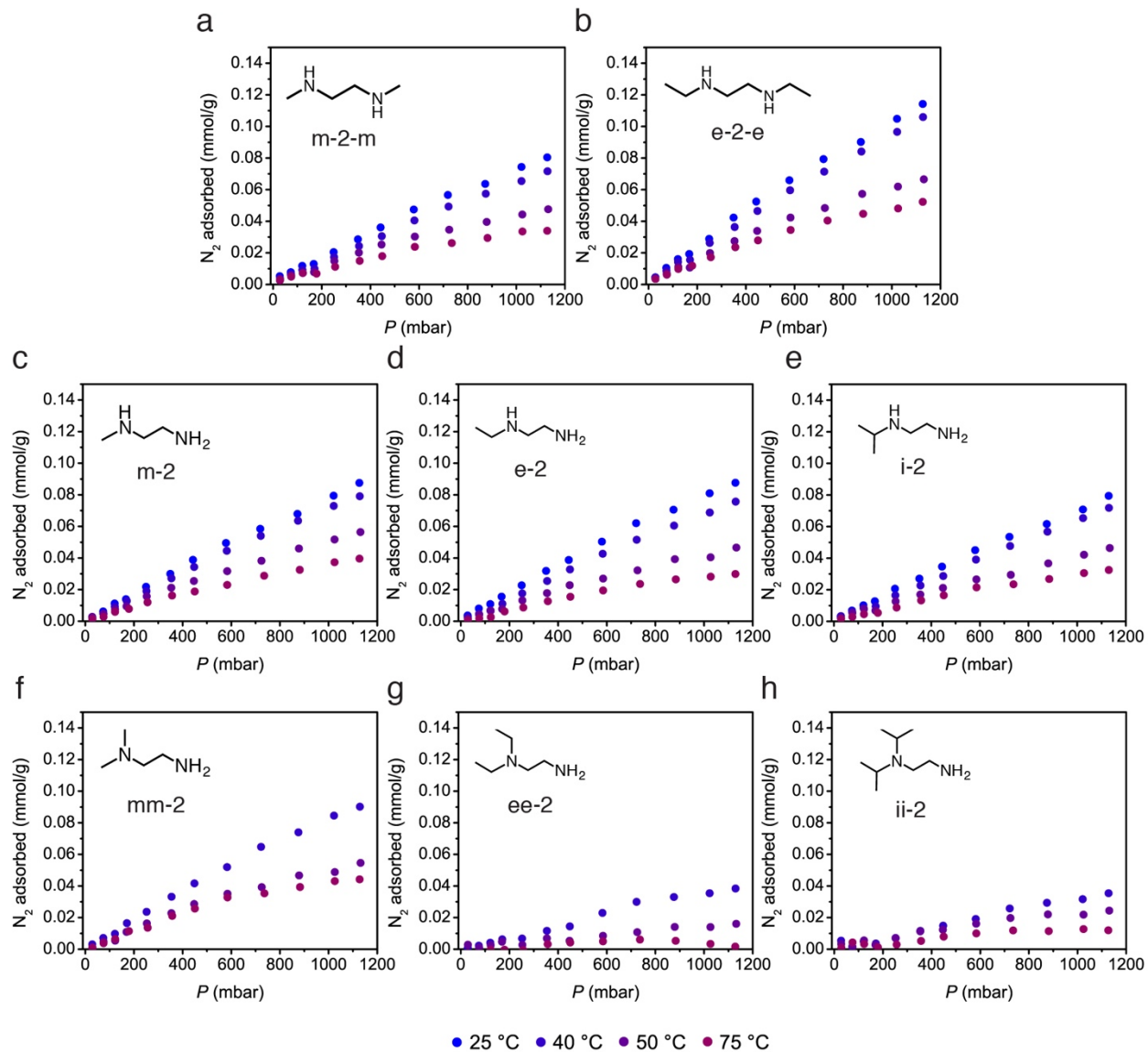


Figure 2.S13. High-throughput N₂ adsorption isotherms for diamine-appended Mg₂(dobpdc) analogues discussed in this work.

2.6.11 High-Throughput H₂O Isotherms

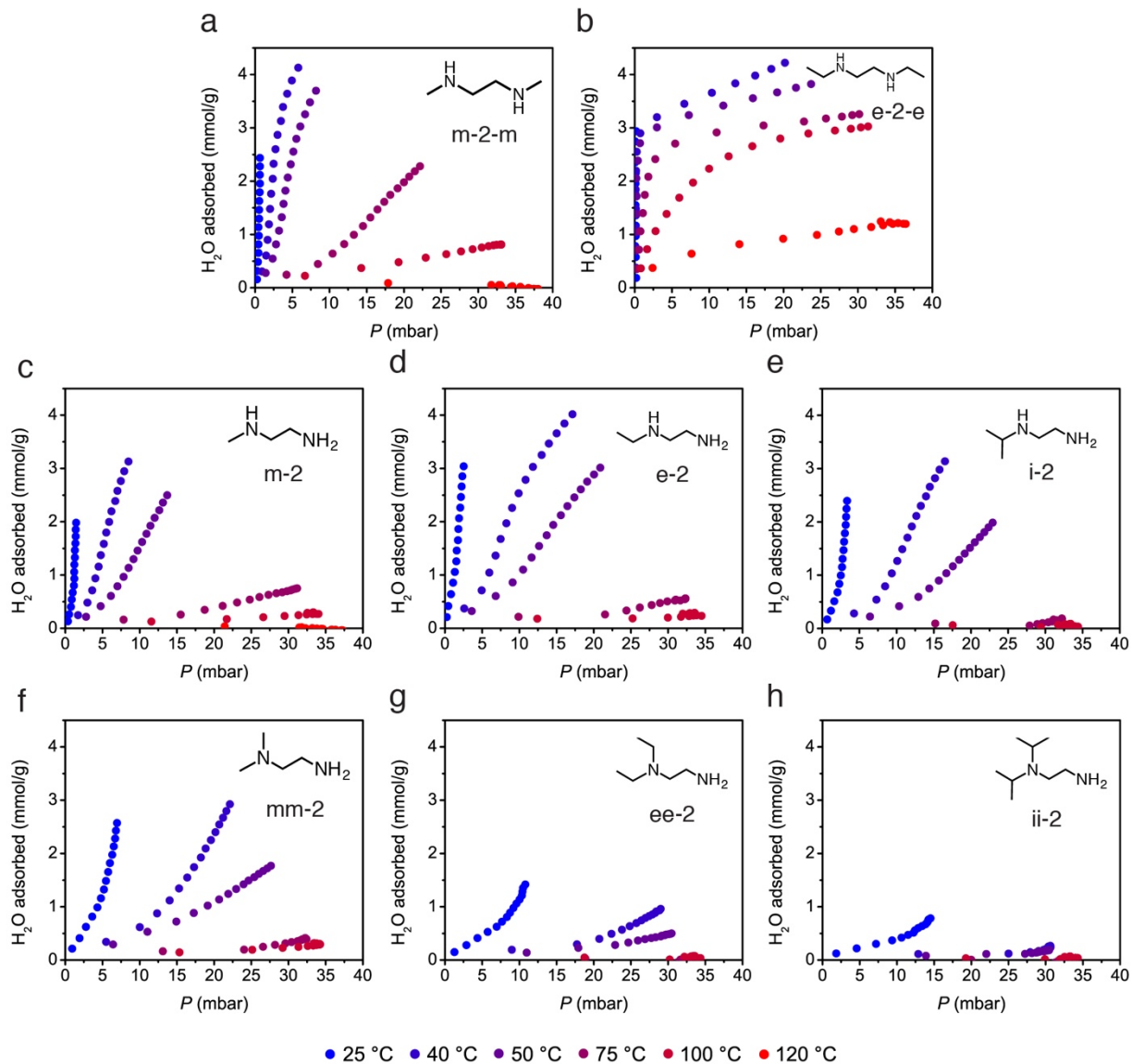


Figure 2.S14. High-throughput H₂O adsorption isotherms for diamine-appended Mg₂(dobpdc) analogues discussed in this work.

2.6.12 Equivalent Energy Results

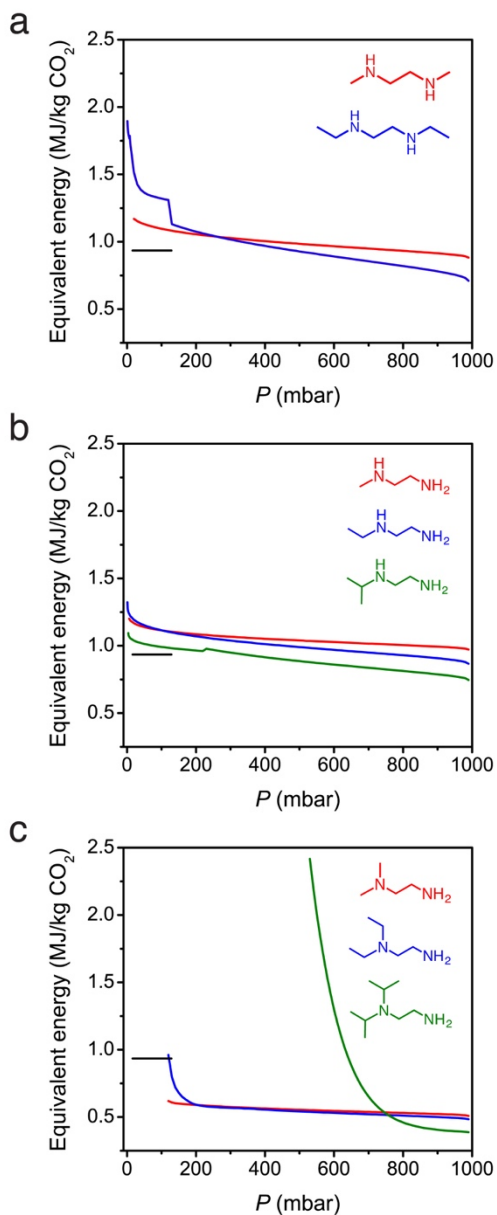


Figure 2.S15. Equivalent energy (MJ/kg CO₂ captured and compressed to 150 bar) as a function of the adsorption partial pressure of CO₂ for diamine-appended Mg₂(dobpdc) frameworks discussed in this work. A minimum adsorption temperature of 40 °C is assumed. Compression of 99% pure CO₂ from 1 bar to 150 bar requires 0.348 MJ/kg CO₂ for a diamine-appended Mg₂(dobpdc) framework; the remainder of the equivalent energy arises from steam extraction for regeneration. The black lines indicate the equivalent energy of 0.935 MJ/kg CO₂ for absorption-based capture with the amine solution Cansolv over a range of 128.8 mbar to 16.3 mbar of CO₂ (DOE baseline case 12B,⁵⁴ supercritical coal-fired power plant), of which 71.4% is from the steam extraction for solvent regeneration in the reboiler and 28.6% is from CO₂ compression.

Table 2.S3. Thermodynamic parameters and performance metrics for diamine-appended M_gz(dobpde) frameworks.

	$-\Delta H_{\text{ads}}$ (kJ/mol) ^a	$-\Delta S_{\text{ads}}$ (J/mol·K) ^{a,b}	$-\Delta G_{\text{ads}}$ at 40 °C (kJ/mol) ^c	Approximate P_{step} at 40 °C (mbar) ^d	T_{des} under 1 bar CO ₂ (°C) ^e	Capture rate, coal flue gas (%) ^f	Equivalent energy, coal flue gas (MJ/kg CO ₂) ^f	Capture rate, natural gas flue gas (%) ^g	Equivalent energy, natural gas flue gas (MJ/kg CO ₂) ^g
m-2-m	78.8 ± 0.7	187 ± 2	20 ± 1	< 0.5	133	> 99	1.07	99	--
e-2-e	100 ± 4	228 ± 10	29 ± 5	< 0.2	156	> 99	1.11	> 99	1.80
m-2	96 ± 3	227 ± 10	25 ± 5	< 0.2	148	> 99	1.10	> 99	--
e-2	84 ± 3	186 ± 14	26 ± 5	< 0.7	134	> 99	1.09	98	1.25
i-2	82 ± 3	203 ± 8	18 ± 4	< 1	123	> 99	0.98	98	1.09
mm-2	52.0 ± 0.6	146 ± 2	6 ± 1	100	88	33	0.60	0	--
ee-2	49 ± 4	141 ± 13	5 ± 6	140	73	7	0.68	0	--
ii-2	40	128	0.08	1000	68	0	--	0	--

^a Calculated at a loading of 1 mmol/g (within the first cooperative adsorption step).

^b Calculated from the relation $\ln(p/p_0) = -\Delta H_{\text{ads}}/RT + \Delta S_{\text{ads}}/R$, which is derived from $\Delta G_{\text{ads}} = -RT \ln(p/p_0) = \Delta H_{\text{ads}} - \Delta S_{\text{ads}}$, where $p_0 = 1$ bar.

^c Calculated using the relation $\Delta G_{\text{ads}} = \Delta H_{\text{ads}} - T\Delta S_{\text{ads}}$.

^d Determined from the approximate inflection point of the 40 °C CO₂ adsorption isotherm step.

^e Determined from the pure CO₂ adsorption and desorption isobars at atmospheric pressure as the point of closure of the hysteresis loop.

^f Calculated assuming a CO₂ partial pressure of 150 mbar with an adsorption temperature of 40 °C ($-\Delta G_{\text{ads}} \geq 10.9$ kJ/mol required for 90% capture).

^g Calculated assuming a CO₂ partial pressure of 40 mbar with an adsorption temperature of 40 °C ($-\Delta G_{\text{ads}} \geq 14.4$ kJ/mol required for 90% capture).

2.6.13 Supplementary Structure Figures and Crystallographic Data

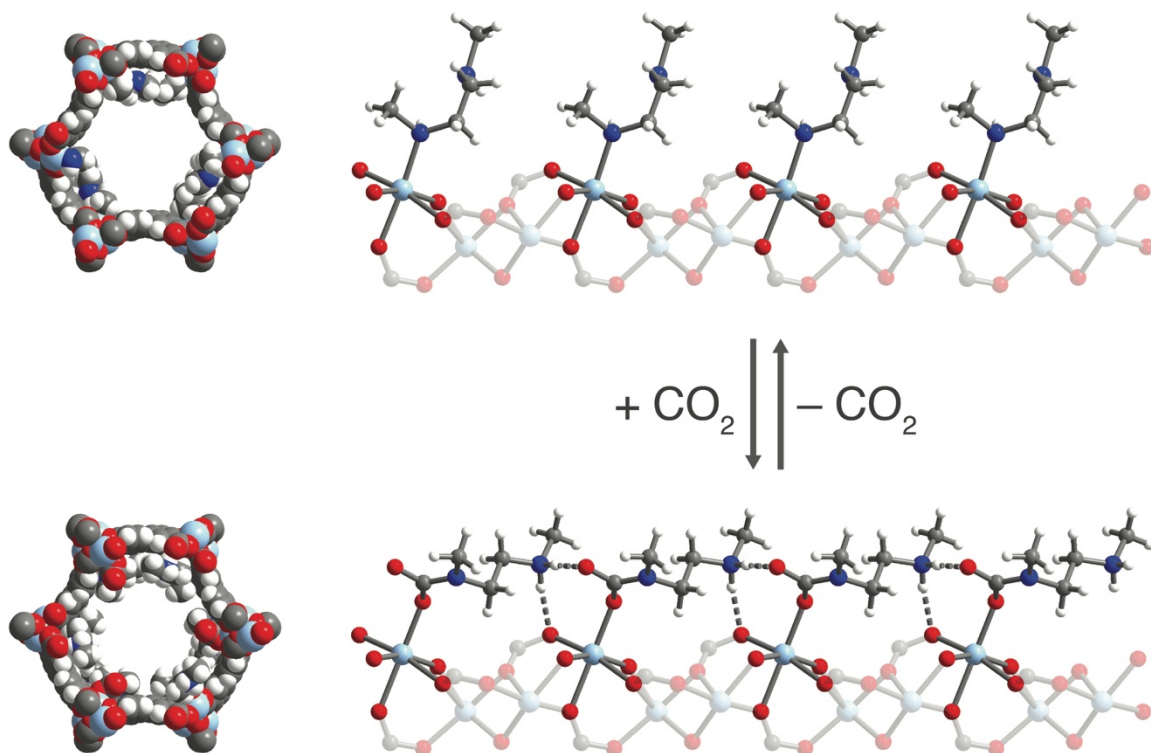


Figure 2.S16. Space-filling models and views along the c axis for the primary conformation of $\text{Zn}_2(\text{dobpdc})(m\text{-}2\text{-}m)_{1.43}$ (top) and for $\text{Zn}_2(\text{dobpdc})(m\text{-}2\text{-}m\text{-CO}_2)_{1.5}$ (bottom). Light blue, blue, gray, red, and white spheres represent Zn, N, C, O, and H atoms, respectively.

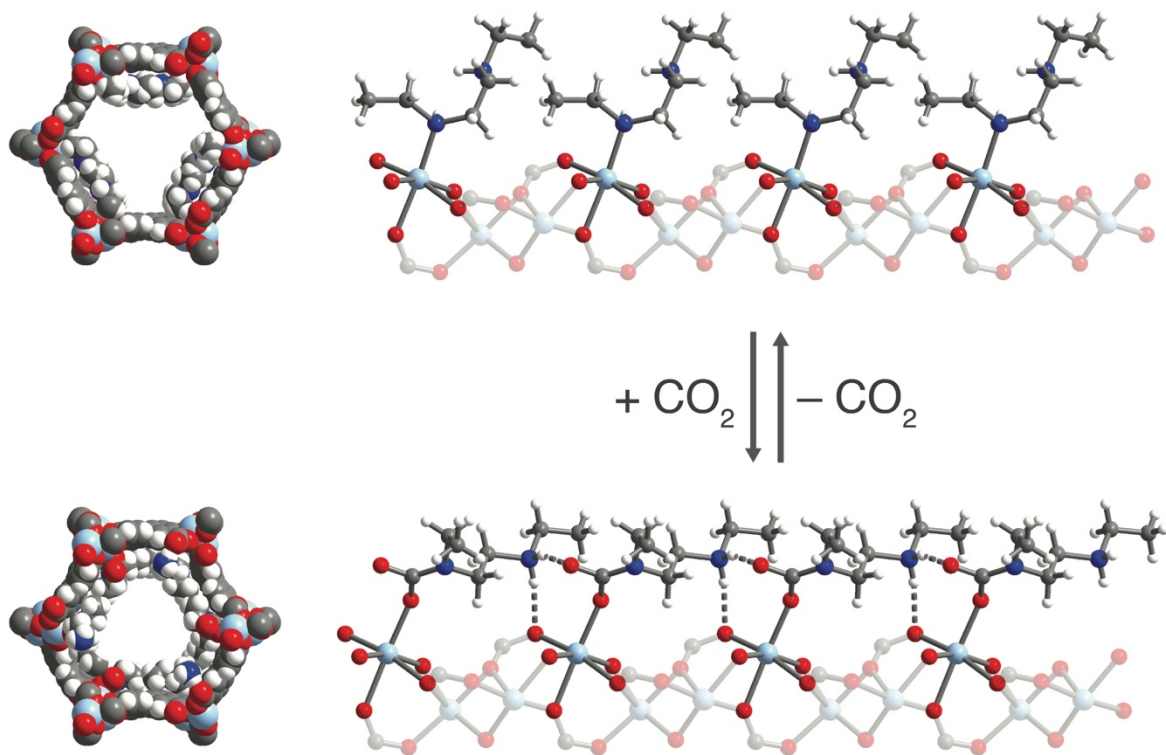


Figure 2.S17. Space-filling models and views along the *c* axis for the primary conformation of Zn₂(dobpdc)(e-2-e)_{1.26} (top) and for Zn₂(dobpdc)(e-2-e)(e-2-e-CO₂) (bottom). Light blue, blue, gray, red, and white spheres represent Zn, N, C, O, and H atoms, respectively.

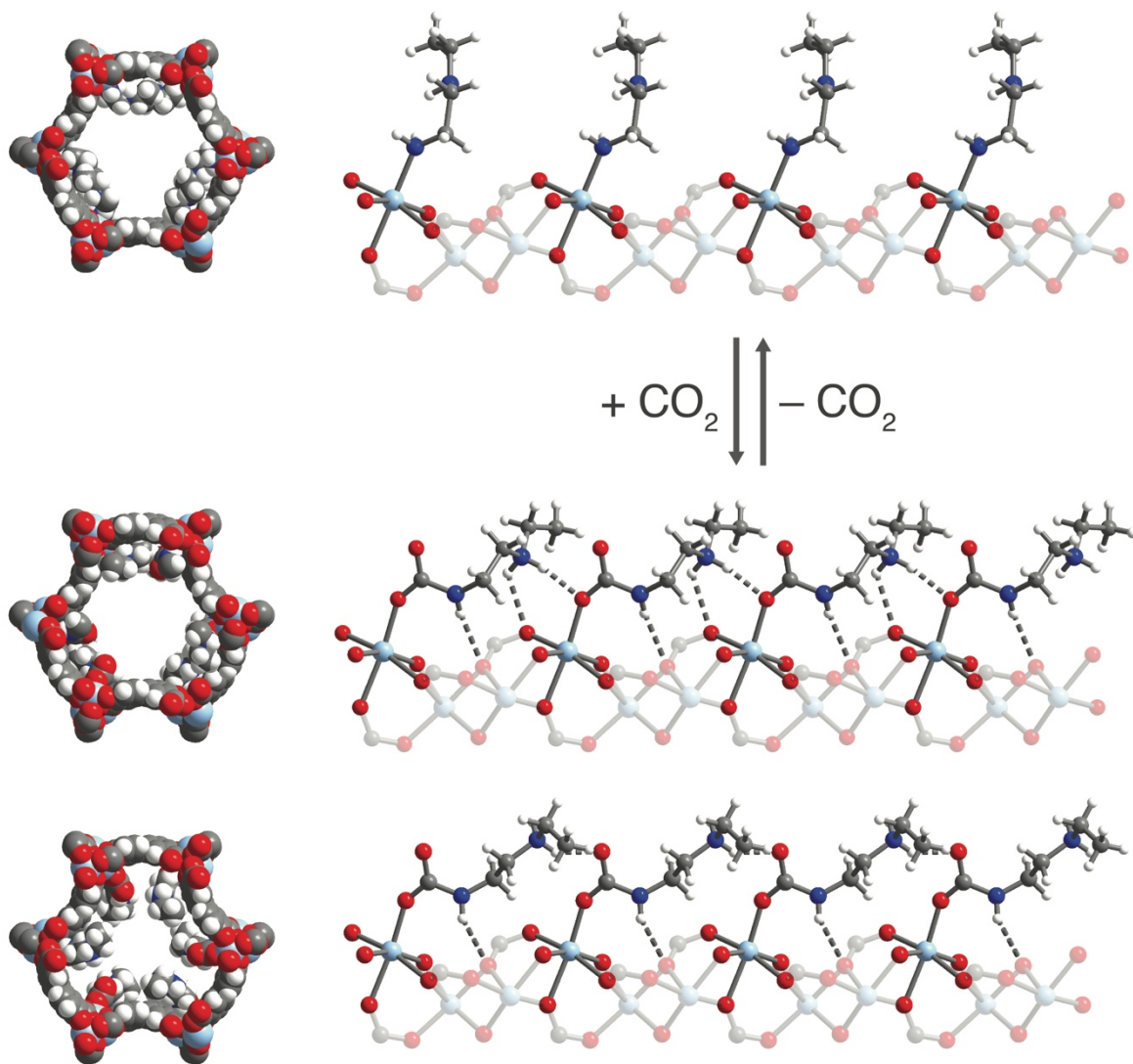


Figure 2.S18. Space-filling models and views along the *c* axis for the primary conformation of $\text{Zn}_2(\text{dobpdc})(e-2)_{1.68}$ (top) and for the two ammonium carbamate chain conformations observed in the structure of $\text{Zn}_2(\text{dobpdc})(e-2-\text{CO}_2)_{1.5}$ with occupancies of 50% (middle) and 25% (bottom). Light blue, blue, gray, red, and white spheres represent Zn, N, C, O, and H atoms, respectively.

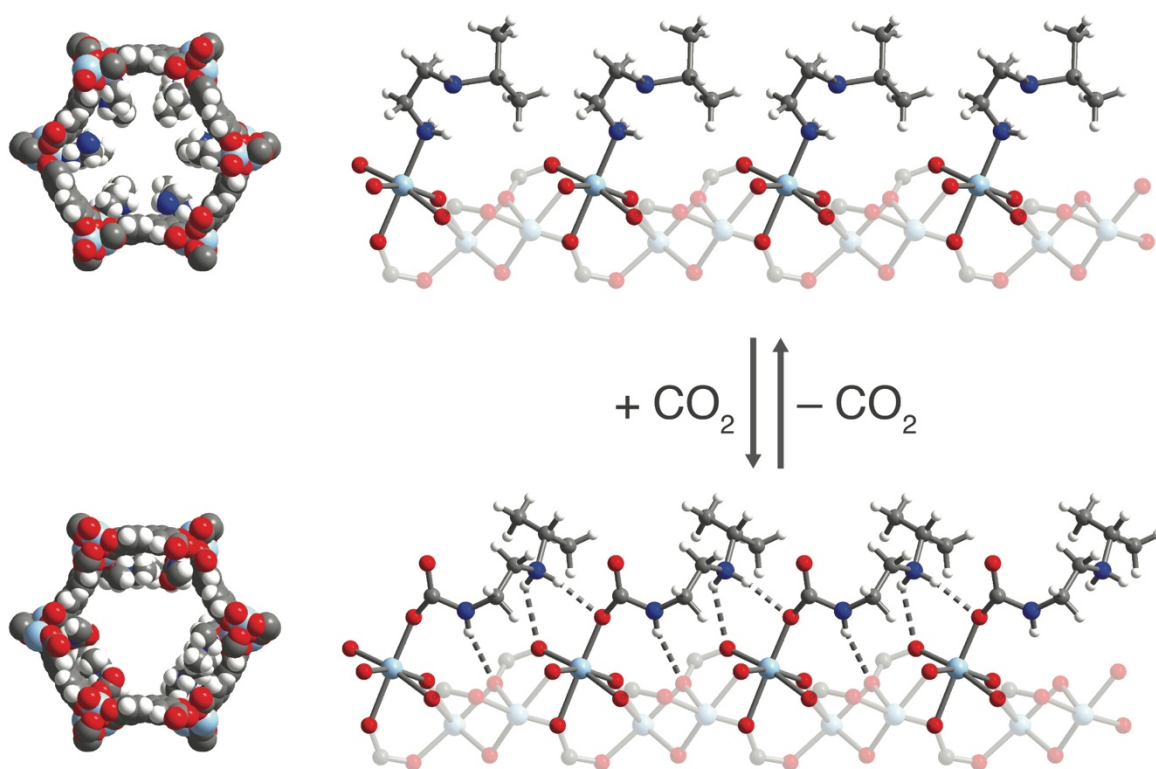


Figure 2.S19. Space-filling models and views along the c axis for the primary conformation of $\text{Zn}_2(\text{dobpdc})(i-2)_{1.94}$ (top) and for $\text{Zn}_2(\text{dobpdc})(i-2)(i-2-\text{CO}_2)$ (bottom). Light blue, blue, gray, red, and white spheres represent Zn, N, C, O, and H atoms, respectively.

Table 2.S4. Crystallographic data.

	Zn ₂ (dobpdc)(m-2-m) _{1.46}	Zn ₂ (dobpdc)(e-2-e) _{1.26}	Zn ₂ (dobpdc)(e-2) _{1.68}	Zn ₂ (dobpdc)(i-2) _{1.94}	Zn ₂ (dobpdc)(mm-2) _{1.83}	Zn ₂ (dobpdc)(ce-2) _{1.65}
Formula	C _{19.84} H _{23.52} N _{2.92} O ₆ Zn ₂	C _{21.56} H _{26.16} N _{2.52} O ₆ Zn ₂	C _{20.72} H _{28.26} N _{3.36} O ₆ Zn ₂	C _{23.7} H _{33.16} N _{3.88} O ₆ Zn ₂	C _{21.32} H _{27.96} N _{3.82} O ₆ Zn ₂	C _{23.89} H _{33.97} N _{3.30} O _{6.80} Zn ₂
Temperature (K)	100(2)	100(2)	100(2)	100(2)	100(2)	100(2)
Crystal System	Trigonal	Trigonal	Trigonal	Trigonal	Trigonal	Trigonal
Space Group	P3 ₁ 21	P3 ₁ 21	P3 ₁ 21	P3 ₁ 21	P3 ₁ 21	P3 ₁ 21
a, b, c (Å)	21.3911(9), 21.3911(9), 6.8959(3)	21.7573(8), 21.7573(8), 6.9089(3)	21.6986(8), 21.6986(8), 6.8708(3)	21.6818(7), 21.6818(7), 6.8741(3)	21.4759(11), 21.4759(11), 6.8613(4)	21.6620(6), 21.6620(6), 6.8262(2)
α, β, γ (°)	90, 90, 120	90, 90, 120	90, 90, 120	90, 90, 120	90, 90, 120	90, 90, 120
V, (Å ³)	2732.7(3)	2832.4(2)	2801.6(2)	2798.6(2)	2740.6(3)	2774.00(17)
Z	3	3	3	3	3	3
Radiation, λ (Å)	Synchrotron, 0.8856	Synchrotron, 0.7293	Synchrotron, 0.8856	Synchrotron, 0.7749	Synchrotron, 0.7749	Synchrotron, 0.8856
2θ Range for Data Collection (°)	4.746 to 78.508	4.436 to 54.250	4.678 to 87.546	4.730 to 87.552	4.776 to 67.290	4.686 to 75.936
Completeness to 2θ	99.6% (2θ = 64.194°)	99.8% (2θ = 51.900°)	99.8% (2θ = 64.194°)	99.9% (2θ = 55.412°)	99.8% (2θ = 55.412°)	99.9% (2θ = 64.194°)
Data / Restraints / Parameters	5556 / 157 / 203	3873 / 258 / 232	7478 / 183 / 239	11148 / 227 / 272	5559 / 76 / 203	5217 / 344 / 294
Goodness of Fit on F ²	1.145	1.163	1.088	1.117	1.103	1.053
R1 ^a , wR2 ^b (I > 2σ(I))	0.0463, 0.1340	0.0478, 0.1343	0.0496, 0.1290	0.0387, 0.1093	0.0413, 0.1334	0.0398, 0.0902
R1 ^a , wR2 ^b (all data)	0.0497, 0.1362	0.0496, 0.1355	0.0550, 0.1323	0.0444, 0.1122	0.0481, 0.1366	0.0509, 0.0944
Largest Diff. Peak and Hole (e Å ⁻³)	0.804 and -1.075	1.705 and -0.635	1.147 and -1.000	1.207 and -0.977	1.425 and -0.461	0.431 and -0.779

$${}^a R_1 = \frac{\sum |F_o| - |F_c|}{\sum |F_o|}, {}^b wR_2 = \frac{\sum [w(F_o^2 - F_c^2)]}{\sum [w(F_o^2)]}^{1/2}$$

	Zn ₂ (dobpdc)(m-2-m-CO ₂) _{1.5}	Zn ₂ (dobpdc)(e-2-e-CO ₂) _{1.62}	Zn ₂ (dobpdc)(e-2-CO ₂) _{1.5}	Zn ₂ (dobpdc)(i-2-CO ₂) _{1.5}
Formula	C _{21.5} H ₂₄ N ₃ O ₉ Zn ₂	C ₂₇ H ₃₈ N ₄ O ₈ Zn ₂	C _{20.48} H _{22.20} N _{3.24} O _{9.24} Zn ₂	C ₂₅ H ₃₄ N ₄ O ₈ Zn ₂
Temperature (K)	195(2)	195(2)	100(2)	195(2)
Crystal System	Trigonal	Trigonal	Trigonal	Trigonal
Space Group	P3 ₁ 21	P3 ₂ 21	P3 ₂ 21	P3 ₁ 21
a, b, c (Å)	21.5457(9), 21.5457(9), 6.9279(3)	21.6857(8), 21.6857(8), 6.8891(3)	21.2594(11), 21.2594(11), 6.7655(4)	21.6521(9), 21.6521(9), 6.8387(3)
α, β, γ (°)	90, 90, 120	90, 90, 120	90, 90, 120	90, 90, 120
V, (Å ³)	2785.2(3)	2805.7(2)	2648.1(3)	2776.5(3)
Z	3	3	3	3
Radiation,	Synchrotron,	Synchrotron,	Synchrotron,	Synchrotron,
λ (Å)	0.7749	0.7749	0.7749	0.7749
2θ Range for Data Collection (°)	4.760 to 59.570	4.730 to 51.034	4.178 to 74.452	4.102 to 53.562
Completeness to 2θ	99.7% (2θ = 55.412°)	99.9% (2θ = 51.034°)	99.8% (2θ = 55.412°)	99.9% (2θ = 53.562°)
Data / Restraints / Parameters	4088 / 0 / 184	2706 / 133 / 200	7037 / 179 / 247	3047 / 102 / 200
Goodness of Fit on F ²	1.123	1.232	1.140	1.109
R1 ^a , wR2 ^b (I > 2σ(I))	0.0409, 0.1152	0.0645, 0.1610	0.0513, 0.1260	0.0457, 0.1354
R1 ^a , wR2 ^b (all data)	0.0457, 0.1177	0.0680, 0.1628	0.0570, 0.1283	0.0514, 0.1392
Largest Diff. Peak and Hole (e Å ⁻³)	0.830 and -0.655	0.829 and -0.842	0.823 and -1.604	0.519 and -0.445

$$^a R_1 = \frac{\sum |F_o| - |F_c|}{\sum |F_o|}, \quad ^b wR_2 = \frac{\sum [w(F_o^2 - F_c^2)]}{\sum [w(F_o^2)]}^{1/2}$$

Zn ₂ (dobpdc)(DMA) ₂	
Formula	C ₂₂ H ₂₄ N ₂ O ₈ Zn ₂
Temperature (K)	100(2)
Crystal System	Trigonal
Space Group	<i>P</i> 3 ₂ 21
a, b, c (Å)	21.5292(11), 21.5292(11), 6.6937(4)
α, β, γ (°)	90, 90, 120
V, (Å ³)	2686.9(3)
Z	3
Radiation, λ (Å)	Synchrotron, 0.7749
2θ Range for Data Collection (°)	6.304 to 80.502
Completeness to 2θ	99.5% (2θ = 55.412°)
Data / Restraints / Parameters	8679 / 0 / 158
Goodness of Fit on F ²	1.100
R1 ^a , wR2 ^b (I > 2σ(I))	0.0645, 0.1602
R1 ^a , wR2 ^b (all data)	0.0743, 0.1645
Largest Diff. Peak and Hole (e Å ⁻³)	1.248 and -2.931
$^a R_1 = \frac{\sum F_o - F_c }{\sum F_o }$, $^b wR_2 = \frac{\{\sum [w(F_o^2 - F_c^2)^2] / \sum [w(F_o^2)^2]\}^{1/2}}$	

2.7 References

- (1) Dlugokencky, E.; Tans, P. ESRL Global Monitoring Division - Global Greenhouse Gas Reference Network www.esrl.noaa.gov/gmd/ccgg/trends/ (accessed Jan 25, 2017).
- (2) International Energy Agency. CO₂ Emissions from Fuel Combustion: Highlights 2016 https://www.iea.org/publications/freepublications/publication/CO2EmissionsfromFuelCombustion_Highlights_2016.pdf (accessed Jan 25, 2017).
- (3) IPCC, 2014: Summary for Policymakers. In *Climate Change 2014: Mitigation of Climate Change. Contribution of Working Group III to the Fifth Assessment Report of the Intergovernmental Panel on Climate Change*; Edenhofer, O., Sokona, Y., Farahani, E., Kadner, S., Seyboth, K., Adler, A., Baum, I., Brunner, S., Eickemeier, P., Kriemann, B., Savolainen, S., Schlömer, S., von Stechow, C., Zwickel, T., Minx, J. C., Eds.; Cambridge University Press: New York, NY, USA.
- (4) Boot-Handford, M. E.; Abanades, J. C.; Anthony, E. J.; Blunt, M. J.; Brandani, S.; Mac Dowell, N.; Fernández, J. R.; Ferrari, M.-C.; Gross, R.; Hallett, J. P.; Haszeldine, R. S.; Heptonstall, P.; Lyngfelt, A.; Makuch, Z.; Mangano, E.; Porter, R. T. J.; Pourkashanian, M.; Rochelle, G. T.; Shah, N.; Yao, J. G.; Fennell, P. S. Carbon Capture and Storage Update. *Energy Environ. Sci.* **2014**, *7* (1), 130–189. <https://doi.org/10.1039/C3EE42350F>.
- (5) Pacala, S.; Socolow, R. Stabilization Wedges: Solving the Climate Problem for the Next 50 Years with Current Technologies. *Science* **2004**, *305* (5686), 968–972. <https://doi.org/10.1126/science.1100103>.
- (6) Holm-Nielsen, J. B.; Al Seadi, T.; Oleskowicz-Popiel, P. The Future of Anaerobic Digestion and Biogas Utilization. *Bioresour. Technol.* **2009**, *100* (22), 5478–5484. <https://doi.org/10.1016/j.biortech.2008.12.046>.
- (7) Rochelle, G. T. Amine Scrubbing for CO₂ Capture. *Science* **2009**, *325* (5948), 1652–1654. <https://doi.org/10.1126/science.1176731>.
- (8) Wang, M.; Lawal, A.; Stephenson, P.; Sidders, J.; Ramshaw, C. Post-Combustion CO₂ Capture with Chemical Absorption: A State-of-the-Art Review. *Chem. Eng. Res. Des.* **2011**, *89* (9), 1609–1624. <https://doi.org/10.1016/j.cherd.2010.11.005>.
- (9) Bhowan, A. S.; Freeman, B. C. Analysis and Status of Post-Combustion Carbon Dioxide Capture Technologies. *Environ. Sci. Technol.* **2011**, *45* (20), 8624–8632. <https://doi.org/10.1021/es104291d>.
- (10) Choi, S.; Drese, J. H.; Jones, C. W. Adsorbent Materials for Carbon Dioxide Capture from Large Anthropogenic Point Sources. *ChemSusChem* **2009**, *2* (9), 796–854. <https://doi.org/10.1002/cssc.200900036>.
- (11) Samanta, A.; Zhao, A.; Shimizu, G. K. H.; Sarkar, P.; Gupta, R. Post-Combustion CO₂ Capture Using Solid Sorbents: A Review. *Ind. Eng. Chem. Res.* **2012**, *51* (4), 1438–1463. <https://doi.org/10.1021/ie200686q>.
- (12) Mason, J. A.; McDonald, T. M.; Bae, T.-H.; Bachman, J. E.; Sumida, K.; Dutton, J. J.; Kaye, S. S.; Long, J. R. Application of a High-Throughput Analyzer in Evaluating Solid Adsorbents for Post-Combustion Carbon Capture via Multicomponent Adsorption of CO₂, N₂, and H₂O. *J. Am. Chem. Soc.* **2015**, *137* (14), 4787–4803. <https://doi.org/10.1021/jacs.5b00838>.
- (13) Sumida, K.; Rogow, D. L.; Mason, J. A.; McDonald, T. M.; Bloch, E. D.; Herm, Z. R.; Bae, T.-H.; Long, J. R. Carbon Dioxide Capture in Metal–Organic Frameworks. *Chem. Rev.* **2012**, *112* (2), 724–781. <https://doi.org/10.1021/cr2003272>.

- (14) Li, J.-R.; Ma, Y.; McCarthy, M. C.; Sculley, J.; Yu, J.; Jeong, H.-K.; Balbuena, P. B.; Zhou, H.-C. Carbon Dioxide Capture-Related Gas Adsorption and Separation in Metal-Organic Frameworks. *Coord. Chem. Rev.* **2011**, *255* (15–16), 1791–1823. <https://doi.org/10.1016/j.ccr.2011.02.012>.
- (15) Wang, Q.; Luo, J.; Zhong, Z.; Borgna, A. CO₂ Capture by Solid Adsorbents and Their Applications: Current Status and New Trends. *Energy Environ. Sci.* **2010**, *4* (1), 42–55. <https://doi.org/10.1039/C0EE00064G>.
- (16) Lin, Y.; Kong, C.; Chen, L. Amine-Functionalized Metal–Organic Frameworks: Structure, Synthesis and Applications. *RSC Adv.* **2016**, *6* (39), 32598–32614. <https://doi.org/10.1039/C6RA01536K>.
- (17) Yu, J.; Xie, L.-H.; Li, J.-R.; Ma, Y.; Seminario, J. M.; Balbuena, P. B. CO₂ Capture and Separations Using MOFs: Computational and Experimental Studies. *Chem. Rev.* **2017**. <https://doi.org/10.1021/acs.chemrev.6b00626>.
- (18) Demessence, A.; D’Alessandro, D. M.; Foo, M. L.; Long, J. R. Strong CO₂ Binding in a Water-Stable, Triazolate-Bridged Metal–Organic Framework Functionalized with Ethylenediamine. *J. Am. Chem. Soc.* **2009**, *131* (25), 8784–8786. <https://doi.org/10.1021/ja903411w>.
- (19) McDonald, T. M.; D’Alessandro, D. M.; Krishna, R.; Long, J. R. Enhanced Carbon Dioxide Capture upon Incorporation of N,N’-Dimethylethylenediamine in the Metal–Organic Framework CuBTri. *Chem. Sci.* **2011**, *2* (10), 2022–2028. <https://doi.org/10.1039/C1SC00354B>.
- (20) Choi, S.; Watanabe, T.; Bae, T.-H.; Sholl, D. S.; Jones, C. W. Modification of the Mg/DOBDC MOF with Amines to Enhance CO₂ Adsorption from Ultradilute Gases. *J. Phys. Chem. Lett.* **2012**, *3* (9), 1136–1141. <https://doi.org/10.1021/jz300328j>.
- (21) McDonald, T. M.; Lee, W. R.; Mason, J. A.; Wiers, B. M.; Hong, C. S.; Long, J. R. Capture of Carbon Dioxide from Air and Flue Gas in the Alkylamine-Appended Metal–Organic Framework mmen-Mg₂(dobpdc). *J. Am. Chem. Soc.* **2012**, *134* (16), 7056–7065. <https://doi.org/10.1021/ja300034j>.
- (22) Lee, W. R.; Hwang, S. Y.; Ryu, D. W.; Lim, K. S.; Han, S. S.; Moon, D.; Choi, J.; Hong, C. S. Diamine-Functionalized Metal–Organic Framework: Exceptionally High CO₂ Capacities from Ambient Air and Flue Gas, Ultrafast CO₂ Uptake Rate, and Adsorption Mechanism. *Energy Environ. Sci.* **2014**, *7* (2), 744–751. <https://doi.org/10.1039/C3EE42328J>.
- (23) McDonald, T. M.; Mason, J. A.; Kong, X.; Bloch, E. D.; Gygi, D.; Dani, A.; Crocellà, V.; Giordanino, F.; Odoh, S. O.; Drisdell, W. S.; Vlasisavljevich, B.; Dzubak, A. L.; Poloni, R.; Schnell, S. K.; Planas, N.; Lee, K.; Pascal, T.; Wan, L. F.; Prendergast, D.; Neaton, J. B.; Smit, B.; Körttricht, J. B.; Gagliardi, L.; Bordiga, S.; Reimer, J. A.; Long, J. R. Cooperative Insertion of CO₂ in Diamine-Appended Metal-Organic Frameworks. *Nature* **2015**, *519* (7543), 303–308. <https://doi.org/10.1038/nature14327>.
- (24) Lee, W. R.; Jo, H.; Yang, L.-M.; Lee, H.; Ryu, D. W.; Lim, K. S.; Song, J. H.; Min, D. Y.; Han, S. S.; Seo, J. G.; Park, Y. K.; Moon, D.; Hong, C. S. Exceptional CO₂ Working Capacity in a Heterodiamine-Grafted Metal–Organic Framework. *Chem. Sci.* **2015**, *6* (7), 3697–3705. <https://doi.org/10.1039/C5SC01191D>.
- (25) Yeon, J. S.; Lee, W. R.; Kim, N. W.; Jo, H.; Lee, H.; Song, J. H.; Lim, K. S.; Kang, D. W.; Seo, J. G.; Moon, D.; Wiers, B.; Hong, C. S. Homodiamine-Functionalized Metal–Organic Frameworks with a MOF-74-Type Extended Structure for Superior Selectivity of CO₂

- over N₂. *J Mater Chem A* **2015**, *3* (37), 19177–19185. <https://doi.org/10.1039/C5TA02357B>.
- (26) Liao, P.-Q.; Chen, X.-W.; Liu, S.-Y.; Li, X.-Y.; Xu, Y.-T.; Tang, M.; Rui, Z.; Ji, H.; Zhang, J.-P.; Chen, X.-M. Putting an Ultrahigh Concentration of Amine Groups into a Metal–Organic Framework for CO₂ Capture at Low Pressures. *Chem. Sci.* **2016**, *7* (10), 6528–6533. <https://doi.org/10.1039/C6SC00836D>.
- (27) Hefti, M.; Joss, L.; Bjelobrk, Z.; Mazzotti, M. On the Potential of Phase-Change Adsorbents for CO₂ Capture by Temperature Swing Adsorption. *Faraday Discuss.* **2016**, *192*, 153–179. <https://doi.org/10.1039/C6FD00040A>.
- (28) Jo, H.; Lee, W. R.; Kim, N. W.; Jung, H.; Lim, K. S.; Kim, J. E.; Kang, D. W.; Lee, H.; Hiremath, V.; Seo, J. G.; Jin, H.; Moon, D.; Han, S. S.; Hong, C. S. Fine-Tuning of the Carbon Dioxide Capture Capability of Diamine-Grafted Metal–Organic Framework Adsorbents Through Amine Functionalization. *ChemSusChem* **2017**, *10* (3), 541–550. <https://doi.org/10.1002/cssc.201601203>.
- (29) Long, J. R.; McDonald, T. M. Cooperative Chemical Adsorption of Acid Gases in Functionalized Metal-Organic Frameworks. US20170087531 A1, March 30, 2017.
- (30) Drisdell, W. S.; Poloni, R.; McDonald, T. M.; Pascal, T. A.; Wan, L. F.; Pemmaraju, C. D.; Vlaisavljevich, B.; Odoh, S. O.; Neaton, J. B.; Long, J. R.; Prendergast, D.; Kortright, J. B. Probing the Mechanism of CO₂ Capture in Diamine-Appended Metal–Organic Frameworks Using Measured and Simulated X-Ray Spectroscopy. *Phys Chem Chem Phys* **2015**, *17* (33), 21448–21457. <https://doi.org/10.1039/C5CP02951A>.
- (31) Irving, H.; Williams, R. J. P. The Stability of Transition-Metal Complexes. *J. Chem. Soc.* **1953**, 3192–3210. <https://doi.org/10.1039/JR9530003192>.
- (32) Lindsey, A. S.; Jeskey, H. The Kolbe-Schmitt Reaction. *Chem. Rev.* **1957**, *57* (4), 583–620. <https://doi.org/10.1021/cr50016a001>.
- (33) Gonzalez, M. I.; Mason, J. A.; Bloch, E. D.; Teat, S. J.; Gagnon, K. J.; Morrison, G. Y.; Queen, W. L.; Long, J. R. Structural Characterization of Framework–Gas Interactions in the Metal–Organic Framework Co₂(Dobdc) by in Situ Single-Crystal X-Ray Diffraction. *Chem. Sci.* **2017**, *8* (6), 4387–4398. <https://doi.org/10.1039/C7SC00449D>.
- (34) *SAINTE, APEX2, and APEX3 Software for CCD Diffractometers*; Bruker Analytical X-ray Systems Inc.: Madison, WI, USA, 2014.
- (35) Sheldrick, G. M. *SADABS*; University of Göttingen, Germany.
- (36) Sheldrick, G. M. SHELXT – Integrated Space-Group and Crystal-Structure Determination. *Acta Crystallogr. Sect. Found. Adv.* **2015**, *71* (1), 3–8. <https://doi.org/10.1107/S2053273314026370>.
- (37) Sheldrick, G. M. Crystal Structure Refinement with SHELXL. *Acta Crystallogr. Sect. C Struct. Chem.* **2015**, *71* (1), 3–8. <https://doi.org/10.1107/S2053229614024218>.
- (38) Dolomanov, O. V.; Bourhis, L. J.; Gildea, R. J.; Howard, J. a. K.; Puschmann, H. OLEX2: A Complete Structure Solution, Refinement and Analysis Program. *J. Appl. Crystallogr.* **2009**, *42* (2), 339–341. <https://doi.org/10.1107/S0021889808042726>.
- (39) Campbell, C. T.; Sellers, J. R. V. Enthalpies and Entropies of Adsorption on Well-Defined Oxide Surfaces: Experimental Measurements. *Chem. Rev.* **2013**, *113* (6), 4106–4135. <https://doi.org/10.1021/cr300329s>.
- (40) Caskey, S. R.; Wong-Foy, A. G.; Matzger, A. J. Dramatic Tuning of Carbon Dioxide Uptake via Metal Substitution in a Coordination Polymer with Cylindrical Pores. *J. Am. Chem. Soc.* **2008**, *130* (33), 10870–10871. <https://doi.org/10.1021/ja8036096>.

- (41) Deng, H.; Grunder, S.; Cordova, K. E.; Valente, C.; Furukawa, H.; Hmadeh, M.; Gándara, F.; Whalley, A. C.; Liu, Z.; Asahina, S.; Kazumori, H.; O'Keeffe, M.; Terasaki, O.; Stoddart, J. F.; Yaghi, O. M. Large-Pore Apertures in a Series of Metal-Organic Frameworks. *Science* **2012**, *336* (6084), 1018–1023. <https://doi.org/10.1126/science.1220131>.
- (42) Vaidhyanathan, R.; Iremonger, S. S.; Shimizu, G. K. H.; Boyd, P. G.; Alavi, S.; Woo, T. K. Direct Observation and Quantification of CO₂ Binding Within an Amine-Functionalized Nanoporous Solid. *Science* **2010**, *330* (6004), 650–653. <https://doi.org/10.1126/science.1194237>.
- (43) Kim, H.; Kim, Y.; Yoon, M.; Lim, S.; Park, S. M.; Seo, G.; Kim, K. Highly Selective Carbon Dioxide Sorption in an Organic Molecular Porous Material. *J. Am. Chem. Soc.* **2010**, *132* (35), 12200–12202.
- (44) Liao, P.-Q.; Zhou, D.-D.; Zhu, A.-X.; Jiang, L.; Lin, R.-B.; Zhang, J.-P.; Chen, X.-M. Strong and Dynamic CO₂ Sorption in a Flexible Porous Framework Possessing Guest Chelating Claws. *J. Am. Chem. Soc.* **2012**, *134* (42), 17380–17383. <https://doi.org/10.1021/ja3073512>.
- (45) Queen, W. L.; Hudson, M. R.; Bloch, E. D.; Mason, J. A.; Gonzalez, M. I.; Lee, J. S.; Gygi, D.; Howe, J. D.; Lee, K.; Darwish, T. A.; James, M.; Peterson, V. K.; Teat, S. J.; Smit, B.; Neaton, J. B.; Long, J. R.; Brown, C. M. Comprehensive Study of Carbon Dioxide Adsorption in the Metal–Organic Frameworks M₂(dobdc) (M = Mg, Mn, Fe, Co, Ni, Cu, Zn). *Chem. Sci.* **2014**, *5* (12), 4569–4581. <https://doi.org/10.1039/C4SC02064B>.
- (46) Takamizawa, S.; Nataka, E.; Akatsuka, T.; Miyake, R.; Kakizaki, Y.; Takeuchi, H.; Maruta, G.; Takeda, S. Crystal Transformation and Host Molecular Motions in CO₂ Adsorption Process of a Metal Benzoate Pyrazine (M^{II} = Rh, Cu). *J. Am. Chem. Soc.* **2010**, *132* (11), 3783–3792. <https://doi.org/10.1021/ja9091598>.
- (47) Lama, P.; Aggarwal, H.; Bezuidenhout, C. X.; Barbour, L. J. Giant Hysteretic Sorption of CO₂: In Situ Crystallographic Visualization of Guest Binding within a Breathing Framework at 298 K. *Angew. Chem. Int. Ed.* **2016**, *55* (42), 13271–13275. <https://doi.org/10.1002/anie.201607076>.
- (48) Castro, J.; Castineiras, A.; Duran, M. L.; Garcia-Vazquez, J. A.; Macias, A.; Romero, J.; Sousa, A. Direct Electrochemical Synthesis and Crystal Structure of the Zinc(II) Carbamate Complex {[N-Methyl-N'-[(2-Pyrrolyl)-Methylene]Ethylenediamine][N-Methyl-N-[2-[(2-Pyrrolato)-Methyleneamino]Ethyl]Carbamato]}zinc(II). *Z. Für Anorg. Allg. Chem.* **1990**, *586* (1), 203–208. <https://doi.org/10.1002/zaac.19905860126>.
- (49) Yamaguchi, S.; Takahashi, T.; Wada, A.; Funahashi, Y.; Ozawa, T.; Jitsukawa, K.; Masuda, H. Fixation of CO₂ by Hydroxozinc(II) Complex with Pyridylamino Type Ligand. *Chem. Lett.* **2007**, *36* (7), 842–843. <https://doi.org/10.1246/cl.2007.842>.
- (50) Notni, J.; Schenk, S.; Görls, H.; Breitzke, H.; Anders, E. Formation of a Unique Zinc Carbamate by CO₂ Fixation: Implications for the Reactivity of Tetra-Azamacrocyclic Ligated Zn(II) Complexes. *Inorg. Chem.* **2008**, *47* (4), 1382–1390. <https://doi.org/10.1021/ic701899u>.
- (51) An, J.; Fiorella, R. P.; Geib, S. J.; Rosi, N. L. Synthesis, Structure, Assembly, and Modulation of the CO₂ Adsorption Properties of a Zinc-Adeninate Macrocyclic. *J. Am. Chem. Soc.* **2009**, *131* (24), 8401–8403. <https://doi.org/10.1021/ja901869m>.

- (52) Tiritiris, I.; Kantlehner, W. Orthoamide Und Iminiumsalsze, LXX [1]. Zur Fixierung von Kohlendioxid Mit Organischen Basen (Teil 1) – Reaktionen von Diaminen Mit Kohlendioxid. *Z. Naturforsch.* **2011**, *66b*, 164–176.
- (53) The unit v/v corresponds to $\text{cm}^3\text{STP}/\text{cm}^3$, where STP is defined as 273.15 K and 1 atm. Volumetric capacities of the frameworks $\text{Mg}_2(\text{dobpdc})(\text{diamine})_2$ were calculated using crystallographic densities approximated from the 100 K single-crystal unit cell volumes of the analogous Zn frameworks.
- (54) *Cost and Performance Baseline for Fossil Energy Plants. Volume 1a: Bituminous Coal (PC) and Natural Gas to Electricity. Revision 3*; DOE/NETL-2015/1723; U.S. Department of Energy, National Energy Technology Laboratory, 2015.
- (55) Garrone, E.; Bonelli, B.; Otero Areán, C. Enthalpy–Entropy Correlation for Hydrogen Adsorption on Zeolites. *Chem. Phys. Lett.* **2008**, *456* (1–3), 68–70. <https://doi.org/10.1016/j.cplett.2008.03.014>.
- (56) Areán, C. O.; Chavan, S.; Cabello, C. P.; Garrone, E.; Palomino, G. T. Thermodynamics of Hydrogen Adsorption on Metal-Organic Frameworks. *ChemPhysChem* **2010**, *11* (15), 3237–3242. <https://doi.org/10.1002/cphc.201000523>.
- (57) Liu, L.; Guo, Q.-X. Isokinetic Relationship, Isoequilibrium Relationship, and Enthalpy–Entropy Compensation. *Chem. Rev.* **2001**, *101* (3), 673–696. <https://doi.org/10.1021/cr990416z>.
- (58) Lemmon, E. W.; Huber, M. L.; McLinden, M. O. *REFPROP: Reference Fluid Thermodynamic and Transport Properties, Version 9*; National Institute of Standards and Technology, 2010.
- (59) *GateCycle*; General Electric Company, 2011.
- (60) Berger, A. H.; Bhowan, A. S. “Impact of Steam Extraction for CCS on Power Plant Performance,” AICHE Annual Meeting, San Francisco, CA, USA, 2013.
- (61) Hill, T. L. *An Introduction to Statistical Thermodynamics*; Dover Publications: New York, 1986.

Chapter 3. Water Enables Efficient CO₂ Capture from Natural Gas Flue Emissions in an Oxidation-Resistant Diamine-Appended Metal–Organic Framework

3.1. Introduction

The combustion of fossil fuels in the energy sector is currently responsible for the release of 32 Gt/year of CO₂ into the atmosphere, or approximately 65% of annual anthropogenic greenhouse gas emissions.^{1,2} To limit the contribution of these emissions to global climate change, mitigation strategies are needed during the transition to cleaner fuel sources.² One of the most widely studied emission mitigation strategies is post-combustion carbon capture and sequestration (CCS), in which CO₂ is selectively removed from the flue gas streams of fossil fuel- or biomass-fired power plants and sequestered underground.^{1–4} To date, the large majority of efforts toward implementing CCS have focused on coal-fired power plants, which are currently responsible for approximately 45% of energy-related CO₂ emissions.^{4,5} However, global consumption of natural gas has been increasing steadily, and its contribution to global primary energy is anticipated to overtake that of coal by 2040 (New Policy Scenario, International Energy Agency).⁶ Furthermore, in economies where natural gas is prevalent, such as that of the United States, the rapid transition away from coal has resulted in CO₂ emissions from the combustion of natural gas already exceeding those from coal, despite the fact that natural gas emits approximately half as much CO₂ as coal per unit electricity produced.⁷ Therefore, new materials are urgently needed for the selective removal of CO₂ from the emissions of natural gas-fired power plants.^{8–10}

The flue gas stream produced at a natural gas combined cycle (NGCC) power plant consists of approximately 74.4% N₂, 12.4% O₂, 8.4% H₂O, 3.9% CO₂, and 0.9% Ar.¹¹ Importantly, emissions from NGCC plants contain fewer pollutants than emission streams from coal-fired plants, which release SO_x, NO_x, heavy metals, and particulate matter.¹¹ These contaminants pose environmental hazards and serve as significant barriers to the deployment of CCS systems in coal-fired plants, particularly due to the known poisoning of a number of CO₂ capture materials by SO_x and NO_x.^{12–19} The CO₂ partial pressure of NGCC flue gas (~40 mbar) is also significantly lower than that of coal flue gas (~150 mbar).¹¹ As a result, gas-fired plants are cleaner-burning than coal-fired plants, but CO₂ capture from the emissions of these power stations is more technically challenging. Specifically, the U.S. Department of Energy (DoE) has set a target of 90% capture of CO₂ from the emission stream,¹¹ requiring that candidate CO₂ capture materials bind CO₂ at concentrations as low as 0.4%. Materials that meet this requirement often possess high CO₂ adsorption enthalpies,²⁰ necessitating energy-intensive cycling conditions and generating a potential tradeoff between heat management and CO₂ cycling capacity.²¹

Owing to decades of development, aqueous amine solutions are the most technology-ready systems for large-scale CO₂ capture applications.^{22,23} However, amine solutions face technological barriers to deployment for CO₂ capture from NGCC power plants due to their high regeneration energy costs and susceptibility to oxidative and thermal degradation.^{24–27} As an alternative, solid adsorbents, such as zeolites, amine-functionalized silicas, porous organic networks, and metal–organic frameworks, may offer enhanced stability, greater CO₂ cycling capacities, and inherently lower regeneration energies.^{4,28–40} Despite the flourishing research areas of adsorptive CO₂ capture from coal flue gas and air, only a handful of reports have yet explored adsorbent design specifically for CCS from gas-fired power plants.^{36,41–48} More research is also needed to design adsorbents with high thermal and oxidative stabilities that can capture CO₂ selectively under humid conditions.

Recently, we^{49–53} and others^{45,54–58} have demonstrated the potential of diamine-appended variants of the metal–organic framework $\text{Mg}_2(\text{dobpdc})$ ($\text{dobpdc}^{4-} = 4,4'$ -dioxidobiphenyl-3,3'-dicarboxylate) as transformative materials for carbon capture applications. The unique step-shaped adsorption profiles of these frameworks enable cycling of the full CO_2 adsorption capacity with minimal temperature swings. We have further shown that the adsorption step of these materials can be tuned post-synthetically by changing the appended diamine,⁵¹ a strategy that we employed to optimize an adsorbent for CO_2 capture from coal flue gas.⁵² Our previous work posited that *primary,secondary* ($1^\circ/2^\circ$) diamine-appended variants of $\text{Mg}_2(\text{dobpdc})$ are likely the most promising for CO_2 capture from NGCC flue gas, on the basis of their low CO_2 adsorption step pressures (<1 mbar at 40°C) and minimal hysteresis upon CO_2 desorption.⁵¹ However, these materials possess a tradeoff between thermal stability and CO_2 adsorption capacity. Specifically, the largest $1^\circ/2^\circ$ diamines were the most resistant to amine volatilization during temperature-swing cycling but also underwent a steric rearrangement at half saturation (0.5 CO_2 per diamine), which led to double-stepped CO_2 adsorption profiles.⁵³ As a result, at the low partial pressures relevant for NGCC CCS systems, only the capacity of the first CO_2 adsorption step (half of the theoretical capacity) would be accessible with such materials. While two similar base frameworks were shown to resolve the issue of steric crowding to enable single-step adsorption profiles with large diamines,⁵³ the initially studied $\text{Mg}_2(\text{dobpdc})(\text{diamine})_2$ variants remain preferable due to their inexpensive components and favorable gravimetric (~ 3.5 – 4.0 mmol/g) and volumetric (~ 79 – 84 v/v) CO_2 adsorption capacities.⁵¹ Additionally, $\text{Mg}_2(\text{dobpdc})$ has already been prepared at the multi-kilogram scale,⁵⁹ facilitating rapid technology development.

Herein, we demonstrate that appending the cyclic $1^\circ/2^\circ$ diamine 2-(aminomethyl)piperidine (2-ampd) to the metal sites in $\text{Mg}_2(\text{dobpdc})$ alters the steric interactions and thermodynamics of CO_2 adsorption, giving rise to a material with two closely-spaced adsorption steps. The adsorbent 2-ampd– $\text{Mg}_2(\text{dobpdc})$ (Figure 3.1) is thermally stable and exhibits two CO_2 adsorption steps at pressures low enough to access the full chemisorptive capacity of the material (1 CO_2 per diamine) from NGCC flue gas. Importantly, we find that the presence of water greatly improves the CO_2 adsorption characteristics of this material, enabling it to achieve $\geq 90\%$ removal of CO_2 from simulated NGCC flue gas in breakthrough measurements. While other amine-functionalized adsorbents have shown improvements in CO_2 capture performance due to a humidity-induced mechanistic shift, our van der Waals (vdW)-corrected density functional theory (DFT) calculations and spectroscopy measurements show that the improved performance of 2-ampd– $\text{Mg}_2(\text{dobpdc})$ under humid conditions can instead be attributed to preferential stabilization of the ammonium carbamate chains formed upon CO_2 insertion. Our results demonstrate that 2-ampd– $\text{Mg}_2(\text{dobpdc})$ is among the most promising adsorbents identified to date for this underexplored but extremely important separation.

3.2. Experimental Procedures

3.2.1. General Synthesis and Characterization Methods

^1H NMR spectra were collected on a Bruker AMX 300 MHz spectrometer and referenced to residual dimethyl sulfoxide ($\delta = 2.50$ ppm). Powder X-ray diffraction (PXRD) patterns were collected with a laboratory Bruker AXS D8 Advance diffractometer with $\text{Cu K}\alpha$ radiation ($\lambda = 1.5418$ Å) or at the Advanced Photon Source with synchrotron radiation ($\lambda = 0.45399$ Å), as specified in the figure captions. Additional details for synchrotron PXRD experiments under

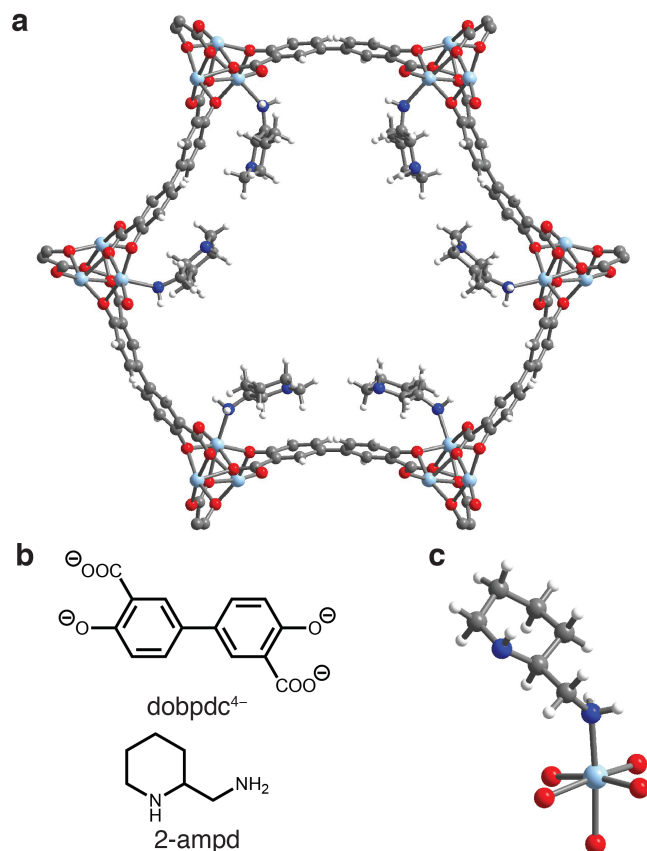


Figure 3.1. (a) Single-crystal X-ray diffraction structure of toluene-solvated 2-ampd-Zn₂(dobpdc), which is isostructural to 2-ampd-Mg₂(dobpdc). The left-handed diamine is depicted in the right-handed framework (space group *P*3₁21). The structure was refined with a racemic mixture of 2-ampd in an inversion-twinned crystal. The enantiomeric diamine and toluene solvent molecules are omitted for clarity. (b) Chemical structures of the ligand dobpc⁴⁻ and the diamine 2-ampd. (c) First coordination sphere of the Zn(II) site depicting coordination of the right-handed enantiomer of the diamine. Light blue, blue, red, gray, and white spheres represent Zn, N, O, C, and H atoms, respectively.

controlled atmospheres are given in the Supporting Information in Section 3.15. All synthetic manipulations were carried out under air unless noted otherwise. All solvents and reagents, including diamines, were purchased from commercial sources and used without further purification unless otherwise noted. The linker H₄dobpdc was purchased from Hangzhou Trylead Chemical Technology Co. The linker H₄dotpdc was prepared according to the literature procedure.⁵³ The metal-organic frameworks Mg₂(dobpdc),⁵¹ Mn₂(dobpdc),⁵² Ni₂(dobpdc),⁵² Co₂(dobpdc),⁵² Zn₂(dobpdc),⁶⁰ and Mg₂(dotpdc)⁵³ were prepared according to literature procedures (Supporting Information, Section 3.6.1). Ultrahigh purity (>99.998%) gases were used for all adsorption experiments.

3.2.2. Infrared Spectra

Attenuated total reflectance (ATR) infrared (IR) spectra were collected on a PerkinElmer Spectrum 400 Fourier Transform (FT) IR spectrometer equipped with a Pike GladiATR and a home-built glovebag accessory used to control the atmosphere. Three vacuum-refill cycles were used to exchange the atmosphere of the glovebag accessory when preparing the system for *in situ*

experiments. For humid FTIR spectra, samples were placed in 4 mL vials and sealed in a 20 mL vapor-dosing chamber containing ~4 mL of water. After at least 15 min of equilibration, the powder was removed, and spectra were collected. Co-adsorption of water in the sample was confirmed by observation of the H₂O IR vibrational bands at 1638 and 3350 (broad) cm⁻¹.⁶¹

3.2.3. Diamine Grafting Procedure

Following a previously reported method,⁵¹ a 20 mL scintillation vial was charged with toluene (4 mL) and 2-ampd (1 mL). Methanol-solvated Mg₂(dobpdc) (~15 mg) was filtered and washed with toluene (2 × 10 mL). (Note: Mg₂(dobpdc) should not be allowed to dry completely in air due to potential decomposition.⁴⁹) The filter-dried Mg₂(dobpdc) was added to the diamine solution, and the vial was swirled several times and allowed to stand at room temperature for at least 12 h. After this time, the mixture was filtered, and the resulting powder was washed with toluene (3 × 20 mL) and allowed to dry for ~3 min under reduced pressure, yielding ~25 mg of toluene-solvated 2-ampd–Mg₂(dobpdc). Other diamine-appended metal–organic frameworks described in this work were prepared using a similar procedure. Full characterization of all new diamine-appended frameworks prepared as part of this work, including PXRD patterns, IR spectra, dry N₂ thermogravimetric decomposition profiles, and CO₂ adsorption/desorption isobars, are included in the Supporting Information. Diamine loadings were determined by suspending ~5 mg of the diamine-appended metal–organic framework in 0.5 mL of DMSO-*d*₆ and then digesting the framework by adding several drops of DCl (35 wt % in D₂O) and heating until the mixture became homogeneous. The resulting solutions were analyzed by ¹H NMR spectroscopy to determine the ratio of diamine to organic linker. Representative diamine loadings for all diamine-appended metal–organic frameworks prepared as part of this work are included in the Supporting Information.

3.2.4. Thermogravimetric Analysis and Cycling Measurements

Dry thermogravimetric analysis (TGA) experiments were conducted using a TA Instruments TGA Q5000. Humid TGA experiments were conducted using a TA Instruments TGA Q50. For humid experiments, the incident gas stream was passed through two room-temperature water bubblers in series, leading to an estimated water content of 2.6%, as determined by comparison to the water isotherms of 2-ampd–Mg₂(dobpdc) (Figure 3.S11). Pre-mixed cylinders of CO₂ in N₂ were obtained from Praxair. Samples were activated under flowing N₂ for 20–30 min until the mass stabilized; exact activation conditions for each diamine-appended material were determined through careful analysis of the dry N₂ thermal decomposition profiles and are included in the Supporting Information. Masses are uncorrected for buoyancy effects. A flow rate of 25 mL/min was used for all TGA experiments. Ramp rates for all isobaric measurements are included in figure captions. A ramp rate of 1.5 °C/min was employed for all dry N₂ decomposition experiments.

3.2.5. Gas Adsorption Measurements

Volumetric adsorption isotherms for N₂, O₂, and CO₂ were obtained using a Micromeritics ASAP 2020 gas adsorption analyzer. Adsorption isotherms for water were obtained using a Micromeritics 3Flex instrument. For water isotherms, the stainless-steel vapor dosing apparatus was subjected to three freeze–pump–thaw cycles to remove any dissolved gases, and heat tape

was used to keep the exposed portion of the glass sample tube at elevated temperature to prevent condensation of water. The maximum relative humidity accessible in measurements with water was limited by the manifold temperature of 45 °C. Isotherms collected at 40, 50, and 60 °C were measured using a circulating water bath to control the sample temperature. Surface area measurements with N₂ were carried out at 77 K using a liquid N₂ bath. Samples were regenerated at 100 °C under reduced pressure (<10 μbar) for 2–4 h between isotherms. The isotherm data points were considered equilibrated after <0.01% change in pressure occurred over an average of 11 intervals of 15 s (for N₂, O₂, and CO₂) or 30 s (for H₂O).

3.2.6. Calculation of Differential Enthalpies and Entropies of Adsorption

Using a linear spline interpolation method and the CO₂ adsorption isotherms for 2-ampd–Mg₂(dobpdc) (Figure 3.S7), the exact pressures (p_q) corresponding to specific CO₂ loadings (q) were determined at different temperatures (T). The Clausius–Clapeyron relationship (eq 3.1) was used to calculate the differential enthalpies of adsorption (Δh_{ads}) based on the slopes of the linear trendlines fit to $\ln(p_q)$ vs. $1/T$ (Figure 3.S8). The y -intercepts of these linear trendlines are equal to $-\Delta s_{ads}/R$ at each loading (assuming $p_0 = 1$ bar)⁶² and thus were used to determine the corresponding differential entropies of adsorption (Figure 3.S9).

$$\ln(p_q) = \left(\frac{\Delta h_{ads}}{R}\right) \left(\frac{1}{T}\right) + c \quad (3.1)$$

3.2.7. Breakthrough Measurements

See Supporting Information in Section 3.6.11 for experimental details and supplementary figures.

3.2.8. Solid-State Magic Angle Spinning (MAS) NMR Experiments

Activation of 2-ampd–Mg₂(dobpdc) was carried out under flowing N₂ at 150 °C for 30 min. The activated material was packed into a 3.2 mm rotor inside a N₂-filled glovebag and further activated under vacuum inside a home-built gas manifold for 10 min at room temperature. This manifold has the key feature of enabling gas dosing of rotors at controlled pressures and subsequent sealing of dosed rotors prior to removal from the manifold.⁶⁰ Samples were dosed with ¹³CO₂ gas (Sigma-Aldrich, 99 atom % ¹³C, <3 atom % ¹⁸O) at room temperature (~22 °C) and allowed to equilibrate for 30 min prior to measurements, unless otherwise specified. For dosing with humid CO₂, a sample that had already been dosed with dry ¹³CO₂ was opened (the top and bottom rotor caps were removed), and the sample was placed in a gas stream of humid CO₂ (relative humidity ~70%, measured using a ThermoPro TP50 Hygrometer) that was generated by flowing natural isotopic abundance CO₂ through a bubbler containing deionized water for 1 h.

All solid-state NMR experiments were carried out at 16.4 T using a Bruker 3.2 mm probe, and MAS rates were 15 kHz in all cases. All solid-state ¹³C NMR spectra were acquired by cross-polarization from ¹H (¹⁵N and ¹H contact RF field strengths of 20 kHz and 35 kHz, respectively). All cross-polarization experiments were acquired with continuous wave ¹H decoupling at 82 kHz RF field strength, and with the contact times stated in the figure captions. All ¹H NMR spectra were acquired using a 90° pulse-acquire sequence with a RF field strength of ~38 kHz, and recycle delays were adjusted to obtain quantitative spectra. The ¹H, ¹³C, and ¹⁵N chemical shifts

were referenced to 1.8 ppm (adamantane), 38.5 ppm (adamantane tertiary carbon, left-hand resonance), and 33.4 ppm (glycine), respectively.⁶³

3.2.9. Single-Crystal X-ray Diffraction

Synthetic and experimental details for single-crystal X-ray diffraction experiments with 2-ampd–Zn₂(dobpdc) and molecular 2-ampd–CO₂ are included in the Supporting Information in Sections 3.6.12–3.6.14.

3.2.10. Density Functional Theory Calculations

Our first-principles DFT calculations used a plane-wave basis and projector augmented-wave (PAW)^{64,65} pseudopotentials with the Vienna ab-initio Simulation Package (VASP)^{66–69} code. To include the effect of the vdW dispersive interactions on binding energies and NMR chemical shifts, we performed structural relaxations with vdW dispersion-corrected functionals (vdW-DF2)⁷⁰ as implemented in VASP. For all calculations, we used (i) a Γ -point sampling of the Brillouin zone (except for NMR calculations, as specified below), (ii) a 1000 eV plane-wave cutoff energy, and (iii) a 10^{-7} eV self-consistency criterion. We explicitly treat two valence electrons for Mg ($3s^2$), six for O ($2s^22p^4$), five for N ($2s^22p^3$), four for C ($2s^22p^2$), and one for H ($1s^1$). All structural relaxations were performed with a Gaussian smearing of 0.05 eV.⁷¹ The ions were relaxed until the Hellmann-Feynman forces were less than $0.001 \text{ eV}\text{\AA}^{-1}$. To compute CO₂ and H₂O binding energies, we optimized the structure of 2-ampd–Mg₂(dobpdc) prior to CO₂ and H₂O adsorption ($E_{\text{ampd-MOF}}$), interacting with CO₂ and H₂O in the gas phase ($E_{\text{CO}_2/\text{H}_2\text{O}}$) within a $15 \text{ \AA} \times 15 \text{ \AA} \times 15 \text{ \AA}$ cubic supercell, and 2-ampd–Mg₂(dobpdc) with adsorbed CO₂ and H₂O molecules ($E_{\text{CO}_2\text{-ampd-MOF}}$) using vdW-corrected DFT. The binding energies (E_B) were obtained via the difference

$$E_B = E_{\text{CO}_2\text{-ampd-MOF}} - (E_{\text{ampd-MOF}} + E_{\text{CO}_2/\text{H}_2\text{O}}) \quad (3.2)$$

For NMR simulations, we used a $1 \times 1 \times 3$ k-point. With this k-point, the isotropic chemical shielding values (σ_{iso}) converged to 0.1 ppm. Since the isotropic chemical shift (δ_{iso}) is obtained from $\delta_{\text{iso}} = -(\sigma_{\text{iso}} - \sigma_{\text{ref}})$ where σ_{ref} is a reference value, we needed to determine a σ_{ref} value by comparing experimental δ_{iso} values to calculated σ_{iso} values. The σ_{ref} values for ¹H (31.4 ppm) and ¹³C (160.1 ppm) were obtained by first computing σ_{iso} values for cocaine (CSD refcode COCAIN10 was used as the starting point, and the structure was geometry optimized before NMR calculation; see Supporting Information for coordinates). The computed values were then compared with experimental values (Table 3.S18, Figure 3.S94).⁷² The σ_{ref} value for ¹⁵N (215.9 ppm) was determined by comparison of DFT-calculated σ_{iso} and the experimental δ_{iso} value for glycine (Table 3.S18).⁶⁰ Additional DFT figures and details are included in the Supporting Information in Section 3.6.21.

3.3. Results and Discussion

3.3.1 Adsorbent Design for NGCC Post-Combustion Capture

Our previous crystallographic and gas adsorption studies of 1°,2° diamine-appended Mg₂(dobpdc) indicated that unfavorable chain-chain interactions in the *ab* plane of the framework give rise to the two-step adsorption profiles of these materials.⁵³ We reasoned that

tethering the alkyl chain to the backbone of the diamine should alleviate these steric interactions, thereby minimizing the gap between the two CO₂ adsorption steps and enabling access to the full theoretical adsorption capacity. Accordingly, we grafted racemic 2-(aminomethyl)piperidine (2-ampd, Figure 3.1b) to Mg₂(dobpdc) using our previously reported procedure⁵¹ to produce the adsorbent 2-ampd–Mg₂(dobpdc). Consistent with our hypothesis, this material exhibits two closely-spaced steps in its CO₂ adsorption isotherms (occurring at 1.0 and 3.7 mbar at 40 °C, respectively; see Figure 3.2). Importantly, both steps occur at pressures low enough to facilitate ≥90% removal of CO₂ (residual pressure of ≤4 mbar) from NGCC flue emissions under idealized, equilibrium conditions at 40 °C. In contrast, variants of Mg₂(dobpdc) functionalized with diamines bearing long alkyl substituents, such as *N*-(*n*-hexyl)ethylenediamine (*n*Hex-2),⁵³ have two widely spaced CO₂ adsorption steps, restricting the quantity of CO₂ that can be captured to the capacity of the lower-pressure step (~1.8 mmol/g at 40 mbar and 40 °C for *n*Hex-2, in contrast to 3.47 mmol/g for 2-ampd under the same conditions; Figure 3.S16).

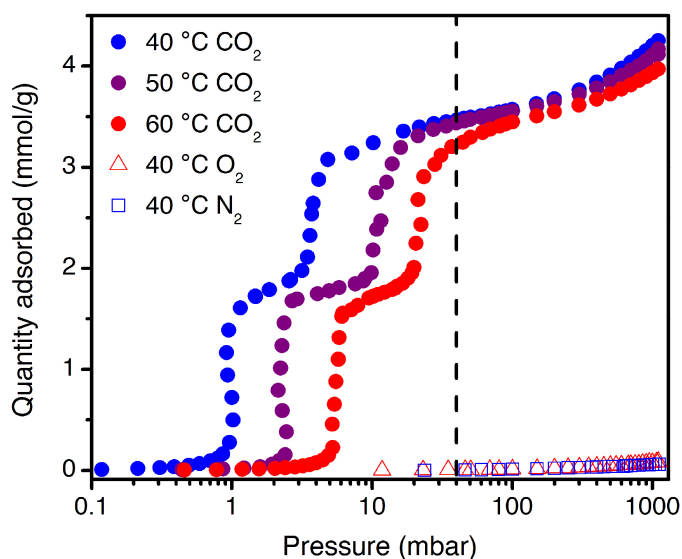


Figure 3.2. Pure CO₂ adsorption isotherms at 40, 50, and 60 °C (purple, blue, and red circles, respectively), and for O₂ (red triangles) and N₂ (blue squares) at 40 °C, for 2-ampd–Mg₂(dobpdc). The dashed black line indicates the approximate partial pressure of CO₂ in flue gas from a NGCC power plant (40 mbar).

We hypothesize that step-shaped CO₂ adsorption in 2-ampd–Mg₂(dobpdc) arises as a result of cooperative insertion of CO₂ into the metal–amine bonds to form chains of ammonium carbamate running along the pore axis, as reported previously for related alkylethylenediamine-appended frameworks.^{49–58} This conclusion is supported by spectroscopic characterization (discussed below) and by the observed metal dependence of the cooperative adsorption step position⁵⁰ for 2-ampd–M₂(dobpdc) variants (M = Mg, Mn, Ni, Co, Zn; Figure 3.S85). In addition, appending 2-ampd within the expanded terephenyl framework Mg₂(dotpdc) (dotpdc⁴⁻ = 4,4'-dioxido-[1,1':4',1''-terphenyl]-3,3''-dicarboxylate) produces an adsorbent with only one step in its CO₂ adsorption isobar (Figure 3.S21), confirming that the two adsorption steps observed for 2-ampd–Mg₂(dobpdc) also arise from steric interactions between adjacent diamines in the framework (Supporting Information, Section 3.6.4). Importantly, 2-ampd–Mg₂(dobpdc) possesses comparable or superior thermal stability to all other 1°/2° diamine-appended variants of Mg₂(dobpdc) evaluated to date (Figure 3.S6), withstanding 12 h of exposure to flowing,

humid CO₂ at a regeneration temperature of 140 °C (or even as high as 180 °C) with minimal diamine volatilization (Table 3.S15, see also discussion below). Therefore, the cyclic diamine 2-ampd uniquely affords the best attributes achieved with 1°/2° diamine-appended Mg₂(dobpdc) materials to date, namely, high thermal stability coupled with a high CO₂ adsorption capacity from a NGCC flue gas stream.

The single crystal X-ray diffraction structure of the isostructural framework 2-ampd–Zn₂(dobpdc) (Figure 3.1) provides insight into the thermal stability and close CO₂ adsorption steps of 2-ampd–Mg₂(dobpdc). The bulky piperidine ring of 2-ampd can maintain a stable chair conformation in the pores of the framework, with efficient packing in the *ab* plane and minimization of unfavorable interactions between adjacent diamines. Consistently, despite the high density of amine groups within the pores, 2-ampd–Mg₂(dobpdc) exhibits a high Brunauer–Emmett–Teller surface area of 618 ± 2 m²/g (Figure 3.S4), which should enable rapid diffusion of CO₂ through the channels of the framework, even after CO₂ adsorption.

3.3.2 Single-Component Adsorption Experiments

Following validation of these initial design criteria, we investigated additional properties relevant to the application of 2-ampd–Mg₂(dobpdc) in CO₂ capture from NGCC flue emissions. Isothermal adsorption profiles were collected at 40, 50, and 60 °C for CO₂ and at 40 °C for N₂ and O₂ (Figure 3.2). For CO₂, two adsorption steps were observed at all temperatures. Both adsorption steps occur below 40 mbar even at 60 °C and are predicted to be operative in this target pressure range up to approximately 69 °C (Figure 3.S14). Importantly, because 2-ampd–Mg₂(dobpdc) adsorbs minimal CO₂ at partial pressures beneath the first step pressure, processes with higher adsorption temperatures can be considered without sacrificing CO₂ adsorption capacity, as would be expected for a typical Langmuir-type adsorbent. Eliminating the need to adsorb at the lowest possible temperature can potentially reduce process costs through relaxed requirements for flue gas cooling,⁷³ minimization of water co-adsorption,⁴⁷ and/or enhanced tolerance to temperature rise in the adsorbent bed upon exothermic CO₂ adsorption.²¹ In addition, despite demonstrating strong adsorption of CO₂ at low partial pressures, 2-ampd–Mg₂(dobpdc) can be fully regenerated by heating to only 140 °C under a flow of dry or humid CO₂ at atmospheric pressure (Figure 3.S37). Furthermore, at the partial pressures relevant to natural gas flue emissions, 2-ampd–Mg₂(dobpdc) demonstrates excellent non-competitive CO₂/N₂ and CO₂/O₂ selectivities of 1320 and 694, respectively (Table 3.S1), which are among the highest reported for a non-size-selective metal–organic framework.^{31,35,74–77} Because N₂ and O₂ cannot participate in the CO₂-selective cooperative adsorption mechanism, these values are anticipated to be reflective of the multicomponent performance of the material.

The thermodynamics of CO₂ adsorption in 2-ampd–Mg₂(dobpdc) were analyzed using the data in Figure 3.2. A spline interpolation method was used to calculate lines of constant loading for the set of CO₂ isotherms from 40 to 60 °C. Employing the Clausius–Clapeyron relationship yielded a differential enthalpy of adsorption (Δh_{ads}) of -73 ± 2 kJ/mol at a loading of 1 mmol/g (Figure 3.S8), similar to that observed for other diamine-appended variants of Mg₂(dobpdc)^{50–52} and smaller in magnitude than the low-coverage enthalpies reported for silicas functionalized with primary or secondary amines.⁷⁸ From this adsorption enthalpy, we calculated a projected regeneration energy of 2.8 MJ/kg CO₂ for a temperature swing adsorption (TSA) process consisting of capture from a 40 mbar stream of CO₂ at 40 °C and desorption under 1 bar of CO₂ at 140 °C (see Supporting Information, Section 3.6.3; note that only CO₂ was considered in this calculation). This value is over 30% lower than the regeneration energy projected for a

polyamine-functionalized silica for a similar process (3.9 MJ/kg CO₂, see Supporting Information, Section 3.6.3),⁴⁸ reflecting the advantage of cooperative adsorbents for CO₂ capture applications. Furthermore, with a higher adsorption temperature of 60 °C, an even lower projected regeneration energy of 2.7 MJ/kg CO₂ may be possible for 2-ampd–Mg₂(dobpdc) (considering only CO₂; see Table 3.S2). Notably, the thermodynamics of adsorption for 2-ampd–Mg₂(dobpdc) were found to adhere to the same enthalpy–entropy correlation as other diamine-appended variants of Mg₂(dobpdc)⁵¹ (Figure 3.S15), corroborating the formation of ammonium carbamate chains upon CO₂ adsorption in this material.

3.3.3 Mixed-Gas Adsorption Experiments

While single-component equilibrium data are needed to guide adsorbent design and characterize fundamental adsorption properties, multicomponent experiments are critical to evaluate adsorbent performance under more realistic process conditions. To that end, we performed extensive dry and humid thermogravimetric experiments with 2-ampd–Mg₂(dobpdc) using CO₂/N₂ mixtures and simulated NGCC flue emission streams. When exposed to a flow of dry simulated NGCC flue gas (4% CO₂ in N₂) at atmospheric pressure, 2-ampd–Mg₂(dobpdc) exhibits a high CO₂ capacity of 16.0 g/100 g (3.63 mmol/g) at 40 °C (Figure 3.3a, purple curve), consistent with the predicted capacity of 3.66 mmol/g for adsorption of 1 CO₂ per diamine. This adsorption capacity is significantly higher than that of other cyclic diamine-appended variants of Mg₂(dobpdc) (2.02–2.33 mmol/g, Figure 3.S30), as well as the representative amine-functionalized silica MCM-41-PEI-50^{79,80} (1.48 mmol/g, Figure 3.S79) under equivalent conditions. However, for a dry 0.4% CO₂ in N₂ stream, representing the lowest adsorption pressure (4 mbar CO₂) required for 90% capture of CO₂ from NGCC emissions, the adsorption capacity at 40 °C (2.81 g/100 g, or 0.639 mmol/g, Figure 3.3a) is significantly lower than that observed in the 40 °C pure CO₂ isotherm at the same CO₂ partial pressure (2.76 mmol/g). Even with extremely slow isobaric cooling rates, similar discrepancies in the threshold conditions for cooperative adsorption have been observed between CO₂ adsorption isobars (collected under flowing CO₂/N₂ mixtures) and volumetric isotherms (collected under pure CO₂ starting from vacuum).^{81,82} In general, the isobaric measurements show lower isobaric step temperatures (equivalent to higher isothermal step pressures) than would be expected given the measured equilibrium adsorption isotherms. These results suggest a smaller thermodynamic driving force for CO₂ capture under the more realistic, mixed-gas flow conditions. Additionally, we found that the adsorption capacity decreased when a faster cooling ramp rate (0.2 versus 0.1 °C/min) was employed, suggesting that the adsorption kinetics are limited in streams with low CO₂ partial pressures (Supporting Information, Section 3.6.9). This result is consistent with a previous report investigating the adsorption kinetics of the related material mmen–Mg₂(dobpdc) (mmen = *N,N'*-dimethylethylenediamine).⁸³ Ultimately, thermodynamic and kinetic factors under process-relevant flow conditions indicate that 2-ampd–Mg₂(dobpdc) falls short of achieving the target of ≥90% CO₂ capture from NGCC flue gas under *dry* conditions.

We also analyzed the ability of 2-ampd–Mg₂(dobpdc) to capture CO₂ in the presence of water, which can constitute up to ~8% of NGCC flue gas by volume. Humid isobars were collected by flowing CO₂/N₂ mixtures through two room-temperature water bubblers to generate an estimated water content of ~2.6 vol % (Figure 3.3b; see Figures 3.S37–3.S46 and Tables 3.S9 and 3.S10 for direct comparisons of dry and humid isobars). Importantly, the temperature of each CO₂ adsorption step increased by 6 °C under humid conditions, with the step inflection points shifting from 111 to 117 °C and from 98 to 104 °C (solid green curves, Figure 3.3). These higher

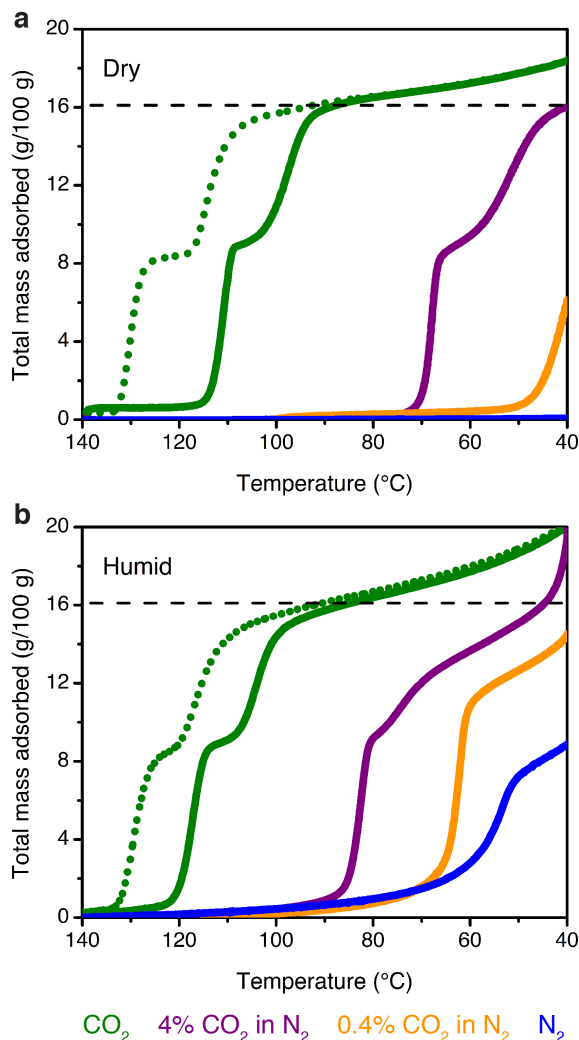


Figure 3.3. Dry (a) and humid (b, ~2.6% H₂O) isobars at atmospheric pressure for pure CO₂ (green), 4% CO₂ in N₂ (purple), 0.4% CO₂ in N₂ (orange), and pure N₂ (blue) in 2-ampd-Mg₂(dobpdc). Solid lines depict adsorption (cooling), and dotted green lines depict desorption (heating) for the pure CO₂ isobars. The dashed black lines indicate the theoretical capacity for adsorption of 1 CO₂ per diamine. Temperature ramp rates: 0.5 °C/min for pure CO₂, 0.1 °C/min for 4% and 0.4% CO₂ in N₂, and 1 °C/min for pure N₂.

adsorption temperatures under humid conditions reflect thermodynamically more favorable cooperative adsorption of CO₂ in the presence of water. Likewise, under a flow of humid 4% CO₂ (40 mbar) in N₂, the inflection point of the higher-temperature adsorption step increased by ~14 °C, from 68 to 82 °C (purple curves, Figure 3.3). Critically, while 2-ampd-Mg₂(dobpdc) captures limited CO₂ from a dry stream containing 0.4% (4 mbar) CO₂ in N₂, the addition of humidity under the same conditions results in a sharp CO₂ step in the adsorption isobar, with an inflection point at 64 °C (orange curves, Figure 3.3). While the composition of the adsorbed phase cannot be determined directly from these experiments, a comparison of the humid CO₂/N₂ mixture isobars with a humid N₂ isobar indicates that the humid 0.4% CO₂ isobar involves the adsorption of CO₂ (orange and blue curves, Figure 3.3b). However, at lower temperatures, the saturation capacities of the humid CO₂/N₂ mixture isobars exceed the gravimetric uptake anticipated for adsorption of 1 CO₂ per diamine, suggesting co-adsorption of water. In sum, the

isobaric adsorption data indicate that while 2-ampd–Mg₂(dobpdc) may fall below the target of $\geq 90\%$ CO₂ capture from dry NGCC flue emissions, the presence of humidity in the gas stream should enable the material to reach this target at temperatures up to at least 60 °C.

To quantify the influence of water on the thermodynamics of CO₂ capture, approximate CO₂ adsorption enthalpies were calculated for the dry and humid CO₂/N₂ mixture isobars by employing the Clausius–Clapeyron relationship at the midpoint of each adsorption step. We note that while slow temperature ramp rates were used to approximate equilibrium conditions (Supporting Information, Section 3.6.9), the enthalpies calculated from the adsorption isobars were found to be systematically higher than those calculated from the single-component, volumetric isotherms. Nonetheless, the difference between the humid and dry isobar enthalpies ($\Delta h_{\text{ads,humid}} - \Delta h_{\text{ads,dry}}$) should reflect the enthalpic benefit of CO₂ adsorption in the presence of water. Using this method, we attribute the increased temperature of the first adsorption step to a 31 ± 2 kJ/mol increase in the effective $-\Delta h_{\text{ads}}$ in the presence of water (dry: 81 ± 1 kJ/mol; humid: 112 ± 2 kJ/mol). Notably, within error, the same increase in effective $-\Delta h_{\text{ads}}$ was found for the lower-temperature adsorption step (30 ± 2 kJ/mol), indicating that water uniformly increases the thermodynamic driving force for both adsorption steps (Tables 3.S7 and 3.S8). Interestingly, minimal change was observed in the isobaric desorption step temperatures following saturation with CO₂/H₂O under the tested humidity, resulting in calculation of equivalent enthalpies within error (dry: 101 ± 1 kJ/mol; humid: 99 ± 1 kJ/mol; difference: -2 ± 2 kJ/mol). While these results are complicated by the lower relative humidities at the elevated desorption temperatures, the similar dry and humid CO₂ desorption step temperatures suggest that water desorbs before CO₂.

In order to quantify the influence of water on the performance of 2-ampd–Mg₂(dobpdc), we collected single-component water adsorption isotherms at 30, 40, 50, and 60 °C. For all temperatures, the isotherms show a plateau at a loading of 1 H₂O per diamine, followed by condensation at higher relative humidities (Figures 3.S10 and 3.S11). Using the same spline interpolation method as for CO₂, a differential adsorption enthalpy of -65 ± 2 kJ/mol was calculated at a loading of 1 mmol H₂O/g (Figure 3.S12). Assuming co-adsorption and desorption cycling of 1 water molecule per diamine–Mg²⁺ site alongside cycled CO₂, the regeneration energy of 2-ampd–Mg₂(dobpdc) would increase by up to 1.5 MJ/kg CO₂ to a total of 4.3 MJ/kg CO₂ (Supporting Information, Section 3.6.3). We note that these values are only approximations, as they do not account for potential differences in the adsorption enthalpy of water on the CO₂-inserted and diamine-bound phases (see DFT calculations below), the potential effect of higher relative humidity levels on adsorption or desorption, and the relative adsorption/desorption kinetics of CO₂ vs. H₂O in the ultimate cycling configuration. Nonetheless, 2-ampd–Mg₂(dobpdc) is still predicted to afford significant energy savings over competing amine-based technologies such as a PEI-functionalized silica, which requires a regeneration energy of 4.7 MJ/kg CO₂ under similar conditions (Supporting Information, Section 3.6.3)⁴⁸ and is susceptible to degradative reaction pathways, such as urea formation (Figures 3.S74–3.S77, discussed in greater detail below). Therefore, while these measurements indicate that the presence of water in the incident gas stream improves the thermodynamic driving force for CO₂ adsorption in 2-ampd–Mg₂(dobpdc), this improvement comes at the potential cost of an increase in the regeneration energy associated with the desorption of co-adsorbed water. The co-cycled water would then need to be condensed prior to compression and transport of the captured CO₂.

3.3.4 Fixed-Bed Adsorption Experiments

To evaluate the performance of 2-ampd–Mg₂(dobpdc) in a fixed-bed adsorption process, we conducted breakthrough experiments under dry and humid simulated NGCC flue gas. These experiments are particularly important for materials with step-shaped isotherms, which often give rise to complex, multimodal breakthrough profiles. Such profiles were originally anticipated for diamine-appended frameworks by Mazzotti and coworkers in a comprehensive modeling study,⁴⁵ and a review of the underlying theory is included in the Supporting Information in Section 3.6.10. In short, the breakthrough profile can be predicted from an isotherm with one or more inflection points by applying “Golden’s Rule,” alternatively known as the rubber band rule or string rule.^{45,84–86} When applying this rule, an operating curve for adsorption is constructed by stretching a hypothetical “rubber band” beneath the adsorption isotherm from the initial state (0% CO₂) to the feed state (4% CO₂). In concentration regimes bounded by individual points of contact with the rubber band, a compressive “shock” is anticipated in the breakthrough profile. In concentration regimes where the rubber band runs along the isotherm, a dispersive “wave” is expected. With a step-shaped isotherm, the result is often a “shock–wave–shock” profile: an initial “shock” is generated as CO₂ slips through the bed at concentrations beneath the step, followed by a “wave” corresponding to a small increase in CO₂ concentration during the onset of the cooperative adsorption step, and finally a second “shock” at full breakthrough (see Figure 3.S52). Intuitively, *the shock–wave–shock profile can be understood as a manifestation of the general inability of a cooperative adsorbent to capture CO₂ once the CO₂ partial pressure in the bed drops below the step pressure.* Accordingly, this behavior is the basis for our design criterion to achieve 90% capture of CO₂ through the selection of adsorbents with step pressures at <10% of the feed concentration.⁵¹

Breakthrough experiments were conducted with 0.73 g of semi-spherical pellets of 2-ampd–Mg₂(dobpdc) (350–700 μm) under 28 sccm of 4% CO₂ in N₂ at 1.1 bar (Figure 3.4; details of pellet preparation and characterization are given in the Supporting Information in Section 3.6.11). Considering the single-component CO₂ adsorption isotherms, a CO₂ “slip” (initial shock) of ~0.02 mol % was predicted under dry flue gas at 40 °C (obtained from Golden’s Rule, see Figure 3.S54), corresponding to a capture rate of 99.5% from a stream containing 4% CO₂ (calculated as (1–0.02/4)×100%). However, with dry simulated flue gas, approximately 0.6 mol % CO₂ slip was detected at the outlet, corresponding to a lower maximum capture rate of 86%. In addition, the CO₂ capacity at exhaustion (full breakthrough) was found to be 2.4 ± 0.2 mmol/g, which fell short of the capacity of 3.5 mmol/g predicted from the adsorption isotherm. The breakthrough profile and capacity were highly reproducible following activation of the material at 120 °C under flowing He (Figure 3.S55). Reducing the flow rate to 14 sccm at 40 °C improved the capture rate (~0.4 mol % slip, or 90% capture rate) and sharpness of the breakthrough profile, reflecting a potential limitation in kinetics, but the breakthrough capacity at exhaustion remained unchanged (Figure 3.S56). As anticipated from the isotherms and isobars, increasing the temperature to 60 °C increased the CO₂ slip, resulting in a measured capture rate of only 62% (Figure 3.S57; predicted capture rate, 88%). The CO₂ breakthrough capacity at exhaustion was calculated as 2.2 ± 0.2 mmol/g, which again fell short of that predicted from the isotherm (3.2 mmol/g) but was consistent with that predicted from the CO₂ mixture isobars (2.2 mmol/g). Therefore, these results suggest that isobars collected by flowing dry CO₂ mixtures (Figure 3.3a) may reflect adsorbent performance in dry breakthrough measurements more accurately than

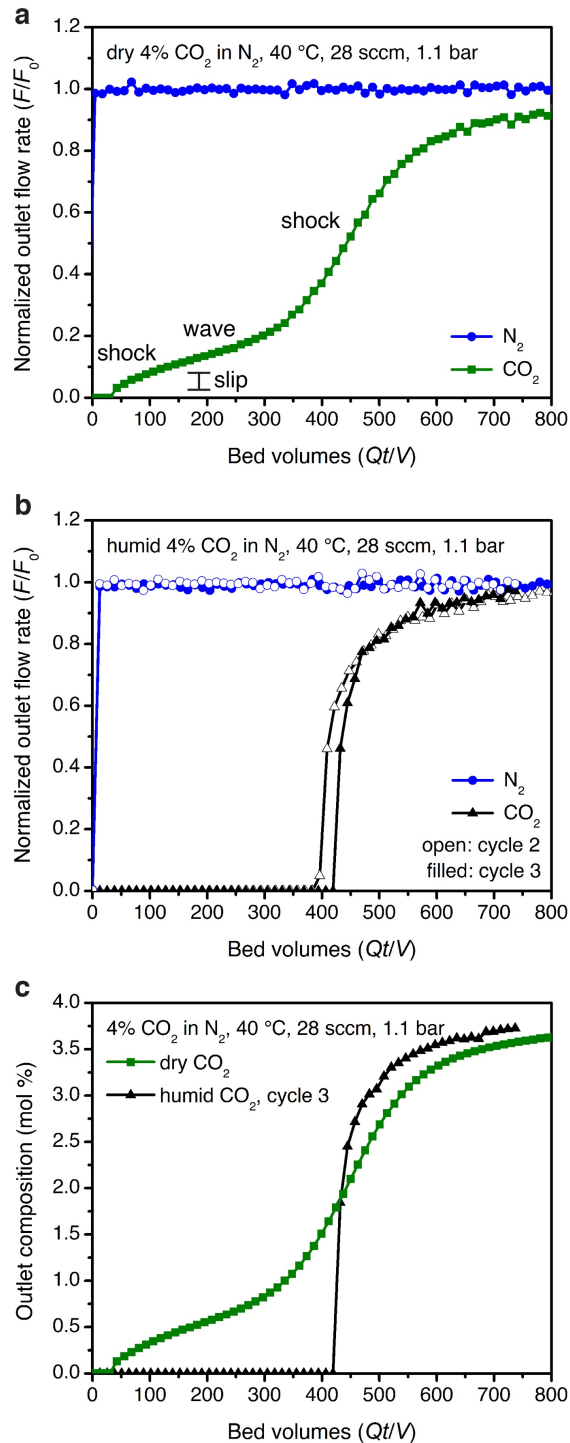


Figure 3.4. Breakthrough experiments with 2-ampd-Mg₂(dobpdc) under 28 sccm of a simulated NGCC flue emission stream of 4% CO₂ in N₂ at 40 °C and ~1.1 bar. (a) Experiment with dry simulated flue gas. Capture rate: 86%; exhaustion capacity: 2.4 ± 0.2 mmol/g. (b) Second (filled symbols) and third (open symbols) breakthrough experiment cycles with humid flue gas following pre-saturation of the adsorbent bed with water. Capture rate: >99%; usable capacity (average ≥90% capture): 2.2 and 2.3 ± 0.1 mmol/g; exhaustion capacity: 2.4 and 2.5 ± 0.1 mmol/g for 2nd and 3rd cycles, respectively. (c) Overlay of dry and humid (3rd cycle) CO₂ breakthrough profiles. The y-axis is shown as normalized outlet flow rate (F/F_0) in (a) and (b) and as outlet composition in mol % in (c).

single-component, volumetric isotherms (Figure 3.2). We anticipate that the greater utility of mixed-gas isobars versus single-component isotherms will apply generally in the evaluation of other carbon capture materials, particularly those with step-shaped adsorption isotherms.

To test the effect of CO₂ concentration on the elution profile, a breakthrough experiment was conducted under 14 sccm of 15% CO₂ in N₂ at 40 °C and atmospheric pressure, simulating coal flue gas (Figure 3.S58). In this experiment, negligible slip was observed (>99% CO₂ capture), and the CO₂ capacity (3.1 ± 0.2 mmol/g) was consistent with that of the equilibrium isotherm (3.6 mmol/g), considering the 92% diamine loading of the pellets. Therefore, the deviations from equilibrium behavior observed in breakthrough experiments with lower CO₂ concentrations (Figure 3.4), particularly with respect to high CO₂ slip and resulting low CO₂ capture rate, can likely be attributed to limitations in kinetics. As a result, non-equilibrium effects may limit the performance of diamine-appended frameworks with *dry* CO₂ mixtures at low partial pressures, a hypothesis supported by a recent investigation of another diamine-appended framework for CO₂ capture from air.⁸³

We also evaluated the breakthrough behavior of the material under humid flue gas mixtures containing ~2 vol % H₂O. Gratifyingly, consistent with the humid isobar measurements (Figure 3.3b), a dramatic enhancement in CO₂ capture performance was observed in breakthrough experiments with humid simulated NGCC flue gas following pre-saturation of the adsorbent bed with water (Figure 3.4b). In particular, humidification completely eliminated the initial CO₂ slip at 40 °C, resulting in a CO₂ capture rate of >99% and a desirable single, sharp CO₂ breakthrough front. The CO₂ exhaustion capacity calculated at full breakthrough (2.4 ± 0.2 mmol/g) was equivalent to that of the dry experiment, with a usable CO₂ capacity of 2.2 ± 0.1 mmol/g satisfying the DoE target of an average of 90% CO₂ capture. This striking improvement in performance is clearly visible in an overlay of the dry and humid CO₂ breakthrough profiles at 40 °C (Figure 3.4c). Breakthrough experiments at 60 °C revealed similarly dramatic improvements in performance upon addition of humidity (Figures 3.S59–3.S60), with an increase in capture rate from 62% to >99% (see Table 3.S11 for a summary of capture rate results). The very high capture rate under humid conditions at 60 °C suggests that even higher adsorption temperatures could be used to achieve smaller temperature swings. In ongoing work, we are developing methods to predict the breakthrough performance as a function of both relative humidity and temperature. The promising performance of 2-ampd–Mg₂(dobpdc) in humid breakthrough experiments supports its utility as a next-generation adsorbent for post-combustion CO₂ capture from NGCC flue emissions.

3.3.5 Influence of Water on CO₂ Adsorption

Due to the sensitivity of the adsorption threshold to the local environment in cooperative adsorbents, it is of interest to determine whether the presence of water changes the nature of the chemisorbed phase or merely enhances the thermodynamic favorability of the ammonium carbamate chain mechanism in diamine-appended metal–organic frameworks. Considering related materials, water is well known to improve the CO₂ adsorption capacity of amine-functionalized silicas.^{30,42,87–98} This effect is generally ascribed to a mechanistic shift from ammonium carbamate formation (0.5 CO₂:amine) to bicarbonate or stabilized carbamic acid formation (1 CO₂ per amine),^{12,88–90,94,95,98–107} although some studies have debated the formation of bicarbonates or carbonates.^{108–111} Furthermore, these reports largely focus on the influence of water on the adsorption capacity, with minimal discussion of the influence of water on the thermodynamics of adsorption and the desorption temperature.^{88,91,112,113} Notably, our related

vdW-corrected DFT study of the framework $\text{mmen-Mg}_2(\text{dobpdc})$ demonstrated a stabilization of up to 41 kJ/mol for the CO_2 -inserted phase in the presence of water.¹¹⁴ This result suggests that water enhances, rather than changes, the ammonium carbamate chain adsorption mechanism, but to date no study has yet combined experimental and computational methods to characterize the effect of water on the CO_2 adsorption pathway, capacity, and breakthrough profile of a diamine-appended metal-organic framework. Accordingly, we employed IR and NMR spectroscopy and vdW-corrected DFT calculations to probe the behavior of $2\text{-ampd-Mg}_2(\text{dobpdc})$ under dry and humid conditions.

We first collected IR spectra of $2\text{-ampd-Mg}_2(\text{dobpdc})$ in the presence of dry N_2 , dry CO_2 , and humid CO_2 (Figure 3.5). Upon exposure to dry CO_2 at 22 °C and atmospheric pressure, new vibrations were observed at 1648 cm^{-1} (C=O) and 1362 and 1342 cm^{-1} (C-N), consistent with the formation of ammonium carbamate chains. These vibrations are shifted to slightly higher energies than those of the molecular 2-ampd ammonium carbamate structure, for which C=O and C-N vibrations were observed at 1637 and 1340 cm^{-1} , respectively (Figures 3.S61–3.S63; crystallographic data available as supporting information in acknowledged associated article). The presence of two C-N stretches further suggests the formation of two distinct ammonium carbamate products upon CO_2 adsorption in $2\text{-ampd-Mg}_2(\text{dobpdc})$. The C-N vibrations persist in the presence of humid CO_2 , consistent with preservation of a chemisorptive mechanism, while the C=O band is obscured by the H-O-H bend at 1630 cm^{-1} arising from co-adsorbed water.¹⁰¹

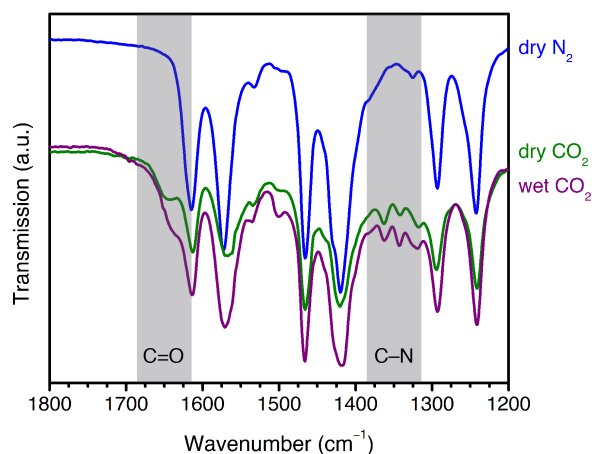


Figure 3.5. Infrared spectra of $2\text{-ampd-Mg}_2(\text{dobpdc})$ under dry N_2 (blue), dry CO_2 (green), and humid CO_2 (purple) at room temperature (~ 22 °C) and atmospheric pressure. The C=O vibration at 1648 cm^{-1} and C-N vibrations at 1362 and 1342 cm^{-1} are consistent with the proposed mechanism of ammonium carbamate chain formation under both dry and humid conditions.

Solid-state NMR spectra obtained under dry and humid conditions provided greater experimental detail for the effect of water on CO_2 adsorption in $2\text{-ampd-Mg}_2(\text{dobpdc})$ (Figure 3.6). The ^{13}C NMR spectrum of $2\text{-ampd-Mg}_2(\text{dobpdc})$ dosed with 1025 mbar of $^{13}\text{CO}_2$ at room temperature shows two predominant overlapping resonances at 162 and 163 ppm, as well as a weak shoulder at a higher chemical shift (Figure 3.6a), all of which can be ascribed to chemisorbed CO_2 species. (See Figure 3.S87 for the ^{13}C spectrum of activated $2\text{-ampd-Mg}_2(\text{dobpdc})$ prior to exposure to CO_2 .) We hypothesize that the two main ^{13}C resonances (Figure 3.6a) correspond to two conformations of ammonium carbamate chains,⁶⁰ consistent with the IR spectrum collected under dry CO_2 (Figure 3.5). Notably, our previous NMR

characterization of diamines exhibiting double-step CO₂ adsorption profiles also revealed multiple resonances for chemisorbed CO₂, which likely arise due to spectroscopically distinct conformations of the sterically hindered ammonium carbamate chains.⁶⁰ The weak shoulder at higher frequencies (Figure 3.6a) may be associated with incomplete equilibration (see Figure 3.S90).

To interpret these results, we carried out additional 2D and ¹⁵N NMR experiments. A ¹H–¹³C HETCOR experiment with a short contact time (100 μs) was performed to probe correlations with hydrogen atoms that are proximal to the chemisorbed carbon species (*i.e.* within a few Å; Figure 3.S89). In the 2D experiment, the two ¹³C resonances each show a major ¹H correlation at ~5 ppm. We assign this feature to the N–H group of an ammonium carbamate species, while the ¹³C peaks are attributed to the carbamate carbon atoms.^{60,115} This N–H correlation supports reaction with CO₂ at the primary amine to produce a metal-bound carbamate species, with proton transfer to a neighboring secondary amine to form a charge-balancing ammonium group. This reactivity is consistent with the previous crystallographic characterization of CO₂ insertion into Zn₂(dobpdc) functionalized with 1°/2° diamines.⁵¹ Additionally, the ¹⁵N NMR spectrum of 2-ampd–Mg₂(dobpdc) dosed with 1025 mbar of ¹³CO₂ featured two peaks at 46 and 76 ppm, consistent with nitrogen atoms in ammonium and carbamate groups, respectively (Figure 3.S86).^{50,60}

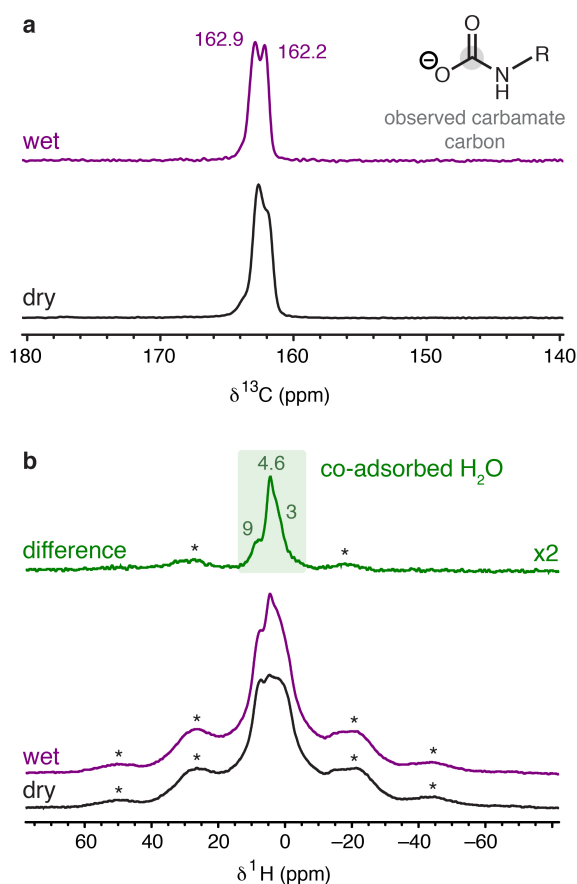


Figure 3.6. (a) ¹³C NMR (16.4 T) MAS spectra of 2-ampd–Mg₂(dobpdc) dosed with 1025 mbar of dry ¹³CO₂ at 22 °C (bottom), and the same sample under a subsequent flow of humid, natural isotopic abundance CO₂ at atmospheric pressure (top). Spectra were obtained by cross-polarization from ¹H (contact time = 1 ms). (b) ¹H NMR spectra obtained by single-pulse excitation for the same samples as in (a). The MAS rate was 15 kHz in all cases. Asterisks mark spinning sidebands.

After exposure of 2-ampd–Mg₂(dobpdc) to a flow of humid CO₂ (natural isotopic abundance) for 1 h, the main two ¹³C resonances were retained, but smaller linewidths were observed (Figure 3.6a; see also Figure 3.S90 for similar data obtained with a longer CO₂ exposure time). Therefore, in further agreement with the IR data, these NMR spectra demonstrate retention of the ammonium carbamate product in the presence of water and exclude a water-induced change in the CO₂ chemisorption mechanism. Co-adsorption of water was also confirmed by collection of ¹H NMR spectra before and after exposure to wet CO₂. The difference ¹H spectrum (Figure 3.6b) shows positive intensity that can be attributed to co-adsorbed water and reveals a narrow component at 4.6 ppm, as well as broad components at ~9 and ~3 ppm. The highly shifted (~9 ppm) water peak supports the formation of strong hydrogen bonds following exposure to water (Figure 3.6b; see also Figure 3.S88 for the ¹H spectrum of activated 2-ampd–Mg₂(dobpdc) prior to exposure to CO₂).

Due to the structural complexity of 2-ampd–Mg₂(dobpdc), the CO₂-inserted structure could not be solved directly from the X-ray diffraction pattern of the microcrystalline powder or from single crystals of the isostructural Zn framework under dry or humid conditions. We thus turned to vdW-corrected DFT calculations to predict the structure and energetics upon CO₂ adsorption, H₂O adsorption, and co-adsorption of CO₂ and H₂O in 2-ampd–Mg₂(dobpdc) (Figure 3.7). For

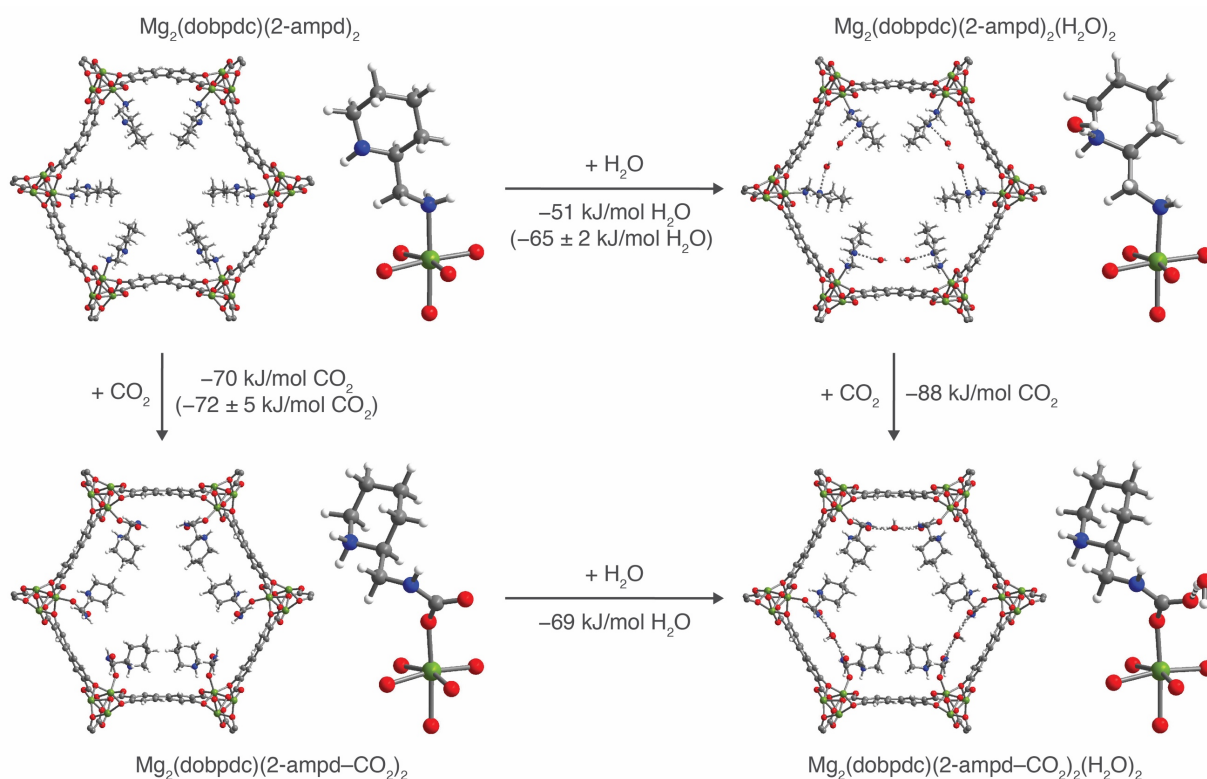


Figure 3.7. Projections along the pore axis and first coordination spheres of Mg(II) sites for the vdW-corrected, DFT-calculated structures of evacuated *L*-2-ampd-*R*-Mg₂(dobpdc) (top left) and the framework following CO₂ insertion (bottom left), water adsorption (top right), and co-adsorption of CO₂ and H₂O (bottom right). The vdW-corrected, DFT-calculated binding energies (ΔE) are provided for each adsorption process, and available experimental differential binding enthalpies (Δh_{ads}) are included in parentheses. Co-adsorption of water was found to enhance the CO₂ binding energy by -18 kJ/mol, and a combined binding energy of -139 kJ/mol 2-ampd was calculated for co-adsorption of 1 CO₂ and 1 H₂O per diamine. Green, blue, gray, red, and white spheres represent Mg, N, C, O, and H atoms, respectively.

simplicity, all calculations were carried out using the left-handed enantiomer of the diamine in the right-handed enantiomer of the framework. An adsorption energy of -70 kJ/mol was calculated for insertion of CO_2 to form ammonium carbamate chains in $\text{Mg}_2(\text{dobpdc})(2\text{-ampd}-\text{CO}_2)_2$. This value is in good agreement with the experimentally determined CO_2 adsorption enthalpy of -72 ± 5 kJ/mol averaged over a loading of 0 to 1 CO_2 per diamine (Figure 3.S8). In the calculated structure of $\text{Mg}_2(\text{dobpdc})(2\text{-ampd})_2(\text{H}_2\text{O})_2$, adsorbed water was found to interact with 2-ampd by donating a hydrogen bond to the secondary amine ($\text{O}\cdots\text{N}$ distance of 2.924 Å). Close $\text{H}_2\text{O}\cdots\text{H}_2\text{O}$ contacts in the *ab* plane ($\text{O}\cdots\text{O}$ distance of 2.867 Å) suggest that additional stabilization is provided by hydrogen bonding between water molecules. In the absence of CO_2 , an adsorption energy of -51 kJ/mol was calculated for H_2O . This value is consistent with the experimental H_2O adsorption enthalpy of -50 ± 2 kJ/mol at low loadings (0.2 mmol/g, or 0.05 mmol H_2O per diamine) but is slightly lower than the average experimental enthalpy of -65 ± 2 kJ/mol over a loading range of 0 to 1 mmol H_2O per diamine (Figure 3.S12). In practice, while the structure shown here represents the lowest-energy H_2O binding mode discovered in our 0 K calculations, H_2O may sample other binding sites or geometries within the pore at room temperature. Overall, the adsorption energies corresponding to the calculated CO_2 - and H_2O -adsorbed structures of 2-ampd- $\text{Mg}_2(\text{dobpdc})$ are in reasonable agreement with those determined from single-component adsorption measurements.

The DFT-calculated structure of $\text{Mg}_2(\text{dobpdc})(2\text{-ampd}-\text{CO}_2)_2(\text{H}_2\text{O})_2$ shows a strong hydrogen bonding interaction between H_2O and the metal-bound oxygen atom of the carbamate ($\text{O}\cdots\text{O}$ distance of 2.786 Å). Additionally, each H_2O molecule accepts a hydrogen bond from a carbamate nitrogen atom of the neighboring ammonium carbamate chain in the *ab* plane ($\text{N}\cdots\text{O}$ distance of 2.939 Å), resulting in a channel of H_2O molecules between adjacent ammonium carbamate chains (Figure 3.S95). A CO_2 adsorption energy of -88 kJ/mol was calculated for co-adsorption of 1 CO_2 and 1 H_2O per diamine, indicating that water increases the magnitude of the CO_2 binding energy by an estimated 18 kJ/mol compared to CO_2 insertion under dry conditions (binding energy of -70 kJ/mol). This value is smaller than the 31 ± 2 kJ/mol increase in $-\Delta h_{\text{ads}}$ calculated from the humid vs. dry pure CO_2 adsorption isobars, but a comparison of the absolute values may be complicated by non-equilibrium effects in the isobars and the inability to determine the precise composition of the adsorbed phase. Notably, the DFT-calculated binding energy of CO_2 is larger than that of water in the co-adsorbed structure, suggesting that the endothermic penalty to desorb H_2O is smaller, and thus H_2O is likely to desorb first. This result is consistent with the minimal differences in the dry and humid CO_2 desorption temperatures observed in mixed-gas isobars (Figure 3.3). We note that the calculated and experimental NMR shifts for 2-ampd- $\text{Mg}_2(\text{dobpdc})$ exposed to dry and humid CO_2 also agree well with the experimental values (Table 3.S20).

Taken together, the humid isobars, breakthrough measurements, spectroscopic data, and vdW-corrected DFT calculations support an increase in the favorability of CO_2 insertion under humid conditions, as a result of an enhancement of the ammonium carbamate chain formation mechanism in the presence of water. In humid breakthrough experiments, the resulting effective decrease in the isothermal CO_2 adsorption step pressure alters the propagation of the adsorption front through the bed. In particular, the single “shock” in the humid CO_2 breakthrough profile suggests that water reduces the effective step pressure and/or alters the shape of the CO_2 adsorption profile at low partial pressures, leading to more favorable performance under humid conditions (Figure 3.S53).

3.3.6 Thermal, Oxidative, and Cycling Stability

Beyond the thermodynamics and kinetics of adsorption, the long-term stability of an adsorbent is a critical consideration for ultimate industrial applications. In particular, the high oxygen content of the NGCC flue gas stream (~12%) is well known to lead to oxidative degradation of aqueous amine solutions.²⁴⁻²⁷ To evaluate the oxidative stability of 2-ampd-Mg₂(dobpdc), the material was exposed to a flow of dry air (~21% O₂ in N₂) at 100 °C and atmospheric pressure for 5 h, and the dry, pure CO₂ isobars were compared before and after exposure. Minimal changes were observed in the CO₂ adsorption profile or capacity after this extensive O₂ treatment (Figure 3.8). In contrast, dry, oxygen-containing streams at 100 °C have been found to cause significant degradation of silicas functionalized with secondary amines.¹¹⁶ In addition, no diamine oxidation products were detected by IR or by ¹H NMR spectroscopy after digestion of the O₂-treated material (Figure 3.S72). The oxidative resistance of 2-ampd-Mg₂(dobpdc) is likely due in part to the fixed, wide spacing of diamines at metal sites ~7 Å apart along the channel direction, which serves to mitigate bimolecular (2 amine molecules) oxidation pathways observed in other materials.¹¹⁶

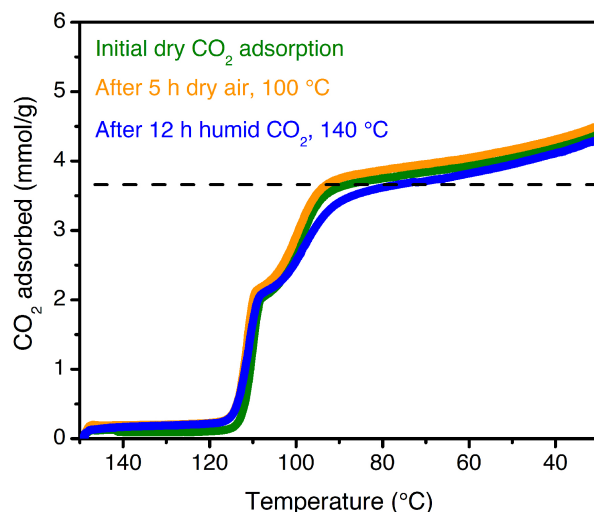


Figure 3.8. Dry, pure CO₂ adsorption isobars for 2-ampd-Mg₂(dobpdc) as synthesized (green curve), after exposure to a flow of dry air (~21% O₂ in N₂) at 100 °C for 5 h (orange curve), and after exposure to a flow of humid CO₂ at 140 °C for 12 h (blue curve). A ramp rate of 1 °C/min was used in all cases. The dashed black line indicates the theoretical capacity for adsorption of 1 CO₂ per diamine.

Adsorbents for carbon capture from NGCC flue gas must also withstand repeated thermal cycling under humid conditions. As part of this work, we found that the stability of diamine-appended variants of Mg₂(dobpdc) and related materials can be rapidly assessed by exposing the adsorbent to a flow of humid CO₂ for 12 h at the relevant desorption temperature (here, 140 °C) in a thermogravimetric analyzer, simulating hundreds of adsorption/desorption cycles (Supporting Information, Section 3.6.16). The humid CO₂ adsorption capacities before and after such accelerated decomposition experiments can be compared in order to evaluate any capacity loss, and the material can be digested after the test to detect diamine volatilization or degradation. Notably, after treatment with flowing humid CO₂ at 140 °C for 12 h, 2-ampd-Mg₂(dobpdc) retains its step-shaped adsorption profile (Figure 3.8, blue curve) with only a slight capacity loss at 40 °C (original: 4.20 mmol/g; after humid CO₂ treatment: 4.11 mmol/g). In addition, almost no diamine volatilization (~2%) from the framework was observed. We further tested the

stability of 2-ampd-Mg₂(dobpdc) to accelerated decomposition experiments at higher temperatures, representative of a potential process failure. At temperatures as high as 180 °C, 2-ampd-Mg₂(dobpdc) retains more than 90% of its adsorption capacity (Table 3.S15), and the material remains highly crystalline even after treatment with a humid CO₂ stream at 220 °C for 12 h (Figure 3.S70). Evaluation of a number of promising diamine-appended variants of Mg₂(dobpdc) for CO₂ capture from NGCC flue gas further revealed that the thermal stability of 2-ampd-Mg₂(dobpdc) is nearly unparalleled among this family of materials (Table 3.S14). In addition, the stability of 2-ampd-Mg₂(dobpdc) is far superior to that of the representative amine-functionalized silica MCM-41-PEI-50, which undergoes urea formation and significant capacity loss (~17%) at 40 °C following exposure to humid CO₂ for 12 h at 140 °C (Figures 3.S75–3.S77). The exceptional stability of 2-ampd-Mg₂(dobpdc) to humid gas streams at high temperatures makes it particularly promising for long-term application in a CO₂ capture process.

The stability of 2-ampd-Mg₂(dobpdc) in a TSA process was further evaluated by performing 750 adsorption (humid 4% CO₂ in N₂, 40 °C) and desorption (humid CO₂, 140 °C) cycles using a thermogravimetric analyzer (Figure 3.9, see Supporting Information Figure 3.S80 for the full cycling data). Consistent with the accelerated decomposition test results (Figure 3.8), 2-ampd-Mg₂(dobpdc) exhibited a stable cycling capacity under humid simulated NGCC flue gas (Figure 3.9). The same final diamine loading (~94%) was observed after both 200 and 750 cycles, suggesting that the loading stabilizes after a small amount of initial diamine volatilization, likely from weakly-bound defect or surface sites. Notably, a high CO₂/H₂O cycling capacity of 16.0 g/100 g was observed for the 750th cycle, comparable to the adsorption capacity from a dry 4% CO₂ in N₂ stream at 40 °C (15.8 g/100 g). Nearly the same cycled capacity (15.3 g/100 g) could also be achieved over 200 tested cycles with a higher adsorption temperature of 60 °C (Figure 3.S81). Short adsorption (5 min) and desorption (1 min) times were used in these experiments,

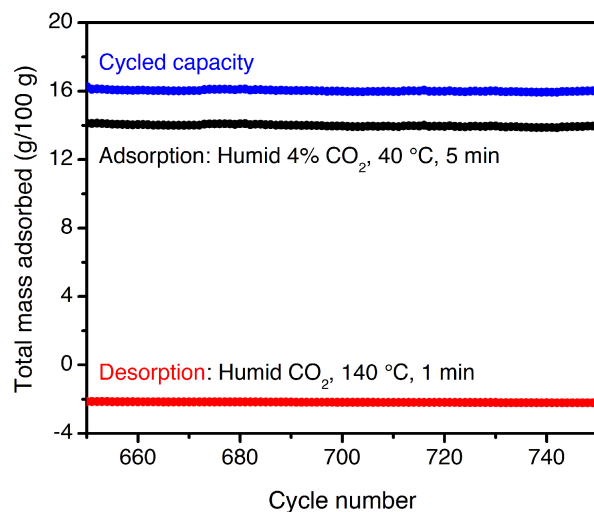


Figure 3.9. Cycling data for the final 100 of 750 adsorption/desorption cycles for 2-ampd-Mg₂(dobpdc) in a simulated temperature swing adsorption process. Adsorption: humid 4% CO₂ in N₂, 40 °C, 5 min (black, cycle maxima). Desorption: Humid CO₂, 140 °C, 1 min (red, cycle minima). The cycled capacity (difference) is shown in blue. The baseline value of 0 g/100 g is defined as the mass after activation under 4% CO₂ in N₂ at 150 °C for 20 min prior to the first cycle. The diamine loading was reduced from 100% to 94% after this experiment. The same final loading was observed after 200 adsorption/desorption cycles, suggesting that the diamine loading stabilizes after initial loss. The weight loss due to diamine volatilization correlates with equilibration of the mass upon desorption to the observed negative baseline value.

indicating rapid kinetics despite the low CO₂ content of the simulated flue gas stream. Overall, the exceptional stability of 2-ampd-Mg₂(dobpdc) and excellent performance in breakthrough and cycling experiments support further development of this promising adsorbent for CO₂ capture from the emissions of gas-fired power plants.

3.4. Conclusions

Natural gas offers significant environmental advantages as an alternative to coal by enabling approximately 50% lower CO₂ emissions per unit of electricity produced. Capturing and sequestering the CO₂ emissions from gas-fired power plants provides an attractive option to achieve even greater emission reductions. We have shown that the metal-organic framework 2-ampd-Mg₂(dobpdc) is a promising candidate for post-combustion CO₂ capture from the emissions of NGCC power stations. In particular, as a result of the constituent cyclic diamine, this material overcomes the tradeoff between stability and capacity encountered with related cooperative adsorbents featuring linear 1°/2° diamines. Importantly, in breakthrough experiments simulating a fixed-bed adsorption process, 2-ampd-Mg₂(dobpdc) exhibits single-shock breakthrough profiles under humid conditions, in contrast to the multimodal elution profiles observed under dry conditions. This advantageous result is attributed to stabilizing H₂O-carbamate interactions, a conclusion supported by mixed-gas adsorption experiments, spectroscopic characterization, and vdW-corrected DFT calculations. Finally, 2-ampd-Mg₂(dobpdc) achieves the challenging practical criteria required of a material for CCS from NGCC emissions, namely a high CO₂ swing capacity as well as high thermal, oxidative, and cycling stability. Continued development of 2-ampd-Mg₂(dobpdc) at larger scales and in structured forms will enable modeling of heat and mass transfer and support bench-scale testing.

More broadly, this report achieves key advances toward the deployment of cooperative adsorbents in industrial CO₂ separations. First, we have reiterated the importance of considering CO₂ “slip” in adsorbent and process design for CO₂ capture applications with dry mixtures.^{45,83} Second, and most importantly, we have established that pre-saturating the adsorbent bed with water can significantly enhance the CO₂ capture performance of diamine-appended, cooperative adsorbents by mitigating or eliminating CO₂ slip. Third, we have shown that experiments under flow conditions (such as isobars collected with slow temperature ramp rates under varying CO₂ concentrations) may predict the performance of cooperative adsorbents more accurately than single-component, volumetric adsorption isotherms. Finally, we have shown that TSA processes with cooperative adsorbents can utilize higher adsorption temperatures (here, 60 °C or higher instead of 40 °C) that could serve to mitigate water co-adsorption and reduce operating costs related to cooling the flue gas stream. Moving forward, we expect that these discoveries will be of value in the design of cooperative adsorbents for other challenging CO₂ capture processes, such as the direct capture of CO₂ from air.

3.5. Acknowledgements

This work has been submitted for publication as an article entitled “Water Enables Efficient CO₂ Capture from Natural Gas Flue Emissions in an Oxidation Resistant Diamine-Appended Metal-Organic Framework” with authors Rebecca L. Siegelman,[§] Phillip J. Milner,[§] Alexander C. Forse, Jung-Hoon Lee, Kristen A. Colwell, Jeffrey B. Neaton, Jeffrey A. Reimer, Simon C. Weston, and Jeffrey R. Long. ([§]Contributed equally.)

We gratefully acknowledge ExxonMobil Research and Engineering Company for financial

support of this work. Work at the Molecular Foundry was supported by the Office of Science, Office of Basic Energy Sciences, U.S. Department of Energy, under Contract DE-AC02-05CH11231, and computational resources were provided by the Department of Energy (LBNL Lawrencium and NERSC). This research also used the Savio computational cluster resource provided by the Berkeley Research Computing program at the University of California, Berkeley (supported by the UC Berkeley Chancellor, Vice Chancellor for Research, and Chief Information Officer). Single-crystal X-ray diffraction data were collected on Beamline 12.2.1 at the Advanced Light Source at Lawrence Berkeley National Laboratory, which is supported by the Director, Office of Science, Office of Basic Energy Sciences, of the U.S. Department of Energy under Contract No. DE-AC02-05CH11231. Synchrotron powder X-ray diffraction data were collected at the Advanced Photon Source, a U.S. Department of Energy Office of Science User Facility operated for the DOE Office of Science by Argonne National Laboratory under Contract No. DE-AC02-06CH11357. We thank Dr. Joseph Falkowski (ExxonMobil Research and Engineering Company), Dr. Miguel Gonzalez (UC Berkeley), and Dr. Jeffrey Martell (UC Berkeley) for helpful discussions; Eugene Kim (UC Berkeley) and Julia Oktawiec (UC Berkeley) for experimental assistance; and Dr. Katie Meihaus (UC Berkeley) for editorial assistance.

3.6. Supporting Information

3.6.1 Preparation of $M_2(\text{dobpdc})$ ($M = \text{Mg}, \text{Mn}, \text{Co}, \text{Ni}, \text{Zn}$) and $\text{Mg}_2(\text{dotpdc})$

$\text{Mg}_2(\text{dobpdc})$. Prepared according to the literature procedure.⁵¹ An Erlenmeyer flask was charged with $\text{Mg}(\text{NO}_3)_2 \cdot 6\text{H}_2\text{O}$ (11.5 g, 45.0 mmol, 1.24 equiv), 4,4'-dihydroxy-[1,1'-biphenyl]-3,3'-dicarboxylic acid (9.90 g, 36.0 mmol, 1.00 equiv), *N,N*-dimethylformamide (90 mL), and methanol (110 mL). The mixture was sonicated until all of the solids dissolved and filtered through filter paper into a 350 mL screw-cap high pressure reaction vessel equipped with a stir bar. The reaction mixture was sparged with N_2 for 1 h. The reaction vessel was sealed, and the reaction mixture was allowed to stir slowly at 120 °C for 14 h, resulting in precipitation of a white solid from solution. The mixture was filtered, and the solid was quickly transferred to a Pyrex jar filled with *N,N*-dimethylformamide (500 mL). The jar was placed in an oven heated to 60 °C and allowed to stand for at least 3 h. The mixture was then filtered and the solid was returned to the jar with fresh *N,N*-dimethylformamide (500 mL) and returned to an oven heated to 60 °C. This washing process was repeated a total of three times. The *N,N*-dimethylformamide was replaced with methanol (500 mL), and this washing process was repeated a further three times with methanol. A small portion of the solid was removed and placed in a vial under flowing N_2 . The solid was activated under flowing N_2 at 180 °C for 24 h, transferred to a glass adsorption tube equipped with a Micromeritics *TransSeal*, and activated for an additional 24 h under reduced pressure (<10 μbar) at 180 °C. Activated $\text{Mg}_2(\text{dobpdc})$ was obtained as a white solid. Langmuir surface area determined from the 77 K N_2 adsorption isotherm: 3896 m^2/g .

$\text{Mn}_2(\text{dobpdc})$. Prepared according to the literature procedure.⁵² An Erlenmeyer flask was charged with $\text{MnCl}_2 \cdot 4\text{H}_2\text{O}$ (990 mg, 5.00 mmol, 2.50 equiv), 4,4'-dihydroxy-[1,1'-biphenyl]-3,3'-dicarboxylic acid (548 mg, 2.00 mmol, 1.00 equiv), *N,N*-dimethylformamide (100 mL), and ethanol (100 mL). The mixture was sonicated until all of the solids dissolved and filtered through filter paper into a 350 mL screw-cap high pressure reaction vessel equipped with a stir bar. The reaction mixture was vigorously sparged with N_2 for 1 h. The reaction vessel was sealed, and the reaction mixture was allowed to stir slowly at 120 °C for 14 h, resulting in precipitation of a pale

yellow solid from solution. The mixture was filtered, and the solid was quickly transferred to a Pyrex jar filled with *N,N*-dimethylformamide (300 mL). The jar was placed in an oven heated to 60 °C and allowed to stand for at least 3 h. The mixture was then filtered and the solid was returned to the jar with fresh *N,N*-dimethylformamide (300 mL) and returned to an oven heated to 60 °C. This washing process was repeated a total of three times. The *N,N*-dimethylformamide was replaced with methanol (300 mL), and this washing process was repeated a further three times with methanol. The mixture was filtered, and the solid was transferred to a Schlenk flask and activated under flowing N₂ at 180 °C for 8 h followed by heating under high vacuum at 180 °C for 24 h. The Schlenk flask was transferred into a N₂-filled glovebox, and the solid was transferred to a glass adsorption tube equipped with a Micromeritics *TransSeal* and activated for an additional 24 h under high vacuum (<10 μbar) at 180 °C. Activated Mn₂(dobpdc) (0.56 g) was obtained as a pale yellow solid. Langmuir surface area determined from the 77 K N₂ adsorption isotherm: 3408 m²/g. **Note: methanol-solvated Mn₂(dobpdc) slowly degrades in the presence of air, turning brown in the process, and thus should be stored activated in a N₂-filled glovebox when not in use.**

Co₂(dobpdc). Prepared according to the literature procedure.⁵² An Erlenmeyer flask was charged with Co(NO₃)₂•6H₂O (1.09 g, 3.75 mmol, 2.50 equiv), 4,4'-dihydroxy-[1,1'-biphenyl]-3,3'-dicarboxylic acid (411 mg, 1.50 mmol, 1.00 equiv), deionized water (50 mL), *N,N*-dimethylformamide (50 mL), and ethanol (50 mL). The mixture was sonicated until all of the solids dissolved and filtered through filter paper into a 350 mL screw-cap high pressure reaction vessel equipped with a stir bar. The reaction mixture was vigorously sparged with N₂ for 1 h. The reaction vessel was sealed, and the reaction mixture was allowed to stir slowly at 120 °C for 14 h, resulting in precipitation of a pink solid from solution. The non-homogeneous mixture was filtered, and the pink solid was quickly transferred to a Pyrex jar filled with *N,N*-dimethylformamide (250 mL). The jar was placed in an oven heated to 60 °C and allowed to stand for at least 3 h. The mixture was then filtered and the solid was returned to the jar with fresh *N,N*-dimethylformamide (300 mL) returned to an oven heated to 60 °C. This washing process was repeated a total of three times. The *N,N*-dimethylformamide was replaced with methanol (300 mL), and this washing process was repeated a further three times with methanol. A small portion of the solid was removed and placed in a vial under flowing N₂. The solid was activated under flowing N₂ at 180 °C for 24 h, transferred to a glass adsorption tube equipped with a Micromeritics *TransSeal*, and activated for an additional 24 h under high vacuum (<10 μbar) at 180 °C. Activated Co₂(dobpdc) was obtained as a purple solid. Langmuir surface area determined from the 77 K N₂ adsorption isotherm: 3665 m²/g.

Ni₂(dobpdc). Prepared according to the literature procedure.⁵² An Erlenmeyer flask was charged with Ni(NO₃)₂•6H₂O (1.09 g, 3.75 mmol, 2.50 equiv), 4,4'-dihydroxy-[1,1'-biphenyl]-3,3'-dicarboxylic acid (411 mg, 1.50 mmol, 1.00 equiv), deionized water (50 mL), *N,N*-dimethylformamide (50 mL), and ethanol (50 mL). The mixture was sonicated until all of the solids dissolved and filtered through filter paper into a 500 mL Pyrex jar. The jar was placed in an oven at 120 °C and allowed to stand for 14 h, resulting in precipitation of a bright green solid from solution. The non-homogeneous mixture was filtered, and the solid was quickly transferred to a Pyrex jar filled with *N,N*-dimethylformamide (250 mL). The jar was placed in an oven heated to 60 °C and allowed to stand for at least 3 h. The mixture was then filtered and the solid was returned to the jar with fresh *N,N*-dimethylformamide (300 mL) and returned to an oven heated to 60 °C. This washing process was repeated a total of three times. The *N,N*-dimethylformamide was replaced with methanol (300 mL), and this washing process was

repeated a further three times with methanol. A small portion of the solid was removed and placed in a vial under flowing N₂. The solid was activated under flowing N₂ at 180 °C for 24 h, transferred to a glass adsorption tube equipped with a Micromeritics *TransSeal*, and activated for an additional 24 h under high vacuum (<10 μbar) at 180 °C. Activated Ni₂(dobpdc) was obtained as a brown solid. Langmuir surface area determined from the 77 K N₂ adsorption isotherm: 3439 m²/g.

Zn₂(dobpdc). Prepared according to the literature procedure.⁶⁰ An Erlenmeyer flask was charged with Zn(NO₃)₂·6H₂O (3.72 g, 12.5 mmol, 2.50 equiv), 4,4'-dihydroxy-[1,1'-biphenyl]-3,3'-dicarboxylic acid (1.37 g, 5.00 mmol, 1.00 equiv), *N,N*-dimethylformamide (250 mL), and methanol (250 mL). The mixture was sonicated until all of the solids dissolved and filtered through filter paper into a 1 L Pyrex jar. The reaction mixture was vigorously sparged with N₂ for 1 h, and the jar was placed in an oven at 120 °C and allowed to stand for 14 h, resulting in precipitation of an off-white solid from solution. The non-homogeneous mixture was filtered, and the solid was quickly transferred to a Pyrex jar filled with *N,N*-dimethylformamide (500 mL). The jar was placed in an oven heated to 60 °C and allowed to stand for at least 3 h. The mixture was then filtered and the solid was returned to the jar with fresh *N,N*-dimethylformamide (500 mL) and returned to an oven heated to 60 °C. This washing process was repeated a total of three times. The *N,N*-dimethylformamide was replaced with methanol (500 mL), and this washing process was repeated a further three times with methanol. The mixture was filtered, and the solid was transferred to a Schlenk flask and activated under flowing N₂ at 180 °C for 8 h followed by heating under high vacuum at 180 °C for 24 h. The Schlenk flask was transferred into a N₂-filled glovebox, and the solid was transferred to a glass adsorption tube equipped with a Micromeritics *TransSeal* and activated for an additional 24 h under high vacuum (<10 μbar) at 180 °C. Activated Zn₂(dobpdc) (1.89 g) was obtained as an off-white solid. Langmuir surface area determined from the 77 K N₂ adsorption isotherm: 3129 m²/g. **Note: methanol-solvated Zn₂(dobpdc) slowly degrades in the presence of air (with no apparent change in color or powder X-ray diffraction pattern) and thus should be stored activated in a N₂-filled glovebox when not in use.**

Mg₂(dotpdc). Prepared according to the literature procedure.⁵³ A 20 mL scintillation vial was charged with 4,4''-dihydroxy-[1,1':4',1''-terphenyl]-3,3''-dicarboxylic acid¹¹⁷ (35.0 mg, 0.100 mmol, 1.00 equiv.) and Mg(NO₃)₂·6H₂O (64.0 mg, 0.250 mmol, 2.50 equiv.). Methanol (5.5 mL) and fresh *N,N*-dimethylformamide (4.5 mL) were added, and the solution was sonicated until all of the solids dissolved. The vial was wrapped in Teflon tape, sealed, and heated to 120 °C for 14 h, during which time an off-white solid precipitated from solution. The vial was cooled to room temperature, and the resulting solid was collected by filtration and washed with *N,N*-dimethylformamide (15 mL). The solid was then transferred to a vial filled with *N,N*-dimethylformamide (10 mL) and allowed to soak at 120 °C for 24 h. The supernatant was decanted and replaced with fresh *N,N*-dimethylformamide (10 mL), and the vial was re-heated to 120 °C. This washing process was repeated a total of three times. Methanol (10 mL) was then added, and the solid was soaked in methanol at 60 °C for 3 h. The supernatant was decanted and replaced with fresh methanol (10 mL), and the vial was re-heated to 60 °C. This washing process was repeated a total of three times. The solid was activated under flowing N₂ at 180 °C for 24 h, transferred to a glass adsorption tube equipped with a Micromeritics *TransSeal*, and activated for an additional 24 h under high vacuum (<10 μbar) at 180 °C. Activated Mg₂(dotpdc) was obtained as a pale yellow solid. Langmuir surface area determined from the 77 K N₂ adsorption isotherm: 5771 m²/g.

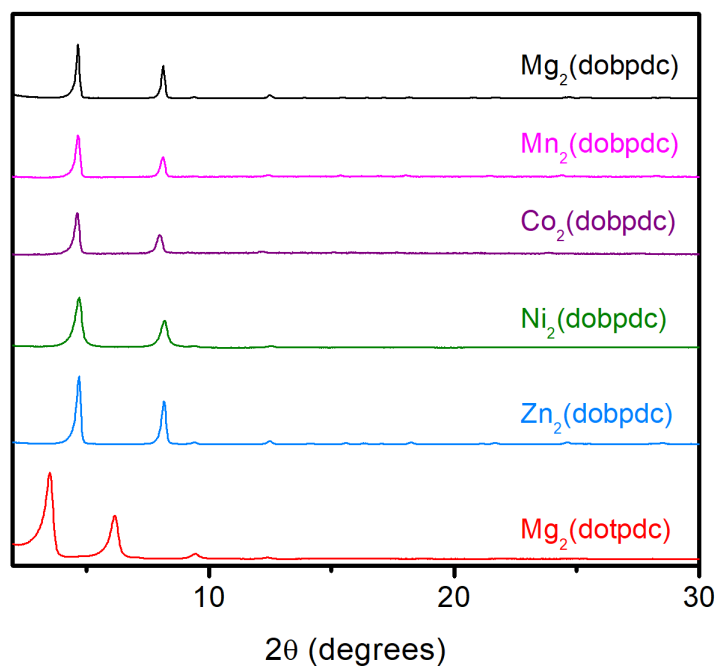


Figure 3.S1. Powder X-ray diffraction patterns (Cu $K\alpha$ radiation, $\lambda = 1.5418 \text{ \AA}$) of methanol-solvated $M_2(\text{dobpdc})$ ($M = \text{Mg, Mn, Ni, Co, Zn}$) and $\text{Mg}_2(\text{dotpdc})$ used in this work.

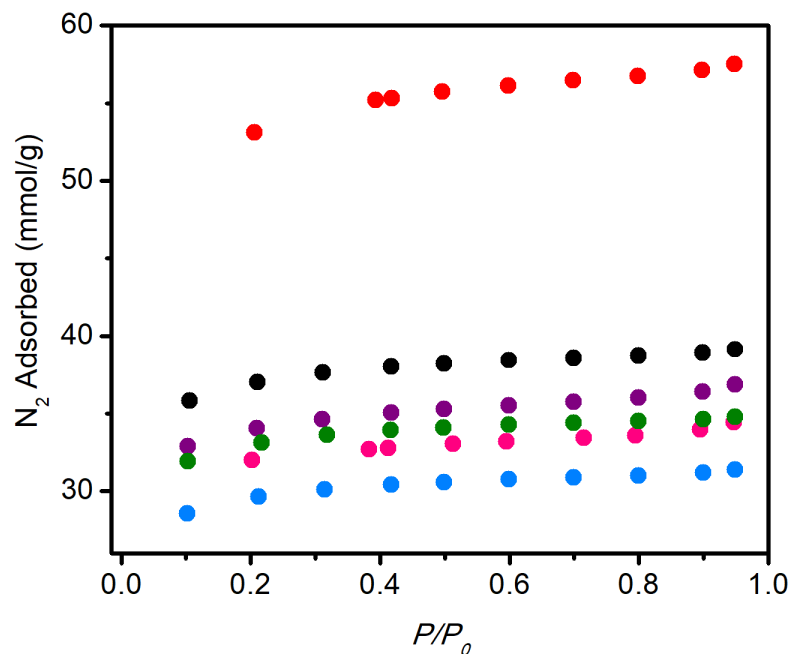


Figure 3.S2. 77 K N_2 adsorption isotherms of activated $\text{Mg}_2(\text{dotpdc})$ (red), $\text{Mg}_2(\text{dobpdc})$ (black), $\text{Co}_2(\text{dobpdc})$ (purple), $\text{Ni}_2(\text{dobpdc})$ (green), $\text{Mn}_2(\text{dobpdc})$ (pink), and $\text{Zn}_2(\text{dobpdc})$ (blue), used in this work. The Langmuir surface areas calculated from these isotherms are indicated in the experimental procedures above and are consistent with those reported in the literature.⁵⁰⁻⁵²

3.6.2 Characterization of 2-ampd–Mg₂(dobpdc)

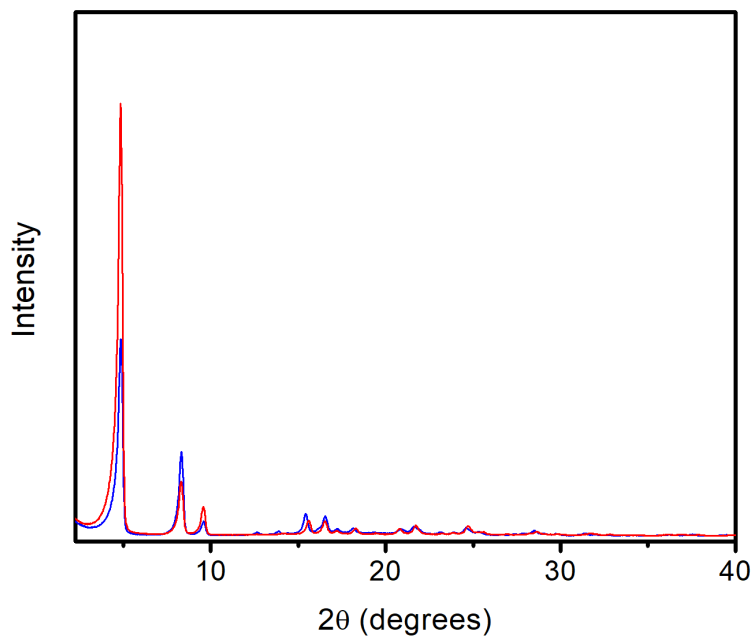


Figure 3.S3. Laboratory powder X-ray diffraction patterns (Cu K α radiation, $\lambda = 1.5418 \text{ \AA}$) of 2-ampd–Mg₂(dobpdc), as-synthesized (blue) and after activation (red) at 150 °C under flowing N₂ for 20 min.

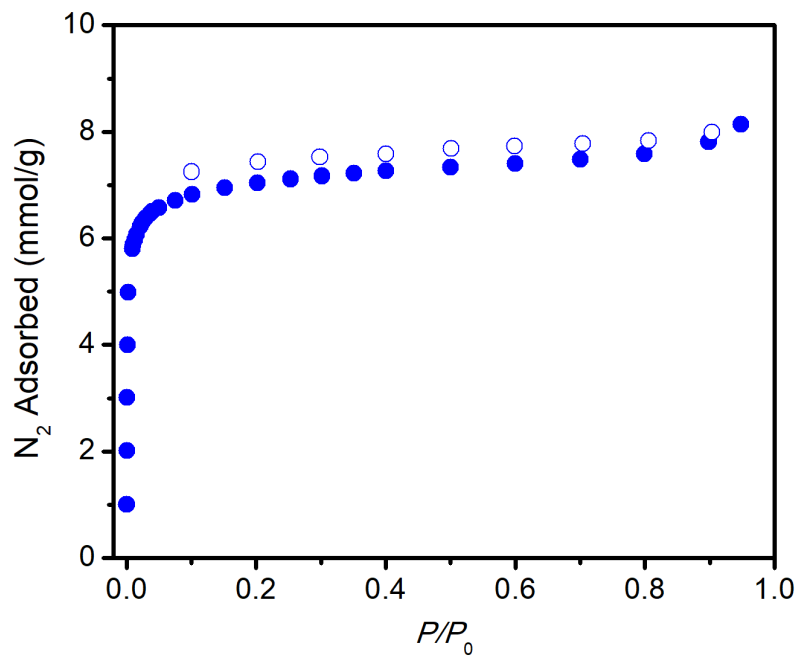


Figure 3.S4. N₂ adsorption (solid circles) and desorption (open circles) isotherms of activated 2-ampd–Mg₂(dobpdc) at 77 K. Brunauer–Emmett–Teller (BET) surface area = $618 \pm 2 \text{ m}^2/\text{g}$.

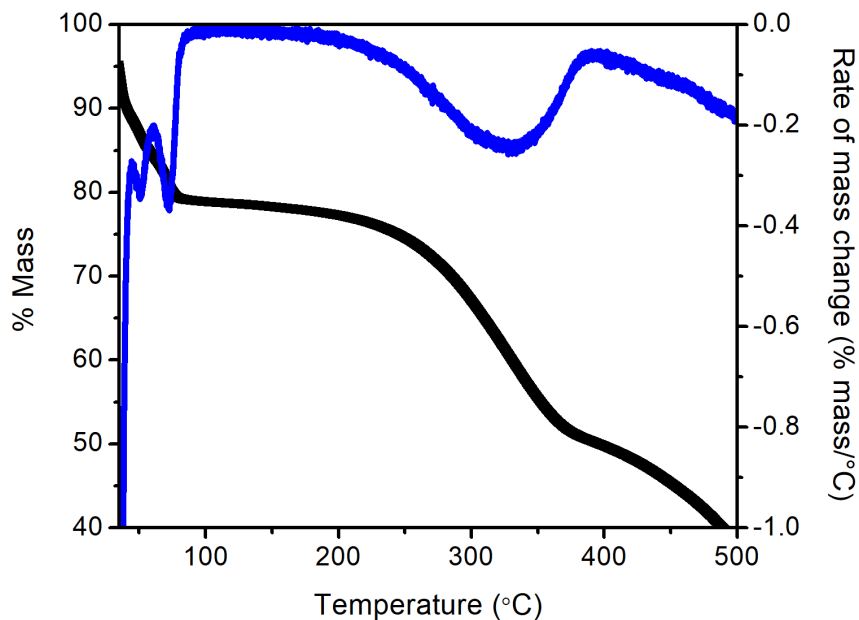


Figure 3.S5. Dry N₂ decomposition profile of 2-ampd-Mg₂(dobpdc) (ramp rate of 1.5 °C/min), plotted in black as % mass change (left-hand y-axis) vs. *T*. The initial mass loss regime (<90 °C) is likely due to the loss of water, toluene, and excess diamine from the pores. The second mass loss regime (190–390 °C) is due to diamine volatilization from the metal sites. The third mass loss regime (>400 °C) is due to decomposition of the framework. The rate of mass change at each temperature is shown in blue and corresponds to the right-hand y-axis.

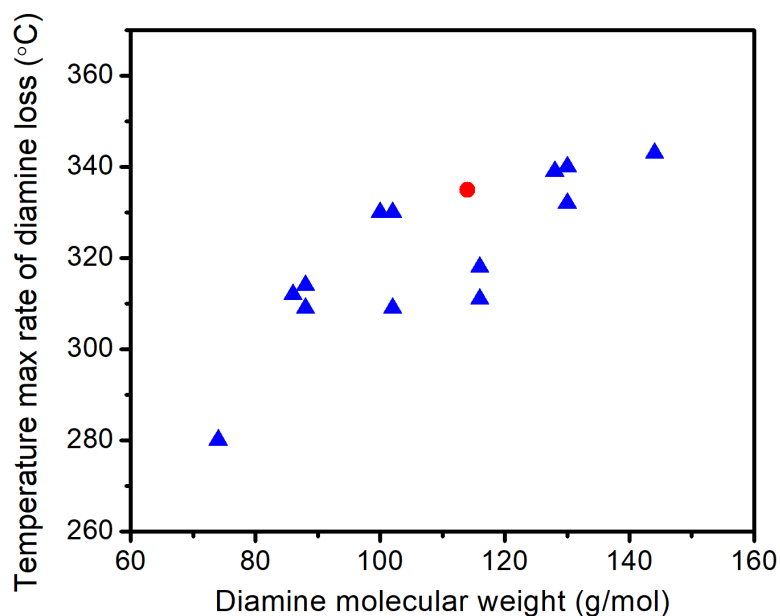


Figure 3.S6. Temperatures of the maximum rates of diamine loss under dry N₂ for a series of *primary, secondary* diamine-appended variants of Mg₂(dobpdc) reported previously^{51,53} and herein (blue triangles), as well as 2-ampd-Mg₂(dobpdc) (red circle). The material 2-ampd-Mg₂(dobpdc) displays comparable or superior thermal stability to related materials. A ramp rate of 1.5 °C/min was used for all decomposition experiments.

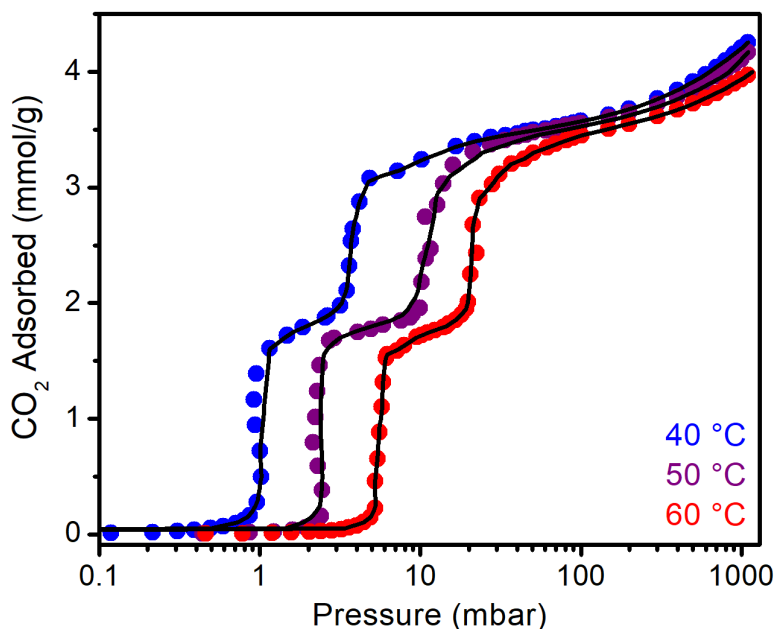


Figure 3.S7. Volumetric equilibrium CO₂ adsorption isotherms for 2-ampd-Mg₂(dobpdc) at 40, 50, and 60 °C. Black lines indicate spline interpolation used to calculate the differential enthalpy and entropy of adsorption. The sample was activated under flowing N₂ at 150 °C for 30 min, followed by activation under high vacuum (<10 μbar) at 100 °C for 4 h. The sample was reactivated under high vacuum (<10 μbar) at 100 °C for 2–4 h between isotherms. Each data point was considered equilibrated after <0.01% pressure change occurred over an average of eleven 15 s intervals. The adsorption of one CO₂ per diamine corresponds to 3.7 mmol/g.

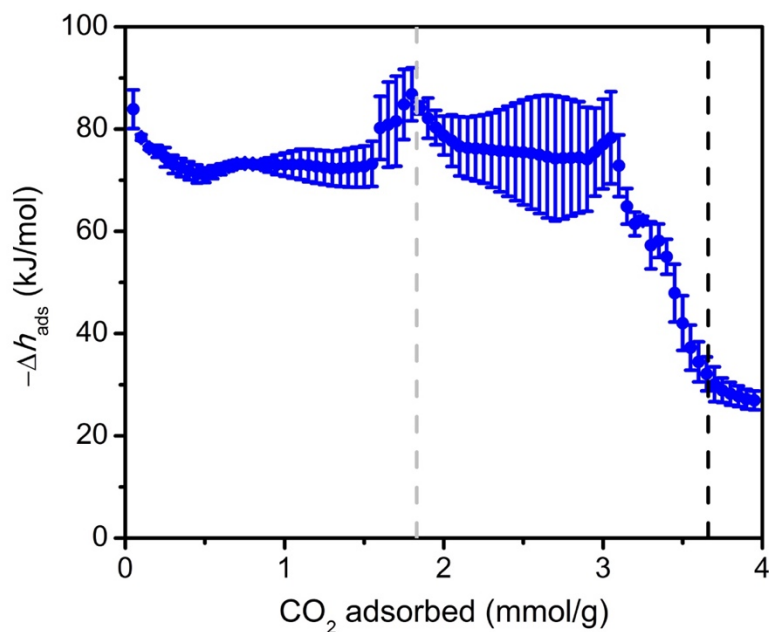


Figure 3.S8. Differential enthalpy of CO₂ adsorption for 2-ampd-Mg₂(dobpdc), determined using the Clausius–Clapeyron relationship and the spline interpolation of the isotherms shown in Figure 3.S7. The expected capacities corresponding to the adsorption of 0.5 and 1 equiv. of CO₂ per diamine are indicated as grey and black dashed lines, respectively.

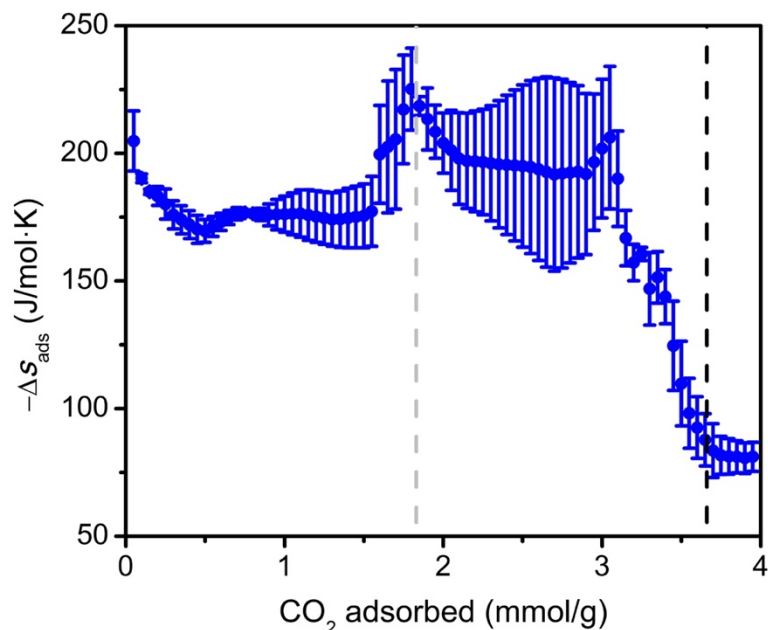


Figure 3.S9. Differential entropy of CO₂ adsorption for 2-ampd-Mg₂(dobpdc), determined from the *y*-intercepts of the linear fits of $\ln(p)$ vs $1/T$ at constant loadings using spline interpolation of the isotherms shown in Figure 3.S7. The expected capacities corresponding to the adsorption of 0.5 and 1 equiv. of CO₂ per diamine are indicated as gray and black dashed lines, respectively.

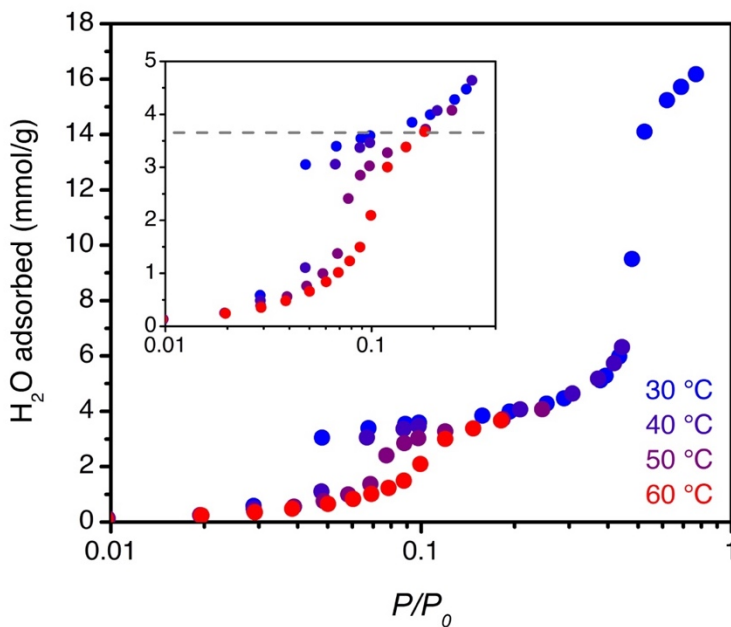


Figure 3.S10. Volumetric H₂O adsorption isotherms for 2-ampd-Mg₂(dobpdc) at 30, 40, 50, and 60 °C plotted as a function of relative pressure. The inset shows an enlargement of the low-pressure region, and the horizontal dashed grey line indicates the capacity corresponding to adsorption of 1 H₂O per diamine (3.7 mmol/g). Each data point was considered equilibrated after <0.01% pressure change occurred over an average of eleven 30 s intervals.

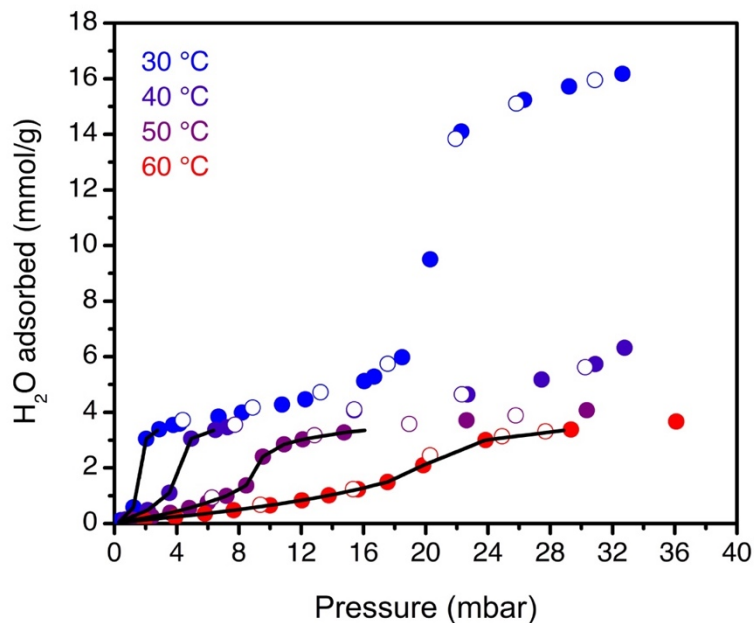


Figure 3.S11. Volumetric H₂O isotherms for 2-ampd-Mg₂(dobpdc) at 30, 40, 50, and 60 °C plotted as a function of absolute pressure. Closed circles show adsorption, and open circles show desorption. The adsorption data are the same as those plotted in Figure 3.S10 above. Black lines indicate spline interpolation used to calculate the differential enthalpy and entropy of adsorption.

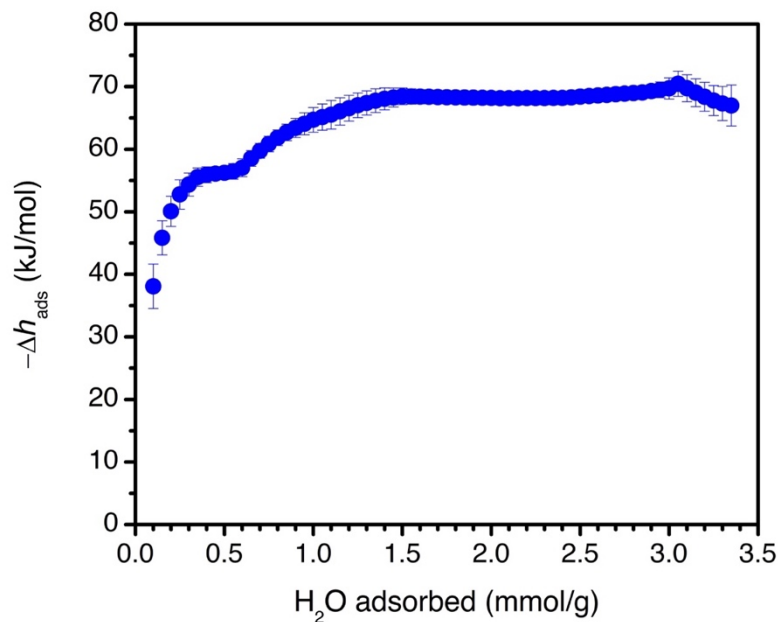


Figure 3.S12. Differential enthalpy of H₂O adsorption for 2-ampd-Mg₂(dobpdc), determined using the Clausius–Clapeyron relationship and the spline interpolation of the isotherms shown in Figure 3.S11.

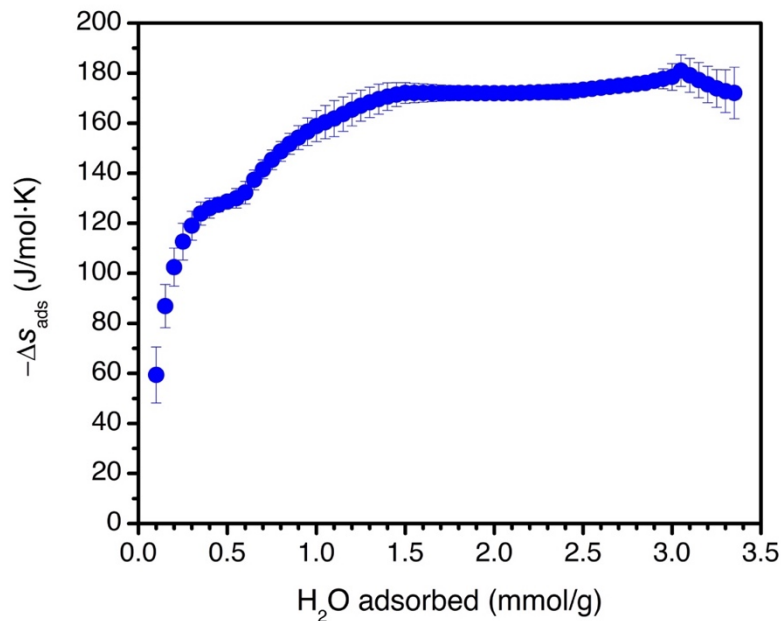


Figure 3.S13. Differential entropy of H₂O adsorption for 2-ampd-Mg₂(dobpdc), determined from the y -intercepts of the linear fits of $\ln(p)$ vs $1/T$ at constant loadings using spline interpolation of the isotherms shown in Figure 3.S11.

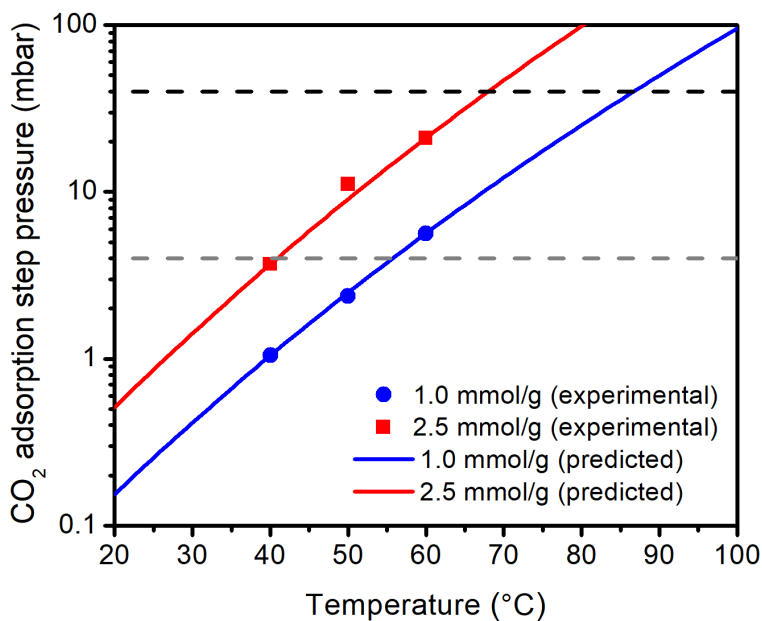


Figure 3.S14. Predicted approximate CO₂ adsorption step pressures for the lower-pressure (blue) and higher-pressure (red) adsorption steps for 2-ampd-Mg₂(dobpdc). The indicated data points correspond to CO₂ pressures determined from the spline interpolation of the CO₂ adsorption isotherms (Figure 3.S7) at loadings of 1.0 mmol/g (*i.e.*, in the lower pressure step, blue circles) and 2.5 mmol/g (*i.e.*, in the higher-pressure step, red squares).

In Figure 3.S14, the red and blue lines were determined using the Clausius–Clapeyron relationship:

$$p_{step,T} = p_{step,T_0} e^{\left(\frac{-\Delta h_{ads}}{R}\right)\left(\frac{1}{T_0} - \frac{1}{T}\right)} \quad (3.S1)$$

Here, $p_{step,T}$ corresponds to the approximate CO₂ adsorption step pressure at a desired temperature T in Kelvin predicted from a measured step pressure p_{step,T_0} at T_0 in Kelvin. For this calculation, T_0 was chosen as 313 K = 40 °C, and thus p_{step,T_0} corresponds to the CO₂ pressure obtained from spline interpolation of the 40 °C CO₂ isotherm at loading of 1.0 mmol/g (*i.e.*, in the lower-pressure adsorption step, blue line, 1.05 mbar of CO₂) or 2.5 mmol/g (*i.e.*, in the higher-pressure adsorption step, red line, 3.69 mbar of CO₂). The differential adsorption enthalpy Δh_{ads} (Figure 3.S8) is taken at a loading of 1.0 mmol/g (-73.0 kJ/mol, blue line) or 2.5 mmol/g (-75.5 kJ/mol, red line). The pressures corresponding to NGCC flue gas (40 mbar, black dashed line) and 90% capture from NGCC flue gas (4.0 mbar, gray dashed line) are indicated. From these equations, we predict that under ideal conditions, the lower pressure CO₂ adsorption step of 2-ampd-Mg₂(dobpdc) (blue line) will be ≤ 4 mbar (*i.e.*, ideally capable of $\geq 90\%$ capture from dry NGCC flue gas) at ≤ 56 °C, and will be ≤ 40 mbar (*i.e.*, ideally capable of CO₂ capture from dry NGCC flue gas) at ≤ 87 °C. Likewise, we can predict that the higher pressure CO₂ adsorption step of 2-ampd-Mg₂(dobpdc) (red line) will be ≤ 4 mbar at ≤ 41 °C, and will be ≤ 40 mbar at ≤ 69 °C. However, these values reflect only ideal scenarios for CO₂ capture from dry NGCC flue gas, as the inflection points of the isobaric CO₂ adsorption steps for 2-ampd-Mg₂(dobpdc) from a dry 4% CO₂ in N₂ stream measured using thermogravimetric analysis (Figure 3.3) occur at significantly lower temperatures for both the lower pressure step (65 °C; predicted from isotherms: 87 °C) and higher pressure step (48 °C; predicted from isotherms: 69 °C) (Figure 3.S7).

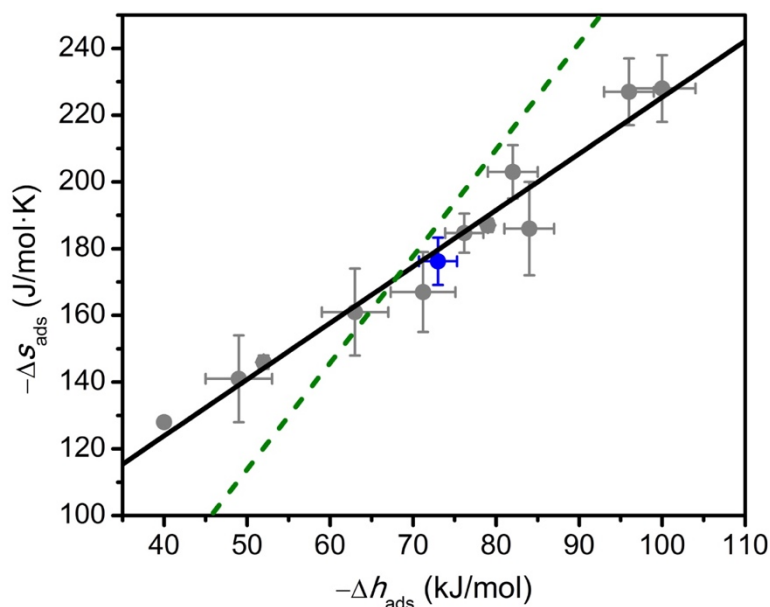


Figure 3.S15. Correlation between the negative differential enthalpy ($-\Delta h_{\text{ads}}$) and negative differential entropy ($-\Delta s_{\text{ads}}$) of CO_2 adsorption in previously reported diamine-appended variants of $\text{Mg}_2(\text{dobpdc})$ that form ammonium carbamate chains (gray circles), determined at a loading of 1.0 mmol/g.^{51,52} The black line is included to guide the eye and demonstrate a general tradeoff between the differential enthalpy and entropy of adsorption, but the statistical significance of a linear correlation has not been definitively proven.¹¹⁸ For 2-ampd- $\text{Mg}_2(\text{dobpdc})$, the lower pressure CO_2 adsorption step (blue circle, calculated at a loading of 1.0 mmol/g) follows this trend, which is consistent with the formation of ammonium carbamate chains. The dashed green line indicates the combinations of Δh_{ads} and Δs_{ads} that yield $\Delta g_{\text{ads}} = -14.4$ kJ/mol, corresponding to $p_{\text{step}} = 4.0$ mbar at 40 °C and thus enabling 90% capture from a natural gas flue gas stream under ideal conditions.⁵¹ All diamine-appended metal-organic frameworks to the right of the dashed green line, including 2-ampd- $\text{Mg}_2(\text{dobpdc})$, are predicted to have CO_2 adsorption steps at ≤ 4 mbar of CO_2 in single-component adsorption isotherms at 40 °C.

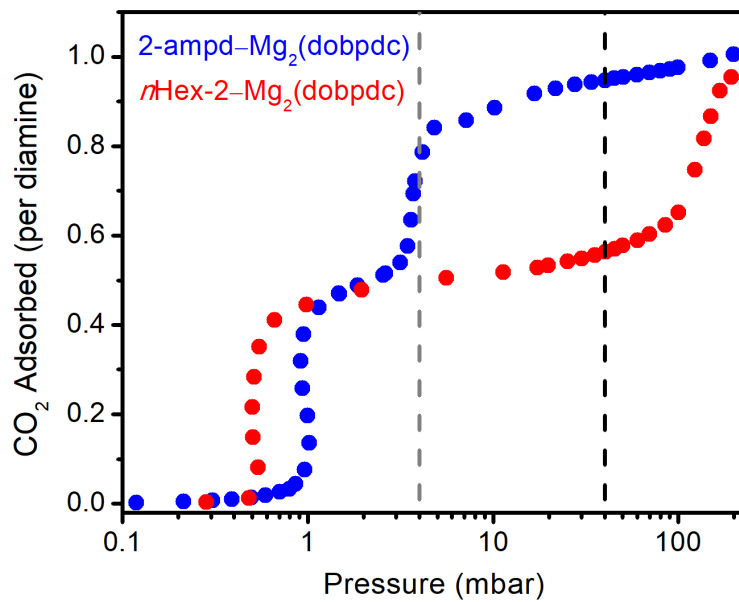


Figure 3.S16. CO₂ adsorption isotherms for 2-ampd-Mg₂(dobpdc) (blue) and the previously reported framework *n*Hex-2-Mg₂(dobpdc) at 40 °C.⁵³ The adsorption steps of 2-ampd-Mg₂(dobpdc) both occur at ≤4 mbar of CO₂ at 40 °C, enabling ≥90% capture from natural gas flue gas under ideal conditions. In contrast, the second CO₂ adsorption step of *n*Hex-2-Mg₂(dobpdc) occurs at approximately 130 mbar at 40 °C, and thus would be inoperative under a 4% CO₂ in N₂ stream.

Table 3.S1. Adsorption capacities and estimated noncompetitive selectivities for CO₂ over O₂ and N₂ in 2-ampd-Mg₂(dobpdc) at 40 °C.

Gas	Partial Pressure (mbar) ^a	Quantity Adsorbed (mmol/g)	Selectivity ($q_{\text{CO}_2}/q_{\text{gas}})/(p_{\text{CO}_2}/p_{\text{gas}})$
CO ₂	40	3.47	-
O ₂	120	0.015	694
N ₂	750	0.049	1320

^aApproximate values in NGCC flue gas.¹¹⁹

3.6.3 Calculation of the Approximate Regeneration Energy of 2-ampd–Mg₂(dobpdc)

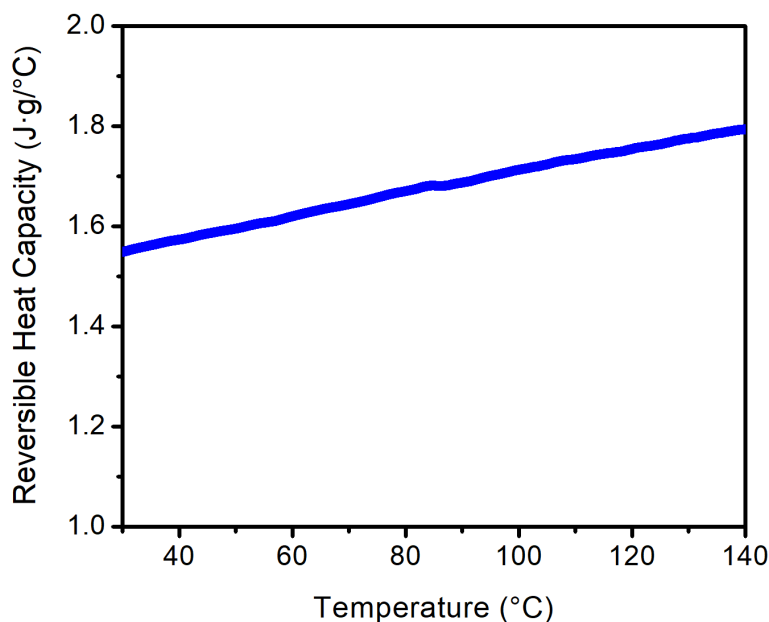


Figure 3.S17. Reversible heat capacity of 2-ampd–Mg₂(dobpdc), determined by modulated differential scanning calorimetry (DSC) under an atmosphere of He. The ramp rate was 2 °C/min. A modulation frequency of 0.75 °C/80 s was used.

Regeneration energies for CO₂ alone were calculated using the following equation:

$$\frac{MJ}{kg\ CO_2} = \left(\frac{1}{q_{WC}}\right) \left(\frac{22.72\ mol\ CO_2}{kg\ CO_2}\right) \left(\frac{1\ MJ}{1000\ kJ}\right) (C_p\Delta T + |\Delta h_{ads}|q_{WC}) \quad (3.S1)$$

where C_p is the heat capacity in J/g_{MOF}•°C = kJ/kg_{MOF}•°C, ΔT is the temperature swing, Δh_{ads} is the differential enthalpy of adsorption in kJ/mol_{CO₂}, and q_{WC} is the working capacity in mmol_{CO₂}/g_{MOF} = mol_{CO₂}/kg_{MOF}. The $C_p\Delta T$ term accounts for the sensible heat, while the $|\Delta h_{ads}|q_{WC}$ term accounts for the regeneration heat.

For a 40–140 °C temperature swing process with 2-ampd–Mg₂(dobpdc), a projected regeneration energy of **2.77 MJ/kg CO₂** was calculated using the following values:

$$C_p = 1.69\ J/g\cdot^{\circ}C \text{ (averaged over 40–140 }^{\circ}C, \text{ as determined from Figure 3.S17)}$$

$$\Delta T = 100\ ^{\circ}C$$

$$|\Delta h_{ads}| = 73.2\ kJ/mol \text{ (averaged from 3.47 to 0.00 mmol/g, as determined from Figure 3.S8)}$$

$$q_{WC} = 3.47\ mol_{CO_2}/kg_{MOF} \text{ (3.47 mmol/g adsorbed at 40 mbar } CO_2, 40\ ^{\circ}C; 0.00\ mmol/g \text{ adsorbed at 1 bar } CO_2, 125\ ^{\circ}C)$$

This regeneration energy value is only an estimate, as it assumes that the framework adsorbs no CO₂ under 1 bar of CO₂ at 140 °C, and it does not account for the effect of water on the heat of adsorption or potential variation of the heat capacity of the adsorbent as a function of CO₂ and/or

H₂O loading. Nonetheless, these values suggest that CO₂ can be desorbed from 2-ampd–Mg₂(dobpdc) with a relatively low energy penalty.

For a 60–140 °C temperature swing process with 2-ampd–Mg₂(dobpdc), a projected regeneration energy of **2.66 MJ/kg CO₂** was calculated using the following values:

$$C_p = 1.71 \text{ J/g}\cdot\text{°C} \text{ (averaged over 60–140 °C, as determined from Figure 3.S17)}$$

$$\Delta T = 80 \text{ °C}$$

$$|\Delta h_{\text{ads}}| = 74.8 \text{ kJ/mol} \text{ (averaged from 3.22 to 0.00 mmol/g, as determined from Figure 3.S8)}$$

$$q_{\text{wc}} = 3.22 \text{ mol}_{\text{CO}_2}/\text{kg}_{\text{MOF}} \text{ (3.22 mmol/g adsorbed at 40 mbar CO}_2\text{, 60 °C; 0.00 mmol/g adsorbed at 1 bar CO}_2\text{, 125 °C)}$$

Using this equation, we determined that the approximate regeneration energies for the previously reported related materials dmpn–Mg₂(dobpdc)⁵³ ($q_{\text{wc}} = 2.42 \text{ mol}_{\text{CO}_2}/\text{kg}_{\text{MOF}}$, $\Delta T = 60 \text{ °C}$) and mmen–Mg₂(dobpdc)⁵⁰ ($q_{\text{wc}} = 3.4 \text{ mol}_{\text{CO}_2}/\text{kg}_{\text{MOF}}$, $\Delta T = 90 \text{ °C}$) to be 2.5 MJ/kg CO₂ and 2.6 MJ/kg CO₂, respectively, for CO₂ capture from the emissions of a coal-fired power plant (15% CO₂, 40 °C, ~1 bar). Therefore, despite the more challenging nature of carbon capture from a more dilute natural gas emission stream, 2-ampd–Mg₂(dobpdc) possesses regeneration energy requirements for post-combustion NGCC capture that are similar to those of previously reported materials in this family in related CO₂ capture processes.

In an analogous calculation, a polyamine-functionalized silica⁴⁸ was found to have a regeneration energy of **3.93 MJ/kg CO₂** for CO₂ capture from natural gas flue gas with the following properties: 32.2 °C, 3.9% CO₂, 4.7% H₂O. We calculated this regeneration energy using the above method and the following reported values: $C_p = 1.4$, $T_{\text{ads}} = 73 \text{ °C}$, $T_{\text{des}} = 138 \text{ °C}$, $|\Delta h_{\text{ads}}| = 91 \text{ kJ/mol CO}_2$, and $q_{\text{wc}} = 1.11 \text{ mmol CO}_2/\text{g}$ (rich loading, 1.60 mmol/g; lean loading, 0.49 mmol/g). The specific silica characterized in this combined experimental and modeling study was prepared by grafting polyethyleneimine (PEI, 600 g/mol) to a commercial porous silica (Vpore, 5 mm spheres crushed and sieved to 0.245–0.425 mm, pore volume 0.90 cm³/g, pore mean diameter 8.5 nm) in methanol to produce a final material with 35 ± 2 wt % PEI.

To estimate the influence of water on the regeneration energy, the following revised formula was used:

$$\frac{\text{MJ}}{\text{kg CO}_2} = \left(\frac{1}{q_{\text{wc}}}\right) \left(\frac{22.72 \text{ mol CO}_2}{\text{kg CO}_2}\right) \left(\frac{1 \text{ MJ}}{1000 \text{ kJ}}\right) \left(C_p \Delta T + |\Delta h_{\text{adsCO}_2}| q_{\text{wcCO}_2} + |\Delta h_{\text{adsH}_2\text{O}}| q_{\text{wcH}_2\text{O}}\right) \quad (3.S2)$$

Here, the adsorption enthalpy ($\Delta h_{\text{ads,H}_2\text{O}}$) and working capacity ($q_{\text{wc,H}_2\text{O}}$) are considered for any co-adsorbed and co-cycled water.

Under a humid stream of 4% CO₂ in N₂, 2-ampd–Mg₂(dobpdc) was found to adsorb a total mass of 20.3 g/100 g at 40 °C (Figure 3.S43). The desorption branch of the humid isobar shows continued mass increase at the onset of heating, suggesting that additional co-adsorption of water is possible with longer adsorption times. The total adsorbed mass at 40 °C is approximately consistent with the theoretical mass of 22.7 g/100 g anticipated for binding of 1 CO₂ and 1 H₂O molecule per diamine, calculated from the theoretical adsorption capacities of 16.1 g CO₂/100 g adsorbent and 6.59 g H₂O/100 g adsorbent. Therefore, to predict the influence of water co-adsorption on the regeneration energy, we treat the most unfavorable case, in which the

adsorbent binds a full equivalent of water (6.59 g H₂O/100 g, or 3.66 mmol H₂O/g), and all of this water is co-cycled with the adsorbed CO₂. From the H₂O adsorption isotherms (Figure 3.S11), an average $|\Delta h_{adsH_2O}|$ of 65 kJ/mol is predicted for co-adsorption of 1 H₂O per CO₂. Therefore, water co-adsorption is anticipated to **add up to 1.56 MJ/kg CO₂** to the regeneration energy with adsorption at 40 °C, leading to a total regeneration energy of **4.33 MJ/kg CO₂**. If adsorption is performed at 60 °C, water co-adsorption is anticipated to **add up to 1.68 MJ/kg CO₂** to the regeneration energy, resulting in the same total regeneration energy of **4.34 MJ/kg CO₂**. We note that these values are only estimates, as they assume that *all* co-adsorbed water is desorbed along with CO₂, and they do not account for the potential difference in the adsorption enthalpy of water on the CO₂-inserted phase. As noted above, this method also does not account for potential variation of the heat capacity of the adsorbent as a function of CO₂ and/or H₂O loading.

For the polyamine-functionalized silica discussed above,⁴⁸ the same calculation can be performed using the provided $q_{wC_{H_2O}}$ of 0.62 mmol/g and $|\Delta h_{adsH_2O}|$ of 60 kJ/mol. These values result in an **increase of 0.76 MJ/kg CO₂**, resulting in a total predicted regeneration energy of **4.69 MJ/kg CO₂** under humid conditions.

The predicted regeneration energies for 2-ampd–Mg₂(dobpdc) and the PEI-functionalized silica are summarized in Table 3.S2 below.

Table 3.S2. Regeneration energy values predicted for 2-ampd–Mg₂(dobpdc) and for a previously-reported⁴⁸ polyamine-functionalized silica.

	2-ampd– Mg ₂ (dobpdc)	2-ampd– Mg ₂ (dobpdc)	PEI- functionalized silica
Adsorption temperature, T_{ads}	40	60	73
Desorption temperature, T_{des}	140	140	138
Temperature swing, ΔT (°C)	100	80	65
Heat capacity, C_p (J/g·°C)	1.69	1.71	1.4
CO ₂ adsorption enthalpy, $ \Delta h_{adsCO_2} $ (kJ/mol CO ₂)	73.2	74.8	91
CO ₂ working capacity, q_{wCO_2} (mmol CO ₂ /g adsorbent)	3.47	3.22	1.11
H ₂ O adsorption enthalpy, $ \Delta h_{adsH_2O} $ (kJ/mol H ₂ O)	65	65	60
H ₂ O working capacity, $q_{wC_{H_2O}}$ (mmol H ₂ O/g adsorbent)	3.66 ^a	3.66 ^a	0.62
Regeneration energy <i>excluding</i> <i>influence of H₂O</i> (MJ/kg CO ₂)	2.77	2.66	3.93
Regeneration energy <i>including</i> <i>influence of H₂O</i> (MJ/kg CO ₂)	4.33 ^a	4.34 ^a	4.69

^aAssumes co-adsorption and co-desorption of 1 H₂O per diamine

3.6.4 Synthesis and Characterization of 2-ampd-Mg₂(dotpdc)

The adsorbent 2-ampd-Mg₂(dotpdc) was prepared following the same procedure used to prepare 2-ampd-Mg₂(dobpdc). The as-synthesized diamine loading of 2-ampd-Mg₂(dotpdc) was found to be 103% by ¹H NMR after digestion with DCl (35 wt% in D₂O) in DMSO-*d*₆.

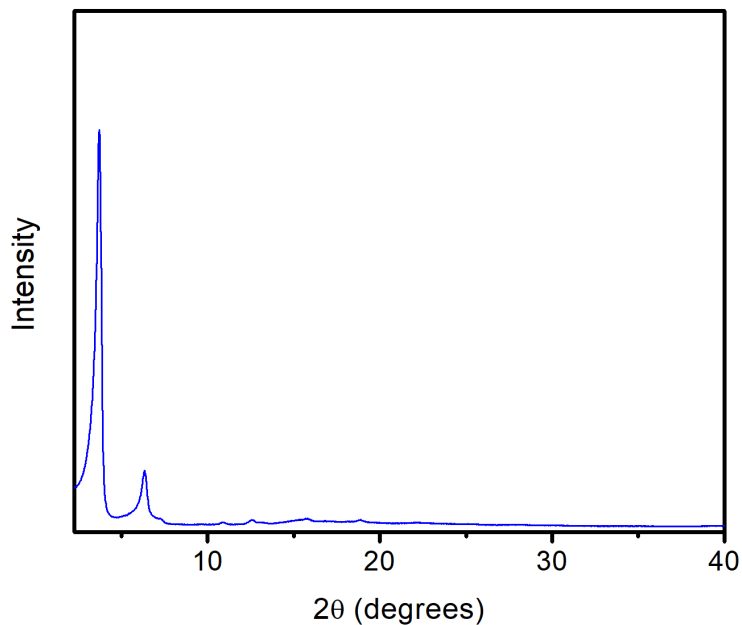


Figure 3.S18. Powder X-ray diffraction pattern (Cu K α radiation, $\lambda = 1.5418 \text{ \AA}$) of as-synthesized 2-ampd-Mg₂(dotpdc).

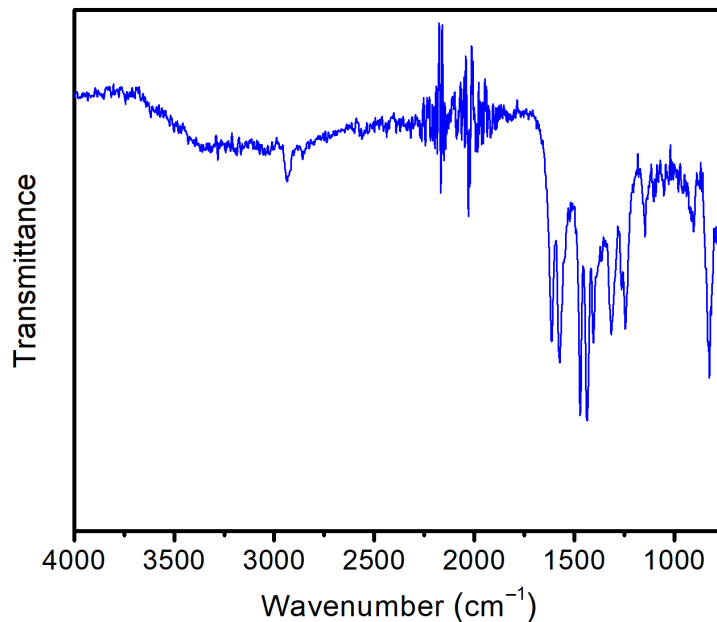


Figure 3.S19. Infrared spectrum of as-synthesized 2-ampd-Mg₂(dotpdc).

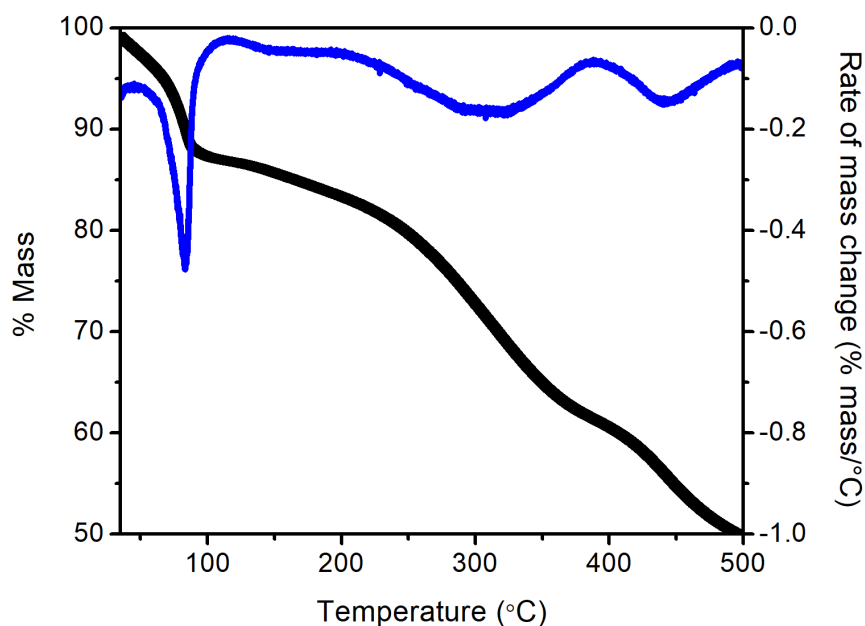


Figure 3.S20. Dry N_2 decomposition profile of 2-ampd- $\text{Mg}_2(\text{dotpdc})$, plotted in black as % mass change (left-hand y-axis) vs. T . The initial mass loss regime ($<110\text{ }^\circ\text{C}$) is likely due to the loss of water, toluene, and excess diamine from the pores. The second mass loss regime ($200\text{--}390\text{ }^\circ\text{C}$) is due to diamine volatilization from the metal sites. The third mass loss regime ($>390\text{ }^\circ\text{C}$) is due to decomposition of the framework. The rate of mass change at each temperature is shown in blue and corresponds to the right-hand y-axis. A ramp rate of $1.5\text{ }^\circ\text{C}/\text{min}$ was used.

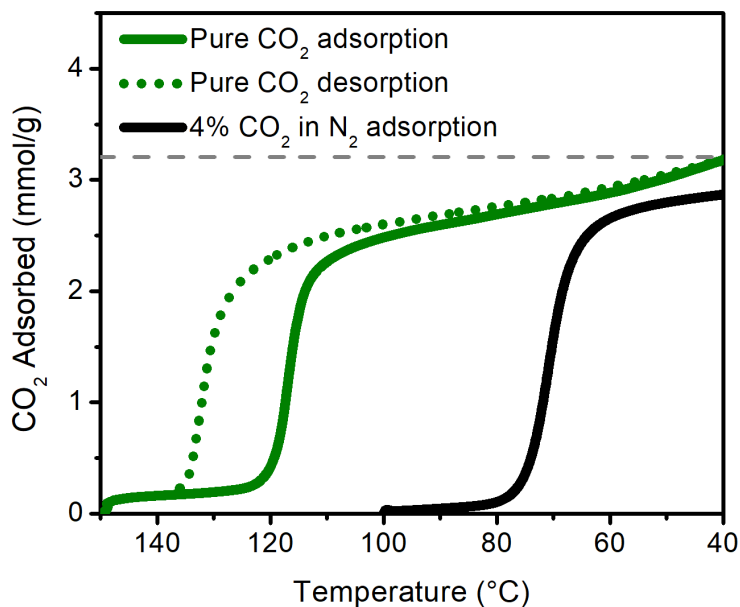


Figure 3.S21. Dry pure CO_2 adsorption (solid green line) and desorption (dotted green line) isobars, as well as the dry 4% CO_2 in N_2 adsorption isobar (solid black line), of 2-ampd- $\text{Mg}_2(\text{dotpdc})$. A ramp rate of $1\text{ }^\circ\text{C}/\text{min}$ was used for the pure CO_2 adsorption/desorption isobars, and a ramp rate of $0.25\text{ }^\circ\text{C}/\text{min}$ was used for the 4% CO_2 in N_2 adsorption isobar. Isobars were collected at atmospheric pressure. The material was activated at $150\text{ }^\circ\text{C}$ under flowing N_2 for 20 min prior to each measurement. The expected adsorption capacity corresponding to the adsorption of one CO_2 per diamine is indicated as a dashed gray line.

These isobars confirm that 2-ampd–Mg₂(dotpdc) displays a single CO₂ adsorption/desorption step, indicating that the double-step adsorption/desorption behavior of 2-ampd–Mg₂(dobpdc) is likely due to unfavorable interactions between adjacent ammonium carbamate chains in the *ab* plane of the framework, as has previously been described.⁵³

3.6.5 Variants of Mg₂(dobpdc) Appended with Acyclic *Primary,Secondary* 1,3-Diaminopropanes

Our previous explorations of *primary,secondary* and *secondary,secondary* diamine-appended variants of Mg₂(dobpdc) were limited to alkylethylenediamines,^{51,53} but our recent work has shown that *primary,primary* 1,3-diaminopropanes can be grafted to Mg₂(dobpdc) to yield adsorbents displaying step-shaped adsorption of CO₂.⁵² Therefore, we were interested in evaluating *primary,secondary* and *secondary,secondary* 1,3-diaminopropane-appended variants of Mg₂(dobpdc) for their potential for CO₂ capture from natural gas flue gas. Thus, the diamines *N*-methyl-1,3-diaminopropane (m-3) and *N*-(*iso*-propyl)-1,3-diaminopropane (i-3) were grafted to Mg₂(dobpdc) using the same procedure used to prepare 2-ampd–Mg₂(dobpdc). However, to date, all attempts to append *secondary,secondary* 1,3-diaminopropanes such as *N,N'*-dimethyl-1,3-diaminopropane and *N,N'*-diethyl-1,3-diaminopropane have resulted in suboptimal diamine loadings (<80%) and materials that cannot be activated because they are extremely prone to diamine volatilization from the metal sites.

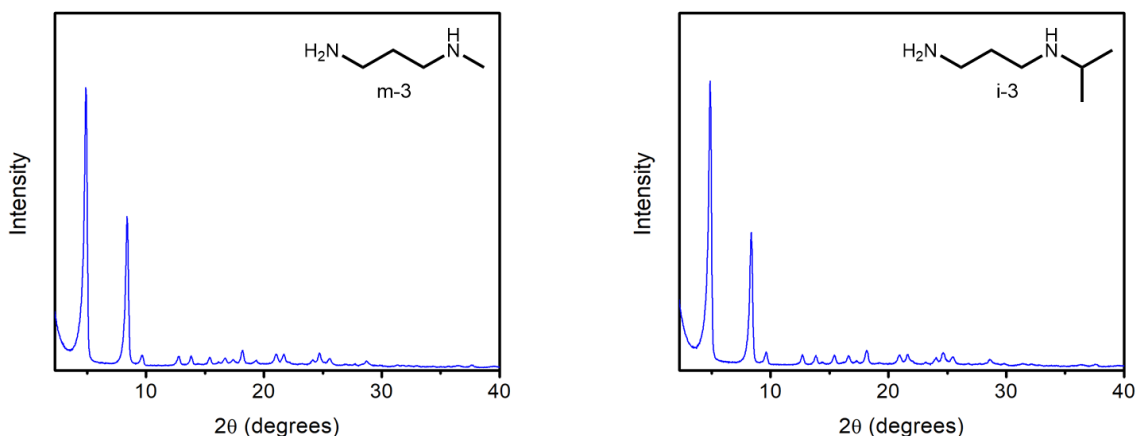


Figure 3.S22. Powder X-ray diffraction patterns (Cu K α radiation, $\lambda = 1.5418 \text{ \AA}$) of as-synthesized variants of Mg₂(dobpdc) appended with acyclic *primary,secondary* 1,3-diaminopropanes.

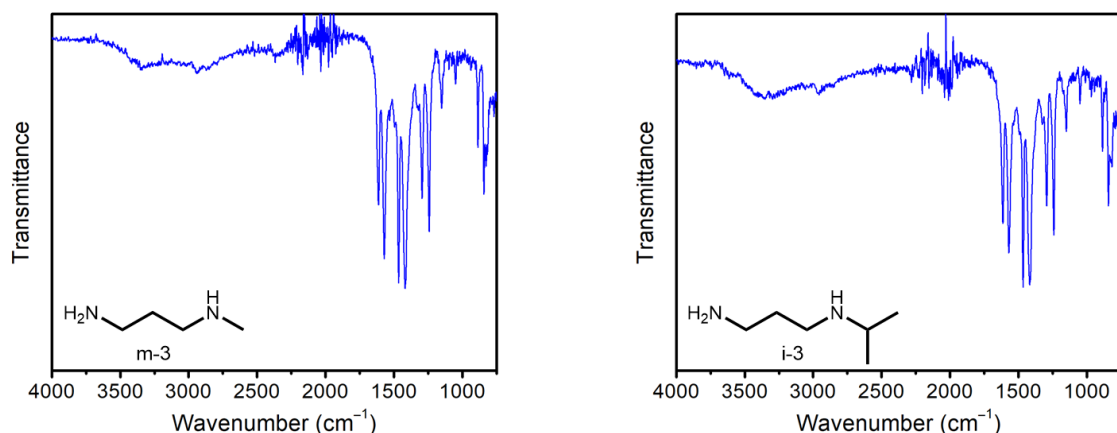


Figure 3.S23. Infrared spectra of as-synthesized variants of $\text{Mg}_2(\text{dobpdc})$ appended with acyclic *primary, secondary* 1,3-diaminopropanes.

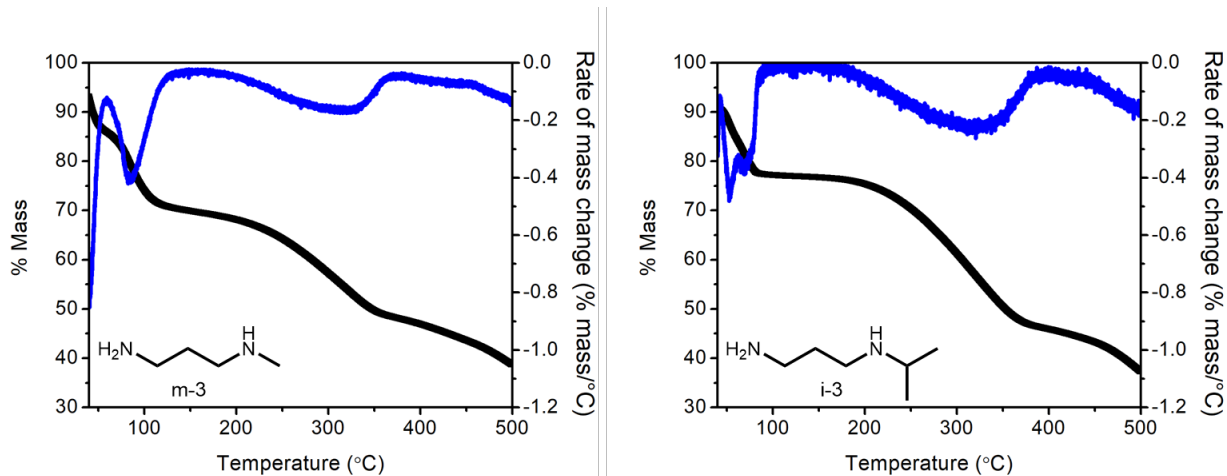


Figure 3.S24. Dry N_2 decomposition profiles of $\text{Mg}_2(\text{dobpdc})$ variants appended with acyclic *primary, secondary* 1,3-diaminopropanes, plotted in black as % mass change (left-hand y -axis) vs. T . The initial mass loss regimes (<130 °C) are likely due to the loss of water, toluene, and excess diamine from the pores. The second mass loss regimes (180–390 °C) are due to diamine volatilization from the metal sites. The third mass loss regimes (>400 °C) are due to decomposition of the framework. The rate of mass change at each temperature is shown in blue and corresponds to the right-hand y -axis. A ramp rate of 1.5 °C/min was used in all cases. Consistent with our previous results,^{51,53} i-3- $\text{Mg}_2(\text{dobpdc})$ displays superior thermal stability to m-3- $\text{Mg}_2(\text{dobpdc})$.

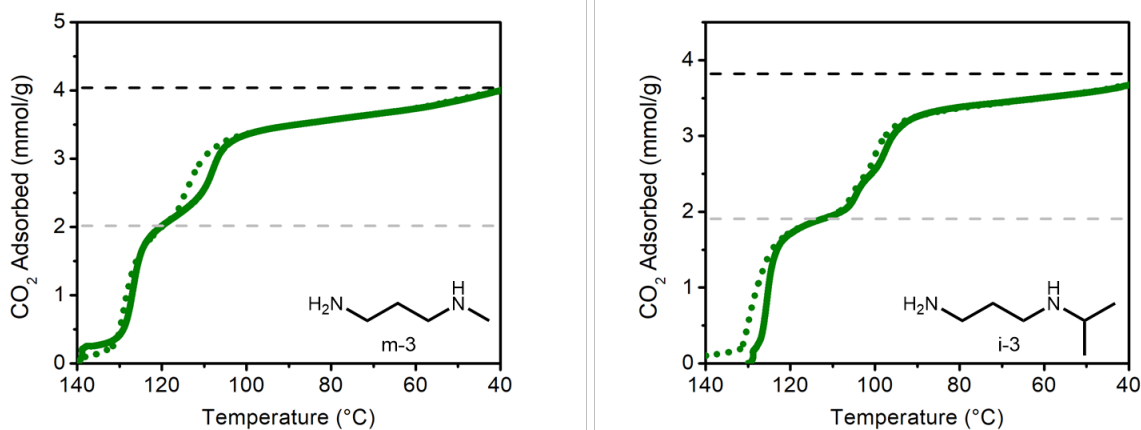


Figure 3.S25. Dry pure CO₂ adsorption (solid green lines) and desorption (dotted green lines) isobars at atmospheric pressure for Mg₂(dobpdc) variants appended with acyclic *primary,secondary* 1,3-diaminopropanes, confirming the presence of two CO₂ adsorption/desorption steps in both cases. A ramp rate of 1 °C/min was used in both cases. The expected capacities corresponding to the adsorption of 1 CO₂ per diamine (black dashed lines) and 0.5 CO₂ per diamine (light gray dotted lines) are indicated.

The observed double-step CO₂ adsorption/desorption profiles of these two diamines are similar to those observed with bulky acyclic *primary,secondary* alkylethylenediamines⁵³ as well as 2-ampd–Mg₂(dobpdc), as the first adsorption step corresponds approximately to the adsorption of 0.5 molecules of CO₂ per diamine. This effect is likely due to unfavorable interactions between adjacent diamines in the *ab* plane of the framework.⁵³

Table 3.S3. Typical diamine loadings and activation temperatures for variants of Mg₂(dobpdc) appended with acyclic *primary,secondary* 1,3-diaminopropanes.

Diamine Structure	Diamine Abbreviation	% Diamine Loading (As Synthesized) ^a	Activation Temperature (°C) ^b	% Diamine Loading (After Activation) ^a
	m-3	108%	130	100%
	i-3	95%	130	94%

^aDetermined by ¹H NMR after digestion with DCl (35 wt% in D₂O) in DMSO-*d*₆.

^bActivated for 20 min under flowing dry N₂.

3.6.6 Variants of Mg₂(dobpdc) Appended with Additional Cyclic *Primary,Secondary* Diamines

To compare the behavior of 2-ampd with related cyclic diamines, variants of Mg₂(dobpdc) appended with 3-aminopiperidine (3-apd), 3-(aminomethyl)piperidine (3-ampd), 4-aminopiperidine (4-apd), 3-aminopyrrolidine (3-apyrr), and 4-(aminomethyl)piperidine (4-ampd) were prepared using the same procedure employed to prepare 2-ampd–Mg₂(dobpdc). Variants of Mg₂(dobpdc) appended with piperazine (pipz) and homopiperazine (hpipz) were prepared using a slightly modified procedure, wherein the diamine grafting was carried out using a solution consisting of approximately 0.5 g of the diamine dissolved in 5 mL of CHCl₃ due to the poor

solubility of these diamines in toluene. The synthesis and characterization of 3-apyr-Mg₂(dobpdc) have been described previously.¹¹⁵

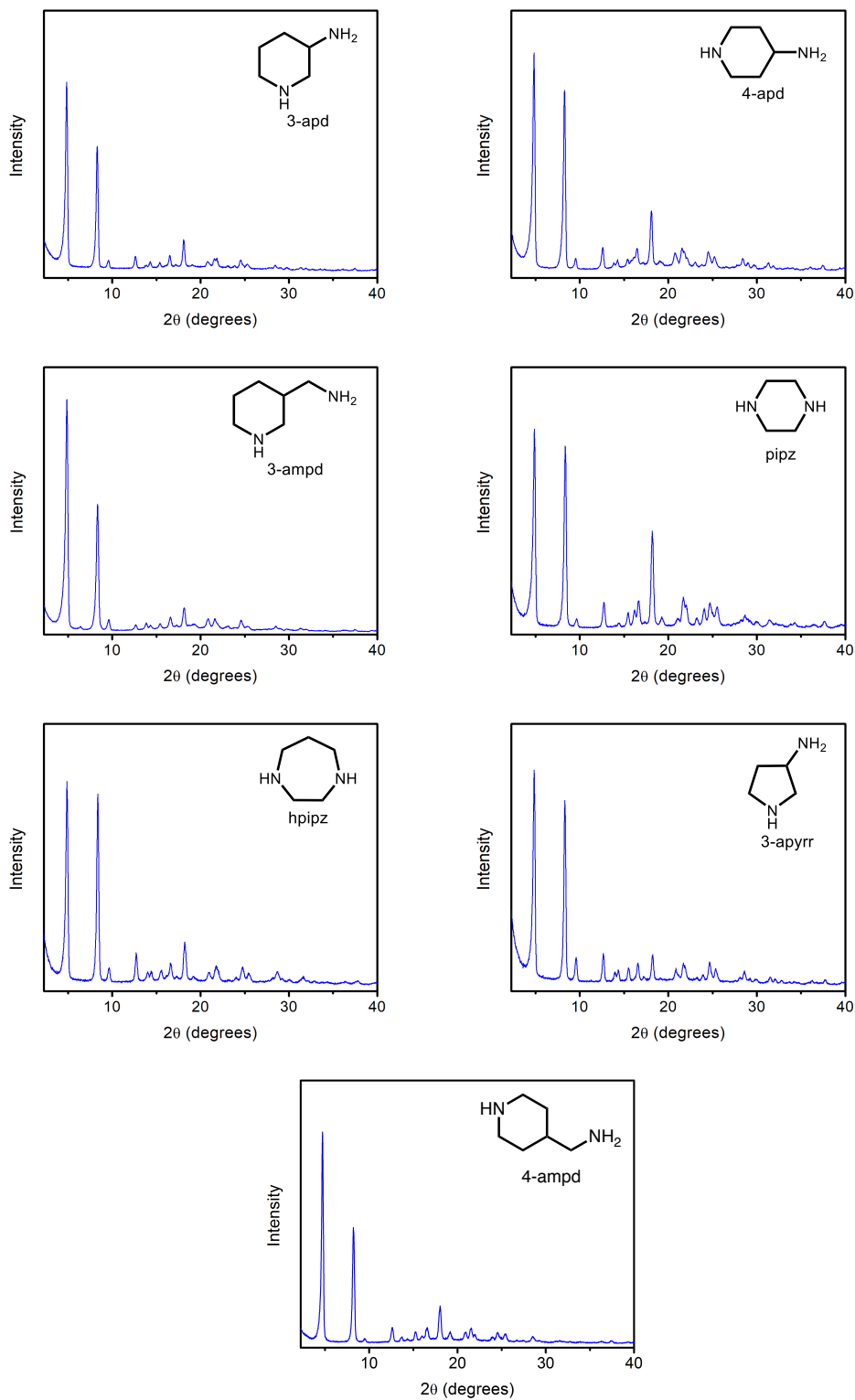


Figure 3.S26. Powder X-ray diffraction patterns (Cu K α radiation, $\lambda = 1.5418 \text{ \AA}$) of as-synthesized variants of Mg₂(dobpdc) appended with cyclic diamines.

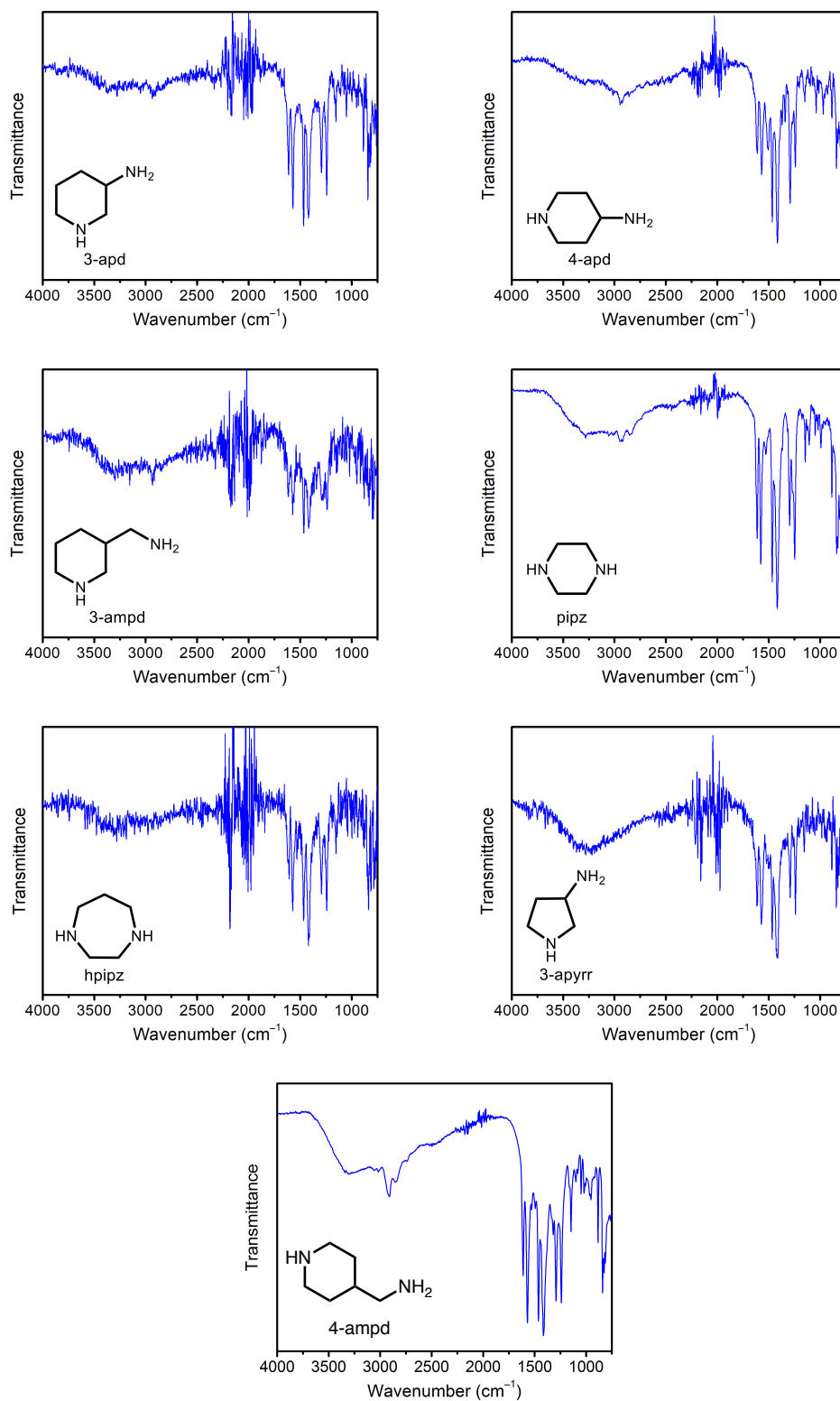


Figure 3.S27. Infrared spectra of as-synthesized variants of Mg₂(dobpdc) appended with cyclic diamines.

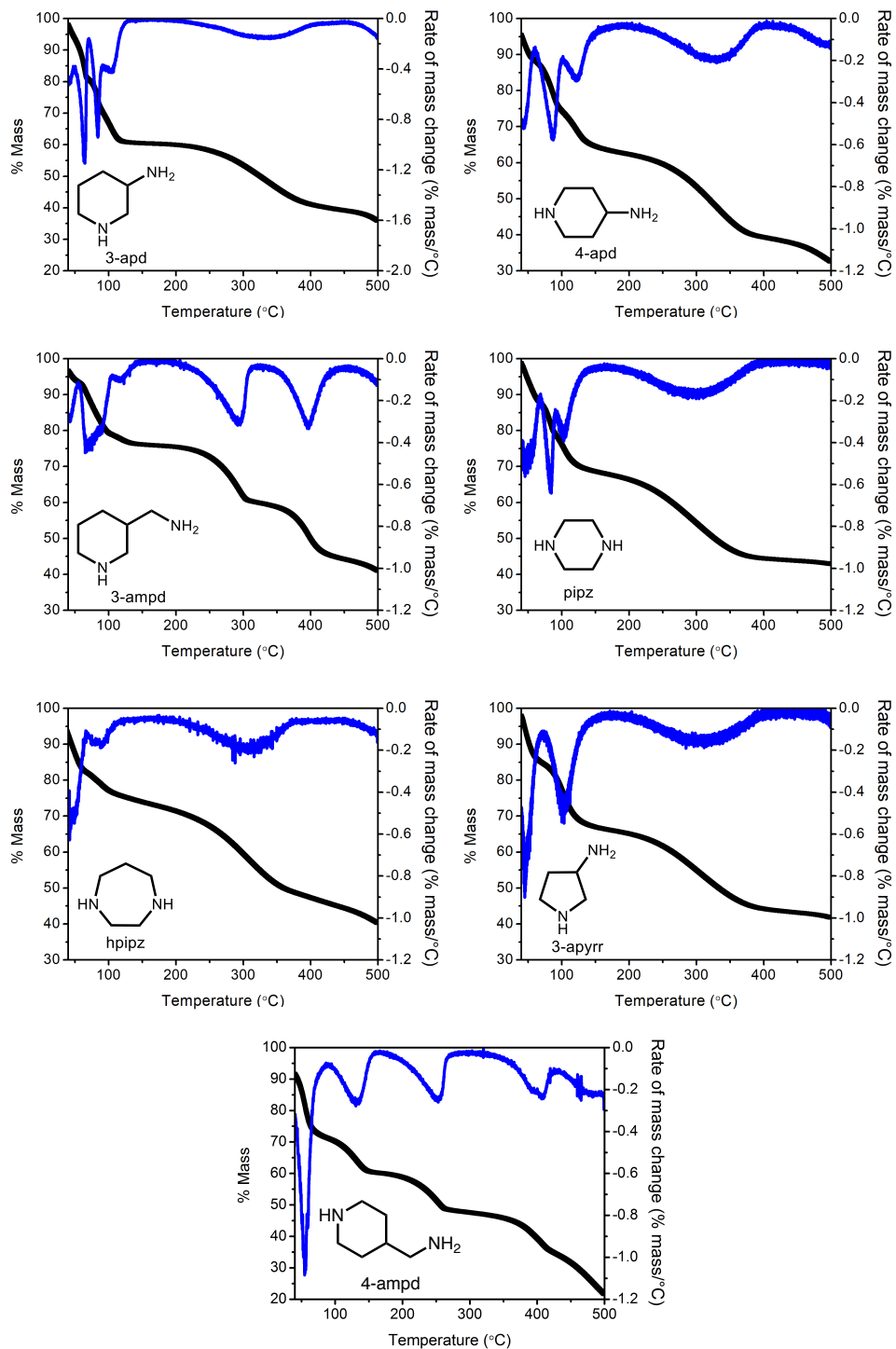


Figure 3.S28. Dry N_2 decomposition profiles of $Mg_2(dobpdc)$ variants appended with cyclic diamines, plotted in black as % mass change (left-hand y-axis) vs. T . The initial mass loss regimes (<130 °C) are likely due to the loss of water, toluene, and excess diamine from the pores. The second mass loss regimes (200–400 °C) are due to diamine volatilization from the metal sites. The third mass regimes (>400 °C) are due to decomposition of the framework. The rate of mass change at each temperature is shown in blue and corresponds to the right-hand y-axis. A ramp rate of 1.5 °C/min was used in all cases.

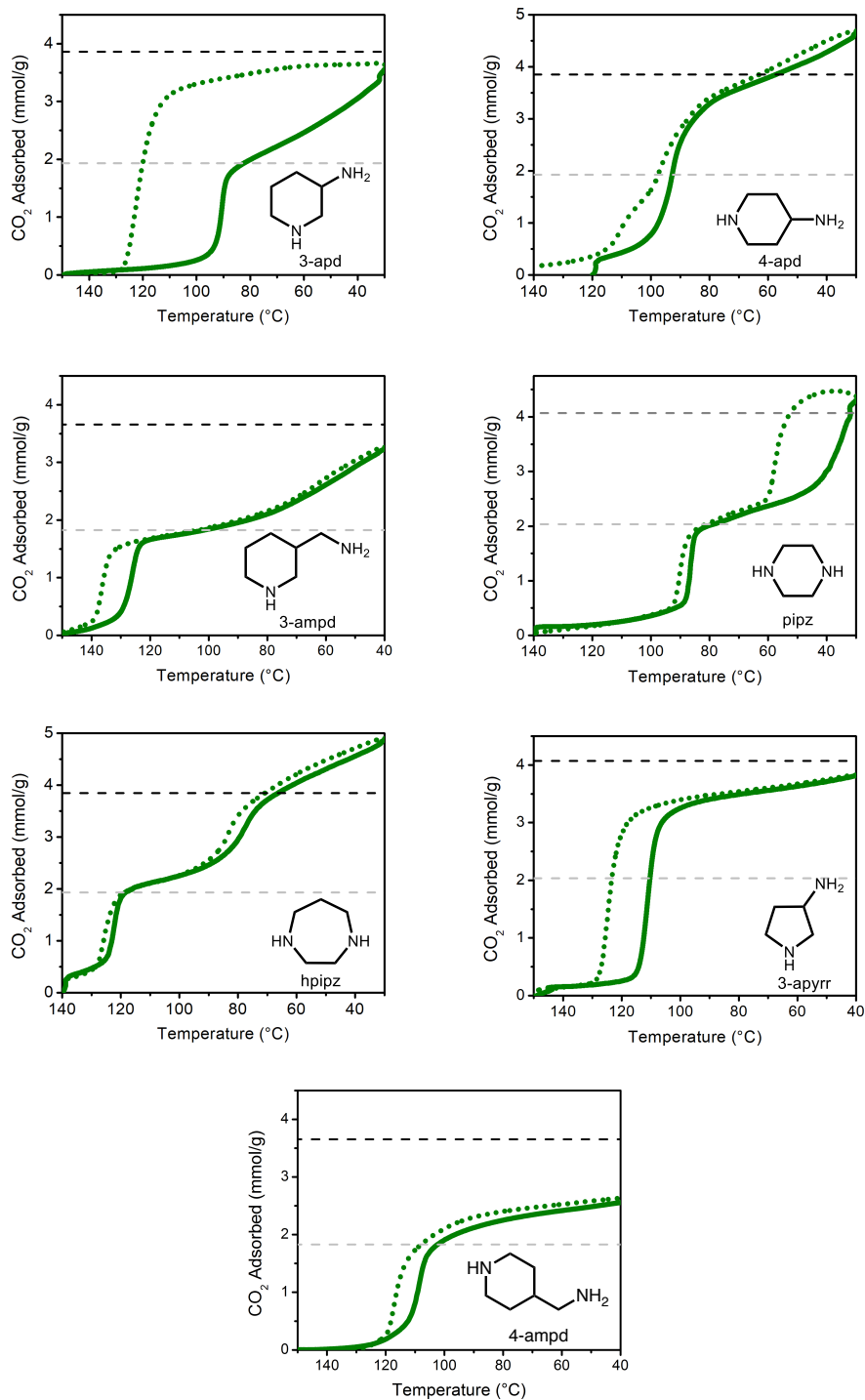


Figure 3.S29. Dry pure CO₂ adsorption (solid green lines) and desorption (dotted green lines) isobars at atmospheric pressure for Mg₂(dobpdc) variants appended with cyclic diamines, confirming the presence of one or two CO₂ adsorption/desorption steps in all cases. A ramp rate of 1 °C/min was used in all cases except for pipz–Mg₂(dobpdc), for which a ramp rate of 0.5 °C/min was used due to the slow adsorption kinetics of this material. The expected capacities corresponding to the adsorption of 1 CO₂ per diamine (black dashed lines) and 0.5 CO₂ per diamine (light gray dashed lines) are indicated.

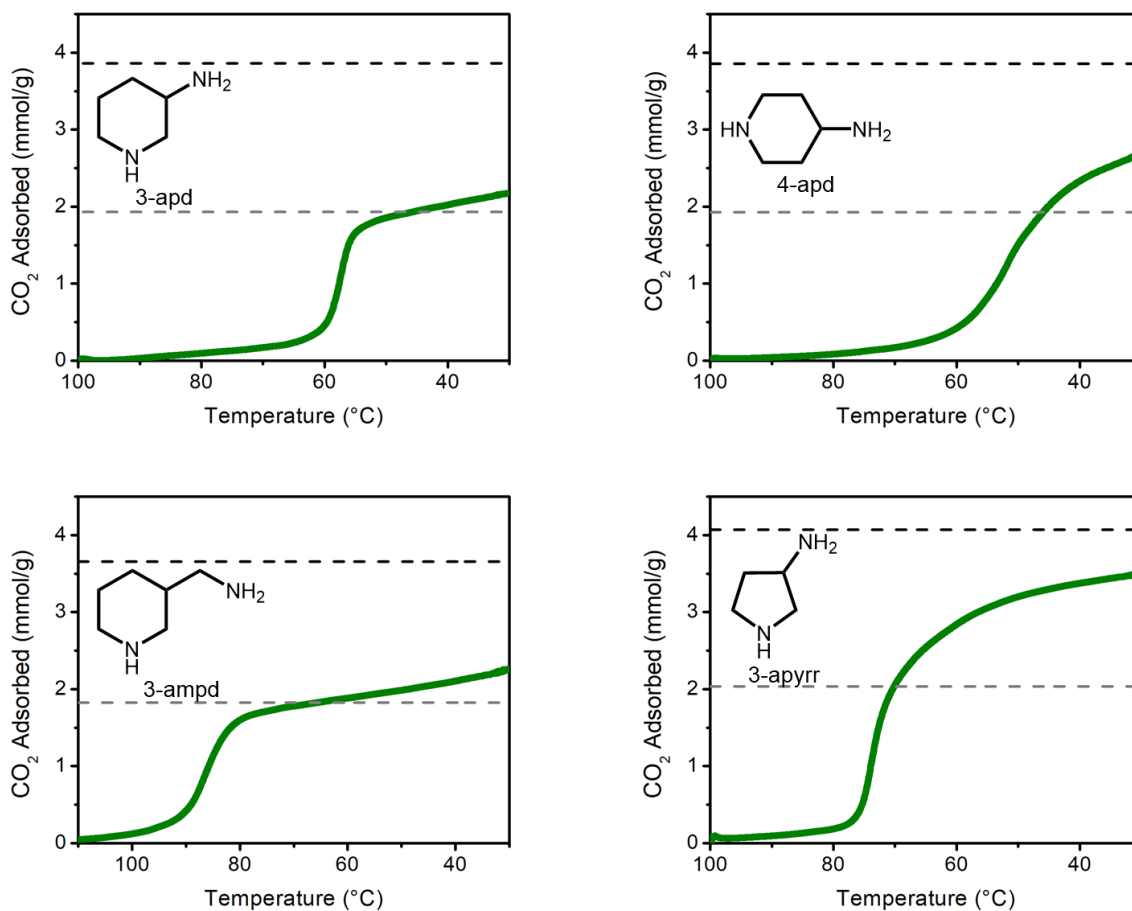
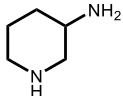
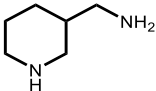
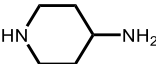
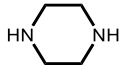
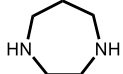
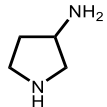
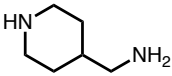


Figure 3.S30. Dry 4% CO₂ in N₂ adsorption isobars at atmospheric pressure for selected Mg₂(dobpdc) variants appended with cyclic diamines. A ramp rate of 0.25 °C/min was used in all cases. The expected adsorption capacities corresponding to 1 CO₂ per diamine (black dashed lines) and 0.5 CO₂ per diamine (light gray dashed lines) are indicated.

In contrast to 2-ampd–Mg₂(dobpdc) (main text Figure 3), none of the cyclic diamine-appended adsorbents in Figure 3.S30 reach their theoretical adsorption capacities under a 4% CO₂ in N₂ stream at 40 °C, or even upon further cooling to 30 °C. Therefore, their adsorption capacities in a simulated natural gas flue gas capture process would be inferior to that of 2-ampd–Mg₂(dobpdc).

Table 3.S4. Typical diamine loadings and activation temperatures for variants of Mg₂(dobpdc) appended with cyclic diamines.

Diamine Structure	Diamine Abbreviation	% Diamine Loading (As Synthesized) ^a	Activation Temperature (°C) ^b	% Diamine Loading (After Activation) ^a
	3-apd	200%	150	100%
	3-ampd	116%	150	104%
	4-apd	171%	150	95%
	pipz	150% ^c	140	94%
	hpipz	110% ^c	140	N/d
	3-apyrr	144%	150	99%
	4-ampd	165%	175	99%

^aDetermined by ¹H NMR after digestion with DCl (35 wt% in D₂O) in DMSO-*d*₆.

^bActivated for 20 min under flowing dry N₂.

^cAppended in CHCl₃ instead of toluene. N/d = not determined.

3.6.7 Relationship Between Isobaric and Isothermal Measurements

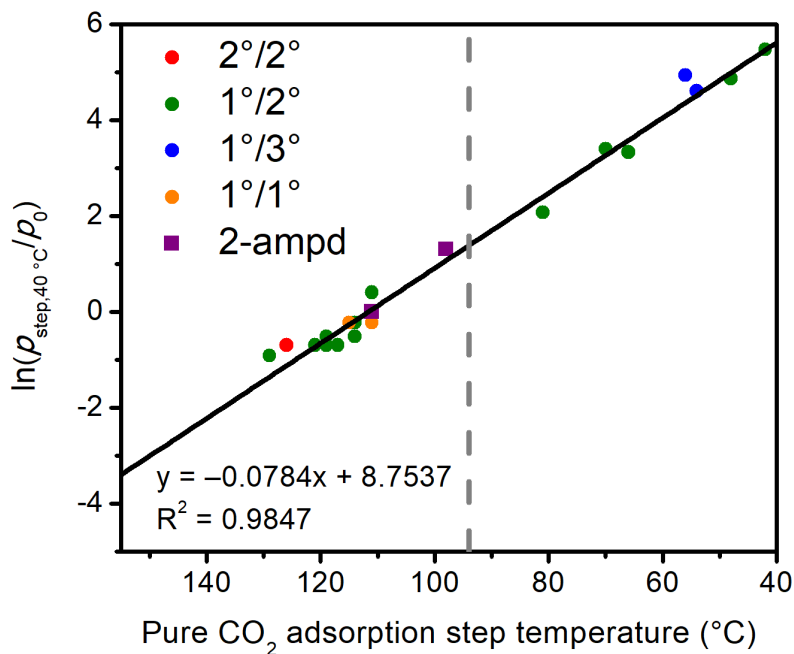
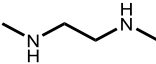
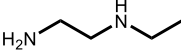
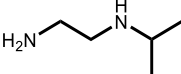
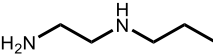
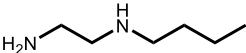
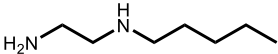
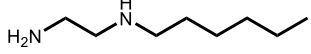
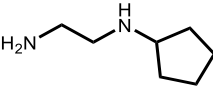
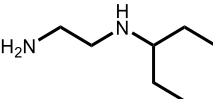
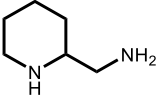
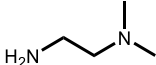
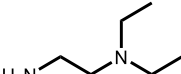

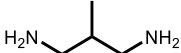


Figure 3.S31. Empirical linear correlation between pure CO₂ adsorption step temperature, as determined by thermogravimetric analysis, and the natural log of the 40 °C CO₂ step pressure divided by p_0 (assumed here as 1 bar), as determined by isothermal volumetric gas adsorption measurements, for a series of diamine-appended variants of Mg₂(dobpc).⁵¹⁻⁵³ The adsorption step temperatures and pressures were determined using the approximate inflection points of the adsorption steps. This correlation suggests that a pure CO₂ adsorption step temperature of $\geq 94 \pm 4$ °C (*i.e.*, to the left of the dashed gray line) is required for a 40 °C CO₂ adsorption step pressure of ≤ 4 mbar under ideal conditions.

Table 3.S5. Pure CO₂ adsorption step temperatures and 40 °C CO₂ adsorption step pressures for a series of diamine-appended variants of Mg₂(dobpdc).

Diamine Structure	Diamine Abbreviation	Pure CO ₂ Adsorption Step Temperature(s) (°C) ^a	40 °C CO ₂ Adsorption Step Pressure(s) (mbar) ^a	Reference
	mmen	126	0.5	49–51
	e-2	119	0.6	51,53
	i-2	114	0.8	51,53
	<i>n</i> Pr-2	117, 81	0.5, 8.0	53
	<i>n</i> Bu-2	119, 70	0.5, 30	53
	<i>n</i> Pent-2	121	0.5	53
	<i>n</i> Hex-2	114, 48	0.6, 130	53
	<i>c</i> Pent-2	129, 66	0.4, 28	53
	3-Pent-2	111, 42	1.5, 240	53
	2-ampd	111, 98	1.0, 3.7	This work
	mm-2	54	100	51
	ee-2	56	140	51
	pn	111	0.8	52
	mpn	115	0.8	52

^aDetermined using the approximate inflection point of the adsorption step.

3.6.8 Effect of Humidity on CO₂ Adsorption in 2-ampd–Mg₂(dobpdc) in Isobaric Measurements

Adsorption and desorption isobars were collected with 2-ampd–Mg₂(dobpdc) under a range of CO₂ concentrations in N₂. These isobars were used to calculate effective differential enthalpies and entropies of CO₂ adsorption under both dry and humid conditions using the Clausius–Clapeyron relationship. The difference between the dry and humid values was interpreted as an approximate measurement of the increase in thermodynamic driving force for CO₂ adsorption under humid conditions. However, we cannot exclude the possibility that water also enhances the adsorption kinetics of 2-ampd–Mg₂(dobpdc) by facilitating proton transfer, leading to higher effective adsorption step temperatures under humid conditions.

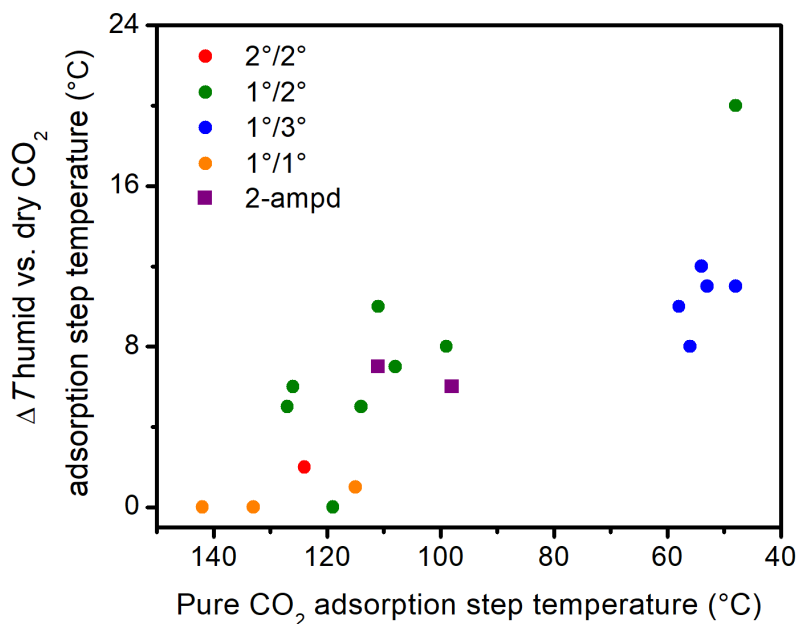


Figure 3.S32. Empirical correlation between the increase in pure CO₂ adsorption step temperature in the presence of humidity (ΔT) and the dry pure CO₂ adsorption step temperature for a series of diamine-appended variants of Mg₂(dobpdc). This qualitative correlation demonstrates that diamine-appended variants of Mg₂(dobpdc) with lower CO₂ adsorption step temperatures (*i.e.*, those with lower magnitude differential enthalpies of adsorption⁵¹) display an increase in the thermodynamic driving force for CO₂ under humid conditions compared to under dry conditions (*i.e.*, $\Delta T > 0$). The trend is likely influenced by the higher relative humidities in the TGA furnace at lower temperatures, because the water bubbler used to humidify the gas inlet is kept at room temperature. However the observed trend appears to support the previously reported trend of weaker ion pairing of ammonium carbamate chains formed by diamines with lower step temperatures.⁵³ A ramp rate of 1 °C/min was used in all cases, except for the adsorption isobars of 2-ampd–Mg₂(dobpdc), for which a ramp rate of 0.5 °C/min was used.

Table 3.S6. Pure CO₂ adsorption step temperatures under dry and humid conditions for a series of diamine-appended variants of Mg₂(dobpdc).

Diamine Structure	Diamine Abbreviation	Dry CO ₂ Adsorption Step Temperature (°C) ^a	Humid CO ₂ Adsorption Step Temperature (°C) ^a	Δ <i>T</i> humid vs. dry CO ₂ (°C)	Reference
	en	142	142	0	52,54,56
	men	133	133	0	52,56
	m-3	127, 108	132, 115	5, 7	This work
	i-3	126, 99	132, 107	6, 8	This work
	mmen	124	126	2	49–51
	e-2	119	119	0	51
	<i>n</i> Bu-2	119, 70	119, broad	0	53
	mpn	115	116	1	52
	<i>n</i> Hex-2	114, 48	119, 68	5, 20	53
	2-ampd	111, 98	118, 104	7, 6	This work
	pyrr-2	58, 53	68, 64	10, 11	53
	mm-2	54	66	12	51
	ee-2	56, 48	64, 59	8, 11	51

^aDetermined using the approximate inflection point of the adsorption step.

With the exception of the data for mm-2-, pyrr-2-, and ee-2-Mg₂(dobpdc) (Figure 3.S33 below), the dry and humid CO₂ isobaric adsorption profiles corresponding to the data in Table 3.S6 and Figure 3.S32 are included in Section 3.6.5.

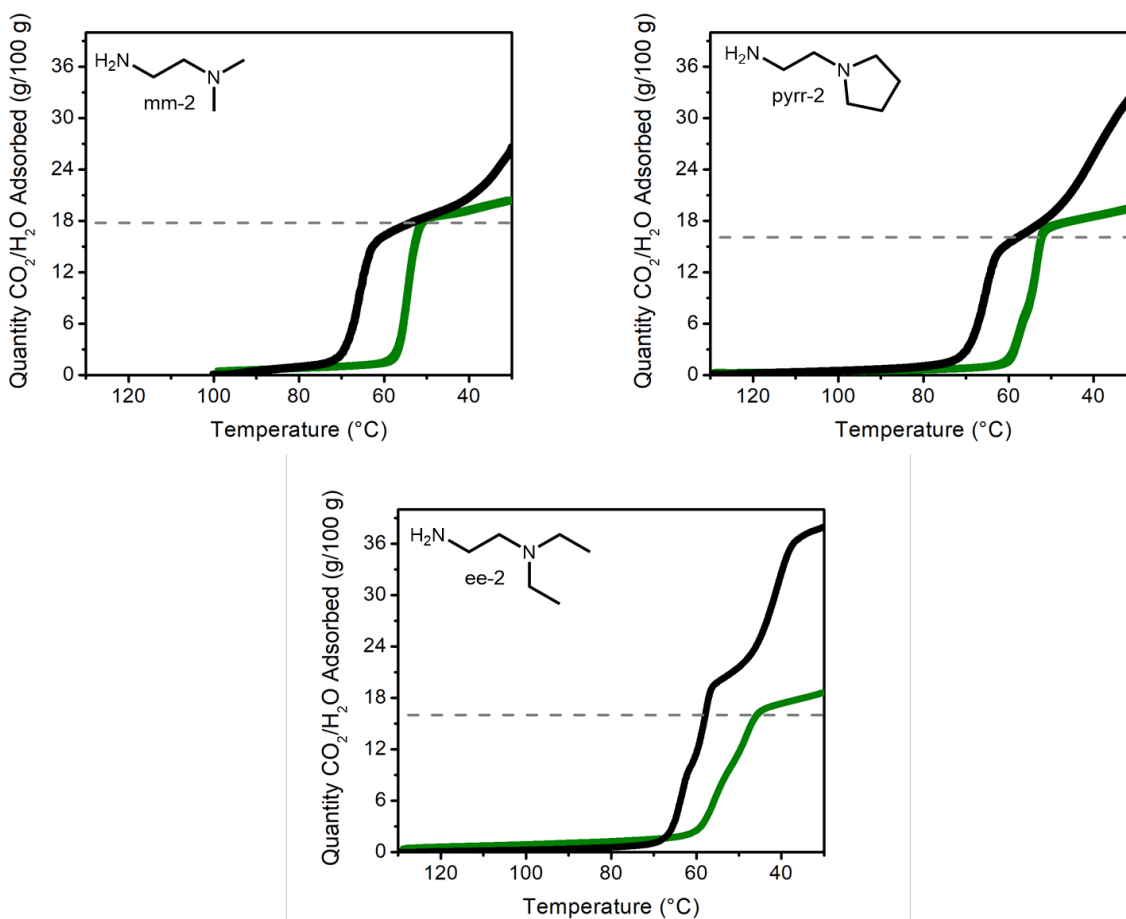


Figure 3.S33. Dry pure CO₂ adsorption isobars (green lines) and humid CO₂ adsorption isobars (black lines) at atmospheric pressure for a series of previously reported Mg₂(dobpdc) variants appended with *primary, tertiary* alkylethylenediamines.^{53,115} A ramp rate of 1 °C/min was used in all cases. The expected adsorption capacities corresponding to 1 CO₂ per diamine (gray dashed lines) are indicated. The adsorption isobars for pyr-2-Mg₂(dobpdc) and ee-2-Mg₂(dobpdc) were previously reported with a ramp rate of 2 °C/min⁵³ and were remeasured here with a ramp rate of 1 °C/min for consistency.

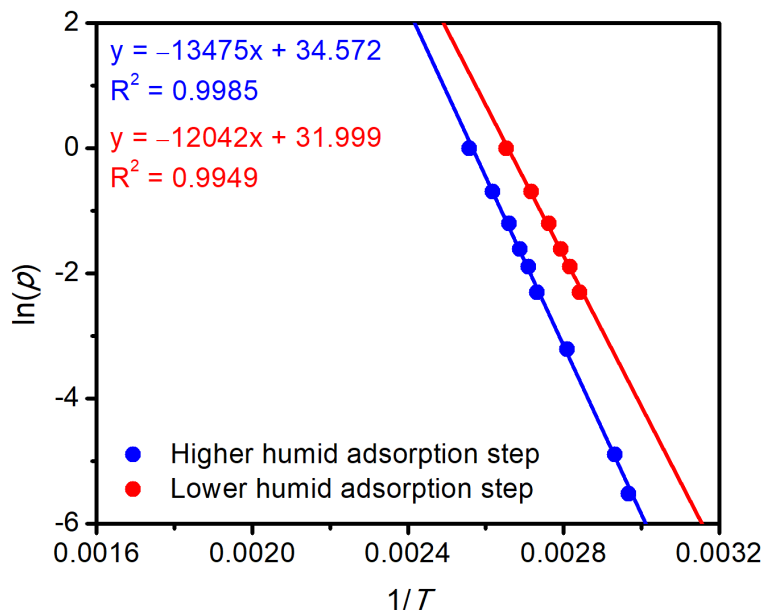


Figure 3.S34. Clausius-Clapeyron plots of the humid CO₂ adsorption isobars of 2-ampd-Mg₂(dobpdc) with a variety of mixtures of CO₂ in N₂. The data and fits for the higher temperature (blue) and lower temperature (red) adsorption steps are shown. The effective differential enthalpies and entropies determined from the linear fits to these data are included in Tables 3.S7 and 3.S8 below. The isobars from which these step temperatures were determined are included below.

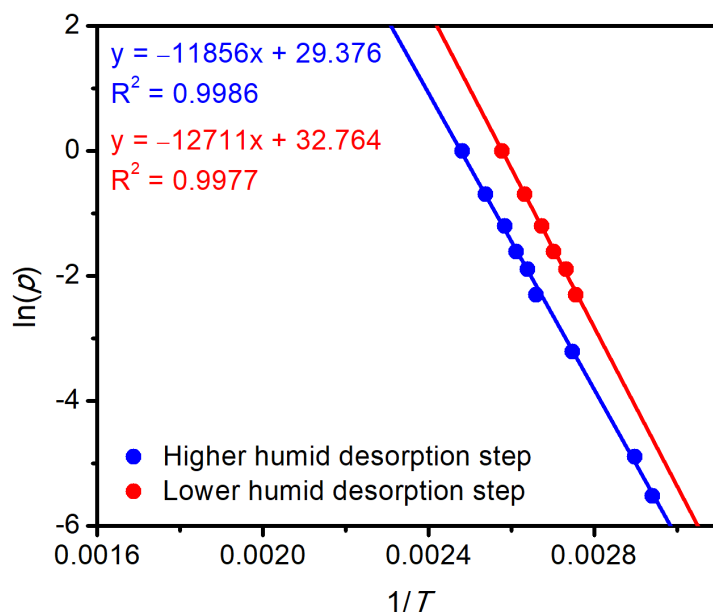


Figure 3.S35. Clausius-Clapeyron plots of the humid CO₂ desorption isobars of 2-ampd-Mg₂(dobpdc) with a variety of mixtures of CO₂ in N₂. The data and fits for the higher temperature (blue) and lower temperature (red) desorption steps are shown. The effective differential enthalpies and entropies determined from the linear fits to these data are included in Tables 3.S7 and 3.S8 below. The isobars from which these step temperatures were determined are included below.

Table 3.S7. Summary of differential enthalpies, entropies, and free energies of adsorption for the higher temperature adsorption step of 2-ampd–Mg₂(dobpdc), determined using the plots in Figures 3.S34 and 3.S35.

Measurement	$-\Delta h_{\text{ads}}$ (kJ/mol)	$-\Delta s_{\text{ads}}$ (kJ/mol)	$-\Delta g_{\text{ads}}$ at 40 °C (kJ/mol)
Dry adsorption isobars	81 ± 1	211 ± 2	15 ± 1
Humid adsorption isobars	112 ± 2	287 ± 5	22 ± 2
Difference	31 ± 2	76 ± 5	7 ± 2
Dry desorption isobars		250 ± 3	23 ± 1
Humid desorption isobars	99 ± 1	244 ± 4	22 ± 2
Difference	-2 ± 2	-6 ± 5	-1 ± 2

Table 3.S8. Summary of differential enthalpies, entropies, and free energies of adsorption for the lower temperature adsorption step of 2-ampd–Mg₂(dobpdc), determined using the plots in Figures 3.S34 and 3.S35.

Measurement	$-\Delta h_{\text{ads}}$	$-\Delta s_{\text{ads}}$	$-\Delta g_{\text{ads}}$ at 40 °C
Dry adsorption isobars	68 ± 1	183 ± 3	11 ± 1
Humid adsorption isobars	98 ± 2	260 ± 6	17 ± 3
Difference	30 ± 2	77 ± 6	6 ± 3
Dry desorption isobars	97 ± 3		
Humid desorption isobars	103 ± 2	265 ± 4	20 ± 2
Difference	5 ± 2	10 ± 6	1 ± 3

Table 3.S9. Summary of CO₂ adsorption step temperatures from a variety of dry and humid CO₂-containing gas streams for 2-ampd–Mg₂(dobpdc).

% CO ₂ in N ₂	Dry higher temperature adsorption step (°C) ^a	Humid higher temperature adsorption step (°C) ^a	ΔT humid vs. dry	Dry lower temperature adsorption step (°C) ^a	Humid lower temperature adsorption step (°C) ^a	ΔT humid vs. dry
100%	111	117	6	98	104	6
50%	100	109	9	87	95	8
30%	92	103	11	79	89	10
20%	87	99	12	72	85	13
15%	84	96	12	69	82	13
10%	78	93	15	63	78	15
4%	68	82	14	40	N/o	N/a
0.75%	48	68	20	N/o	N/o	N/a
0.4%	42	64	22	N/o	N/o	N/a

^aDetermined using the approximate inflection point of the adsorption step. N/o = not clearly observed. N/a = not applicable.

The general **increase in adsorption step temperatures** under humid conditions compared to under dry conditions reflects the thermodynamically more favorable adsorption of CO₂ in the presence of water. This effect is increasingly pronounced with lower partial pressure streams, which is likely due at least in part to the higher relative humidity of the gas stream inside of the furnace at lower temperatures.

Table 3.S10. Summary of CO₂ desorption step temperatures from a variety of dry and humid CO₂-containing gas streams for 2-ampd-Mg₂(dobpdc).

% CO ₂ in N ₂	Dry higher temperature desorption step (°C) ^a	Humid higher temperature desorption step (°C) ^a	ΔT humid vs. dry	Dry lower temperature desorption step (°C) ^a	Humid lower temperature desorption step (°C) ^a	ΔT humid vs. dry
100%	130	130	0	113	115	2
50%	122	121	-1	104	107	3
30%	115	114	-1	98	101	3
20%	110	110	0	94	97	3
15%	106	106	0	90	93	3
10%	101	103	2	86	89	3
4%	91	91	0		N/o	N/a
0.75%	73	72	-1	N/o	N/o	N/a
0.4%	68	67	-1	N/o	N/o	N/a

^aDetermined using the approximate inflection point of the desorption step. N/o = not clearly observed. N/a = not applicable.

In contrast to the results observed upon adsorption (Table 3.S9), minimal changes to the desorption step temperatures occurred under humid conditions compared to dry conditions. The decreased extent of hysteresis observed for both steps under humid conditions (see Figure 3.S36 below) suggests that in addition to increasing the thermodynamic driving force for CO₂ adsorption (Table 3.S9), water likely also decreases the activation barrier for cooperative CO₂ adsorption, potentially by facilitating proton transfer. This effect remains an active area of investigation in our group.

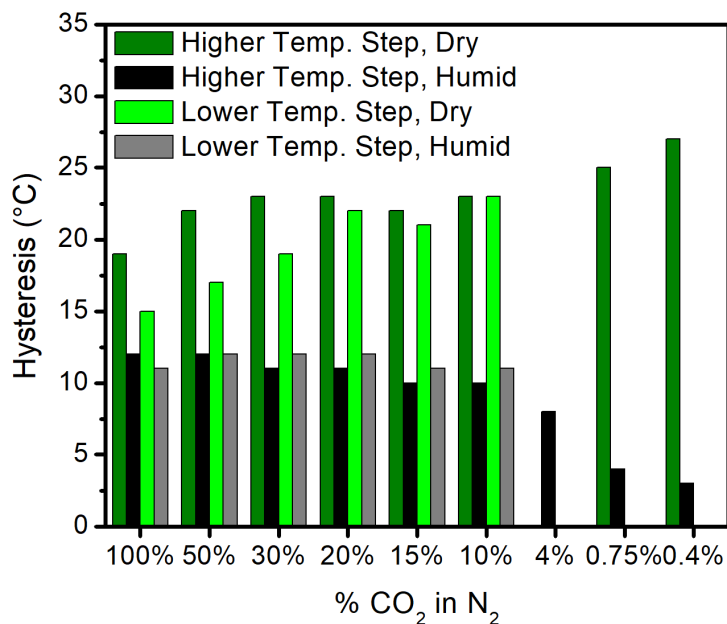


Figure 3.S36. The extent of hysteresis (difference between desorption and adsorption step temperatures) for both steps in 2-ampd-Mg₂(dobpdc) under dry and humid conditions for a range of CO₂ in N₂ mixtures. In all cases, diminished hysteresis is observed in the presence of water, particularly with streams with low partial pressures of CO₂. The lower temperature adsorption and desorption steps were not clearly observed from humid 4%, 0.75%, and 0.4% CO₂ in N₂ streams, as well as from dry 0.75% and 0.4% CO₂ in N₂ streams at temperatures >30 °C.

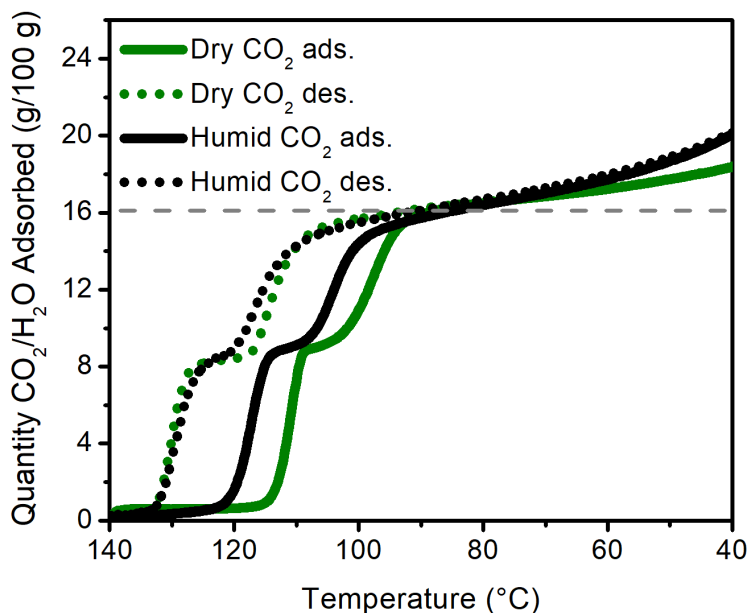


Figure 3.S37. Dry pure CO₂ adsorption (solid green) and desorption (dotted green) isobars, and humid pure CO₂ adsorption (solid black) and desorption (dotted black) isobars, for 2-ampd-Mg₂(dobpdc). The material was activated at 140 °C under flowing dry (green) or humid (black) N₂ for 20 min. Isobars were collected at atmospheric pressure using a ramp rate of 0.5 °C/min. The gray dashed line indicates the expected adsorption capacity corresponding to 1 CO₂ per diamine.

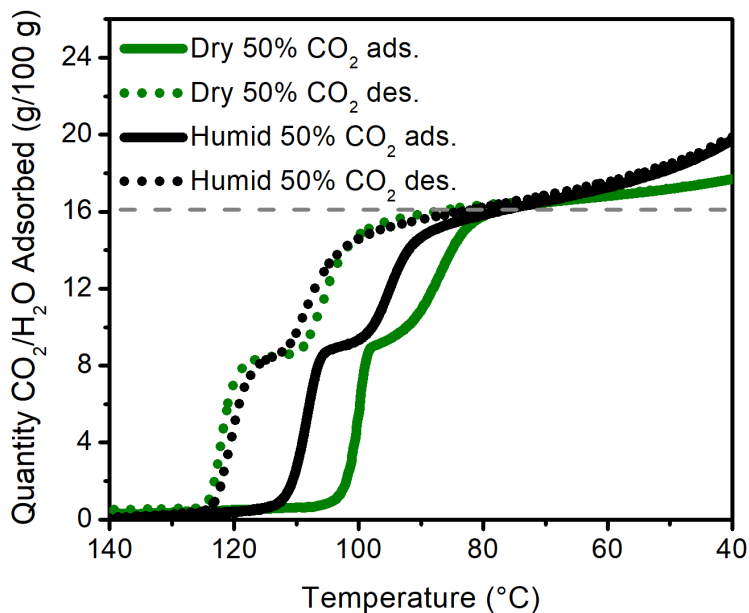


Figure 3.S38. Dry 50% CO₂ in N₂ adsorption (solid green) and desorption (dotted green) isobars, and humid 50% CO₂ in N₂ adsorption (solid black) and desorption (dotted black) isobars, for 2-ampd-Mg₂(dobpdc). The material was activated at 140 °C under flowing dry (green) or humid (black) N₂ for 20 min. Isobars were collected at atmospheric pressure using a ramp rate of 0.5 °C/min. The gray dashed line indicates the expected adsorption capacity corresponding to 1 CO₂ per diamine.

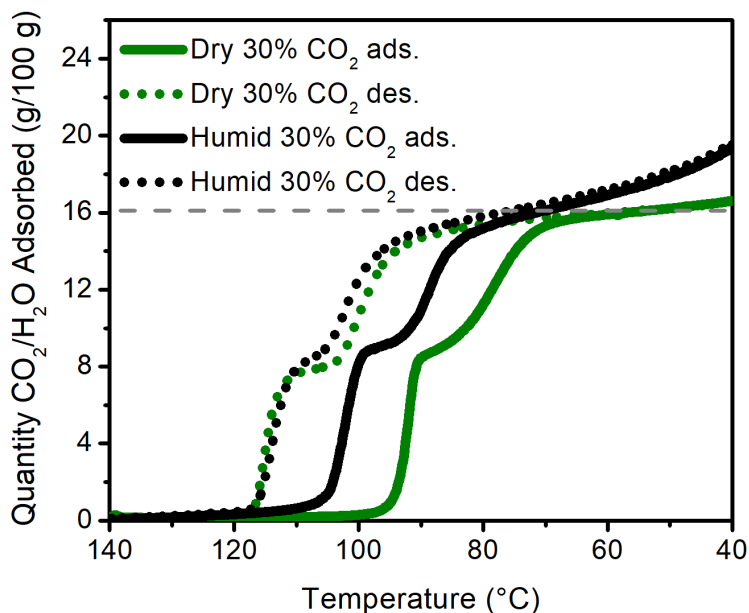


Figure 3.S39. Dry 30% CO₂ in N₂ adsorption (solid green) and desorption (dotted green) isobars, and humid 30% CO₂ in N₂ adsorption (solid black) and desorption (dotted black) isobars, for 2-ampd-Mg₂(dobpdc). The material was activated at 140 °C under flowing dry (green) or humid (black) N₂ for 20 min. Isobars were collected at atmospheric pressure using a ramp rate of 0.5 °C/min. The gray dashed line indicates the expected adsorption capacity corresponding to 1 CO₂ per diamine.

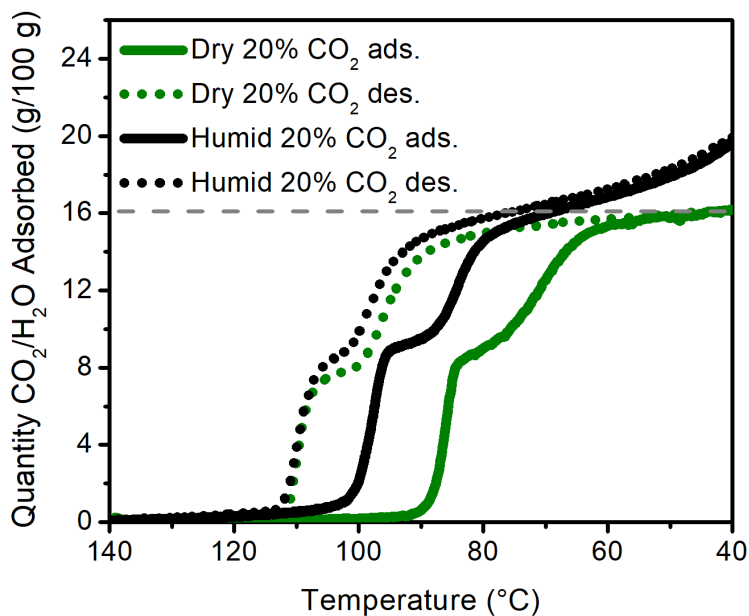


Figure 3.S40. Dry 20% CO₂ in N₂ adsorption (solid green) and desorption (dotted green) isobars, and humid 20% CO₂ in N₂ adsorption (solid black) and desorption (dotted black) isobars, for 2-ampd-Mg₂(dobpdc). The material was activated at 140 °C under flowing dry (green) or humid (black) N₂ for 20 min. Isobars were collected at atmospheric pressure using a ramp rate of 0.5 °C/min. The gray dashed line indicates the expected adsorption capacity corresponding to 1 CO₂ per diamine.

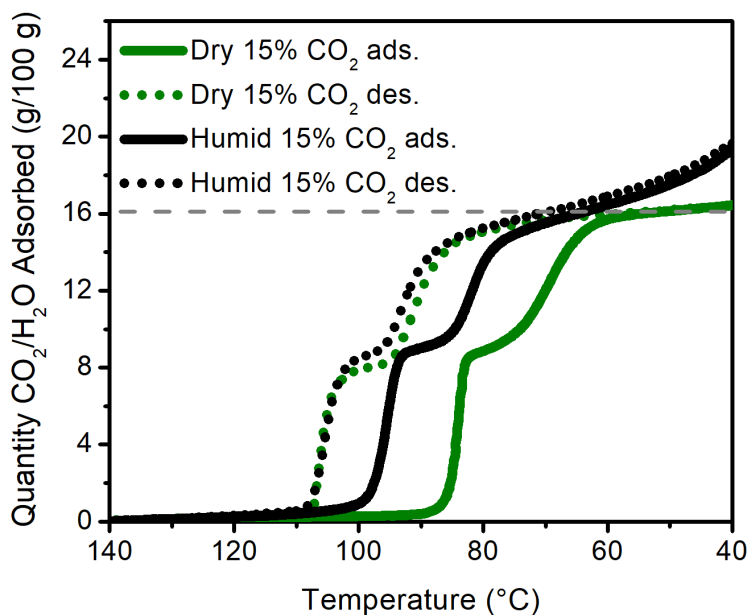


Figure 3.S41. Dry 15% CO₂ in N₂ adsorption (solid green) and desorption (dotted green) isobars, and humid 15% CO₂ in N₂ adsorption (solid black) and desorption (dotted black) isobars, for 2-ampd-Mg₂(dobpdc). The material was activated at 140 °C under flowing dry (green) or humid (black) N₂ for 20 min. Isobars were collected at atmospheric pressure using a ramp rate of 0.2 °C/min. The gray dashed line indicates the expected adsorption capacity corresponding to 1 CO₂ per diamine.

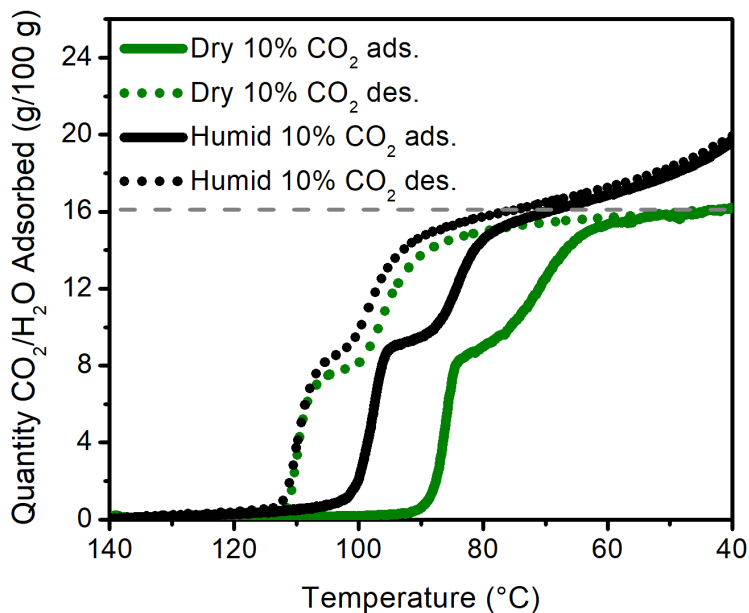


Figure 3.S42. Dry 10% CO₂ in N₂ adsorption (solid green) and desorption (dotted green) isobars, and humid 10% CO₂ in N₂ adsorption (solid black) and desorption (dotted black) isobars, for 2-ampd-Mg₂(dobpdc). The material was activated at 140 °C under flowing dry (green) or humid (black) N₂ for 20 min. Isobars were collected at atmospheric pressure using a ramp rate of 0.2 °C/min. The gray dashed line indicates the expected adsorption capacity corresponding to 1 CO₂ per diamine.

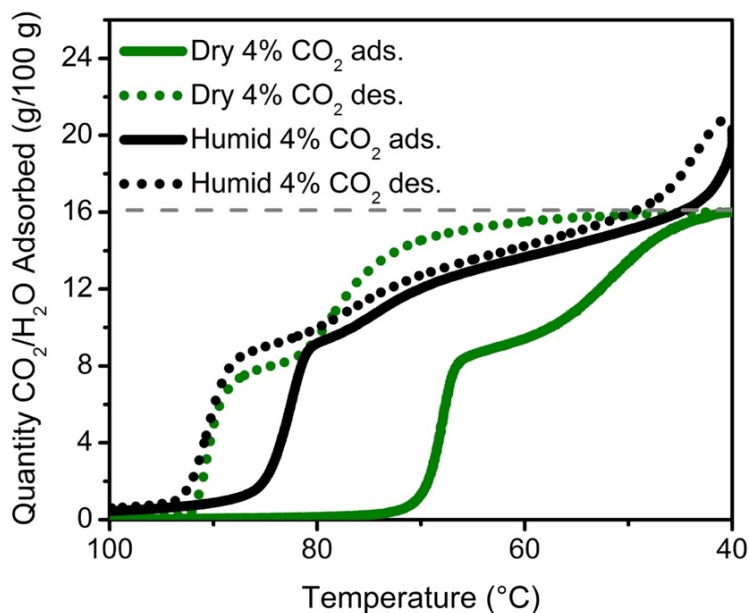


Figure 3.S43. Dry 4% CO₂ in N₂ adsorption (solid green) and desorption (dotted green) isobars, and humid 4% CO₂ in N₂ adsorption (solid black) and desorption (dotted black) isobars, for 2-ampd-Mg₂(dobpdc). The material was activated at 140 °C under flowing dry (green) or humid (black) N₂ for 20 min. Isobars were collected at atmospheric pressure using a ramp rate of 0.1 °C/min. The gray dashed line indicates the expected adsorption capacity corresponding to 1 CO₂ per diamine.

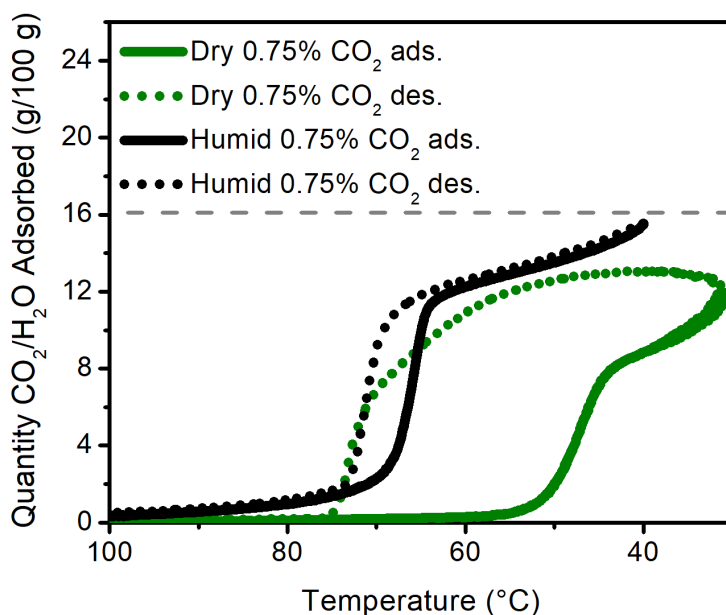


Figure 3.S44. Dry 0.75% CO₂ in N₂ adsorption (solid green) and desorption (dotted green) isobars, and humid 0.75% CO₂ in N₂ adsorption (solid black) and desorption (dotted black) isobars, for 2-ampd-Mg₂(dobpdc). The material was activated at 140 °C under flowing dry (green) or humid (black) N₂ for 20 min. Isobars were collected at atmospheric pressure using a ramp rate of 0.1 °C/min. The gray dashed line indicates the expected adsorption capacity corresponding to 1 CO₂ per diamine. Under dry and humid conditions, the second adsorption step is not clearly operative.

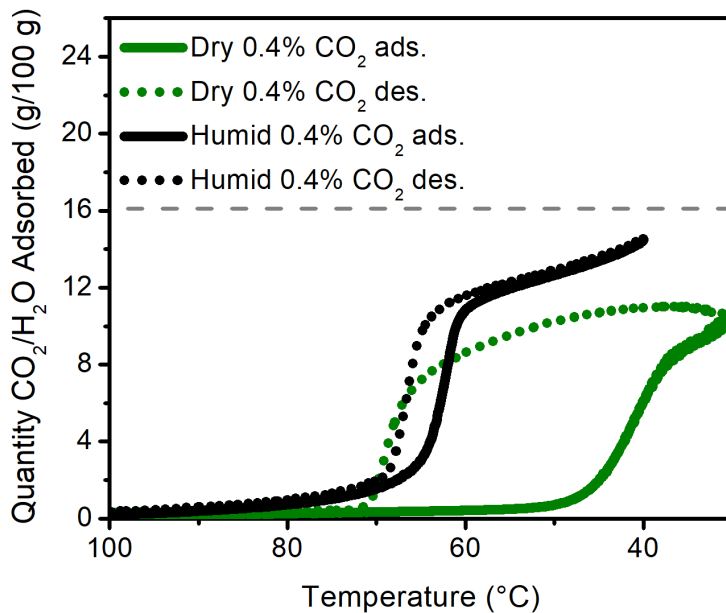


Figure 3.S45. Dry 0.4% CO₂ in N₂ adsorption (solid green) and desorption (dotted green) isobars, and humid 0.4% CO₂ in N₂ adsorption (solid black) and desorption (dotted black) isobars, for 2-ampd-Mg₂(dobpdc). The material was activated at 140 °C under flowing dry (green) or humid (black) N₂ for 20 min. Isobars were collected at atmospheric pressure using a ramp rate of 0.1 °C/min. The gray dashed line indicates the expected adsorption capacity corresponding to 1 CO₂ per diamine. Under dry and humid conditions, the second adsorption step is not clearly operative.

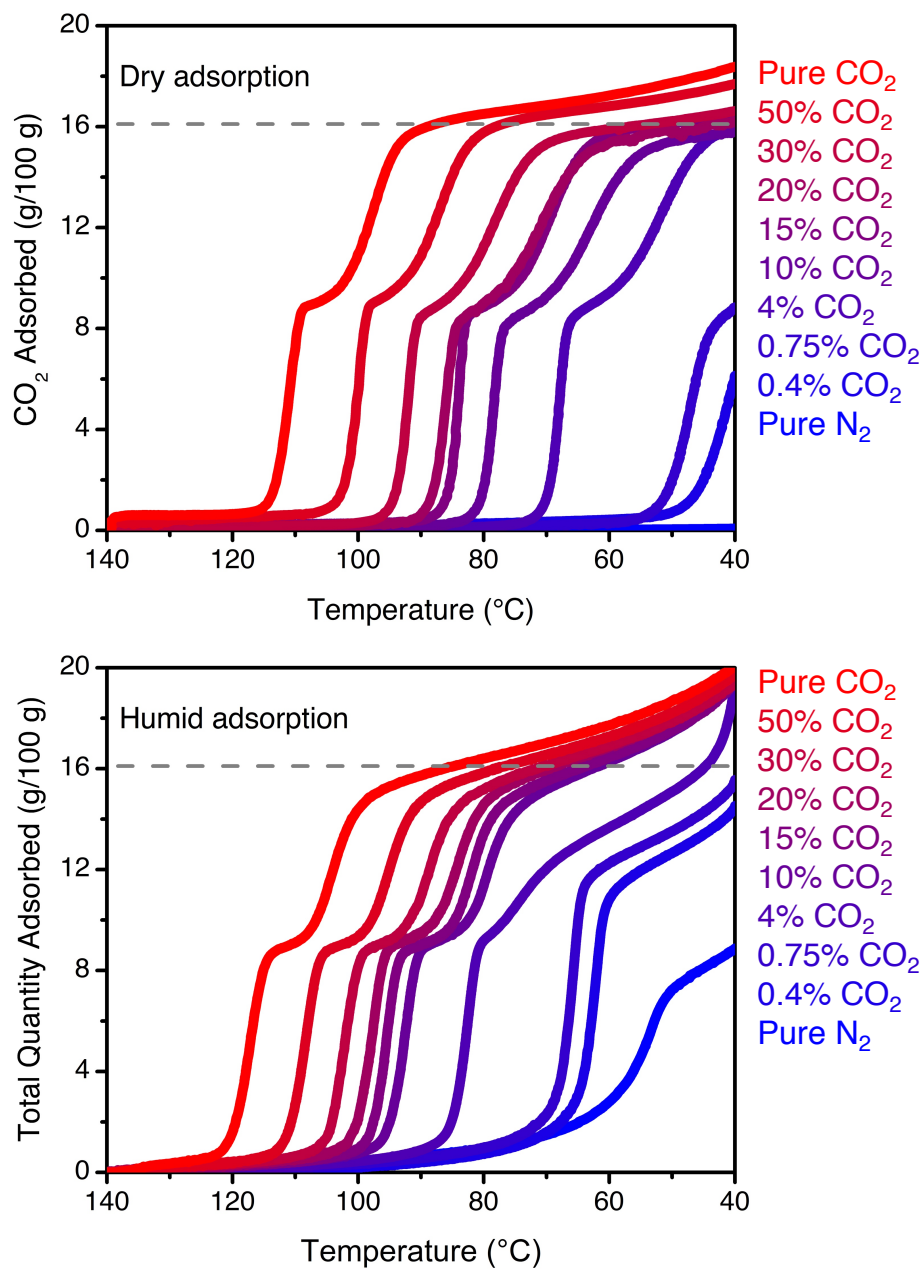


Figure 3.S46. Full series of dry (top) and humid (bottom) adsorption isobars for pure CO₂, CO₂/N₂ mixtures, and pure N₂ at atmospheric pressure. Temperature ramp rates for individual isobars are specified in Figure 3.S37–3.S45.

3.6.9 Ramp Rate Effects on Adsorption Isobars

During the course of this work, we found adsorption isobars conducted with fast ramp rates are far from equilibrated. Because of this, adsorption isobars conducted with slower ramp rates often possessed sharper adsorption steps that were shifted to higher temperatures. Therefore, in order to accurately measure the adsorption characteristics of adsorbents under quasi-equilibrium conditions, **very slow ramp rates should be employed**, particularly with low partial pressure CO₂ streams for which the adsorption kinetics may be slow. This effect appears to be particularly pronounced under dry conditions, likely because water can mediate proton transfer and accelerate the kinetics of adsorption. Several representative adsorption isobars are included here to demonstrate the effect of the temperature ramp rate on the adsorption profile of 2-ampd-Mg₂(dobpdc). The effect of temperature ramp rates on the adsorption kinetics of diamine-appended metal-organic frameworks remains an active area of investigation in our group.

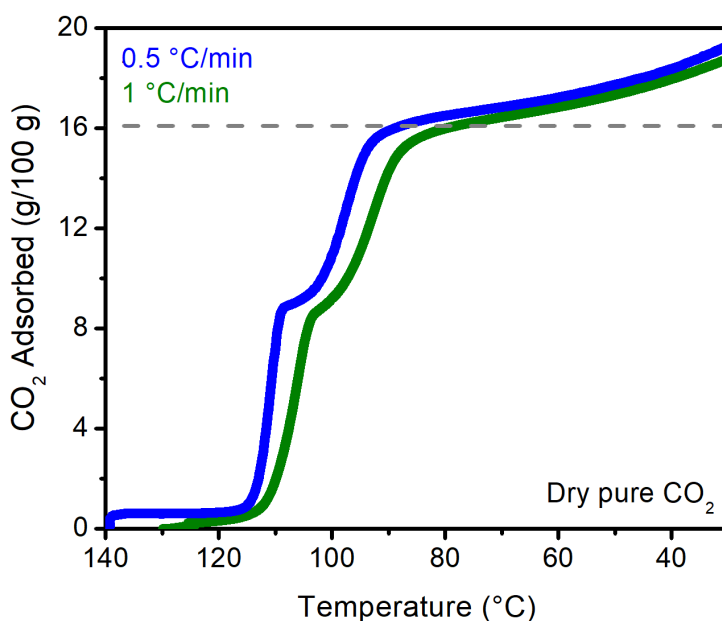


Figure 3.S47. Dry pure CO₂ adsorption isobars for 2-ampd-Mg₂(dobpdc) at atmospheric pressure with cooling ramp rates of 1 °C/min (green) and 0.5 °C/min (blue). The material was activated at 140 °C under flowing dry N₂ for 20 min. The gray dashed line indicates the expected adsorption capacity corresponding to 1 CO₂ per diamine. The adsorption steps are sharper and occur at higher temperatures with a slower ramp rate.

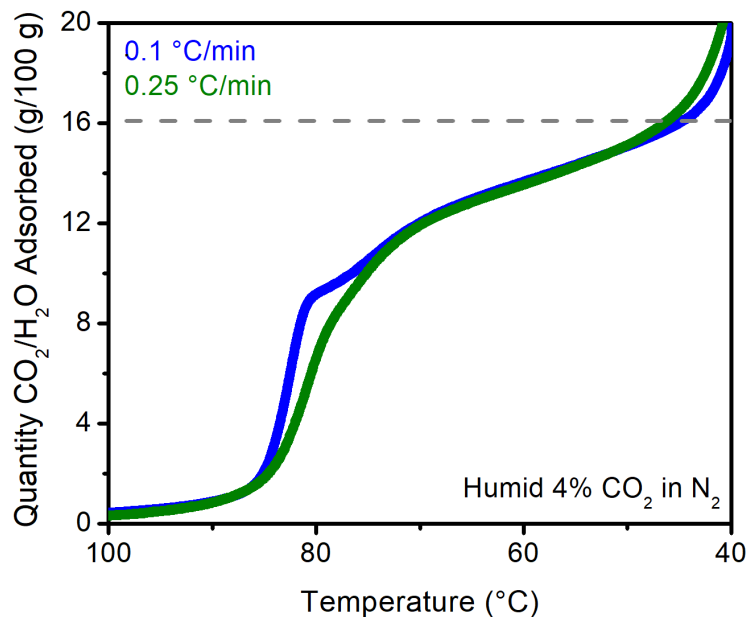


Figure 3.S48. Humid 4% CO₂ in N₂ adsorption isobars for 2-ampd-Mg₂(dobpdc) at atmospheric pressure with cooling ramp rates of 0.25 °C/min (green) and 0.1 °C/min (blue). The material was activated at 140 °C under flowing humid N₂ for 20 min. The gray dashed line indicates the expected adsorption capacity corresponding to 1 CO₂ per diamine. The adsorption step is sharper and more clearly pronounced with a slower ramp rate.

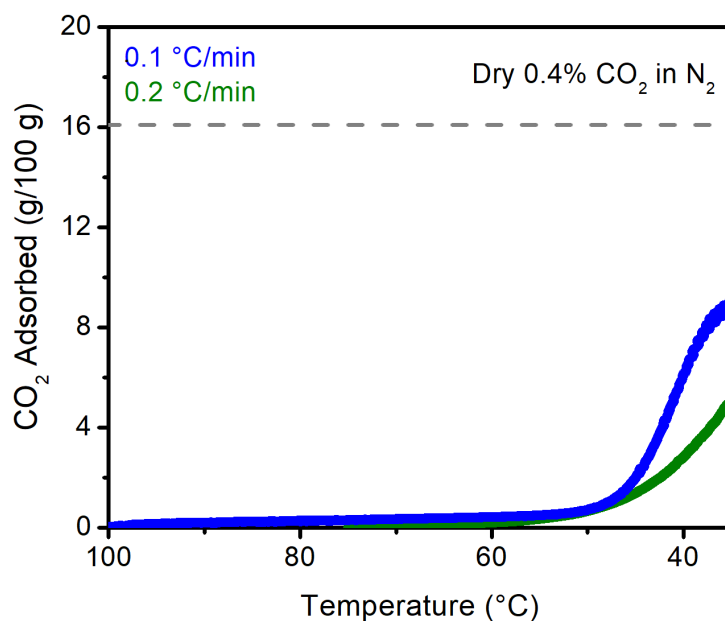


Figure 3.S49. Dry 0.4% CO₂ in N₂ adsorption isobars for 2-ampd-Mg₂(dobpdc) at atmospheric pressure with cooling ramp rates of 0.2 °C/min (green) and 0.1 °C/min (blue). The material was activated at 140 °C under flowing dry N₂ for 20 min. The gray dashed line indicates the expected adsorption capacity corresponding to 1 CO₂ per diamine. The adsorption step is sharper with a slower ramp rate, and a higher adsorption capacity is observed at temperatures below 45 °C.

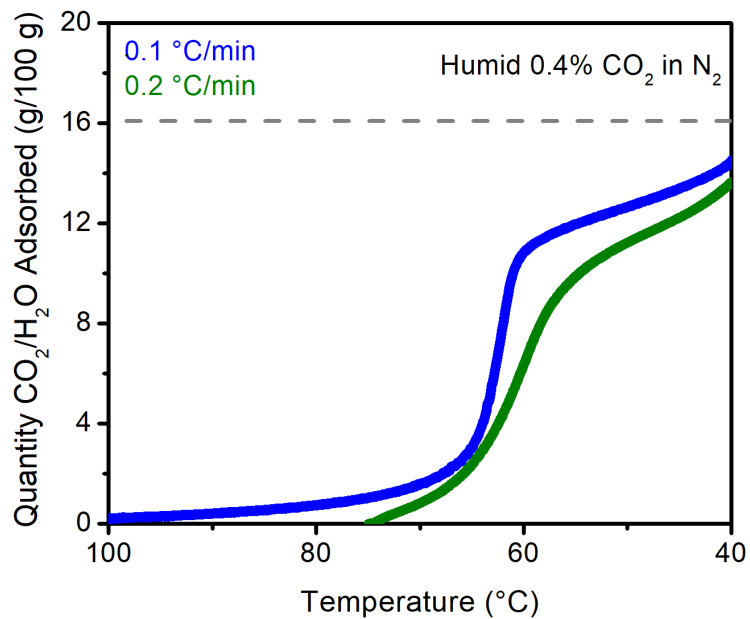


Figure 3.S50. Humid 0.4% CO₂ in N₂ adsorption isobars for 2-ampd-Mg₂(dobpdc) at atmospheric pressure with cooling ramp rates of 0.2 °C/min (green) and 0.1 °C/min (blue). The material was activated at 140 °C under flowing humid N₂ for 20 min. The gray dashed line indicates the expected adsorption capacity corresponding to 1 CO₂ per diamine. The adsorption step is significantly sharper with a slower ramp rate.

3.6.10 Predicting Breakthrough Curves from Step-Shaped Adsorption Isotherms

Small-scale breakthrough experiments enable characterization of adsorbent performance under realistic process conditions and can inform process models in the development of full-scale fixed bed adsorption units. Importantly, simple graphical approaches can be used to predict breakthrough profiles directly from the adsorption isotherms. An excellent review of this topic is provided by Helfferich and Carr,⁸⁵ and the key points of this analysis are reproduced here. To relate isotherms and elution profiles, the primary quantity of interest is the velocity v_{c_i} of a given concentration c_i of solute i as it flows through the adsorption column. This concentration velocity is defined as

$$v_{c_i} \equiv \left(\frac{\partial z}{\partial t} \right)_{c_i}, \quad (3.S4)$$

where z is the linear distance in the direction of flow, and t is time. Neglecting axial dispersion, ideal plug flow under isotherm conditions gives the following equation for conservation of mass:

$$\frac{\rho}{\varepsilon} \left(\frac{\partial q_i}{\partial t} \right)_z + \left(\frac{\partial c_i}{\partial t} \right)_z + v^0 \left(\frac{\partial c_i}{\partial z} \right)_t = 0 \quad (3.S5)$$

Here, v^0 is the velocity of the moving-phase flow, q_i is the adsorbent loading, ρ is the bulk density of the adsorbent, and ε is the fractional void volume of the adsorbent bed. The resulting “wave equation” for the concentration velocity is thus

$$v_{c_i} = \frac{v^0}{\left(1 + \frac{\rho}{\varepsilon}\right) \left(\frac{\partial q_i}{\partial c_i} \right)_z} \quad (3.S6)$$

If local equilibrium is further assumed, the adsorbent loading becomes solely a function of concentration, and the partial differential can be replaced by the corresponding total differential:

$$v_{c_i} = \frac{v^0}{\left(1 + \frac{\rho}{\varepsilon}\right) \left(\frac{dq_i}{dc_i} \right)_z} \quad (3.S7)$$

Therefore, the concentration velocity is inversely proportional to dq_i/dc_i , which is the slope of the tangent to the equilibrium adsorption isotherm at the corresponding concentration c_i . In other words, under local equilibrium, *the “natural” wave velocity is lower at concentrations where the isotherm is steeper*. With this knowledge, the propagation of adsorption and desorption waves is straightforward to predict for simple linear, Type I, and Type III isotherms (Figure 3.S51 below).

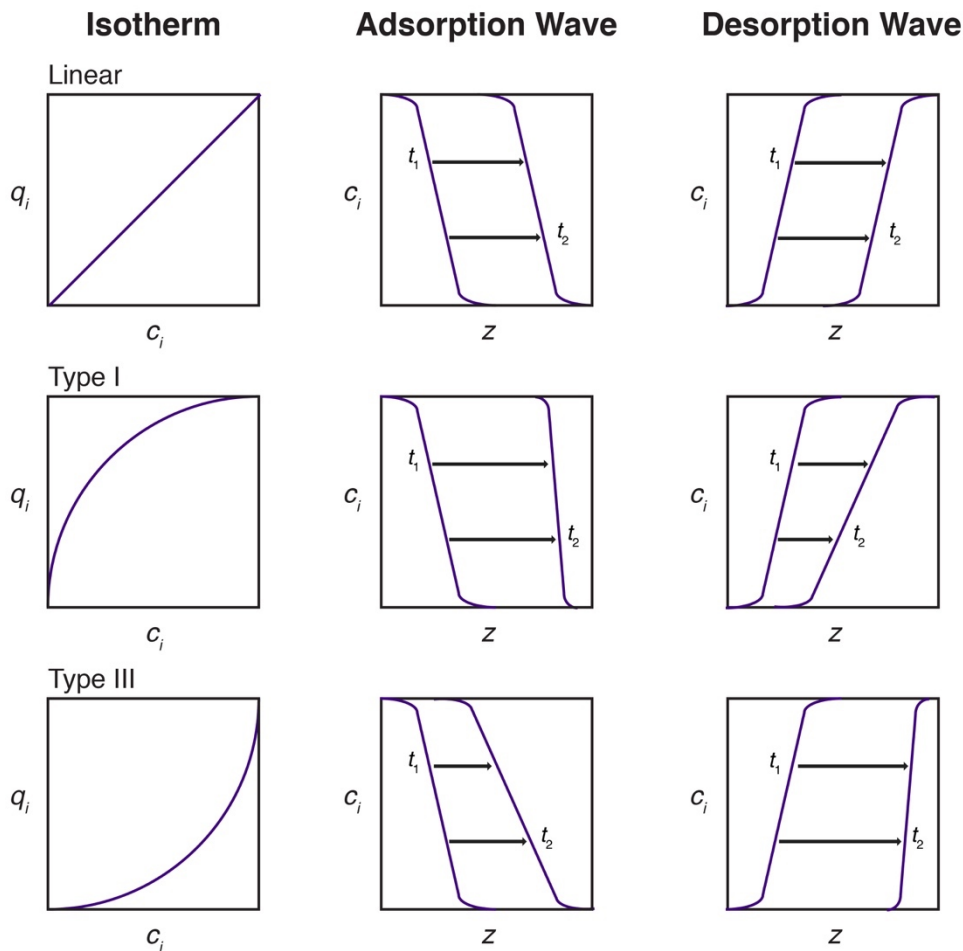


Figure 3.S51. Propagation of adsorption and desorption waves for linear (top), Type I (middle), and Type III (bottom) isotherms under ideal conditions. The left column shows the isotherm profile as loading (q_i) vs. concentration (c_i). The center and right columns show the propagation of the adsorption and desorption waves, respectively, as c_i vs. distance z along the column for a wave initially diffuse at t_1 to a later time t_2 . Figure adapted from the work of Helfferich and Carr.⁸⁵

For linear isotherms, the slope of the isotherm is constant, and thus the adsorption and desorption waves propagate through the bed unchanged under ideal conditions. For Type I isotherms, higher concentrations, where the isotherm slope is shallower, move through the bed faster than lower concentrations. On adsorption, this results in a wave that sharpens to a “shock,” or discontinuity, while on desorption, the wave broadens as it travels. Similarly, for adsorption Type III isotherm, lower concentrations move faster than higher concentrations, and the adsorption wave spreads as it moves through the column.

More complex “composite” waves may be generated in the case of isotherms with inflection points. A simple graphical approach known as “Golden’s rule,” or alternatively the “string” or “rubber band” rule, can be used to predict the shape of the breakthrough profile directly from an isotherm of arbitrary shape.^{85,86,84,120,45,121,83} In this method, an operating curve is constructed from an imaginary rubber band stretched between the initial state (typically, no adsorbate) and the feed state (here, 40 mbar of CO_2). For adsorption, the rubber band operating curve falls below the isotherm, while for desorption, it falls above it. In regions where the rubber band is stretched tightly between individual points of contact with the isotherm, compressive waves, or

“shocks” are generated in the breakthrough profile. In regions where the rubber band instead runs along the isotherm, dispersive waves are generated. As a result, inflection points in isotherms often lead to multi-moment breakthrough profiles containing both shocks and waves, an example of which is demonstrated in Figure 3.S52 below. Importantly, in most cases of interest for diamine-appended frameworks with step-shaped isotherms, this behavior results in an intuitive conclusion: once the CO₂ concentration in the bed drops below the step pressure, the cooperative adsorption mechanism is no longer active, and thus *CO₂ at concentrations below the step pressure “slips” through the bed*. Hefti, Joss, and coworkers first discussed the importance of considering CO₂ slip for diamine-appended frameworks in a 2016 modeling study,⁴⁵ and Darunte and coworkers⁸³ recently demonstrated CO₂ slip experimentally in breakthrough experiments targeting direct air capture with mmen–Mg₂(dobpdc) (mmen = *N,N'*-dimethylethylenediamine).

In the present study, “shock–wave–shock” breakthrough profiles were observed for CO₂ with dry streams simulating natural gas flue emissions, but upon incorporation of humidity, single-shock breakthrough profiles were observed under the same conditions. This favorable result enables significant improvements in capture rate under the more realistic H₂O-containing streams. As discussed in the main text, we attribute this enhanced performance to preferential stabilization of the CO₂-bound phase in the presence of water, as reflected in the higher isobaric step temperatures under humid CO₂-containing streams (Figures 3.S37–3.S45). This is consistent with a lower effective step pressure in the CO₂ isotherm in the presence of water. The single-shock breakthrough profiles therefore suggest that water reduces the step pressure and/or modifies the pre-step region of the isotherm such that the operating curve no longer intersects the isotherm (Figure 3.S53).

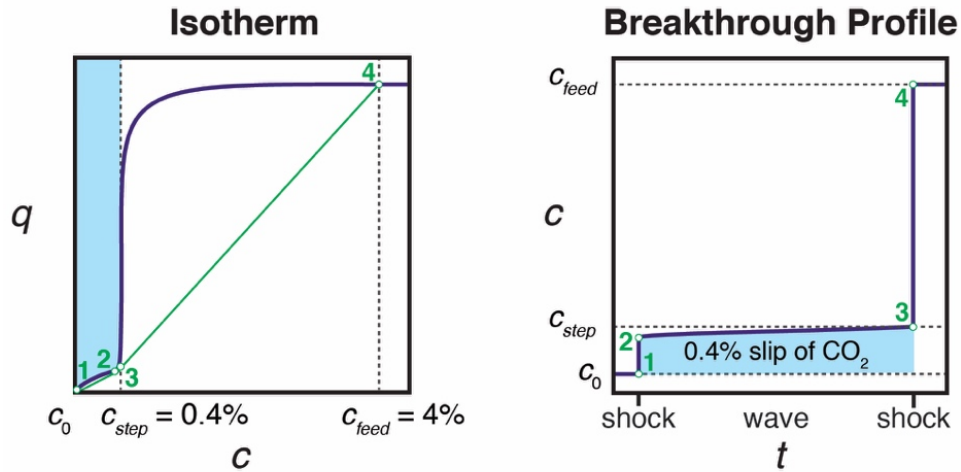


Figure 3.S52. Use of Golden’s rule to predict the breakthrough profile (right) from a hypothetical step-shaped adsorption isotherm (left). An operating curve is constructed by stretching an imaginary rubber band (green line) from the initial concentration ($c_0 = 0$) to the feed concentration ($c_f = 4\%$) beneath the adsorption isotherm. In regions where the rubber band is stretched between points of tangency with the isotherm, such as between points 1 and 2 and between points 3 and 4, a compressive “shock” is generated in the breakthrough profile. In regions where the rubber band runs along the adsorption isotherm, such as between points 2 and 3, a dispersive “wave” is generated in the breakthrough profile. The shaded blue region marks CO_2 beneath the step that cannot be captured, resulting in “slip” in the breakthrough curve. To capture 90% of the CO_2 emitted from a NGCC flue gas stream containing 4% CO_2 , the CO_2 isotherm must show a step at $\leq 0.4\%$ CO_2 , or 4 mbar for a stream at a total pressure 1 bar. Here, the capture rate is calculated as $(1 - 0.4/4) \times 100\%$. Figure adapted from reference 45.

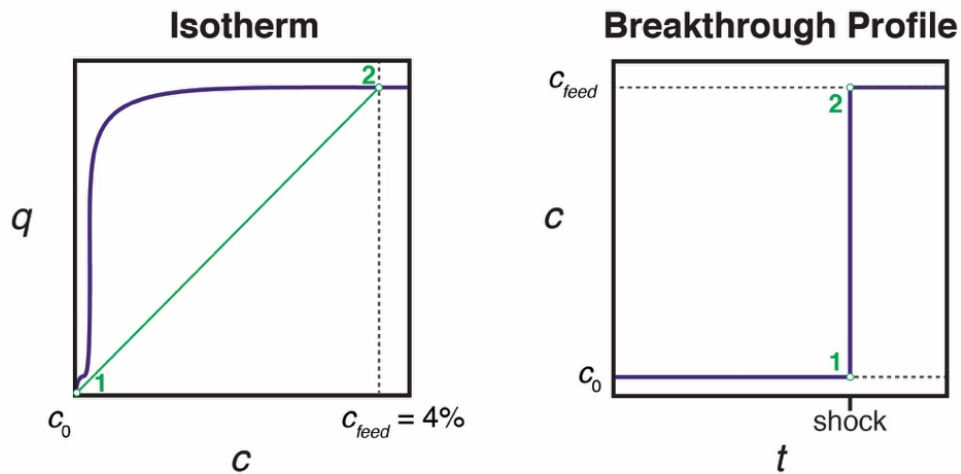


Figure 3.S53. Hypothetical isotherm (left) and breakthrough profile (right) for a case in which application of Golden’s rule predicts single-shock behavior for a step-shaped isotherm. While the initial and feed concentrations (c_i and c_f , respectively) are equivalent to those in Figure 3.S52, the isotherm step pressure is lower, which eliminates the intersection between the isotherm and the “rubber band” operating curve (green line). The case depicted here is representative of the breakthrough curves for humid simulated flue gas streams depicted in this work.

3.6.11 Breakthrough Experiments with 2-ampd–Mg₂(dobpdc)

For breakthrough experiments, semi-spherical pellets of 2-ampd–Mg₂(dobpdc) (approximately 350–700 μm in diameter) were prepared by repeatedly compressing the powdered material between two stainless steel disks and sieving the resulting tablet between 25 and 45 mesh grids. The initial diamine loading of the pellets was 92% by NMR digestion. A 6" stainless steel column (0.25" OD, wall thickness 0.035") was packed with 0.73 g of activated 2-ampd–Mg₂(dobpdc) pellets. The column was fitted with quarter-turn Swagelok plug valves and attached to a U-shaped piece of 1/8" stainless steel tubing with VCR fittings and 2 μm fritted stainless steel gaskets. The column inlet was attached to a manifold consisting of 1/8" copper tubing fed by 4 individual Parker-Porter mass flow controllers. An SRI Instruments 8610C GC equipped with a 6' Haysep-D column and a TCD was used to monitor the breakthrough profile of the effluent at 1 min intervals. The GC was calibrated using a series of pre-mixed, Certified Standard tanks of varying percent CO₂ (4, 10, 15, 20, 30, and 50%) in N₂ purchased from Praxair as well as pure, research-grade CO₂ and N₂. The system deadspace was estimated by measuring the Ar breakthrough time after the system had been pre-equilibrated under He. A total inlet flow rate of 14 or 28 sccm was used for all gases and gas mixtures in both experiments and calibrations. Flow rates were validated using an Agilent ADM200 Universal Flow Meter and were monitored every 0.5 s at the GC outlet over the course of each experiment. The material was initially activated at 120 °C under 28 sccm of He flow for 30 min. Subsequent reactivation between breakthrough cycles was performed under 28 sccm of He or Ar flow at 100 °C for 30–60 min. The column was submerged in a well-stirred water bath at 40 °C or 60 °C during each experiment, and near-isothermal operation was assumed.

Dry breakthrough experiments were conducted with the column pre-equilibrated under flowing He. To begin the experiment, He flow to the column was stopped as a flow of 4% CO₂ in N₂ was simultaneously switched from a purge line (to equilibrate the flow rate) to the column inlet. Following complete breakthrough of CO₂, the capacity of each gas (q_i , mmol/g) was determined using the following equation:

$$q_i = \left[\frac{Q}{22.414 \frac{\text{ccSTP}}{\text{mmol}}} \int_0^t \left(1 - \frac{F_i}{F_{0,i}} \right) dt - \varepsilon V \left(\frac{y_i P}{RT} \right) \right] \left(\frac{y_i}{m} \right) \quad (3.S8)$$

Here, Q is the average total mass flow rate in sccm, t is the corrected time in min, F_i is the molar flow rate of species i at time t , $F_{0,i}$ is the inlet molar flow rate of species i , ε is the interparticle void fraction, V is the volume of pelletized adsorbent in cm³, y_i is the mole fraction of species i , P is the total pressure, R is the universal gas constant, T is the column temperature during the experiment, and m is the mass of adsorbent. The interparticle void fraction ε is calculated as

$$\varepsilon = 1 - \frac{\rho_{\text{bulk}}}{\rho_{\text{particle}}} \quad (3.S9)$$

where ρ_{bulk} is the bulk density in kg/m³, calculated as m/V , and ρ_{particle} is the particle density in kg/m³ and is estimated as 1000 kg/m³.

The error in capacity calculations was estimated by propagating the standard deviation of the flow rate and the integrated breakthrough time corresponding to the time resolution set by the GC scan rate (1 min). In all experiments, N₂ breakthrough capacities were within error of zero.

For humid breakthrough experiments, a water bubbler was inserted immediately before the

column inlet. The water concentration was estimated as 2–3 vol % on the basis of the measured differences between the dry and humid flow rates. The bed was pre-saturated with H₂O using humid He prior to each experiment. Pre-saturation of the adsorbent with H₂O was confirmed by placing a column of indicating Drierite at the adsorbent column outlet. The Drierite column was removed prior to each humid breakthrough experiment to avoid errors in breakthrough capacity resulting from adsorption of CO₂ by Drierite. It was further necessary to pre-saturate the water bubbler with CO₂ prior to each experiment to maintain a constant feed concentration of CO₂. After sealing the column of H₂O-saturated material under He, the simulated flue gas mixture was flowed through the water bubbler to a bypass line fed directly to the GC until the CO₂ concentration equilibrated, indicating saturation of the bubbler with CO₂. The breakthrough experiment was then begun. Between humid breakthrough cycles, the adsorbent was reactivated under a flow of 28 sccm of humid He for 30–60 min, and pre-saturation with H₂O was again verified using a Drierite column. Breakthrough capacities for humid experiments were calculated by subtracting the estimated flow rate of water from the total flow rate prior to integration.

For 2-ampd–Mg₂(dobpdc), the predicted and observed “slip” concentrations are shown below in Figure 3.S54 and Table 3.S11. Under dry conditions, more slip is consistently observed in the breakthrough profiles than would be predicted from the single-component, equilibrium adsorption isotherms. This is consistent with a previous report⁸³ and suggests that kinetic factors may contribute to the ultimate observed capture rate. (As discussed in the main text, we have also found quasi-equilibrium, gravimetric, mixed-gas isobars to be a better predictor of capture rate than the single-component isotherms, which are measured using a volumetric method starting from vacuum.) In addition, thermal effects may contribute to deviations from the capture rate predicted from single-component adsorption isotherms. To quantify the temperature increase in the bed upon adsorption, an internal thermocouple will be incorporated in future breakthrough studies.

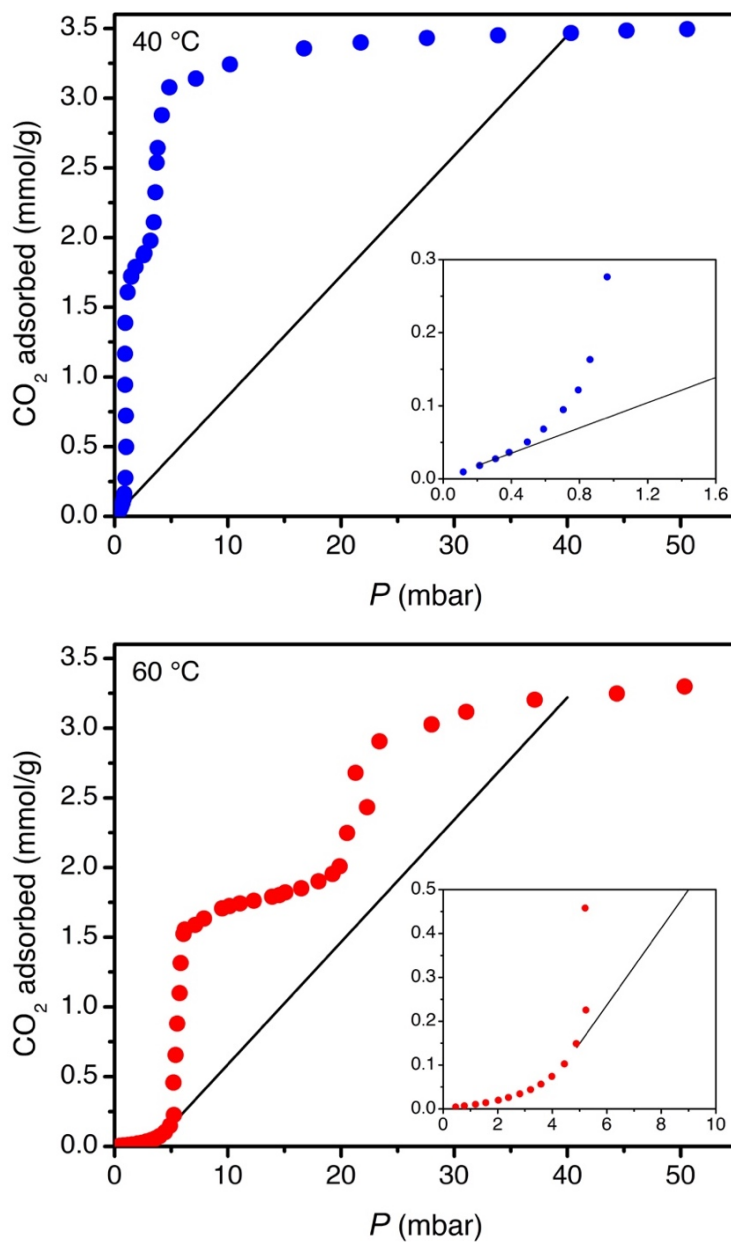


Figure 3.S54. Application of Golden's rule to the isotherms of 2-ampd-Mg₂(dobpdc) to generate operating curves for post-combustion CO₂ capture from NGCC flue emissions containing 40 mbar of CO₂. Only the final portion of the operating curve is shown. Slip of ~0.2 mbar of CO₂ is predicted at 40 °C (top), resulting in a predicted capture rate of 99.5% (calculated as $(1 - 0.2 \text{ mbar}/40 \text{ mbar}) \times 100\%$). Slip of ~4.9 mbar of CO₂ is predicted at 60 °C (bottom), resulting in a capture rate of ~88% (calculated as $(1 - 4.9 \text{ mbar}/40 \text{ mbar}) \times 100\%$). The insets show enlarged views of the low-pressure region.

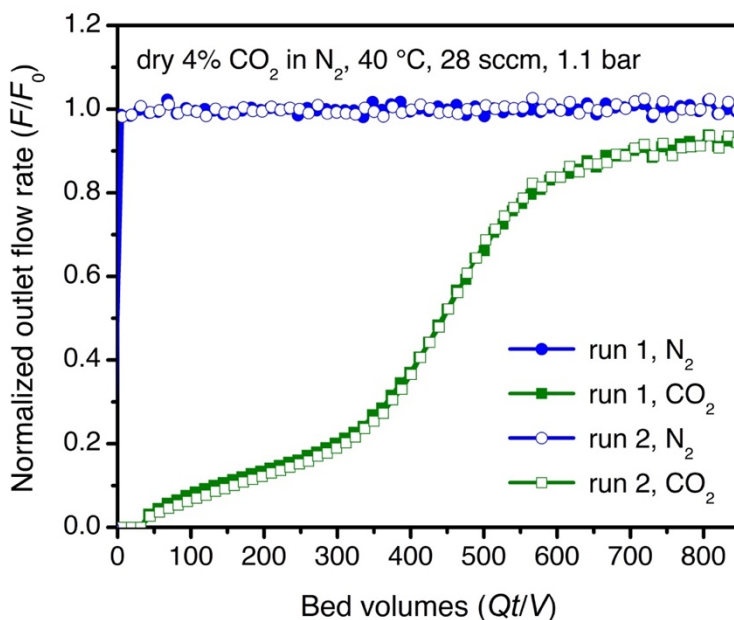


Figure 3.S55. Two breakthrough experiments with 2-ampd-Mg₂(dobpdc) under 28 sccm of dry simulated NGCC flue gas (4% CO₂ in N₂) at ~1.1 bar and 40 °C. A capture rate of 86% was observed, with a calculated CO₂ capacity of 2.4 ± 0.2 mmol/g at exhaustion.

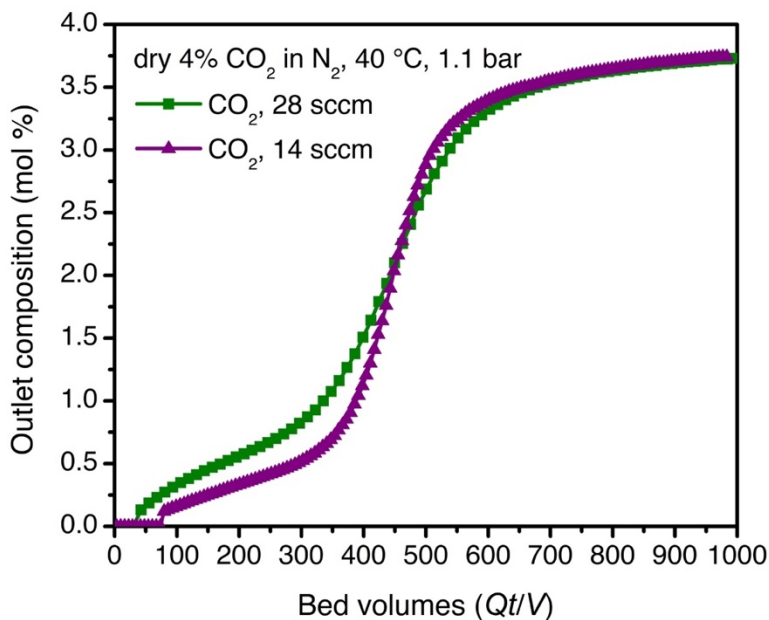


Figure 3.S56. Comparison of CO₂ breakthrough profiles for 2-ampd-Mg₂(dobpdc) under 28 sccm (green squares) or 14 sccm (purple triangles) of a dry simulated NGCC flue gas (4% CO₂ in N₂) at ~1.1 bar and 40 °C. The CO₂ capacity at exhaustion was calculated as 2.4 ± 0.2 mmol/g in both cases.

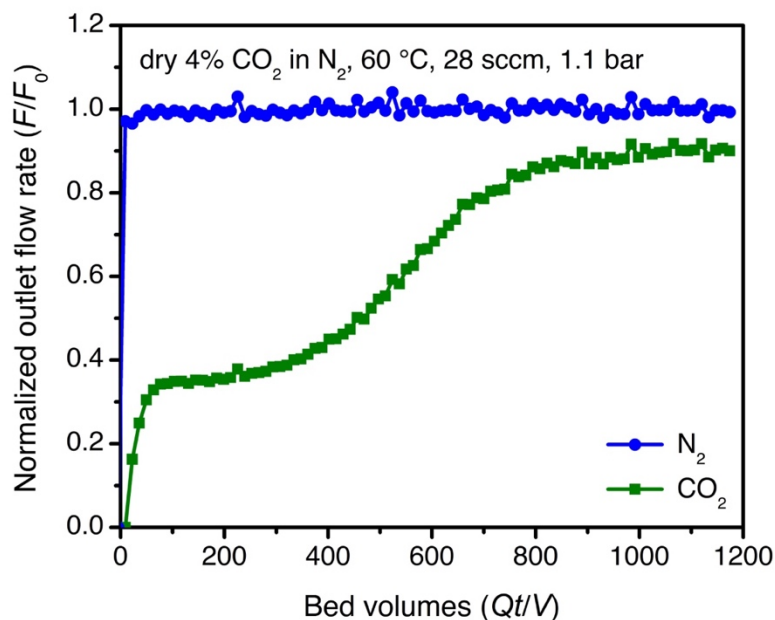


Figure 3.S57. Breakthrough experiment with 2-ampd-Mg₂(dobpdc) under 28 sccm of dry simulated NGCC flue gas (4% CO₂ in N₂) at ~1.1 bar and 60 °C. A capture rate of 62% was observed, with a calculated CO₂ capacity of 2.2 ± 0.2 mmol/g at exhaustion.

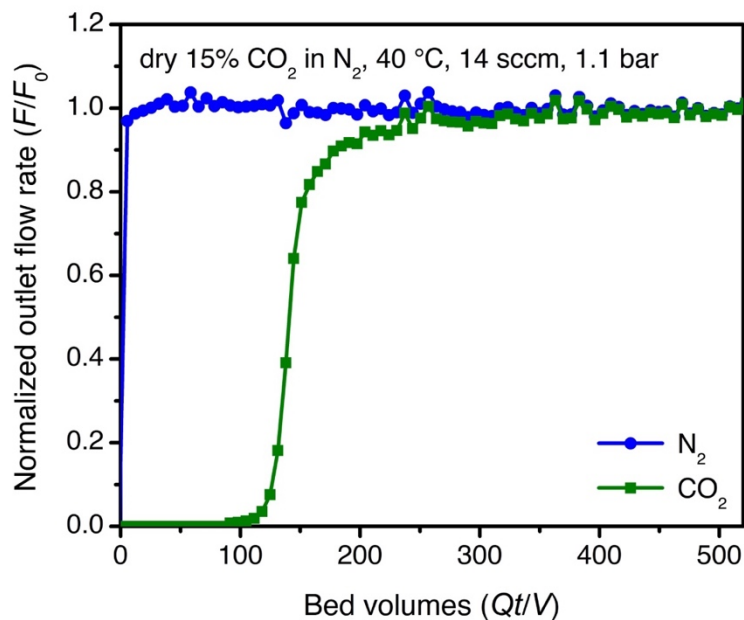


Figure 3.S58. Breakthrough experiment with 2-ampd-Mg₂(dobpdc) under 14 sccm of dry simulated coal flue gas (15% CO₂ in N₂) at ~1.1 bar at 40 °C. Negligible slip was observed, and a CO₂ breakthrough capacity of 3.1 ± 0.2 mmol/g was calculated at exhaustion.

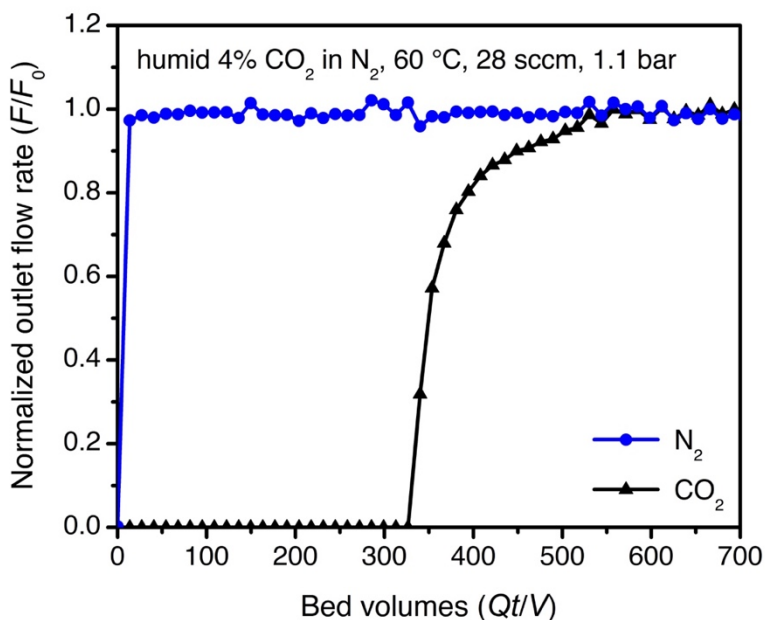


Figure 3.S59. Breakthrough experiment with 2-ampd-Mg₂(dobpdc) under 28 sccm of humid simulated coal flue gas (4% CO₂ in N₂) at ~1.1 bar at 60 °C. The bed was pre-saturated with H₂O prior to the experiment, and the feed gas was humidified using a CO₂-saturated water bubbler at room temperature. Negligible slip was observed, and a CO₂ breakthrough capacity of 1.8 ± 0.2 mmol/g was calculated at exhaustion.

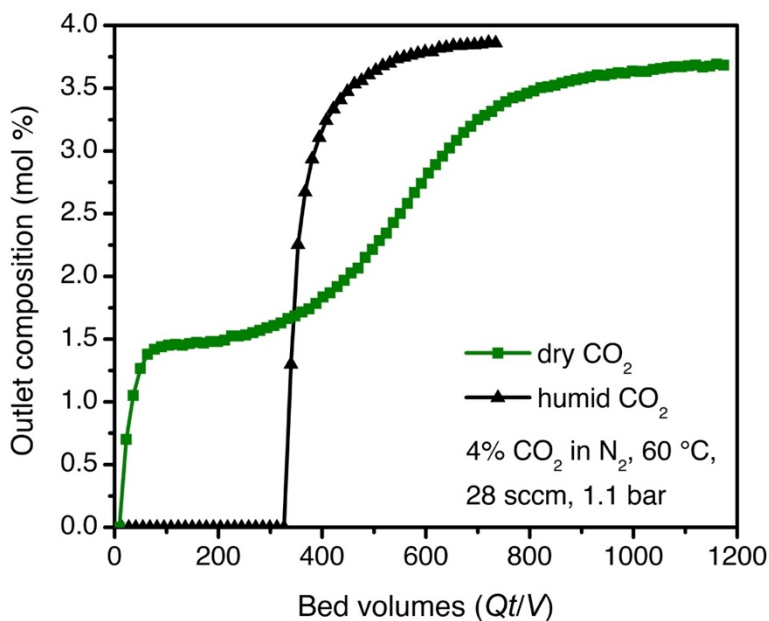


Figure 3.S60. Overlay of dry and humid CO₂ breakthrough profiles under 28 sccm of simulated NGCC flue gas (4% CO₂ in N₂) at ~1.1 bar and 60 °C.

Table 3.S11. Predicted CO₂ slip and capture rate for 2-ampd–Mg₂(dobpdc) from Golden’s rule and the values observed experimentally in breakthrough experiments under 28 sccm of 4% CO₂ at 1.1 bar and the specified temperature.

	Predicted CO ₂ slip	Experimental CO ₂ slip, dry	Experimental CO ₂ slip, humid
40 °C	0.2 mbar (99.5% capture)	5.8 mbar (86% capture)	not observed (>99% capture)
60 °C	4.9 mbar (88% capture)	15 mbar (62% capture)	not observed (>99% capture)

3.6.12 Synthesis of 2-ampd–Zn₂(dobpdc) Single Crystals

Glassware used for single-crystal synthesis was silanized to suppress nucleation on the glassware surface. Silanization was performed using 1 vol % solution of chlorotrimethylsilane in toluene. For small-scale synthesis of single-crystals, 20 mL scintillation vials were used. Prior to silanization, the vials were rinsed with acetone and dried in an oven at 160 °C for at least 1 h. The vials were removed from the oven and filled slightly more than halfway with silanization solution while still hot. The vials were sealed with Teflon-lined caps and placed in a Vortex-Genie 2 Lab Mixer for 30 s to ensure thorough coating of the inner surface with silanization solution. The vials were then left sealed for a minimum of 12 h at room temperature. Prior to synthesis, the silanization solution was removed, and the vials were rinsed twice with acetone and dried in an oven at 160 °C for at least 1 h.

To prepare single crystals of Zn₂(dobpdc), a solution of 14 mg of H₄dobpdc (0.05 mmol) was dissolved in 5.0 mL of ethanol. The solution was sonicated until the ligand was fully dissolved. Separately, a solution of 39 mg (0.18 mmol, 3.5 eq) of Zn(OAc)₂·2H₂O was dissolved in 5 mL of H₂O and sonicated to ensure complete dissolution. The metal and ligand precursor solutions were filtered through syringe filters (Spectrum, 0.45 μm porosity/13 mm diameter) and combined in a silanized 20 mL scintillation vial with the threads pre-taped with Teflon tape. For larger-scale preparations, stock solutions of the metal and ligand precursors were prepared and were dispensed into multiple 20 mL scintillation vials. (Alternatively, a Schlenk flask can be silanized following the above procedure and used in place of vials for large-scale single-crystal synthesis.) The vials were sparged for ~15 min with N₂ and quickly sealed with Teflon-lined caps, which were then wrapped with electrical tape. The vials were heated at 75 °C for 12 h in an oil bath.

Following synthesis, the crystals were quickly transferred to a Schlenk flask using a pipette and kept under N₂ atmosphere. The residual synthesis solution was removed via cannula, and the crystals were soaked three times in dimethylformamide (DMF) for at least 3 h each at room temperature, followed by three times in dry methanol for at least 3 h each at room temperature. Residual non-metal-bound coordinating solvent was removed by soaking three times in dry toluene for at least 3 h each at room temperature, followed by soaking three times in dry hexanes for at least 3 h each at room temperature. After the final wash with hexanes, the majority of solvent was removed using a cannula, and the crystals were evacuated for 30 min at room temperature, at which point they were heated to 180 °C *in vacuo* for at least 3 h. The crystals were then brought into a N₂-filled glovebox, where they were submerged in dry hexanes in a 20 mL vial for long-term storage. Care was taken to purge the atmosphere of the glovebox to remove coordinating solvents prior to exposing the crystals to the box atmosphere.

To prepare single-crystals of 2-ampd–Zn₂(dobpdc), the diamine 2-ampd (2-

(aminomethyl)piperidine) was first dried over Na and distilled under vacuum. This rigorous diamine drying procedure was found to be necessary to achieve high loadings of 2-ampd in single crystals of 2-ampd–Zn₂(dobpdc). The dry diamine was brought into the same N₂-filled glovebox as the activated single crystals of Zn₂(dobpdc). After purging the glovebox atmosphere to remove any residual coordinating solvents, a small portion of activated single crystals of Zn₂(dobpdc) was transferred to a 4 mL vial. The majority of hexanes solvent was removed using a pipette, after which the crystals were submerged in ~2 mL of dry toluene and 50 μL of dry 2-ampd was added. The vial threads were wrapped with Teflon tape, and the vial was sealed with a Teflon-lined cap wrapped with electrical tape. The crystals were stored in the solution of toluene and diamine in the N₂-filled glovebox for 1 week prior to collection of single-crystal diffraction data.

3.6.13 Synthesis and Characterization of Molecular 2-ampd–CO₂ Single Crystals

To prepare single crystals of (piperidin-1-ium-2-ylmethyl)carbamate (2-ampd–CO₂), 1 mL of 2-(aminomethylpiperidine) (2-ampd) was dissolved in 4 mL of toluene in a 20 mL scintillation vial. The vial was left unsealed at room temperature. Slow reaction of 2-ampd with CO₂ from air over the course of several days produced colorless, plate-like crystals of 2-ampd–CO₂ that were suitable for single-crystal X-ray diffraction.

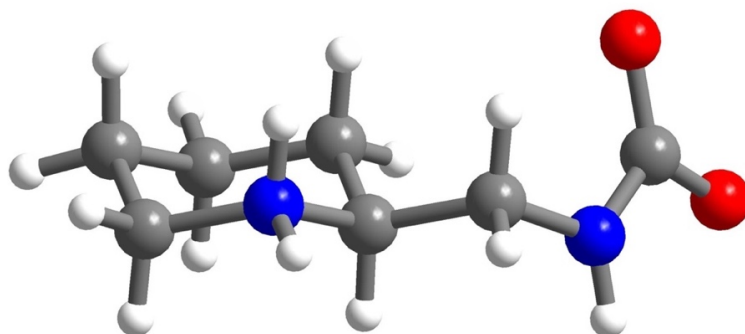


Figure 3.S61. Asymmetric unit for the single-crystal structure of molecular 2-ampd–CO₂.

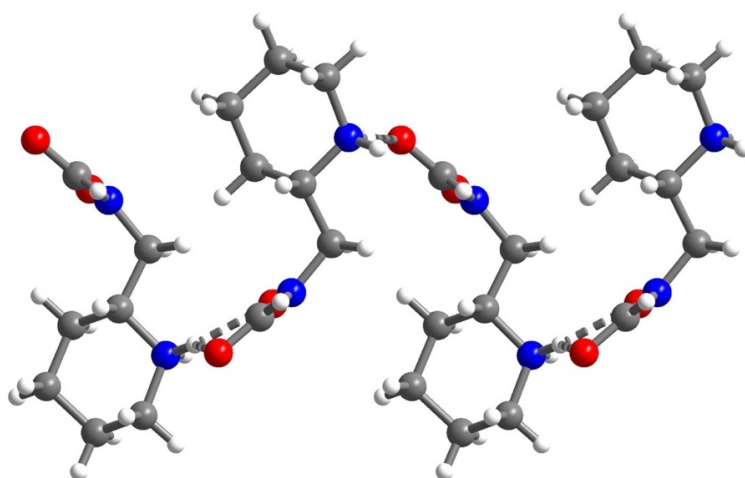


Figure 3.S62. Extended structure for the molecular single-crystal structure of 2-ampd–CO₂. Relevant bond distances: carbamate C1–N1, 1.354(3) Å; carbamate C1–O1, 1.273(3) Å; carbamate C1–O2, 1.259(3) Å; N···O for hydrogen bonds, 2.705(3)–2.941(3) Å. Atom labels refer to atom names in the cif.

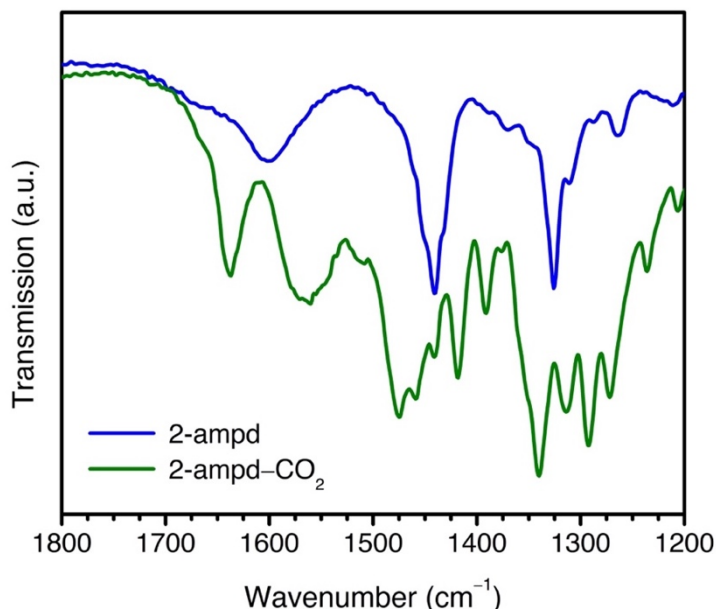


Figure 3.S63. Infrared spectra of molecular 2-ampd (blue) and 2-ampd-CO₂ (green). Following reaction with CO₂, new vibrations are observed at 1637 cm⁻¹ and 1340 cm⁻¹. These values are similar to the C=O (1648 cm⁻¹) and C-N (1362, 1342 cm⁻¹) vibrations observed in 2-ampd-Mg₂(dobpdc) following cooperative adsorption of CO₂.

3.6.14 Single-Crystal X-ray Diffraction

All single-crystal X-ray diffraction data were collected at Beamline 12.2.1 at the Advanced Light Source, Lawrence Berkeley National Laboratory using synchrotron radiation ($\lambda = 0.7288$ Å) and a Bruker AXS D8 diffractometer equipped with a Bruker PHOTON II CMOS detector. Structures were collected at 100 K using an Oxford Cryosystems Cryostream 700 Plus. Raw data were corrected for Lorentz and polarization effects using Bruker AXS SAINT software¹²² and were corrected for absorption using SADABS.¹²³ The structures were solved using SHELXT¹²⁴ and refined using SHELXL¹²⁵ operated in the OLEX2¹²⁶ interface. Thermal parameters were refined anisotropically for all non-hydrogen atoms. Except where noted otherwise below, all hydrogen atoms were placed geometrically and refined using a riding model.

The single-crystal structure of Zn₂(dobpdc)(2-ampd)_{1.76}(C₇H₈)_{0.79} was refined as an inversion twin in space group *P*3₁21 based on a Flack parameter value of 0.49(2). The racemic diamine 2-ampd was found to be disordered over two positions from the nitrogen bound to Zn (atom N1 in the cif), requiring distance (SADI for C-C and C-N bonds) and displacement parameter (SIMU and RIGU) restraints. Refinement of the chemical occupancy of each of the disordered positions resulted in occupancies of 0.589(9) (part 1, atoms with suffix A) and 0.291(9) (part 2, atoms with suffix B). These occupancies were fixed in the final refinement cycle. On the basis of bond lengths and electron density distribution, we assigned the conformation in part 1 (atoms with suffix A) as the right-handed diamine enantiomer in the right-handed space group. The diamine conformation in part 2 (atoms with suffix B) was therefore assigned as the left-handed enantiomer in the right-handed space group. However, due to the disorder in the structure and

single-electron difference between C and N, we cannot exclude the possibility that the conformations in parts 1 and 2 are each a mixture of diamine enantiomers, with atoms assigned as N2A, N2B, C13A and C13B instead existing as mixtures of C and N.

The hydrogen atom for each piperidine nitrogen atom (N2A and N2B) could not be located in the difference map. As an alternative, the piperidine hydrogen atoms were modeled geometrically as equivalently disordered over axial and equatorial positions. The overall diamine occupancy is 88.0(18)%; however, the occupancy of the nitrogen atom bound to Zn (N1) was kept at full occupancy to account for solvent or water that is bound on sites where the diamine is absent. The reported formula, however, reflects the nitrogen content for the diamine alone.

Additionally, a toluene molecule was located in the pore, with a C2 axis running through the C2 axis of the molecule. The occupancy of the toluene molecule refined to 0.787(11) and was fixed in the final refinement cycle. Large displacement parameters and an excess of modeled electron density centered at the methyl group of the carbon suggest that this toluene molecule may be disordered or display significant thermal motion within the pore; however, attempts to model this disorder further were unsuccessful. Distance restraints (SADI for 1,2 and 1,3 C–C distances in the aromatic ring; DFIX for the C–C(methyl) bond) and displacement parameter restraints (RIGU and strong SIMU) were used in modeling the toluene molecule.

Four instances of OMIT were used (OMIT 0 1 0, OMIT 0 2 0, OMIT -1 3 0, OMIT 1 2 0). These reflections were suspected to be affected by the beamstop.

For the single-crystal structure of 2-ampd–CO₂, semi-free refinement was used for hydrogen atoms bound to the carbamate nitrogen (N1 in the cif) and ammonium nitrogen (N2) atoms. These hydrogen atoms (H1 and H2A, H2B) were located in the difference map, and the corresponding N–H distances were restrained to ideal values (DFIX).

Table 3.S12. Crystallographic data for single-crystal X-ray diffraction.

	Zn ₂ (dobpdc)(2-ampd) _{1.76} (C ₇ H ₈) _{0.79}	2-ampd-CO ₂
Formula	C _{30.09} H _{36.96} N _{3.52} O ₆ Zn ₂	C ₇ H ₁₄ N ₂ O ₂
Temperature (K)	100(2)	100(2)
Crystal System	Trigonal	Monoclinic
Space Group	<i>P</i> 3 ₁ 21	<i>P</i> 2 ₁ / <i>n</i>
<i>a</i> , <i>b</i> , <i>c</i> (Å)	21.4691(5), 21.4691(5), 6.8480(2)	5.0969(3), 18.5652(11), 8.4393(5)
<i>α</i> , <i>β</i> , <i>γ</i> (°)	90, 90, 120	90, 102.214(4), 90
<i>V</i> (Å ³)	2733.52(15)	780.49(8)
<i>Z</i>	3	4
Radiation, <i>λ</i> (Å)	Synchrotron, 0.7288	Synchrotron, 0.7288
2 <i>θ</i> Range for Data Collection (°)	3.890 to 60.792	4.500 to 49.094
Completeness to 2 <i>θ</i>	99.8% (2 <i>θ</i> = 51.860°)	99.8% (2 <i>θ</i> = 49.094°)
Data / Restraints / Parameters	5134 / 204 / 197	1208 / 3 / 109
Goodness of Fit on <i>F</i> ²	1.061	1.127
<i>R</i> ₁ ^{<i>a</i>} , <i>wR</i> ₂ ^{<i>b</i>} (<i>I</i> > 2 <i>σ</i> (<i>I</i>))	0.0371, 0.0915	0.0522, 0.1291
<i>R</i> ₁ ^{<i>a</i>} , <i>wR</i> ₂ ^{<i>b</i>} (all data)	0.0474, 0.0973	0.0643, 0.1362
Largest Diff. Peak and Hole (e Å ⁻³)	0.555, -0.539	0.266, -0.277

$${}^a R_1 = \frac{\sum ||F_o| - |F_c||}{\sum |F_o|}, {}^b wR_2 = \left\{ \frac{\sum [w(F_o^2 - F_c^2)^2]}{\sum [w(F_o^2)^2]} \right\}^{1/2}$$

3.6.15 Synchrotron Powder X-ray Diffraction

High-resolution powder X-ray diffraction patterns of 2-ampd-Mg₂(dobpdc) and 2-ampd-Mg₂(dobpdc)-CO₂ were collected at beamline 17-BM at the Advance Photon Source of Argonne National Laboratory. An average wavelength of 0.45399 Å was used. Scattered intensity was recorded with a PerkinElmer a-Si Flat Panel detector. Prior to measurement, the sample was packed in a borosilicate glass capillary of 1.0 mm diameter under a N₂ atmosphere. The capillary was then attached to a custom-designed gas-dosing cell, which was then mounted onto the goniometer head and connected to a gas-dosing manifold for *in situ* diffraction measurements. The sample temperature was controlled by an Oxford Cryosystems Cryostream 800. The diffraction pattern of 2-ampd-Mg₂(dobpdc) was collected at 300 K under dynamic vacuum. The gas-dosing manifold was then used to dose the sample with 970 mbar of dry CO₂ at 300 K. The diffraction pattern of 2-ampd-Mg₂(dobpdc)-CO₂ was collected upon equilibration, as determined by stabilization of the diffraction pattern over several scans. Initial unit cell dimensions were determined by a standard peak search followed by indexing via single-value decomposition in TOPAS-Academic v4.1. Using TOPAS-Academic, precise unit cell dimensions were then determined by performing a structureless Pawley refinement.

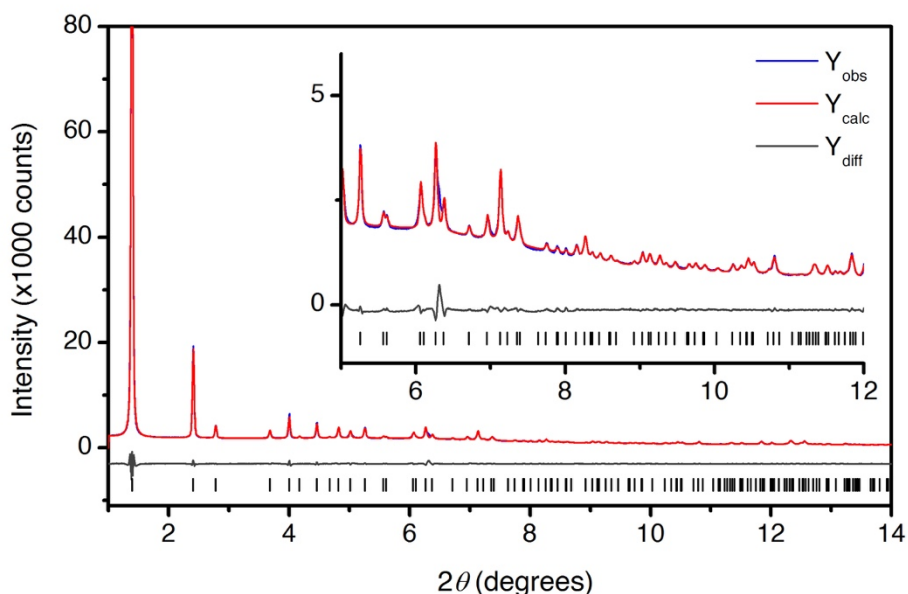


Figure 3.S64. Pawley refinement of synchrotron powder X-ray diffraction data ($\lambda = 0.45399$ Å) for evacuated 2-ampd-Mg₂(dobpdc) at 300 K. Blue and red lines depict the observed and calculated diffraction patterns, respectively. The gray line depicts the difference between the observed and calculated patterns, and the black tick marks indicate the calculated Bragg peak positions. The inset shows the high-angle region at magnified scale. Figures-of-merit (as defined by TOPAS): $R_{wp} = 2.59\%$, $R_{exp} = 2.10\%$, $R_p = 1.63\%$, $GoF = 1.24$.

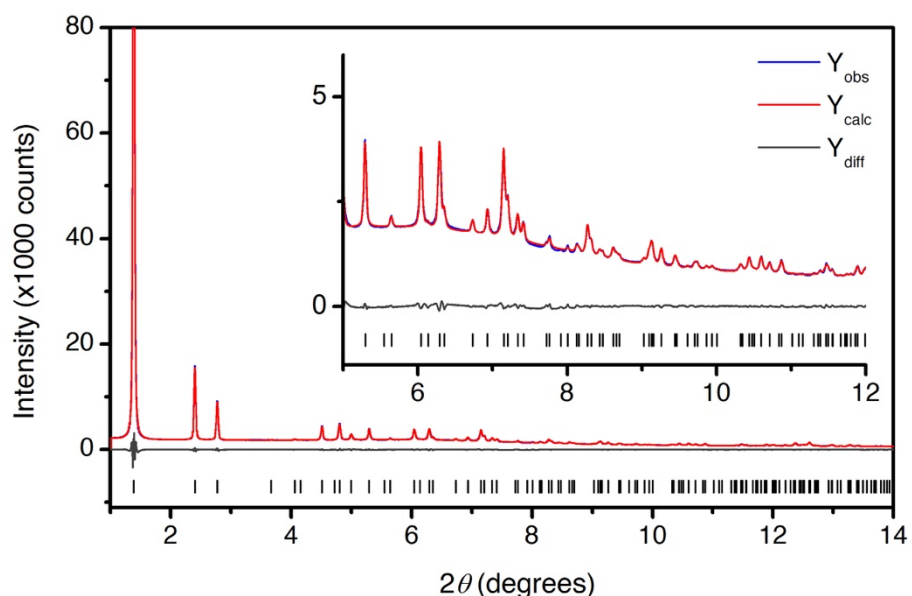


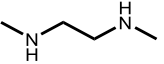
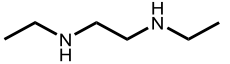
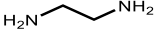
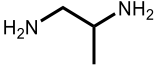
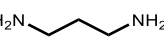
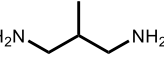
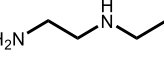
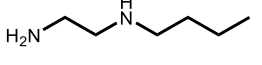
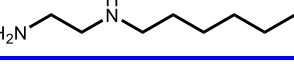
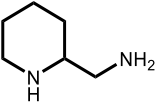
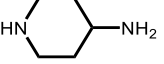
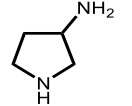
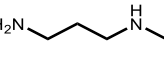
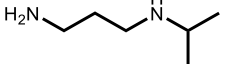
Figure 3.S65. Pawley refinement of synchrotron powder X-ray diffraction data ($\lambda = 0.45399 \text{ \AA}$) for 2-ampd– $\text{Mg}_2(\text{dobpc})$ dosed with 970 mbar of CO_2 at 300 K. Blue and red lines depict the observed and calculated diffraction patterns, respectively. The gray line depicts the difference between the observed and calculated patterns, and the black tick marks indicate the calculated Bragg peak positions. The inset shows the high-angle region at magnified scale. Figures-of-merit (as defined by TOPAS): $R_{\text{wp}} = 2.11\%$, $R_{\text{exp}} = 2.09\%$, $R_{\text{p}} = 1.46\%$, $\text{GoF} = 1.01$.

Table 3.S13. Crystallographic data for Pawley refinement of synchrotron powder X-ray diffraction data.

	2-ampd– $\text{Mg}_2(\text{dobpc})$, evacuated	2-ampd– $\text{Mg}_2(\text{dobpc})$, 970 mbar CO_2
Temperature (K)	300	300
Crystal System	Trigonal	Trigonal
Space Group	$P3_221$	$P3_221$
a, b, c (\AA)	21.580(2) 21.580(2), 6.9289(5)	21.673(1) 21.673(1), 6.8145(4)
α, β, γ ($^\circ$)	90, 90, 120	90, 90, 120
V (\AA^3)	2794.5(5)	2772.1(4)
Radiation, λ (\AA)	Synchrotron, 0.45399	Synchrotron, 0.45399
R_{wp}	2.59	2.11
R_{exp}	2.10	2.09
R_{p}	1.63	1.46
Goodness of Fit	1.24	1.01

3.6.16 Accelerated Decomposition of Diamine-Appended Variants of Mg₂(dobpdc)

Table 3.S14. Summary of the results of accelerated decomposition tests^a for diamine-appended variants of Mg₂(dobpdc). Colors indicate loss of <5% (green), 5–15% (yellow), or >15% (red).

Diamine Structure	Diamine Abbreviation	Diamine Loss (%)	Gravimetric Adsorption Step Capacity Loss (humid CO ₂) at 94 °C (%) ^b	Reference
	mmen ^c	39	- ^d	49–51
	e-2-e ^c	>50	- ^d	51
	en ^c	37	<5	52,54,56
	men ^c	20	4	52,56
	pn	19	- ^d	52
	mpn	13	20	52
	e-2	13	7	51,53
	nBu-2	10	6 ^e	53
	nHex-2	1	3 ^e	53
	2-ampd	2	2	This work
	4-apd	25	- ^d	This work
	3-apyrr	10	12	115
	m-3 ^c	23	22	This work
	i-3 ^c	12	14	This work

^aAccelerated decomposition tests were conducted as described below.

^b94 °C was chosen due to the correlation in Figure 3.S31.

^cHumid N₂ was used in place of humid CO₂ during the accelerated decomposition test.

^dAdsorption step not clearly observed after accelerated decomposition.

^eDetermined at 40 °C.

Accelerated decomposition tests were conducted by activating the material under humid N₂ for 20 min at the indicated activation temperature, collecting a humid CO₂ adsorption isobar, heating the material to 140 °C and holding it under a humid flowing CO₂ (or N₂) stream for 12 h at 140 °C, reactivating the material under humid N₂ for 10 min, and then collecting a second humid CO₂ adsorption isobar. In cases where the humid pure CO₂ desorption step temperature was found to be >140 °C, humid N₂ was used in place of humid CO₂ for the accelerated decomposition tests. The diamine loading after accelerated decomposition was then determined by ¹H NMR after digestion of the sample with DCl (35 wt% in D₂O) in DMSO-*d*₆.

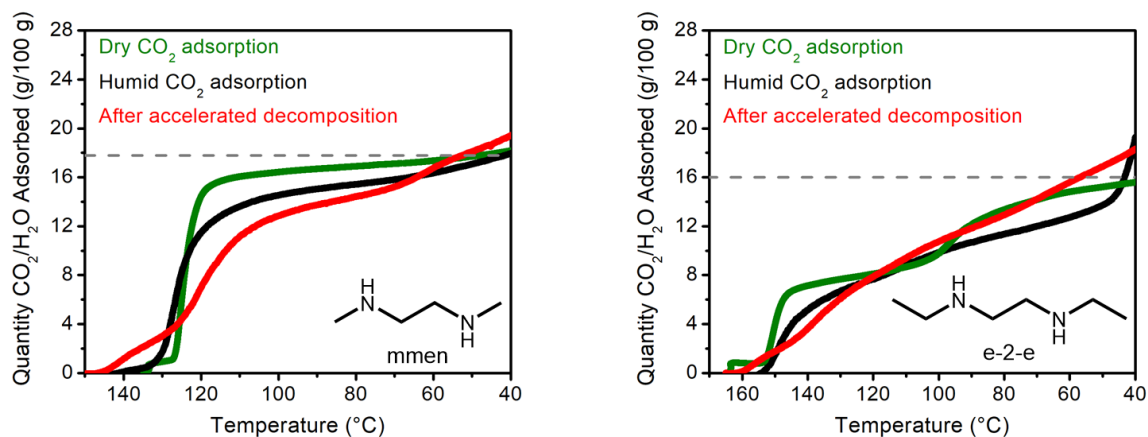


Figure 3.S66. Isobars for dry pure CO₂ adsorption isobars (green lines), humid CO₂ adsorption isobars (black lines), and humid CO₂ adsorption after exposure to humid flowing N₂ at 140 °C for 12 h (red lines) for a series of previously reported Mg₂(dobpdc) variants appended with *secondary,secondary* alkylethylenediamines.^{49–51} Isobars were collected at atmospheric pressure using a ramp rate of 1 °C/min. Gray dashed lines indicate the expected adsorption capacities corresponding to 1 CO₂ per diamine.

In both cases, significant diamine loss and broadening of the adsorption profiles were observed after accelerated decomposition under flowing humid N₂. This finding corroborates recent reports of the poor thermal stability of mmen–Mg₂(dobpdc) under humid conditions.^{127,128} This is likely due to the weak interactions between the metal sites and *secondary* amines in these materials leading to facile diamine volatilization.⁵¹

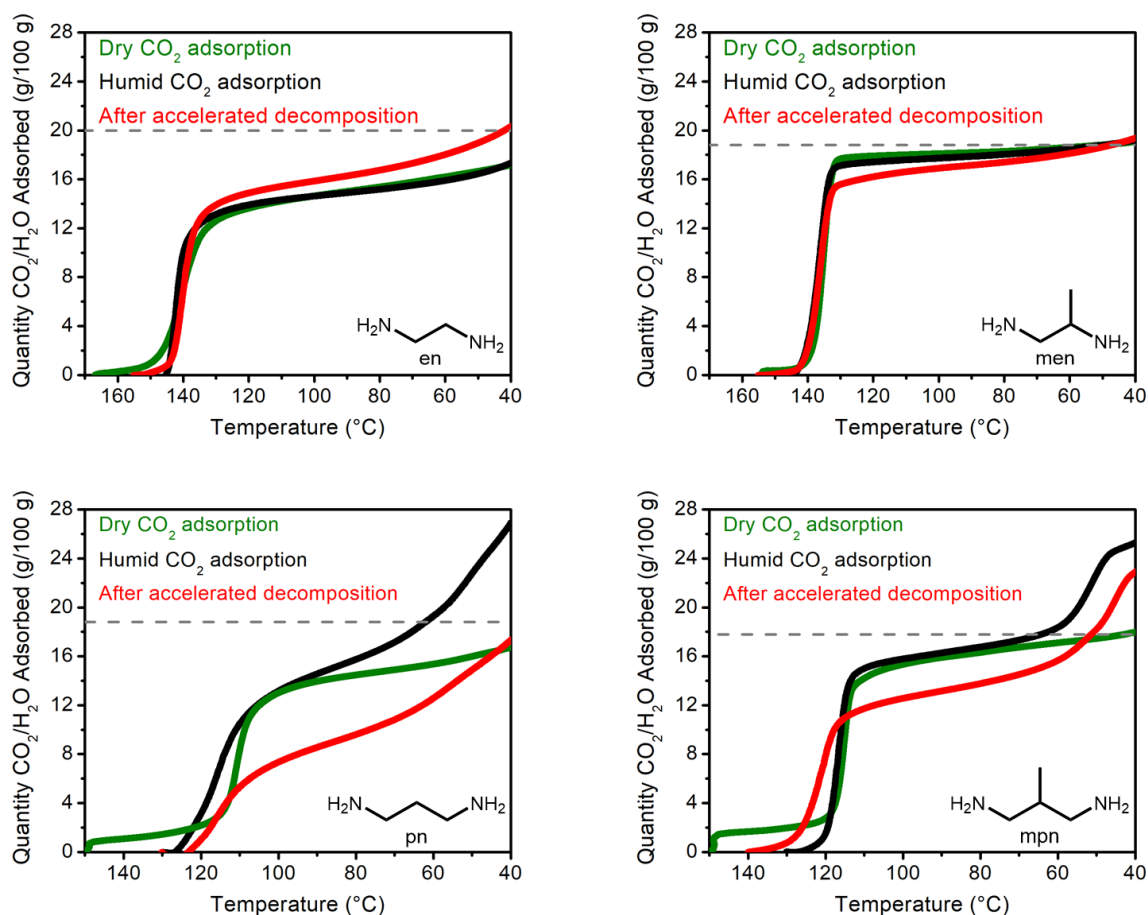


Figure 3.S67. Dry pure CO₂ adsorption isobars (green lines), humid CO₂ adsorption isobars (black lines), and humid CO₂ adsorption isobars after exposure to humid flowing N₂ (en, men) or CO₂ (pn, mpn) at 140 °C for 12 h (red lines) for a series of Mg₂(dobpdc) variants appended with *primary,primary* diamines.^{52,54,56} A ramp rate of 1 °C/min was used in all cases, and isobars were collected at atmospheric pressure. The expected adsorption capacities corresponding to 1 CO₂ per diamine (dark gray dashed lines) are shown.

Both en-Mg₂(dobpdc) and men-Mg₂(dobpdc) display suboptimal diamine loadings upon initial activation, but they do not display significant reduction in CO₂/H₂O adsorption capacities after holding at 140 °C under humid N₂ for 12 h. This finding suggests that the diamine loss from weakly bound sites occurs primarily during activation and not during the accelerated decomposition tests. However, the extremely high regeneration temperatures of these adsorbents under dry pure CO₂ (>180 °C) precludes their use in a temperature swing adsorption process.⁵² In contrast, pn-Mg₂(dobpdc) and mpn-Mg₂(dobpdc) demonstrate poor thermal stability.

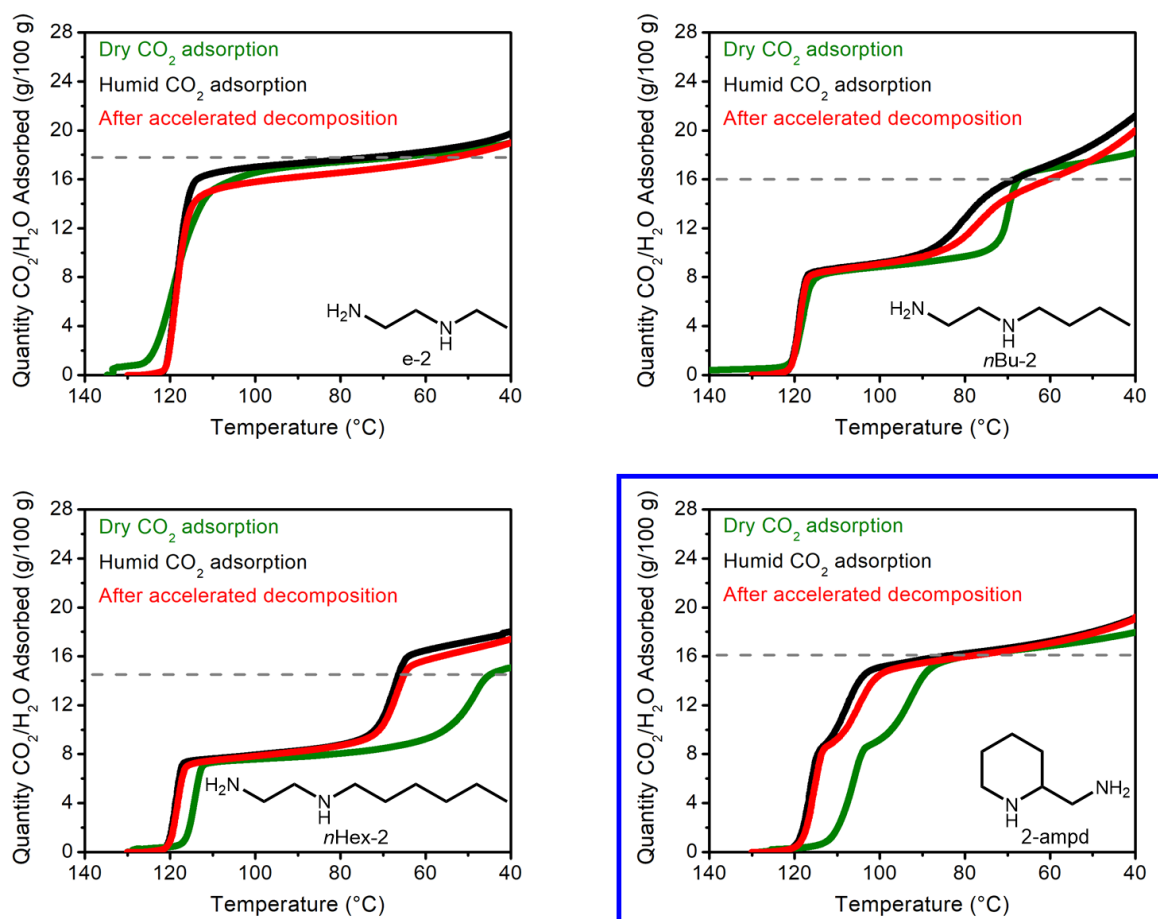


Figure 3.S68. Dry pure CO₂ adsorption isobars (green lines), humid CO₂ adsorption isobars (black lines), and humid CO₂ adsorption isobars after exposure to humid flowing CO₂ at 140 °C for 12 h (red lines) for a series of previously reported Mg₂(dobpdc) variants appended with *primary, secondary* alkylethylenediamines^{51,53} as well as 2-ampd–Mg₂(dobpdc). A ramp rate of 1 °C/min was used in all cases, and isobars were collected at atmospheric pressure. The expected adsorption capacities corresponding to 1 CO₂ per diamine (dark gray dashed lines) are shown.

The stability trend of e-2–Mg₂(dobpdc) < nBu-2–Mg₂(dobpdc) < nHex-2–Mg₂(dobpdc) observed in these accelerated decomposition tests is consistent with the stability trend previously observed upon adsorption/desorption cycling in a simulated temperature swing adsorption process with these materials.⁵³ The material 2-ampd–Mg₂(dobpdc) shows the best thermal stability of this series with almost no lost in CO₂/H₂O capacity (~2%) upon being subjected to flowing humid CO₂ at 140 °C for 12 h.

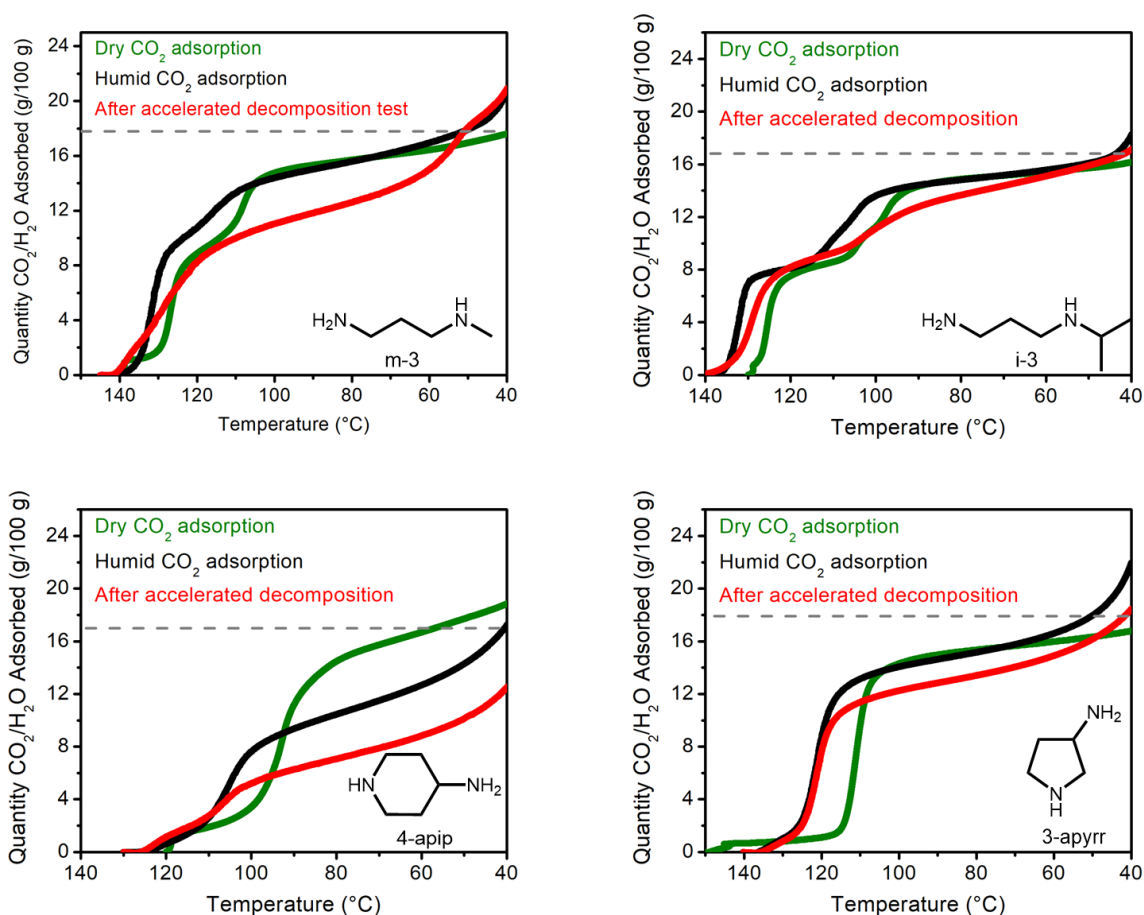


Figure 3.S69. Dry pure CO₂ adsorption isobars (green lines), humid CO₂ adsorption isobars (black lines), and humid CO₂ adsorption isobars after exposure to humid flowing CO₂ at 140 °C for 12 h (red lines) for a series of additional Mg₂(dobpdc) variants appended with *primary, secondary* diamines. A ramp rate of 1 °C/min was used in all cases, and isobars were collected at atmospheric pressure. The expected adsorption capacities corresponding to 1 CO₂ per diamine (dark gray dashed lines) are shown.

Both m-3-Mg₂(dobpdc) and 4-apip-Mg₂(dobpdc) undergo significant decomposition under flowing humid CO₂ at 140 °C. In addition, the second CO₂ adsorption step of i-3-Mg₂(dobpdc) is severely compromised after the accelerated decomposition test. The material 3-apyrr-Mg₂(dobpdc) is more robust, but still displays a diminished CO₂/H₂O adsorption capacity after the accelerated decomposition test (Figure 3.S69). Notably, all four of these diamine-appended frameworks possess higher CO₂ adsorption step temperatures in the presence of water, although 4-apip-Mg₂(dobpdc) is unique among all diamine-appended variants of Mg₂(dobpdc) investigated to date in displaying a reproducible decrease in apparent CO₂ adsorption capacity under humid conditions.

Table 3.S15. Summary of accelerated decomposition tests for 2-ampd–Mg₂(dobpdc) at different temperatures. Colors indicate loss of <5% (green), 5–15% (yellow), and >15% (red) in diamine loading or adsorption capacity.

Accelerated Decomposition Temperature (°C)	Diamine Loss ^a (%)	CO ₂ /H ₂ O Adsorption Step Capacity Loss at 94 °C ^a (%)
140	2	2
160	3	7
180	8	15
200	21	30
220	29	44

^aAccelerated decomposition tests were conducted by activating the material under humid N₂ at 130 °C for 20 min, collecting a humid CO₂ adsorption isobar, heating the material to the indicated temperature and holding it under a humid flowing CO₂ steam for 12 h at the indicated temperature, reactivating the material under humid N₂ for 10 min at 130 °C, and then collecting a second humid CO₂ adsorption isobar.

The material 2-ampd–Mg₂(dobpdc) does not undergo significant decomposition under humid gas streams until heating above 200 °C and notably retains crystallinity even following significant diamine loss after being subjected to flowing humid CO₂ at 220 °C for 12 h (Figure 3.S70).

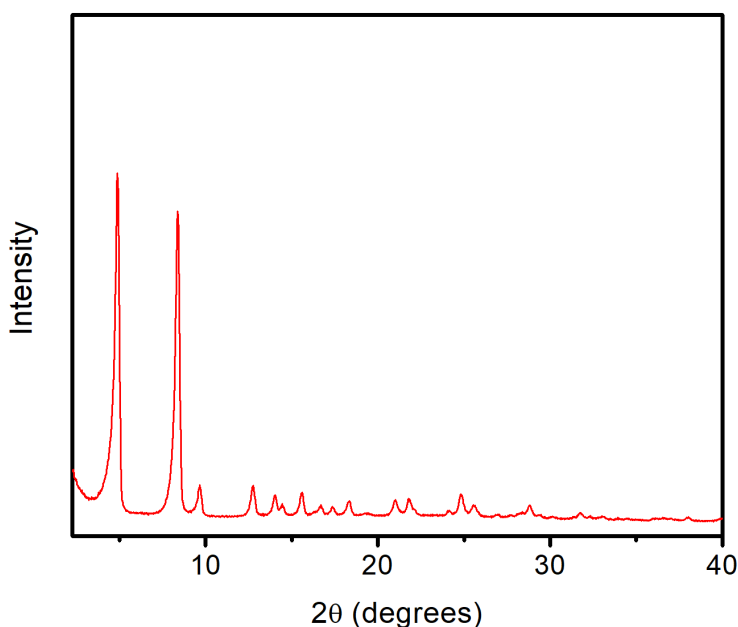


Figure 3.S70. Laboratory powder X-ray diffraction pattern (Cu K α radiation, $\lambda = 1.5418 \text{ \AA}$) of 2-ampd–Mg₂(dobpdc) after exposure to flowing humid CO₂ at 220 °C for 12 h, confirming that the framework maintains crystallinity after exposure to a humid gas stream at high temperatures.

Due to the high O₂ content of the flue gas emissions of natural gas-fired power plants (up to 12%),¹²⁹ the stability of 2-ampd–Mg₂(dobpdc) to O₂ was evaluated by flowing dry air (~21% O₂)

over the material at 100 °C for 6 h. The CO₂ adsorption profiles before and after exposure to dry air were found to be nearly identical (Figure 3.S71). The adsorption profiles of the previously reported material dmpn–Mg₂(dobpdc)⁵² were also found to be identical before and after exposure to dry air at 100 °C for 6 h, suggesting that stability to O₂ may be a general feature of diamine-appended variants of Mg₂(dobpdc).

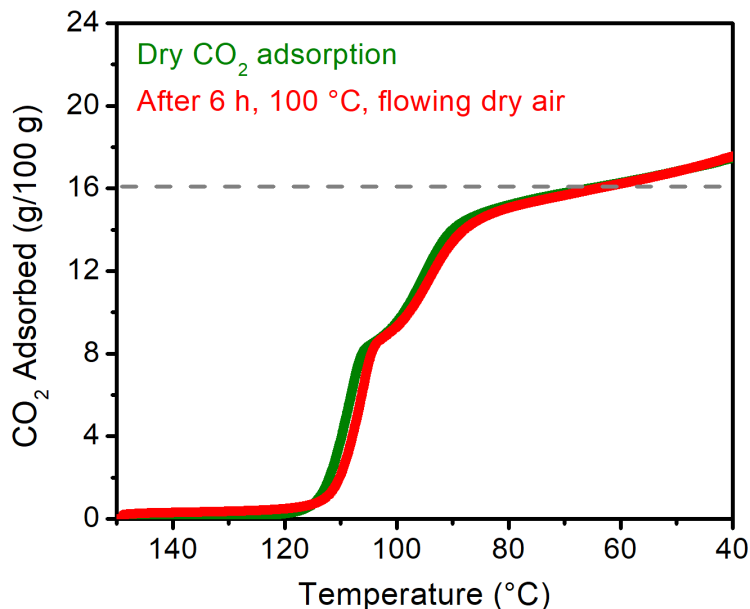


Figure 3.S71. Initial dry CO₂ adsorption isobar for 2-ampd–Mg₂(dobpdc) (green) and CO₂ adsorption isobar collected after exposure to 6 h of flowing dry air at 100 °C (red). The dashed grey line indicates the adsorption capacity corresponding to 1 CO₂ per diamine. Isobars were collected at atmospheric pressure using a ramp rate of 1 °C/min.

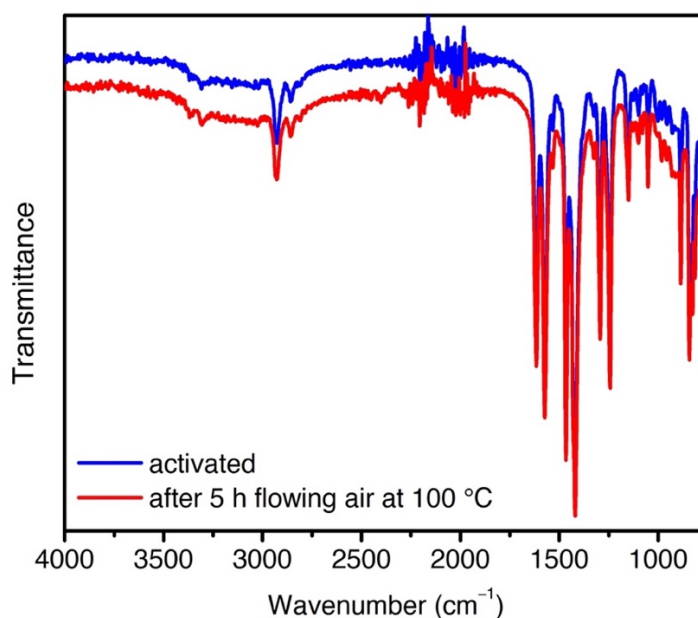


Figure 3.S72. Infrared spectra of 2-ampd–Mg₂(dobpdc) as-synthesized (blue) and after exposure to flowing dry air at 100 °C for 5 h (red).

3.6.17 Comparison of 2-ampd-Mg₂(dobpdc) and MCM-41-PEI-50

In order to compare the stability of 2-ampd-Mg₂(dobpdc) to amine-functionalized silicas, which are among the state-of-the-art adsorbents for CO₂ capture processes, its performance and stability were compared with those of MCM-41-PEI-50.

Synthesis of MCM-41-PEI-50. Prepared according to the literature procedure.⁷⁹ Branched polyethyleneimine (average molecular weight ~800 g/mol, 0.5 g, purchased from Sigma-Aldrich) was dissolved in methanol (4 mL) in a 20 mL scintillation vial with vigorous stirring. Next, MCM-41 (0.5 g, purchased from Sigma-Aldrich) was added slowly to the solution, resulting in formation of a thick slurry. The slurry was stirred vigorously for 30 min, at which time it was dried at 70 °C for 16 h under flowing N₂. All experiments were performed on material from the same batch for consistency.

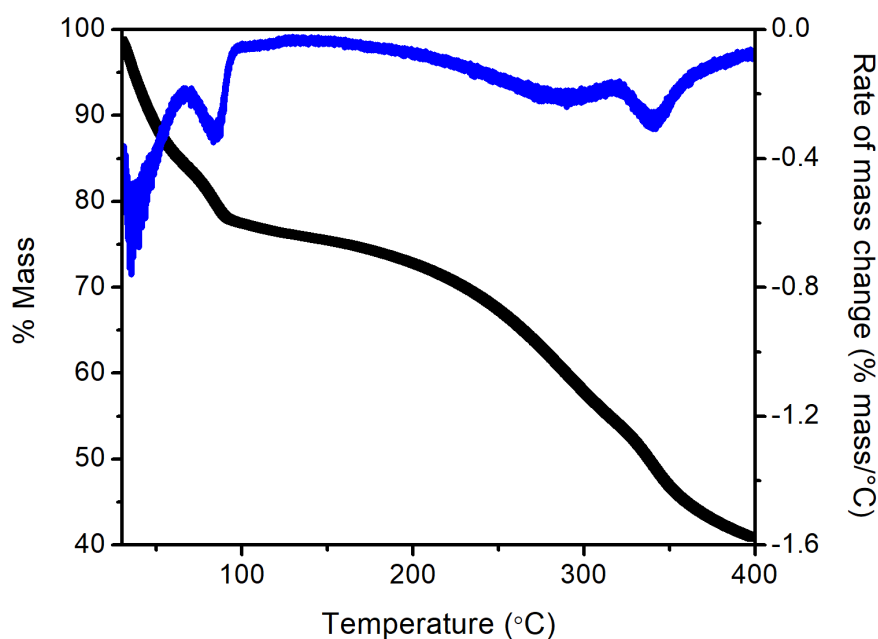


Figure 3.S73. Dry N₂ decomposition profile of MCM-41-PEI-50, plotted in black as % mass change (left-hand y-axis) vs. *T*. The initial mass loss regime (<100 °C) is likely due to the loss of methanol, water, and CO₂. The rate of mass change at each temperature is shown in blue and corresponds to the right-hand y-axis. A ramp rate of 1.5 °C/min was used.

Based on this decomposition profile, as well as isobaric CO₂ adsorption experiments with activation at various temperatures (not shown), 140 °C was determined to be the optimal activation temperature for this material.

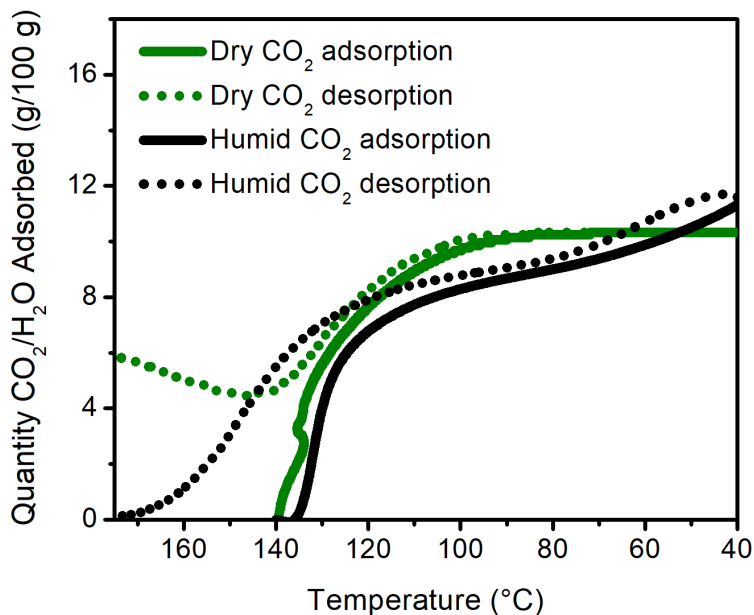


Figure 3.S74. Dry pure CO₂ adsorption (solid green) and desorption (dotted green) isobars, and humid CO₂ adsorption (solid black) and desorption (dotted black) isobars, for MCM-41-PEI-50. The material was activated at 140 °C under flowing dry (green) or humid (black) N₂ for 1 h. The observed adsorption capacity of 10.4 g/100 g from a dry pure CO₂ stream at 40 °C is close to that previously reported for this material (~10.8 g/100 g CO₂).⁸⁰

Consistent with the literature,¹³⁰ MCM-41-PEI-50 could not be regenerated efficiently under dry pure CO₂ (dotted green line) due to irreversible urea formation at higher temperatures. **This is in contrast to the behavior of all diamine-appended variants of Mg₂(dobpdc) reported to date, which can be fully regenerated under dry pure CO₂ by heating to the proper desorption temperature.** Because water mitigates urea formation, nearly full regeneration could be achieved by heating the material to 175 °C under humid CO₂. This is significantly higher than the temperature required to fully regenerate 2-ampd-Mg₂(dobpdc) under humid CO₂ (~140 °C).

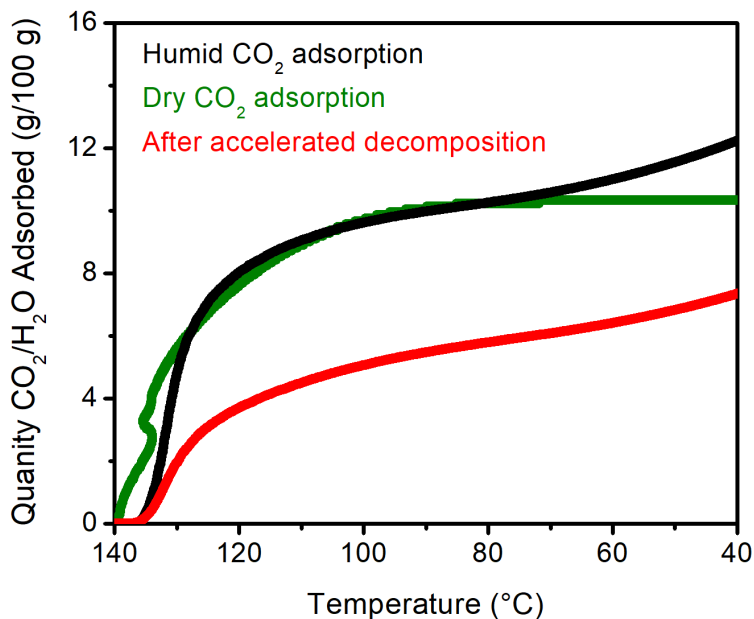


Figure 3.S75. Dry pure CO₂ adsorption isobar (green line), humid CO₂ adsorption isobar (black line), and humid CO₂ adsorption isobar after exposure to humid flowing CO₂ at 140 °C for 12 h (red line) for MCM-41-PEI-50. The material was activated at 140 °C under flowing dry (green) or humid (black) N₂ for 1 h and reactivated at 140 °C under flowing humid N₂ for 1 h after the accelerated decomposition test (red). After the accelerated decomposition test, the initially white material was found to have turned yellow, suggesting that urea formation had taken place.¹³⁰

Due to the difficulty of reactivating MCM-41-PEI-50 with humid N₂, the CO₂/H₂O capacity loss observed upon accelerated decomposition of MCM-41-PEI-50 (difference between red and green lines, Figure 3.S75) was corroborated by thoroughly reactivating the material with dry N₂ and collecting a dry CO₂ adsorption isobar (Figure 3.S76). These isobars confirm that treatment with flowing humid CO₂ at 140 °C results in a 17% decrease in dry CO₂ adsorption capacity at 40 °C (10.3 g/100g → 8.5 g/100 g), which is likely due to slow, irreversible urea formation even under flowing humid CO₂.

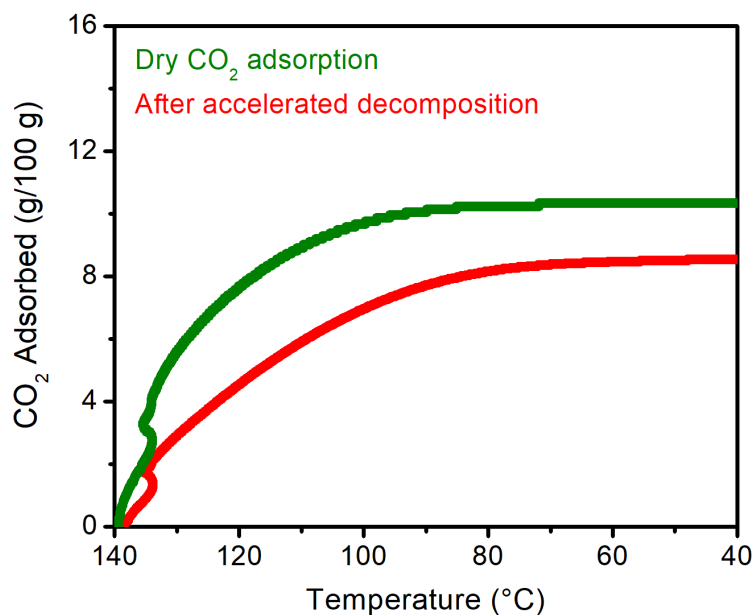


Figure 3.S76. Dry pure CO₂ adsorption isobars for MCM-41-PEI-50 samples as synthesized (green line) and after being subjected to flowing humid CO₂ at 140 °C for 12 h (red line). The samples were (re)activated at 140 °C under flowing dry N₂ for 1 h in each case.

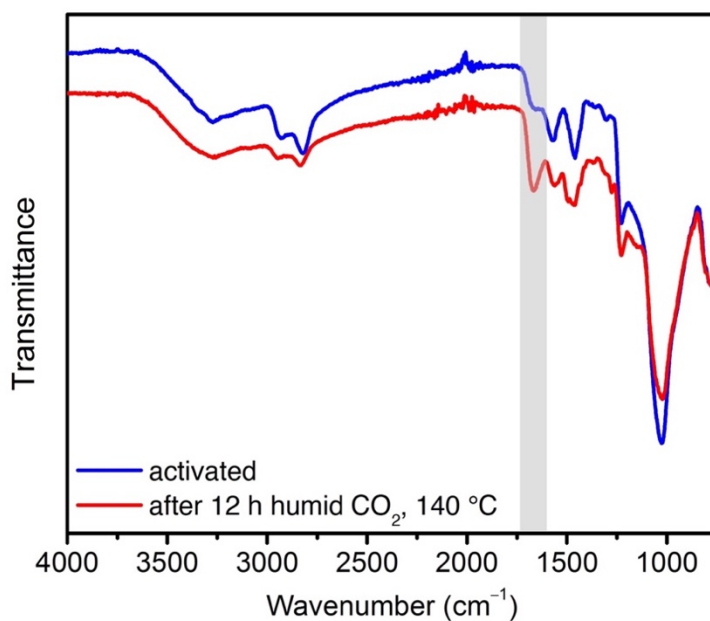


Figure 3.S77. Infrared spectra of MCM-41-PEI-50 as-synthesized (blue) and after exposure to flowing humid CO₂ at 140 °C for 12 h (red). An increase in intensity at approximately 1660 cm⁻¹ was observed after exposure to humid CO₂ at high temperatures, which is likely due to urea formation.¹³⁰ Irreversible urea formation likely accounts for the observed reduction in CO₂ adsorption capacity upon accelerated decomposition (Figure 3.S76).

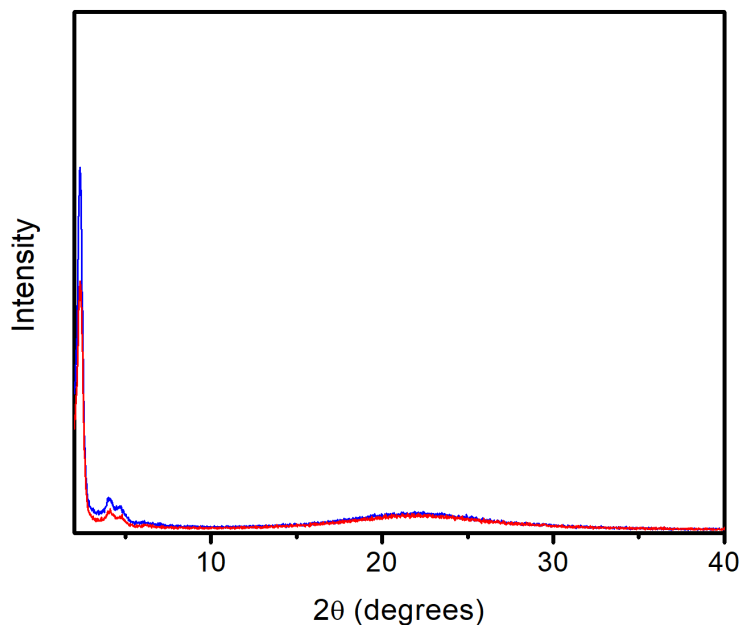


Figure 3.S78. Laboratory powder X-ray diffraction patterns (Cu K α radiation, $\lambda = 1.5418 \text{ \AA}$) of MCM-41-PEI-50 as-synthesized (blue) and after exposure to flowing humid CO₂ at 140 °C for 12 h (red).

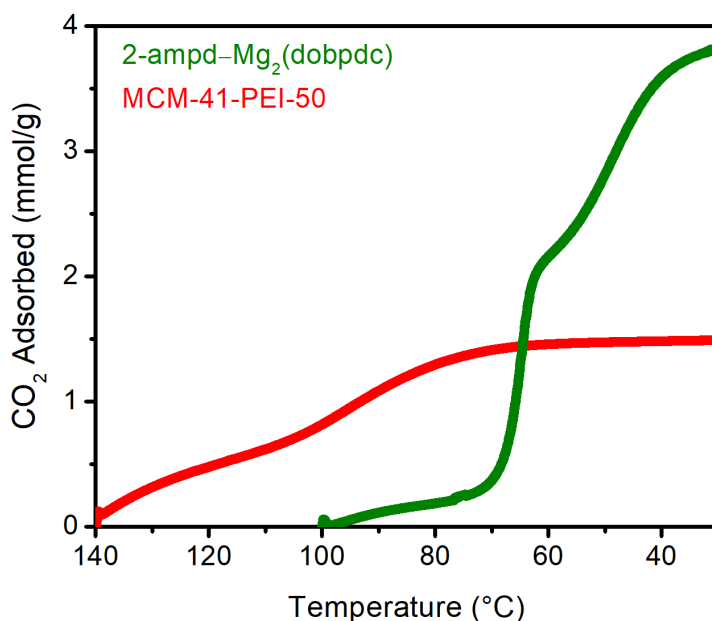


Figure 3.S79. Comparison of the dry pure 4% CO₂ in N₂ adsorption isobars for 2-ampd-Mg₂(dobpdc) (green line) and MCM-41-PEI-50 (red line). The material MCM-41-PEI-50 was activated at 140 °C under flowing dry N₂ for 1 h, and 2-ampd-Mg₂(dobpdc) was activated at 150 °C under flowing dry N₂ for 20 min. A ramp rate of 0.25 °C/min was used in both cases.

At $\geq 65 \text{ }^\circ\text{C}$, MCM-41-PEI-50 displays a higher adsorption capacity from a dry simulated natural gas flue gas stream than 2-ampd-Mg₂(dobpdc), but at 40 °C, 2-ampd-Mg₂(dobpdc) possesses a much higher CO₂ adsorption capacity (3.6 mmol/g) than MCM-41-PEI-50 (1.5 mmol/g).

3.6.18 Adsorption/Desorption Cycling of 2-ampd-Mg₂(dobpdc)

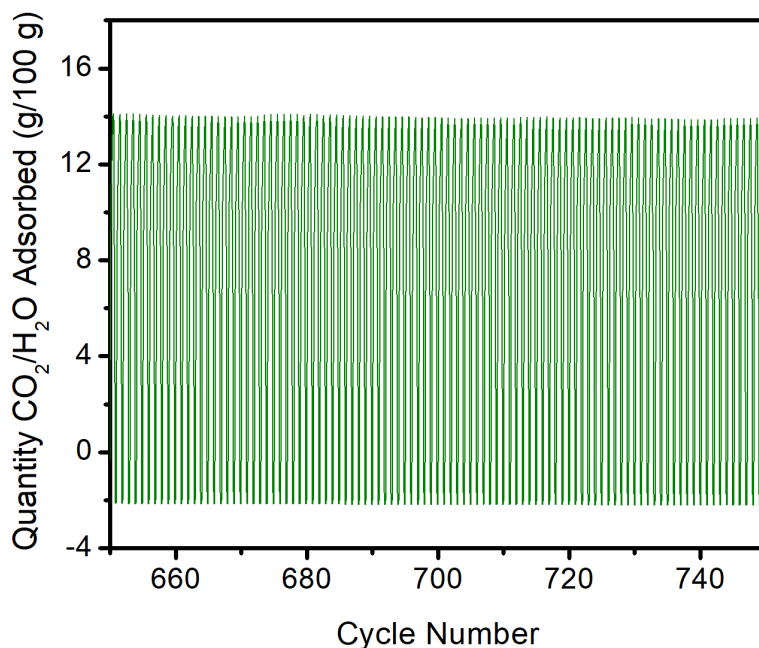


Figure 3.S80. The last 100 of 750 humid adsorption/desorption cycles with 2-ampd-Mg₂(dobpdc) in a simulated natural gas flue gas temperature-swing adsorption process. Adsorption conditions: humid 4% CO₂ in N₂, 40 °C, 5 min (correspond to maxima). Desorption conditions: humid pure CO₂, 140 °C, 1 min (correspond to minima). The cycling capacity of the 750th cycle was found to be 16.0 g/100 g. The baseline value of 0 g/100 g is defined as the mass after activation under 4% CO₂ in N₂ at 150 °C for 20 min prior to the first cycle. The diamine loading was found to be 94% after this experiment. The weight loss due to gradual diamine volatilization from weakly bound sites accounts for the negative baseline value in this experiment. The diamine loading was found to be 93% after 200 humid/adsorption cycles under the same conditions, indicating that continuous diamine loss does not occur upon adsorption/desorption cycling.

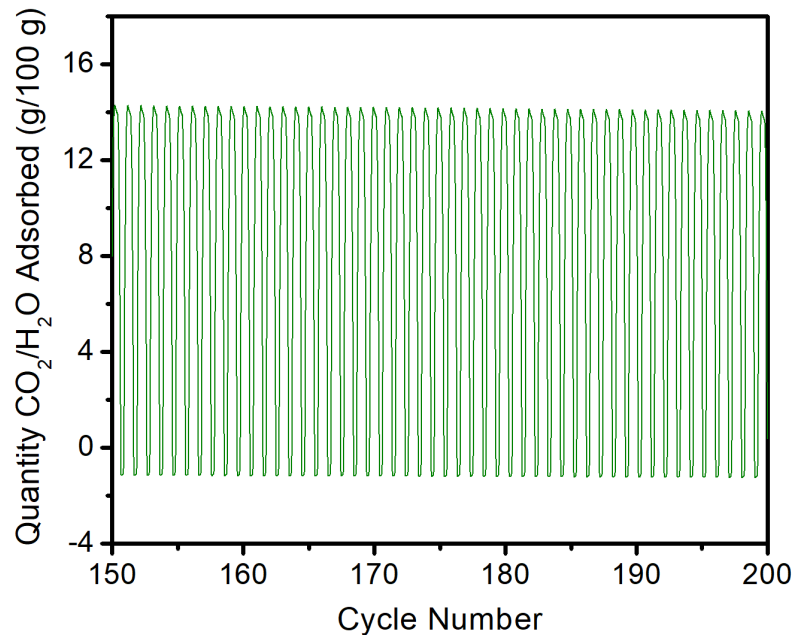


Figure 3.S81. The last 50 of 200 humid adsorption/desorption cycles with 2-ampd-Mg₂(dobpdc) in a simulated natural gas flue gas temperature-swing adsorption process with a higher adsorption temperature of 60 °C to minimize water co-adsorption. Adsorption: humid 4% CO₂ in N₂, 60 °C, 5 min (correspond to maxima). Desorption: humid pure CO₂, 140 °C, 1 min (correspond to minima). The cycling capacity of the 200th cycle was found to be 15.3 g/100 g. The baseline value of 0 g/100 g is defined as the mass after activation under 4% CO₂ in N₂ at 150 °C for 20 min prior to the first cycle. The diamine loading was found to be 93% after this experiment. The weight loss due to gradual diamine volatilization from weakly bound sites likely accounts for the negative baseline value in this experiment.

3.6.19 Synthesis and Characterization of 2-ampd–M₂(dobpdc) (M = Mn, Co, Ni, Zn)

The diamine 2-ampd was grafted to methanol-solvated Ni₂(dobpdc) and Co₂(dobpdc) using the same procedure employed to prepare the Mg analogue. The diamine 2-ampd was grafted to activated Mn₂(dobpdc) and Zn₂(dobpdc) using a modified procedure.^{50–52} A solution of 2-ampd (3 mL) and toluene (12 mL) was dried by stirring over CaH₂ at 100 °C for 1 h while being sparged with N₂. The mixture was allowed to settle and transferred to a N₂-filled glovebag. Activated M₂(dobpdc) (M = Mn or Zn, ~20 mg) was transferred out of a N₂-filled glovebox in a sealed 20 mL scintillation vial and transferred into the N₂-filled glovebag. The solution of 2-ampd and toluene (5 mL) was transferred to the activated framework, taking care not to disturb the CaH₂. The mixture was swirled several times and allowed to stand for 24 h in a N₂-filled glovebag. The diamine-appended frameworks were removed from the glovebag, filtered in air, and characterized immediately.

Table 3.S16. Typical diamine loadings and activation temperatures for M₂(dobpdc) (M = Mg, Mn, Co, Ni, Zn) variants appended with 2-ampd.

Metal	% Diamine Loading (As Synthesized) ^a	Activation Temperature (°C) ^b	% Diamine Loading (After Activation) ^a
Mg	~115%	140	~100
Mn	N/d ^c	150	N/d ^c
Co	~122%	150	~102
Ni	~113%	170	~94
Zn	112%	150	102

^aDetermined by ¹H NMR after digestion with DCl (35 wt% in D₂O) in DMSO-*d*₆.

^bActivated for 20 min under flowing dry N₂.

^cDue to the presence of highly paramagnetic Mn²⁺ ions in solution, reliable diamine loadings could not be determined. However, the presence of the diamine before and after activation was confirmed by ¹H NMR.

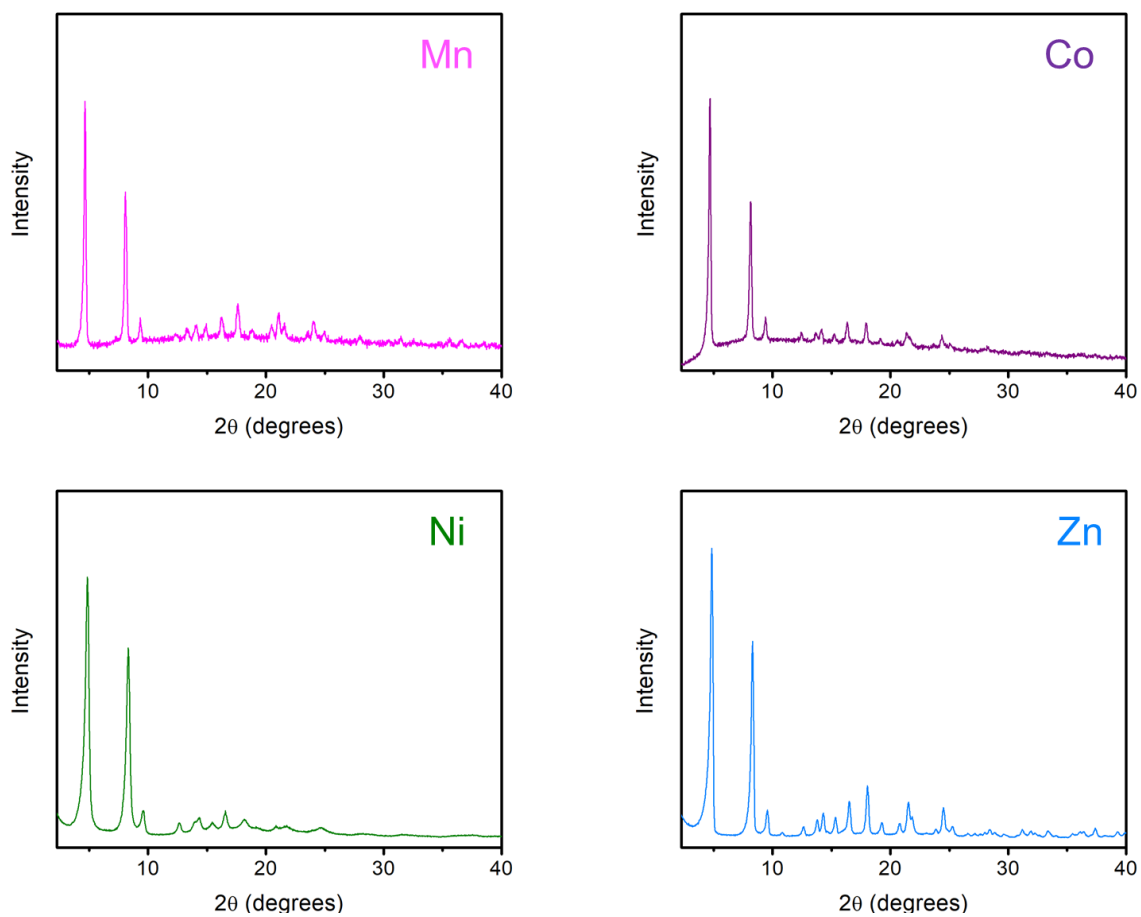


Figure 3.S82. Powder X-ray diffraction patterns (Cu $K\alpha$ radiation, $\lambda = 1.5418 \text{ \AA}$) of as-synthesized 2-ampd- $M_2(\text{dobpdc})$ ($M = \text{Mn, Co, Ni, Zn}$).

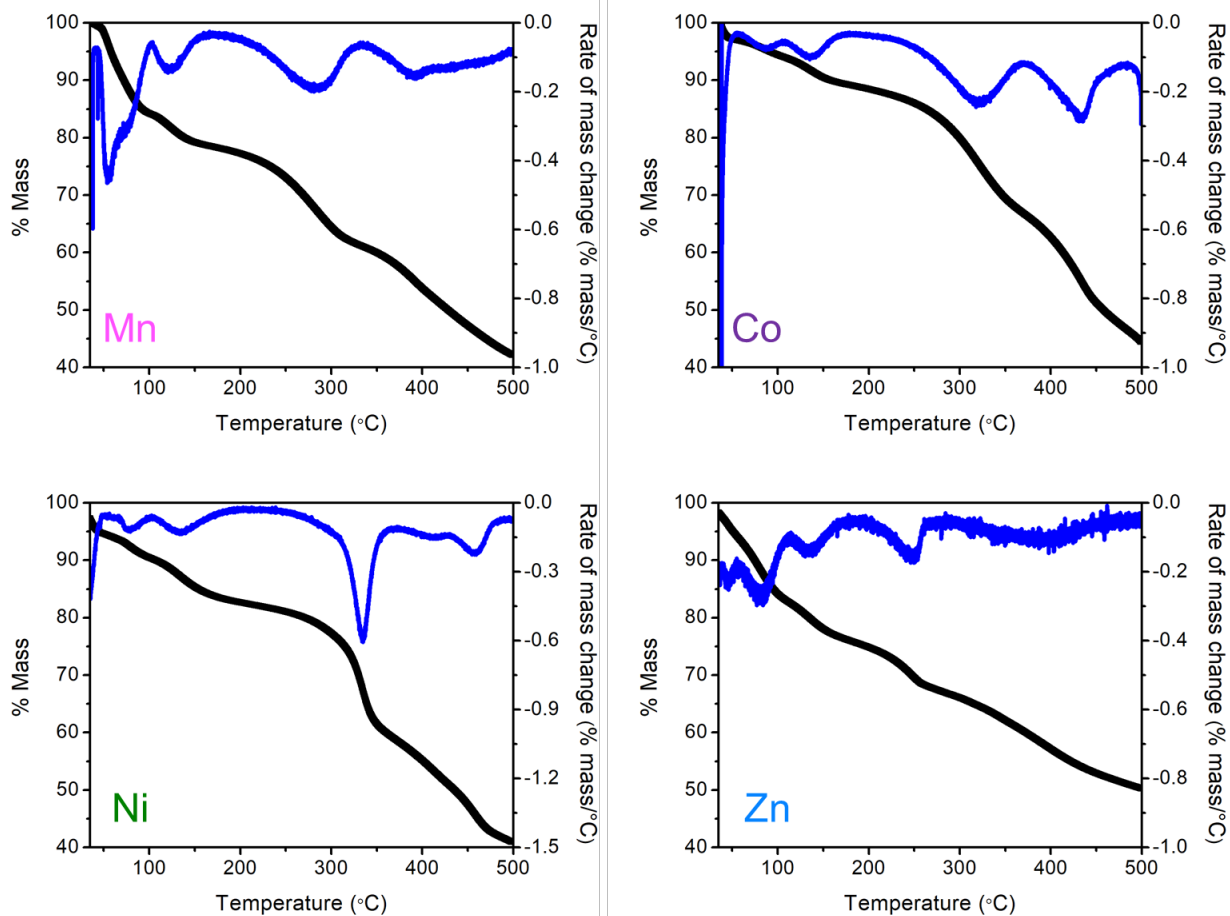


Figure 3.S83. Dry N₂ decomposition profiles of 2-ampd-M₂(dobpdc) (M = Mn, Co, Ni, Zn), plotted in black as % mass change (left-hand y-axis) vs. *T*. The rate of mass change at each temperature is shown in blue and corresponds to the right-hand y-axis. A ramp rate of 1.5 °C/min was used in all cases.

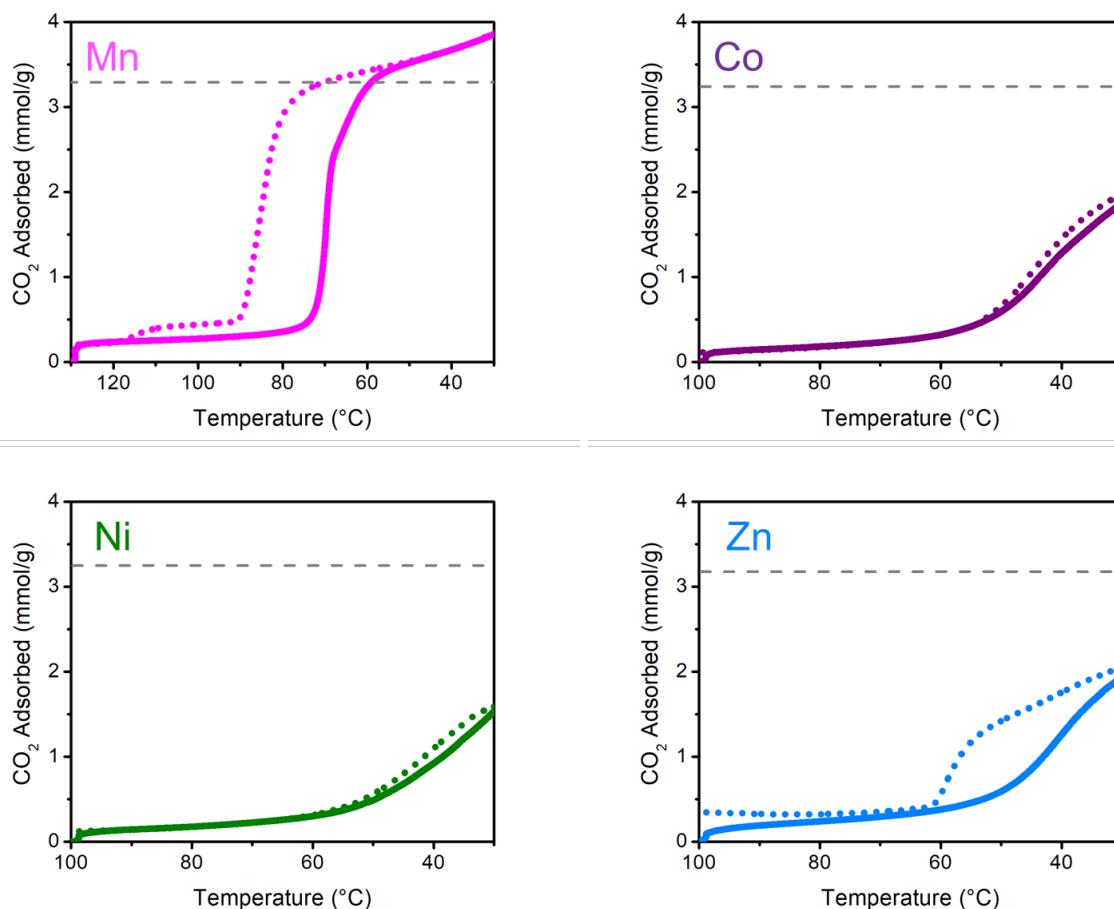


Figure 3.S84. Dry pure CO₂ adsorption (solid line) and desorption (dotted line) isobars of 2-ampd–M₂(dobpdc) (M = Mn, Co, Ni, Zn). A ramp rate of 1 °C/min was in all cases. The materials were activated under flowing N₂ for 20 min at the temperatures indicated in Table 3.S16. The expected adsorption capacity corresponding to the adsorption of one CO₂ per diamine is indicated as a dashed dark gray line.

The adsorbent 2-ampd–Mn₂(dobpdc) displays step-shaped adsorption/desorption of CO₂ at temperatures lower than the corresponding Mg analogue, which is consistent with ammonium carbamate chain formation via the insertion of CO₂ into the M–N bonds.⁵⁰ In addition, step-shaped desorption of CO₂ from 2-ampd–Zn₂(dobpdc) was observed. The adsorption steps of 2-ampd–Co₂(dobpdc) and 2-ampd–Zn₂(dobpdc) likely occur around 30 °C and thus cannot be reliably measured by thermogravimetric analysis. Consistent with our previous results, 2-ampd–Ni₂(dobpdc) does not display a CO₂ adsorption step.⁵⁰

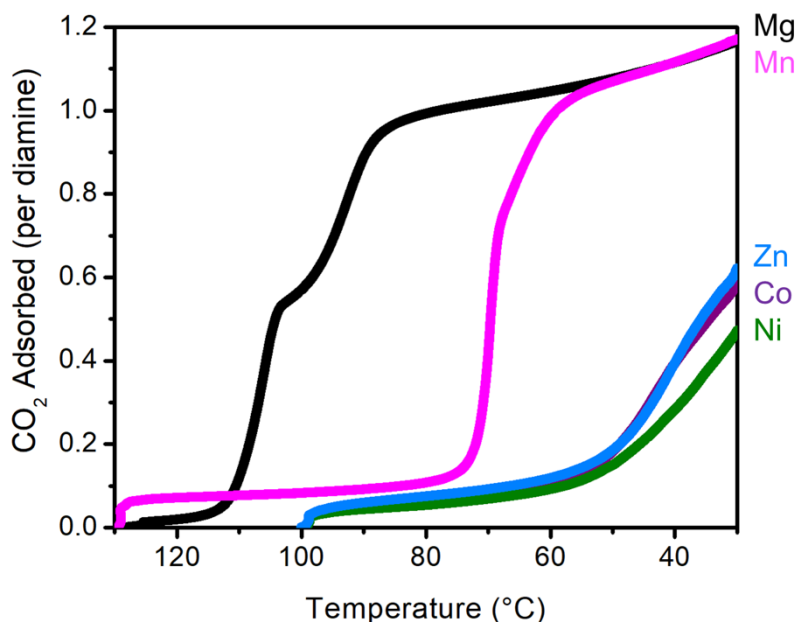


Figure 3.S85. Comparison of the dry pure CO₂ adsorption isobars of 2-ampd-M₂(dobpdc) (M = Mg, Mn, Co, Ni, Zn). A ramp rate of 1 °C/min was in all cases. The materials were activated under flowing N₂ for 20 min at the temperatures indicated in Table 3.S16. The adsorption temperature trend of Mg > Mn > Zn ≈ Co > Ni is consistent with previous reports and corroborates the formation of ammonium carbamate chains upon CO₂ adsorption in 2-ampd-M₂(dobpdc) variants.⁵⁰

3.6.20 Additional Solid-State Magic Angle Spinning (MAS) NMR Spectra and Details

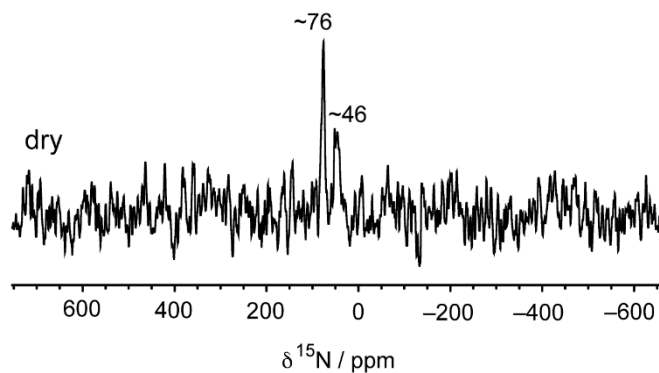


Figure 3.S86. Solid-state ¹⁵N MAS NMR (16.4 T) spectrum of 2-ampd-Mg₂(dobpdc) dosed with 1025 mbar of dry ¹³CO₂. The spectrum was obtained by cross-polarization from ¹H (contact time = 1 ms). The ¹⁵N nuclear spins are present at natural abundance. The resonance at ~76 ppm is assigned to a carbamate (RNHC(O)O⁻) nitrogen, while the resonance at ~46 ppm is assigned to an ammonium (R₂NH₂⁺) nitrogen.⁵⁰ The sample spinning rate was 15 kHz. This spectrum corroborates the formation of ammonium carbamate chains in 2-ampd-Mg₂(dobpdc) upon CO₂ adsorption.

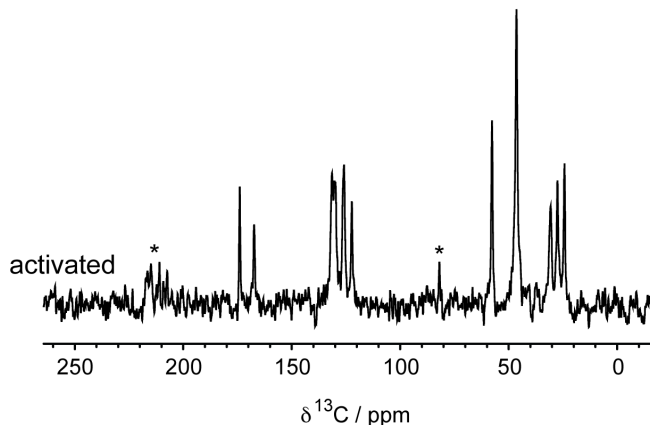


Figure 3.S87. Solid-state ^{13}C NMR (16.4 T) MAS spectrum of activated 2-ampd- $\text{Mg}_2(\text{dobpdc})$. This spectrum was obtained by cross-polarization from ^1H (contact time = 1 ms). The observed resonances can be assigned either to the linker (δ 173.9 ppm, 167.3 ppm, 132–122 ppm) or to 2-ampd (δ 58–24 ppm). The asterisks indicate spinning side bands. The sample spinning rate was 15 kHz.

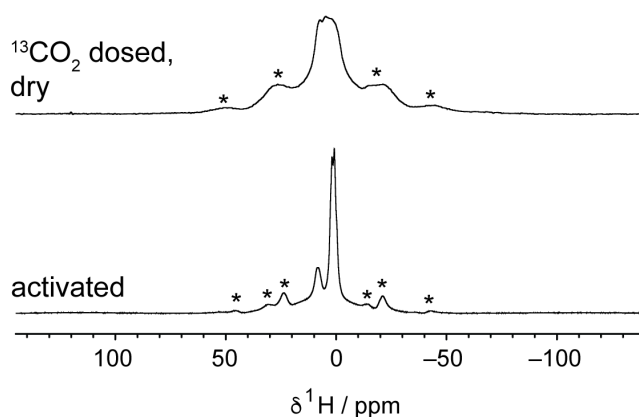


Figure 3.S88. Solid-state ^1H NMR (16.4 T) MAS spectra of activated 2-ampd- $\text{Mg}_2(\text{dobpdc})$ (bottom) and 2-ampd- $\text{Mg}_2(\text{dobpdc})$ after dosing with $^{13}\text{CO}_2$ gas at 1009 mbar (top). Spectra were obtained by single pulse excitation. In the spectrum of activated 2-ampd- $\text{Mg}_2(\text{dobpdc})$ (bottom), resolvable peaks can be observed for the linker aromatic hydrogens (8–9 ppm) and amine hydrogens (0–4 ppm). Following dosing with $^{13}\text{CO}_2$, a broad poorly resolved ^1H NMR spectrum is observed (top). The increase of linewidth in the spectrum likely arises from a reduction in amine dynamics following the formation of ammonium carbamate chains upon $^{13}\text{CO}_2$ adsorption. Asterisks mark spinning side bands.

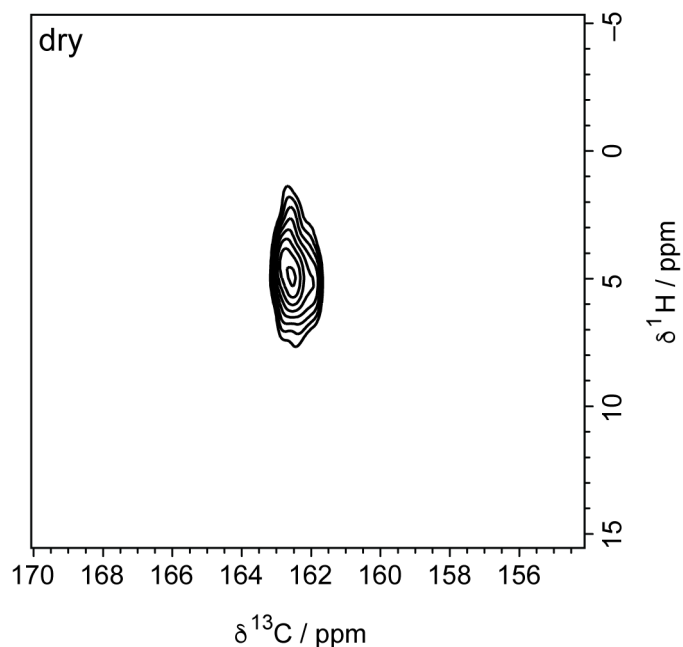


Figure 3.S89. Solid-state ^1H - ^{13}C HETCOR experiment (contact time for cross polarization = 100 μs) for dry, $^{13}\text{CO}_2$ -dosed 2-ampd-Mg₂(dobpdc). The sample spinning rate was 15 kHz.

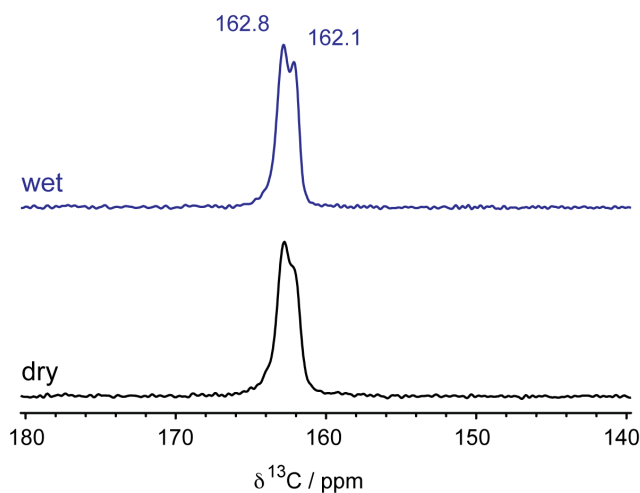


Figure 3.S90. Solid-state ^{13}C NMR (16.4 T) MAS spectra of a second sample of 2-ampd-Mg₂(dobpdc) dosed with 1009 mbar of $^{13}\text{CO}_2$ for 5 h; this data was collected in order to independently validate the spectra in Figure 6a of the main text. Spectra were obtained by cross-polarization from ^1H (contact time = 1 ms). Spectra are shown following initial gas dosing with dry $^{13}\text{CO}_2$ (with a longer dosing time of 5 h), as well as following subsequent treatment with humid CO_2 at natural isotopic abundance. These spectra are analogous to those in Figure 3.6a, but a longer gas dosing time of 5 h was used. Notably the shoulder feature present at high frequencies (Figure 3.6a) appears to be diminished in intensity here, suggesting its presence may be associated with incomplete equilibration.

3.6.21 Additional DFT Figures and Details

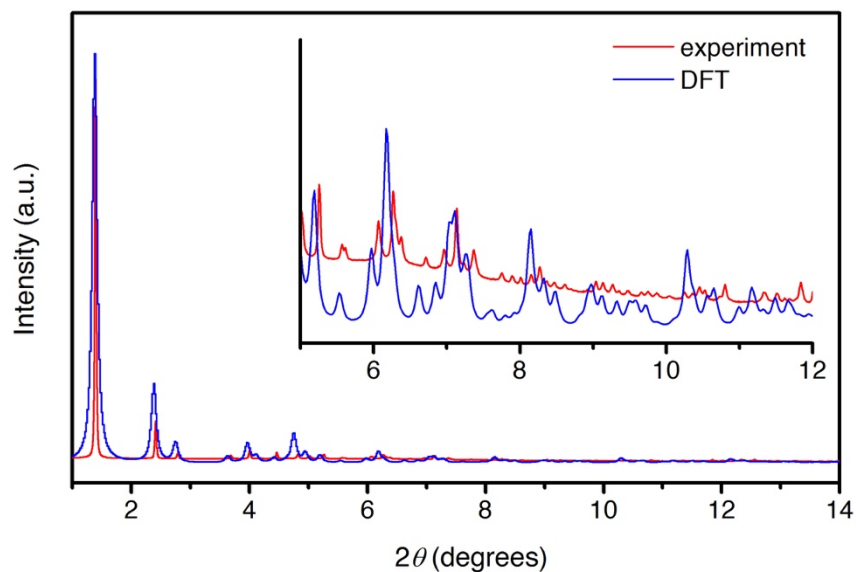


Figure 3.S91. Comparison of the experimental synchrotron powder X-ray diffraction pattern of evacuated 2-ampd-Mg₂(dobpdc) at 300 K (red, $\lambda = 0.45399$ Å) and the powder diffraction pattern simulated from the DFT-calculated structure of 2-ampd-Mg₂(dobpdc) at 0 K (blue). The inset shows an enlargement of the low-angle region.

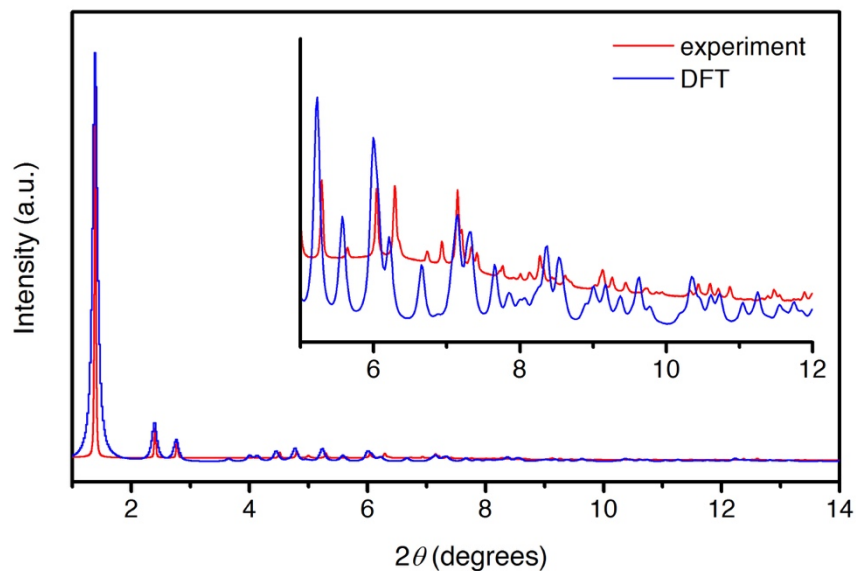


Figure 3.S92. Comparison of the experimental synchrotron powder X-ray diffraction pattern of 2-ampd-Mg₂(dobpdc) under 970 mbar of CO₂ at 300 K (red, $\lambda = 0.45399$ Å) and the powder diffraction pattern simulated from the DFT-calculated structure of Mg₂(dobpdc)(2-ampd-CO₂)₂ at 0 K (blue). The inset shows an enlargement of the low-angle region.

Table 3.S17. Lattice parameters for DFT-calculated structures in space group $P3_121$.

	$\text{Mg}_2(\text{dobpdc})(2\text{-ampd})_2$	$\text{Mg}_2(\text{dobpdc})(2\text{-ampd}-\text{CO}_2)_2$	$\text{Mg}_2(\text{dobpdc})(2\text{-ampd})_2(\text{H}_2\text{O})_2$	$\text{Mg}_2(\text{dobpdc})(2\text{-ampd}-\text{CO}_2)_2(\text{H}_2\text{O})_2$
a (Å)	21.9537	21.8601	21.9059	21.7949
c (Å)	7.0093	6.9379	7.0306	7.0185
Volume (Å ³)	2925.61	2871.20	2921.77	2887.2470

To obtain the σ_{ref} values for ^1H , ^{13}C , and ^{15}N , we performed structural relaxations and NMR calculations for cocaine and glycine crystals with vdW-DF2 functional.⁷⁰ We use Γ -point sampling of the Brillouin zone and a 1000 eV plane-wave cutoff energy. The ions were relaxed until the forces were less than 0.01 eV Å⁻¹. Figure 3.S93 shows the optimized structures of cocaine and glycine molecular crystals; their lattice parameters appear in Table 3.S18.

Since the measured NMR chemical shift δ (net magnetic field \mathbf{B}) is a difference between the absolute σ_{ref} (external magnetic field \mathbf{B}_0) and induced σ_{ind} (induced magnetic field \mathbf{B}_{ind}) NMR shieldings, and since only σ_{ind} is accessible with DFT, we need σ_{ref} to compare the DFT-computed σ_{ind} to the measured δ . By computing σ_{ind} for molecules well-studied by solid-state NMR spectroscopy^{63,72}, such as cocaine and glycine, and then comparing the computed σ_{ind} to the measured δ , we are able to get σ_{ref} for these reference molecules and apply σ_{ref} to other systems having the same isotopes (^1H , ^{13}C , and ^{15}N).

For the cocaine molecule, there are many ^1H and ^{13}C magnetic resonances that are well-assigned by solid-state NMR spectroscopy.⁷² Thus, we plot measured δ_{iso}^{exp} vs computed σ_{iso}^{DFT} for ^1H and ^{13}C as shown in Figure 3.S94. In δ_{iso}^{exp} vs σ_{iso}^{DFT} (see Figure 3.S94), we assume a slope of -1 and find the intercept (σ_{ref}) from a linear fit since $\delta_{iso}^{exp} = -(\sigma_{iso}^{DFT} - \sigma_{ref})$. The computed σ_{ref} for ^1H and ^{13}C are 31.4 ppm and 160.1 ppm, respectively. For glycine, there is a well-defined ^{15}N resonance.⁶³ The σ_{iso}^{DFT} and δ_{iso}^{exp} of ^{15}N are 182.5 ppm and 33.4 ppm. Thus, the σ_{ref} of ^{15}N becomes 215.9 ppm. Tables 3.S19 and 3.S20 show the computed σ_{iso} and δ_{iso} for 2-ampd- $\text{Mg}_2(\text{dobpdc})$.

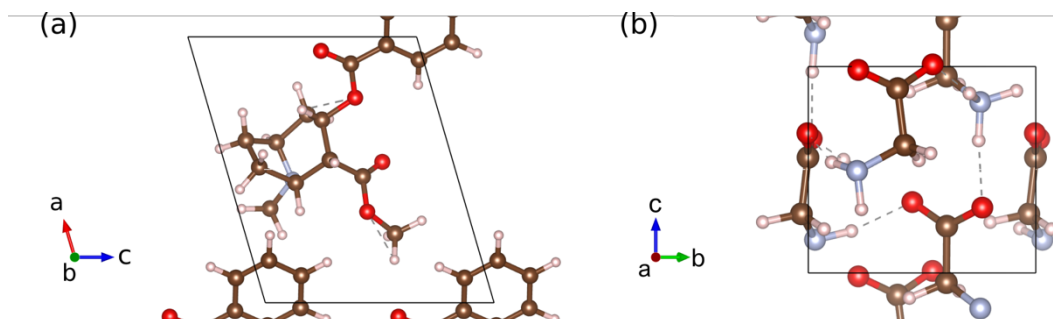
**Figure 3.S93.** Optimized molecular structures of (a) cocaine and (b) glycine.

Table 3.S18. Lattice parameters optimized with vdW-DF2 functional of the cocaine and glycine molecular crystals compared to experimental values. Their space groups are $P2_1$ and $P3_1$, respectively.

	Cocaine		Glycine	
	DFT	Experiment ¹³¹	DFT	Experiment ¹³²
a (Å)	10.187	10.130	7.125	7.037
b (Å)	9.671	9.866	7.125	7.037
c (Å)	8.424	8.445	5.594	5.483
α (°)	90	90	90	90
β (°)	106.251	106.920	90	90
γ (°)	90	90	120	120

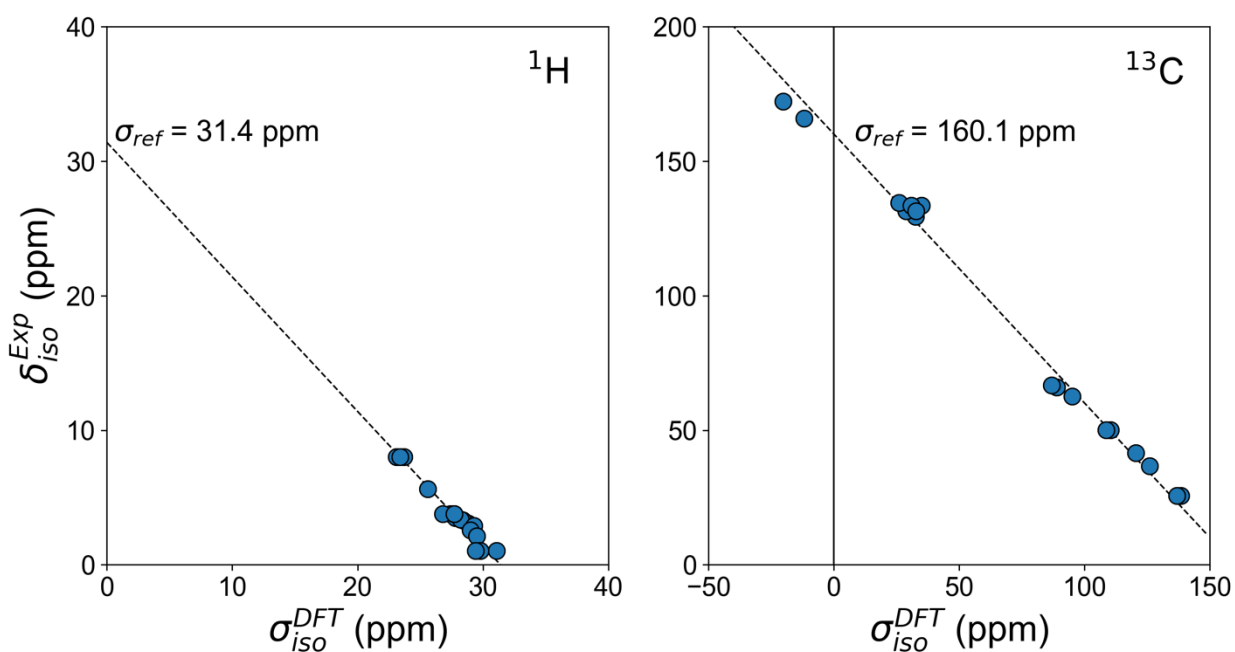


Figure 3.S94. Experimental δ_{iso}^{exp} vs computed σ_{iso}^{DFT} for ^1H and ^{13}C in cocaine. The dotted lines represent $\delta_{iso}^{exp} = -(\sigma_{iso}^{DFT} - \sigma_{ref})$.

Table 3.S19. Calculated σ_{iso} values for 2-ampd-Mg₂(dobpdc). Not applicable: N/A.

	DFT, Dry CO₂	DFT, Humid CO₂
$\sigma^{13}\text{C}$ (ppm) COO ⁻	-6.9	-6.8
$\sigma^1\text{H}$ (ppm) NHCOO ⁻	27.5	24.4
HOH...COO ⁻	N/A	25.8
HOH...COO ⁻	N/A	31.3
$\sigma^{15}\text{N}$ (ppm) RNHCOO ⁻	136.1	131.0
R ₂ NH ₂ ...COO ⁻	164.4	164.2

Table 3.S20. Comparison of experimental and DFT-calculated NMR shifts for 2-ampd-Mg₂(dobpdc). In a previous NMR and computational study of diamine-appended frameworks,⁶⁰ root-mean-square deviations of 1.3 ppm for ¹H, 2.2 ppm for ¹³C, and 6.3 ppm for ¹⁵N were observed between experimental and vdW-corrected DFT values. Not applicable: N/A.

	DFT, Dry CO₂	Experiment, Dry CO₂	DFT, Humid CO₂	Experiment, Humid CO₂
$\delta^{13}\text{C}$ (ppm) COO ⁻	167.0	162, 163	166.9	162.2, 162.9
$\delta^1\text{H}$ (ppm) NHCOO ⁻	3.9	broad, 0–10	7.0	~5
HOH...COO ⁻	N/A	N/A	5.6	9
HOH...COO ⁻	N/A	N/A	0.1	3
$\delta^{15}\text{N}$ (ppm) RNHCOO ⁻	79.8	76	84.9	not measured
R ₂ NH ₂ ...COO ⁻	51.5	46	51.7	not measured

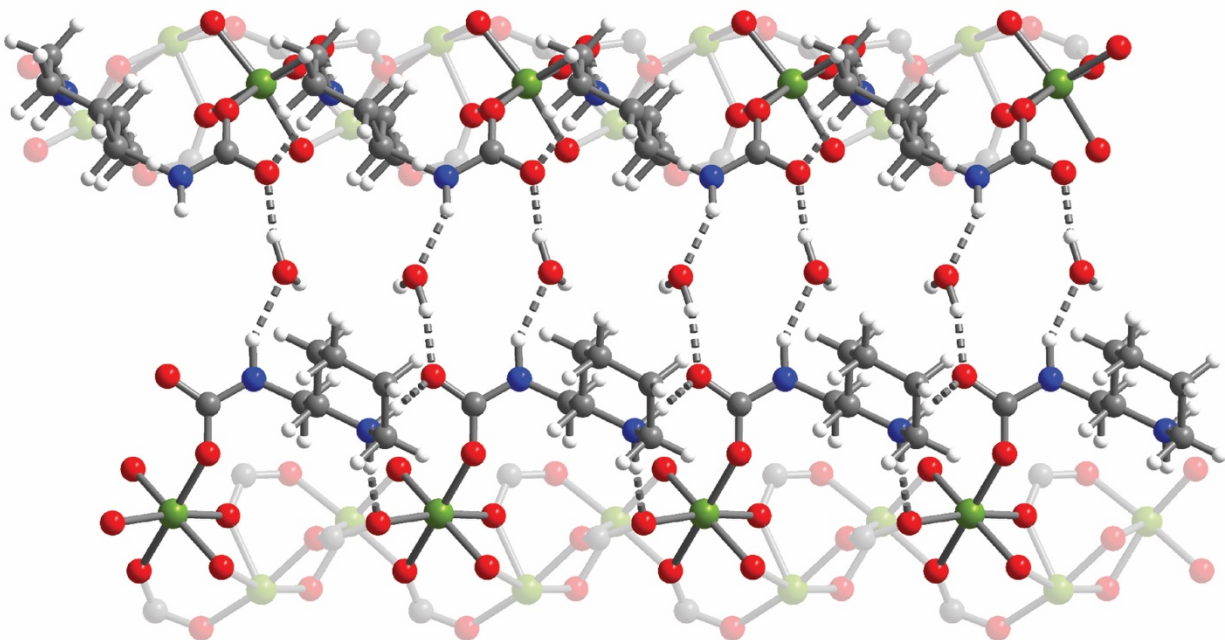


Figure 3.S95. Additional view of the vdW-corrected DFT structure of $\text{Mg}_2(\text{dobpdc})(2\text{-ampd-CO}_2)_2(\text{H}_2\text{O})_2$ showing a channel of water molecules hydrogen bonded to the carbamate groups of two adjacent ammonium carbamate chains along the c axis of the framework. Green, blue, gray, red, and white spheres represent Mg, N, C, O, and H atoms, respectively.

3.7. References

- (1) *CO₂ Emissions from Fuel Combustion 2017 - Highlights*; International Energy Agency: Paris, France, 2017.
- (2) Pachauri, R. K.; Allen, M. R.; Barros, V. R.; Broome, J.; Cramer, W.; Christ, R.; Church, J. A.; Clarke, L.; Dahe, Q.; Dasgupta, P. *Climate Change 2014: Synthesis Report. Contribution of Working Groups I, II and III to the Fifth Assessment Report of the Intergovernmental Panel on Climate Change*; IPCC, 2014.
- (3) Chu, S. Carbon Capture and Sequestration. *Science* **2009**, 325 (5948), 1599–1599. <https://doi.org/10.1126/science.1181637>.
- (4) Bui, M.; Adjiman, C. S.; Bardow, A.; Anthony, E. J.; Boston, A.; Brown, S.; Fennell, P. S.; Fuss, S.; Galindo, A.; Hackett, L. A.; Hallett, J. P.; Herzog, H. J.; Jackson, G.; Kemper, J.; Krevor, S.; Maitland, G. C.; Matuszewski, M.; Metcalfe, I. S.; Petit, C.; Puxty, G.; Reimer, J.; Reiner, D. M.; Rubin, E. S.; Scott, S. A.; Shah, N.; Smit, B.; Trusler, J. P. M.; Webley, P.; Wilcox, J.; Mac Dowell, N. Carbon Capture and Storage (CCS): The Way Forward. *Energy Environ. Sci.* **2018**, 11, 1062–1076. <https://doi.org/10.1039/C7EE02342A>.
- (5) Stauffer, P. H.; Keating, G. N.; Middleton, R. S.; Viswanathan, H. S.; Berchtold, K. A.; Singh, R. P.; Pawar, R. J.; Mancino, A. Greening Coal: Breakthroughs and Challenges in Carbon Capture and Storage. *Environ. Sci. Technol.* **2011**, 45 (20), 8597–8604. <https://doi.org/10.1021/es200510f>.
- (6) *World Energy Outlook 2017*; International Energy Agency, 2017. <https://doi.org/10.1787/weo-2017-en>.
- (7) *Annual Energy Outlook 2018 with Projections to 2050*; U.S. Energy Information Administration, 2018.
- (8) *CO₂ Capture at Gas Fired Power Plants*; IEAGHG, 2012.
- (9) *Carbon Dioxide Capture for Natural Gas and Industrial Applications*; Quadrennial Technology Review 2015; U.S. Department of Energy, 2015.
- (10) *Carbon Capture Opportunities for Natural Gas Fired Power Systems*; U.S. Department of Energy, 2017.
- (11) *Cost and Performance Baseline for Fossil Energy Plants. Volume 1a: Bituminous Coal (PC) and Natural Gas to Electricity. Revision 3*; DOE/NETL-2015/1723; U.S. Department of Energy, National Energy Technology Laboratory, 2015.
- (12) Khatri, R. A.; Chuang, S. S. C.; Soong, Y.; Gray, M. Thermal and Chemical Stability of Regenerable Solid Amine Sorbent for CO₂ Capture. *Energy Fuels* **2006**, 20 (4), 1514–1520. <https://doi.org/10.1021/ef050402y>.
- (13) Uyanga, I. J.; Idem, R. O. Studies of SO₂- and O₂-Induced Degradation of Aqueous MEA during CO₂ Capture from Power Plant Flue Gas Streams. *Ind. Eng. Chem. Res.* **2007**, 46 (8), 2558–2566. <https://doi.org/10.1021/ie0614024>.
- (14) Belmabkhout, Y.; Sayari, A. Isothermal versus Non-Isothermal Adsorption–Desorption Cycling of Triamine-Grafted Pore-Expanded MCM-41 Mesoporous Silica for CO₂ Capture from Flue Gas. *Energy Fuels* **2010**, 24 (9), 5273–5280. <https://doi.org/10.1021/ef100679e>.
- (15) Sjoström, S.; Krutka, H. Evaluation of Solid Sorbents as a Retrofit Technology for CO₂ Capture. *Fuel* **2010**, 89 (6), 1298–1306. <https://doi.org/10.1016/j.fuel.2009.11.019>.

- (16) Han, S.; Huang, Y.; Watanabe, T.; Dai, Y.; Walton, K. S.; Nair, S.; Sholl, D. S.; Meredith, J. C. High-Throughput Screening of Metal–Organic Frameworks for CO₂ Separation. *ACS Comb. Sci.* **2012**, *14* (4), 263–267. <https://doi.org/10.1021/co3000192>.
- (17) Yu, K.; Kiesling, K.; Schmidt, J. R. Trace Flue Gas Contaminants Poison Coordinatively Unsaturated Metal–Organic Frameworks: Implications for CO₂ Adsorption and Separation. *J. Phys. Chem. C* **2012**, *116* (38), 20480–20488. <https://doi.org/10.1021/jp307894e>.
- (18) Hallenbeck, A. P.; Kitchin, J. R. Effects of O₂ and SO₂ on the Capture Capacity of a Primary-Amine Based Polymeric CO₂ Sorbent. *Ind. Eng. Chem. Res.* **2013**, *52* (31), 10788–10794. <https://doi.org/10.1021/ie400582a>.
- (19) Rezaei, F.; Jones, C. W. Stability of Supported Amine Adsorbents to SO₂ and NO_x in Postcombustion CO₂ Capture. 1. Single-Component Adsorption. *Ind. Eng. Chem. Res.* **2013**, *52* (34), 12192–12201. <https://doi.org/10.1021/ie4019116>.
- (20) Berger, A. H.; Bhowan, A. S. Selection of Optimal Solid Sorbents for CO₂ Capture Based on Gas Phase CO₂ Composition. *Energy Procedia* **2014**, *63*, 2092–2099. <https://doi.org/10.1016/j.egypro.2014.11.225>.
- (21) Rezaei, F.; Grahn, M. Thermal Management of Structured Adsorbents in CO₂ Capture Processes. *Ind. Eng. Chem. Res.* **2012**, *51* (10), 4025–4034. <https://doi.org/10.1021/ie201057p>.
- (22) Rochelle, G. T. Amine Scrubbing for CO₂ Capture. *Science* **2009**, *325* (5948), 1652–1654. <https://doi.org/10.1126/science.1176731>.
- (23) Bhowan, A. S.; Freeman, B. C. Analysis and Status of Post-Combustion Carbon Dioxide Capture Technologies. *Environ. Sci. Technol.* **2011**, *45* (20), 8624–8632. <https://doi.org/10.1021/es104291d>.
- (24) Gouedard, C.; Picq, D.; Launay, F.; Carrette, P.-L. Amine Degradation in CO₂ Capture. I. A Review. *Int. J. Greenh. Gas Control* **2012**, *10*, 244–270. <https://doi.org/10.1016/j.ijggc.2012.06.015>.
- (25) Fredriksen, S. B.; Jens, K.-J. Oxidative Degradation of Aqueous Amine Solutions of MEA, AMP, MDEA, Pz: A Review. *Energy Procedia* **2013**, *37*, 1770–1777. <https://doi.org/10.1016/j.egypro.2013.06.053>.
- (26) Vega, F.; Sanna, A.; Navarrete, B.; Maroto-Valer, M. M.; Cortés, V. J. Degradation of Amine-based Solvents in CO₂ Capture Process by Chemical Absorption. *Greenh. Gases Sci. Technol.* **2014**, *4* (6), 707–733. <https://doi.org/10.1002/ghg.1446>.
- (27) Mazari, S. A.; Si Ali, B.; Jan, B. M.; Saeed, I. M.; Nizamuddin, S. An Overview of Solvent Management and Emissions of Amine-Based CO₂ Capture Technology. *Int. J. Greenh. Gas Control* **2015**, *34*, 129–140. <https://doi.org/10.1016/j.ijggc.2014.12.017>.
- (28) Choi, S.; Drese, J. H.; Jones, C. W. Adsorbent Materials for Carbon Dioxide Capture from Large Anthropogenic Point Sources. *ChemSusChem* **2009**, *2* (9), 796–854. <https://doi.org/10.1002/cssc.200900036>.
- (29) Bae, Y.-S.; Snurr, R. Q. Development and Evaluation of Porous Materials for Carbon Dioxide Separation and Capture. *Angew. Chem. Int. Ed.* **2011**, *50* (49), 11586–11596. <https://doi.org/10.1002/anie.201101891>.
- (30) Bollini, P.; Didas, S. A.; Jones, C. W. Amine-Oxide Hybrid Materials for Acid Gas Separations. *J. Mater. Chem.* **2011**, *21* (39), 15100–15120. <https://doi.org/10.1039/C1JM12522B>.

- (31) Li, J.-R.; Ma, Y.; McCarthy, M. C.; Sculley, J.; Yu, J.; Jeong, H.-K.; Balbuena, P. B.; Zhou, H.-C. Carbon Dioxide Capture-Related Gas Adsorption and Separation in Metal-Organic Frameworks. *Coord. Chem. Rev.* **2011**, *255* (15–16), 1791–1823. <https://doi.org/10.1016/j.ccr.2011.02.012>.
- (32) Wang, Q.; Luo, J.; Zhong, Z.; Borgna, A. CO₂ Capture by Solid Adsorbents and Their Applications: Current Status and New Trends. *Energy Env. Sci* **2011**, *4* (1), 42–55. <https://doi.org/10.1039/C0EE00064G>.
- (33) Liu, J.; Thallapally, P. K.; McGrail, B. P.; Brown, D. R.; Liu, J. Progress in Adsorption-Based CO₂ Capture by Metal–Organic Frameworks. *Chem Soc Rev* **2012**, *41* (6), 2308–2322. <https://doi.org/10.1039/C1CS15221A>.
- (34) Samanta, A.; Zhao, A.; Shimizu, G. K. H.; Sarkar, P.; Gupta, R. Post-Combustion CO₂ Capture Using Solid Sorbents: A Review. *Ind. Eng. Chem. Res.* **2012**, *51* (4), 1438–1463. <https://doi.org/10.1021/ie200686q>.
- (35) Sumida, K.; Rogow, D. L.; Mason, J. A.; McDonald, T. M.; Bloch, E. D.; Herm, Z. R.; Bae, T.-H.; Long, J. R. Carbon Dioxide Capture in Metal–Organic Frameworks. *Chem. Rev.* **2012**, *112* (2), 724–781. <https://doi.org/10.1021/cr2003272>.
- (36) Huck, J. M.; Lin, L.-C.; Berger, A. H.; Shahrak, M. N.; Martin, R. L.; Bhowm, A. S.; Haranczyk, M.; Reuter, K.; Smit, B. Evaluating Different Classes of Porous Materials for Carbon Capture. *Energy Environ. Sci.* **2014**, *7* (12), 4132–4146. <https://doi.org/10.1039/C4EE02636E>.
- (37) Webley, P. A. Adsorption Technology for CO₂ Separation and Capture: A Perspective. *Adsorption* **2014**, *20* (2–3), 225–231. <https://doi.org/10.1007/s10450-014-9603-2>.
- (38) Lee, S.-Y.; Park, S.-J. A Review on Solid Adsorbents for Carbon Dioxide Capture. *J. Ind. Eng. Chem.* **2015**, *23*, 1–11. <https://doi.org/10.1016/j.jiec.2014.09.001>.
- (39) Sanz-Pérez, E. S.; Murdock, C. R.; Didas, S. A.; Jones, C. W. Direct Capture of CO₂ from Ambient Air. *Chem. Rev.* **2016**, *116* (19), 11840–11876. <https://doi.org/10.1021/acs.chemrev.6b00173>.
- (40) Ünveren, E. E.; Monkul, B. Ö.; Sariođlan, Ş.; Karademir, N.; Alper, E. Solid Amine Sorbents for CO₂ Capture by Chemical Adsorption: A Review. *Petroleum* **2017**, *3* (1), 37–50. <https://doi.org/10.1016/j.petlm.2016.11.001>.
- (41) Siegelman, R. L.; Milner, P. J.; Kim, E. J.; Weston, S. C.; Long, J. R. Challenges and Opportunities for Adsorption-Based CO₂ Capture from Natural Gas Combined Cycle Emissions. *Energy Environ. Sci.* **2019**, *Advance Article*. <https://doi.org/10.1039/C9EE00505F>.
- (42) Xu, X.; Song, C.; Miller, B. G.; Scaroni, A. W. Adsorption Separation of Carbon Dioxide from Flue Gas of Natural Gas-Fired Boiler by a Novel Nanoporous “Molecular Basket” Adsorbent. *Fuel Process. Technol.* **2005**, *86* (14), 1457–1472. <https://doi.org/10.1016/j.fuproc.2005.01.002>.
- (43) Grande, C. A.; Ribeiro, R. P. P. L.; Rodrigues, A. E. CO₂ Capture from NGCC Power Stations Using Electric Swing Adsorption (ESA). *Energy Fuels* **2009**, *23* (5), 2797–2803. <https://doi.org/10.1021/ef8010756>.
- (44) Seif El Nasr, A.; Nelson, T.; Kataria, A.; Abu-Zahra, M. R. M. Benchmarking of a Novel Solid Sorbent CO₂ Capture Process for NGCC Power Generation. *Int. J. Greenh. Gas Control* **2015**, *42*, 583–592. <https://doi.org/10.1016/j.ijggc.2015.09.014>.

- (45) Hefti, M.; Joss, L.; Bjelobrk, Z.; Mazzotti, M. On the Potential of Phase-Change Adsorbents for CO₂ Capture by Temperature Swing Adsorption. *Faraday Discuss.* **2016**, *192*, 153–179. <https://doi.org/10.1039/C6FD00040A>.
- (46) Gibson, J. A. A.; Mangano, E.; Shiko, E.; Greenaway, A. G.; Gromov, A. V.; Lozinska, M. M.; Friedrich, D.; Campbell, E. E. B.; Wright, P. A.; Brandani, S. Adsorption Materials and Processes for Carbon Capture from Gas-Fired Power Plants: AMPGas. *Ind. Eng. Chem. Res.* **2016**, *55* (13), 3840–3851. <https://doi.org/10.1021/acs.iecr.5b05015>.
- (47) Zhang, W.; Sun, C.; Snape, C. E.; Irons, R.; Stebbing, S.; Alderson, T.; Fitzgerald, D.; Liu, H. Process Simulations of Post-Combustion CO₂ Capture for Coal and Natural Gas-Fired Power Plants Using a Polyethyleneimine/Silica Adsorbent. *Int. J. Greenh. Gas Control* **2017**, *58*, 276–289. <https://doi.org/10.1016/j.ijggc.2016.12.003>.
- (48) Dijkstra, J. W.; Walspurger, S.; Elzinga, G. D.; Pieterse, J. A. Z.; Boon, J.; Haije, W. G. Evaluation of Postcombustion CO₂ Capture by a Solid Sorbent with Process Modeling Using Experimental CO₂ and H₂O Adsorption Characteristics. *Ind. Eng. Chem. Res.* **2018**, *57* (4), 1245–1261. <https://doi.org/10.1021/acs.iecr.7b03552>.
- (49) McDonald, T. M.; Lee, W. R.; Mason, J. A.; Wiers, B. M.; Hong, C. S.; Long, J. R. Capture of Carbon Dioxide from Air and Flue Gas in the Alkylamine-Appended Metal–Organic Framework mmen-Mg₂(dobpdc). *J. Am. Chem. Soc.* **2012**, *134* (16), 7056–7065. <https://doi.org/10.1021/ja300034j>.
- (50) McDonald, T. M.; Mason, J. A.; Kong, X.; Bloch, E. D.; Gygi, D.; Dani, A.; Crocellà, V.; Giordanino, F.; Odoh, S. O.; Drisdell, W. S.; Vlasisavljevich, B.; Dzubak, A. L.; Poloni, R.; Schnell, S. K.; Planas, N.; Lee, K.; Pascal, T.; Wan, L. F.; Prendergast, D.; Neaton, J. B.; Smit, B.; Kortright, J. B.; Gagliardi, L.; Bordiga, S.; Reimer, J. A.; Long, J. R. Cooperative Insertion of CO₂ in Diamine-Appended Metal–Organic Frameworks. *Nature* **2015**, *519* (7543), 303–308. <https://doi.org/10.1038/nature14327>.
- (51) Siegelman, R. L.; McDonald, T. M.; Gonzalez, M. I.; Martell, J. D.; Milner, P. J.; Mason, J. A.; Berger, A. H.; Bhowan, A. S.; Long, J. R. Controlling Cooperative CO₂ Adsorption in Diamine-Appended Mg₂(dobpdc) Metal–Organic Frameworks. *J. Am. Chem. Soc.* **2017**, *139* (30), 10526–10538. <https://doi.org/10.1021/jacs.7b05858>.
- (52) Milner, P. J.; Siegelman, R. L.; Forse, A. C.; Gonzalez, M. I.; Runčevski, T.; Martell, J. D.; Reimer, J. A.; Long, J. R. A Diaminopropane-Appended Metal–Organic Framework Enabling Efficient CO₂ Capture from Coal Flue Gas via a Mixed Adsorption Mechanism. *J. Am. Chem. Soc.* **2017**, *139* (38), 13541–13553. <https://doi.org/10.1021/jacs.7b07612>.
- (53) Milner, P. J.; Martell, J. D.; Siegelman, R. L.; Gygi, D.; Weston, S. C.; Long, J. R. Overcoming Double-Step CO₂ Adsorption and Minimizing Water Co-Adsorption in Bulky Diamine-Appended Variants of Mg₂(dobpdc). *Chem. Sci.* **2018**, *9* (1), 160–174. <https://doi.org/10.1039/C7SC04266C>.
- (54) Lee, W. R.; Hwang, S. Y.; Ryu, D. W.; Lim, K. S.; Han, S. S.; Moon, D.; Choi, J.; Hong, C. S. Diamine-Functionalized Metal–Organic Framework: Exceptionally High CO₂ Capacities from Ambient Air and Flue Gas, Ultrafast CO₂ Uptake Rate, and Adsorption Mechanism. *Energy Environ. Sci.* **2014**, *7* (2), 744–751. <https://doi.org/10.1039/C3EE42328J>.
- (55) Lee, W. R.; Jo, H.; Yang, L.-M.; Lee, H.; Ryu, D. W.; Lim, K. S.; Song, J. H.; Min, D. Y.; Han, S. S.; Seo, J. G.; Park, Y. K.; Moon, D.; Hong, C. S. Exceptional CO₂ Working Capacity in a Heterodiamine-Grafted Metal–Organic Framework. *Chem. Sci.* **2015**, *6* (7), 3697–3705. <https://doi.org/10.1039/C5SC01191D>.

- (56) Jo, H.; Lee, W. R.; Kim, N. W.; Jung, H.; Lim, K. S.; Kim, J. E.; Kang, D. W.; Lee, H.; Hiremath, V.; Seo, J. G.; Jin, H.; Moon, D.; Han, S. S.; Hong, C. S. Fine-Tuning of the Carbon Dioxide Capture Capability of Diamine-Grafted Metal–Organic Framework Adsorbents Through Amine Functionalization. *ChemSusChem* **2017**, *10* (3), 541–550. <https://doi.org/10.1002/cssc.201601203>.
- (57) Lee, W. R.; Kim, J. E.; Lee, S. J.; Kang, M.; Kang, D. W.; Lee, H. Y.; Hiremath, V.; Seo, J. G.; Jin, H.; Moon, D.; Cho, M.; Jung, Y.; Hong, C. S. Diamine-Functionalization of a Metal–Organic Framework Adsorbent for Superb Carbon Dioxide Adsorption and Desorption Properties. *ChemSusChem* **2018**, *11* (10), 1694–1707. <https://doi.org/10.1002/cssc.201800363>.
- (58) Kang, M.; Eun Kim, J.; Won Kang, D.; Young Lee, H.; Moon, D.; Seop Hong, C. A Diamine-Grafted Metal–Organic Framework with Outstanding CO₂ Capture Properties and a Facile Coating Approach for Imparting Exceptional Moisture Stability. *J. Mater. Chem. A* **2019**, *7* (14), 8177–8183. <https://doi.org/10.1039/C8TA07965J>.
- (59) Mosaic Materials, Inc. <http://mosaicmaterials.com/>.
- (60) Forse, A. C.; Milner, P. J.; Lee, J.-H.; Redfearn, H. N.; Oktawiec, J.; Siegelman, R. L.; Martell, J. D.; Dinakar, B.; Porter-Zasada, L. B.; Gonzalez, M. I.; Neaton, J. B.; Long, J. R.; Reimer, J. A. Elucidating CO₂ Chemisorption in Diamine-Appended Metal–Organic Frameworks. *J. Am. Chem. Soc.* **2018**, *140* (51), 18016–18031. <https://doi.org/10.1021/jacs.8b10203>.
- (61) NIST WebBook <https://webbook.nist.gov/>.
- (62) Campbell, C. T.; Sellers, J. R. V. Enthalpies and Entropies of Adsorption on Well-Defined Oxide Surfaces: Experimental Measurements. *Chem. Rev.* **2013**, *113* (6), 4106–4135. <https://doi.org/10.1021/cr300329s>.
- (63) Bertani, P.; Raya, J.; Bechinger, B. ¹⁵N Chemical Shift Referencing in Solid State NMR. *Solid State Nucl. Magn. Reson.* **2014**, *61–62*, 15–18. <https://doi.org/10.1016/j.ssnmr.2014.03.003>.
- (64) Blöchl, P. E. Projector Augmented-Wave Method. *Phys. Rev. B* **1994**, *50* (24), 17953–17979. <https://doi.org/10.1103/PhysRevB.50.17953>.
- (65) Kresse, G.; Joubert, D. From Ultrasoft Pseudopotentials to the Projector Augmented-Wave Method. *Phys. Rev. B* **1999**, *59* (3), 1758–1775. <https://doi.org/10.1103/PhysRevB.59.1758>.
- (66) Kresse, G.; Hafner, J. Ab Initio Molecular Dynamics for Liquid Metals. *Phys. Rev. B* **1993**, *47* (1), 558–561. <https://doi.org/10.1103/PhysRevB.47.558>.
- (67) Kresse, G.; Hafner, J. Ab Initio Molecular-Dynamics Simulation of the Liquid-Metal–Amorphous-Semiconductor Transition in Germanium. *Phys. Rev. B* **1994**, *49* (20), 14251–14269. <https://doi.org/10.1103/PhysRevB.49.14251>.
- (68) Kresse, G.; Furthmüller, J. Efficient Iterative Schemes for Ab Initio Total-Energy Calculations Using a Plane-Wave Basis Set. *Phys. Rev. B* **1996**, *54* (16), 11169–11186. <https://doi.org/10.1103/PhysRevB.54.11169>.
- (69) Kresse, G.; Furthmüller, J. Efficiency of Ab-Initio Total Energy Calculations for Metals and Semiconductors Using a Plane-Wave Basis Set. *Comput. Mater. Sci.* **1996**, *6* (1), 15–50. [https://doi.org/10.1016/0927-0256\(96\)00008-0](https://doi.org/10.1016/0927-0256(96)00008-0).
- (70) Lee, K.; Murray, É. D.; Kong, L.; Lundqvist, B. I.; Langreth, D. C. Higher-Accuracy van Der Waals Density Functional. *Phys. Rev. B* **2010**, *82* (8), 081101. <https://doi.org/10.1103/PhysRevB.82.081101>.

- (71) Elsässer, C.; Fähnle, M.; Chan, C. T.; Ho, K. M. Density-Functional Energies and Forces with Gaussian-Broadened Fractional Occupations. *Phys. Rev. B* **1994**, *49* (19), 13975–13978. <https://doi.org/10.1103/PhysRevB.49.13975>.
- (72) Baias, M.; Widdifield, C. M.; Dumez, J.-N.; Thompson, H. P. G.; Cooper, T. G.; Salager, E.; Bassil, S.; Stein, R. S.; Lesage, A.; Day, G. M.; Emsley, L. Powder Crystallography of Pharmaceutical Materials by Combined Crystal Structure Prediction and Solid-State ¹H NMR Spectroscopy. *Phys. Chem. Chem. Phys.* **2013**, *15* (21), 8069–8080. <https://doi.org/10.1039/C3CP41095A>.
- (73) Ali, U.; Agbonghae, E. O.; Hughes, K. J.; Ingham, D. B.; Ma, L.; Pourkashanian, M. Techno-Economic Process Design of a Commercial-Scale Amine-Based CO₂ Capture System for Natural Gas Combined Cycle Power Plant with Exhaust Gas Recirculation. *Appl. Therm. Eng.* **2016**, *103*, 747–758. <https://doi.org/10.1016/j.applthermaleng.2016.04.145>.
- (74) Zhang, Z.; Yao, Z.-Z.; Xiang, S.; Chen, B. Perspective of Microporous Metal–Organic Frameworks for CO₂ Capture and Separation. *Energy Environ. Sci.* **2014**, *7* (9), 2868. <https://doi.org/10.1039/C4EE00143E>.
- (75) Sabouni, R.; Kazemian, H.; Rohani, S. Carbon Dioxide Capturing Technologies: A Review Focusing on Metal Organic Framework Materials (MOFs). *Environ. Sci. Pollut. Res.* **2014**, *21* (8), 5427–5449. <https://doi.org/10.1007/s11356-013-2406-2>.
- (76) Wang, Q.; Bai, J.; Lu, Z.; Pan, Y.; You, X. Finely Tuning MOFs towards High-Performance Post-Combustion CO₂ Capture Materials. *Chem. Commun.* **2016**, *52* (3), 443–452. <https://doi.org/10.1039/C5CC07751F>.
- (77) Yu, J.; Xie, L.-H.; Li, J.-R.; Ma, Y.; Seminario, J. M.; Balbuena, P. B. CO₂ Capture and Separations Using MOFs: Computational and Experimental Studies. *Chem. Rev.* **2017**, *117* (14), 9674–9754. <https://doi.org/10.1021/acs.chemrev.6b00626>.
- (78) Alkhabbaz, M. A.; Bollini, P.; Foo, G. S.; Sievers, C.; Jones, C. W. Important Roles of Enthalpic and Entropic Contributions to CO₂ Capture from Simulated Flue Gas and Ambient Air Using Mesoporous Silica Grafted Amines. *J. Am. Chem. Soc.* **2014**, *136* (38), 13170–13173. <https://doi.org/10.1021/ja507655x>.
- (79) Xu, X.; Song, C.; Andresen, J. M.; Miller, B. G.; Scaroni, A. W. Novel Polyethylenimine-Modified Mesoporous Molecular Sieve of MCM-41 Type as High-Capacity Adsorbent for CO₂ Capture. *Energy Fuels* **2002**, *16* (6), 1463–1469. <https://doi.org/10.1021/ef020058u>.
- (80) Mason, J. A.; McDonald, T. M.; Bae, T.-H.; Bachman, J. E.; Sumida, K.; Dutton, J. J.; Kaye, S. S.; Long, J. R. Application of a High-Throughput Analyzer in Evaluating Solid Adsorbents for Post-Combustion Carbon Capture via Multicomponent Adsorption of CO₂, N₂, and H₂O. *J. Am. Chem. Soc.* **2015**, *137* (14), 4787–4803. <https://doi.org/10.1021/jacs.5b00838>.
- (81) Liao, P.-Q.; Chen, X.-W.; Liu, S.-Y.; Li, X.-Y.; Xu, Y.-T.; Tang, M.; Rui, Z.; Ji, H.; Zhang, J.-P.; Chen, X.-M. Putting an Ultrahigh Concentration of Amine Groups into a Metal–Organic Framework for CO₂ Capture at Low Pressures. *Chem. Sci.* **2016**, *7* (10), 6528–6533. <https://doi.org/10.1039/C6SC00836D>.
- (82) Bien, C. E.; Chen, K. K.; Chien, S.-C.; Reiner, B. R.; Lin, L.-C.; Wade, C. R.; Ho, W. S. W. Bioinspired Metal–Organic Framework for Trace CO₂ Capture. *J. Am. Chem. Soc.* **2018**, *140* (40), 12662–12666. <https://doi.org/10.1021/jacs.8b06109>.
- (83) Darunte, L.; Sen, T.; Bhawanani, C.; Walton, K. S.; Sholl, D. S.; Realff, M. J.; Jones, C. W. Moving Beyond Adsorption Capacity in Design of Adsorbents for CO₂ Capture from

- Ultra-Dilute Feeds: Kinetics of CO₂ Adsorption in Materials with Stepped Isotherms. *Ind. Eng. Chem. Res.* **2019**, *58* (1), 366–377. <https://doi.org/10.1021/acs.iecr.8b05042>.
- (84) Zhang, W.; Shan, Y.; Seidel-Morgenstern, A. Breakthrough Curves and Elution Profiles of Single Solutes in Case of Adsorption Isotherms with Two Inflection Points. *J. Chromatogr. A* **2006**, *1107* (1–2), 216–225. <https://doi.org/10.1016/j.chroma.2005.12.094>.
- (85) Helfferich, F. G.; Carr, P. W. Non-Linear Waves in Chromatography. *J. Chromatogr. A* **1993**, *629* (2), 97–122. [https://doi.org/10.1016/0021-9673\(93\)87026-I](https://doi.org/10.1016/0021-9673(93)87026-I).
- (86) Golden, F. M. Theory of Fixed-Bed Performance for Ion Exchange Accompanied by Chemical Reaction. Ph.D. Thesis, University of California, Berkeley: United States, 1973.
- (87) Satyapal, S.; Filburn, T.; Trela, J.; Strange, J. Performance and Properties of a Solid Amine Sorbent for Carbon Dioxide Removal in Space Life Support Applications. *Energy Fuels* **2001**, *15* (2), 250–255. <https://doi.org/10.1021/ef0002391>.
- (88) Huang, H. Y.; Yang, R. T.; Chinn, D.; Munson, C. L. Amine-Grafted MCM-48 and Silica Xerogel as Superior Sorbents for Acidic Gas Removal from Natural Gas. *Ind. Eng. Chem. Res.* **2003**, *42* (12), 2427–2433. <https://doi.org/10.1021/ie020440u>.
- (89) Xu, X.; Song, C.; Miller, B. G.; Scaroni, A. W. Influence of Moisture on CO₂ Separation from Gas Mixture by a Nanoporous Adsorbent Based on Polyethylenimine-Modified Molecular Sieve MCM-41. *Ind. Eng. Chem. Res.* **2005**, *44* (21), 8113–8119. <https://doi.org/10.1021/ie050382n>.
- (90) Serna-Guerrero, R.; Belmabkhout, Y.; Sayari, A. Further Investigations of CO₂ Capture Using Triamine-Grafted Pore-Expanded Mesoporous Silica. *Chem. Eng. J.* **2010**, *158* (3), 513–519. <https://doi.org/10.1016/j.cej.2010.01.041>.
- (91) Serna-Guerrero, R.; Belmabkhout, Y.; Sayari, A. Triamine-Grafted Pore-Expanded Mesoporous Silica for CO₂ Capture: Effect of Moisture and Adsorbent Regeneration Strategies. *Adsorption* **2010**, *16* (6), 567–575. <https://doi.org/10.1007/s10450-010-9253-y>.
- (92) Goeppert, A.; Czaun, M.; May, R. B.; Prakash, G. K. S.; Olah, G. A.; Narayanan, S. R. Carbon Dioxide Capture from the Air Using a Polyamine Based Regenerable Solid Adsorbent. *J. Am. Chem. Soc.* **2011**, *133* (50), 20164–20167. <https://doi.org/10.1021/ja2100005>.
- (93) Fan, Y.; Lively, R. P.; Labreche, Y.; Rezaei, F.; Koros, W. J.; Jones, C. W. Evaluation of CO₂ Adsorption Dynamics of Polymer/Silica Supported Poly(ethylenimine) Hollow Fiber Sorbents in Rapid Temperature Swing Adsorption. *Int. J. Greenh. Gas Control* **2014**, *21*, 61–71. <https://doi.org/10.1016/j.ijggc.2013.11.021>.
- (94) Didas, S. A.; Sakwa-Novak, M. A.; Foo, G. S.; Sievers, C.; Jones, C. W. Effect of Amine Surface Coverage on the Co-Adsorption of CO₂ and Water: Spectral Deconvolution of Adsorbed Species. *J. Phys. Chem. Lett.* **2014**, *5* (23), 4194–4200. <https://doi.org/10.1021/jz502032c>.
- (95) Hahn, M. W.; Steib, M.; Jentys, A.; Lercher, J. A. Mechanism and Kinetics of CO₂ Adsorption on Surface Bonded Amines. *J. Phys. Chem. C* **2015**, *119* (8), 4126–4135. <https://doi.org/10.1021/jp512001t>.
- (96) Wang, D.; Wang, X.; Song, C. Comparative Study of Molecular Basket Sorbents Consisting of Polyallylamine and Polyethylenimine Functionalized SBA-15 for CO₂ Capture from Flue Gas. *ChemPhysChem* **2017**, *18* (22), 3163–3173. <https://doi.org/10.1002/cphc.201700828>.

- (97) Zhang, H.; Goeppert, A.; Olah, G. A.; Prakash, G. K. S. Remarkable Effect of Moisture on the CO₂ Adsorption of Nano-Silica Supported Linear and Branched Polyethylenimine. *J. CO₂ Util.* **2017**, *19*, 91–99. <https://doi.org/10.1016/j.jcou.2017.03.008>.
- (98) Zhao, P.; Zhang, G.; Sun, Y.; Xu, Y. CO₂ Adsorption Behavior and Kinetics on Amine-Functionalized Composites Silica with Trimodal Nanoporous Structure. *Energy Fuels* **2017**, *31* (11), 12508–12520. <https://doi.org/10.1021/acs.energyfuels.7b02292>.
- (99) Leal, O.; Bolívar, C.; Ovalles, C.; García, J. J.; Espidel, Y. Reversible Adsorption of Carbon Dioxide on Amine Surface-Bonded Silica Gel. *Inorganica Chim. Acta* **1995**, *240* (1), 183–189. [https://doi.org/10.1016/0020-1693\(95\)04534-1](https://doi.org/10.1016/0020-1693(95)04534-1).
- (100) Chang, A. C. C.; Chuang, S. S. C.; Gray, M.; Soong, Y. In-Situ Infrared Study of CO₂ Adsorption on SBA-15 Grafted with γ -(Aminopropyl)Triethoxysilane. *Energy Fuels* **2003**, *17* (2), 468–473. <https://doi.org/10.1021/ef020176h>.
- (101) Khatri, R. A.; Chuang, S. S. C.; Soong, Y.; Gray, M. Carbon Dioxide Capture by Diamine-Grafted SBA-15: A Combined Fourier Transform Infrared and Mass Spectrometry Study. *Ind. Eng. Chem. Res.* **2005**, *44* (10), 3702–3708. <https://doi.org/10.1021/ie048997s>.
- (102) Moore, J. K.; Sakwa-Novak, M. A.; Chaikittisilp, W.; Mehta, A. K.; Conradi, M. S.; Jones, C. W.; Hayes, S. E. Characterization of a Mixture of CO₂ Adsorption Products in Hyperbranched Aminosilica Adsorbents by ¹³C Solid-State NMR. *Environ. Sci. Technol.* **2015**, *49* (22), 13684–13691. <https://doi.org/10.1021/acs.est.5b02930>.
- (103) Lee, J. J.; Chen, C.-H.; Shimon, D.; Hayes, S. E.; Sievers, C.; Jones, C. W. Effect of Humidity on the CO₂ Adsorption of Tertiary Amine Grafted SBA-15. *J. Phys. Chem. C* **2017**, *121* (42), 23480–23487. <https://doi.org/10.1021/acs.jpcc.7b07930>.
- (104) Yu, J.; Chuang, S. S. C. The Role of Water in CO₂ Capture by Amine. *Ind. Eng. Chem. Res.* **2017**, *56* (21), 6337–6347. <https://doi.org/10.1021/acs.iecr.7b00715>.
- (105) Chen, C.-H.; Shimon, D.; Lee, J. J.; Didas, S. A.; Mehta, A. K.; Sievers, C.; Jones, C. W.; Hayes, S. E. Spectroscopic Characterization of Adsorbed ¹³CO₂ on 3-Aminopropylsilyl-Modified SBA15 Mesoporous Silica. *Environ. Sci. Technol.* **2017**, *51* (11), 6553–6559. <https://doi.org/10.1021/acs.est.6b06605>.
- (106) Yu, J.; Zhai, Y.; Chuang, S. S. C. Water-Enhancement in CO₂ Capture by Amines: An Insight into CO₂-H₂O Interactions on Amine Films and Sorbents. *Ind. Eng. Chem. Res.* **2018**, *57* (11), 4052–4062. <https://doi.org/10.1021/acs.iecr.7b05114>.
- (107) Chen, C.-H.; Shimon, D.; Lee, J. J.; Mentink-Vigier, F.; Hung, I.; Sievers, C.; Jones, C. W.; Hayes, S. E. The “Missing” Bicarbonate in CO₂ Chemisorption Reactions on Solid Amine Sorbents. *J. Am. Chem. Soc.* **2018**, *140* (28), 8648–8651. <https://doi.org/10.1021/jacs.8b04520>.
- (108) Bacsik, Z.; Ahlsten, N.; Ziadi, A.; Zhao, G.; Garcia-Bennett, A. E.; Martín-Matute, B.; Hedin, N. Mechanisms and Kinetics for Sorption of CO₂ on Bicontinuous Mesoporous Silica Modified with n-Propylamine. *Langmuir* **2011**, *27* (17), 11118–11128. <https://doi.org/10.1021/la202033p>.
- (109) Danon, A.; Stair, P. C.; Weitz, E. FTIR Study of CO₂ Adsorption on Amine-Grafted SBA-15: Elucidation of Adsorbed Species. *J. Phys. Chem. C* **2011**, *115* (23), 11540–11549. <https://doi.org/10.1021/jp200914v>.
- (110) Aziz, B.; Hedin, N.; Bacsik, Z. Quantification of Chemisorption and Physisorption of Carbon Dioxide on Porous Silica Modified by Propylamines: Effect of Amine Density.

- Microporous Mesoporous Mater.* **2012**, *159*, 42–49. <https://doi.org/10.1016/j.micromeso.2012.04.007>.
- (111) Mafra, L.; Čendak, T.; Schneider, S.; Wiper, P. V.; Pires, J.; Gomes, J. R. B.; Pinto, M. L. Structure of Chemisorbed CO₂ Species in Amine-Functionalized Mesoporous Silicas Studied by Solid-State NMR and Computer Modeling. *J. Am. Chem. Soc.* **2017**, *139* (1), 389–408. <https://doi.org/10.1021/jacs.6b11081>.
- (112) Serna-Guerrero, R.; Da'na, E.; Sayari, A. New Insights into the Interactions of CO₂ with Amine-Functionalized Silica. *Ind. Eng. Chem. Res.* **2008**, *47* (23), 9406–9412. <https://doi.org/10.1021/ie801186g>.
- (113) Yu, J.; Chuang, S. S. C. The Structure of Adsorbed Species on Immobilized Amines in CO₂ Capture: An in Situ IR Study. *Energy Fuels* **2016**, *30* (9), 7579–7587. <https://doi.org/10.1021/acs.energyfuels.6b01423>.
- (114) Lee, J.-H.; Siegelman, R. L.; Maserati, L.; Rangel, T.; Helms, B. A.; Long, J. R.; Neaton, J. B. Enhancement of CO₂ Binding and Mechanical Properties upon Diamine Functionalization of M₂(dobpdc) Metal–Organic Frameworks. *Chem. Sci.* **2018**, *9* (23), 5197–5206. <https://doi.org/10.1039/C7SC05217K>.
- (115) Martell, J. D.; Porter-Zasada, L. B.; Forse, A. C.; Siegelman, R. L.; Gonzalez, M. I.; Oktawiec, J.; Runčevski, T.; Xu, J.; Srebro-Hooper, M.; Milner, P. J.; Colwell, K. A.; Autschbach, J.; Reimer, J. A.; Long, J. R. Enantioselective Recognition of Ammonium Carbamates in a Chiral Metal–Organic Framework. *J. Am. Chem. Soc.* **2017**, *139* (44), 16000–16012. <https://doi.org/10.1021/jacs.7b09983>.
- (116) Bollini, P.; Choi, S.; Drese, J. H.; Jones, C. W. Oxidative Degradation of Aminosilica Adsorbents Relevant to Postcombustion CO₂ Capture. *Energy Fuels* **2011**, *25* (5), 2416–2425. <https://doi.org/10.1021/ef200140z>.
- (117) Xiao, D. J.; Oktawiec, J.; Milner, P. J.; Long, J. R. Pore Environment Effects on Catalytic Cyclohexane Oxidation in Expanded Fe₂(dobdc) Analogues. *J. Am. Chem. Soc.* **2016**, *138* (43), 14371–14379. <https://doi.org/10.1021/jacs.6b08417>.
- (118) Krug, R. R.; Hunter, W. G.; Grieger, R. A. Statistical Interpretation of Enthalpy–Entropy Compensation. *Nature* **1976**, *261* (5561), 566–567. <https://doi.org/10.1038/261566a0>.
- (119) Tim Fout; Alexander Zoelle; Dale Keairns; Marc Turner; Mark Woods; Norma Kuehn; Vasant Shah; Vincent Chou; Lora Pinkerton. *Cost and Performance Baseline for Fossil Energy Plants Volume 1a: Bituminous Coal (PC) and Natural Gas to Electricity Revision 3*; National Energy Technology Laboratory, 2015.
- (120) Mazzotti, M.; Rajendran, A. Equilibrium Theory-Based Analysis of Nonlinear Waves in Separation Processes. *Annu. Rev. Chem. Biomol. Eng.* **2013**, *4* (1), 119–141. <https://doi.org/10.1146/annurev-chembioeng-061312-103318>.
- (121) Sinha, A.; Darunte, L. A.; Jones, C. W.; Realff, M. J.; Kawajiri, Y. Systems Design and Economic Analysis of Direct Air Capture of CO₂ through Temperature Vacuum Swing Adsorption Using MIL-101(Cr)-PEI-800 and mmen-Mg₂(dobpdc) MOF Adsorbents. *Ind. Eng. Chem. Res.* **2017**, *56* (3), 750–764. <https://doi.org/10.1021/acs.iecr.6b03887>.
- (122) *SAINT, APEX2, and APEX3 Software for CCD Diffractometers*; Bruker Analytical X-ray Systems Inc.: Madison, WI, USA, 2014.
- (123) Sheldrick, G. M. *SADABS*; University of Göttingen, Germany.
- (124) Sheldrick, G. M. SHELXT – Integrated Space-Group and Crystal-Structure Determination. *Acta Crystallogr. Sect. Found. Adv.* **2015**, *71* (1), 3–8. <https://doi.org/10.1107/S2053273314026370>.

- (125) Sheldrick, G. M. Crystal Structure Refinement with SHELXL. *Acta Crystallogr. Sect. C Struct. Chem.* **2015**, *71* (1), 3–8. <https://doi.org/10.1107/S2053229614024218>.
- (126) Dolomanov, O. V.; Bourhis, L. J.; Gildea, R. J.; Howard, J. a. K.; Puschmann, H. OLEX2: A Complete Structure Solution, Refinement and Analysis Program. *J. Appl. Crystallogr.* **2009**, *42* (2), 339–341. <https://doi.org/10.1107/S0021889808042726>.
- (127) Adil, K.; Bhatt, P. M.; Belmabkhout, Y.; Abtab, S. M. T.; Jiang, H.; Assen, A. H.; Mallick, A.; Cadiou, A.; Aqil, J.; Eddaoudi, M. Valuing Metal-Organic Frameworks for Postcombustion Carbon Capture: A Benchmark Study for Evaluating Physical Adsorbents. *Adv. Mater.* **2017**, *29* (39), 1702953. <https://doi.org/10.1002/adma.201702953>.
- (128) Minguez, I. L.; Soukri, M.; Lail, M. A. Flying MOFs: Polyamine-Containing Fluidized MOF/SiO₂ Hybrid Materials for CO₂ Capture from Post-Combustion Flue Gas. *Chem. Sci.* **2018**. <https://doi.org/10.1039/C7SC05372J>.
- (129) Vaccarelli, M.; Carapellucci, R.; Giordano, L. Energy and Economic Analysis of the CO₂ Capture from Flue Gas of Combined Cycle Power Plants. *Energy Procedia* **2014**, *45*, 1165–1174. <https://doi.org/10.1016/j.egypro.2014.01.122>.
- (130) Drage, T. C.; Arenillas, A.; Smith, K. M.; Snape, C. E. Thermal Stability of Polyethylenimine Based Carbon Dioxide Adsorbents and Its Influence on Selection of Regeneration Strategies. *Microporous Mesoporous Mater.* **2008**, *116* (1), 504–512. <https://doi.org/10.1016/j.micromeso.2008.05.009>.
- (131) Hrynchuk, R. J.; Barton, R. J.; Robertson, B. E. The Crystal Structure of Free Base Cocaine, C₁₇H₂₁NO₄. *Can. J. Chem.* **1983**, *61* (3), 481–487. <https://doi.org/10.1139/v83-085>.
- (132) Itaka, Y. The Crystal Structure of γ -glycine. *Acta Crystallogr.* **1961**, *14* (1), 1–10. <https://doi.org/10.1107/S0365110X61000012>.

Chapter 4. A Cooperative Adsorbent for Switch-Like CO₂ Capture from Crude Natural Gas

4.1. Introduction

Natural gas currently supplies over 22% of global primary energy,¹⁻⁴ and its share is projected to rise to 25% by 2040, accompanied by an anticipated 40% increase in worldwide gas demand.^{3,4} Both economic and environmental incentives are supporting this growth: gas reserves are abundant and largely untapped, and the low carbon intensity of natural gas has encouraged its use as a cleaner-burning alternative to coal.³ Furthermore, natural gas significantly reduces emissions of NO_x, particulate matter, and mercury as compared to oil or coal.⁵

Despite the abundance of crude gas reserves, approximately 25% of U.S. reserves^{5,6} and up to 50% of worldwide reserves⁷ are estimated to be sub-quality due to CO₂ contamination in excess of 2%. This CO₂ must be removed from the crude gas prior to transport in a pipeline to avoid dilution of the heating value of the gas and to prevent corrosion in the presence of moisture. Aqueous amine solutions, which utilize acid–base chemistry to absorb and separate CO₂ by forming ammonium carbamate or bicarbonate, remain the industry standard for natural gas purification.⁸ Despite the maturity of aqueous amine technology, these solutions suffer from a number of disadvantages, including high regeneration energies, low CO₂ capacities, and issues with corrosivity, oxidation, and volatilization.⁸ The limitations of amine solutions and the burgeoning market for natural gas purification have led to exploration of a number of alternative technologies in various stages of development. Physical absorption,⁹ low-temperature (<0 °C) separations,¹⁰ membrane-based processes,¹¹ separations using clathrate hydrates,¹² and adsorptive separations have all received growing interest in recent years.

Pressure-swing adsorption (PSA)¹³ processes have generated particular interest as modular systems with the potential to reduce the energy intensity and environmental hazards of natural gas purification relative to amine solutions.^{14,15} In PSA, a porous solid selectively binds CO₂ from a crude natural gas feed at elevated pressure, generating a methane-enriched product stream. Following saturation of the adsorbent bed with CO₂, desorption is achieved by depressurization and purge steps, after which the bed is repressurized to begin a new cycle. Two or more adsorption beds are used in parallel to allow continuous operation through concurrent adsorption and desorption steps.

PSA for CO₂ removal has seen early commercial-scale success, notably in Guild Associates' Molecular Gate™ process¹⁶ and Xebec's Rotary-Valve, Fast-Cycle PSA process,¹⁷ which incorporate proprietary titanosilicate and metal-based adsorbents, respectively. Further advances in material design are attractive to achieve improved performance in PSA processes. New adsorbents for natural gas conditioning must (1) possess high capacity and selectivity for CO₂, (2) co-adsorb minimal CH₄ to maximize recovery, (3) release the bound CO₂ with minimal energetic input, and (4) demonstrate rapid adsorption–desorption kinetics. Additionally, adsorbents with the ability to function in the presence of moisture are highly desirable, as natural gas feeds are typically saturated with water.⁵ Because water tends to displace acid gases on adsorbents that utilize exposed metal ions as binding sites,¹⁸⁻²¹ the presence of water has hindered the development of PSA for CO₂ removal. The ability to segregate binding sites for CO₂ and H₂O would therefore enable greater bed utilization, eliminate costly pre-drying of the gas feed, and/or simplify complex process configurations relying on separation of CO₂ and H₂O.

Amine-functionalized adsorbents are promising candidates to meet each of the above criteria. As with amine solutions, these materials selectively bind CO₂ through acid–base chemistry to

form ammonium carbamate or bicarbonate species. This strategy has already been applied in the design of amine-grafted mesoporous silicas for natural gas purification.^{22,23} Amine-functionalized metal–organic frameworks have likewise received growing attention for CO₂ removal from humid gas streams.²⁴ These materials feature inorganic ions or clusters bridged by organic ligands to form highly porous and crystalline coordination solids. Amine functionality can be incorporated within the ligand^{25,26} or post-synthetically introduced by grafting to open metal coordination sites within the pores.^{27,28}

The latter approach led to the recent discovery of a new class of frameworks of the form M₂(dobpdc)(diamine)₂ (M = Mg, Mn, Fe, Co, Ni, Zn; dobpdc⁴⁻ = 4,4'-dioxidobiphenyl-3,3'-dicarboxylate) that feature one-dimensional hexagonal channels densely lined with metal(II) cations, each bearing an appended diamine (Figure 4.1a).^{29,30} The ideal spacing between metal sites facilitates an unprecedented adsorption mechanism in which CO₂ inserts into the metal–amine bonds (Figure 4.1b); the resulting metal-bound carbamate and dangling ammonium groups interact with neighboring sites to form chains of ammonium carbamate running along the framework channel.³⁰ This switch-like mechanism manifests as sharp, high-capacity steps in the

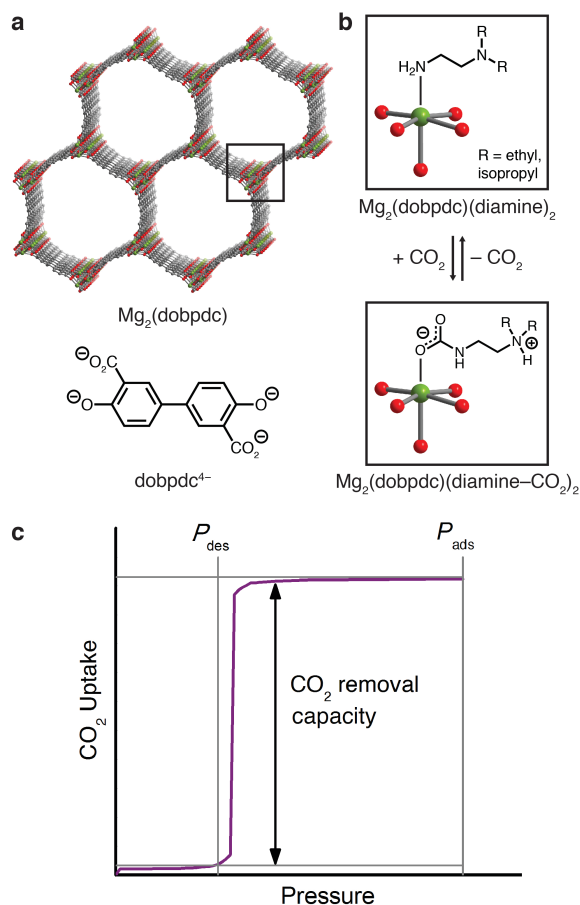


Figure 4.1. a) Structure of the metal–organic framework Mg₂(dobpdc) (top) and the ligand dobpdc⁴⁻ (bottom). Green, gray, and red spheres correspond to Mg, C, and O atoms, respectively; H atoms have been omitted for clarity. (b) Post-synthetic functionalization of the open Mg(II) coordination sites with diamines to yield Mg₂(dobpdc)(diamine)₂ (top), and chemisorption of CO₂ through insertion into the metal–amine bond (bottom), resulting in cooperative formation of ammonium carbamate chains along the pore axis. (c) Hypothetical isotherm and schematic of a pressure-swing adsorption process with a cooperative adsorbent, for which the full adsorption capacity of the material can be accessed as working capacity.

CO₂ adsorption isotherms, and the full capacity of bound CO₂ can accordingly be desorbed with minimal changes in temperature or pressure (Figure 4.1c). The threshold pressure for CO₂ insertion can be precisely tailored to a given CO₂ separation process through judicious choice of the constituent metal and diamine.³¹

Previous exploration of diamine-appended M₂(dobpdc) has been limited to CO₂ capture from low-pressure air or flue gas streams in temperature-swing processes.^{29,30,32–36} Here, we demonstrate the design of a diamine-appended framework as a next-generation adsorbent for pressure-swing conditioning of CO₂-rich natural gas. We further demonstrate that humidity enhances the CO₂ capture performance of these materials and discuss the mechanistic effects underlying this advantageous behavior.

4.2. Experimental Procedures

4.2.1. General Materials and Methods

The ligand 4,4'-dihydroxy-(1,1'-biphenyl)-3,3'-dicarboxylic acid (H₄dobpdc) was obtained from Hangzhou Trylead Chemical Technology Co. and used as received; or was obtained from Combi-Blocks and purified by recrystallization from a 3:1 (v:v) acetone:water mixture; or was synthesized as previously reported.³⁷ All other reagents and solvents were obtained from commercial suppliers at reagent grade purity or higher and were used without further purification. Synthetic procedures were conducted under air unless otherwise noted. Zeolite 13X was obtained from Sigma Aldrich as 60–80 mesh pellets (product code 20305, Supelco). Full characterization of this material is included in the Supporting Information, Section 4.6.7. The metal–organic framework Mg₂(dobpdc) was prepared as a gram-scale powder and characterized following a previously reported procedure (Supporting Information, Section 4.6.1).³¹ Ultrahigh purity (99.999%) He, N₂, CH₄, and H₂ and research grade (99.998%) CO₂ were used for all adsorption experiments. Elemental analyses were conducted at the Microanalytical Laboratory of the University of California, Berkeley, using a PerkinElmer 2400 Series II combustion analyzer. ¹H NMR spectra were collected on a Bruker AMX 300 MHz NMR spectrometer. Details regarding use of dynamic scanning calorimetry for heat capacity measurements and kinetics experiments are given in the Supporting Information, Sections 4.6.8 and 4.6.9, respectively. Powder X-ray diffraction (PXRD) patterns were collected with a laboratory Bruker AXS D8 Advance diffractometer with CuK α radiation ($\lambda = 1.5418 \text{ \AA}$) or at the Advanced Photon Source with synchrotron radiation ($\lambda = 0.45399 \text{ \AA}$), as specified in the figure captions. Details for synchrotron PXRD experiments under controlled atmospheres are given in the Supporting Information in Section 4.6.17. Single-crystal synthesis and X-ray diffraction details are included in the Supporting Information in Section 4.6.18.

4.2.2. Gram-Scale Synthesis of Diamine-Appended M₂(dobpdc)

Diamine-grafting conditions for preparing gram-scale diamine-appended Mg₂(dobpdc) powders were adapted from a previous report.³⁰ A 20% (v/v) solution of diamine in toluene was dried by stirring over CaH₂ for 3 h at 60 °C. Separately, several grams of washed, methanol-solvated Mg₂(dobpdc) was dried under flowing N₂ at 250 °C for 12 h. The desolvated parent framework was then cooled to room temperature under N₂, and a quantity of diamine solution corresponding to 10 equivalents of diamine per Mg^{II} site was added by cannula transfer. (We note that at the milligram scale, direct diamine grafting has been demonstrated without activation

of the methanol-solvated parent framework or diamine drying agents such as CaH_2 .³¹) The reaction vessel was sonicated for 15 min under N_2 and then left undisturbed under N_2 for a minimum of 12 h at room temperature. The solid was isolated by filtration and washed three times with 100 mL portions of toluene and three times with 100 mL portions of hexanes in air at room temperature. Prior to adsorption measurements, the sample was desolvated (activated) by heating *in vacuo* or under flowing N_2 at 100 °C for 12 h. Diamine loadings were determined by collecting NMR spectra of ~5 mg of activated, diamine-appended framework samples digested with a solution of ~20 μL of 35 wt % DCl in ~0.75 mL of $\text{DMSO-}d_6$. The ratio of the diamine to ligand peak integrals indicated typical diamine loadings of 100% within error ($\pm 5\%$). Combustion elemental analysis calculated for $\text{Mg}_2(\text{dobpdc})(\text{ee-2})_2$ ($\text{C}_{26}\text{H}_{38}\text{Mg}_2\text{N}_4\text{O}_6$; ee-2 = *N,N*-diethylethylenediamine): C, 56.65; H, 6.95; N, 10.16. Found: C, 56.42; H, 6.77; N, 10.15. Combustion elemental analysis calculated for $\text{Mg}_2(\text{dobpdc})(\text{ii-2})_{2.1}$ ($\text{C}_{30.8}\text{H}_{48}\text{Mg}_2\text{N}_{4.2}\text{O}_6$; ii-2 = *N,N*-diisopropylethylenediamine): C, 59.50; H, 7.78; N, 9.46. Found: C, 59.50, H, 7.62; N, 9.46.

4.2.3. Volumetric Gas Adsorption Experiments

Low-pressure gas adsorption experiments. Single-component isotherms in the range of 0–1.2 bar were measured by a volumetric method using ASAP 2020 or 3Flex instruments from Micromeritics. In a typical measurement, 50–200 mg of sample was transferred to a pre-weighed glass measurement tube under a N_2 atmosphere and capped with a Micromeritics *TranSeal*. The sample was then degassed for 12 h at 250 °C for the parent $\text{Mg}_2(\text{dobpdc})$ framework or 4 h at 100 °C for diamine-appended frameworks until the outgas rate was less than 3 $\mu\text{bar}/\text{min}$. The evacuated tube was then weighed to determine the mass of the degassed sample. The sample was transferred to the analysis port of the instrument, where the outgas rate was again confirmed to fall below 3 $\mu\text{bar}/\text{min}$. For cryogenic measurements, the sample tube was fitted with an isothermal jacket and submerged in a liquid nitrogen bath. Langmuir surface areas were calculated from the 77 K N_2 adsorption data using Micromeritics software, assuming a cross-sectional area of 16.2 \AA^2 for N_2 . Brunauer–Emmett–Teller (BET) surface areas were calculated using the method and consistency criteria of Walton and Snurr.³⁸ For H_2O isotherms (Figures 4.S29 and 4.S36), the stainless-steel vapor dosing apparatus was subjected to three freeze–pump–thaw cycles to remove any dissolved gases, and heat tape was used to keep the exposed portion of the glass sample tube at elevated temperature to prevent condensation of water. The maximum relative humidity accessible in measurements with H_2O was limited by the fixed manifold temperature of 45 °C. The isotherm data points were considered equilibrated after <0.01% change in pressure occurred over an average of 11 intervals of 15 s (for N_2 , CO_2 , and CH_4) or 30 s (for H_2O). Diamine-appended samples were regenerated at 100 °C under reduced pressure (<10 μbar) for 2–4 h between isotherms unless noted otherwise. Adsorption isotherms between 25 and 75 °C were measured in water baths using a recirculating dewar connected to a Julabo F32-MC isothermal bath. Oil-free vacuum pumps and oil-free pressure regulators were used for all measurements.

High-pressure gas adsorption experiments. High-pressure gas adsorption measurements in the range of 0 to 100 bar were conducted using a HPVA-II-100 from Particulate Systems, a subsidiary of Micromeritics. A tared, stainless steel sample holder was loaded with approximately 1 g of activated diamine-appended framework inside a glovebox under N_2 . The sample was weighed, and the holder was sealed with VCR fittings and an air-tight valve and transferred to the analysis port of the instrument. The sample holder was placed inside an aluminum recirculating dewar connected to a Julabo FP89-HL isothermal bath filled with

Syltherm XLT fluid (temperature stability: ± 0.02 °C) and evacuated for 2 h prior to measurement. Methods for determining the sample freespace have been described in detail previously.³⁹ The NIST REFPROP database⁴⁰ was used to perform non-ideality corrections at each measured temperature and pressure.

Prior to sample measurement, an empty sample holder was used to collect background CO₂ adsorption isotherms at the analysis temperatures and target pressure points. A small negative background was observed at high pressures and can likely be attributed to volume or temperature calibration errors or errors in the equation of state used to correct for non-ideality. The background adsorption was found to be consistent over several measurements, and polynomial fits of replicate data sets at each temperature were used to perform background subtraction on the experimental data sets (Figure 4.S13). A negligible background was observed for high-pressure CH₄ measurements, and these datasets were therefore not corrected. For each material, total adsorption (n_{tot}) was calculated from the experimentally measured, background-corrected excess adsorption data (n_{ex}) using equation 4.1:

$$n_{tot} = n_{ex} + V_p \cdot \rho_{bulk}(T, P) \quad (4.1)$$

The pore volume (V_p) was determined from the 77 K N₂ adsorption experiments using the Gurvich rule⁴¹ (Figures 4.S3, 4.S8, and 4.S33), and the bulk gas density was determined from the NIST REFPROP database⁴⁰ at each experimental temperature and pressure.

Selectivity calculations. Preliminary, non-competitive selectivities for CO₂ were calculated directly from the single-component adsorption isotherms. Mixed-gas selectivities were calculated from breakthrough experiments. In both cases, the following formula was used:

$$s = (q_{CO_2}/q_{CH_4})/(p_{CO_2}/p_{CH_4}) \quad (4.2)$$

Here, q_i is the quantity of gas i adsorbed at the corresponding partial pressure of interest p_i .

Calculation of differential enthalpies and entropies of adsorption. To calculate the differential enthalpy (Δh_{ads}) and entropy (Δs_{ads}) of adsorption, the exact pressures (p_q) corresponding to specific adsorbate loadings (q) were determined at different temperatures (T). For Type I isotherms, p_q values were obtained using single- or dual-site Langmuir or Langmuir–Freundlich models (see Supporting Information in Sections 4.6.4–4.6.7 for fits, fit parameters, and additional details). For step-shaped CO₂ adsorption isotherms, a linear spline interpolation method was used to obtain p_q values. The Clausius–Clapeyron relationship given in eq 4.3 was then applied to calculate the differential enthalpies of adsorption from the slopes of the linear trendlines fit to $\ln(p_q)$ vs. $1/T$. The differential entropies of adsorption were determined from the y -intercepts of these linear trendlines, which are equal to $-\Delta s_{ads}/R$ at each loading (assuming $p_0 = 1$ bar).

$$\ln(p_q) = \left(\frac{\Delta h_{ads}}{R}\right)\left(\frac{1}{T}\right) + c \quad (4.3)$$

4.2.4. Thermogravimetric Analysis

Dry thermogravimetric analysis (TGA) experiments were conducted at atmospheric pressure using a TA Instruments TGA Q5000. Humid TGA experiments were conducted using a TA Instruments TGA Q50 by passing the incident gas stream through two water bubblers in series, leading to an estimated water content of 1.3% at 25 °C (~30% R.H.). All adsorption and

desorption isobars were collected at a ramp rate of 1 °C/min. Pre-mixed CO₂/N₂ blends (5%, 10%, 15%, 20%, 30%, and 50% CO₂ in N₂) were purchased from Praxair. Initial sample activation was performed at 120 °C under flowing N₂ for 20–30 min until stabilization of the mass was observed. Decomposition experiments were conducted at a ramp rate of 1.5 °C/min under dry N₂.

4.2.5. Breakthrough Experiments and Pressure Cycling

For all dynamic breakthrough measurements, pellets of adsorbent were prepared by mechanical compression. Prior to activation from toluene or hexanes, the powdered diamine-appended material was placed in a stainless-steel cylinder between highly polished faces of a stainless-steel platform and corresponding plunger. A mechanical press was used to compress the powder between the platform and plunger to form a tablet. This tablet was then broken to the desired particle size between copper mesh sieves (Figure 4.S50) to produce pellets of either 25–45 mesh (350–700 μm) or 60–80 mesh (180–250 μm), as specified below. Pellets were activated by heating *in vacuo* or under flowing N₂ at 100 °C for 12 h.

Quantitative, dry breakthrough measurements at 1, 35, and 70 bar were conducted on a custom-built breakthrough apparatus at the Chevron Energy Technology Company in Richmond, CA (Figure 4.S51). A 5 cm³ stainless steel column (30.5 cm length, 0.46 cm diameter) was packed with 25–45 mesh pellets of activated ii-2-Mg₂(dobpdc) (2.50 g) or ee-2-Mg₂(dobpdc) (3.31 g). Glass wool was placed before the end fittings to secure the adsorbent in place. Capacities for CO₂ are reported with an error of ±0.3 mmol/g, as calculated by assuming a 30 s error in integrated breakthrough time and a flow rate deviation of ±1%.

Qualitative dry and humid breakthrough experiments at 7 and 50 bar and extended pressure cycling were performed on a customized PSA-1000 instrument built by L&C Science and operated at the Chevron Energy Technology Company. A 3.2 cm³ stainless steel bed (16.5 cm length, 0.5 cm diameter) was packed with 0.90 g of activated ee-2-Mg₂(dobpdc) or 1.98 g of activated zeolite 13X as 60–80 mesh pellets. Additional experimental details and breakthrough experiments are included in the Supporting Information in Sections 4.6.13–4.6.15.

4.2.6. Infrared Spectra

Attenuated total reflectance (ATR) infrared (IR) spectra were collected on a PerkinElmer Spectrum 400 Fourier Transform (FT) IR spectrometer equipped with a Pike GladiATR and a home-built glovebag accessory used to control the atmosphere. Three vacuum–refill cycles were used to exchange the atmosphere of the glovebag accessory when preparing the system for *in situ* experiments. For humid FTIR spectra, samples were placed in 4 mL vials and sealed in a 20 mL vapor-dosing chamber containing ~4 mL of water. After at least 15 min of equilibration, the powder was removed, and spectra were collected. Co-adsorption of water in the sample was confirmed by observation of the broad H₂O IR vibrational band at 3350 cm⁻¹.⁴²

4.3. Results and Discussion

4.3.1. Material Design Considerations

Effective use of diamine-appended $M_2(\text{dobpdc})$ for PSA requires thoughtful manipulation of several design features unique to this class of materials. Critically, for adsorbents with step-shaped isotherms, CO_2 binding is only possible at partial pressures exceeding the step pressure. Once the adsorbate partial pressure in the column drops below this threshold pressure, the switch-like mechanism is disabled, and any remaining CO_2 will “slip” through the bed with the CH_4 product (Figure 4.2). More specifically, the breakthrough profile for adsorption can be predicted from the CO_2 isotherm using a graphical method known as Golden’s rule, or the “rubber band” or “string” rule.^{32,43–45} In short, an operating curve is constructed by stretching an imaginary rubber band (green curve, Figure 4.2) beneath the adsorption isotherm between the initial state (0% CO_2) and the feed state (10% CO_2). In regions bounded by points of tangency with the isotherm, a compressive “shock” is anticipated in the breakthrough profile. In regions where the rubber band runs along the isotherm, a dispersive wave is generated. With step-shaped isotherms, a multi-moment “shock–wave–shock” breakthrough profile is therefore frequently observed, with the initial “shock” corresponding to CO_2 slip at concentrations beneath the step. (See Supporting Information in Section 4.6.12 for additional details.) As a result, the adsorbent must be designed such that the adsorption step occurs not simply below the CO_2 partial pressure in the feed, but instead at a minimum partial pressure dictated by the desired product purity and/or CO_2 capture rate. For natural gas purification, this variable is fixed by the maximum allowable CO_2 content of 2 mol % in the product CH_4 stream.

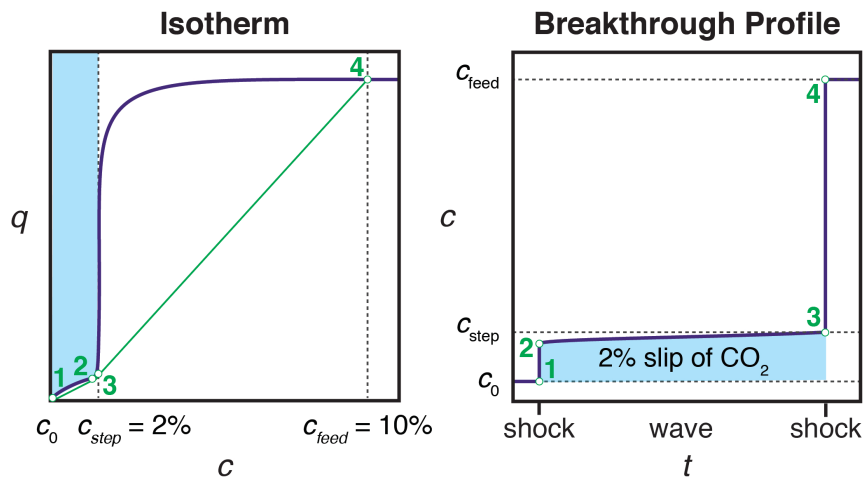


Figure 4.2. Schematic of a “shock–wave–shock” breakthrough profile (right, concentration, c , vs. time, t) anticipated for an adsorbent with a step-shaped isotherm (left, quantity adsorbed, q , vs. c). The operating curve used to predict the breakthrough profile from the isotherm is shown in green, and the numerical labels indicate corresponding points in the isotherm and breakthrough profile. At concentrations beneath the step, CO_2 “slips” through the bed (shaded blue area). To achieve a CH_4 product purity of $\geq 98\%$, an adsorbent with $< 2\%$ slip is desirable. Figure adapted from ref. 32.

Crude natural gas may be recovered from reserves coupled with crude oil (associated gas) or in independent reserves (non-associated or wellhead gas) and can therefore exhibit a broad range of total pressures (up to ~ 70 bar), compositions (up to $\sim 80\%$ CO_2), and temperatures.^{5,7} For this

study, we chose two representative cases: (1) simulated non-associated gas, 70 bar, 10% CO₂, and (2) simulated associated gas, 7 bar, 10% CO₂, both in the range of 25–50 °C. To reduce the CO₂ concentration below 2%, a diamine-appended framework must operate with a step pressure of ≤ 1.4 bar for the non-associated gas in case (1) and ≤ 140 mbar for the associated gas in case (2) (Table 4.1).

Table 4.1. Target total stream pressure, CO₂ partial pressure, and CO₂ adsorption step pressure for the separations explored in this work.

	Wellhead Gas	Associated Gas
Target Total Pressure	70 bar	7 bar
Target CO₂ Partial Pressure	7 bar	0.7 bar
Target CO₂ adsorption step Pressure	≤ 1.4 bar	≤ 0.14 bar

Previous exploration of diamine-appended frameworks for cooperative CO₂ capture has generated a library of adsorbents with step pressures ranging from 10⁻⁴ bar to 1 bar at 40 °C.³¹ For the high-pressure separations in this work, the adsorbents ee-2–Mg₂(dobpdc) (ee-2 = *N,N*-diethylethylenediamine) and ii-2–Mg₂(dobpdc) (ii-2 = *N,N*-diisopropylethylenediamine) were identified as promising candidate materials for low-energy CO₂ capture. The primary/tertiary (1°/3°) diamines in these materials promote high thermal stability due to the strong interaction between the magnesium centers and the primary amines. The sterically bulky tertiary amines further suppress amine volatilization (see Figure 4.S12 for a two-year stability test) and destabilize the CO₂-adsorbed phase, leading to high CO₂ step pressures and low differential enthalpies of CO₂ adsorption ($-\Delta h_{\text{ads}} < 70$ kJ/mol). These favorable characteristics supported further investigation of 1°/3° diamine-appended frameworks for PSA.

4.3.2. Pressure-Swing Adsorption with a Cooperative Adsorption Threshold at Atmospheric Pressure

The target CO₂ insertion step pressure of 1.4 bar for non-associated gas purification suggests an attractive possibility for energy-efficient PSA: following saturation of the adsorbent at high pressure, the bound CO₂ could be completely desorbed at atmospheric pressure without need for vacuum or heat. The adsorbent ii-2–Mg₂(dobpdc) was previously found to have a step pressure of 1 bar at 40 °C³¹ and was therefore initially investigated for CO₂ capture from non-associated gas.

High-pressure, single component CO₂ and CH₄ isotherms were first collected for ii-2–Mg₂(dobpdc) (Figure 4.3). Step-like CO₂ isotherms were observed at all temperatures, with the step capacity corresponding to the anticipated binding of 1 CO₂ molecule per diamine (3.3 mmol/g). Application of the Clausius–Clapeyron relationship indicated differential adsorption enthalpies of -45 ± 4 kJ/mol for CO₂ and -13.4 ± 0.6 kJ/mol for CH₄ at a loading of 1 mmol/g. (See Figures 4.S16 and 4.S20 for plots of $-\Delta h_{\text{ads}}$ as a function of loading for CO₂ and CH₄, respectively.) Compared to other amine-based adsorbents, which frequently exhibit low-coverage adsorption enthalpies with magnitudes of >70 kJ/mol CO₂,^{46,47,27} the moderate adsorption enthalpies of 1°/3° diamine-appended frameworks reduce both heat management requirements upon adsorption and the energetic input required for desorption. For a target stream

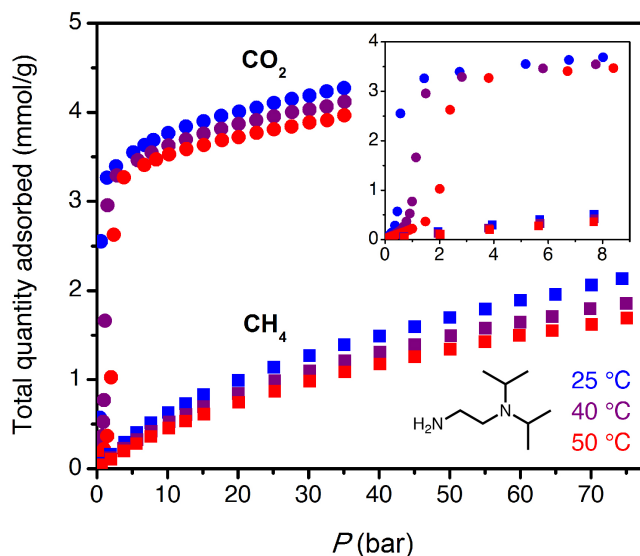


Figure 4.3. High-pressure CO₂ (circles) and CH₄ (squares) adsorption isotherms for ii-2-Mg₂(dobpdc) at 25 °C (blue), 40 °C (purple), and 50 °C (red). The inset shows an enlarged view of the low-pressure region.

of 10% CO₂ at 70 bar, non-competitive CO₂/CH₄ selectivities of 17, 19, and 20 were calculated from the single-component isotherms at 25, 40, and 50 °C under the target conditions for wellhead gas purification. These values are anticipated to represent lower bounds for selectivity, as CO₂ and CH₄ have separate primary binding sites in diamine-appended frameworks.

High-pressure, dry breakthrough experiments were conducted to analyze the CO₂ capacity and mixed-gas selectivity of ii-2-Mg₂(dobpdc) from dry, simulated wellhead gas. With 300 scem of 10% CO₂ in CH₄ at 70 bar and 30 °C, a shock-wave-shock breakthrough profile was observed (Figure 4.4), consistent with the general schematic shown in Figure 2 (see Supporting Information in Section 4.6.14 for a duplicate measurement and additional experiments with different temperatures, pressures, and gas compositions). Integrating over the full breakthrough profile yielded a high CO₂ exhaustion capacity of 3.3 mmol/g (equivalent to 1 CO₂ per diamine) and a moderate CO₂/CH₄ selectivity of 7.7. Despite these promising performance metrics, several limitations were noted that would inhibit the realistic application of this material for PSA. Importantly, the breakthrough experiments show greater CO₂ “slip” than would be anticipated based on the single-component, equilibrium isotherms. Specifically, while application of Golden’s rule predicted a CO₂ slip of <1 mol % (Table 4.S9), the initial shock in the CO₂ breakthrough curve instead yielded a slip concentration of 3 mol % CO₂ (2 bar of CO₂). As a result, the CH₄ product purity was limited to ~97%, and the material displayed negligible usable CO₂ capacity for production of pipeline-quality CH₄ (≥98%).

The partial pressure of CO₂ in the initial shock is consistent with an effective step temperature of 53 °C, as calculated from the adsorption isotherms and the differential enthalpy of adsorption (Supporting Information, Section 4.6.5). In part, this can be attributed to temperature rise in the bed during adsorption. Thermocouples at 3" and 9" from the inlet along the 12" bed indicated a small temperature rise during the experiment, to a maximum of 38 °C (Figure 4.S52). Kinetics limitations may also contribute to the high level of CO₂ slip observed in breakthrough experiments. Examination of the temperature dependence of the rate of CO₂ adsorption by dynamic scanning calorimetry revealed slow CO₂ adsorption kinetics at conditions approaching the step (Supporting Information, Section 4.6.9). Furthermore, a 25 °C adsorption isotherm

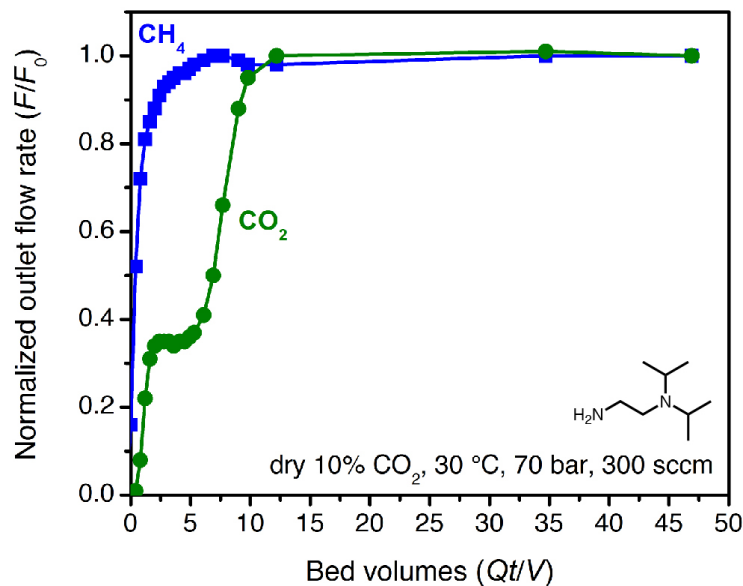


Figure 4.4. Breakthrough profile for ii-2-Mg₂(dobpdc) under 300 sccm of dry 10% CO₂ in CH₄ at 70 bar and 30 °C. The CO₂ in the initial shock corresponds to a slip concentration of 3 mol %.

collected for the pelletized adsorbent revealed a shift in the step pressure to >0.6 bar, vs ~0.4 bar for the powder under the same equilibration criteria (Figure 4.S21). Extending the time allotted for equilibration shifted the pellet isotherm step position back to that of the powder, indicating that kinetics limitations likely contribute to the complex CO₂ breakthrough profiles observed for this material and that the adsorption properties may be sensitive to external stimuli, including compaction. Similar kinetics limitations were recently discussed for this class of adsorbents in the context of direct air capture.³⁶ Note that this behavior is anticipated for such materials, because the driving force for reactive CO₂ adsorption is small at conditions near the cooperative adsorption step but increases at lower temperature or with an increasing partial pressure of CO₂ beyond the step (Figures 4.S38–4.S39). Regardless, these results suggest that predictions made from single-component adsorption isotherms alone may not provide an accurate depiction of adsorbent performance under flow conditions (additional discussion below).

In addition, the equilibrium adsorption isotherms show hysteresis, with the desorption branch of the isotherm closing at 0.25 bar at 25 °C and 0.5 bar at 50 °C (Figure 4.S14). As a result, vacuum or heat would be required to desorb CO₂ between cycles. In sum, ii-2-Mg₂(dobpdc) may be valuable as an adsorbent for bulk separation of CO₂ from high-pressure streams, but to produce pipeline-quality natural gas, the material would either need to be paired with a polishing adsorbent or replaced with an adsorbent with a slightly lower step pressure. The latter strategy motivated us to explore ee-2-Mg₂(dobpdc) for both associated and non-associated gas separations.

4.3.3. Evaluation of ee-2-Mg₂(dobpdc) for Natural Gas Purification

The smaller steric profile of the tertiary amine in *N,N*-diethylethylenediamine (ee-2) results in lower CO₂ insertion pressures for ee-2-Mg₂(dobpdc) as compared to ii-2-Mg₂(dobpdc), as a result of stronger ion pairing in the ammonium carbamate chains formed upon CO₂ adsorption.³¹ As shown in Figure 4.5, the inflection point of the first CO₂ adsorption step for this material

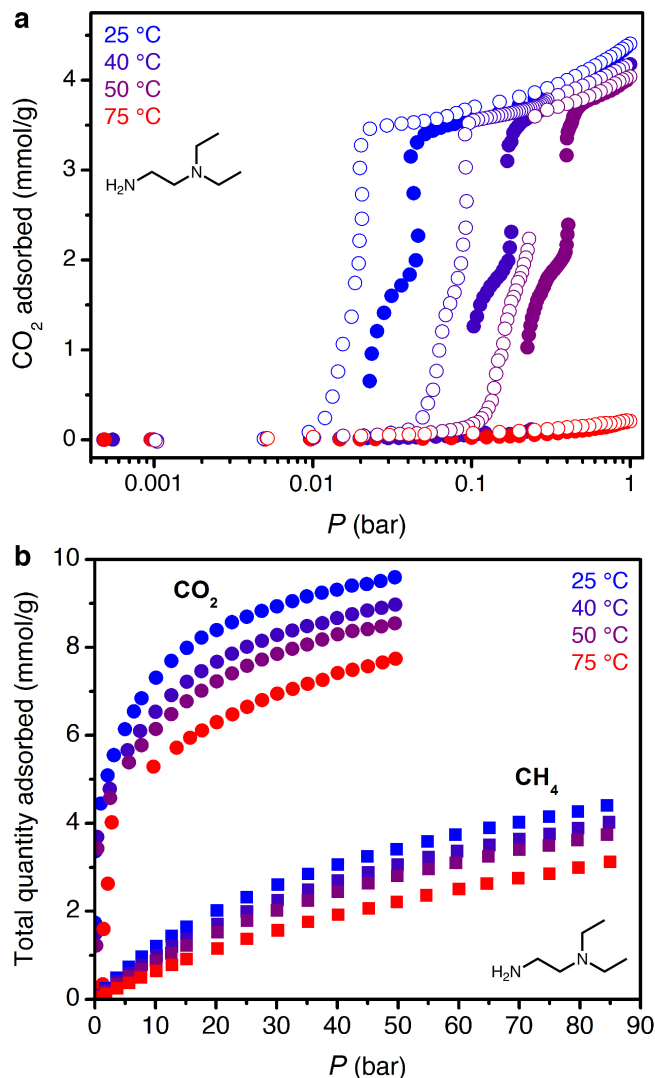


Figure 4.5. (a) Low-pressure CO₂ adsorption (filled circles) and desorption (open circles) isotherms for ee-2-Mg₂(dobpdc). (b) High-pressure CO₂ (circles) and CH₄ (squares) adsorption isotherms for ee-2-Mg₂(dobpdc).

shifts from ~0.11 bar at 40 °C to 0.24 bar at 50 °C and exceeds 1 bar slightly below 75 °C, suggesting that regeneration could be achieved with a moderate concentration swing or combined pressure–vacuum or pressure–temperature swing process. The two-step CO₂ adsorption profile has been attributed to steric crowding within the pore, which necessitates a rearrangement at half capacity to allow full occupancy of ammonium carbamate chains.^{‡,35} The full capacity of both adsorption steps (3.6 mmol/g) is consistent with the binding of 1 CO₂ molecule per diamine, with a slight increase in the gravimetric capacity from that of ii-2-Mg₂(dobpdc) due to the smaller appended diamine. In addition, the high-pressure isotherms show greater uptake of CO₂ beyond the step as compared to the material grafted with ii-2, consistent with a larger accessible surface area (911 ± 4 m²/g, vs. 490 ± 4 m²/g for ii-2-Mg₂(dobpdc); Figures 4.S3 and 4.S8) that likely facilitates faster diffusion through the pores. High-pressure methane isotherms likewise show increased uptake compared to that of ii-2-Mg₂(dobpdc), leading to a non-competitive selectivity of 15–16 over a temperature range of 25–

50 °C for wellhead gas containing 10% CO₂ at 70 bar. Desorption isotherms for CO₂ show closure of the hysteresis loop at 0.01, 0.04, and 0.1 bar at 25, 40, and 50 °C, respectively (Figure 4.5a). Differential enthalpies of adsorption of -65 ± 1 and -13.1 ± 0.2 kJ/mol were calculated for CO₂ and CH₄, respectively, at a loading of 1 mmol/g (Figures 4.S23 and 4.S28). Note, however, that the CH₄ adsorption enthalpy within the diamine-appended framework may deviate from that in the CO₂-inserted framework, in which the pores are lined with ion-paired chains of ammonium carbamate.

Multicomponent performance was first evaluated in dry breakthrough experiments, as with ii-2-Mg₂(dobpdc). The powdered adsorbent was compressed and sieved to form binderless pellets, which were found to perform identically to the powder with a standard equilibration interval (<0.01% change in pressure over an average of 11 intervals of 15 s). For a simulated wellhead gas stream containing 10% CO₂ at 70 bar, 30 °C, and 300 sccm, a CH₄ purity of 99.6% was achieved (Figure 4.6a), easily satisfying the target pipeline specification of 98% (see Figure 4.S58 for a duplicate experiment). Exothermic CO₂ adsorption produced a moderate ΔT of ~ 8 °C

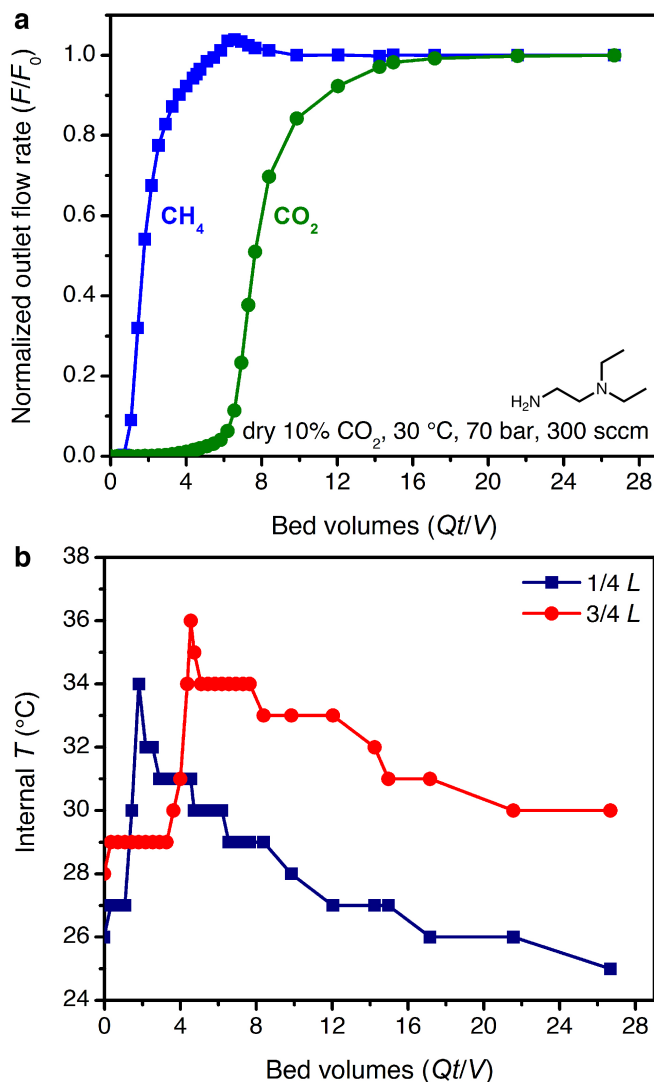


Figure 4.6. (a) Breakthrough profile for ee-2-Mg₂(dobpdc) under 300 sccm of dry 10% CO₂ in CH₄ at 70 bar and 30 °C. (b) Corresponding temperature profile, as measured with two internal thermocouples.

(Figure 4.6b). A small amount of “roll-up” (normalized outlet flow rate, F/F_0 , > 1) is visible in the CH₄ breakthrough curve as strong binding of CO₂ displaces adsorbed CH₄. Co-adsorption of CH₄ was higher than anticipated from the single-component adsorption isotherms, reaching 7.8 mmol/g and resulting in a mixture selectivity of 4.8 for CO₂. However, we note that the CH₄ capacity and associated CO₂ selectivity calculations are susceptible to large errors due to the short breakthrough times for CH₄. For example, a 5% error for a typical integrated CH₄ breakthrough time of 160 s would result in an error of ± 0.5 mmol/g in calculated CH₄ capacity. In a subsequent breakthrough experiment at a lower total pressure of 35 bar, a product purity of 99.2% and CO₂/CH₄ selectivity of 5.8 were achieved (Figure 4.S59). For varying total pressures with 10% CO₂ at 30 °C, consistent CO₂ slip of ~ 0.3 bar was observed, signifying an effective step temperature of 52 °C, as calculated from the adsorption enthalpy and adsorption isotherms (see Supporting Information, Section 4.6.6, Table 4.S10, and Figure 4.S60). These results indicate that like ii-2-Mg₂(dobpdc), ee-2-Mg₂(dobpdc) shows greater slip than anticipated from the equilibrium CO₂ isotherms alone. However, breakthrough results suggest that ee-2-Mg₂(dobpdc) possesses sufficiently favorable thermodynamics and kinetics of CO₂ adsorption to produce pipeline quality methane from dry wellhead gas feeds.

4.3.4. Performance Under Humid Conditions

The promising CO₂ capture performance of ee-2-Mg₂(dobpdc) from dry, high-pressure feeds prompted our further investigation of this material for CO₂ capture under humid conditions. Water isotherms (Figure 4.S29) were first collected and indicated minimal adsorption below condensation at pressures of ~ 15 , 20, and 40 mbar at 25, 30, and 40 °C, respectively. A differential enthalpy of H₂O adsorption of -49 ± 1 kJ/mol was calculated from the adsorption isotherms at a loading of 3.6 mmol/g (1 H₂O per diamine, Figure 4.S30); however, this value does not account for potential differences in the binding site and interaction energy of water with the framework after CO₂ insertion.

The mixture selectivity of ee-2-Mg₂(dobpdc) was then evaluated through breakthrough experiments under humidified gas feeds. With simulated associated gas (7 bar, 10% CO₂ in CH₄, 30 °C, 300 sccm), a five-fold increase in the CO₂ breakthrough volume and elimination of the CO₂ slip were observed in the second cycle of a feed at 55% relative humidity (RH) as compared to a dry feed (Figure 4.7a; activation at 30 °C with a vacuum pressure of 0.02 mbar between cycles). Similarly, improved performance was observed for humid simulated non-associated gas. Following pre-saturation of the bed with water at 30 °C, the bed was evacuated at 30 °C and fed a dry mixture of 10% CO₂ in CH₄ at 50 bar, 30 °C, and 300 sccm. Negligible slip and an increased breakthrough time were observed compared to an equivalent experiment with a dry bed and dry feed (Figure 4.S61). To corroborate these results, equilibrium CO₂ isotherms were collected for the powdered and pelletized materials before and after saturation with water ($P/P_0 = \sim 0.7$) and after saturation and subsequent evacuation with a turbomolecular pump at 30 °C (Figure 4.S32). The step-shaped CO₂ isotherms of the water-exposed materials matched those of the pristine material, although a 5% decrease in post-step CO₂ capacity was observed at 1 bar (Figure 4.S32).

In stark contrast, zeolite 13X showed an eight-fold decrease in CO₂ breakthrough volume in the second cycle with simulated associated gas at 55% RH due to passivation of the CO₂ binding sites by water (Figure 4.7b). As a result, if the H₂O front were to advance through the bed in a PSA process, utilizing zeolite 13X as the adsorbent would require either costly pre-drying of the stream or periodic full regeneration at temperatures of 250–300 °C. Employing amine-

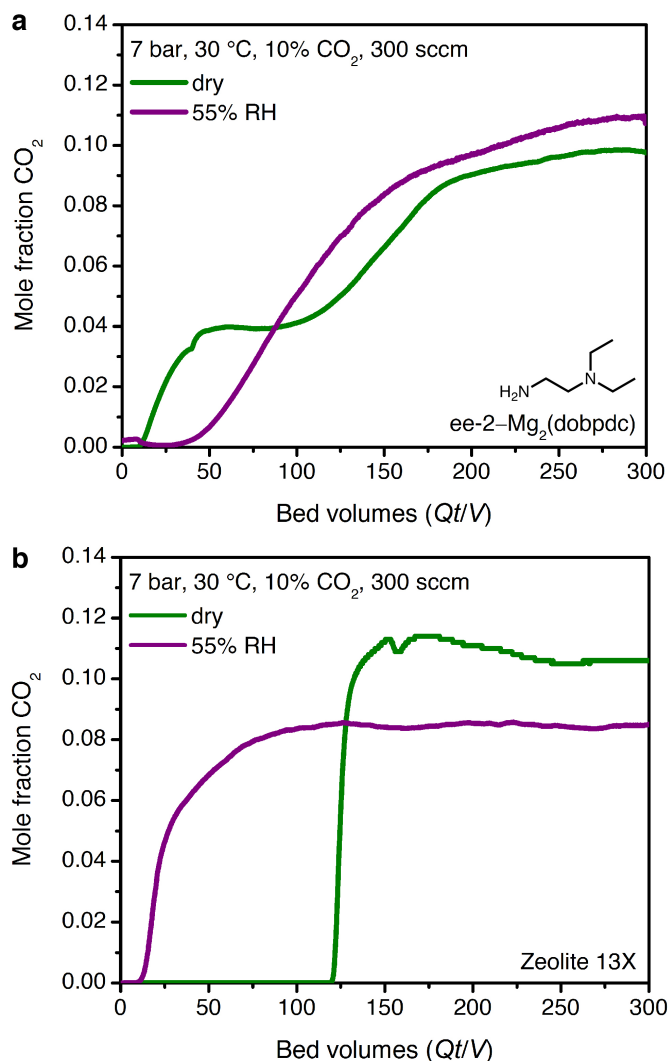


Figure 4.7. Dry (green) and humid (purple, 55% RH, second cycle) qualitative breakthrough curves for (a) ee-2-Mg₂(dobpdc) and (b) zeolite 13X. Humidity eliminates CO₂ slip for ee-2-Mg₂(dobpdc) and generates a five-fold increase in breakthrough volume, while zeolite 13X shows an eight-fold decrease in breakthrough volume under humid conditions. Materials were evacuated at 30 °C with a vacuum pressure of 0.02 mbar for 12 h between cycles.

functionalized adsorbents for direct removal of CO₂ from humid streams may therefore provide significant energy savings in a PSA process, although post-purification drying of CH₄ would still be required prior to pipeline transport. Several previous reports have noted equivalent or improved CO₂ capture performance in the presence of water for amine-functionalized silicas and diamine-appended frameworks.^{21,23,33,48–53} However, to our knowledge, the dramatic humidity-induced improvement in capture rate in the breakthrough profile of ee-2-Mg₂(dobpdc) has not been observed previously for other classes of amine-functionalized adsorbents. We therefore sought to determine the mechanism underlying the improved performance of ee-2-Mg₂(dobpdc) under humid conditions.

4.3.5. Mechanism of CO₂ Adsorption and Proposed Role of Water

X-ray diffraction, infrared spectroscopy, and thermogravimetric analysis were used to probe the structural nuances underlying differences in the observed CO₂ adsorption behavior under dry and humid conditions. Previous characterization of ee-2-Mg₂(dobpdc) by ¹H, ¹³C, and ¹⁵N NMR spectroscopy, combined with DFT calculations, confirmed that ee-2-Mg₂(dobpdc) forms ammonium carbamate chains upon CO₂ adsorption;⁵⁴ however, crystallographic characterization of the chain structure has not been reported to date. While diffraction-quality crystals could not be obtained for the magnesium framework, single-crystals of the corresponding ee-2-Zn₂(dobpdc) framework were synthesized and could be analyzed by single-crystal X-ray diffraction. Here, we report the first CO₂-inserted structure for a 1^o/3^o diamine-appended framework (Figure 4.8; see Figure 4.S69 for a thermal ellipsoid plot). Insertion of CO₂ into the

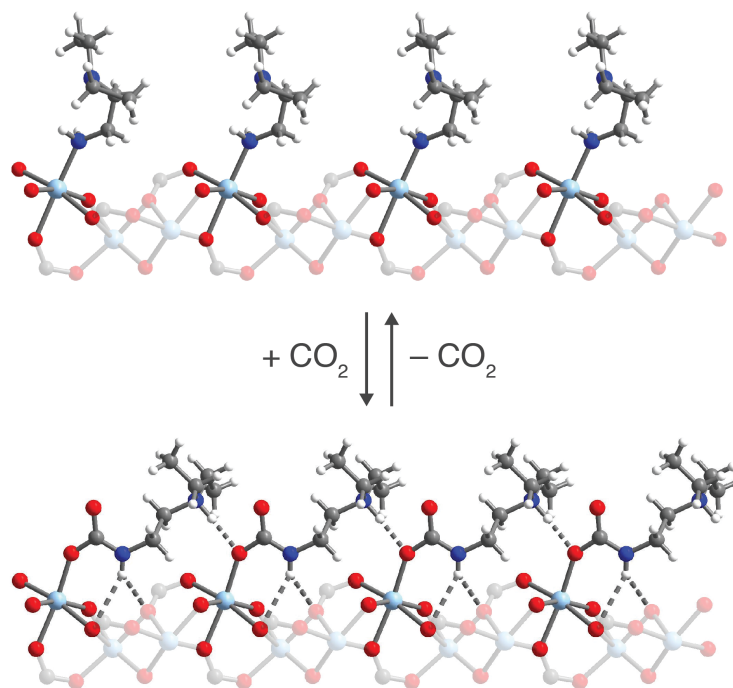


Figure 4.8. Structure of ee-2-Zn₂(dobpdc) before (top) and after (bottom) CO₂ insertion to form ammonium carbamate chains, as observed by single-crystal X-ray diffraction. Light blue, blue, red, gray, and white spheres represent Zn, N, O, C, and H atoms, respectively. The structure of ee-2-Zn₂(dobpdc) prior to CO₂ adsorption was obtained from ref. 31.

Zn–N bonds generates planar, O-bound carbamate species, with corresponding proton transfer to each unbound amine to yield ion-paired ammonium groups.

Attempts at crystallographic observation of water binding within the CO₂-inserted structure are ongoing but have not yet proven successful. As an alternative, we probed the interaction of water with the framework through collection of *in situ* infrared spectra of ee-2-Mg₂(dobpdc) under N₂, dry CO₂, and humid CO₂ (Figure 4.S40). Upon exposure to CO₂, characteristic ammonium carbamate C–N and C–O vibrations are observed at 1320 and 1629 cm⁻¹, respectively. When the CO₂-inserted sample is exposed to humidity, the C–N vibration persists but shifts to slightly higher energy (~1326 cm⁻¹; note that the C–O vibration is obscured by the H–O–H bend at 1630 cm⁻¹). These observations are consistent with preservation of the CO₂ insertion mechanism in the presence of water and suggest hydrogen bonding of water with the carbamate, which would stabilize the CO₂-inserted phase.

Multicomponent isobars were collected to study the effect of water on the CO₂ insertion threshold. Due to safety considerations preventing the use of flammable gases in the TGA furnace, pre-mixed cylinders of CO₂ in N₂ were used to approximate the behavior of ee-2-Mg₂(dobpdc) under CO₂/CH₄ mixtures. Dry isobaric adsorption and desorption profiles were compared to humid isobars obtained by bubbling the incident CO₂/N₂ mixtures through two water bubblers prior to the furnace inlet (Figure 4.9; see Figures 4.S41–4.S48 for other mixture compositions, as well as dry and humid N₂ isobars). Under humid streams (~1.3% H₂O), the step temperature for each mixture increases relative to the step temperature in the corresponding dry isobar, equivalent to a lower CO₂ step pressure in an adsorption isotherm. This shift is again consistent with preferential stabilization of the CO₂-bound phase under humid conditions, which can likely be attributed to hydrogen bonding of water with the metal-bound carbamate species. Importantly, step-like adsorption and desorption behavior is still observed in the humid isobars. Under humid CO₂ at atmospheric pressure, the hysteresis loop closes by 75 °C, supporting a small temperature swing as one potential process configuration. Vacuum-swing or concentration-

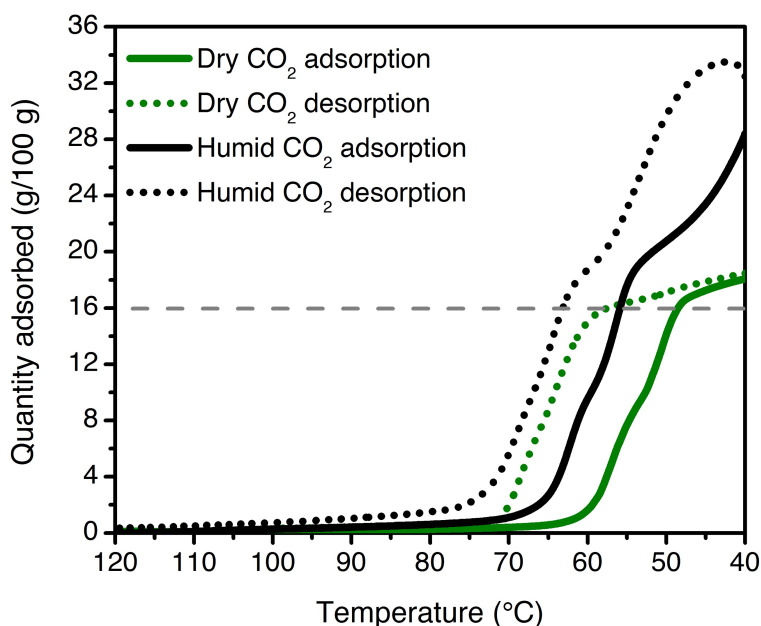


Figure 4.9. Dry (green) and humid (black) CO₂ adsorption (solid lines) and desorption (dotted lines) isobars for ee-2-Mg₂(dobpdc) at atmospheric pressure (ramp rate: 1 °C/min). The cooperative adsorption threshold shifts to higher temperatures under humid conditions, indicating more favorable adsorption in the presence of H₂O. The grey dashed line indicates the capacity anticipated for binding 1 CO₂ per diamine (16.0 g/100 g).

swing processes may also be viable for this material, and optimization of process design is currently in progress.

In light of the humid infrared spectra and isobaric data, the elimination of CO₂ slip in humid breakthrough experiments can be explained using Golden’s rule, as introduced in Figure 4.2. By reducing the effective step pressure for cooperative CO₂ adsorption, water removes the intersection between the operating curve and the adsorption isotherm, resulting in a favorable single-shock breakthrough profile (Figure 4.10). In ongoing work, we are investigating the correlation between relative humidity and capture rate in greater detail, as well as studying the influence of humidity on the kinetics of CO₂ adsorption.

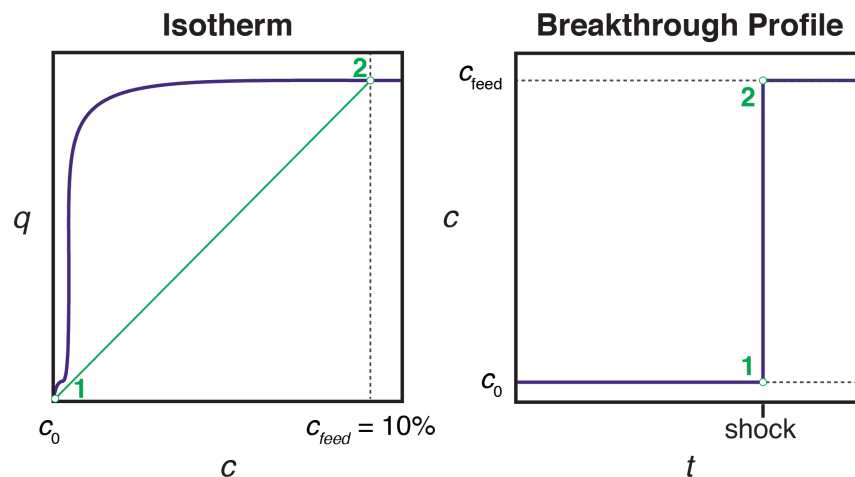


Figure 4.10. Schematic showing generation of a single-shock breakthrough profile (right, concentration vs. time) for an adsorbent with a step-shaped isotherm (left, quantity adsorbed vs. concentration). The operating curve used to predict the breakthrough profile from the isotherm is shown in green, and the numerical labels indicate corresponding points in the isotherm and breakthrough profile. When the operating curve does not intersect the isotherm, CO₂ slip is not observed.

4.3.6. Mechanical Pressure Cycling

The promising breakthrough results obtained with ee-2-Mg₂(dobpdc) prompted us to evaluate the performance of the material following extended pressure cycling. While the binderless pellets investigated in this work do not possess mechanical strength sufficient for evaluation in a true PSA process, the material was evaluated before and after extended mechanical pressure cycling under both dry and humid conditions. A dual-bed system was used, with ~0.85 g of 60–80 mesh (~180–250 μm) semi-spherical, binderless pellets per bed. A total of 250 cycles were completed with the following modified Skarstrom cycle:⁵⁵ (1) adsorption (5 min, 250 sccm of 10% CO₂, 50 bar, 40 °C), (2) pressure equilibration, (3) blowdown to ~1 bar, (4) vacuum desorption (~0.1 bar), (5) pressure equilibration, and (6) repressurization. Approximately 100 cycles were performed first with a dry feed, after which 150 cycles were performed with the feed passed through a water saturation vessel at 20 °C, leading to an estimated water content of 609 ppmv (33% RH at 40 °C). Within the first 10 cycles of the initial dry experiment, the depressurization time increased, which we attribute to collapse of the binderless pellets and subsequent fluidization of the material (Figure 4.S62). In post-cycling analysis, the adsorbent remained crystalline, and no diamine loss was observed in the NMR spectrum of the digested material (Supporting Information, Section 4.6.16). Additionally, sharp, step-shaped CO₂ adsorption was maintained in the CO₂ isobar of ee-2-Mg₂(dobpdc) following mechanical pressure cycling (Figure 4.S66), suggesting that the material can withstand the mechanical strain of both extended pressure cycling and fluidization. These results support further development of ee-2-Mg₂(dobpdc) as a promising adsorbent for natural gas purification directly from humid streams.

4.4. Conclusions

As natural gas continues to supply a growing share of global primary energy, new strategies are needed to remove CO₂ contamination from currently unusable reserves. Here, we have

shown that the framework ee-2-Mg₂(dobpdc) is a promising candidate for natural gas purification in a PSA process, the first-such demonstration with a diamine-appended metal-organic framework. Using dry breakthrough experiments, we have also reiterated the importance of considering CO₂ “slip” for adsorbents with step-shaped adsorption isotherms.^{32,36} Humid breakthrough experiments subsequently revealed that water significantly improves the CO₂ capture performance of ee-2-Mg₂(dobpdc) by eliminating pre-breakthrough slip. In contrast, an equivalent experiment with the benchmark material zeolite 13X revealed a rapid loss of CO₂ capacity following saturation with water, an observation consistent with previous results for adsorbents relying on exposed metal cations as binding sites. Through spectroscopic characterization and multicomponent isobars, we have traced the origin of improved performance under humid conditions to stabilizing H₂O-carbamate interactions. Finally, we have shown that ee-2-Mg₂(dobpdc) retains its cooperative adsorption properties following extended mechanical pressure cycling under both dry and humid simulated natural gas feeds. These results support further development of ee-2-Mg₂(dobpdc) for this important separation.

In future work, we aim to model the influence of both the relative humidity and temperature on the CO₂ capture performance of ee-2-Mg₂(dobpdc). Additionally, we will evaluate the potential for co-removal of H₂S, which can be present in crude natural gas streams at concentrations as high as 16 mol % and must be reduced to a level of ~5–15 ppm.⁵⁶ A number of recent studies have explored the interaction of H₂S with metal-organic frameworks,^{57,56,58–63} but the effect of H₂S on diamine-appended Mg₂(dobpdc) frameworks remains untested. Furthermore, shaped particles or other structured forms are needed to evaluate the material in a full PSA process and to determine the CH₄ recovery and purity achievable in an optimized cycle configuration. Co-adsorption of heavier hydrocarbons and the influence of heat effects should also be evaluated at that stage. Finally, as these materials advance toward commercialization, innovative process design strategies are needed to leverage the cooperative adsorption mechanism while managing the corresponding thermal front.

4.5. Acknowledgements

This work has been submitted for publication as an article entitled “A Cooperative Adsorbent for the Switch-Like Capture of Carbon Dioxide from Crude Natural Gas” with authors Rebecca L. Siegelman, Joshua A. Thompson, Jarad A. Mason, Thomas M. McDonald, and Jeffrey R. Long.

We gratefully acknowledge Chevron Energy Technology Company for financial support of this work. Structural and spectroscopic studies were supported through the Center for Gas Separations, an Energy Frontier Research Center funded by the U.S. Department of Energy, Office of Science, Office of Basic Energy Sciences under Award DE-SC0001015. Single-crystal X-ray diffraction data were collected on Beamline 12.2.1 at the Advanced Light Source at Lawrence Berkeley National Laboratory, which is supported by the Director, Office of Science, Office of Basic Energy Sciences, of the U.S. Department of Energy under Contract No. DE-AC02-05CH11231. Synchrotron powder X-ray diffraction data were collected at the Advanced Photon Source, a U.S. Department of Energy Office of Science User Facility operated for the DOE Office of Science by Argonne National Laboratory under Contract No. DE-AC02-06CH11357. We thank Levi Merrell (Chevron Energy Technology Company), Eugene Kim (UC Berkeley), and Kristen Colwell (UC Berkeley) for experimental assistance; Stephen DeWitt (Georgia Institute of Technology) and Dr. Miguel I. Gonzalez, Dr. Jeffrey Martell, Dr. Phillip Milner, Dr. Jonathan Bachman, and Ever Velasquez (all of UC Berkeley) for helpful discussions;

and Dr. Katie Meihaus (UC Berkeley) for editorial assistance.

4.6. Supporting Information

4.6.1. Characterization of Mg₂(dobpdc)

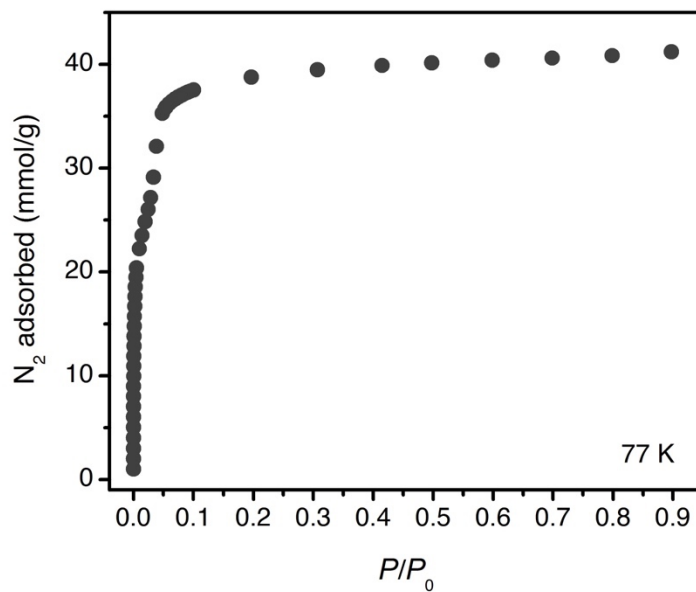


Figure 4.S1. Surface area measurement of Mg₂(dobpdc) with N₂ at 77 K. The Brunauer-Emmett-Teller (BET) surface area was calculated as 2520 ± 40 m²/g, and the Langmuir surface area was calculated as 4090 ± 12 m²/g.

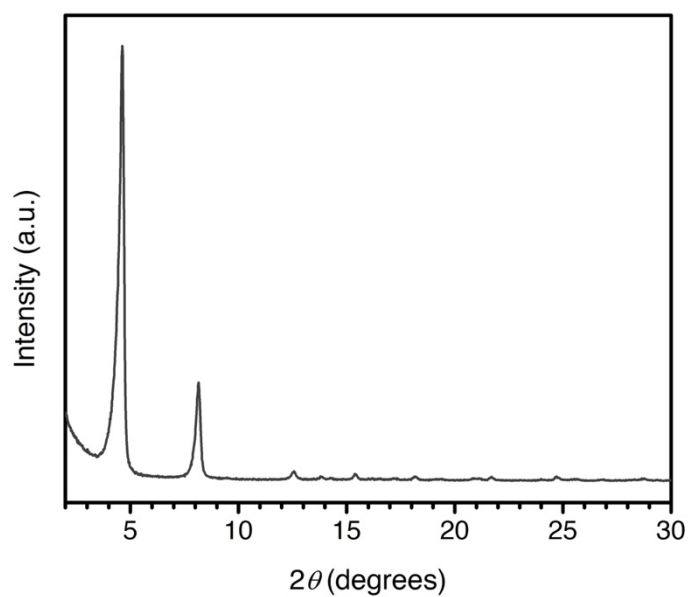


Figure 4.S2. Laboratory powder X-ray diffraction pattern ($\lambda = 1.5418$ Å) of activated Mg₂(dobpdc) in air.

4.6.2. Additional Characterization of ii-2-Mg₂(dobpdc)

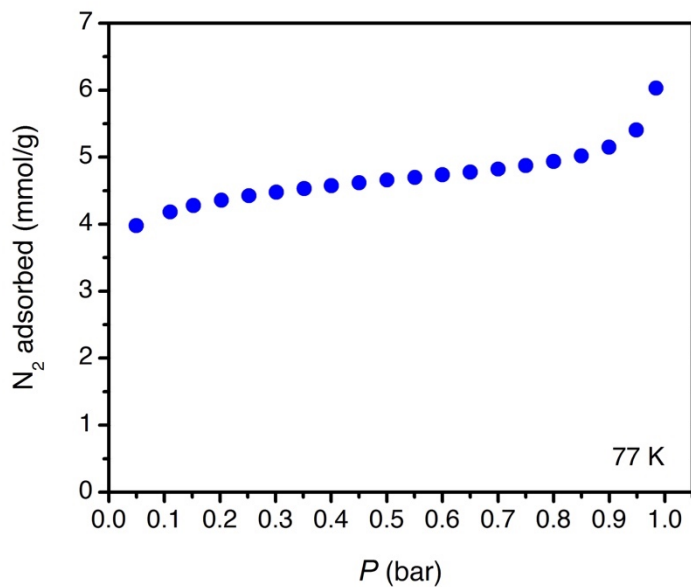


Figure 4.S3. Surface area measurement of ii-2-Mg₂(dobpdc) with N₂ at 77 K. The Langmuir surface area was calculated as 490 ± 4 m²/g. A pore volume of 0.17 cm³/g was calculated from the loading at $P/P_0 = 0.70$.

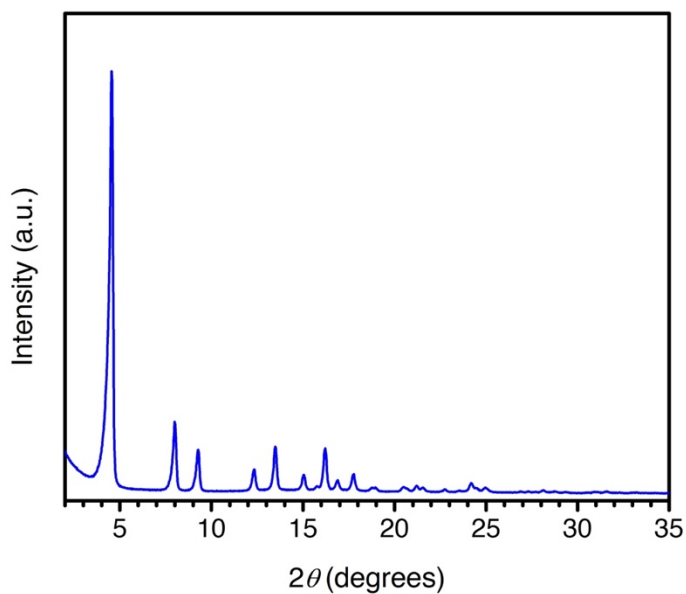


Figure 4.S4. Laboratory powder X-ray diffraction pattern ($\lambda = 1.5418$ Å) for as-synthesized ii-2-Mg₂(dobpdc).

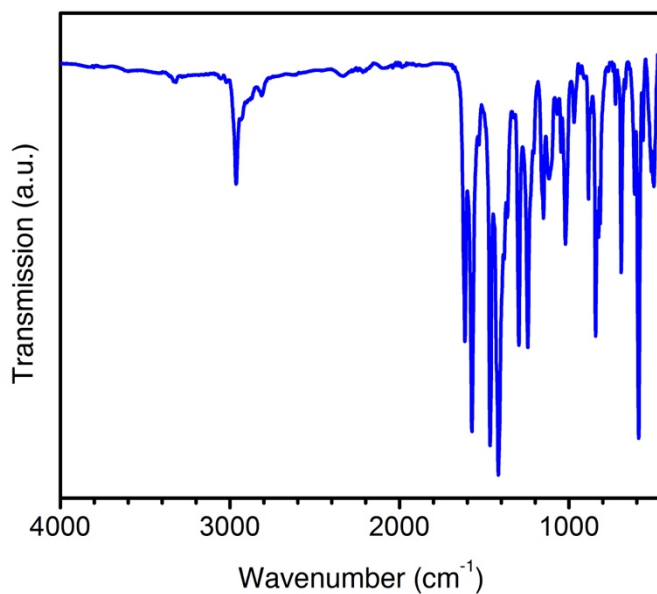


Figure 4.S5. Infrared spectrum of ii-2-Mg₂(dobpdc) following activation from hexanes.

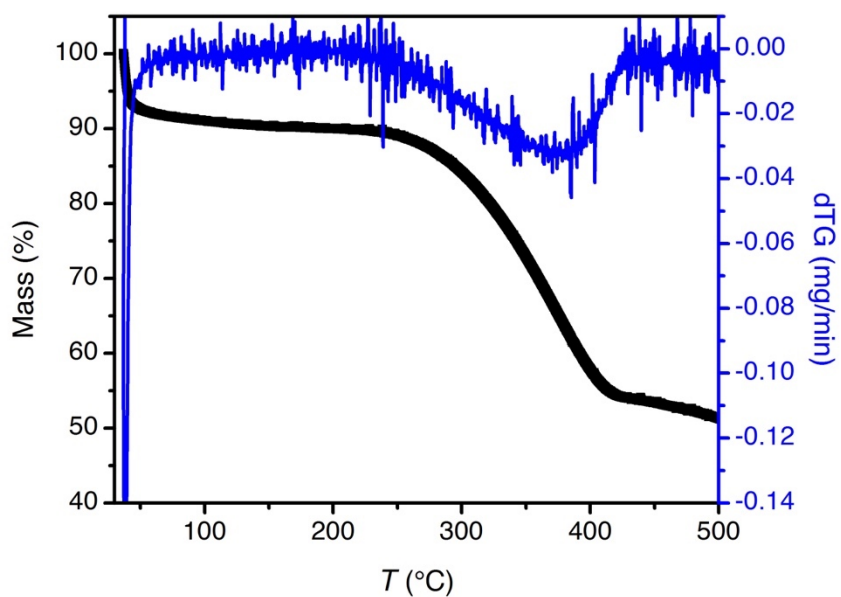


Figure 4.S6. Thermogravimetric decomposition traces (black) and derivative decomposition traces (dTG, blue) for ii-2-Mg₂(dobpdc). A temperature ramp rate of 2 °C/min was used. The dTG peak at lowest temperature is due to excess solvent (toluene or hexanes) in the framework pores, while the higher temperature peak is due to volatilization of the diamine.

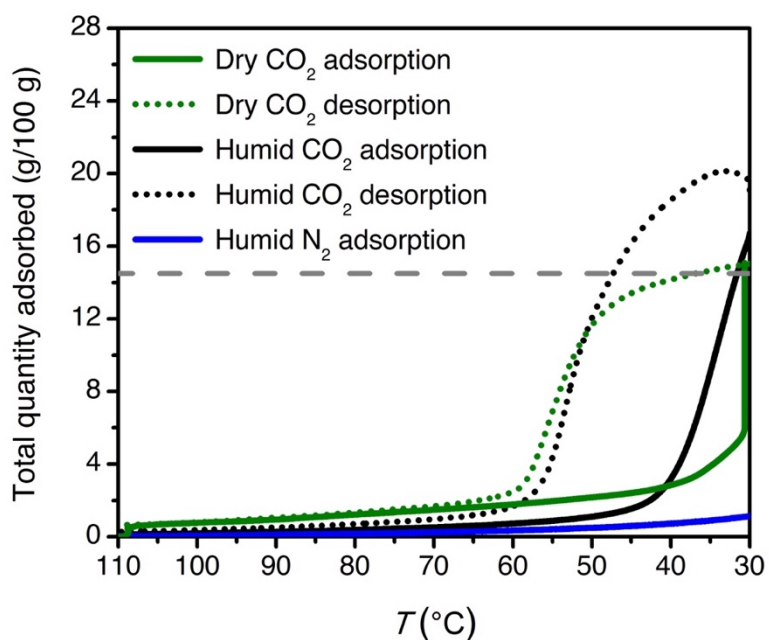


Figure 4.S7. Dry (green) and humid (black) adsorption (solid lines) and desorption (dotted lines) isobars for pure CO₂, as well as a humid N₂ adsorption isobar (blue), for ii-2-Mg₂(dobpdc). The material was activated at 110 °C under flowing dry (green) or humid (black) N₂ for 20 min. A ramp rate of 1 °C/min was used, and isobars were collected at atmospheric pressure. The expected adsorption capacity corresponding to 1 CO₂ per diamine is indicated as a dashed gray line. For the dry CO₂ isobar, the temperature was held isothermally at 30 °C for 45 min prior to beginning the desorption branch of the isobar. The dry CO₂ isobar is reproduced from reference ³¹.

4.6.3. Additional Characterization of ee-2-Mg₂(dobpdc)

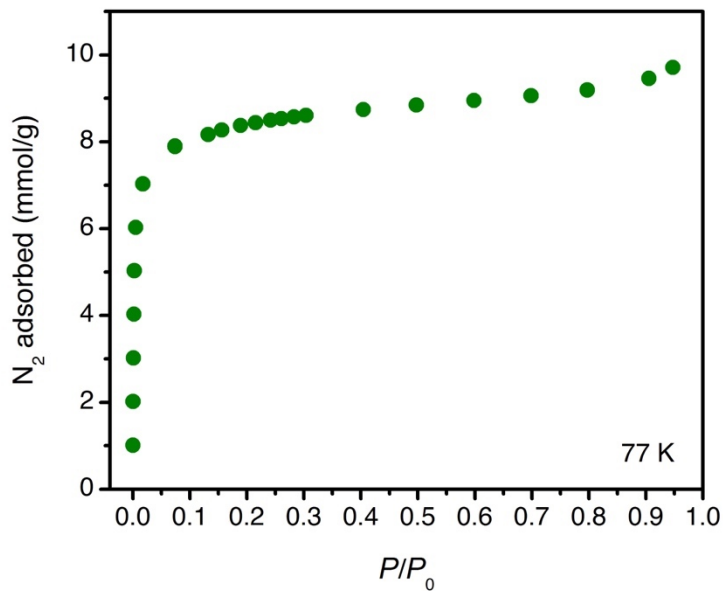


Figure 4.S8. Surface area measurement of ee-2-Mg₂(dobpdc) with N₂ at 77 K. The Brunauer-Emmett-Teller (BET) surface area was calculated as 726 ± 2 m²/g, and the Langmuir surface area was calculated as 911 ± 4 m²/g. A pore volume of 0.32 cm³/g was calculated from the loading at $P/P_0 = 0.80$.

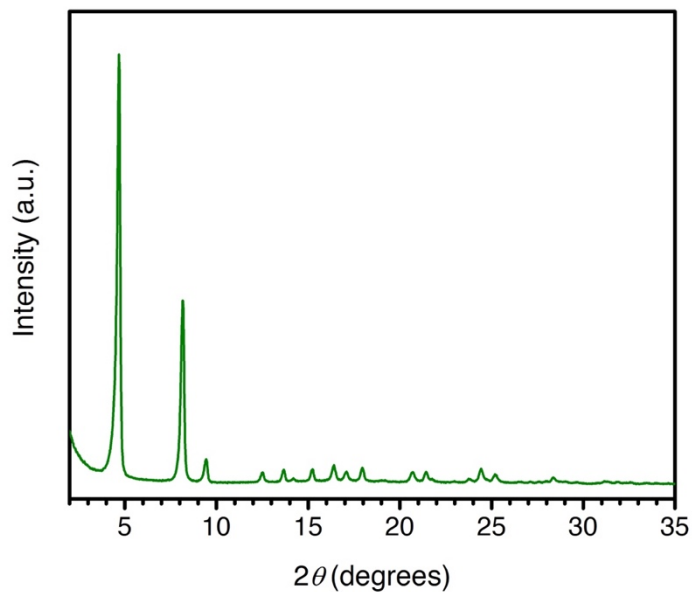


Figure 4.S9. Laboratory powder X-ray diffraction pattern ($\lambda = 1.5418 \text{ \AA}$) for as-synthesized ee-2-Mg₂(dobpdc).

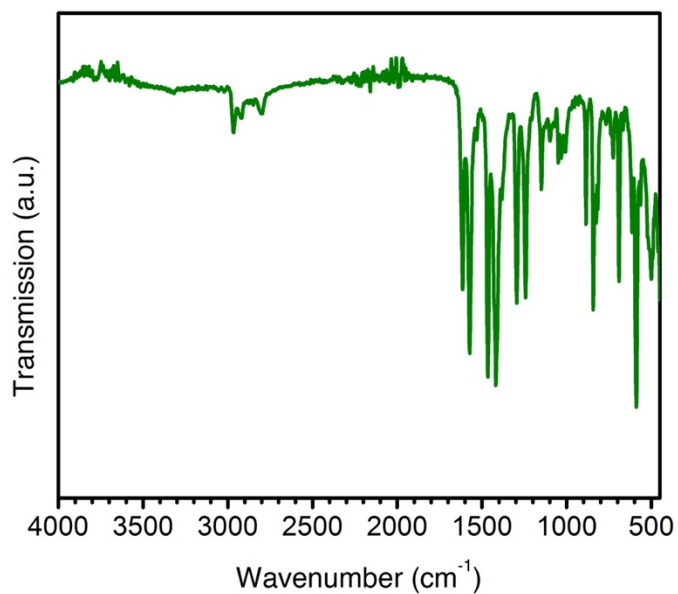


Figure 4.S10. Infrared spectrum of ee-2-Mg₂(dobpdc) following activation from hexanes.

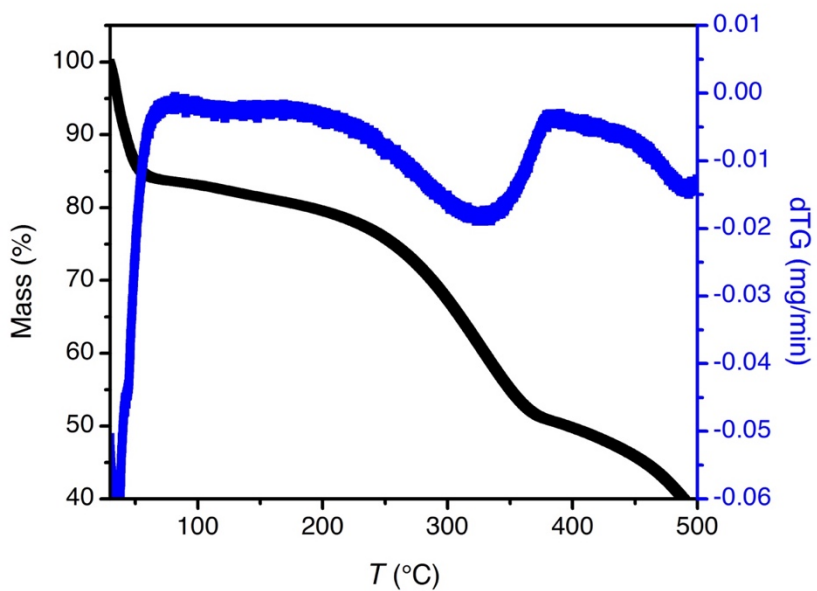


Figure 4.S11. Thermogravimetric decomposition traces (black) and derivative decomposition traces (dTG, blue) for ee-2-Mg₂(dobpdc). A temperature ramp rate of 2 °C/min was used. The dTG peak at lowest temperature is due to excess solvent (toluene or hexanes) in the framework pores, while the higher temperature peak is due to volatilization of the diamine.

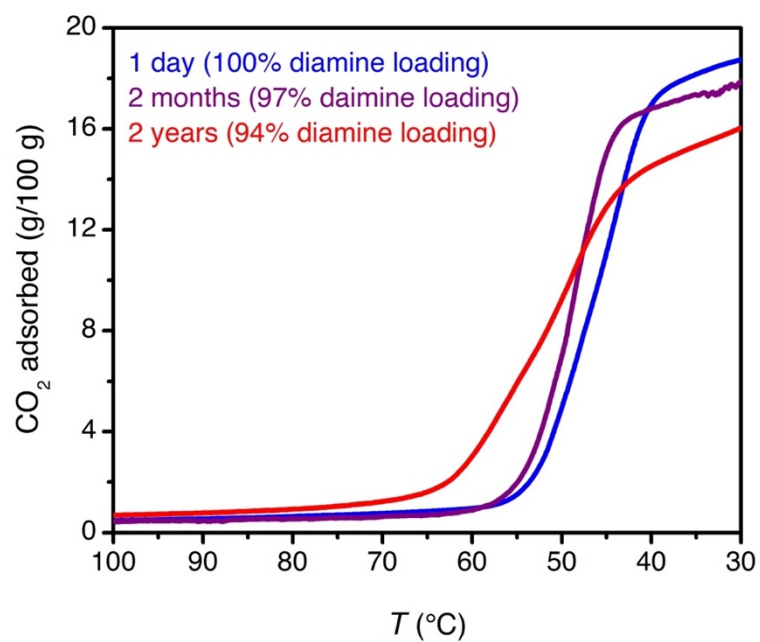


Figure 4.S12. Pure CO₂ adsorption isobars of ee-2-Mg₂(dobpdc) after storage in a sealed vial in air for 1 day (blue), 2 months (purple), and 2 years (red). The reported diamine loadings were determined after isobar collection by digesting the samples with DCI following the procedure in the main text and comparing the diamine and ligand peak integrals in the NMR spectra.

4.6.4. Isotherm Backgrounds and Fits

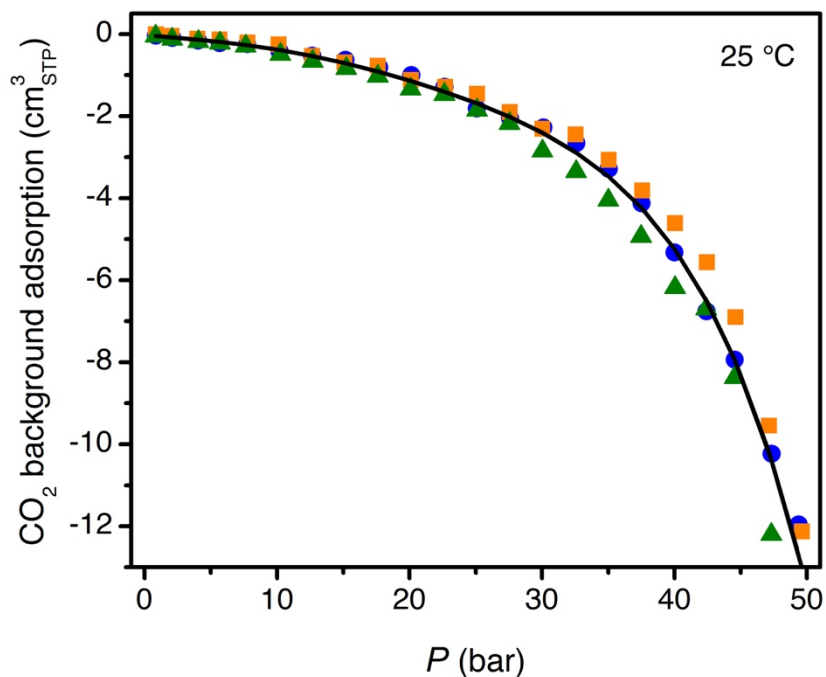


Figure 4.S13. Three background CO₂ adsorption isotherms (symbols) at 25 °C for an empty high-pressure sample holder. The black line represents a 5th order polynomial fit to the background adsorption and was used to correct high-pressure adsorption data at 25 °C. The same background correction procedure was used for high-pressure data at other temperatures. The negative background adsorption likely results from a temperature gradient between the exposed portion of the sample holder and the portion in the isothermal bath.

Type I isotherms for each material were fit with a single- or dual-site Langmuir ($v_i = 1$) or Langmuir–Freundlich ($v_i \neq 1$) equation (eq 4.S1), where q is the total amount adsorbed in mmol/g, P is the pressure in bar, $q_{sat,i}$ is the saturation capacity in mmol/g, and b_i is the Langmuir parameter in bar^{- v} for up to two sites 1 and 2. Isotherms were fit either individually at each temperature or simultaneously as a function of temperature, as specified in the figure and table captions. For simultaneous fits, the Langmuir parameter was expressed using eq 4.S2, where S_i is the site-specific molar entropy of adsorption in J/mol·K, E_i is the site-specific binding energy in kJ/mol, R is the gas constant in J/mol·K, and T is the temperature in K. The fit parameters for each material can be found alongside the corresponding fits in Sections S4.6.5–4.6.7 below.

$$q = \frac{q_{sat,1}b_1P^{v_1}}{1+b_1P^{v_1}} + \frac{q_{sat,2}b_2P^{v_2}}{1+b_2P^{v_2}} \quad (4.S1)$$

$$b_i = e^{-\frac{S_i}{R}} e^{E_i \frac{1000}{RT}} \quad (4.S2)$$

4.6.5. Additional Isotherms, Fits, and Thermodynamic Data for ii-2-Mg₂(dobpdc)

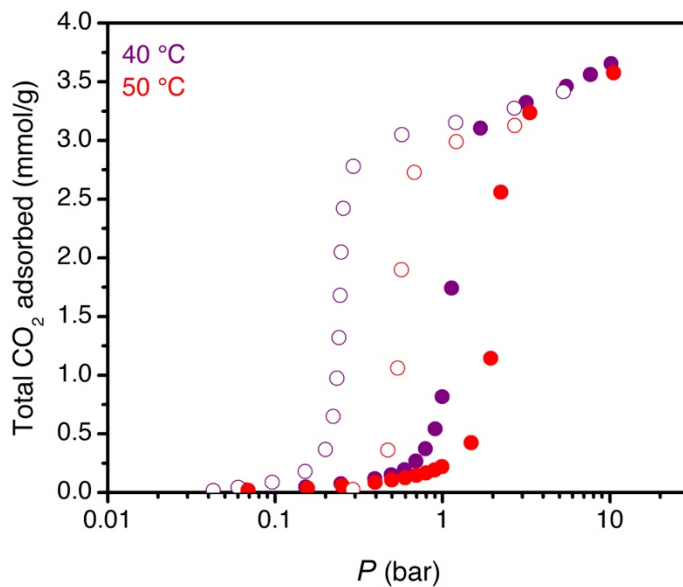


Figure 4.S14. High-pressure CO₂ adsorption (filled circles) and desorption (open circles) isotherms for ii-2-Mg₂(dobpdc). A maximum of 60 min was allotted for equilibration for each data point.

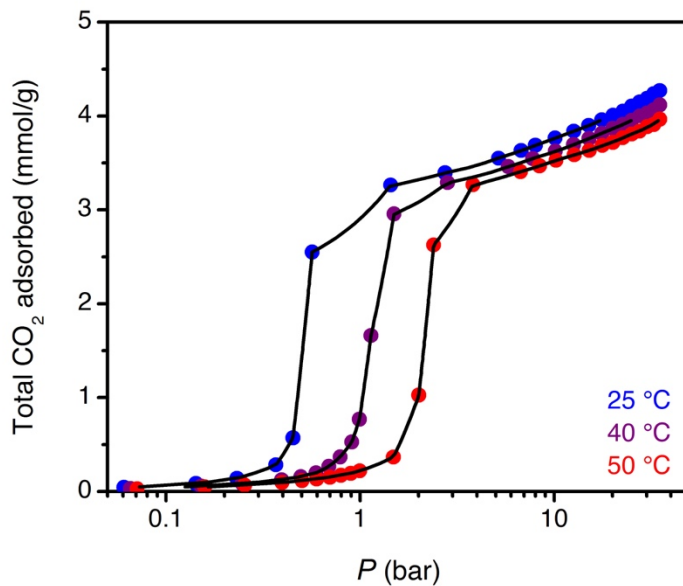


Figure 4.S15. Spline interpolation of CO₂ isotherms for ii-2-Mg₂(dobpdc) used in the calculation of loading-dependent differential enthalpies and entropies of adsorption.

Using the adsorption enthalpy of -45 kJ/mol CO_2 within the cooperative adsorption step and the measured step onset pressure of 1 bar at 40 °C, the step onset pressure can be predicted at any temperature using the Clausius–Clapeyron relationship, as shown in eq 4.S3:

$$p_{step}(T) = p_{step,T_0} e^{\left(\frac{\Delta H_{step}}{R}\right)\left(\frac{1}{T_0} - \frac{1}{T}\right)} \quad (4.S3)$$

Here, p_{step,T_0} is a reference step pressure at temperature T_0 in (K), ΔH_{step} is the differential adsorption enthalpy in kJ/mol within the cooperative adsorption step, and R is the universal gas constant in kJ/(mol·K).

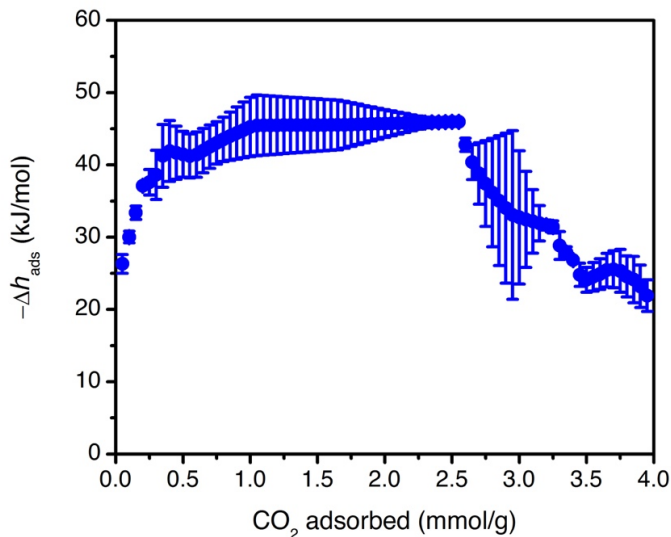


Figure 4.S16. Loading-dependent differential enthalpy of CO_2 adsorption for ii-2- $\text{Mg}_2(\text{dobpdc})$ calculated from spline interpolation of the CO_2 adsorption isotherms at 25, 40, and 50 °C.

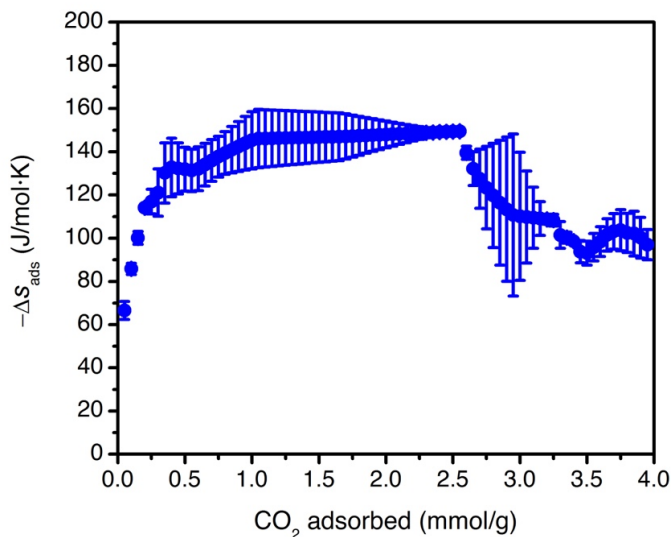


Figure 4.S17. Loading-dependent differential entropy of CO_2 adsorption for ii-2- $\text{Mg}_2(\text{dobpdc})$ calculated from spline interpolation of the CO_2 adsorption isotherms at 25, 40, and 50 °C.

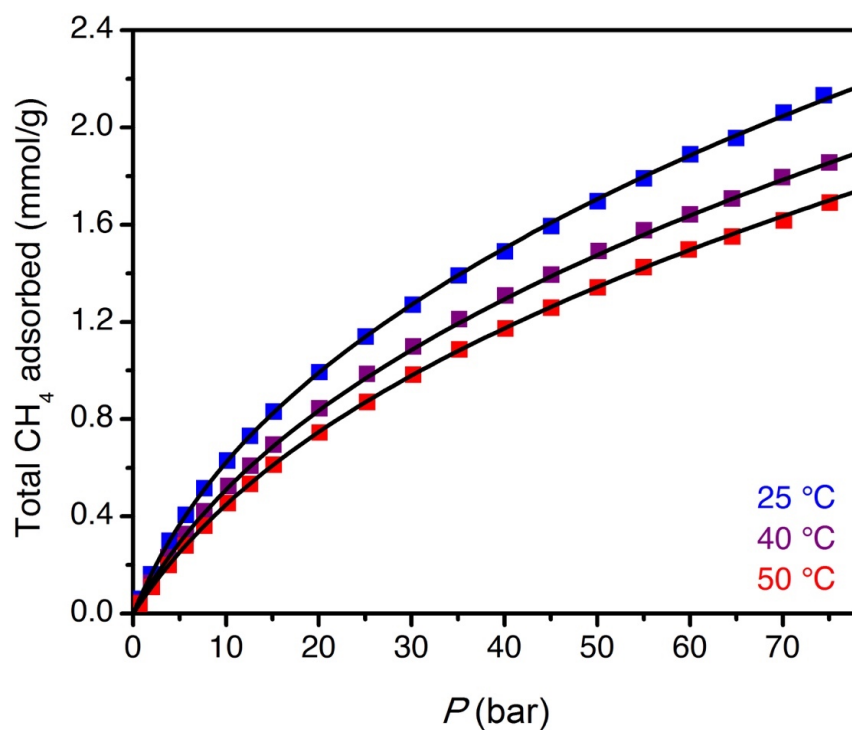


Figure 4.S18. High-pressure CH₄ adsorption isotherms for ii-2-Mg₂(dobpdc) (squares) and corresponding simultaneous dual-site Langmuir fits (black lines).

Table 4.S1. Dual-site Langmuir fit parameters for the CH₄ adsorption isotherms of ii-2-Mg₂(dobpdc) at 25, 40, and 50 °C (fit simultaneously for all temperatures); $q_{sat,i}$ is the saturation capacity, S_i is the site-specific molar entropy of adsorption, E_i is the site-specific binding energy, and R is the gas constant in J/mol·K.

$q_{sat,1}$ (mmol/g)	$-S_1$ (R)	$-E_1$ (kJ/mol)	$q_{sat,2}$ (mmol/g)	$-S_2$ (R)	$-E_2$ (kJ/mol)
0.88	8.6	15.2	5	10.5	12.8

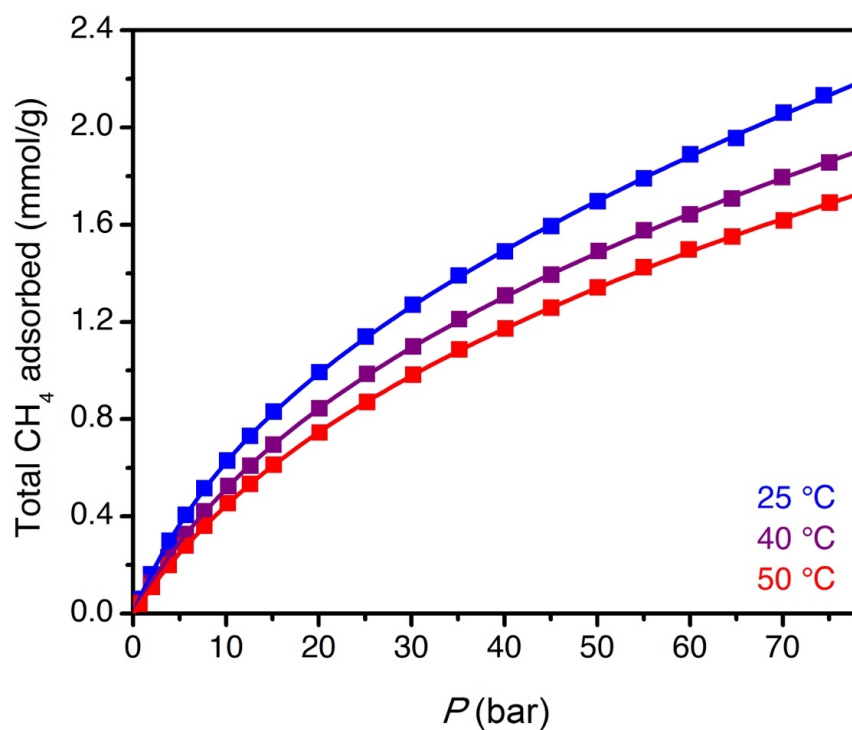


Figure 4.S19. High-pressure CH₄ adsorption isotherms for ii-2-Mg₂(dobpdc) (squares) and corresponding dual-site Langmuir fits at individual temperatures (lines).

Table 4.S2. Dual-site Langmuir fit parameters for the CH₄ adsorption isotherms of ii-2-Mg₂(dobpdc) at 25, 40, and 50 °C (fit independently for all temperatures); $q_{sat,i}$ is the saturation capacity, S_i is the site-specific molar entropy of adsorption, E_i is the site-specific binding energy, and R is the gas constant in J/mol·K.

T (K)	$q_{sat,1}$ (mmol/g)	$-S_1$ (R)	$-E_1$ (kJ/mol)	$q_{sat,2}$ (mmol/g)	$-S_2$ (R)	$-E_2$ (kJ/mol)
298	1.1	8.0	13.2	8.0	7.2	3.0
313	1.0	8.0	13.1	5.3	7.1	3.6
323	1.0	6.9	10.0	4.7	6.8	3.0

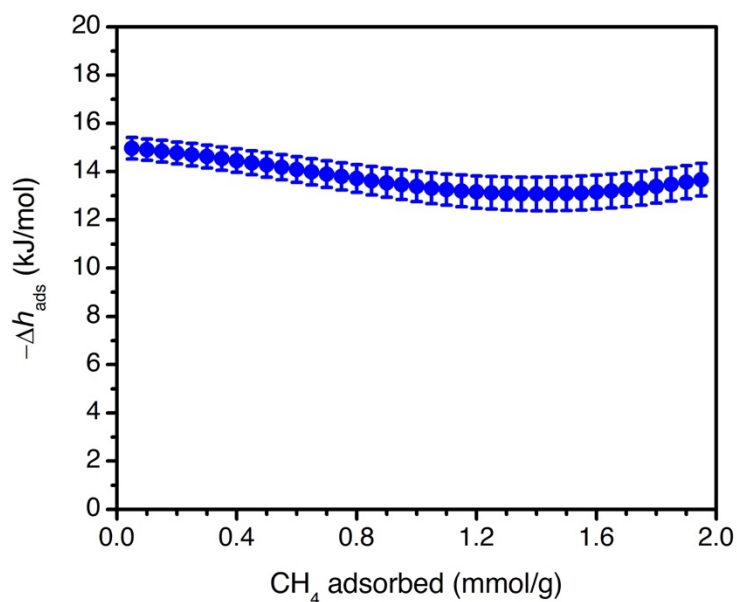


Figure 4.S20. Loading-dependent differential enthalpy of CH₄ adsorption for ii-2-Mg₂(dobpdc), as calculated from individual, dual-site Langmuir fits of the high-pressure total adsorption isotherms at 25, 40, and 50 °C.

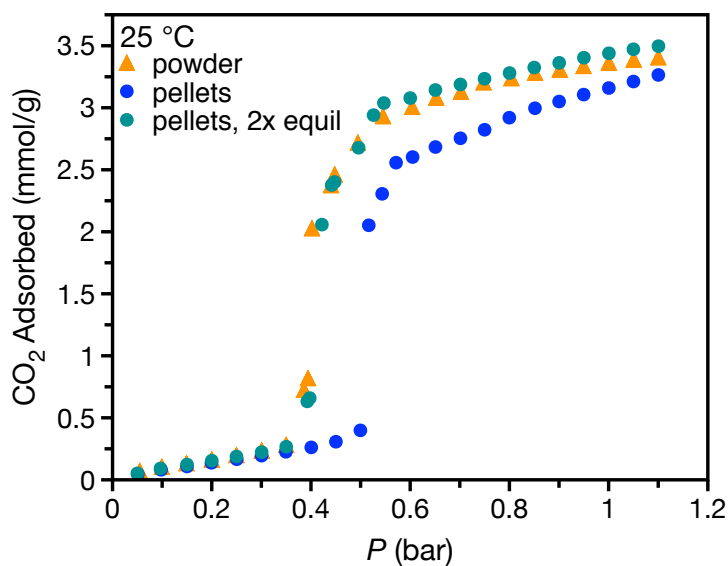


Figure 4.S21. Comparison of low-pressure CO₂ adsorption isotherms at 25 °C for as-synthesized ii-2-Mg₂(dobpdc) powder (orange triangles), 25–45 mesh binderless pellets (blue circles), and the pelletized adsorbent with twice the standard equilibration time (teal circles). Equilibration is defined as <0.01% change in pressure over an average of 11 intervals of the user-specified equilibration interval, with the standard interval set as 15 s. The isotherm of the pelletized adsorbent was found to match that of the powder only when longer equilibration times were allotted, consistent with a kinetics limitation.

4.6.6. Additional Isotherms, Fits, and Thermodynamic Data for ee-2-Mg₂(dobpdc)

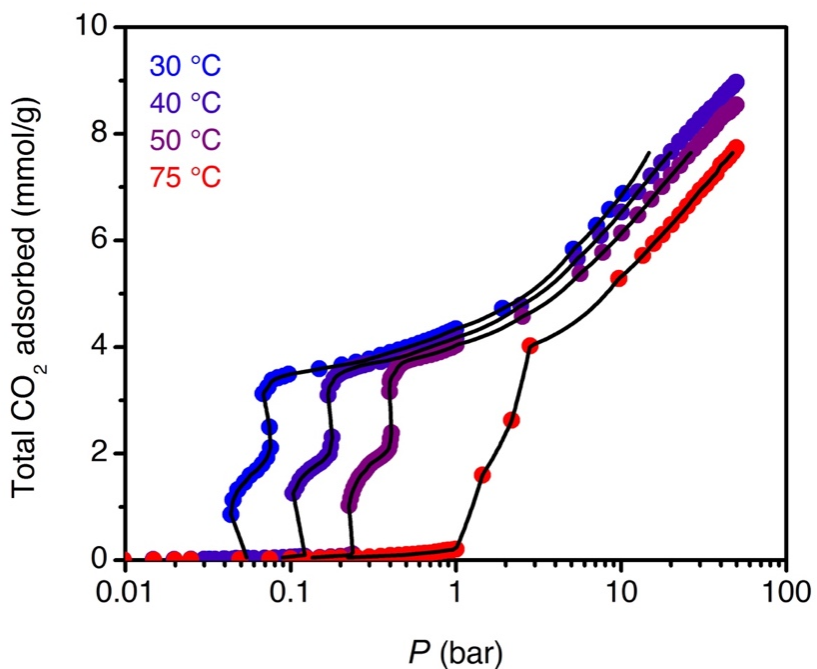


Figure 4.S22. Spline interpolation of CO₂ isotherms (black lines) for ee-2-Mg₂(dobpdc) used in the calculation of loading-dependent differential enthalpies and entropies of adsorption.

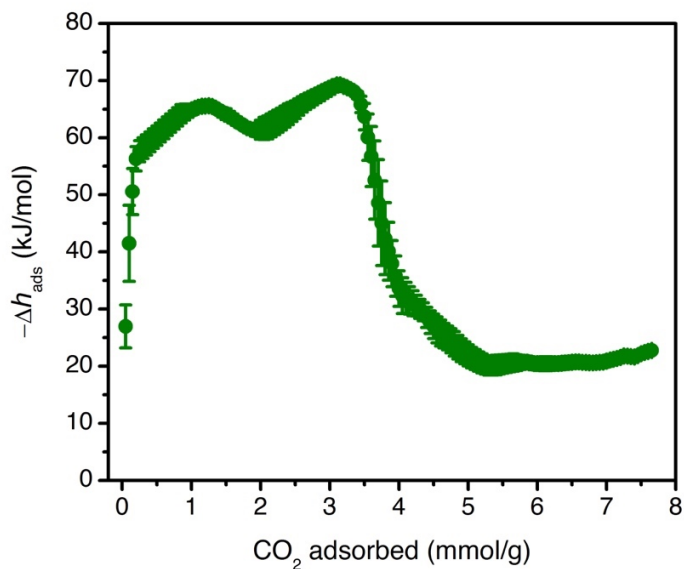


Figure 4.S23. Loading-dependent differential enthalpy of CO₂ adsorption for ee-2-Mg₂(dobpdc) calculated from spline interpolation of the CO₂ adsorption isotherms at 30, 40, 50, and 75 °C.

Using the average adsorption enthalpy of -64 kJ/mol CO_2 within the first cooperative adsorption step and the measured onset pressure of 0.24 bar for the first adsorption step at 50 °C, the step onset pressure for the first step can be predicted at any temperature using the Clausius–Clapeyron relationship, as shown in eq 4.S3.

Table 4.S3. Measured onset pressures for the first cooperative CO_2 adsorption step of ee-2-Mg₂(dobpc), and onset pressures predicted from the Clausius–Clapeyron relationship and a reference step pressure of 0.24 bar at 50 °C.

T (°C)	$P_{\text{step, measured}}$ (bar)	$P_{\text{step, predicted}}$ (bar)
25	0.02	0.03
30	0.05	0.05
40	0.11	0.11
55	not measured	0.35
60	not measured	0.50
65	not measured	0.70
70	not measured	0.98
75	$1.0 < P_{\text{step}} < 1.4$	1.36

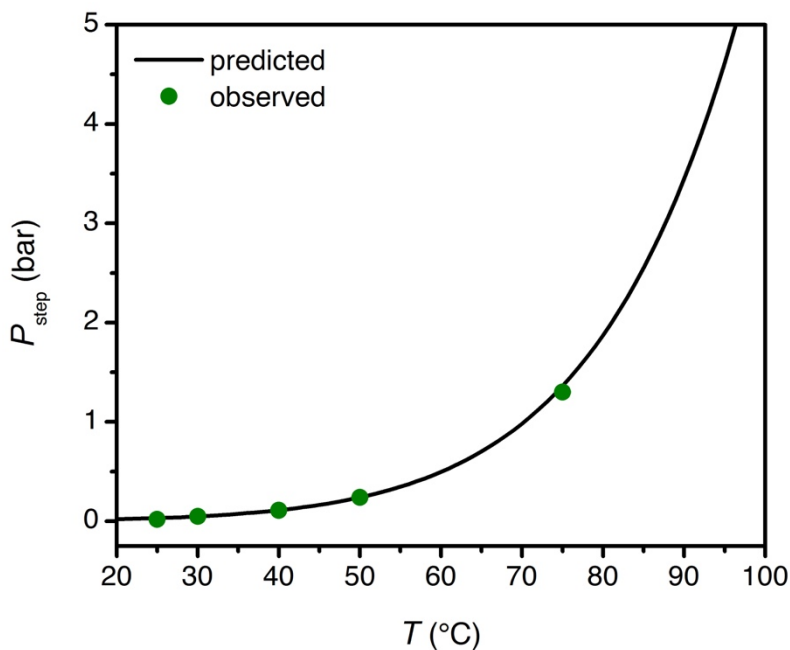


Figure 4.S24. Measured onset pressures for the first cooperative CO_2 adsorption step of ee-2-Mg₂(dobpc), and onset pressures predicted from the Clausius–Clapeyron relationship.

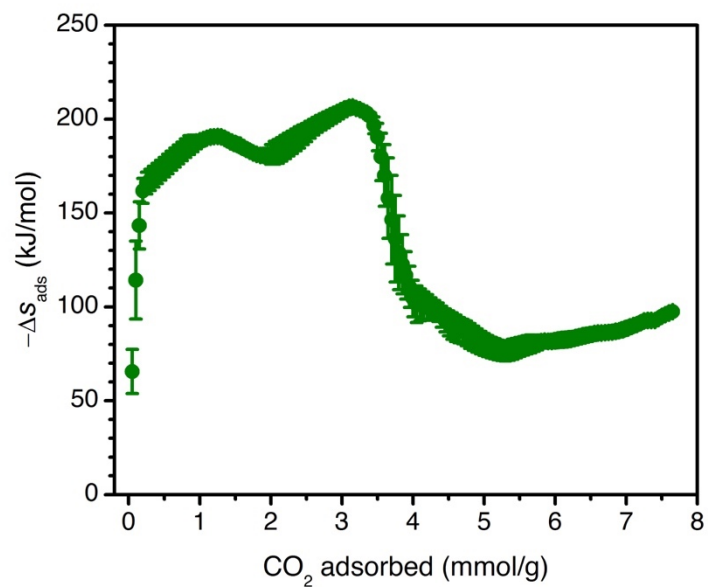


Figure 4.S25. Loading-dependent differential entropy of CO₂ adsorption for ee-2-Mg₂(dobpdc) calculated from spline interpolation of the CO₂ adsorption isotherms at 30, 40, 50, and 75 °C.

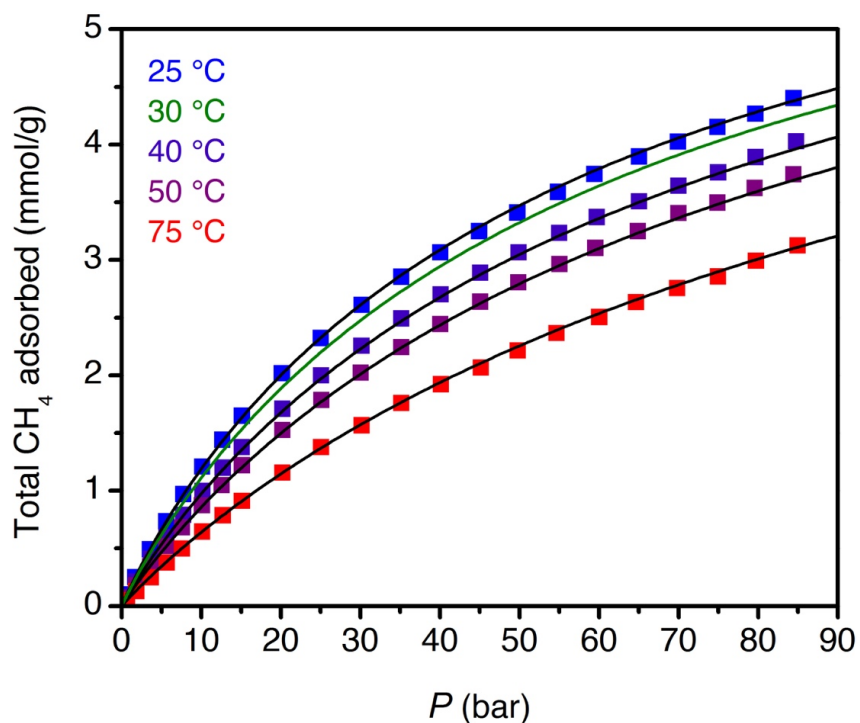


Figure 4.S26. High-pressure CH₄ adsorption isotherms for ee-2-Mg₂(dobpdc) (squares) and corresponding simultaneous single-site Langmuir fits (black lines). The green line shows the simulated CH₄ adsorption isotherm at 30 °C, the temperature used for several breakthrough experiments in this work.

Table 4.S4. Single-site Langmuir fit parameters for the CH₄ adsorption isotherms of ee-2-Mg₂(dobpdc) at 25, 40, 50, and 75 °C (fit simultaneously for all temperatures); q_{sat} is the saturation capacity, S is the site-specific molar entropy of adsorption, E is the site-specific binding energy, and R is the gas constant in J/mol·K.

q_{sat} (mmol/g)	$-S$ (R)	$-E$ (kJ/mol)
7.33	8.75	12.2

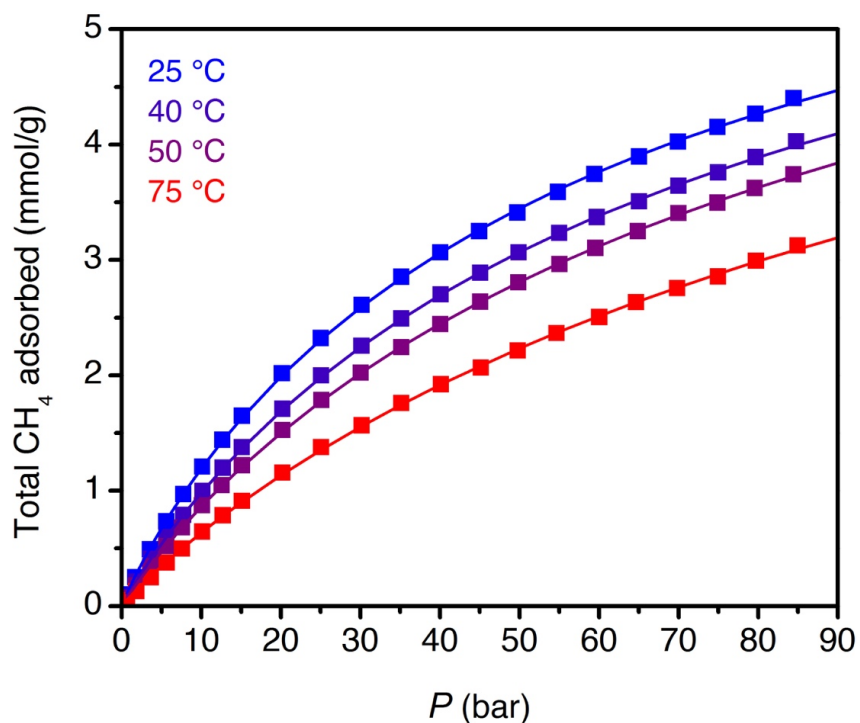


Figure 4.S27. High-pressure CH₄ adsorption isotherms for ee-2-Mg₂(dobpdc) (squares) and corresponding single-site Langmuir–Freundlich fits at individual temperatures (lines).

Table 4.S5. Single-site Langmuir–Freundlich fit parameters for the CH₄ adsorption isotherms of ee-2-Mg₂(dobpdc) at 25, 40, 50, and 75 °C (fit independently for all temperatures); q_{sat} is the saturation capacity, b is the Langmuir constant, and ν is the Freundlich parameter.

T (K)	q_{sat} (mmol/g)	b (bar ^{-ν)}	ν
298	7.54	0.0220	0.932
313	7.37	0.0170	0.955
323	7.561	0.0145	0.948
348	7.684	0.0104	0.939

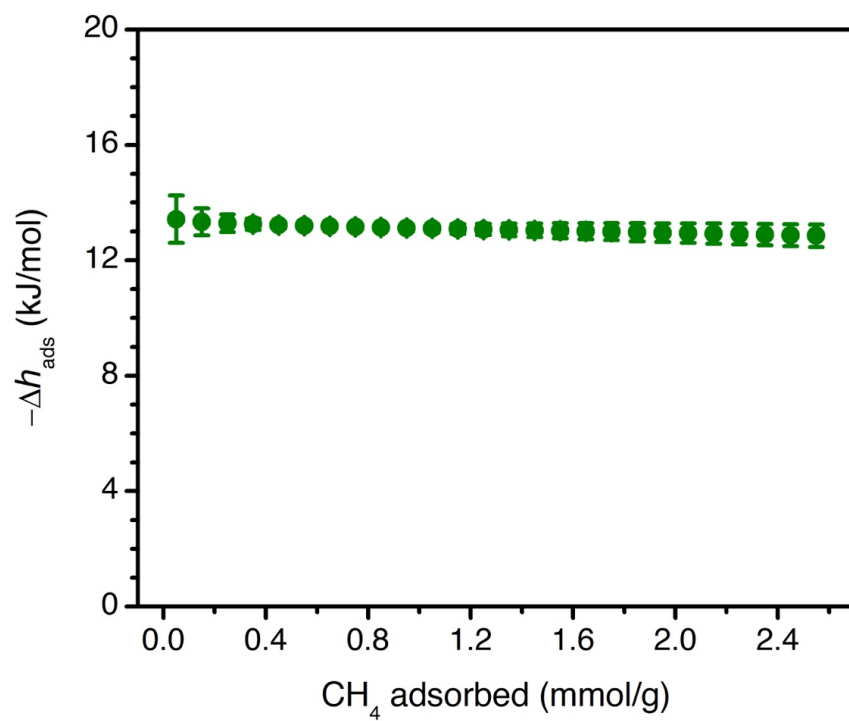


Figure 4.S28. Loading-dependent differential enthalpy of CH_4 adsorption for ee-2- $\text{Mg}_2(\text{dobpdc})$, as calculated from individual, single-site Langmuir–Freundlich fits of the high-pressure total adsorption isotherms at 25, 40, 50, and 75 °C.

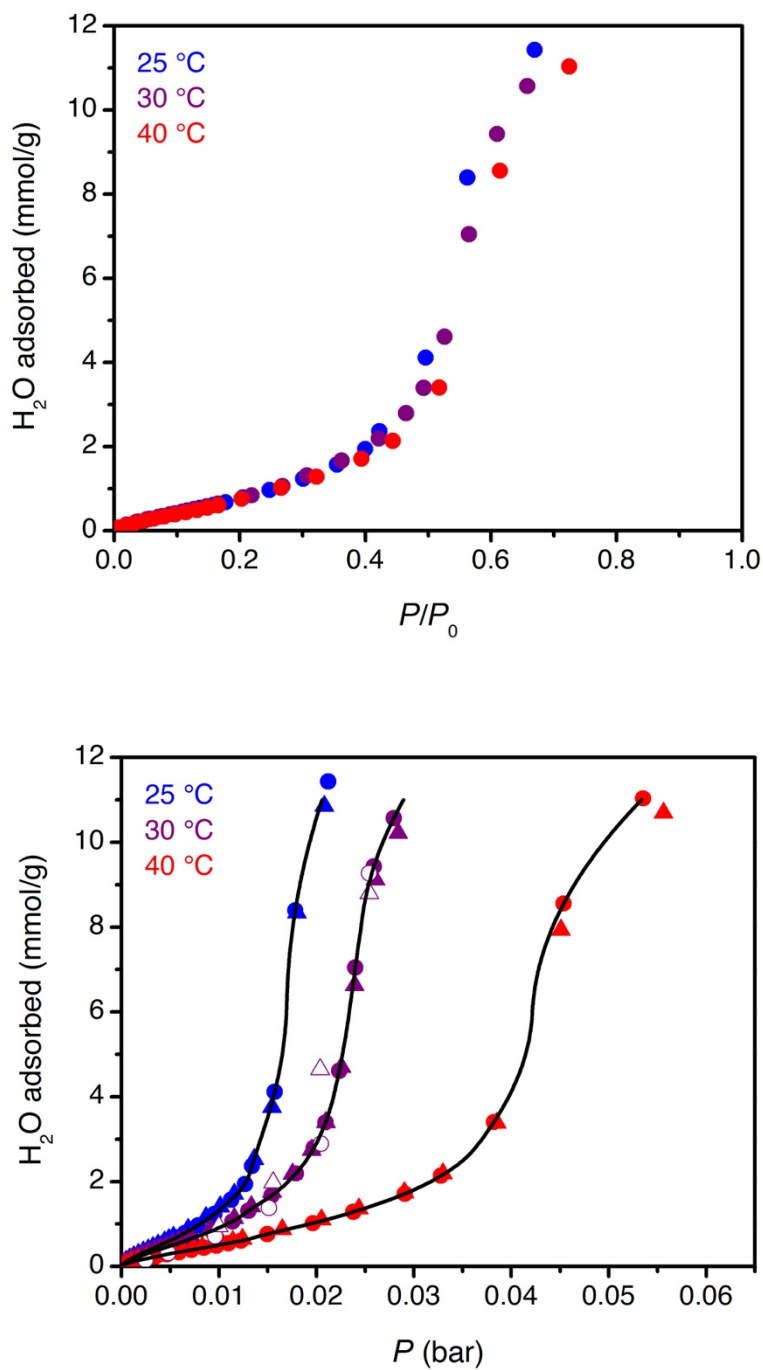


Figure 4.S29. Adsorption (filled symbols) and desorption (open symbols) H₂O isotherms for ee-2-Mg₂(dobpdc) powder (circles) and pellets (triangles). Data are plotted as a function of both relative pressure (top) and absolute pressure (bottom). The black lines in the absolute pressure plot depict the second-order spline interpolation used to calculate the loading-dependent differential enthalpies and entropies of adsorption.

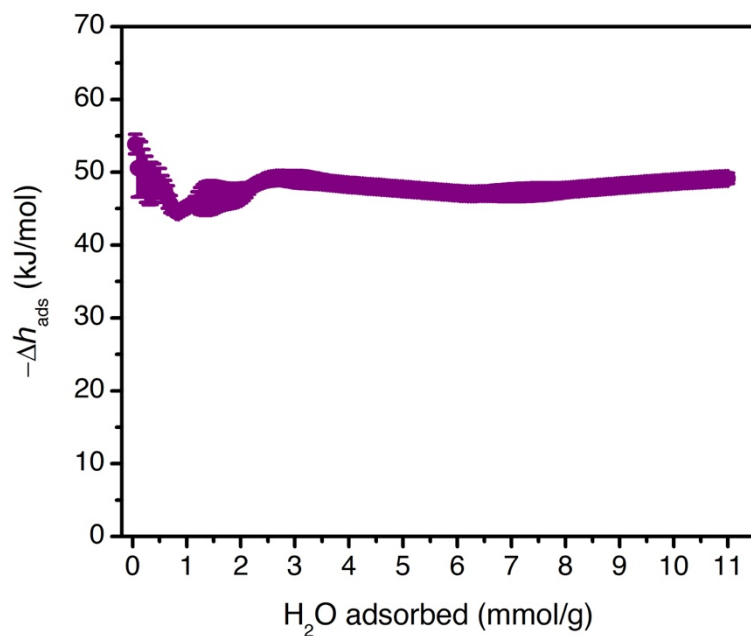


Figure 4.S30. Loading-dependent differential enthalpy of H₂O adsorption for ee-2-Mg₂(dobpdc) calculated from spline interpolation of the H₂O adsorption isotherms at 25, 30, and 40 °C.

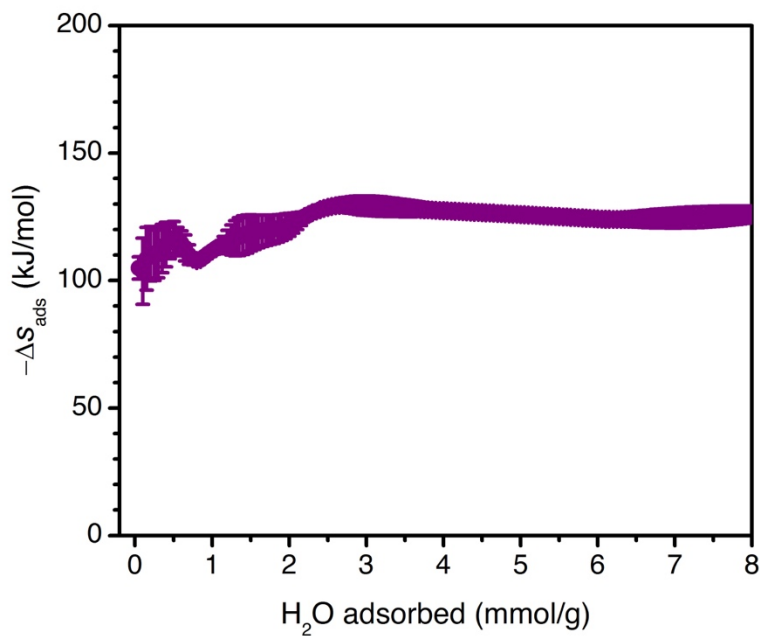


Figure 4.S31. Loading-dependent differential entropy of H₂O adsorption for ee-2-Mg₂(dobpdc) calculated from spline interpolation of the H₂O adsorption isotherms at 25, 30, and 40 °C.

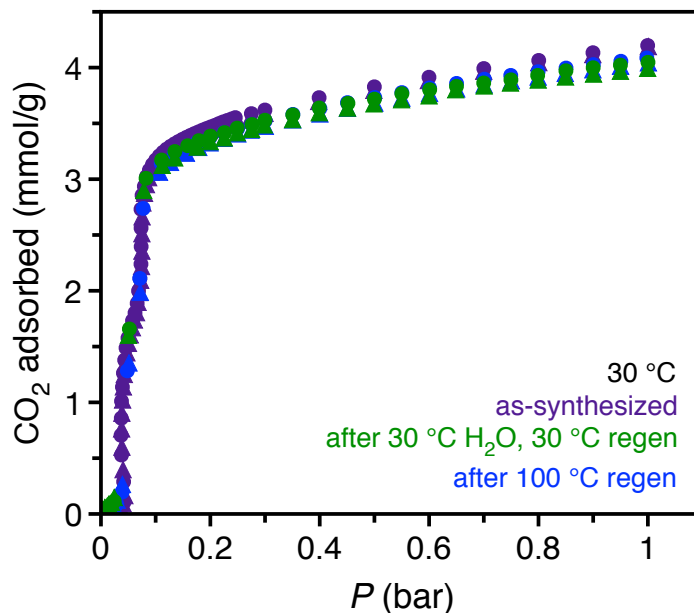


Figure 4.S32. Low-pressure CO₂ adsorption isotherms for ee-2-Mg₂(dobpdc) initially (purple), after collection of a 30 °C H₂O isotherm and regeneration with a turbomolecular pump at 30 °C (green), and after vacuum regeneration at 100 °C (blue). Circles show the as-synthesized powdered material; triangles show binderless pellets prepared by mechanical compaction.

4.6.7. Adsorption Isotherms, Fits, and Thermodynamic Data for Zeolite 13X

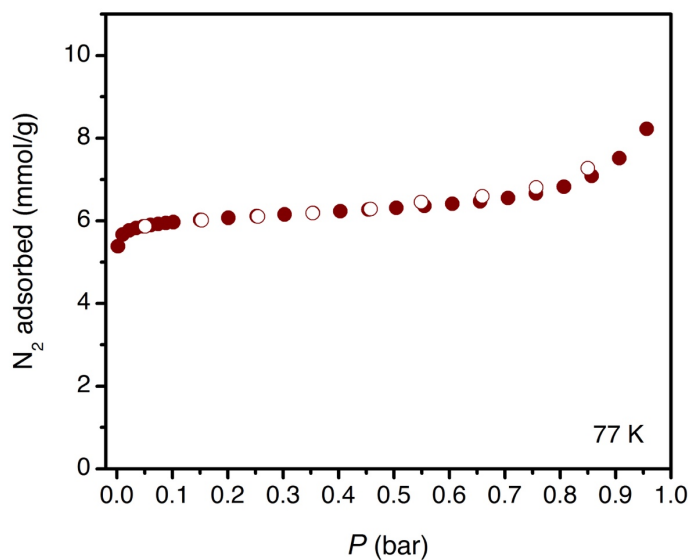


Figure 4.S33. Surface area measurement of zeolite 13X with N₂ at 77 K. Filled circles indicate adsorption; open circles indicate desorption. The Langmuir surface area was calculated as 631 ± 4 m²/g. A pore volume of 0.24 cm³/g was calculated from the loading at $P/P_0 = 0.80$.

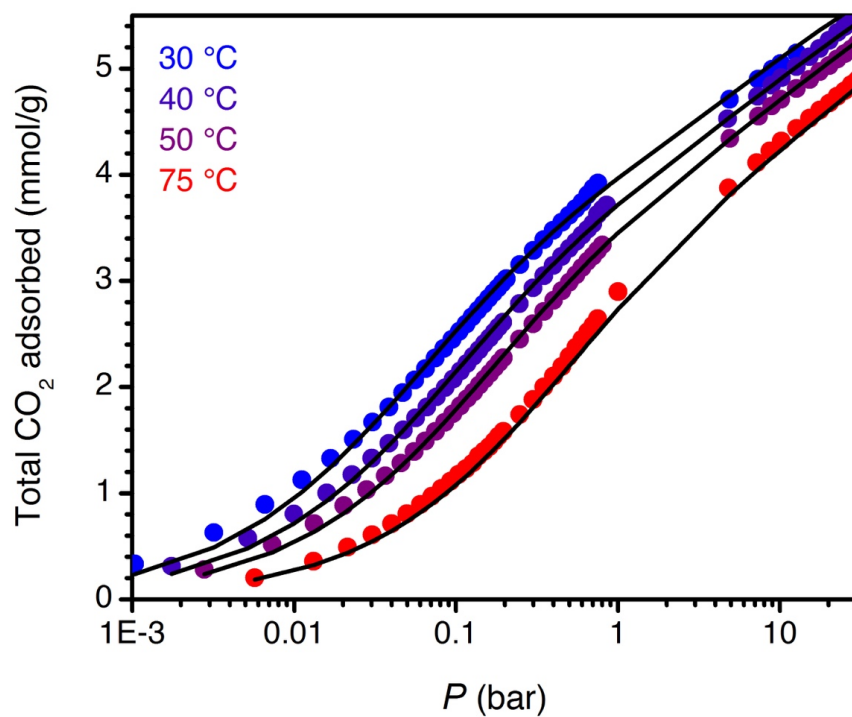


Figure 4.S34. Low- and high-pressure CO₂ adsorption isotherms for zeolite 13X (circles) and corresponding simultaneous dual-site Langmuir–Freundlich fits (lines).

Table 4.S6. Dual-site Langmuir–Freundlich fit parameters for the CO₂ adsorption isotherms of zeolite 13X at 30, 40, 50, and 75 °C (fit simultaneously for all temperatures); $q_{sat,i}$ is the saturation capacity, S_i is the site-specific molar entropy of adsorption, E_i is the site-specific binding energy, and v_i is the Freundlich parameter.

$q_{sat,1}$ (mmol/g)	$-S_1$ (R)	$-E_1$ (kJ/mol)	v_1	$q_{sat,2}$ (mmol/g)	$-S_2$ (R)	$-E_2$ (kJ/mol)	v_2
4.11	9.28	28.4	0.7	2.36	9.99	20.8	0.7

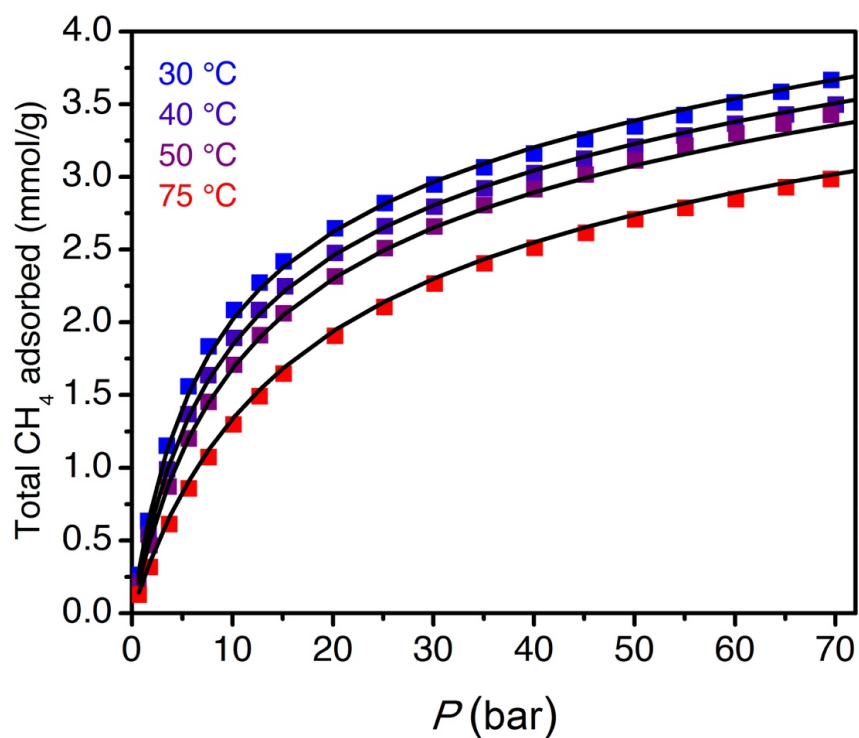


Figure 4.S35. High-pressure CH₄ adsorption isotherms for zeolite 13X (squares) and corresponding simultaneous dual-site Langmuir fits (lines).

Table 4.S7. Dual-site Langmuir fit parameters for the CH₄ adsorption isotherms of zeolite 13X at 30, 40, and 50 °C (fit simultaneously for all temperatures); $q_{sat,i}$ is the saturation capacity, S_i is the site-specific molar entropy of adsorption, E_i is the site-specific binding energy, and R is the gas constant in J/mol·K.

$q_{sat,1}$ (mmol/g)	$-S_1$ (R)	$-E_1$ (kJ/mol)	$q_{sat,2}$ (mmol/g)	$-S_2$ (R)	$-E_2$ (kJ/mol)
3.09	7.93	15.2	2.92	11.2	15.2

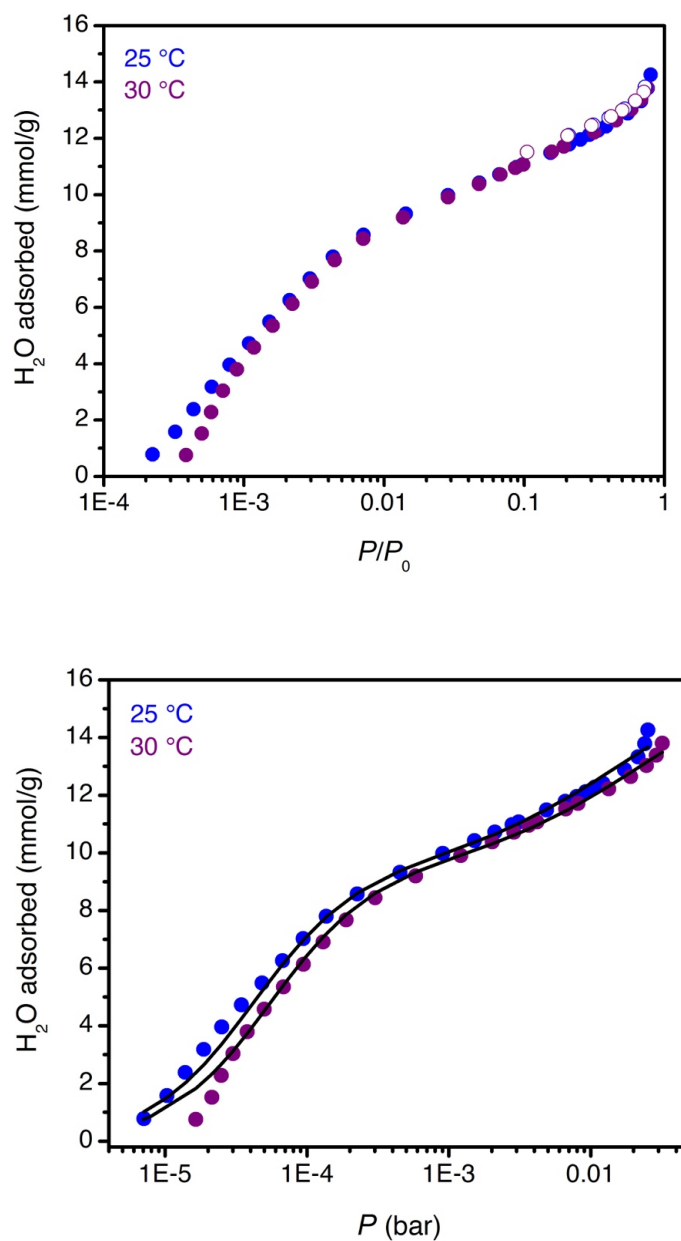


Figure 4.S36. Adsorption (filled circles) and desorption (open circles) H₂O isotherms for zeolite 13X. Data are plotted as a function of both relative pressure (top) and absolute pressure (bottom). Simultaneous dual-site Langmuir Freundlich fits are depicted as black lines in the absolute pressure plot.

Table 4.S8. Dual-site Langmuir–Freundlich fit parameters for the H₂O adsorption isotherms of zeolite 13X at 25 and 30 °C (fit simultaneously); $q_{sat,i}$ is the saturation capacity, S_i is the site-specific molar entropy of adsorption, E_i is the site-specific binding energy, and v_i is the Freundlich parameter.

$q_{sat,1}$ (mmol/g)	$-S_1$ (R)	$-E_1$ (kJ/mol)	v_1	$q_{sat,2}$ (mmol/g)	$-S_2$ (R)	$-E_2$ (kJ/mol)	v_2
9.38	16	49.1	1.2	7.61	18	39.5	0.72

4.6.8. Heat Capacity Measurements with Dynamic Scanning Calorimetry

All dynamic scanning calorimetry (DSC) experiments were conducted under 25 mL/min of He using a TA Instruments DSC Q200. Sensor capacitance and resistance were calibrated using factory-provided sapphire disks and ultra-high purity indium. For heat capacity experiments, an additional calibration of the modulated (MDSC) mode⁶⁴ was conducted using factory-provided sapphire disks in Tzero™ pans. Cell constants for the MDSC mode were calculated by taking the ratio of the experimental reversing and non-reversing heat capacities to the literature values for sapphire. All MDSC calibration and experimental datasets were conducted with a modulation period of 80 s, an amplitude of 0.75 °C, and a ramp rate of 2 °C/min. Accurate sample masses were obtained by taring the Tzero™ pan on a TGA Q5000, loading the sample into the Tzero™ pan, and activating the sample under flowing N₂ in the TGA furnace. The sample was then transferred to the DSC Q200 in air and reactivated under flowing He within the DSC instrument prior to measurement. Note that the lid of the Tzero™ pan was not completely sealed to allow removal of adsorbed guest molecules during activation within the DSC.

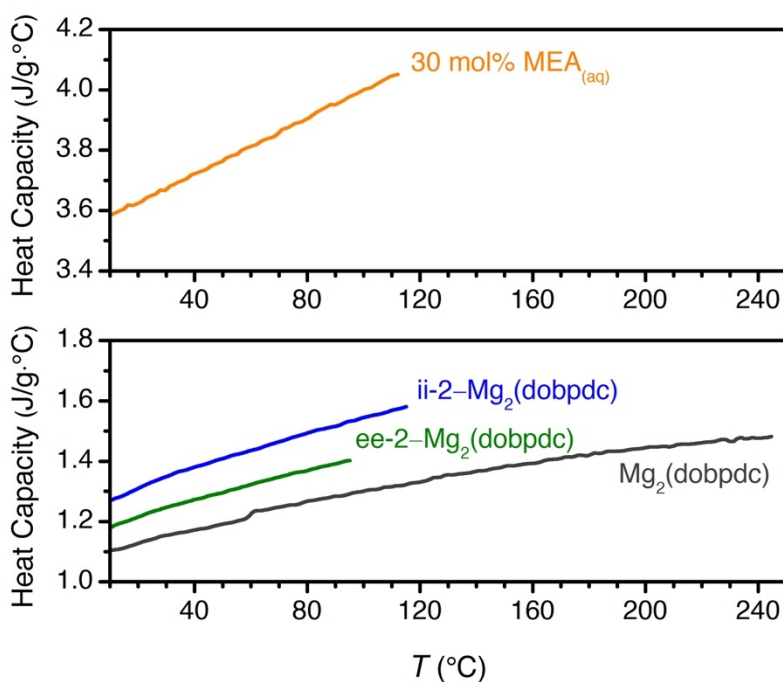


Figure 4.S37. Reported heat capacity for 30 mol% aqueous monoethanolamine (MEA, top),⁶⁵ and measured reversible heat capacity for Mg₂(dobpdc) (gray), ee-2-Mg₂(dobpdc) (green), and ii-2-Mg₂(dobpdc) (blue).

4.6.9. Kinetics Experiments with Dynamic Scanning Calorimetry

Kinetics experiments with DSC were performed using the same calibration and sample preparation methods discussed in section S4.6.8 above. All DSC experiments were performed at atmospheric pressure. After activating the sample under flowing He, the sample was cooled to the specified temperature and switched to a flow of pure CO₂, and the exotherm corresponding to CO₂ adsorption was monitored as a function of time. Time t_0 was selected as the onset of the exotherm. The samples were reactivated at 100 °C under flowing He between each adsorption cycle. For diamine-appended frameworks, the exotherm was found to broaden and flatten as a function of time, consistent with slower CO₂ adsorption kinetics as the experiment temperature approaches the CO₂ adsorption step temperature.

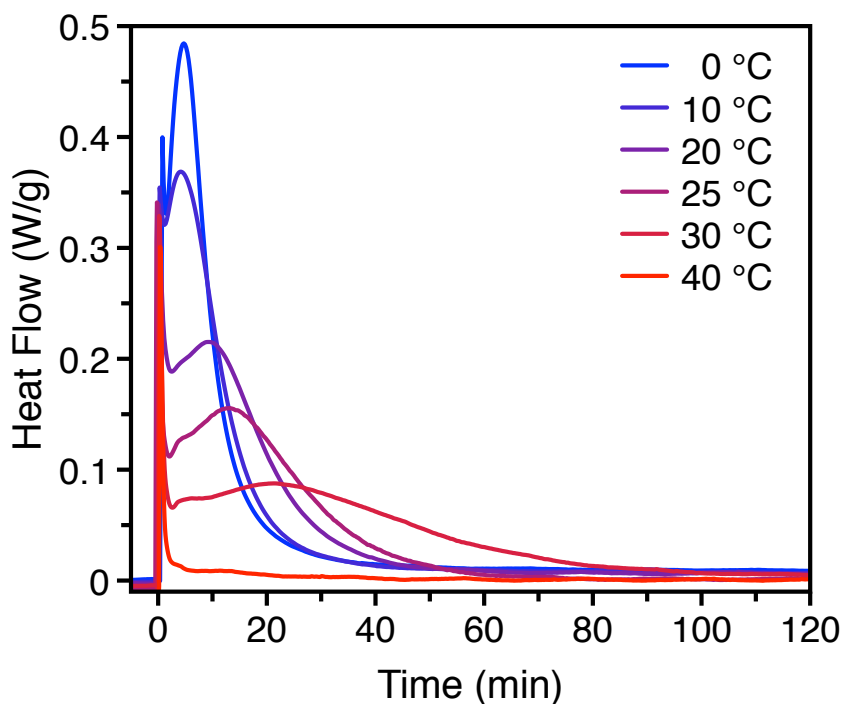


Figure 4.S38. Adsorption kinetics of ii-2-Mg₂(dobpdc) as measured by DSC under a flow of pure CO₂ at atmospheric pressure. Minimal exothermic adsorption was observed at 40 °C, the temperature at which the step position reaches atmospheric pressure for this material.

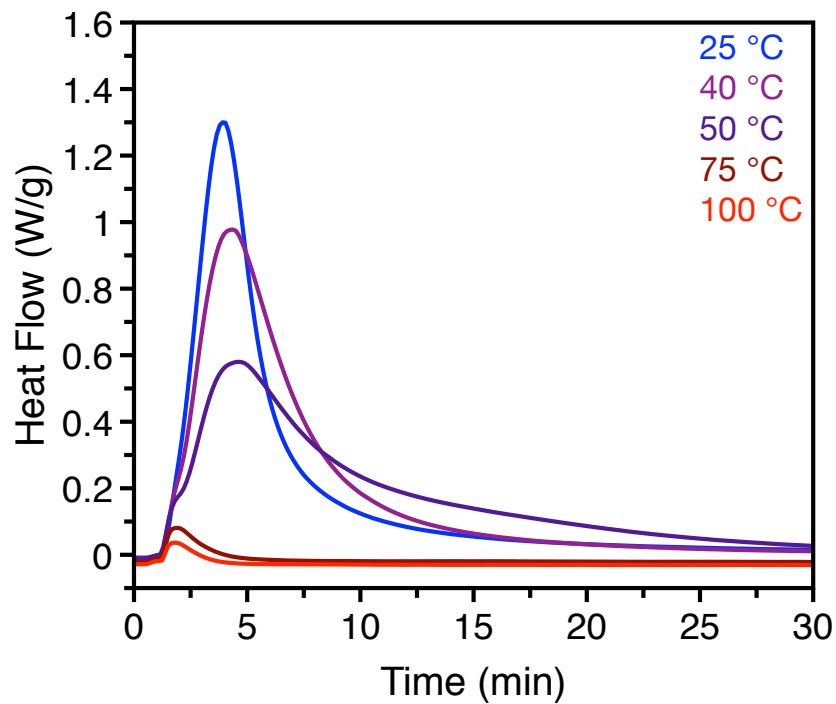


Figure 4.S39. Adsorption kinetics of ee-2-Mg₂(dobpdc) as measured by DSC under a flow of pure CO₂ at atmospheric pressure. Minimal exothermic adsorption was observed at 75 °C, the temperature at which the step position reaches atmospheric pressure for this material.

4.6.10. *In Situ* Infrared Spectra for ee-2-Mg₂(dobpdc)

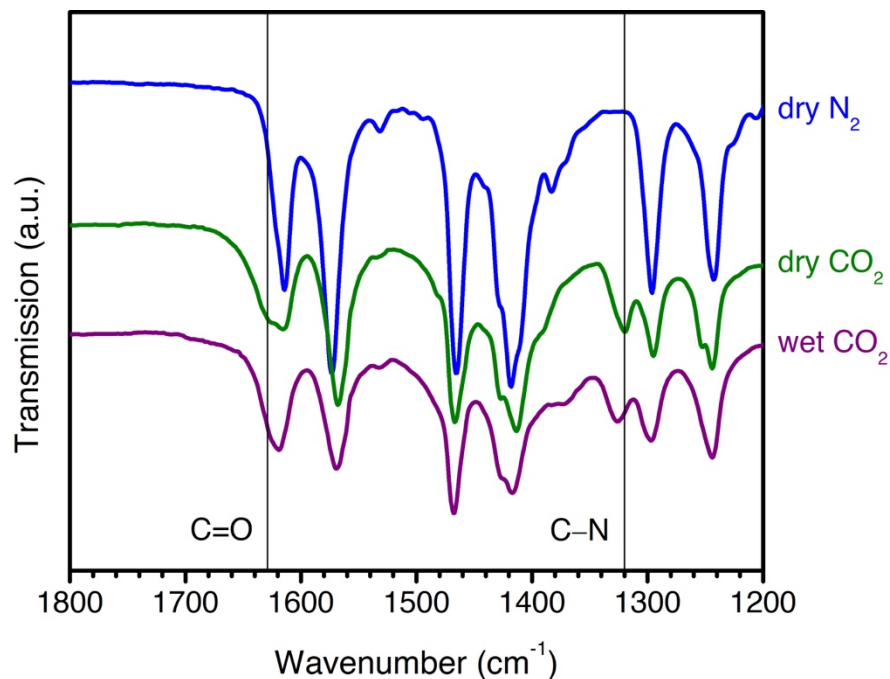


Figure 4.S40. *In situ* infrared spectra at room temperature under N₂ (blue), dry CO₂ (green), and humid CO₂ (purple) for ee-2-Mg₂(dobpdc). Gray lines mark the positions of the diagnostic carbamate $\nu(\text{C}=\text{O})$ (1629 cm⁻¹) and $\nu(\text{C}-\text{N})$ (~ 1320 cm⁻¹) bands under dry CO₂.

4.6.11. Effect of Humidity on CO₂ Adsorption in ee-2-Mg₂(dobpdc)

Adsorption and desorption isobars were collected with ee-2-Mg₂(dobpdc) for a range of CO₂ concentrations in N₂ under both dry and humid conditions at atmospheric pressure. For humid isobars, the inlet stream to the TGA furnace was humidified by flowing through two room-temperature (~ 20 °C) water bubblers in series. The estimated water content was 1.3%, as determined by the pressure at which the same quantity of water was adsorbed in the single-component 40 °C H₂O isotherm and the humid N₂ isobar (simulating a H₂O isobar). This estimated water content is equivalent to that determined for the same humid TGA apparatus in a previous report.³³

For all CO₂ concentrations, an increase in the isobaric step temperature was observed under humid conditions. The higher step temperature (equivalent to a lower isothermal step pressure) under humid conditions suggests an increase in the thermodynamic driving force for CO₂ adsorption in the presence of H₂O, consistent with previous reports.^{66,67} However, H₂O may also enhance the kinetics of CO₂ adsorption by facilitating proton transfer. We are continuing to investigate the thermodynamics and kinetics of CO₂ and H₂O co-adsorption in ongoing work. We note that for humid isobars, continued mass increase was observed during the desorption branch of the isobar, suggesting incomplete equilibration of the total mass of CO₂ and H₂O adsorbed with the temperature ramp rates used for these experiments.

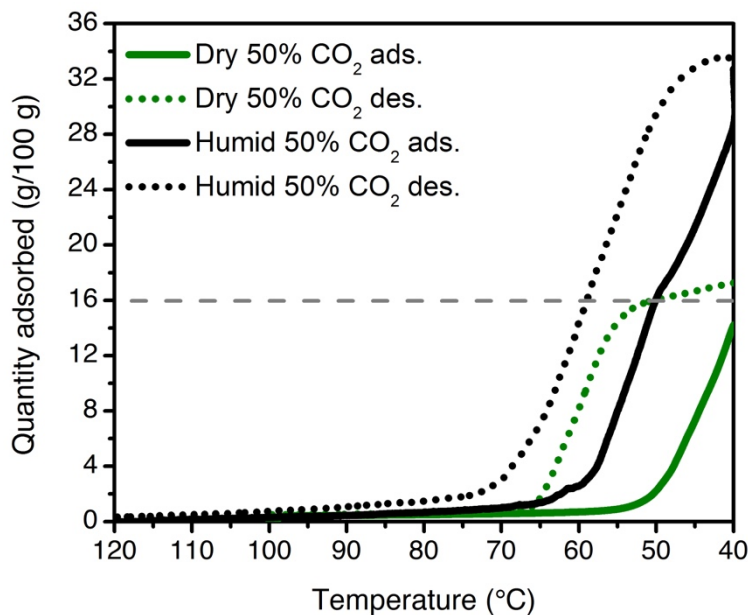


Figure 4.S41. Dry 50% CO₂ in N₂ adsorption (solid green) and desorption (dotted green) isobars, and humid 50% CO₂ in N₂ adsorption (solid black) and desorption (dotted black) isobars, for ee-2-Mg₂(dobpdc). The material was activated at 120 °C under flowing dry (green) or humid (black) N₂ for 20 min. Isobars were collected at atmospheric pressure using a ramp rate of 1 °C/min. The gray dashed line indicates the expected adsorption capacity corresponding to 1 CO₂ per diamine.

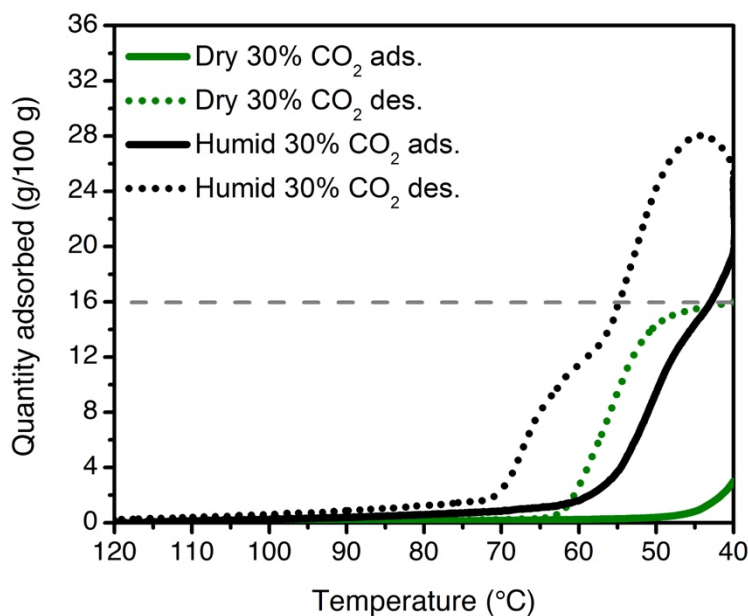


Figure 4.S42. Dry 30% CO₂ in N₂ adsorption (solid green) and desorption (dotted green) isobars, and humid 30% CO₂ in N₂ adsorption (solid black) and desorption (dotted black) isobars, for ee-2-Mg₂(dobpdc). The material was activated at 120 °C under flowing dry (green) or humid (black) N₂ for 20 min. Isobars were collected at atmospheric pressure using a ramp rate of 1 °C/min. The gray dashed line indicates the expected adsorption capacity corresponding to 1 CO₂ per diamine.

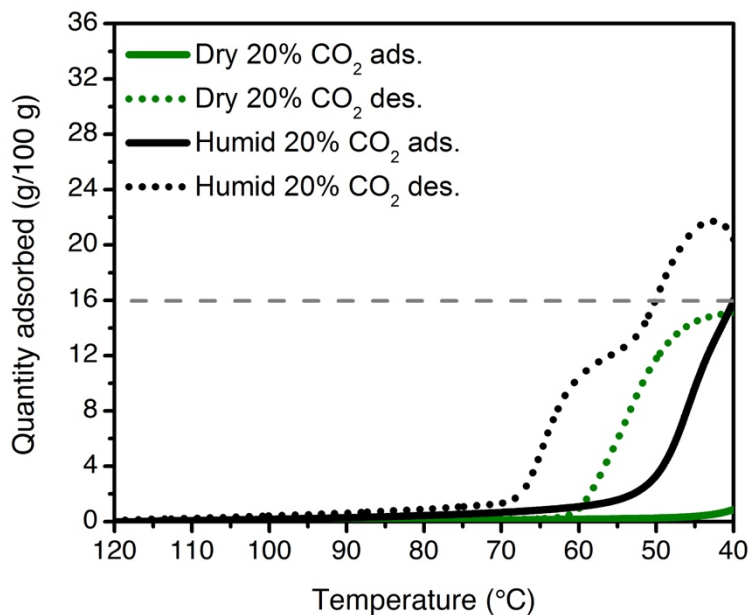


Figure 4.S43. Dry 20% CO₂ in N₂ adsorption (solid green) and desorption (dotted green) isobars, and humid 20% CO₂ in N₂ adsorption (solid black) and desorption (dotted black) isobars, for ee-2-Mg₂(dobpdc). The material was activated at 120 °C under flowing dry (green) or humid (black) N₂ for 20 min. Isobars were collected at atmospheric pressure using a ramp rate of 1 °C/min. The gray dashed line indicates the expected adsorption capacity corresponding to 1 CO₂ per diamine.

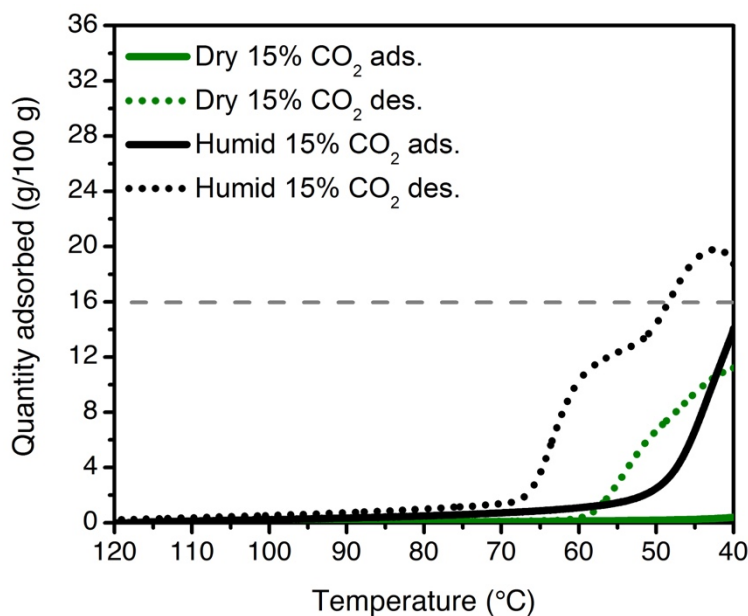


Figure 4.S44. Dry 15% CO₂ in N₂ adsorption (solid green) and desorption (dotted green) isobars, and humid 15% CO₂ in N₂ adsorption (solid black) and desorption (dotted black) isobars, for ee-2-Mg₂(dobpdc). The material was activated at 120 °C under flowing dry (green) or humid (black) N₂ for 20 min. Isobars were collected at atmospheric pressure using a ramp rate of 1 °C/min. The gray dashed line indicates the expected adsorption capacity corresponding to 1 CO₂ per diamine.

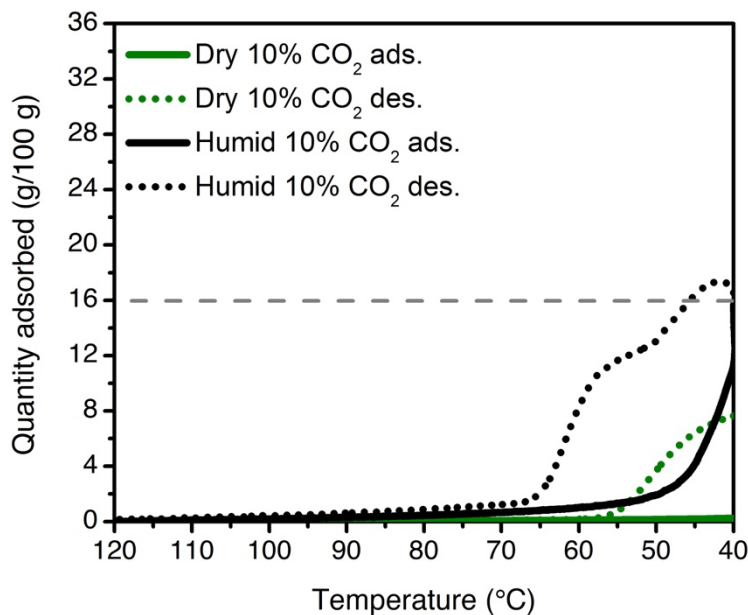


Figure 4.S45. Dry 10% CO₂ in N₂ adsorption (solid green) and desorption (dotted green) isobars, and humid 10% CO₂ in N₂ adsorption (solid black) and desorption (dotted black) isobars, for ee-2-Mg₂(dobpdc). The material was activated at 120 °C under flowing dry (green) or humid (black) N₂ for 20 min. Isobars were collected at atmospheric pressure using a ramp rate of 1 °C/min. The gray dashed line indicates the expected adsorption capacity corresponding to 1 CO₂ per diamine.

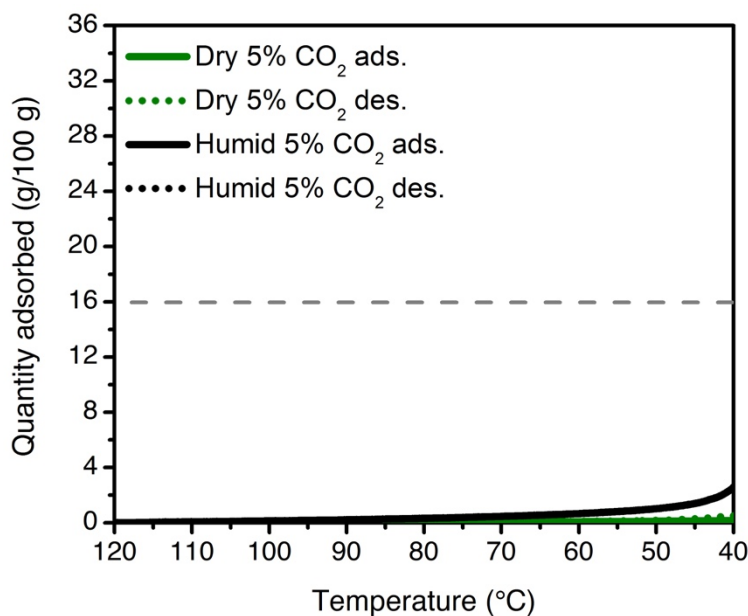


Figure 4.S46. Dry 5% CO₂ in N₂ adsorption (solid green) and desorption (dotted green) isobars, and humid 5% CO₂ in N₂ adsorption (solid black) and desorption (dotted black) isobars, for ee-2-Mg₂(dobpdc). The material was activated at 120 °C under flowing dry (green) or humid (black) N₂ for 20 min. Isobars were collected at atmospheric pressure using a ramp rate of 1 °C/min. The gray dashed line indicates the expected adsorption capacity corresponding to 1 CO₂ per diamine.

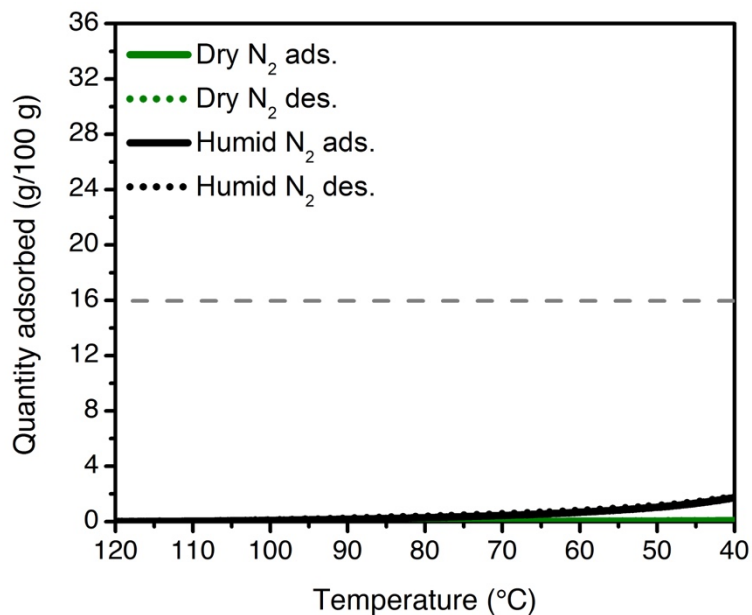


Figure 4.S47. Dry N₂ adsorption (solid green) and desorption (dotted green) isobars, and humid N₂ adsorption (solid black) and desorption (dotted black) isobars, for ee-2-Mg₂(dobpdc). The material was activated at 120 °C under flowing dry (green) or humid (black) N₂ for 20 min. Isobars were collected at atmospheric pressure using a ramp rate of 1 °C/min. The gray dashed line indicates the expected adsorption capacity corresponding to 1 CO₂ per diamine.

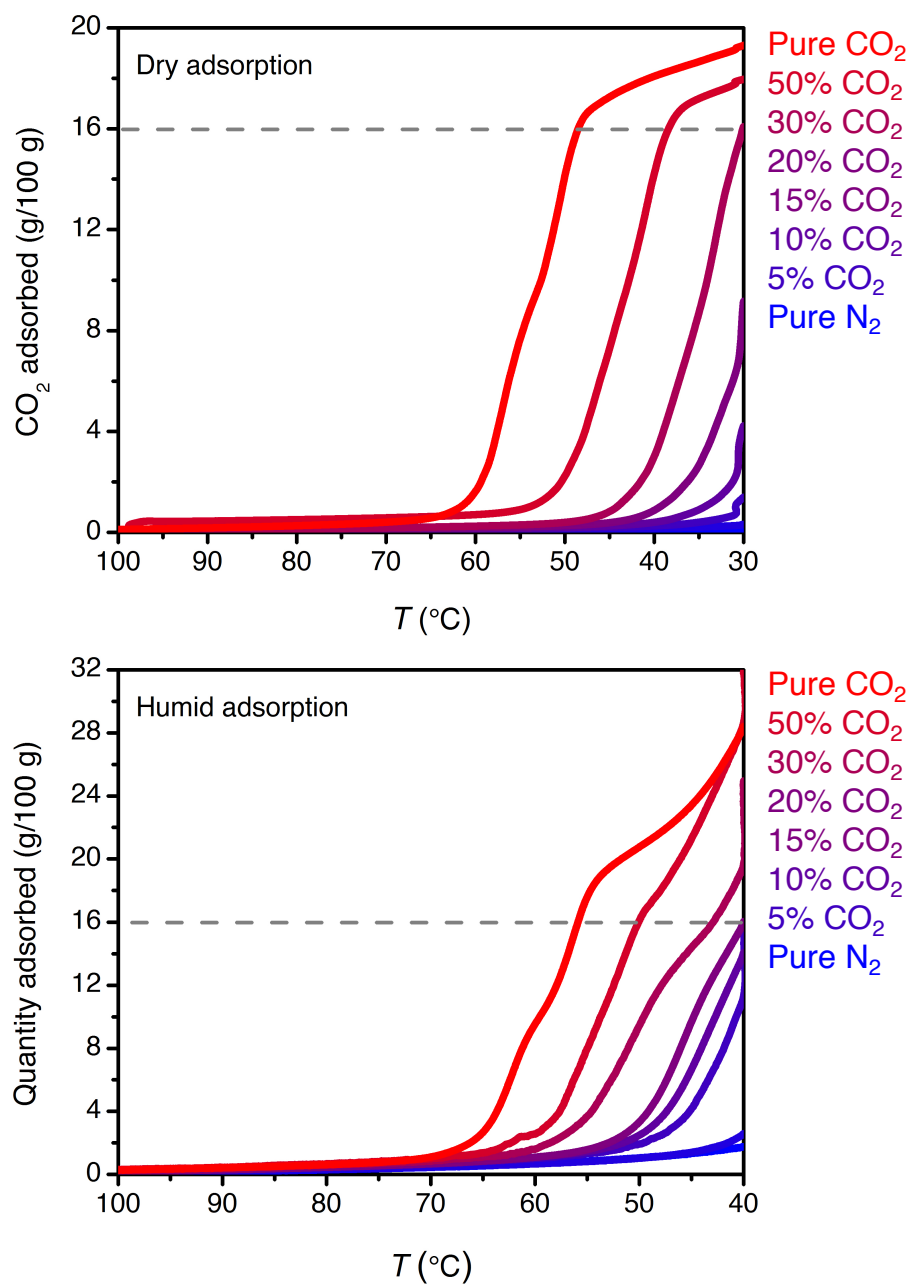


Figure 4.S48. Full series of dry (top) and humid (bottom) adsorption isobars for pure CO₂, CO₂/N₂ mixtures, and pure N₂ at atmospheric pressure (note different temperature scales on horizontal axes). A temperature ramp rate of 1 °C/min was used for all experiments.

4.6.12. Predicting Breakthrough Curves from Step-Shaped Adsorption Isotherms

Simple graphical approaches can be used to predict breakthrough profiles directly from adsorption isotherms. An excellent review of this topic is provided by Helfferich and Carr,⁴⁴ and the key points of this analysis are reproduced here. This analysis is also included in a parallel study by our group regarding CO₂ capture from the emissions of natural gas-fired power plants.⁶⁷

To relate isotherms and elution profiles, the primary quantity of interest is the velocity v_{c_i} of a given concentration c_i of solute i as it flows through the adsorption column. This concentration velocity is defined as

$$v_{c_i} \equiv \left(\frac{\partial z}{\partial t} \right)_{c_i}, \quad (4.S4)$$

where z is the linear distance in the direction of flow, and t is time. Neglecting axial dispersion, ideal plug flow under isotherm conditions gives the following equation for conservation of mass:

$$\frac{\rho}{\varepsilon} \left(\frac{\partial q_i}{\partial t} \right)_z + \left(\frac{\partial c_i}{\partial t} \right)_z + v^0 \left(\frac{\partial c_i}{\partial z} \right)_t = 0 \quad (4.S5)$$

Here, v^0 is the velocity of the moving-phase flow, q_i is the adsorbent loading, ρ is the bulk density of the adsorbent, and ε is the fractional void volume of the adsorbent bed. The resulting “wave equation” for the concentration velocity is thus

$$v_{c_i} = \frac{v^0}{\left(1 + \frac{\rho}{\varepsilon} \right) \left(\frac{\partial q_i}{\partial c_i} \right)_z} \quad (4.S6)$$

If local equilibrium is further assumed, the adsorbent loading becomes solely a function of concentration, and the partial differential can be replaced by the corresponding total differential:

$$v_{c_i} = \frac{v^0}{\left(1 + \frac{\rho}{\varepsilon} \right) \left(\frac{dq_i}{dc_i} \right)_z} \quad (4.S7)$$

Therefore, the concentration velocity is inversely proportional to dq_i/dc_i , which is the slope of the tangent to the equilibrium adsorption isotherm at the corresponding concentration c_i . In other words, under local equilibrium, *the “natural” wave velocity is lower at concentrations where the isotherm is steeper*. With this knowledge, the propagation of adsorption and desorption waves is straightforward to predict for simple linear, Type I, and Type III isotherms, as illustrated in Figure 4.S49 below.

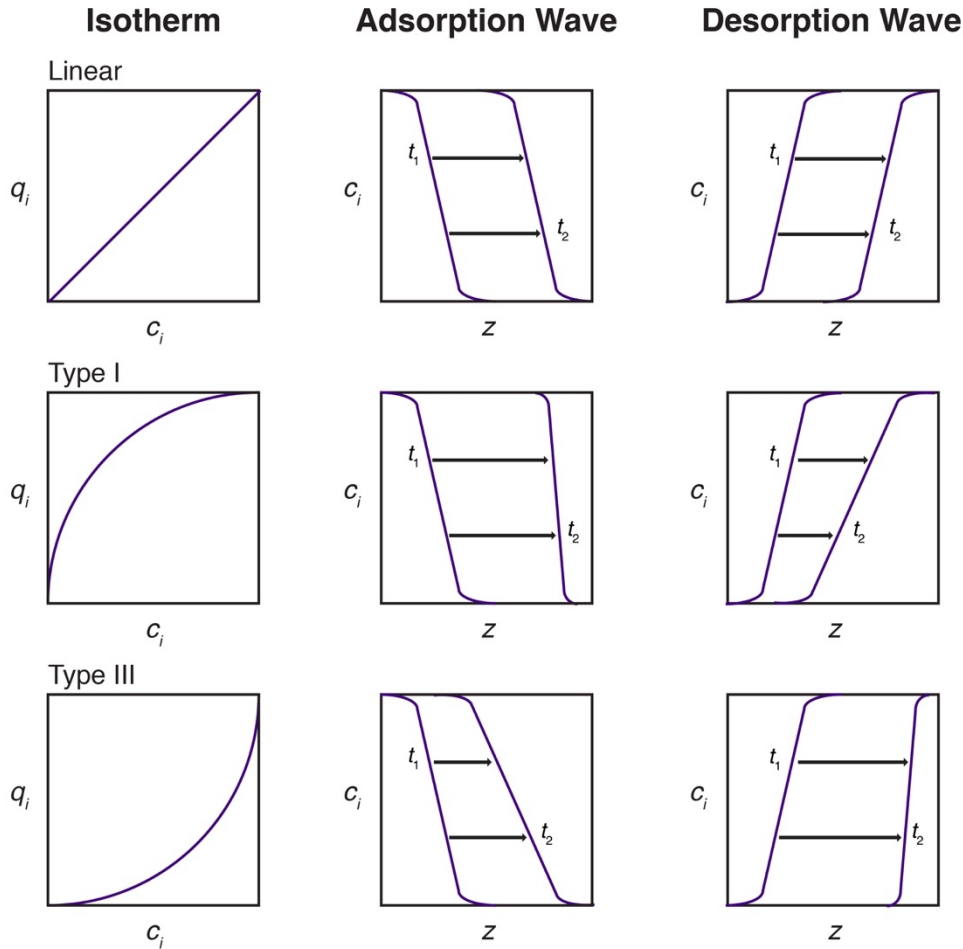


Figure 4.S49. Propagation of adsorption and desorption waves for linear (top), Type I (middle), and Type III (bottom) isotherms under ideal conditions. The left column shows the isotherm profile as loading (q_i) vs. concentration (c_i). The center and right columns show the propagation of the adsorption and desorption waves, respectively, as c_i vs. distance z along the column for a wave initially diffuse at t_1 to a later time t_2 . Figure adapted from the work of Helfferich and Carr.⁴⁴

For linear isotherms, the slope of the isotherm is constant, and thus the adsorption and desorption waves propagate through the bed unchanged under ideal conditions. For Type I isotherms, higher concentrations, where the isotherm slope is shallower, move through the bed faster than lower concentrations. On adsorption, this results in a wave that sharpens to a “shock,” or discontinuity, while on desorption, the wave broadens as it travels. Similarly, for adsorption Type III isotherm, lower concentrations move faster than higher concentrations, and the adsorption wave spreads as it moves through the column.

More complex “composite” waves may be generated in the case of isotherms with inflection points. A simple graphical approach known as “Golden’s rule,” or alternatively the “string” or “rubber band” rule, can be used to predict the shape of the breakthrough profile directly from an isotherm of arbitrary shape.^{44,43,45,68,32,69,36} In this method, an operating curve is constructed from an imaginary rubber band stretched between the initial state (typically, no adsorbate) and the feed state (here, 10% CO₂). For adsorption, the rubber band operating curve falls below the isotherm, while for desorption, it falls above it. In regions where the rubber band is stretched tightly between individual points of contact with the isotherm, compressive waves, or “shocks”

are generated in the breakthrough profile. In regions where the rubber band instead runs along the isotherm, dispersive waves are generated. As a result, inflection points in isotherms often lead to multi-moment breakthrough profiles containing both shocks and waves, a schematic of which is shown in Figure 2 of the main text. Importantly, in most cases of interest for diamine-appended frameworks with step-shaped isotherms, this behavior results in an intuitive conclusion: once the CO₂ partial pressure in the bed drops below the step pressure, the cooperative adsorption mechanism is no longer active, and thus CO₂ at concentrations below the step pressure “slips” through the bed. Hefti, Joss and coworkers first discussed the importance of considering CO₂ slip for diamine-appended frameworks in a 2016 modeling study,³² and Darunte and coworkers³⁶ recently demonstrated CO₂ slip experimentally in breakthrough experiments targeting direct air capture with mmen–Mg₂(dobpdc) (mmen = *N,N'*-dimethylethylenediamine).

In the present study, “shock–wave–shock” breakthrough profiles were observed for CO₂ with dry mixtures simulating crude natural gas streams, but upon incorporation of humidity, single-shock breakthrough profiles were observed under the same conditions. This favorable result enables significant improvements in capture rate under the more realistic H₂O-containing streams. As discussed in the main text, we attribute this enhanced performance to preferential stabilization of the CO₂-bound phase in the presence of water, as reflected in the higher isobaric step temperatures under humid CO₂-containing streams (Figures 4.S41–4.S48). This is consistent with a lower effective step pressure in the CO₂ isotherm in the presence of water. The single-shock breakthrough profiles therefore suggest that water reduces the step pressure and/or modifies the pre-step region of the isotherm such that the operating curve no longer intersects the isotherm (Figure 4.10). These results are consistent with a parallel study by our group investigating CO₂ capture from simulated natural gas flue emissions with a diamine-appended metal–organic framework.⁶⁷

4.6.13. Additional Experimental Details for Breakthrough Measurements

Breakthrough experiments were conducted with the adsorbent column pre-equilibrated under flowing He unless otherwise noted. To begin the experiment, He flow to the column was stopped as a flow of simulated natural gas was introduced. For quantitative experiments, following complete breakthrough of CO₂, the capacity of each gas (q_i , mmol/g) was determined using the following equation:

$$q_i = \left[\frac{Q}{22.414 \frac{\text{ccSTP}}{\text{mmol}}} \int_0^t \left(1 - \frac{F_i}{F_{0,i}} \right) dt - \varepsilon V \left(\frac{y_i P}{RT} \right) \right] \left(\frac{y_i}{m} \right) \quad (4.S8)$$

Here, Q is the average total mass flow rate in sccm, t is the corrected time in min, F_i is the molar flow rate of species i at time t , $F_{0,i}$ is the inlet molar flow rate of species i , ε is the interparticle void fraction, V is the volume of pelletized adsorbent in cm³, y_i is the mole fraction of species i , P is the total pressure, R is the universal gas constant, T is the column temperature in K, and m is the mass of adsorbent. The interparticle void fraction ε is calculated as

$$\varepsilon = 1 - \frac{\rho_{\text{bulk}}}{\rho_{\text{particle}}} \quad (4.S9)$$

where Q_{bulk} is the bulk density in kg/m^3 , calculated as m/V , and $Q_{particle}$ is the particle density in kg/m^3 and is estimated as $1000 \text{ kg}/\text{m}^3$ for diamine-appended frameworks.

For the custom dry breakthrough apparatus (Figure 4.S51), reported data were corrected for the system deadtime, which was determined by running breakthrough experiments with an empty column. A representative deadtime of 392 s was determined for experiments at 70 bar under 300 sccm of 10% CO_2 in CH_4 . An insulated clamshell furnace (Applied Test Systems) was used to control the bed temperature, and a manual back-pressure regulator was used to control the bed pressure. The internal bed temperature was measured with thermocouples at 3" and 9" along the 12" column. The composition of the outlet stream was monitored using an OmniStar mass spectrometer. A standard flow rate of 300 sccm was supplied using a Brooks flow controller. The flow rate of the outlet stream was measured using a thermal mass flow meter calibrated to CH_4 , and the recorded values were corrected for the true composition at each time point using the viscosity calculated from the Wilke model. Flow, pressure, and temperature data were recorded every 30 s until breakthrough and every several minutes thereafter until complete bed saturation was observed. Diamine-appended frameworks were activated at $100 \text{ }^\circ\text{C}$ under house vacuum ($\sim 0.15 \text{ bar}$) for 12 h between runs unless specified otherwise.

For qualitative dry and humid breakthrough experiments at 7 and 50 bar, a customized PSA-1000 apparatus from L&C Science was used. Additional information is available from the manufacturer.⁷⁰ The outlet composition was monitored using a mass spectrometer. Diamine-appended frameworks were activated at $100 \text{ }^\circ\text{C}$ with a rotary vacuum pump ($\sim 0.02 \text{ mbar}$) for 12 h between runs unless specified otherwise. Zeolite 13X was activated with a rotary vacuum pump ($\sim 0.02 \text{ mbar}$) for 2 h at $100 \text{ }^\circ\text{C}$ and 8 h at $300 \text{ }^\circ\text{C}$ between runs unless specified otherwise.

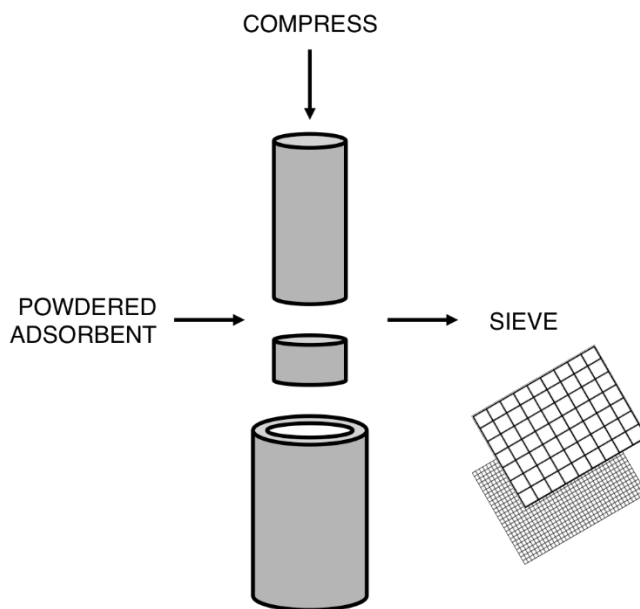


Figure 4.S50. Schematic of compression method used to prepare pelletized adsorbent from microcrystalline powder.

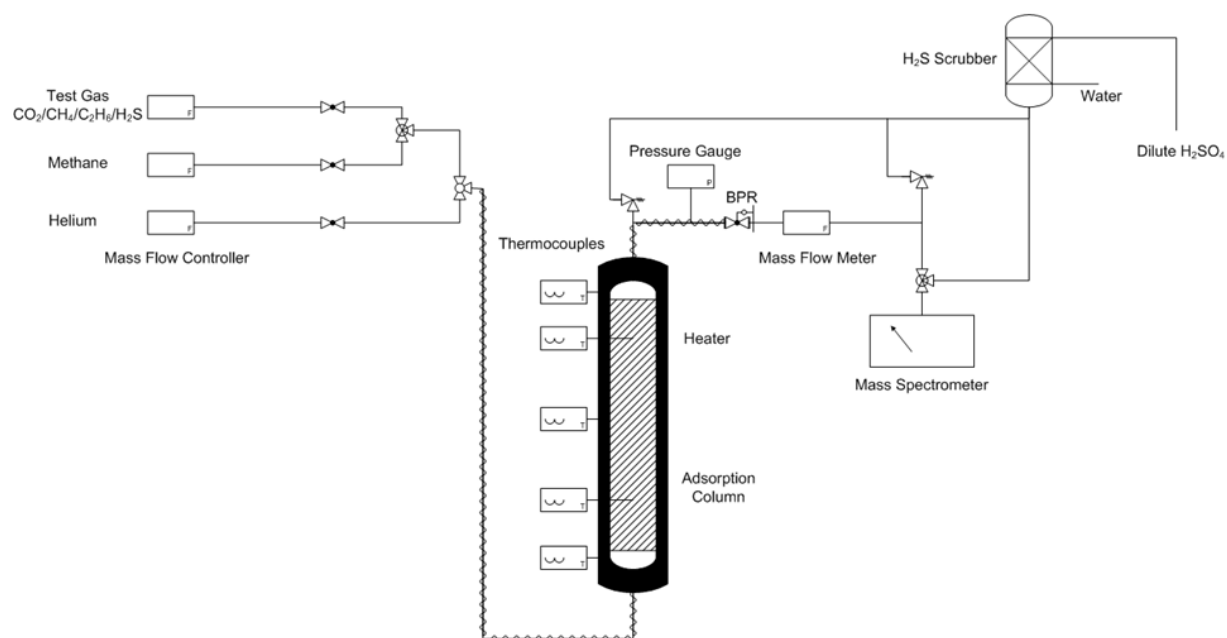


Figure 4.S51. Schematic of home-built breakthrough apparatus used for quantitative breakthrough experiments with dry gas streams. The column pressure was controlled using a back-pressure regulator (BPR).

4.6.14. Additional Breakthrough Experiments with ii-2-Mg₂(dobpdc)

Table 4.S9. Summary of breakthrough results for ii-2-Mg₂(dobpdc) with 10% CO₂ in CH₄. A capacity of 3.3 mmol/g corresponds to adsorption of 1 CO₂ per diamine. The CO₂ exhaustion capacities (integrated over the full breakthrough curve) are reported with an estimated error of ±0.3 mmol/g. All experiments listed below were performed on the home-built breakthrough apparatus.

<i>T</i> (°C)	<i>P</i> _{total} (bar)	Flow rate (sccm)	Predicted CO ₂ slip (mol %, bar)	Observed CO ₂ slip (mol %, bar)	Observed CH ₄ purity (mol %)	CO ₂ exhaustion capacity (mmol/g)
30	70	300	<1%, <0.7	3%, 2	97	3.3
50	70	300	~2.2%, ~1.5	6%, 4	94	3.4
30	35	300	~1%, ~0.7	6%, 2	94	3.8

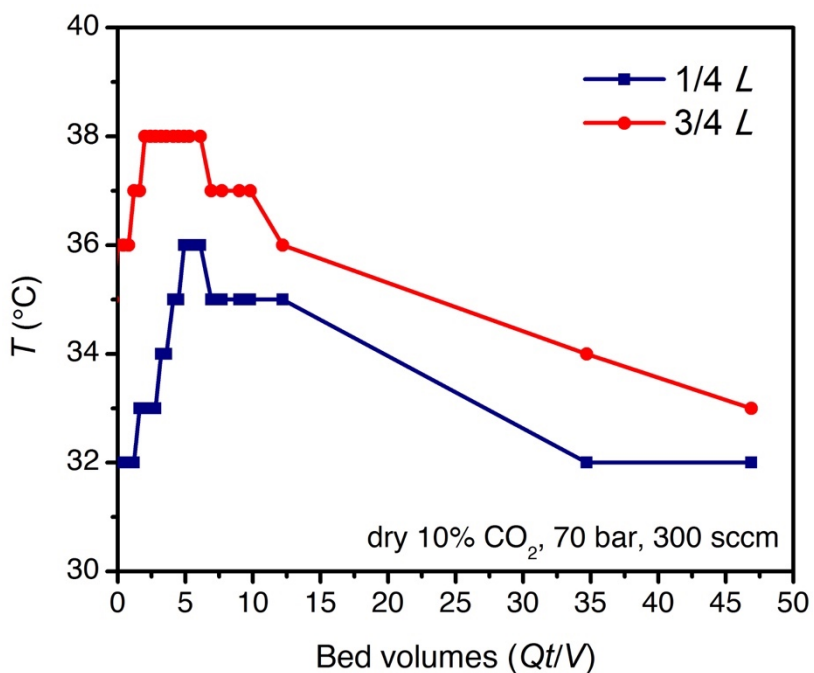


Figure 4.S52. Temperature profile for the breakthrough experiment with ii-2-Mg₂(dobpdc) shown in main text Figure 4.

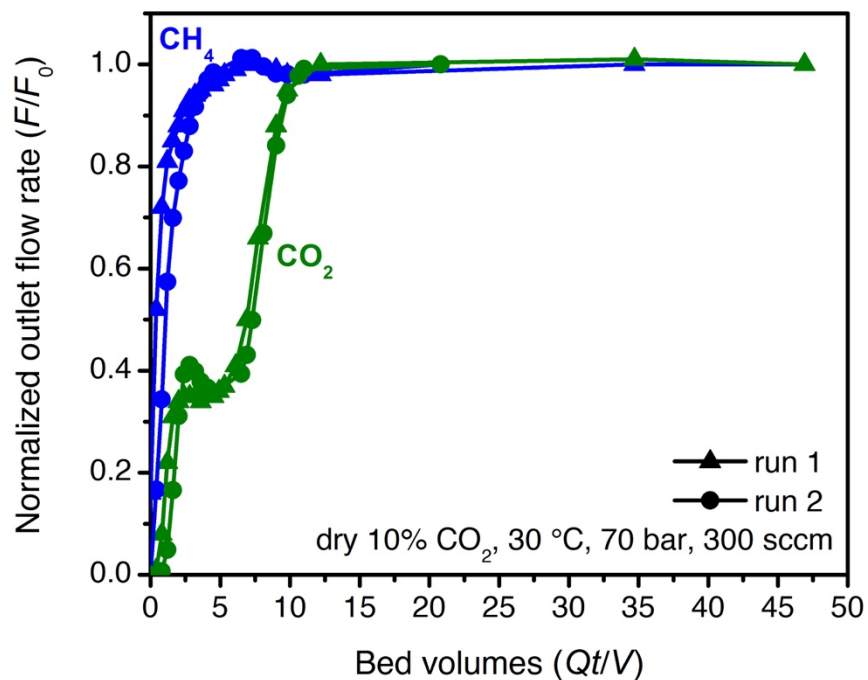


Figure 4.S53. Duplicate breakthrough experiments for ii-2-Mg₂(dobpdc) under 300 sccm of dry 10% CO₂ in CH₄ at 30 °C and 70 bar. The data shown for run 1 are the same as those shown in the main text.

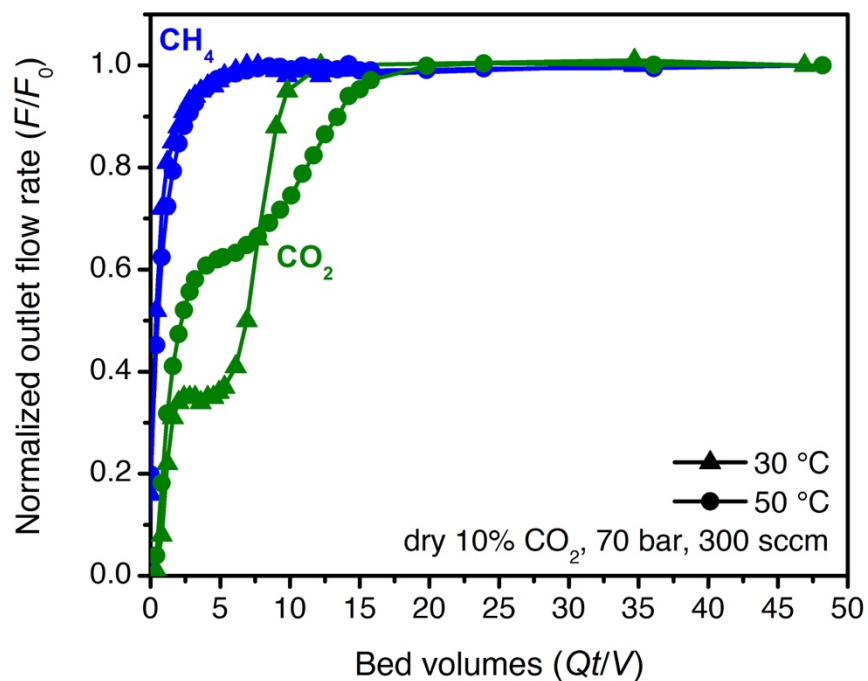


Figure 4.S54. Breakthrough curves for ii-2-Mg₂(dobpdc) at 30 °C (triangles) and 50 °C (circles) under 300 sccm of dry 10% CO₂ in CH₄ at 70 bar. The data shown for 30 °C are the same as those shown in the main text.

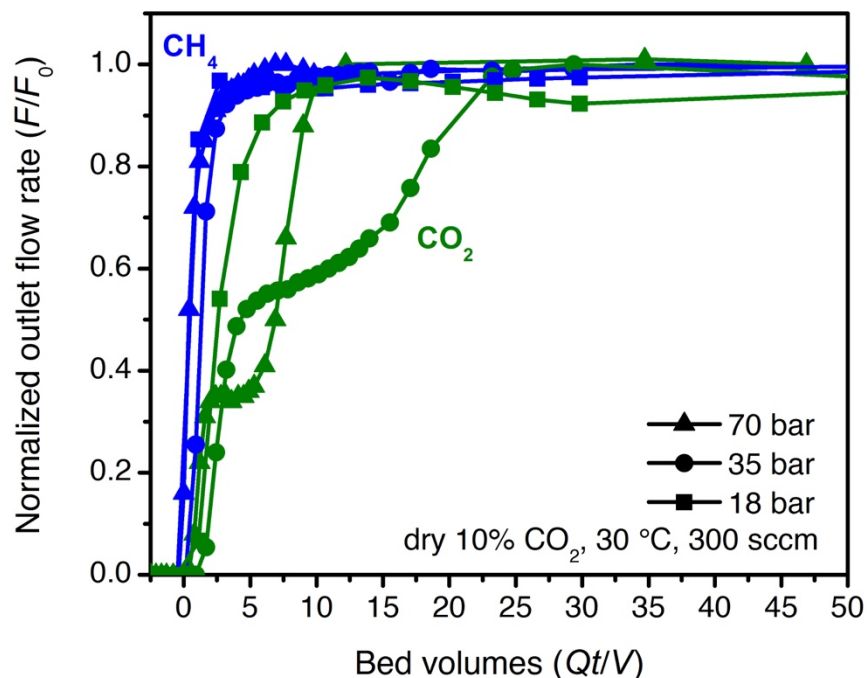


Figure 4.S55. Breakthrough curves for ii-2-Mg₂(dobpdc) at 70 bar (triangles), 35 bar (circles), and 18 bar (squares) under 300 sccm of dry 10% CO₂ in CH₄ at 30 °C. The data shown for 70 bar are the same as those shown in the main text.

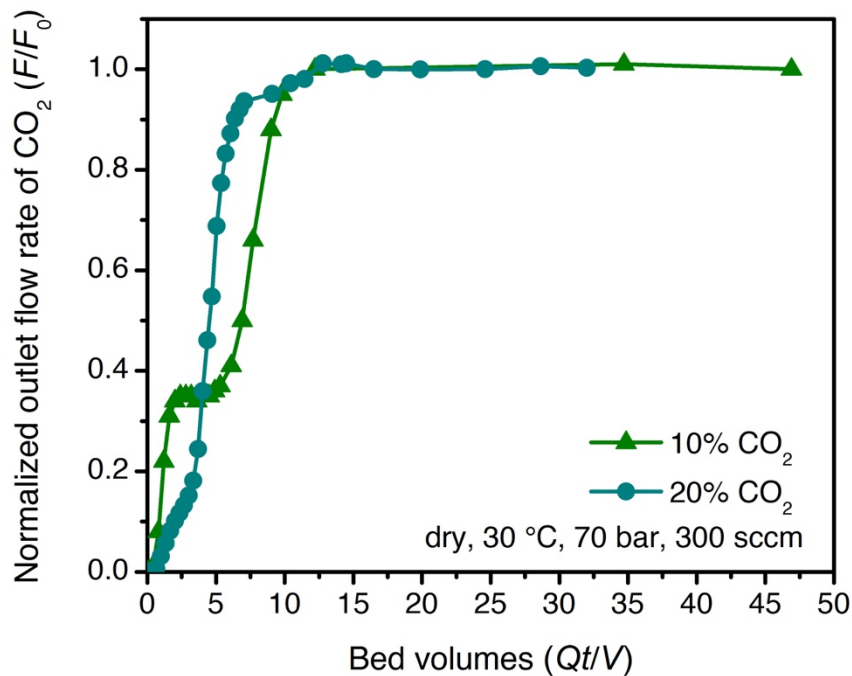


Figure 4.S56. Breakthrough curves for ii-2-Mg₂(dobpdc) under 300 sccm of varying inlet concentrations of CO₂ in CH₄ at 70 bar and 30 °C. The data shown for 10% CO₂ are the same as those shown in the main text. For the experiment with 20% CO₂ in CH₄, the column was pre-equilibrated under pure CH₄ rather than He.

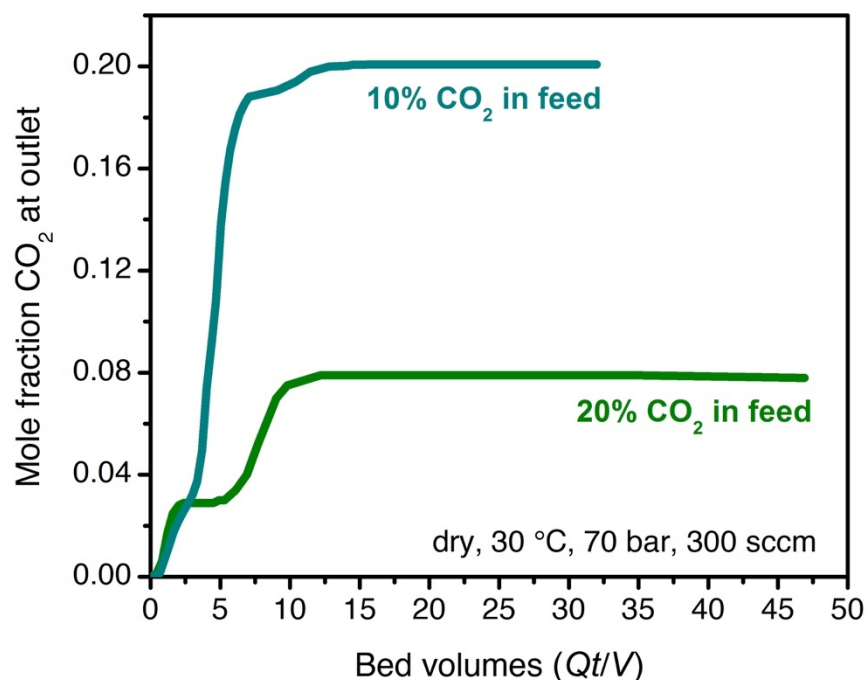


Figure 4.S57. Mole fraction data from the breakthrough experiment shown in Figure 4.S56.

4.6.15. Additional Breakthrough Experiments with ee-2-Mg₂(dobpdc)

Table 4.S10. Summary of breakthrough results for ee-2-Mg₂(dobpdc) with 10% CO₂ in CH₄. A capacity of 3.6 mmol/g corresponds to adsorption of 1 CO₂ per diamine. For quantitative experiments at 70, 35, and 1 bar, CO₂ exhaustion capacities (integrated over the full breakthrough curve) are reported with an estimated error of ±0.3 mmol/g. Quantitative experiments were performed on the home-built breakthrough apparatus. The qualitative experiment at 7 bar was performed on the customized L&C PSA instrument.

<i>T</i> (°C)	<i>P</i> _{total} (bar)	Flow rate (sccm)	Predicted CO ₂ slip (mol %, bar)	Observed CO ₂ slip (mol %, bar)	Observed CH ₄ purity (mol %)	CO ₂ exhaustion capacity (mmol/g)
30	70	300	0.09%, 0.06	0.4%, 0.3	99.6	4.2
30	35	300	0.2%, 0.06	0.8%, 0.3	99.2	4.9
30	7	300	0.9%, 0.06	4%, 0.3	96.0	not calculated
30	1	300	6%, 0.06	5%, 0.05	95.0	1.6

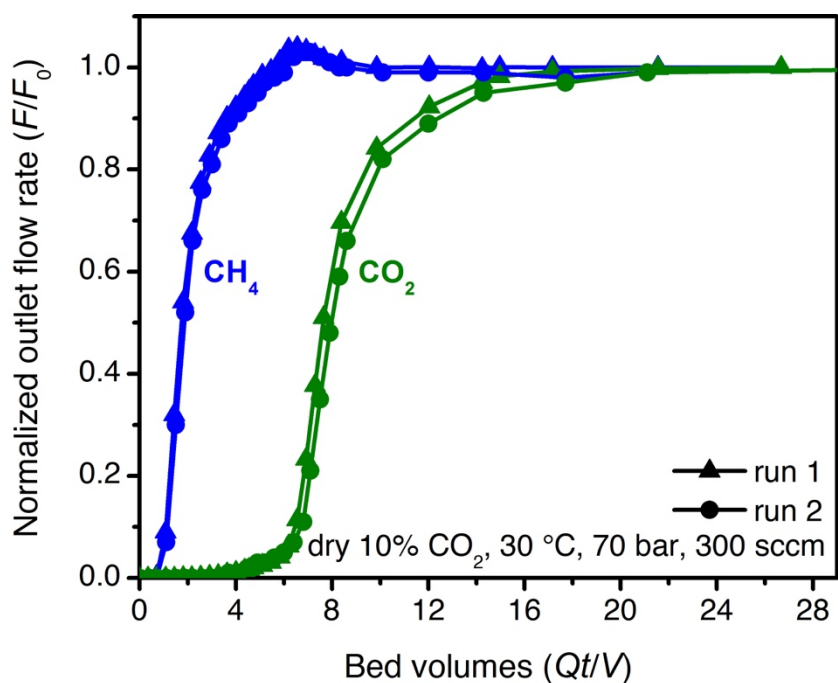


Figure 4.S58. Duplicate breakthrough experiments for ee-2-Mg₂(dobpdc) under 300 sccm of dry 10% CO₂ in CH₄ at 30 °C and 70 bar. The data shown for run 1 are the same as those shown in the main text.

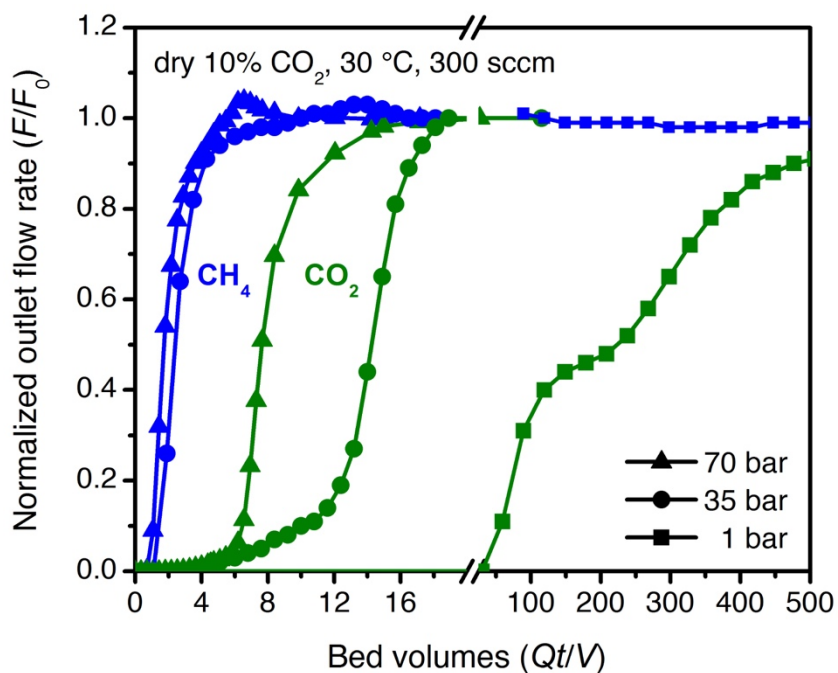


Figure 4.S59. Breakthrough curves for ee-2-Mg₂(dobpdc) at 70 bar (triangles), 35 bar (circles), and 1 bar (squares) under 300 sccm of dry 10% CO₂ in CH₄ at 30 °C. The data shown for 70 bar are the same as those shown in the main text.

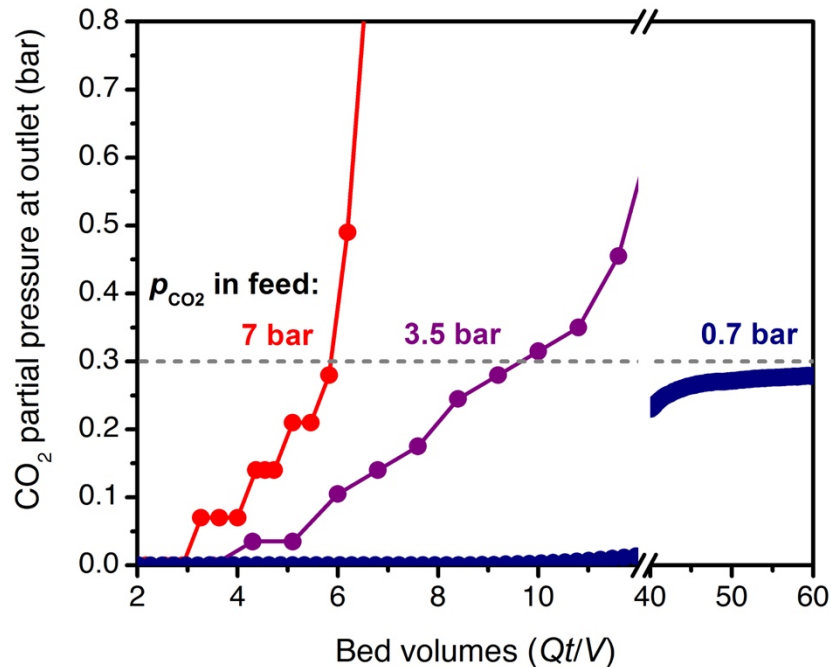


Figure 4.S60. Breakthrough curves for ee-2-Mg₂(dobpdc) with 300 sccm of dry 10% CO₂ at 30 °C and a total pressure of 70 bar (red), 35 bar (purple), and 7 bar (blue). Experiments are plotted in terms of CO₂ partial pressure at the outlet vs bed volumes to demonstrate the consistent slip of ~0.3 bar of CO₂ (gray dashed line) prior to full breakthrough.

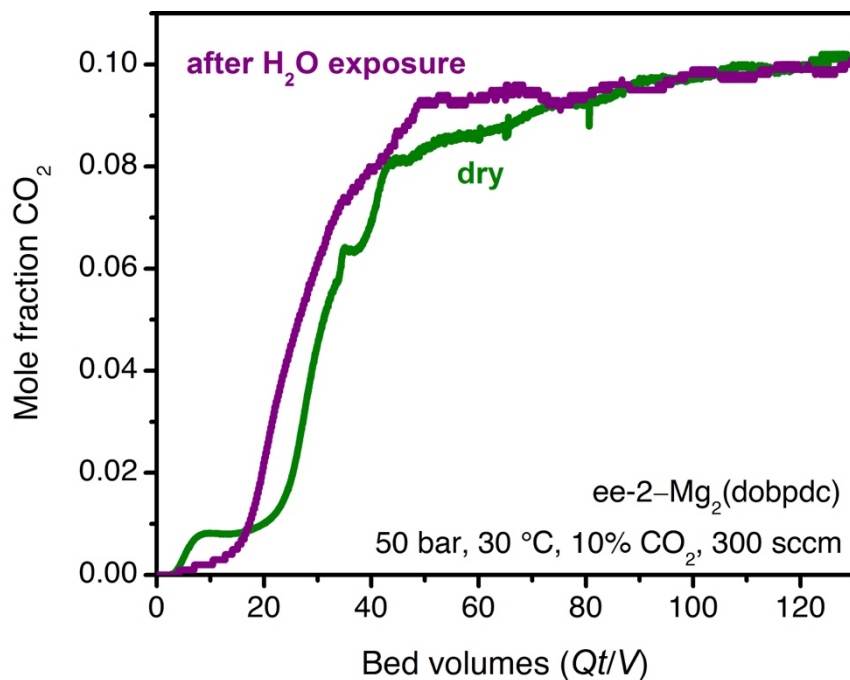


Figure 4.S61. Dry breakthrough curve for ee-2-Mg₂(dobpdc) under 300 sccm of 10% CO₂ in CH₄ at 30 °C (green), and the same experiment performed after exposure of the material to H₂O (purple).

4.6.16. Characterization of ee-2-Mg₂(dobpdc) Following Extended Pressure Cycling

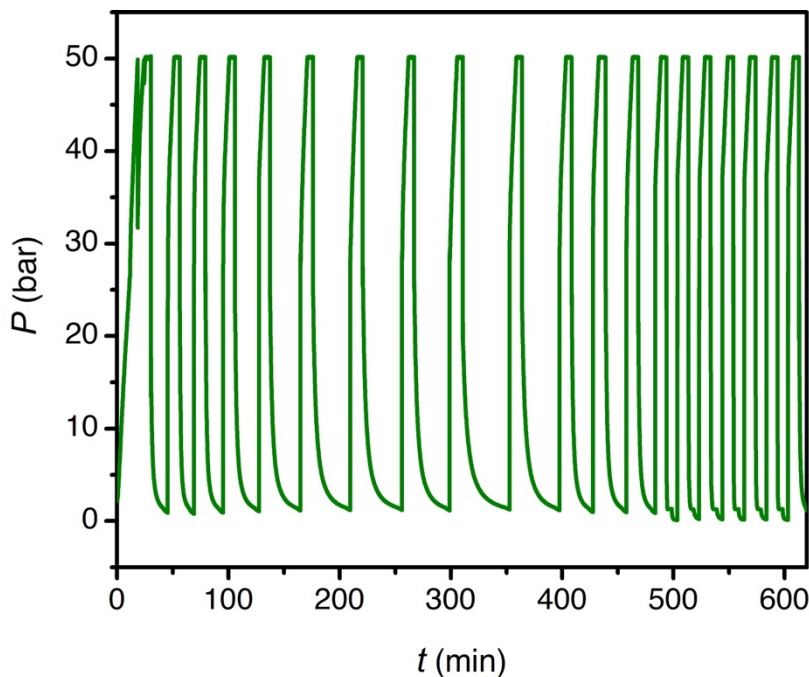


Figure 4.S62. Pressure vs temperature data for one bed in the first 20 of 100 mechanical pressure cycles of ee-2-Mg₂(dobpdc) under 250 sccm of dry 10% CO₂ in CH₄ at 40 °C.

Table 4.S11. Predicted and measured elemental analysis for ee-2-Mg₂(dobpdc) before and after extended pressure cycling. Materials were activated at 120 °C under vacuum for 2 h and stored in a N₂-filled glovebox prior to air-free elemental analysis. These results suggest contamination with co-fluidized glass wool packing, as confirmed with additional data below.

	Predicted for Mg ₂ (dobpdc)(ee-2) ₂	Measured, pre- cycling	Measured, post- cycling
C	56.65	56.42	49.88
H	6.95	6.77	5.66
N	10.16	10.15	7.94

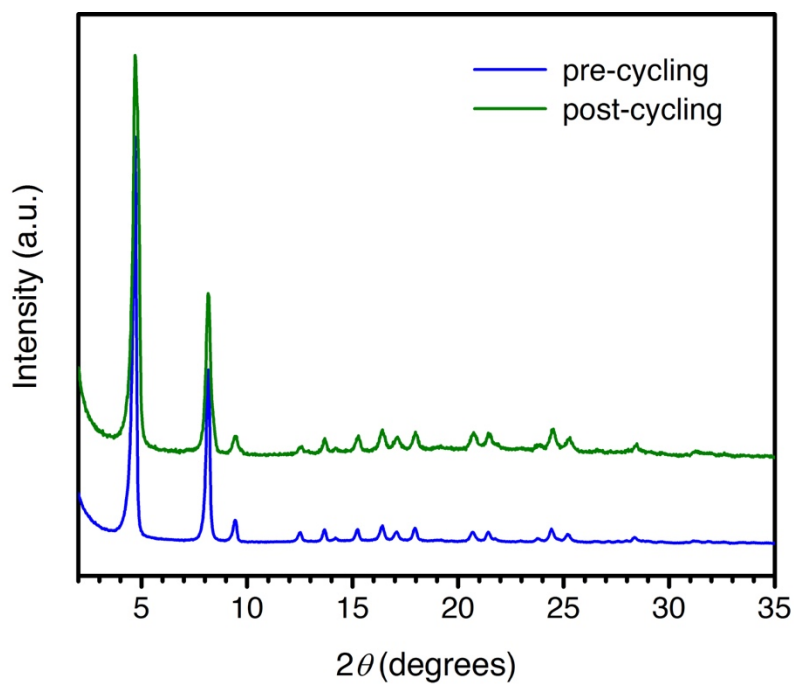


Figure 4.S63. Laboratory powder X-ray diffraction patterns ($\lambda = 1.5418 \text{ \AA}$) for ee-2-Mg₂(dobpdc) before (blue) and after (green) extended pressure–vacuum cycling, demonstrating negligible changes in crystallinity.

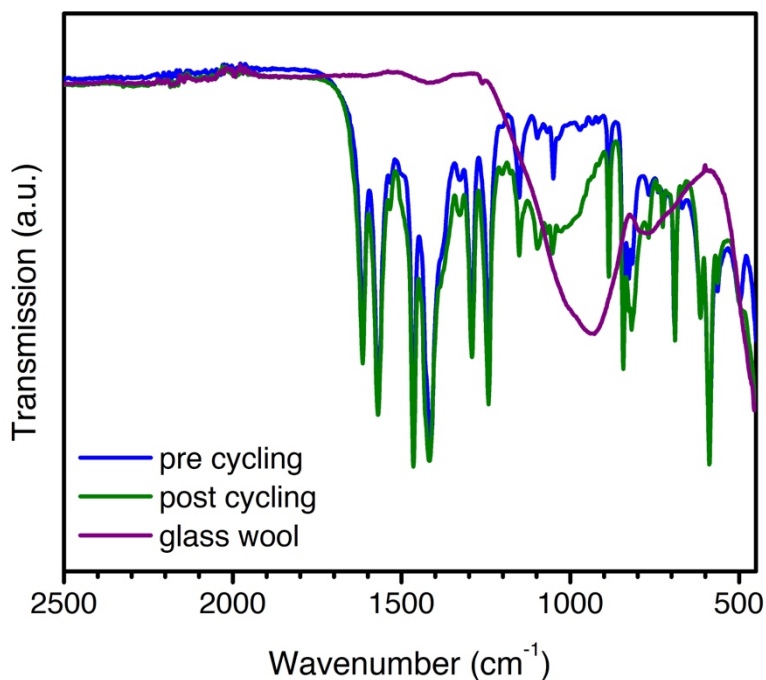


Figure 4.S64. Infrared spectra of ee-2-Mg₂(dobpdc) before (blue) and after (green) extended pressure–vacuum cycling. A broad vibration was observed around 950 cm⁻¹ and was assigned as glass wool packing (purple) that fluidized with the sample during cycling.

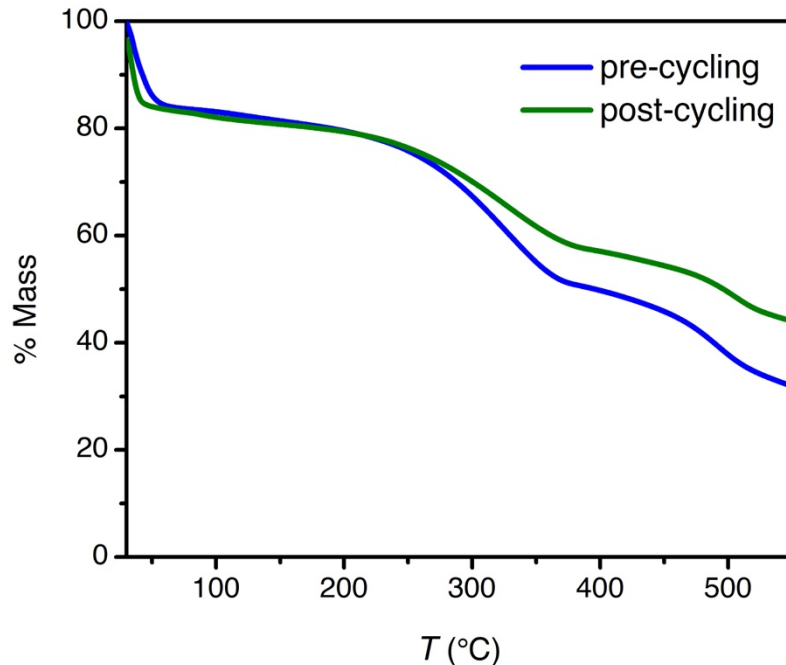


Figure 4.S65. Thermogravimetric decomposition traces for ee-2-Mg₂(dobpdc) before (blue) and after (green) extended pressure–vacuum cycling. A temperature ramp rate of 1.5 °C/min was used. The higher baseline mass for the post-cycling sample at elevated temperatures is consistent with buildup of fluidized glass wool packing in the sample. To estimate the amount of co-fluidized glass wool, the apparent weight percent of diamine in the adsorbent calculated from the post-cycling decomposition curve (31 wt % between 150 and 420 °C) was compared to the weight percent of diamine in the adsorbent calculated from the pre-cycling decomposition curve (42 wt %). These results suggest glass wool contamination of approximately 26% by mass ($100\% \times (1 - 0.31/0.42) = 26\%$), assuming no diamine loss during cycling. The assumption of negligible diamine loss was validated by collection of NMR spectra of the digested material before and after cycling. In both cases, full diamine loading was calculated from the ratio of the ligand and diamine peak integrals.

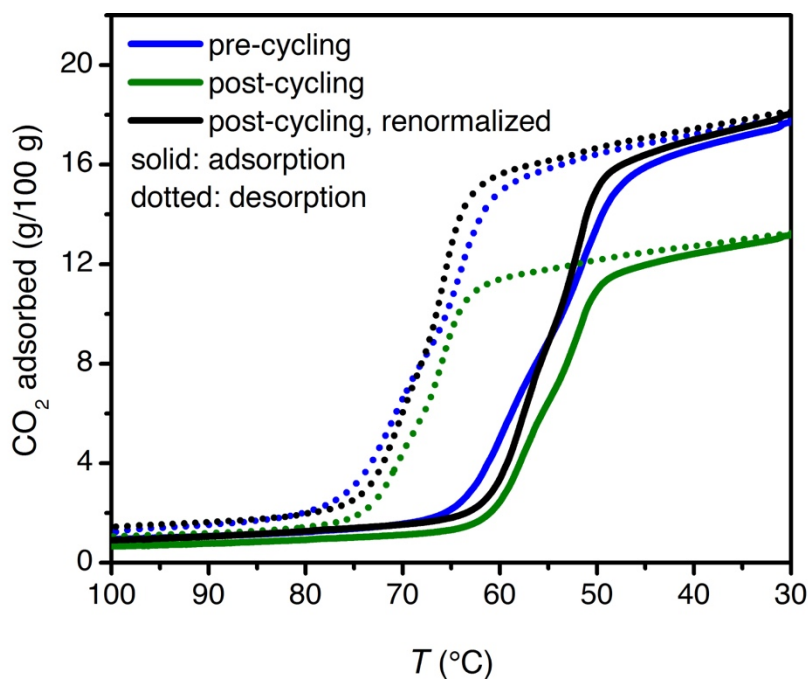


Figure 4.S66. Dry, pure CO₂ adsorption isobars at atmospheric pressure for ee-2-Mg₂(dobpdc) before (blue) and after (green) extended pressure–vacuum cycling. Samples were activated at 120 °C under flowing N₂ for 30 min prior to isobar collection. A ramp rate of 1 °C/min was used. To account for the mass of co-fluidized glass wool contamination, the activated mass of adsorbent in the post-cycling isobar was renormalized using the estimated mass % of glass wool contamination determined from the TGA decomposition traces (Figure 4.S65).

4.6.17. Synchrotron Powder X-ray Diffraction

High-resolution powder X-ray diffraction patterns of ee-2-Mg₂(dobpdc) and ee-2-Mg₂(dobpdc)–CO₂ were collected at beamline 17-BM at the Advance Photon Source of Argonne National Laboratory. An average wavelength of 0.45399 Å was used. Scattered intensity was recorded with a PerkinElmer a-Si Flat Panel detector. Prior to measurement, the sample was packed in a borosilicate glass capillary of 1.0 mm diameter under a N₂ atmosphere. The capillary was then attached to a custom-designed gas-dosing cell, which was then mounted onto the goniometer head and connected to a gas-dosing manifold for *in situ* diffraction measurements. The sample temperature was controlled by an Oxford Cryosystems Cryostream 800. The diffraction pattern of ee-2-Mg₂(dobpdc) was collected at 300 K under dynamic vacuum. The gas-dosing manifold was then used to dose the sample with 970 mbar of dry CO₂ at 300 K. The diffraction pattern of ee-2-Mg₂(dobpdc)–CO₂ was collected upon equilibration, as determined by stabilization of the diffraction pattern over several scans. Initial unit cell dimensions were determined by a standard peak search followed by indexing via single-value decomposition in TOPAS-Academic v4.1. Using TOPAS-Academic, precise unit cell dimensions were then determined by performing a structureless Pawley refinement.

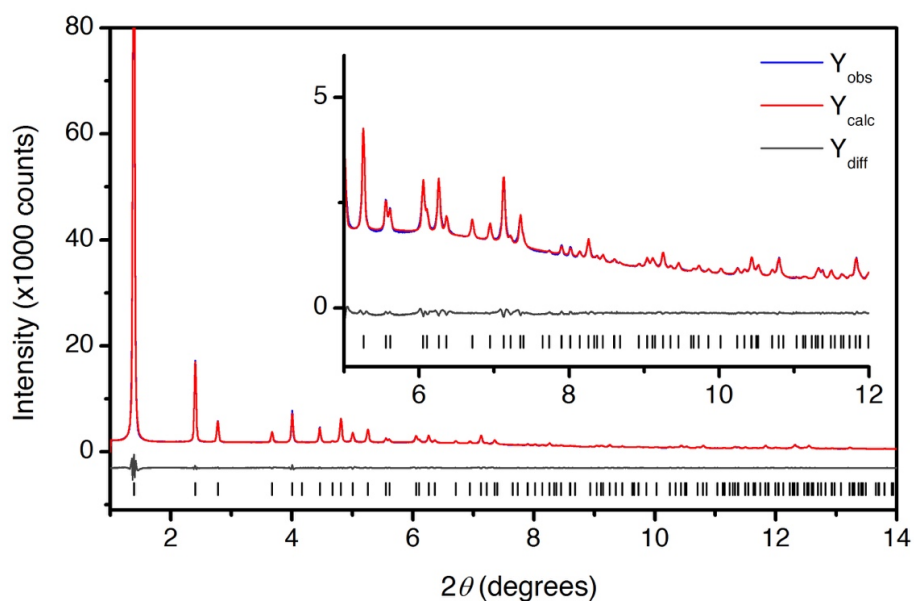


Figure 4.S67. Pawley refinement of synchrotron powder X-ray diffraction data ($\lambda = 0.45399 \text{ \AA}$) for evacuated ee-2-Mg₂(dobpdc) at 300 K. Blue and red lines depict the observed and calculated diffraction patterns, respectively. The gray line depicts the difference between the observed and calculated patterns, and the black tick marks indicate the calculated Bragg peak positions. The inset shows the high-angle region at magnified scale. Figures-of-merit (as defined by TOPAS): $R_{wp} = 2.13\%$, $R_{exp} = 2.14\%$, $R_p = 1.39\%$, $GoF = 0.998$.

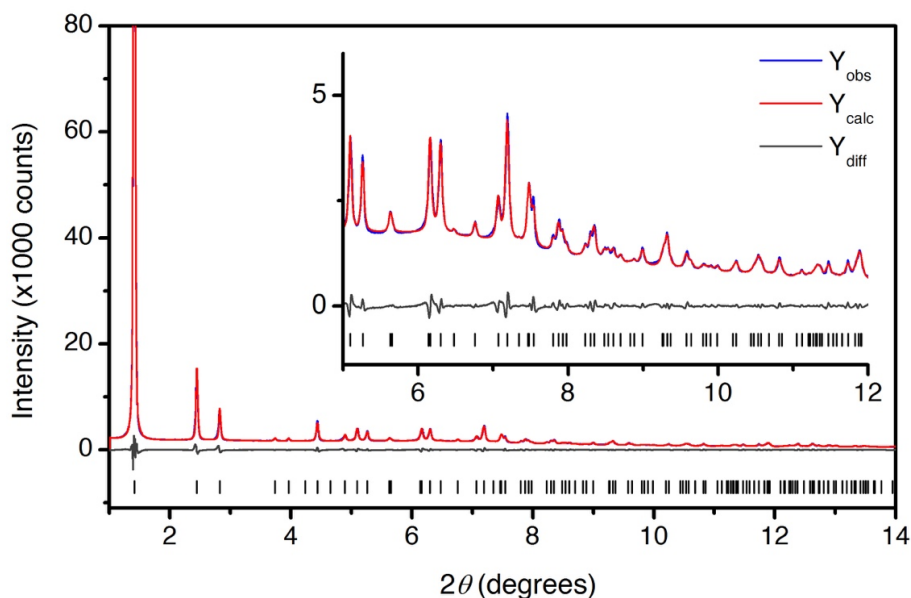


Figure 4.S68. Pawley refinement of synchrotron powder X-ray diffraction data ($\lambda = 0.45399 \text{ \AA}$) for ee-2-Mg₂(dobpdc) dosed with 970 mbar of CO₂ at 300 K. Blue and red lines depict the observed and calculated diffraction patterns, respectively. The gray line depicts the difference between the observed and calculated patterns, and the black tick marks indicate the calculated Bragg peak positions. The inset shows the high-angle region at magnified scale. Figures-of-merit (as defined by TOPAS): $R_{wp} = 3.37\%$, $R_{exp} = 2.07\%$, $R_p = 2.21\%$, $GoF = 1.63$.

Table 4.S12. Crystallographic data for Pawley refinement of synchrotron powder X-ray diffraction data.

	ee-2- Mg ₂ (dobpdc), evacuated	ee-2- Mg ₂ (dobpdc), 970 mbar CO ₂
Temperature (K)	300	300
Crystal System	Trigonal	Trigonal
Space Group	<i>P</i> 3 ₂ 21	<i>P</i> 3 ₂ 21
<i>a, b, c</i> (Å)	21.6248(1) 21.6248(1), 6.9188(3)	21.264(2) 21.264(2), 7.0289(5)
α, β, γ (°)	90, 90, 120	90, 90, 120
<i>V</i> (Å ³)	2801.9(3)	2752.3(4)
Radiation, λ (Å)	Synchrotron, 0.45399	Synchrotron, 0.45399
<i>R</i> _{wp}	2.13	3.37
<i>R</i> _{exp}	2.14	2.07
<i>R</i> _p	1.39	2.21
Goodness of Fit	0.998	1.63

4.6.18. Single-Crystal X-ray Diffraction

Single crystals of Zn₂(dobpdc) were prepared as reported previously.⁶⁷ The crystals were functionalized with the diamine ee-2 following a previously reported procedure.³¹

For CO₂ dosing, crystals of ee-2-Zn₂(dobpdc) were activated for 1 h at 100 °C under vacuum (<10 microbar) and then transferred to the analysis port of a Micromeritics ASAP 2420 gas sorption analyzer. The crystals were placed under 1100 mbar of CO₂ for 5 min at room temperature. The glass adsorption tube was then sealed under this CO₂ atmosphere, removed from the instrument, and stored over dry ice for 28 h. Immediately after removing the seal on the glass adsorption tube, the crystals were coated with Paratone oil, and a single crystal was rapidly mounted on a MiTeGen loop and frozen at a temperature of 100 K in a cryostream of N₂.

Single-crystal X-ray diffraction data were collected at Beamline 12.2.1 at the Advanced Light Source, Lawrence Berkeley National Laboratory using synchrotron radiation ($\lambda = 0.7288$ Å) and a Bruker AXS D8 diffractometer equipped with a Bruker PHOTON II CMOS detector. Structures were collected at 100 K using an Oxford Cryosystems Cryostream 700 Plus. Raw data were corrected for Lorentz and polarization effects using Bruker AXS SAINT software⁷¹ and were corrected for absorption using SADABS.⁷² The structures were solved using SHELXT⁷³ and refined using SHELXL⁷⁴ operated in the OLEX2⁷⁵ interface.

Thermal parameters were refined anisotropically for all non-hydrogen atoms. All hydrogen atoms were placed in ideal positions and refined using a riding model. The ammonium carbamate chains formed upon CO₂ adsorption (part -1 in the .cif) freely refined to an occupancy of 0.345(5). In addition, unreacted diamine was resolved in the structure (part -2 in the .cif) and

freely refined to an occupancy of 0.451(8). These occupancies were fixed in the final refinement. Additionally, the occupancy of atom O4 (the bound oxygen atom of the carbamate) was fixed as $(1 - \text{the occupancy of the unreacted diamine}) = 0.549$ to account for water, solvent, or unreacted CO₂ at the open Zn(II) coordination sites not bound to carbamate groups or unreacted diamine. This decision was made on the basis of free refinement of the bound nitrogen and oxygen atoms, which gave occupancies of N3 = 0.41(5) (within error of the occupancy of unreacted diamine) and O4 = 0.55(5) (within error of $1 - \text{the occupancy of unreacted diamine}$), respectively.

To model the disorder, the following distance and displacement parameter restraints were used:

SADI for 1,2 distances of C–C bonds in the ethyl groups of the diamine,

SADI for 1,2 distances of the C–N bonds of the tertiary amine in part -2,

DFIX for the C–N bonds of the ammonium, and

RIGU and SIMU for the unreacted diamine (part -2)

Four instances of OMIT were used (OMIT 0 1 0, OMIT -1 1 1, OMIT 0 3 0, OMIT -4 4 2). These reflections were suspected to be affected by the beamstop.

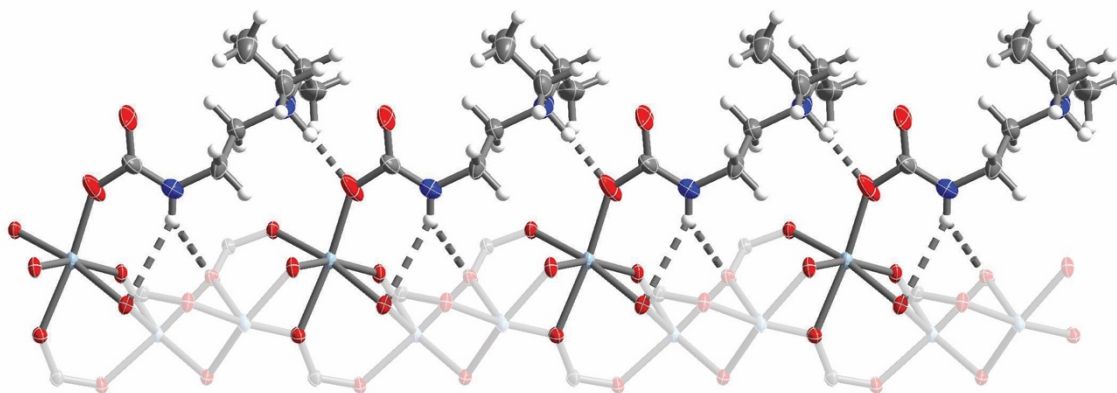


Figure 4.S69. Thermal ellipsoid plot of the ammonium carbamate chains in Zn₂(dobpdc)(ee-2)_{0.902}(ee-2-CO₂)_{0.690} at 100 K drawn at 50% probability level, as determined by single crystal X-ray diffraction. Light blue, gray, blue, red, and white represent Zn, C, N, O, and H atoms, respectively.

Table 4.S13. Crystallographic data for single-crystal X-ray diffraction.

	<u>Zn₂(dobpdc)(ee-2)_{0.902}(ee-2-CO₂)_{0.690}</u>
Formula	C _{24.24} H _{31.47} N _{3.18} O _{7.38} Zn ₂
Temperature (K)	100(2)
Crystal System	Trigonal
Space Group	<i>P</i> 3 ₁ 21
<i>a</i> , <i>b</i> , <i>c</i> (Å)	21.5982(10), 21.5982(10), 6.9071(4)
<i>α</i> , <i>β</i> , <i>γ</i> (°)	90, 90, 120
<i>V</i> (Å ³)	2790.4(3)
<i>Z</i>	3
Radiation, <i>λ</i> (Å)	Synchrotron, 0.7288
2 <i>θ</i> Range for Data Collection (°)	3.868 to 59.814
Completeness to 2 <i>θ</i>	99.8% (2 <i>θ</i> = 51.860°)
Data / Restraints / Parameters	5009/ 95 / 274
Goodness of Fit on <i>F</i> ²	1.086
<i>R</i> ₁ ^{<i>a</i>} , <i>wR</i> ₂ ^{<i>b</i>} (<i>I</i> > 2 <i>σ</i> (<i>I</i>))	0.0335, 0.0877
<i>R</i> ₁ ^{<i>a</i>} , <i>wR</i> ₂ ^{<i>b</i>} (all data)	0.0395, 0.0906
Largest Diff. Peak and Hole (e Å ⁻³)	0.379, -0.446

4.7. Notes and References

‡In light of the double-stepped adsorption profiles observed here for ee-2-Mg₂(dobpdc) and observed previously for Mg₂(dobpdc) functionalized with bulky 1°/2° diamines,³⁵ the single-stepped adsorption profile of ii-2-Mg₂(dobpdc), which bears an even larger diisopropyl-substituted tertiary amine, is surprising. This result suggests that the 50% CO₂-inserted structure in ii-2-Mg₂(dobpdc) is energetically unfavorable, and further work is needed to elucidate the structure of the CO₂-adsorbed phase for this material.

- (1) *Key World Energy Statistics 2017*; International Energy Agency, 2017.
- (2) *BP Statistical Review of World Energy, 66th Edition*; BP, 2017.
- (3) *International Energy Outlook 2017*; DOE/EIA-0484(2017); Energy Information Administration, U.S. Department of Energy, 2017.
- (4) *2017 Outlook for Energy: A View to 2040*; ExxonMobil, 2017.
- (5) Parrish, W. R.; Kidnay, A. J. *Fundamentals of Natural Gas Processing*; CRC Press, 2006.
- (6) Leppin, D.; Meyer, H. S. Gas Research Institute Program in Natural Gas Processing. In *SPE-21505-MS*; Society of Petroleum Engineers: SPE, 1991. <https://doi.org/10.2118/21505-MS>.
- (7) Burgers, W. F. J.; Northrop, P. S.; Kheshgi, H. S.; Valencia, J. A. Worldwide Development Potential for Sour Gas. *Energy Procedia* **2011**, *4* (Supplement C), 2178–2184. <https://doi.org/10.1016/j.egypro.2011.02.104>.
- (8) Rufford, T. E.; Smart, S.; Watson, G. C. Y.; Graham, B. F.; Boxall, J.; Diniz da Costa, J. C.; May, E. F. The Removal of CO₂ and N₂ from Natural Gas: A Review of Conventional and Emerging Process Technologies. *J. Pet. Sci. Eng.* **2012**, *94* (Supplement C), 123–154. <https://doi.org/10.1016/j.petrol.2012.06.016>.
- (9) Burr, B.; Lyddon, L. *A Comparison of Physical Solvents for Acid Gas Removal*; Bryan Research & Engineering, Inc, 2008.
- (10) Maqsood, K.; Mullick, A.; Ali, A.; Kargupta, K.; Ganguly, S. Cryogenic Carbon Dioxide Separation from Natural Gas: A Review Based on Conventional and Novel Emerging Technologies. *Rev. Chem. Eng.* **2014**, *30* (5), 453–477. <https://doi.org/10.1515/revce-2014-0009>.
- (11) Alcheikhhamdon, Y.; Hoorfar, M. Natural Gas Purification from Acid Gases Using Membranes: A Review of the History, Features, Techno-Commercial Challenges, and Process Intensification of Commercial Membranes. *Chem. Eng. Process. - Process Intensif.* **2017**, *120*, 105–113. <https://doi.org/10.1016/j.cep.2017.07.009>.
- (12) van Denderen, M.; Ineke, E.; Golombok, M. CO₂ Removal from Contaminated Natural Gas Mixtures by Hydrate Formation. *Ind. Eng. Chem. Res.* **2009**, *48* (12), 5802–5807. <https://doi.org/10.1021/ie8017065>.
- (13) Ruthven, D. M.; Farooq, S.; Knaebel, K. S. *Pressure Swing Adsorption*; VCH Publishers: New York, N.Y., 1994.
- (14) Tagliabue, M.; Farrusseng, D.; Valencia, S.; Aguado, S.; Ravon, U.; Rizzo, C.; Corma, A.; Mirodatos, C. Natural Gas Treating by Selective Adsorption: Material Science and Chemical Engineering Interplay. *Chem. Eng. J.* **2009**, *155* (3), 553–566. <https://doi.org/10.1016/j.cej.2009.09.010>.
- (15) Sircar, S. Separation of Methane and Carbon Dioxide Gas Mixtures by Pressure Swing Adsorption. *Sep. Sci. Technol.* **1988**, *23* (6–7), 519–529. <https://doi.org/10.1080/01496398808057650>.

- (16) Guild Associates, Inc. Molecular Gate® Carbon Dioxide Removal Systems <http://www.moleculargate.com/carbon-dioxide-removal-adsorption-system.html> (accessed Oct 1, 2017).
- (17) Toreja, J.; Chan, N.; VanNostrand, B.; Dickinson, J. P. Rotary-Valve, Fast-Cycle Pressure-Swing Adsorption Technology Allows West Coast Platform to Meet Tight California Specifications and Recover Stranded Gas. In *Laurance Reid Gas Conditioning Conference*; University of Oklahoma Norman, OK, 2011.
- (18) Liu, J.; Wang, Y.; Benin, A. I.; Jakubczak, P.; Willis, R. R.; LeVan, M. D. CO₂/H₂O Adsorption Equilibrium and Rates on Metal–Organic Frameworks: HKUST-1 and Ni/DOBDC. *Langmuir* **2010**, *26* (17), 14301–14307. <https://doi.org/10.1021/la102359q>.
- (19) Wang, Y.; LeVan, M. D. Adsorption Equilibrium of Binary Mixtures of Carbon Dioxide and Water Vapor on Zeolites 5A and 13X. *J. Chem. Eng. Data* **2010**, *55* (9), 3189–3195. <https://doi.org/10.1021/je100053g>.
- (20) Kizzie, A. C.; Wong-Foy, A. G.; Matzger, A. J. Effect of Humidity on the Performance of Microporous Coordination Polymers as Adsorbents for CO₂ Capture. *Langmuir* **2011**, *27* (10), 6368–6373. <https://doi.org/10.1021/la200547k>.
- (21) Mason, J. A.; McDonald, T. M.; Bae, T.-H.; Bachman, J. E.; Sumida, K.; Dutton, J. J.; Kaye, S. S.; Long, J. R. Application of a High-Throughput Analyzer in Evaluating Solid Adsorbents for Post-Combustion Carbon Capture via Multicomponent Adsorption of CO₂, N₂, and H₂O. *J. Am. Chem. Soc.* **2015**, *137* (14), 4787–4803. <https://doi.org/10.1021/jacs.5b00838>.
- (22) Belmabkhout, Y.; De Weireld, G.; Sayari, A. Amine-Bearing Mesoporous Silica for CO₂ and H₂S Removal from Natural Gas and Biogas. *Langmuir* **2009**, *25* (23), 13275–13278. <https://doi.org/10.1021/la903238y>.
- (23) Huang, H. Y.; Yang, R. T.; Chinn, D.; Munson, C. L. Amine-Grafted MCM-48 and Silica Xerogel as Superior Sorbents for Acidic Gas Removal from Natural Gas. *Ind. Eng. Chem. Res.* **2003**, *42* (12), 2427–2433. <https://doi.org/10.1021/ie020440u>.
- (24) Ibarra, I. A.; González-Zamora, E. CO₂ Capture under Humid Conditions in Metal–Organic Frameworks. *Mater. Chem. Front.* **2017**, *1* (8), 1471–1484. <https://doi.org/10.1039/C6QM00301J>.
- (25) Couck, S.; Denayer, J. F. M.; Baron, G. V.; Rémy, T.; Gascon, J.; Kapteijn, F. An Amine-Functionalized MIL-53 Metal–Organic Framework with Large Separation Power for CO₂ and CH₄. *J. Am. Chem. Soc.* **2009**, *131* (18), 6326–6327. <https://doi.org/10.1021/ja900555r>.
- (26) Flaig, R. W.; Osborn Popp, T. M.; Fracaroli, A. M.; Kapustin, E. A.; Kalmutzki, M. J.; Altamimi, R. M.; Fathieh, F.; Reimer, J. A.; Yaghi, O. M. The Chemistry of CO₂ Capture in an Amine-Functionalized Metal–Organic Framework under Dry and Humid Conditions. *J. Am. Chem. Soc.* **2017**, *139* (35), 12125–12128. <https://doi.org/10.1021/jacs.7b06382>.
- (27) Hong, C. S.; Kang, M.; Kang, D. W. Post-Synthetic Diamine-Functionalization of MOF-74 Type Frameworks for Effective Carbon Dioxide Separation. *Dalton Trans.* **2019**, *48*, 2263–2270. <https://doi.org/10.1039/C8DT04339F>.
- (28) McDonald, T. M.; D’Alessandro, D. M.; Krishna, R.; Long, J. R. Enhanced Carbon Dioxide Capture upon Incorporation of N,N’-Dimethylethylenediamine in the Metal–Organic Framework CuBTri. *Chem. Sci.* **2011**, *2* (10), 2022–2028. <https://doi.org/10.1039/C1SC00354B>.

- (29) McDonald, T. M.; Lee, W. R.; Mason, J. A.; Wiers, B. M.; Hong, C. S.; Long, J. R. Capture of Carbon Dioxide from Air and Flue Gas in the Alkylamine-Appended Metal–Organic Framework mmen-Mg₂(dobpdc). *J. Am. Chem. Soc.* **2012**, *134* (16), 7056–7065. <https://doi.org/10.1021/ja300034j>.
- (30) McDonald, T. M.; Mason, J. A.; Kong, X.; Bloch, E. D.; Gygi, D.; Dani, A.; Crocellà, V.; Giordanino, F.; Odoh, S. O.; Drisdell, W. S.; Vlaisavljevich, B.; Dzubak, A. L.; Poloni, R.; Schnell, S. K.; Planas, N.; Lee, K.; Pascal, T.; Wan, L. F.; Prendergast, D.; Neaton, J. B.; Smit, B.; Kortright, J. B.; Gagliardi, L.; Bordiga, S.; Reimer, J. A.; Long, J. R. Cooperative Insertion of CO₂ in Diamine-Appended Metal–Organic Frameworks. *Nature* **2015**, *519* (7543), 303–308. <https://doi.org/10.1038/nature14327>.
- (31) Siegelman, R. L.; McDonald, T. M.; Gonzalez, M. I.; Martell, J. D.; Milner, P. J.; Mason, J. A.; Berger, A. H.; Bhowan, A. S.; Long, J. R. Controlling Cooperative CO₂ Adsorption in Diamine-Appended Mg₂(dobpdc) Metal–Organic Frameworks. *J. Am. Chem. Soc.* **2017**, *139* (30), 10526–10538. <https://doi.org/10.1021/jacs.7b05858>.
- (32) Hefti, M.; Joss, L.; Bjelobrk, Z.; Mazzotti, M. On the Potential of Phase-Change Adsorbents for CO₂ Capture by Temperature Swing Adsorption. *Faraday Discuss.* **2016**, *192*, 153–179. <https://doi.org/10.1039/C6FD00040A>.
- (33) Milner, P. J.; Siegelman, R. L.; Forse, A. C.; Gonzalez, M. I.; Runčevski, T.; Martell, J. D.; Reimer, J. A.; Long, J. R. A Diaminopropane-Appended Metal–Organic Framework Enabling Efficient CO₂ Capture from Coal Flue Gas via a Mixed Adsorption Mechanism. *J. Am. Chem. Soc.* **2017**, *139* (38), 13541–13553. <https://doi.org/10.1021/jacs.7b07612>.
- (34) Jo, H.; Lee, W. R.; Kim, N. W.; Jung, H.; Lim, K. S.; Kim, J. E.; Kang, D. W.; Lee, H.; Hiremath, V.; Seo, J. G.; Jin, H.; Moon, D.; Han, S. S.; Hong, C. S. Fine-Tuning of the Carbon Dioxide Capture Capability of Diamine-Grafted Metal–Organic Framework Adsorbents Through Amine Functionalization. *ChemSusChem* **2017**, *10* (3), 541–550. <https://doi.org/10.1002/cssc.201601203>.
- (35) Milner, P. J.; Martell, J. D.; Siegelman, R. L.; Gygi, D.; Weston, S. C.; Long, J. R. Overcoming Double-Step CO₂ Adsorption and Minimizing Water Co-Adsorption in Bulky Diamine-Appended Variants of Mg₂(dobpdc). *Chem. Sci.* **2018**, *9* (1), 160–174. <https://doi.org/10.1039/C7SC04266C>.
- (36) Darunte, L.; Sen, T.; Bhawanani, C.; Walton, K. S.; Sholl, D. S.; Realff, M. J.; Jones, C. W. Moving Beyond Adsorption Capacity in Design of Adsorbents for CO₂ Capture from Ultra-Dilute Feeds: Kinetics of CO₂ Adsorption in Materials with Stepped Isotherms. *Ind. Eng. Chem. Res.* **2019**, *58* (1), 366–377. <https://doi.org/10.1021/acs.iecr.8b05042>.
- (37) Lindsey, A. S.; Jeskey, H. The Kolbe-Schmitt Reaction. *Chem. Rev.* **1957**, *57* (4), 583–620. <https://doi.org/10.1021/cr50016a001>.
- (38) Walton, K. S.; Snurr, R. Q. Applicability of the BET Method for Determining Surface Areas of Microporous Metal–Organic Frameworks. *J. Am. Chem. Soc.* **2007**, *129* (27), 8552–8556. <https://doi.org/10.1021/ja071174k>.
- (39) Mason, J. A.; Veenstra, M.; Long, J. R. Evaluating Metal–Organic Frameworks for Natural Gas Storage. *Chem Sci* **2014**, *5* (1), 32–51. <https://doi.org/10.1039/C3SC52633J>.
- (40) Lemmon, E. W.; Huber, M. L.; McLinden, M. O. *REFPROP: Reference Fluid Thermodynamic and Transport Properties, Version 9*; National Institute of Standards and Technology, 2010.
- (41) Gurvich, L. *J. Phys. Chem. Soc. Russ.* **1915**, *47*, 805.
- (42) NIST WebBook <https://webbook.nist.gov/>.

- (43) Golden, F. M. Theory of Fixed-Bed Performance for Ion Exchange Accompanied by Chemical Reaction. Ph.D. Thesis, University of California, Berkeley: United States, 1973.
- (44) Helfferich, F. G.; Carr, P. W. Non-Linear Waves in Chromatography. *J. Chromatogr. A* **1993**, *629* (2), 97–122. [https://doi.org/10.1016/0021-9673\(93\)87026-I](https://doi.org/10.1016/0021-9673(93)87026-I).
- (45) Zhang, W.; Shan, Y.; Seidel-Morgenstern, A. Breakthrough Curves and Elution Profiles of Single Solutes in Case of Adsorption Isotherms with Two Inflection Points. *J. Chromatogr. A* **2006**, *1107* (1–2), 216–225. <https://doi.org/10.1016/j.chroma.2005.12.094>.
- (46) Sumida, K.; Rogow, D. L.; Mason, J. A.; McDonald, T. M.; Bloch, E. D.; Herm, Z. R.; Bae, T.-H.; Long, J. R. Carbon Dioxide Capture in Metal–Organic Frameworks. *Chem. Rev.* **2012**, *112* (2), 724–781. <https://doi.org/10.1021/cr2003272>.
- (47) Alkhabbaz, M. A.; Bollini, P.; Foo, G. S.; Sievers, C.; Jones, C. W. Important Roles of Enthalpic and Entropic Contributions to CO₂ Capture from Simulated Flue Gas and Ambient Air Using Mesoporous Silica Grafted Amines. *J. Am. Chem. Soc.* **2014**, *136* (38), 13170–13173. <https://doi.org/10.1021/ja507655x>.
- (48) Xu, X.; Song, C.; Miller, B. G.; Scaroni, A. W. Influence of Moisture on CO₂ Separation from Gas Mixture by a Nanoporous Adsorbent Based on Polyethylenimine-Modified Molecular Sieve MCM-41. *Ind. Eng. Chem. Res.* **2005**, *44* (21), 8113–8119. <https://doi.org/10.1021/ie050382n>.
- (49) Serna-Guerrero, R.; Belmabkhout, Y.; Sayari, A. Triamine-Grafted Pore-Expanded Mesoporous Silica for CO₂ Capture: Effect of Moisture and Adsorbent Regeneration Strategies. *Adsorption* **2010**, *16* (6), 567–575. <https://doi.org/10.1007/s10450-010-9253-y>.
- (50) Bollini, P.; Didas, S. A.; Jones, C. W. Amine-Oxide Hybrid Materials for Acid Gas Separations. *J. Mater. Chem.* **2011**, *21* (39), 15100–15120. <https://doi.org/10.1039/C1JM12522B>.
- (51) Didas, S. A.; Sakwa-Novak, M. A.; Foo, G. S.; Sievers, C.; Jones, C. W. Effect of Amine Surface Coverage on the Co-Adsorption of CO₂ and Water: Spectral Deconvolution of Adsorbed Species. *J. Phys. Chem. Lett.* **2014**, *5* (23), 4194–4200. <https://doi.org/10.1021/jz502032c>.
- (52) Zhang, H.; Goeppert, A.; Olah, G. A.; Prakash, G. K. S. Remarkable Effect of Moisture on the CO₂ Adsorption of Nano-Silica Supported Linear and Branched Polyethylenimine. *J. CO₂ Util.* **2017**, *19*, 91–99. <https://doi.org/10.1016/j.jcou.2017.03.008>.
- (53) Yu, J.; Zhai, Y.; Chuang, S. S. C. Water-Enhancement in CO₂ Capture by Amines: An Insight into CO₂-H₂O Interactions on Amine Films and Sorbents. *Ind. Eng. Chem. Res.* **2018**, *57* (11), 4052–4062. <https://doi.org/10.1021/acs.iecr.7b05114>.
- (54) Forse, A. C.; Milner, P. J.; Lee, J.-H.; Redfearn, H. N.; Oktawiec, J.; Siegelman, R. L.; Martell, J. D.; Dinakar, B.; Porter-Zasada, L. B.; Gonzalez, M. I.; Neaton, J. B.; Long, J. R.; Reimer, J. A. Elucidating CO₂ Chemisorption in Diamine-Appended Metal–Organic Frameworks. *J. Am. Chem. Soc.* **2018**, *140* (51), 18016–18031. <https://doi.org/10.1021/jacs.8b10203>.
- (55) Skarstrom, C. W. Method and Apparatus for Fractionating Gaseous Mixtures by Adsorption. US2944627A, July 12, 1960.
- (56) Shah, M. S.; Tsapatsis, M.; Siepmann, J. I. Hydrogen Sulfide Capture: From Absorption in Polar Liquids to Oxide, Zeolite, and Metal–Organic Framework Adsorbents and Membranes. *Chem. Rev.* **2017**, *117* (14), 9755–9803. <https://doi.org/10.1021/acs.chemrev.7b00095>.

- (57) Ethiraj, J.; Bonino, F.; Lamberti, C.; Bordiga, S. H₂S Interaction with HKUST-1 and ZIF-8 MOFs: A Multitechnique Study. *Microporous Mesoporous Mater.* **2015**, *207*, 90–94. <https://doi.org/10.1016/j.micromeso.2014.12.034>.
- (58) Liu, J.; Wei, Y.; Li, P.; Zhao, Y.; Zou, R. Selective H₂S/CO₂ Separation by Metal–Organic Frameworks Based on Chemical-Physical Adsorption. *J. Phys. Chem. C* **2017**, *121* (24), 13249–13255. <https://doi.org/10.1021/acs.jpcc.7b04465>.
- (59) Bhatt, P. M.; Belmabkhout, Y.; Assen, A. H.; Weseliński, Ł. J.; Jiang, H.; Cadiau, A.; Xue, D.-X.; Eddaoudi, M. Isorecticular Rare Earth fcu-MOFs for the Selective Removal of H₂S from CO₂ Containing Gases. *Chem. Eng. J.* **2017**, *324*, 392–396. <https://doi.org/10.1016/j.cej.2017.05.008>.
- (60) Kim, K. C. Design Strategies for Metal–Organic Frameworks Selectively Capturing Harmful Gases. *J. Organomet. Chem.* **2018**, *854*, 94–105. <https://doi.org/10.1016/j.jorganchem.2017.11.017>.
- (61) Belmabkhout, Y.; Bhatt, P. M.; Adil, K.; Pillai, R. S.; Cadiau, A.; Shkurenko, A.; Maurin, G.; Gongping, L.; Koros, W. J.; Eddaoudi, M. Natural Gas Upgrading Using a Fluorinated MOF with Tuned H₂S and CO₂ Adsorption Selectivity. *Nat. Energy* **2018**, *1*. <https://doi.org/10.1038/s41560-018-0267-0>.
- (62) Joshi, J. N.; Zhu, G.; Lee, J. J.; Carter, E. A.; Jones, C. W.; Lively, R. P.; Walton, K. S. Probing Metal–Organic Framework Design for Adsorptive Natural Gas Purification. *Langmuir* **2018**, *34* (29), 8443–8450. <https://doi.org/10.1021/acs.langmuir.8b00889>.
- (63) Belmabkhout, Y.; Pillai, R. S.; Alezi, D.; Shekhah, O.; Bhatt, P. M.; Chen, Z.; Adil, K.; Vaesen, S.; Weireld, G. D.; Pang, M.; Suetin, M.; Cairns, A. J.; Solovyeva, V.; Shkurenko, A.; Tall, O. E.; Maurin, G.; Eddaoudi, M. Metal–Organic Frameworks to Satisfy Gas Upgrading Demands: Fine-Tuning the soc-MOF Platform for the Operative Removal of H₂S. *J. Mater. Chem. A* **2017**, *5* (7), 3293–3303. <https://doi.org/10.1039/C6TA09406F>.
- (64) Boller, A.; Jin, Y.; Wunderlich, B. Heat Capacity Measurement by Modulated DSC at Constant Temperature. *J. Therm. Anal.* **1994**, *42* (2–3), 307–330. <https://doi.org/10.1007/BF02548519>.
- (65) *Gas Treating Chemicals, Vol. 1*; Union Carbide Chemicals Company, 1957.
- (66) Lee, J.-H.; Siegelman, R. L.; Maserati, L.; Rangel, T.; Helms, B. A.; Long, J. R.; Neaton, J. B. Enhancement of CO₂ Binding and Mechanical Properties upon Diamine Functionalization of M₂(dobpdc) Metal–Organic Frameworks. *Chem. Sci.* **2018**, *9* (23), 5197–5206. <https://doi.org/10.1039/C7SC05217K>.
- (67) Siegelman, R. L.; Milner, P. J.; Forse, A. C.; Lee, J.-H.; Colwell, K. A.; Neaton, J. B.; Reimer, J. A.; Weston, S. C.; Long, J. R. Water Enables Efficient CO₂ Capture from Natural Gas Flue Emissions in an Oxidation-Resistant Diamine-Appended Metal–Organic Framework. *Submitted*.
- (68) Mazzotti, M.; Rajendran, A. Equilibrium Theory-Based Analysis of Nonlinear Waves in Separation Processes. *Annu. Rev. Chem. Biomol. Eng.* **2013**, *4* (1), 119–141. <https://doi.org/10.1146/annurev-chembioeng-061312-103318>.
- (69) Sinha, A.; Darunte, L. A.; Jones, C. W.; Realff, M. J.; Kawajiri, Y. Systems Design and Economic Analysis of Direct Air Capture of CO₂ through Temperature Vacuum Swing Adsorption Using MIL-101(Cr)-PEI-800 and mmen-Mg₂(dobpdc) MOF Adsorbents. *Ind. Eng. Chem. Res.* **2017**, *56* (3), 750–764. <https://doi.org/10.1021/acs.iecr.6b03887>.

- (70) L&C Science: PSA Bench-Top Testing System Series <http://www.landscience.com/PSA-1000.html> (accessed Apr 26, 2019).
- (71) *SAINTE, APEX2, and APEX3 Software for CCD Diffractometers*; Bruker Analytical X-ray Systems Inc.: Madison, WI, USA, 2014.
- (72) Sheldrick, G. M. *SADABS*; University of Göttingen, Germany.
- (73) Sheldrick, G. M. SHELXT – Integrated Space-Group and Crystal-Structure Determination. *Acta Crystallogr. Sect. Found. Adv.* **2015**, *71* (1), 3–8. <https://doi.org/10.1107/S2053273314026370>.
- (74) Sheldrick, G. M. Crystal Structure Refinement with SHELXL. *Acta Crystallogr. Sect. C Struct. Chem.* **2015**, *71* (1), 3–8. <https://doi.org/10.1107/S2053229614024218>.
- (75) Dolomanov, O. V.; Bourhis, L. J.; Gildea, R. J.; Howard, J. a. K.; Puschmann, H. OLEX2: A Complete Structure Solution, Refinement and Analysis Program. *J. Appl. Crystallogr.* **2009**, *42* (2), 339–341. <https://doi.org/10.1107/S0021889808042726>.

Chapter 5. A Cooperative Adsorbent for Biogas Upgrading

5.1. Introduction

To accelerate the transition to a clean-energy future, renewable energy sources are urgently needed to displace CO₂-emitting fossil fuels. Biogas, produced through anaerobic digestion of plant or animal waste, can be upgraded to a renewable natural gas equivalent (“biomethane”) by purifying the crude fuel to meet pipeline specifications.^{1–4} In addition to complementing intermittent renewable energy sources, such as solar and wind power, biomethane can support a number of related clean-energy initiatives. Importantly, biogas production can divert organic waste from landfills, where it would otherwise generate emissions of methane, a greenhouse gas with over 20 times the warming potential of CO₂.⁵ In addition, if biofuel production is coupled with capture and sequestration of CO₂ in a pre- or post-combustion process, “negative emissions” are possible through net CO₂ removal from the atmosphere, a process termed BECCS (bioenergy with carbon capture and storage).^{6,7} However, market penetration of biomethane has been hindered by stringent purification standards for pipeline injection. In particular, the selective removal of carbon dioxide (CO₂) from crude biogas streams remains a primary barrier to large-scale implementation of upgrading technologies due to the large energy costs associated with this separation. Crude biogas contains CO₂ contamination on the order of 25–50 vol %, and upgrading technologies must reduce this contamination to low levels (<2–3%) in order to meet pipeline specifications, avoid corrosion, and increase the heating value of the resulting fuel.⁴ While a number of technologies have been explored for CO₂ removal, including membranes, water or physical solvent scrubbing, and aqueous amine solutions, these technologies can suffer from issues with reliability, high capital or operating costs, or large methane losses.^{8–11,4} As an alternative, pressure- or vacuum-swing adsorption can provide a simple and scalable route to biomethane production through the selective interaction of CO₂ with a porous material.^{12–17} However, new adsorbent materials are needed to improve the energy efficiency and methane recovery of these systems.

Our group recently reported a new class of diamine-appended metal–organic frameworks of the form Mg₂(dobpdc)(diamine)₂ (dobpdc⁴⁻ = 4,4'-dioxidobiphenyl-3,3'-dicarboxylate) as highly promising materials for reversible, energy-efficient CO₂ capture.^{18–20} The efficiency of these materials arises from an unprecedented “switch-like” cooperative adsorption mechanism. At a temperature-dependent threshold pressure, CO₂ reversibly polymerizes along the pore surface to form chains of ammonium carbamate.²⁰ This reaction can be reversed with small changes in temperature or pressure, enabling access to the full adsorption capacity of the material as working capacity.²⁰ Due to the chemical specificity of this mechanism and the reduced energy requirements for adsorption–desorption cycling, Mg₂(dobpdc)(diamine)₂ frameworks offer the potential for improved efficiency over commercial biogas upgrading technologies. Furthermore, the commercial viability of these materials is supported by the use of an earth-abundant base metal and inexpensive organic constituents. Indeed, these frameworks have already been prepared at the multi-kilogram scale.²¹

To maximize the utility of Mg₂(dobpdc)(diamine)₂ adsorbents for biogas upgrading, the cooperative adsorption threshold must be matched to the target CH₄ product purity and process conditions. In this study, we focus on production of biomethane (≤2% CO₂) from crude biogas containing approximately 36% CO₂, representative of a typical digester output from a wastewater source. We discuss the optimization of the adsorbent design for this separation at the milligram scale, followed by gram-scale demonstration of the material in breakthrough

experiments simulating a fixed-bed adsorption process. Through a collaboration with Mosaic Materials, a start-up company working to commercialize metal–organic frameworks for CO₂ separations, we then characterize heat and mass transfer in breakthrough experiments at the 30–50 g scale with composite pellets of adsorbent. Finally, we provide early results from slipstream tests following exposure of the candidate diamine-appended adsorbent to a slipstream of real biogas containing H₂S, siloxanes, and heavier hydrocarbons. We conclude with a discussion of next steps toward commercialization of this promising new class of adsorbents for biogas upgrading.

5.2. Experimental Procedures

The compound 4,4'-dihydroxy-(1,1'-biphenyl)-3,3'-dicarboxylic acid (H₄dobpdc) was obtained from Trylead Chemical Company. All other reagents and solvents were obtained from commercial suppliers at reagent grade purity or higher and were used without further purification. Ultrahigh purity (>99.998%) gases were used for all adsorption experiments. The adsorbents Mg₂(dobpdc) and dmpn–Mg₂(dobpdc) were prepared and characterized as previously reported.²² For small-scale breakthrough measurements, dmpn–Mg₂(dobpdc) was prepared at the gram scale by air-free transfer of a 20% (v/v) solution of CaH₂-dried dmpn in toluene to a sample of activated Mg₂(dobpdc), as described previously.¹⁸ While complete diamine functionalization at the milligram-scale was previously performed by direct grafting of a large excess (~50 equiv) of as-received dmpn to methanol-solvated Mg₂(dobpdc),²² the use of dry diamine and activated Mg₂(dobpdc) enables the use of approximately stoichiometric dmpn.

Elemental analyses were conducted at the Microanalytical Laboratory of the University of California, Berkeley, using a PerkinElmer 2400 Series II combustion analyzer. ¹H NMR spectra were collected on a Bruker AMX 300 MHz NMR spectrometer. Diamine loading was characterized by collecting NMR spectra of materials digested with ~20 μL of DCI (35 wt % in D₂O) in 0.75 mL of DMSO-*d*₆. Powder X-ray diffraction (PXRD) patterns were collected with a laboratory Bruker AXS D8 Advance diffractometer with CuKα radiation (λ = 1.5418 Å). Low-pressure adsorption isotherms were collected using Micromeritics ASAP 2420, 2020, or 3Flex instruments following previously reported procedures.¹⁸ High-pressure CO₂ and CH₄ isotherms were obtained using a HPVA-II-10 from Particulate Systems, a subsidiary of Micromeritics, using the freespace collection, data collection, and background correction methods reported previously.²³ A pore volume of 0.422 cm³/g was calculated for dmpn–Mg₂(dobpdc) from the previously reported 77 K N₂ adsorption isotherm²² using the Gurvich rule²⁴ and the quantity adsorbed at $P/P_0 = 0.9$. Differential enthalpies and entropies of CO₂ adsorption were calculated using spline interpolation methods and the Clausius–Clapeyron relationship, as described in the Supporting Information (Section 5.6.1). Thermogravimetric analysis was performed using a Q5000 TGA from TA instruments using gas flow rates of 25 mL/min. All thermogravimetric experiments were performed at atmospheric pressure, and masses were not corrected for buoyancy effects. Binderless pellets of dmpn–Mg₂(dobpdc) (~350–700 μm) were prepared by sieving compressed powder between 25 and 45 mesh grids. Proprietary composite pellets of dmpn–Mg₂(dobpdc) were obtained from Mosaic Materials. Experimental details for breakthrough experiments are included in the Supporting Information (Section 5.6.2). Slipstream tests were performed at the Davis Wastewater Treatment Plant in Davis, CA.

5.3. Results and Discussion

To meet pipeline specifications for biomethane, an upgrading technology must reduce the CO₂ concentration of crude biogas to $\leq 2\%$. For a cooperative adsorbent, this criterion dictates that a candidate material must capture CO₂ at partial pressures $\leq 2\%$ of the total feed pressure. The competitive advantage of adsorbents will likely be best realized with low-pressure streams to avoid compression costs; thus, we focus on either direct purification of a near-ambient pressure feed, or single-stage compression to a total pressure of ≤ 6 bar. Compared to Langmuir adsorbents, which may require deep vacuum to achieve moderate CO₂ cycling capacities, cooperative adsorbents offer the potential for larger swing capacities with smaller pressure or temperature swings (Figure 5.1a).

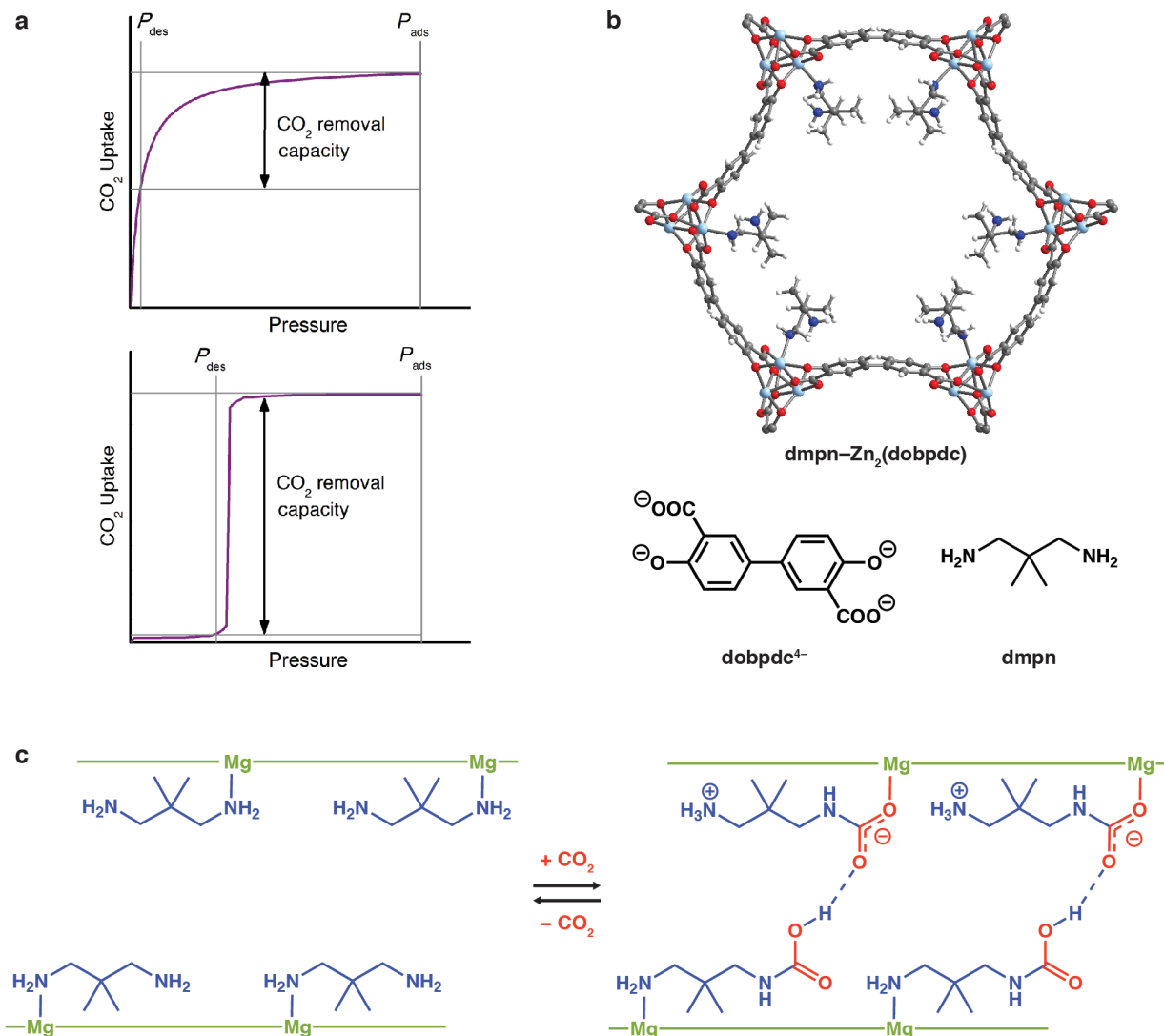


Figure 5.1. (a) Schematic showing a PSA process for a hypothetical adsorbent with a Langmuir isotherm (top) and a step-shaped isotherm (bottom). Larger CO₂ cycling capacities can be achieved with smaller pressure swings in the case of a step-shaped isotherm. To achieve $< 2\%$ CO₂ at the bed exit, a step-shaped adsorbent must bind CO₂ at $\leq 2\%$ of the total pressure. (b) Single-crystal structure of the dmpn-functionalized zinc congener of M₂(dobpdc).²² Light blue, blue, red, gray, and white spheres represent Zn, N, O, C, and H atoms, respectively. (c) Depiction of cooperative CO₂ adsorption within adjacent chains of Mg^{II}-diamine sites to form a mixed chemisorption product containing both ammonium carbamate and carbamic acid, as proposed in a recent study combining NMR spectroscopy and van der Waals-corrected density functional theory.²⁵

In a survey of the large library of diamine-appended adsorbents discovered to date, the material $\text{dmpn-Mg}_2(\text{dobpdc})$ ($\text{dmpn} = 2,2\text{-dimethyl-1,3-diaminopropane}$) was identified as the top candidate material for this separation (Figure 5.1b). The three-carbon backbone of dmpn enables hydrogen bonding between adjacent free and metal-bound amines down the pore axis of the material, resulting in enhanced stability and resistance to diamine volatilization. This material also possesses favorable CO_2 adsorption step pressures of $\sim 5\text{--}25$ mbar at the representative feed temperatures of $25\text{--}40$ °C (Figure 5.S1). Such low CO_2 adsorption pressures should enable production of pipeline-quality biomethane ($<2\%$ CO_2) at total feed pressures of ≤ 1.25 bar. Intriguingly, $\text{dmpn-Mg}_2(\text{dobpdc})$ was previously found to bind CO_2 through a mixed mechanism involving both ammonium carbamate chains and carbamic acids (Figure 5.1c), resulting in greater curvature in the step region of the adsorption profile.²⁵ The potential advantage of this unique mechanism is discussed in greater detail in subsequent sections.

We first collected high-pressure CO_2 and CH_4 adsorption isotherms for $\text{dmpn-Mg}_2(\text{dobpdc})$ to evaluate the single-component adsorption behavior of this material at equilibrium (Figure 5.2). Interestingly, a second step was observed in the CO_2 isotherms at pressures above 10 bar. While the isotherm region bearing this second step is unlikely to have direct relevance for a low-pressure PSA process at near-ambient temperature, the second adsorption step suggests that the CO_2 -adsorbed phase of $\text{dmpn-Mg}_2(\text{dobpdc})$ may sample previously unobserved configurations at higher pressures. Further spectroscopic investigation is needed to elucidate the specific binding modes in this high-pressure regime. For the CH_4 isotherms, simple Langmuir adsorption was observed, with an approximate adsorption enthalpy of -10 kJ/mol (Figure 5.S4). Importantly, $\text{dmpn-Mg}_2(\text{dobpdc})$ adsorbs <0.5 mmol/g of CH_4 over the tested temperature region of $25\text{--}75$ °C in the target partial pressure range (0.6–3.8 bar, assuming a 1–6 bar stream containing 64% CH_4). Such low adsorption of CH_4 is favorable to maximize CH_4 recovery in a PSA process. We further note that because CH_4 cannot compete with CO_2 for chemisorptive binding sites, the CH_4 adsorption capacity of $\text{dmpn-Mg}_2(\text{dobpdc})$ may be even lower under mixed-gas conditions.

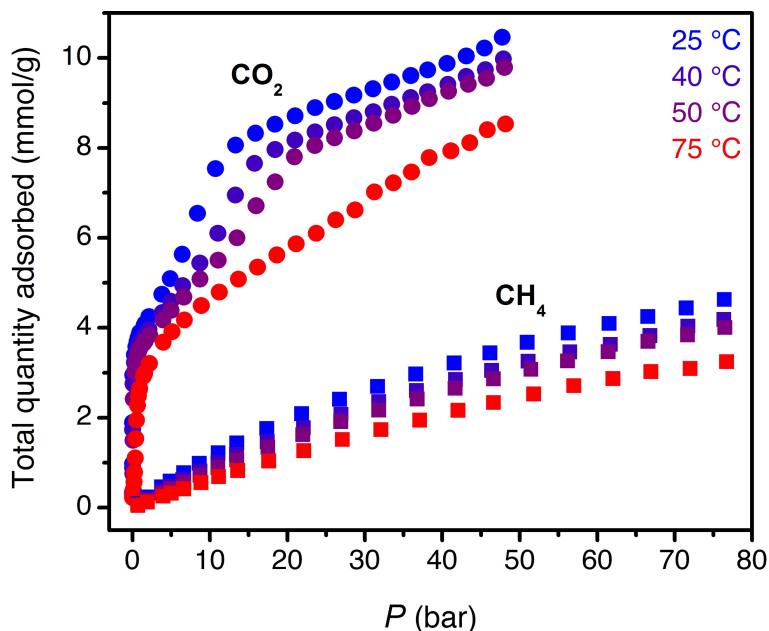


Figure 5.2. High-pressure CO_2 (circles) and CH_4 (squares) adsorption isotherms for $\text{dmpn-Mg}_2(\text{dobpdc})$.

To evaluate the stability of $\text{dmpn-Mg}_2(\text{dobpdc})$, cycling experiments were conducted using a thermogravimetric analyzer (TGA). Because the TGA cannot be pressurized or evacuated, the exact cycling conditions could not be replicated in these experiments. Additionally, safety concerns prevented the use of flammable CH_4 in the TGA furnace, and thus CO_2/N_2 mixtures were used to approximate CO_2/CH_4 mixtures. Nonetheless, TGA cycling experiments can be used to characterize the behavior of $\text{dmpn-Mg}_2(\text{dobpdc})$ under the minimum CO_2 concentration that the framework must adsorb in order to reach the pipeline specification of $\leq 2\%$ CO_2 in the effluent. Here, a mixture of 10% CO_2 in N_2 at atmospheric pressure (0.10 bar CO_2) was used to approximate a desired target minimum partial pressure of CO_2 for a stream at 5 bar. The temperature-swing cycling results of adsorption at 40°C under 10% CO_2 in N_2 with desorption under 100% CO_2 at 100°C are shown in Figure 5.3. A stable CO_2 swing capacity of $\sim 9.2\text{ g}/100\text{ g}$ was observed. Importantly, the baseline in these experiments remained stable and in fact increased slightly for the last few cycles, suggesting that lack of full reactivation between cycles, rather than diamine loss, is responsible for the relative capacity loss of 4.1% over 26 cycles (0.16% per cycle). It is likely that improved cycling performance could be achieved by a slight increase in the desorption temperature. Longer adsorption periods or higher partial pressures of CO_2 may also lead to improved working capacity, as the sharp spike in uptake upon switching to 100% CO_2 indicates that the material has not yet saturated with CO_2 at the onset of desorption.

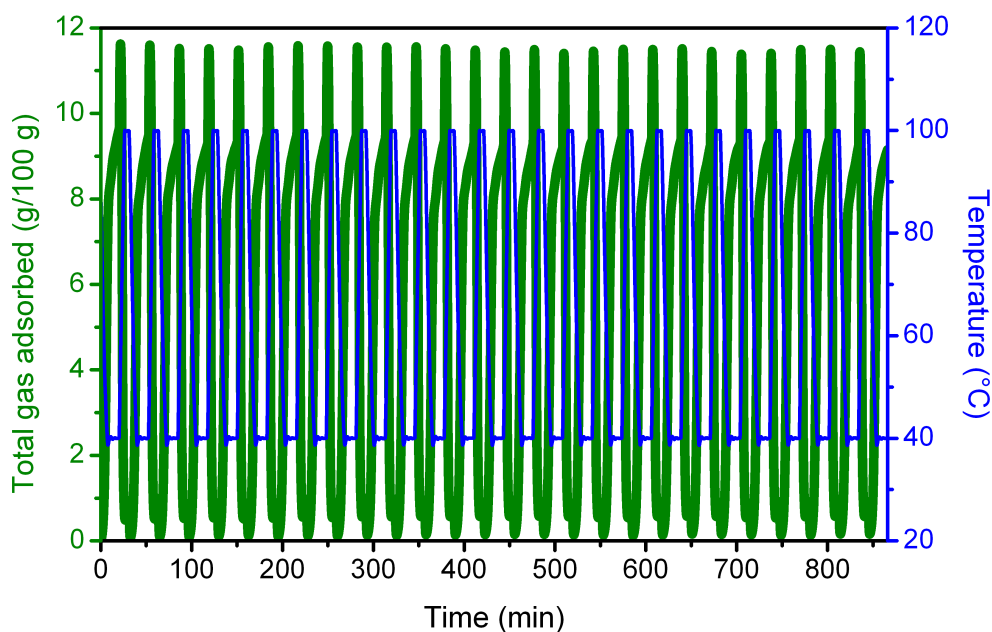


Figure 5.3. Temperature-swing cycling of $\text{dmpn-Mg}_2(\text{dobpdc})$ at atmospheric pressure with adsorption under 10% CO_2 in N_2 at 40°C and desorption under pure CO_2 at 100°C .

The single-component results prompted further evaluation of $\text{dmpn-Mg}_2(\text{dobpdc})$ in multicomponent breakthrough experiments. Initial small-scale experiments were performed with a 6" column of 1/4" stainless-steel pipe containing 0.69 g of $\text{dmpn-Mg}_2(\text{dobpdc})$ as 25–45 mesh (350–700 μm) binderless pellets. The material was equilibrated under flowing He prior to data collection. A higher CO_2 concentration of 50% was used in these early experiments. With a flow rate of 3.1 sccm at 40°C and ~ 1 bar, sharp, rapid breakthrough of CH_4 was observed, followed

by single-shock breakthrough of CO₂ corresponding to a capacity of 3.2 ± 0.1 mmol/g (Figure 5.4). Consistent with the strong anticipated binding of CO₂, “roll-up” of CH₄ (normalized outlet flow rate, $F/F_0 > 1$) was observed upon displacement of weakly-bound CH₄ from the bed by strongly-adsorbed CO₂. Similar results were obtained at a total pressure of 4 bar (Figure 5.S7). The observation of a single-shock CO₂ breakthrough profile is notable and is consistent with previously reported breakthrough curves for dmpn–Mg₂(dobpdc) with dry and humid simulated coal flue gas (15% CO₂ in N₂).²² For other adsorbents with step-shaped isotherms, early “slip” of CO₂ at concentrations beneath the step is commonly observed, because such adsorbents typically become inoperative for further CO₂ capture once the CO₂ partial pressure in the bed drops below the step pressure.^{26–29} As has been demonstrated previously, Golden’s rule, also known as the “rubber band” or “string” rule, can be used to predict the breakthrough profile from an isotherm of arbitrary shape.^{29–32} Applying this rule suggests that the high feed concentration and high curvature of the adsorption isotherm prevent the intersection of the operating curve with the adsorption isotherm, resulting in the observed single-shock breakthrough profile (Figure 5.S8). From a process standpoint, this single-shock breakthrough profile is favorable for deeper removal of CO₂ or for deployment of the adsorbent in upgrading of landfill biogas, which may contain slightly lower CO₂ concentrations.

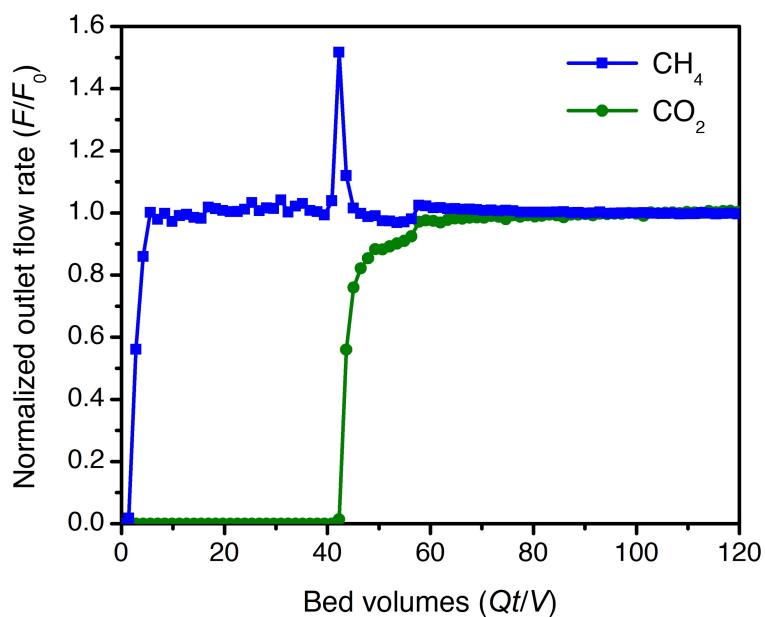


Figure 5.4. Small-scale breakthrough experiment with binderless pellets of dmpn–Mg₂(dobpdc) under 3 sccm of dry 50% CO₂ in CH₄ at ~1 bar and 40 °C. A CO₂ capacity of 3.2 ± 0.1 mmol/g was calculated at full breakthrough.

Large-scale breakthrough experiments were subsequently performed using cylindrical composite pellets of dmpn–Mg₂(dobpdc) (6 mm diameter; ~1 mm height) supplied by Mosaic Materials (Figure 5.5). For these experiments, a 7.5" section of stainless-steel pipe (1" outer diameter, 0.065" wall thickness) was packed with 34 g of composite pellets secured with glass wool on each end. A multipoint thermocouple profile probe (Omega, PP6-36-K-U-18) was inserted through the center of the column, enabling simultaneous measurement of heat and mass transport through the bed. The column was insulated with 0.5" thick Buna-N/PVC insulation to approximate adiabatic operation. Under a flow of 75 sccm of 36.5% CO₂ in CH₄ at 22 °C,

similar CH₄ and CO₂ breakthrough profiles were observed as for the gram-scale breakthrough experiment. The calculated CO₂ breakthrough capacity of 2.5 ± 0.1 mmol/g was equivalent to the theoretical capacity anticipated for the composite pellets. The temperature profile across the bed reflected the strongly exothermic CO₂ adsorption process, with temperatures peaking at ~ 52 °C ($\Delta T = 30$ °C) near the column exit. Management of this heat release will be a critical consideration in process design for diamine-appended frameworks. Heat management will be particularly important for dmpn–Mg₂(dobpdc), which shows greater temperature dependence in its step saturation capacity compared to related diamine-appended frameworks due to its mixed

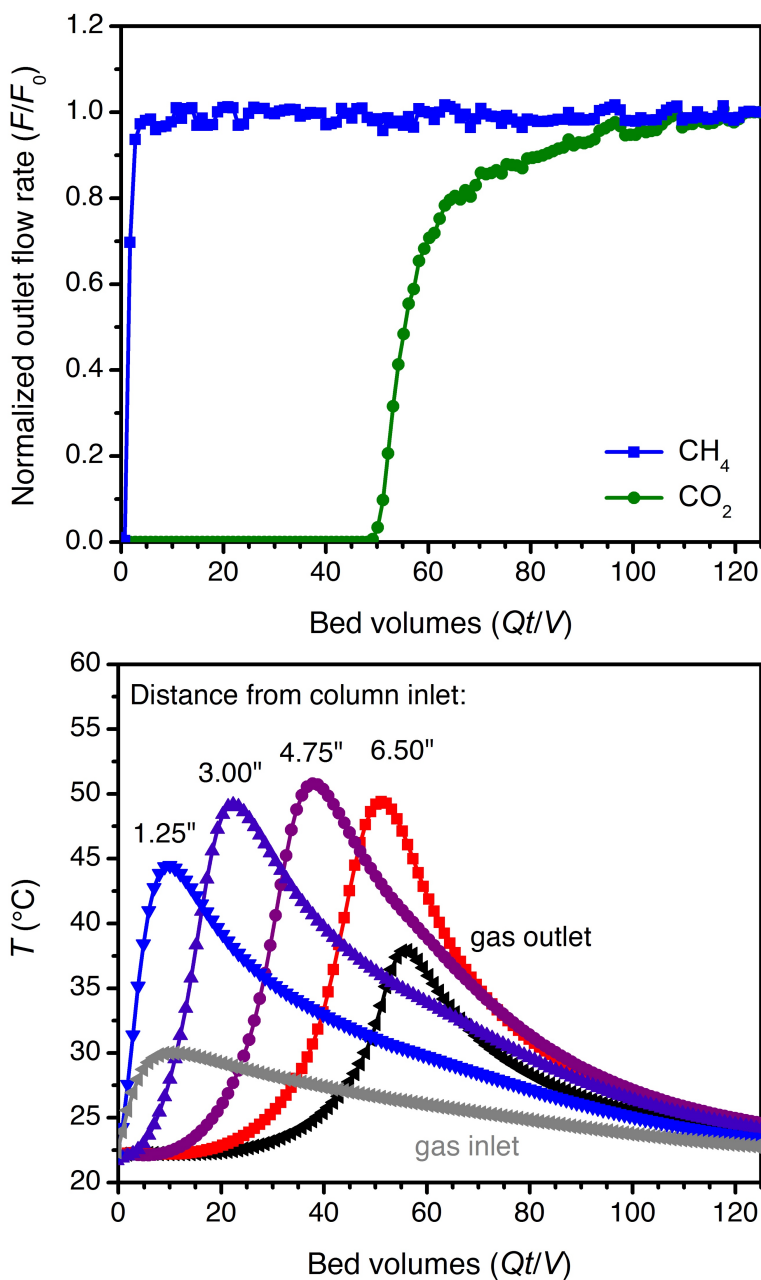


Figure 5.5. Large-scale breakthrough experiment (top) and corresponding temperature profile (bottom) with composite pellets of dmpn–Mg₂(dobpdc) under 75 sccm of dry 36.5% CO₂ in CH₄ at ~ 1 bar and 22 °C. The total length of packed adsorbent was 7.5".

adsorption mechanism. Therefore, innovative process, reactor, or structured contactor designs will play a key role in further development of these materials toward commercialization.

The promising CO₂ capture performance of dmpn–Mg₂(dobpdc) in large-scale breakthrough experiments prompted our continued evaluation of this material in a slipstream of crude biogas. Composite pellets of dmpn–Mg₂(dobpdc) produced by Mosaic Materials were encased in wire mesh sachets and exposed to a 200 mL/min slipstream at ~1 bar at the Davis Wastewater Treatment Plant in Davis, CA. The stream was saturated in water and contained 35.8 vol % CO₂, as well as 0.90% N₂, 0.22% O₂, 1800 ppmv H₂S, 2 ppmv non-CH₄ hydrocarbons, and 130 ppbv equiv. Si. (Note that Si present in the stream arises from siloxanes, which originate from consumer products such as shampoos.⁸) In the ultimate upgrading process, H₂O and H₂S would need to be removed prior to pipeline injection, and these steps would likely be performed in pretreatment stages prior to CO₂ removal. Therefore, an adsorbent for CO₂ removal is unlikely to contact the crude biogas feed, and thus the slipstream tests performed here simulate conditions only anticipated during a process failure.

Pure CO₂ adsorption isobars collected for dmpn–Mg₂(dobpdc) pellets before and after exposure to the crude biogas stream showed a gradual broadening of the cooperative adsorption step with increasing exposure time (Figure 5.6). (Note that an exposure time of 5 h corresponds to 2 H₂S molecules per diamine.) Characterization of the diamine loading after each exposure period revealed a plateau in diamine content at ~85%, indicating that the diamine–framework interactions are relatively robust to the water and H₂S contaminants in the crude feed. Elemental analysis of the samples exposed for 3 and 4 weeks revealed sulfur content of 0.29% and 0.26% (detection limit: 0.2%), respectively, after vacuum activation for 1 h at 120 °C. The nature of any bound sulfur species remains an area of ongoing investigation, and we are further investigating the potential to re-functionalize the material with diamine to replace any potentially deactivated, sulfur-bound sites.

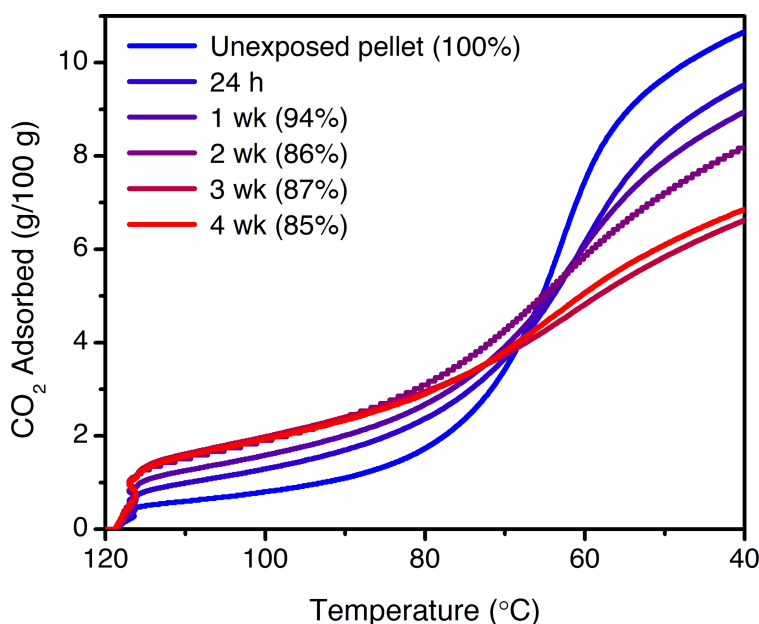


Figure 5.6. Pure CO₂ adsorption isobars at atmospheric pressure for composite pellets of dmpn–Mg₂(dobpdc) after varying exposure times to a crude biogas stream. Numbers in parentheses indicate the diamine loadings, as determined from the peak integrals of the NMR spectra of digested samples.

5.4. Conclusions

Modular, efficient biogas upgrading technologies, such as low-pressure PSA, have the potential to increase the contribution of renewable fuels to the energy sector while diverting harmful methane emissions. Here, we have shown the potential of $\text{dmpn-Mg}_2(\text{dobpdc})$ as a promising new cooperative adsorbent for CO_2 removal from crude biogas to produce pipeline-quality biomethane. Furthermore, we have shown the progression of the material from gram-scale demonstration to early bench-scale development with simultaneous monitoring of heat and mass transfer in realistic pellets of adsorbent. Finally, we have shown the ability of the adsorbent to withstand short-term exposure to crude biogas feeds, representative of a process failure.

In ongoing work, the single-component adsorption data and breakthrough results reported herein are being used to develop a process model, which will inform optimization of the cycle conditions. Additionally, further investigation of the impurity tolerance of $\text{dmpn-Mg}_2(\text{dobpdc})$ will inform placement of any pre-treatment units, such as removal of H_2O , H_2S , or siloxanes. Finally, rapid temperature rise in the bed upon exothermic CO_2 adsorption will require careful design of the ultimate composites, reactor, and/or process to mitigate any deleterious heat effects on the capture performance. Successful developments toward these engineering challenges will enable access to the full potential of cooperative adsorbents for efficient CO_2 capture.

5.5. Acknowledgements

This work was funded by the California Energy Commission under award number PIR-14-021, in collaboration with Mosaic Materials. Initial discovery of $\text{dmpn-Mg}_2(\text{dobpdc})$ was sponsored by ExxonMobil Research and Engineering Company. Dr. Thomas McDonald, Dr. Zoey Herm, Dr. Graham Wenz, Dr. Carly Anderson, and Justin Lim (all of Mosaic Materials), as well as Dr. John Wind and Dr. Paul Bryan (Partners in Sustainability Integration, PSI), are acknowledged for contributions to this work. We further thank Dr. Paul Bryan (PSI) and Eric Granlund (UC Berkeley) for assistance with the design and fabrication of the large-scale breakthrough apparatus.

5.6. Supporting Information

5.6.1. Additional Adsorption Data, Fits, and Thermodynamic Calculations

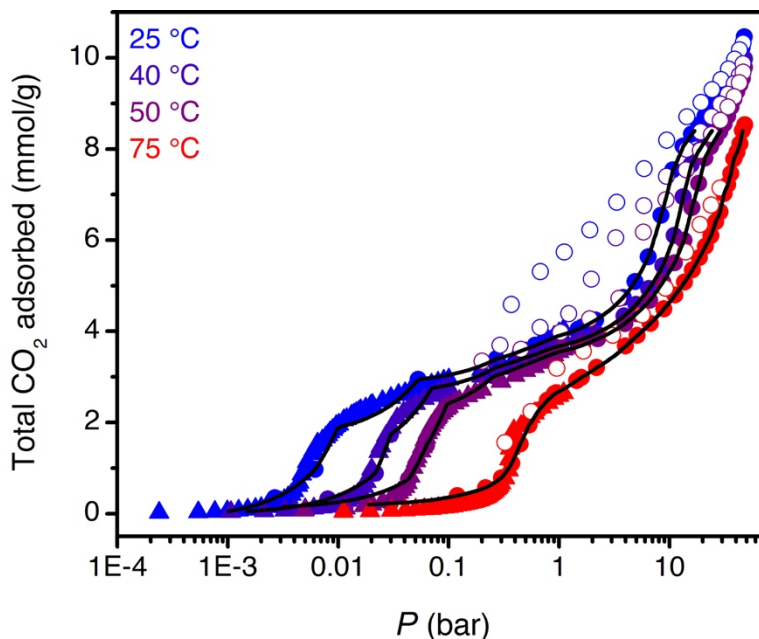


Figure 5.S1. Logarithmic plot of the CO₂ adsorption isotherms of dmpn–Mg₂(dobpdc). Circles indicate high-pressure adsorption (solid) and desorption (open) isotherms collected as part of this work. Traingles indicate previously reported²² low-pressure CO₂ adsorption isotherms. Black lines indicate the first-order spline interpolation used to calculate the differential enthalpy and entropy of adsorption.

To calculate the differential enthalpy (Δh_{ads}) and entropy (Δs_{ads}) of adsorption, the exact pressures (p_q) corresponding to specific adsorbate loadings (q) were determined at different temperatures (T). For step-shaped CO₂ adsorption isotherms, a linear spline interpolation method was used to obtain p_q values. The Clausius–Clapeyron relationship given in eq 5.S1 was then applied to calculate the differential enthalpies of adsorption from the slopes of the linear trendlines fit to $\ln(p_q)$ vs. $1/T$. The differential entropies of adsorption were determined from the y -intercepts of these linear trendlines, which are equal to $-\Delta s_{\text{ads}}/R$ at each loading (assuming $p_0 = 1$ bar).

$$\ln(p_q) = \left(\frac{\Delta h_{\text{ads}}}{R}\right)\left(\frac{1}{T}\right) + c \quad (5.S1)$$

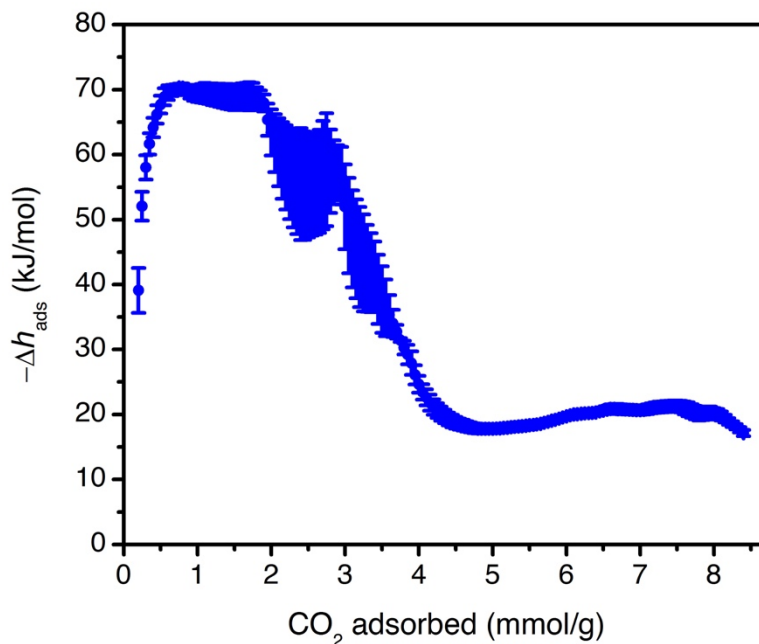


Figure 5.S2. Loading-dependent differential enthalpy of CO₂ adsorption for dmpn–Mg₂(dobpdc), calculated from spline interpolation of the high-pressure CO₂ adsorption isotherms at 25, 40, 50, and 75 °C.

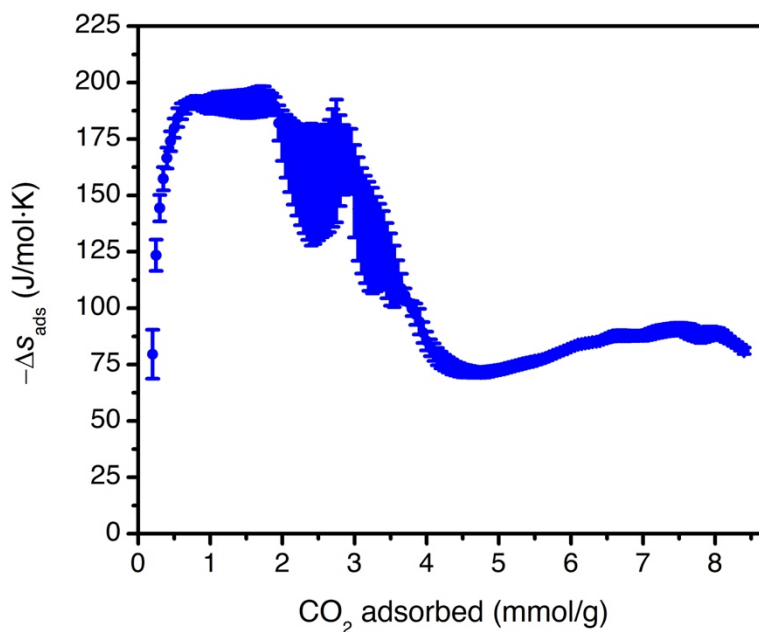


Figure 5.S3. Loading-dependent differential entropy of CO₂ adsorption for dmpn–Mg₂(dobpdc), calculated from spline interpolation of the CO₂ adsorption isotherms at 25, 40, 50, and 75 °C.

Type I CH₄ isotherms were fit using a single-site Langmuir model (eq 5.S2), where q is the total amount adsorbed in mmol/g, P is the pressure in bar, q_{sat} is the saturation capacity in mmol/g, and b is the Langmuir parameter, expressed using eq 5.S3, where S is the site-specific molar entropy of adsorption in J/mol·K, E is the site-specific binding energy in kJ/mol, R is the gas constant in J/mol·K, and T is the temperature in K.

$$q = \frac{q_{\text{sat}}bP}{1+q_{\text{sat}}bP} \quad (5.S2)$$

$$b = e^{-\frac{S}{R}} e^{E \cdot \frac{1000}{RT}} \quad (5.S3)$$

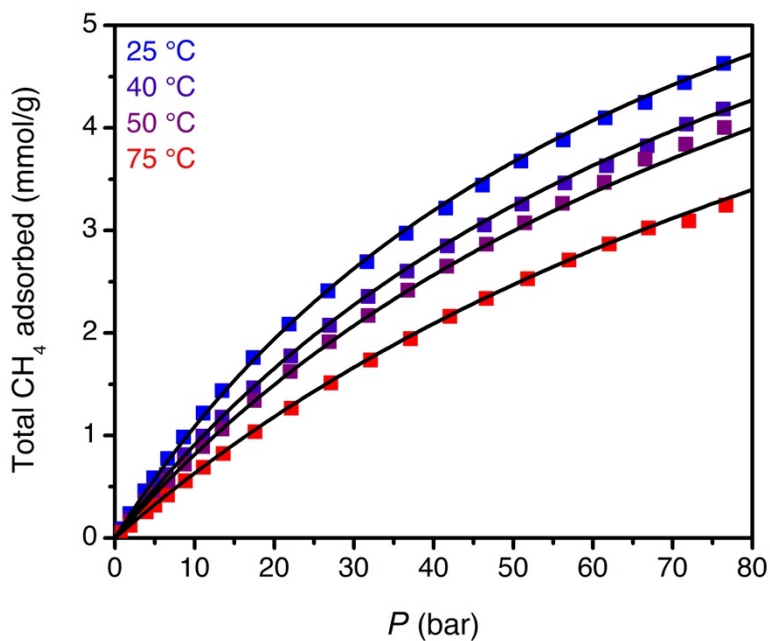


Figure 5.S4. High-pressure CO₂ adsorption isotherms (squares) and corresponding fits (black lines) using a simultaneous, single-site Langmuir model: $q_{\text{sat}} = 9.04$ mmol/g, $S = -8.45$ R, $E = -10.3$ kJ/mol.

5.6.2. Additional Breakthrough Details and Results

An SRI Instruments 8610V GC with a 6' Haysep-D column and a thermal conductivity detector (TCD) was used to monitor the breakthrough profile at 1 min intervals. The TCD was calibrated using a series of pre-mixed, Certified Standard tanks of varying percent CO₂ (10, 50, and 90%) in CH₄ as well as pure, research-grade CO₂ and CH₄. Flow rates were monitored every 0.5 s at the GC outlet using an Agilent ADM Universal Flow Meter. A Swagelok KPB series back-pressure regulator was placed between the column outlet and GC inlet to control the column pressure. An Ashcroft DG25 digital pressure gauge was placed at the column inlet to determine the pressure drop across the column. Activation between breakthrough experiments was performed under He at the experimental flow rate for 1 h at 100 °C. The system deadspace was estimated by measuring the initial breakthrough time of Ar (a non-adsorbing probe gas) on a column pre-equilibrated under He with equivalent experimental conditions. For small-scale breakthrough experiments, the temperature was controlled using a hot plate and well-stirred 4 L water bath with continuous temperature monitoring. Large-scale breakthrough experiments were performed starting at room temperature (~22 °C) under quasi-adiabatic conditions by insulating the column with 0.5" thick Buna-N/PVC insulation (McMaster-Carr part number 44745K25).

Prior to each experiment, the column was equilibrated under He at the experimental temperature and pressure. To begin each experiment, He flow to the column was stopped as a flow of simulated biogas was simultaneously switched to the column inlet. Following complete breakthrough of CO₂, the capacity of each gas (q_i , mmol/g) was determined using the following formula:

$$q_i = \left[\frac{Q}{22.414 \frac{ccSTP}{mmol}} \left(\int_0^t \left(1 - \frac{F_i}{F_{0,i}} \right) dt - t_{0,Ar} \right) - \varepsilon V \left(\frac{y_i P}{RT} \right) \right] \left(\frac{y_i}{m} \right) \quad (5.S4)$$

Here, Q is the average total flow rate in sccm, t is the corrected time in min, F_i is the molar flow rate of species i at time t , $F_{0,i}$ is the inlet molar flow rate of species i , ε is the interparticle void fraction, V is the volume of pelletized adsorbent in cm³, $t_{0,Ar}$ is the initial breakthrough time of Ar under equivalent experimental conditions, y_i is the mole fraction of species i , P is the total pressure, R is the universal gas constant, T is the column temperature during the experiment, and m is the mass of adsorbent.

The interparticle void fraction ε is calculated as

$$\varepsilon = 1 - \frac{\rho_{bulk}}{\rho_{particle}} \quad (5.S5)$$

where ρ_{bulk} is the bulk density, calculated as $m/V = 315 \text{ kg/m}^3$ (binderless pellets) or 417 kg/m^3 (composite pellets), and $\rho_{particle}$ is the particle density, estimated as 1000 kg/m^3 (binderless pellets) or 723 kg/m^3 (composite pellets).

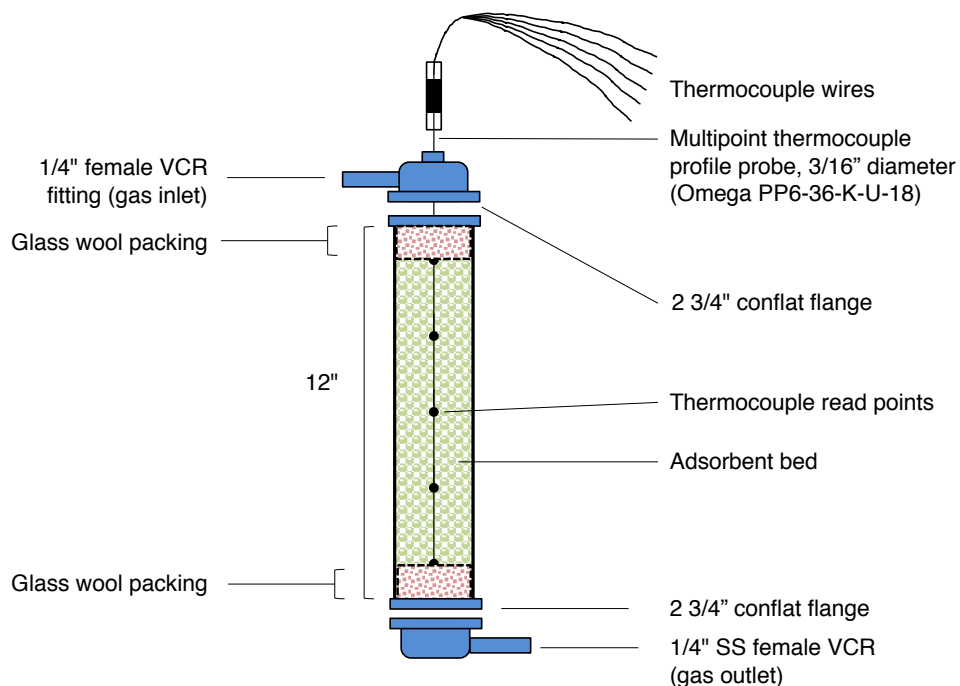


Figure 5.S5. Schematic of large-scale breakthrough column used in this work. The column was constructed from 1" outer diameter stainless-steel pipe with a wall thickness of 0.065". The multipoint thermocouple profile probe was obtained from Omega (PP6-36-K-U-18).



Figure 5.S6. Photograph of large-scale (1" OD pipe, 12" long) and small-scale (1/4" OD pipe, 6" long) breakthrough columns used in this work.

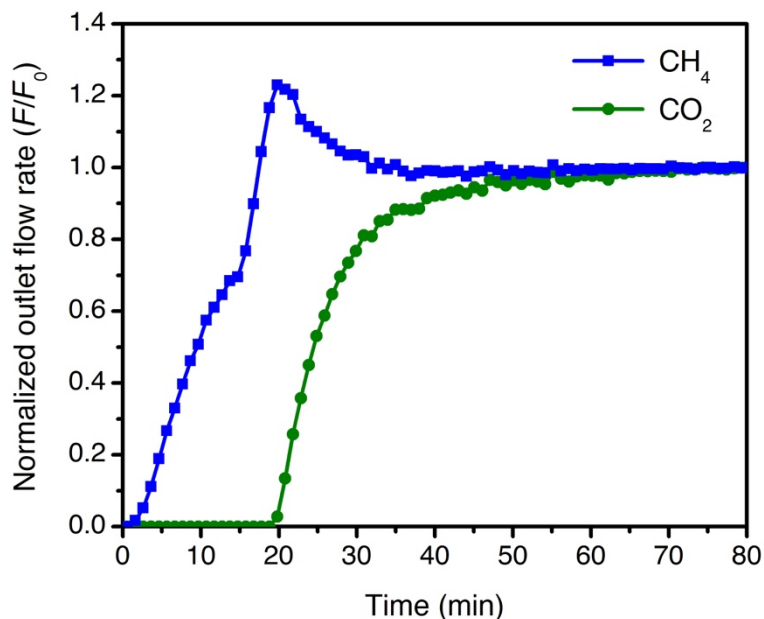


Figure 5.S7. Small-scale breakthrough experiment with binderless pellets of $\text{dmpn-Mg}_2(\text{dobpdc})$ under 5 sccm of dry 50% CO_2 in CH_4 at 4 bar and 40 °C. A CO_2 capacity of 4.0 ± 0.2 mmol/g was calculated at full breakthrough. Broadening in the CH_4 breakthrough curve is likely due to back-mixing in the experimental setup at elevated pressure.

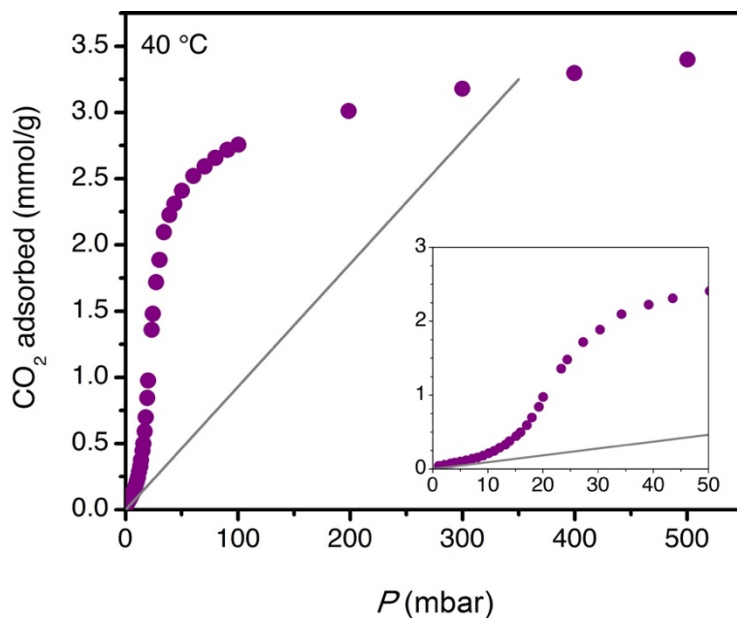


Figure 5.S8. Application of Golden's rule to predict the shape of the breakthrough profile from the CO_2 adsorption isotherm of $\text{dmpn-Mg}_2(\text{dobpdc})$. Here, the initial condition is taken as 0 mbar CO_2 at 40 °C, while the feed condition is taken as 350 mbar of CO_2 (35% CO_2 in CH_4 at 1 bar) at 40 °C. The inset shows an enlargement of the low-pressure region. Because the chord between the initial condition and the feed does not intersect the adsorption isotherm, a single-shock breakthrough profile is predicted, consistent with experimental observation.

5.6.3. Additional Characterization Following Exposure Tests

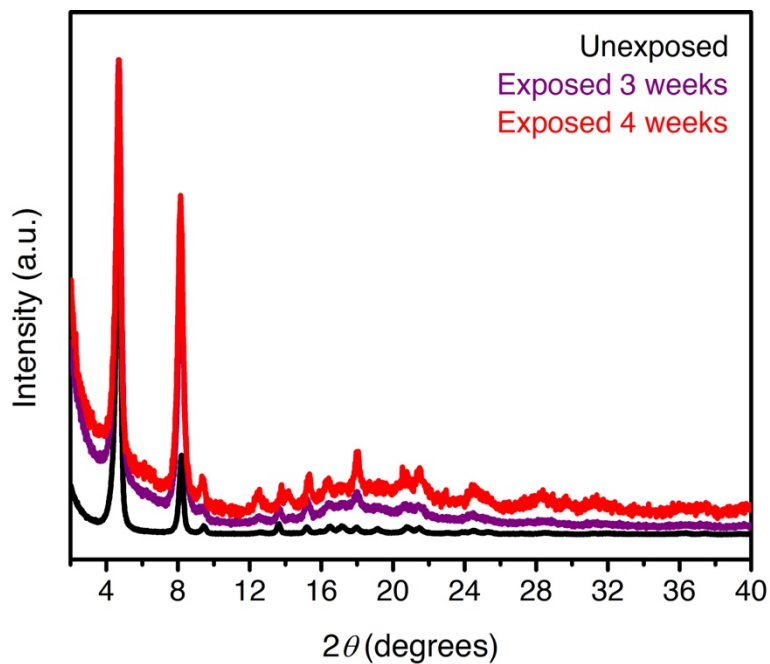


Figure 5.S9. Powder X-ray diffraction patterns for a pristine composite pellet of dmpn–Mg₂(dobpdc) (black) and for pellets after 3 weeks (purple) and 4 weeks (red) of exposure to a slipstream of crude biogas. Patterns were normalized to the intensity of the lowest-angle peak.

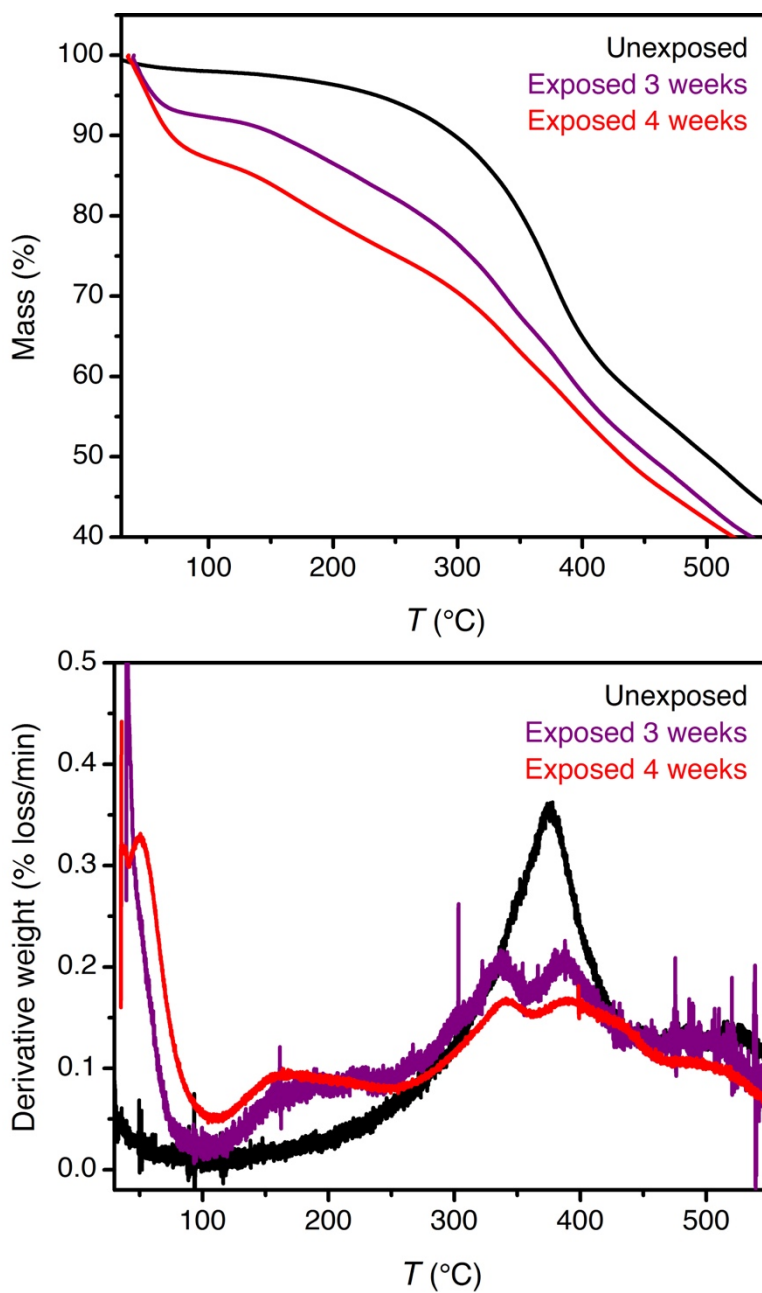


Figure 5.S10. Thermogravimetric decomposition curves (top) and corresponding derivative plots (bottom) for a pristine composite pellet of dmpn-Mg₂(dobpdc) (black) and for pellets after 3 weeks (purple) and 4 weeks (red) of exposure to a slipstream of crude biogas.

5.7. References

- (1) Vasco-Correa, J.; Khanal, S.; Manandhar, A.; Shah, A. Anaerobic Digestion for Bioenergy Production: Global Status, Environmental and Techno-Economic Implications, and Government Policies. *Bioresour. Technol.* **2018**, *247*, 1015–1026. <https://doi.org/10.1016/j.biortech.2017.09.004>.
- (2) Scarlat, N.; Dallemand, J.-F.; Fahl, F. Biogas: Developments and Perspectives in Europe. *Renew. Energy* **2018**, *129*, 457–472. <https://doi.org/10.1016/j.renene.2018.03.006>.
- (3) Sun, Q.; Li, H.; Yan, J.; Liu, L.; Yu, Z.; Yu, X. Selection of Appropriate Biogas Upgrading Technology-a Review of Biogas Cleaning, Upgrading and Utilisation. *Renew. Sustain. Energy Rev.* **2015**, *51*, 521–532. <https://doi.org/10.1016/j.rser.2015.06.029>.
- (4) Yang, L.; Ge, X.; Wan, C.; Yu, F.; Li, Y. Progress and Perspectives in Converting Biogas to Transportation Fuels. *Renew. Sustain. Energy Rev.* **2014**, *40*, 1133–1152. <https://doi.org/10.1016/j.rser.2014.08.008>.
- (5) Holm-Nielsen, J. B.; Al Seadi, T.; Oleskowicz-Popiel, P. The Future of Anaerobic Digestion and Biogas Utilization. *Bioresour. Technol.* **2009**, *100* (22), 5478–5484. <https://doi.org/10.1016/j.biortech.2008.12.046>.
- (6) Gough, C.; Upham, P. *Biomass Energy with Carbon Capture and Storage (BECCS): A Review*; The Tyndall Centre, University of Manchester, Manchester Institute of Innovation Research, 2010.
- (7) *Biomass Energy and Carbon Capture and Storage (BECCS): Unlocking Negative Emissions*, First edition.; Gough, C., Thornley, P., Mander, S., Vaughan, N., Falano, T., Eds.; John Wiley & Sons: Hoboken, NJ, 2018.
- (8) Petersson, A.; Wellinger, A. *Biogas Upgrading Technologies – Developments and Innovations*; IEA Bioenergy, 2009.
- (9) Ryckebosch, E.; Drouillon, M.; Vervaeren, H. Techniques for Transformation of Biogas to Biomethane. *Biomass Bioenergy* **2011**, *35* (5), 1633–1645. <https://doi.org/10.1016/j.biombioe.2011.02.033>.
- (10) Bauer, F.; Hulteberg, C.; Persson, T.; Tamm, D. *Biogas Upgrading – Review of Commercial Technologies*; 2013:270; Svenskt Gastekniskt Center AB: Malmö, Sweden, 2013.
- (11) Scholz, M.; Melin, T.; Wessling, M. Transforming Biogas into Biomethane Using Membrane Technology. *Renew. Sustain. Energy Rev.* **2013**, *17*, 199–212. <https://doi.org/10.1016/j.rser.2012.08.009>.
- (12) Grande, C. A.; Rodrigues, A. E. Biogas to Fuel by Vacuum Pressure Swing Adsorption I. Behavior of Equilibrium and Kinetic-Based Adsorbents. *Ind. Eng. Chem. Res.* **2007**, *46* (13), 4595–4605. <https://doi.org/10.1021/ie061341+>.
- (13) Alonso-Vicario, A.; Ochoa-Gómez, J. R.; Gil-Río, S.; Gómez-Jiménez-Aberasturi, O.; Ramírez-López, C. A.; Torrecilla-Soria, J.; Domínguez, A. Purification and Upgrading of Biogas by Pressure Swing Adsorption on Synthetic and Natural Zeolites. *Microporous Mesoporous Mater.* **2010**, *134* (1), 100–107. <https://doi.org/10.1016/j.micromeso.2010.05.014>.
- (14) Grande, C. A. Biogas Upgrading by Pressure Swing Adsorption. *Biofuels Eng. Process Technol.* **2011**. <https://doi.org/10.5772/18428>.
- (15) Chaemchuen, S.; Kabir, N. A.; Zhou, K.; Verpoort, F. Metal–Organic Frameworks for Upgrading Biogas via CO₂ Adsorption to Biogas Green Energy. *Chem. Soc. Rev.* **2013**, *42* (24), 9304–9332. <https://doi.org/10.1039/C3CS60244C>.

- (16) Wu, B.; Zhang, X.; Xu, Y.; Bao, D.; Zhang, S. Assessment of the Energy Consumption of the Biogas Upgrading Process with Pressure Swing Adsorption Using Novel Adsorbents. *J. Clean. Prod.* **2015**, *101*, 251–261. <https://doi.org/10.1016/j.jclepro.2015.03.082>.
- (17) Arya, A.; Divekar, S.; Rawat, R.; Gupta, P.; Garg, M. O.; Dasgupta, S.; Nanoti, A.; Singh, R.; Xiao, P.; Webley, P. A. Upgrading Biogas at Low Pressure by Vacuum Swing Adsorption. *Ind. Eng. Chem. Res.* **2015**, *54* (1), 404–413. <https://doi.org/10.1021/ie503243f>.
- (18) Siegelman, R. L.; McDonald, T. M.; Gonzalez, M. I.; Martell, J. D.; Milner, P. J.; Mason, J. A.; Berger, A. H.; Bhowan, A. S.; Long, J. R. Controlling Cooperative CO₂ Adsorption in Diamine-Appended Mg₂(dobpdc) Metal–Organic Frameworks. *J. Am. Chem. Soc.* **2017**, *139* (30), 10526–10538. <https://doi.org/10.1021/jacs.7b05858>.
- (19) McDonald, T. M.; Lee, W. R.; Mason, J. A.; Wiers, B. M.; Hong, C. S.; Long, J. R. Capture of Carbon Dioxide from Air and Flue Gas in the Alkylamine-Appended Metal–Organic Framework mmen-Mg₂(dobpdc). *J. Am. Chem. Soc.* **2012**, *134* (16), 7056–7065. <https://doi.org/10.1021/ja300034j>.
- (20) McDonald, T. M.; Mason, J. A.; Kong, X.; Bloch, E. D.; Gygi, D.; Dani, A.; Crocellà, V.; Giordanino, F.; Odoh, S. O.; Drisdell, W. S.; Vlasisavljevich, B.; Dzubak, A. L.; Poloni, R.; Schnell, S. K.; Planas, N.; Lee, K.; Pascal, T.; Wan, L. F.; Prendergast, D.; Neaton, J. B.; Smit, B.; Kortright, J. B.; Gagliardi, L.; Bordiga, S.; Reimer, J. A.; Long, J. R. Cooperative Insertion of CO₂ in Diamine-Appended Metal-Organic Frameworks. *Nature* **2015**, *519* (7543), 303–308. <https://doi.org/10.1038/nature14327>.
- (21) Mosaic Materials, Inc. <http://mosaicmaterials.com/>.
- (22) Milner, P. J.; Siegelman, R. L.; Forse, A. C.; Gonzalez, M. I.; Runčevski, T.; Martell, J. D.; Reimer, J. A.; Long, J. R. A Diaminopropane-Appended Metal–Organic Framework Enabling Efficient CO₂ Capture from Coal Flue Gas via a Mixed Adsorption Mechanism. *J. Am. Chem. Soc.* **2017**, *139* (38), 13541–13553. <https://doi.org/10.1021/jacs.7b07612>.
- (23) Mason, J. A.; Veenstra, M.; Long, J. R. Evaluating Metal–Organic Frameworks for Natural Gas Storage. *Chem Sci* **2014**, *5* (1), 32–51. <https://doi.org/10.1039/C3SC52633J>.
- (24) Gurvich, L. *J. Phys. Chem. Soc. Russ.* **1915**, *47*, 805.
- (25) Forse, A. C.; Milner, P. J.; Lee, J.-H.; Redfearn, H. N.; Oktawiec, J.; Siegelman, R. L.; Martell, J. D.; Dinakar, B.; Porter-Zasada, L. B.; Gonzalez, M. I.; Neaton, J. B.; Long, J. R.; Reimer, J. A. Elucidating CO₂ Chemisorption in Diamine-Appended Metal–Organic Frameworks. *J. Am. Chem. Soc.* **2018**, *140* (51), 18016–18031. <https://doi.org/10.1021/jacs.8b10203>.
- (26) Hefti, M.; Joss, L.; Bjelobrk, Z.; Mazzotti, M. On the Potential of Phase-Change Adsorbents for CO₂ Capture by Temperature Swing Adsorption. *Faraday Discuss.* **2016**, *192*, 153–179. <https://doi.org/10.1039/C6FD00040A>.
- (27) Sotomayor, F. J.; Lastoskie, C. M. Predicting the Breakthrough Performance of “Gating” Adsorbents Using Osmotic Framework-Adsorbed Solution Theory. *Langmuir* **2017**, *33* (42), 11670–11678. <https://doi.org/10.1021/acs.langmuir.7b02036>.
- (28) Taylor, M. K.; Runčevski, T.; Oktawiec, J.; Bachman, J. E.; Siegelman, R. L.; Jiang, H.; Mason, J. A.; Tarver, J. D.; Long, J. R. Near-Perfect CO₂/CH₄ Selectivity Achieved through Reversible Guest Templating in the Flexible Metal–Organic Framework Co(bdp). *J. Am. Chem. Soc.* **2018**, *140* (32), 10324–10331. <https://doi.org/10.1021/jacs.8b06062>.
- (29) Darunte, L.; Sen, T.; Bhawanani, C.; Walton, K. S.; Sholl, D. S.; Realff, M. J.; Jones, C. W. Moving Beyond Adsorption Capacity in Design of Adsorbents for CO₂ Capture from

- Ultra-Dilute Feeds: Kinetics of CO₂ Adsorption in Materials with Stepped Isotherms. *Ind. Eng. Chem. Res.* **2019**, *58* (1), 366–377. <https://doi.org/10.1021/acs.iecr.8b05042>.
- (30) Golden, F. M. Theory of Fixed-Bed Performance for Ion Exchange Accompanied by Chemical Reaction. Ph.D. Thesis, University of California, Berkeley: United States, 1973.
- (31) Helfferich, F. G.; Carr, P. W. Non-Linear Waves in Chromatography. *J. Chromatogr. A* **1993**, *629* (2), 97–122. [https://doi.org/10.1016/0021-9673\(93\)87026-I](https://doi.org/10.1016/0021-9673(93)87026-I).
- (32) Zhang, W.; Shan, Y.; Seidel-Morgenstern, A. Breakthrough Curves and Elution Profiles of Single Solutes in Case of Adsorption Isotherms with Two Inflection Points. *J. Chromatogr. A* **2006**, *1107* (1–2), 216–225. <https://doi.org/10.1016/j.chroma.2005.12.094>.